242
2-24-82
I-1590

(2)

Lh. 284

ornl

OAK RIDGE NATIONAL LABORATORY

UNION CARBIDE

OPERATED BY
UNION CARBIDE CORPORATION
FOR THE UNITED STATES
DEPARTMENT OF ENERGY

ORNL/TM-7948/V1

(25)

MASTER

Fusion Engineering Device Design Description Volume 1

C. A. Flanagan
D. Steiner
G. E. Smith
Fusion Engineering Design Center Staff

ORNL/TM--7948/V1

DE82 011294

ORNL/TM--7948/V1

DE82 011294

Contract No. W-7405-eng-26

FUSION ENERGY DIVISION

FUSION ENGINEERING DEVICE DESIGN DESCRIPTION

C. A. Flanagan, D. Steiner, and G. E. Smith
Fusion Engineering Design Center Staff

Volume 1

Date Published: December 1981

Prepared by the
OAK RIDGE NATIONAL LABORATORY
Oak Ridge, Tennessee 37830
operated by
UNION CARBIDE CORPORATION
for the
DEPARTMENT OF ENERGY

ORNL - DWG 81 - 19198 FED

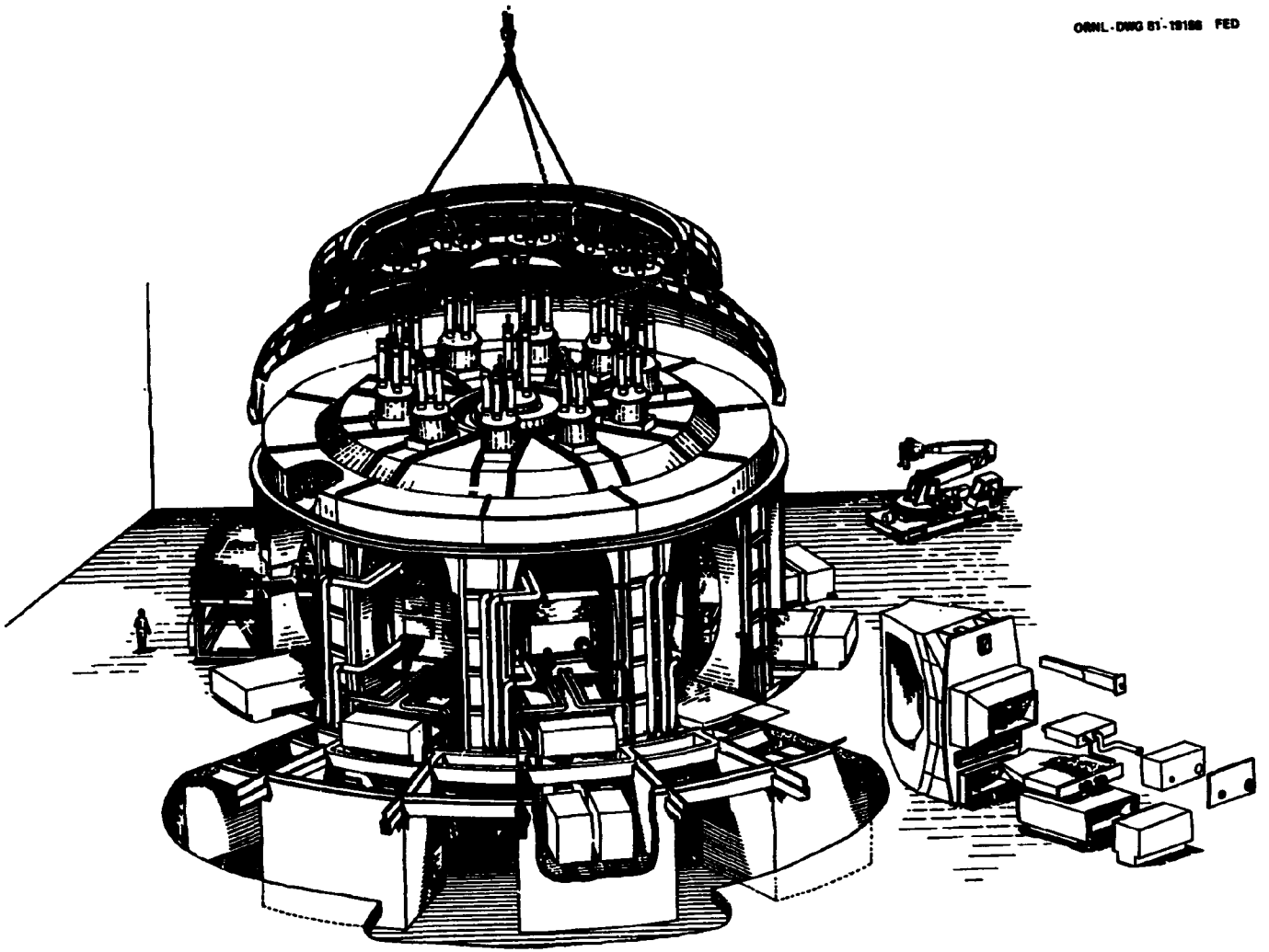

FED REFERENCE CONFIGURATION
DIMETRIC VIEW

ABSTRACT

The U.S. Magnetic Fusion Engineering Act of 1980 calls for the operation of a Fusion Engineering Device (FED) by 1990. It is the intent of the Act that the FED, in combination with other testing facilities, will establish the engineering feasibility of magnetic fusion energy. During 1981, the Fusion Engineering Design Center (FEDC), under the guidance of a Technical Management Board (TMB), developed a baseline design for the FED. This design is summarized herein.

The device has a major radius of 5.0 m with a plasma minor radius of 1.3 m elongated by 1.6. Capability is provided for operating the toroidal field coils up to 10 T, but the bulk of the operations is designed for 8 T. At 8-T conditions, the fusion power is ∿180 MW (neutron wall loading ∿0.4 MW/m^2) and a plasma Q of ∿5 is expected. At 10-T conditions, which are expected to be limited to about 10% of the total operations, the fusion power is ∿450 MW (∿1.0 MW/m^2) and ignition is expected.

Based on constant 1981 dollars, the projected direct capital cost of the FED is $1044 million and the total capital cost (direct plus indirect) is estimated to be $2172 million. The construction schedule from the beginning of preliminary design through the end of pre-operational testing is estimated to take seven years and eight months (92 months).

As presently envisioned, there will be four phases of device operation. These phases are: integrated systems checkout, occupying the first year of operation; a hydrogen or deuterium phase expected to require an additional two years; a D-T plasma burn phase of one-year duration; and the remainder of the presumed 10-year facility life devoted to D-T engineering testing.

Although feasible solutions were developed for each of the major systems and subsystems of the FED baseline, further design effort is expected to yield significant improvement in the design. Key design issues are identified, which if resolved, could enhance the feasibility

ACKNOWLEDGMENTS

We wish to acknowledge the dedication and skill of Linda Caldwell, Shirlene Dale, Nancy Raulston, Sandra Vaughan, and Kathie Zell, who provided the secretarial services essential to preparation of this report. We appreciate their pleasant and willing attitude which was maintained through numerous retyping efforts. We also wish to thank Paul Fogarty and Bill Kunselman for the high level of cooperation in the preparation of many of the drawings and figures and E. L. Watkin and staff for preparation of all the final artwork for the document. We express our thanks to Christina Sekula and her colleagues for their assistance in final layout, proofing, and processing the document. Without their efforts, this report would not have been possible.

In the technical area, we would like to acknowledge the collaborative involvement of the "Resource Physicists" who made significant contributions in the design evolution as well as in the physics analysis of the FED. These individuals and their technical area of involvement are: B. A. Carreras — Disruption Characterization; W. A. Houlberg — Particle and Power Flux; H. C. Howe — Pump Limiter; D. Q. Hwang — ICRH Heating; J. A. Schmidt — Poloidal Divertor; L. D. Stewart — Neutral Beam Heating; M. Ulrickson — Pump Limiter; J. Wesley — Disruption Control. The coordination of the "Resource Physicists" input with Design Center personnel was carried out by J. F. Lyon who also made significant contributions in documenting the Plasma Engineering chapter. The overall guidance of the "Resource Physicists" effort and development of the FED physics basis was provided by Paul H. Rutherford.

Finally, we wish to acknowledge the involvement of J. F. Clarke, Deputy Director of the Office of Fusion Energy, Office of Energy Research, U.S. Department of Energy, and the members of the Technical Management Board who provided guidance for the FED activities in FY 1981.

C. A. Flanagan
G. E. Smith
D. Steiner — Editors

LIST OF FIGURES

TABLE OF CONTENTS

and/or reduce the cost of the FED. In addition, the critical technological research and development required to perform final design and to build the FED are identified.

The FY 1981 FED activities focused on the development of a concept and supporting programs for moving ahead with the demonstration of engineering feasibility. The baseline design, along with the supporting information, constitutes a basis upon which a full design effort can be initiated.

LIST OF CONTRIBUTORS*

M. Anderson
S. E. Attenberger
R. J. Barrett
J. F. Baur
K. L. Black
S. K. Borowski
G. Bronner
J. N. Brooks
T. G. Brown
B. A. Carreras
B. A. Cramer
J. P. Davisson
R. W. Derby
B. A. Engholm
C. A. Flanagan
G. M. Fuller
S. K. Ghose
G. E. Gorker
M. W. Griffin
J. R. Haines
L. M. Hively
J. A. Holmes
W. G. Homeyer
R. J. Hooper
J. C. Hosea
W. A. Houlberg
H. C. Howe
B. L. Hunter
D. Q. Hwang
G. J. Inukai
S. S. Kalsi
S. Kim
J. Kirchner
J. F. Lyon
R. McGrath
D. H. Metzler
D. Mikkelsen
J. G. Murray
W. D. Nelson
M. Pelovitz
Y-K. M. Peng
M. Petravic
D. E. Post
R. L. Reid
W. T. Reiersen
M. L. Rogers
J. A. Rome
P. H. Sager
J. A. Schmidt
J. Schultz
S. W. Schwenterly
T. E. Shannon
S. S. Shen
C. E. Singer
G. E. Smith
P. T. Spampinato
V. C. Srivastava
D. Steiner
L. D. Stewart
W. L. Stirling
W. Stodiek
D. J. Strickler
R. J. Thome
S. L. Thomson
C. A. Trachsel
L. R. Turner
M. Ulrickson
H. F. Vogel
J. Wesley
S. Whitley
J. B. Wilgen
W. R. Wing
K. F. Wu
K. M. Young

*Contributor affiliations are footnoted at the beginning of each chapter.

LIST OF TABLES

1. DESIGN OVERVIEW

D. Steiner* C. A. Flanagan†

The nature of the device to follow the Tokamak Fusion Test Reactor (TFTR) has been evolving in design studies during the last seven years. From 1974 to 1976, design studies were directed toward a device designated the Experimental Power Reactor (EPR). The mission of the EPR was to demonstrate the production of net electricity. Although it was concluded that a commitment to such a device would be premature, the EPR studies provided the basis for a new round of design studies covering the period 1976-1978. The concept pursued in these studies was designated The Next Step (TNS). The mission of TNS was to provide a focus for developing reactor-relevant technology and engineering.

A DOE review of the fusion program led to a policy statement[1] which identified the Engineering Test Facility (ETF) as the next step in the fusion program. The mission of the ETF was to bridge the gap between the base of magnetic fusion knowledge at the start of operations and the base required to design the demonstration device. Thus, the ETF was to serve as a test-bed to test and qualify components that would be used in demonstration devices. In order to achieve this mission, it was judged that the ETF would require the following device characteristics: (1) an ignited, long-burn D-T fusion plasma, (2) availabilities of the order of 50% in the testing phase, and (3) annual fluence capabilities of about 1 MWyear/m^2 in the testing phase. The TNS studies were used as the starting point for the Engineering Test Facility (ETF) design activity which was initiated in 1978.

A review of the ETF design activities led to the consensus that: (1) the ETF design effort was sound; and (2) the ETF mission was too ambitious with regard to role, availability and fluence targets, and testing objectives. It was recommended that the role of the device to follow TFTR be the investigation of engineering feasibility, rather than

*Fusion Engineering Design Center/Oak Ridge National Laboratory.
†Fusion Engineering Design Center/Westinghouse Electric Corporation.

engineering testing and qualification of components for demonstration reactors. This recommendation was incorporated into the Magnetic Fusion Energy Engineering Act of 1980 which calls for the operation of a Fusion Engineering Device (FED) by 1990. It is the intent of the Act that the FED, in combination with other facilities, will establish the engineering feasibility of magnetic fusion energy. The goals of the FED are (1) to provide a D-T-burning plasma, (2) to explore issues of operator and public safety, and (3) to provide a focus for developing reactor technologies and engineering. In addressing these goals, the FED must represent acceptable capital and life-cycle costs.

In order to proceed with planning for the FED program, the Office of Fusion Energy (OFE) established at the beginning of FY 81 a Technical Management Board (TMB) to oversee all FED-related activities. The elements working under the board's direction include: the Fusion Engineering Design Center (FEDC) which is reponsible for FED design activities; the Physics Group which establishes the physics basis for the FED and gives physics guidance to the design evolution; the Nuclear Technology Group which examines the scope of nuclear testing which can be accomplished by the FED and other facilities; the Plasma Engineering Technology Group which examines the FED and complementary programs required in the plasma related technology areas; and finally, the U.S. International Tokamak Reactor (INTOR) activity which ensures that the FED effort benefits from the INTOR design effort.

The primary objectives of the FY 81 FED activity were twofold: (1) to select the FED concept and (2) to document the concept and the selection process. During the period from October 1980 to March 1981, the focus of the Design Center was on trade and design studies. The objectives of these studies were to develop a baseline concept for the FED and to examine the design space around the baseline. The results of these studies are documented in ORNL/TM-7777.[2]

During the period from March 1981 through September 1981 the focus of the Design Center effort was to develop (1) the FED design, (2) a cost and schedule, and (3) a facilities layout. In addition, a preliminary test program was defined and the research and development necessary for the final design and construction of FED was identified.

The purpose of this document is to describe the FED baseline design together with a discussion of the major systems options considered and the rationale for the baseline choices. This overview section provides a summary of the FED design including: a discussion of the principal design guidelines (Sect. 1.2); a description of the FED baseline design (Sect. 1.3); a discussion of the expected mode of operations and a preliminary scope for the test plan (Sect. 1.4); a summary of the projected costs along with a construction schedule (Sect. 1.5); a listing of the key design issues that require emphasis in future design activity (Sect. 1.6); a summary of the research and development needs required for the final design and construction of FED (Sect. 1.7); and finally, concluding remarks (Sect. 1.8).

1.2 PRINCIPAL DESIGN GUIDELINES

During FY 81 a baseline design was developed for the FED. Although not optimized, it represents a reasonable design with feasible concepts for all the major systems and components. The development of the FED baseline design was an evolutionary process as indicated in Fig. 1-1. Initially, the Technical Management Board (TMB) established the mission and a set of working parameters and design guidelines; these parameters and guidelines are summarized in Table 1-1. These parameters and guidelines reflect the FED mission and are based on the following considerations: (1) the requirement to satisfy the general FED technical objectives as articulated in the Magnetic Fusion Energy Engineering Act of 1980, (2) the assessment of the existing and anticipated physics and technology data base supporting FED, and (3) the desire to develop an FED with acceptable capital costs, engineering requirements, and risks. Although the parameters and guidelines were influenced by all three considerations, certain considerations were dominant for each entry in the table, as indicated below.

- The fusion power level, the neutron wall loading, and the burn time specifications were a compromise between the need to satisfy the general FED technical objectives and cost considerations.

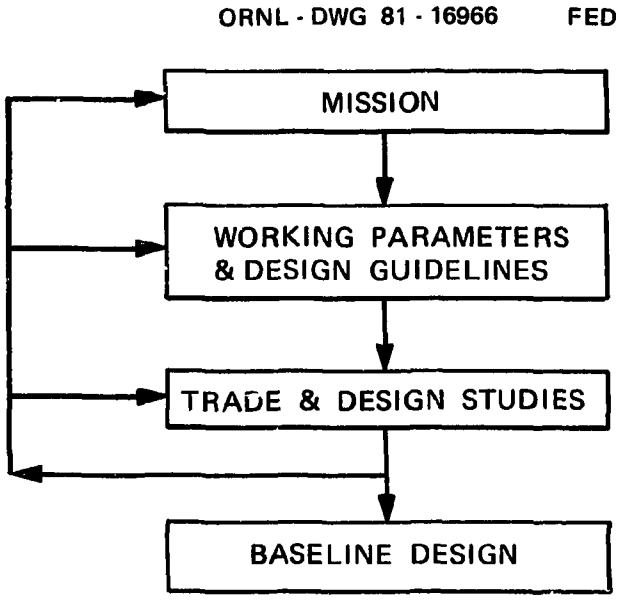

Fig. 1-1. The FED design evolution process.

Table 1-1. Working parameters and design guidelines established by the TMB for FED trade and design studies

Fusion Power (MW)	∿200
Neutron wall loading (MW/m^2)	∿0.5
Burn time (s)	∿100
Plasma elongation	∿1.6
Plasma radius (m)	∿1.3
Major radius (m)	∿4.8
Plasma burn mode	Driven, Q ∿ 5
Start-up technique	RF assist
Bulk heating technique	ICRH
Particle and impurity control	Pump limiter

- The plasma elongation was based on physics considerations about beta and confinement enhancement with elongation.
- The plasma radius and major radius were influenced both by physics considerations (confinement and beta) and by cost considerations.
- A driven mode of operation ($Q \sim 5$) eliminates the additional risk associated with ensuring an ignition requirement based on present uncertainties.
- The rf assist, ion cyclotron resonance heating (ICRH), and the pump limiter reflect an attempt to reduce complexity and cost by seeking relatively simple engineering solutions for plasma initiation and startup, heating, and particle and impurity control, respectively.

The TMB also specified that the FED should incorporate toroidal field coils designed to operate nominally at a maximum field of 8 T at the conductor, but which would be capable of limited operation at 10 T. The 10-T capability is viewed as a desirable perturbation to the basic device but does not drive the design; only about 10% of the total machine operation is to be at the 10-T level. The 10-T capability allows for limited operation with enhanced plasma performance and provides for additional engineering scaling tests.

A full set of system parameters and configuration layouts was developed from the parameters and guidelines given in Table 1-1. These were used as the basis for a number of trade and design studies. The trade studies focused on cost and performance implications of variations about the working parameters; the design studies focused on the engineering feasibility of systems. Emphasis was given to those issues and systems that represent major cost drivers, major performance drivers, and major engineering drivers. These trade and design studies were reported in ORNL/TM-7777.[2] The key results of the studies are summarized below:

1. Mission alternatives. A study was performed at the outset of the FY 81 design activities to consider various mission and device alternatives. Three mission alternatives and devices were defined in terms of test objectives with increasing levels of achievement.

The first level device, with mission to demonstrate plasma engineering and engineering operations, assumes D-D-T operation at low neutron wall loading, $\sim 10^{-3}$ MW/m^2, in a configuration with a minor radius of 0.8 m and a major radius of 3.5 m. The second level device demonstrates nuclear engineering testing in addition to the first level demonstration, assumes D-T driven operation at modest wall loading, ~ 0.5 MW/m^2, in a configuration with a minor radius of 1.3 m and a major radius of 4.8 m. The third level device demonstrates component and material qualification in addition to the other demonstrations, assumes ignited D-T operation with high wall loading, ~ 1 MW/m^2, and high availability, $\sim 50\%$, in a configuration with a minor radius of 1.5 m and a major radius of 6.0 m.

On the basis of relative cost, complexity, and risk, it appears that the third level device (similar to ETF/INTOR) may be too ambitious a step for FED. The first level device offers attractive relative cost, complexity, and risk; however, it does not provide a demonstration of either blanket performance or the total tritium fuel cycle. These demonstrations are currently considered to be essential parts of the FED mission.[3] Therefore, it was concluded that the second level mission be used as the context for the FED mission and FED baseline concept.

2. Plasma performance. The plasma engineering analyses suggest that FED can achieve its nominal performance goals ($Q \sim 5$, neutron wall loading ~ 0.5 MW/m^2, and burn time ~ 100 s) at a toroidal field of 8 T (maximum) under a range of reasonable assumptions and eventualities. At the 10-T field level, the same assumptions predict ignition and about twice the neutron wall loading (~ 1.0 MW/m^2) as that at 8 T.
3. Number of pulses. An assessment of the number of pulses that FED might sustain over a projected 10-year life was performed. A range of 5×10^4 to 10^6 pulses was considered. Values of 2.5×10^5 pulses at 8 T and 2.5×10^4 pulses at 10 T were adopted.
4. Toroidal field coils. Several credible toroidal field coil options were identified for achieving the desired capability of nominal operations at 8 T with limited operation at 10 T. Each of these

options fits into the same winding cavity and requires that the machine *major radius be increased from 4.8 m* (see Table 1-1) *to 5.0 m.*

5. Device size. While the current baseline may not be fully optimized with respect to size, the trade studies suggest that it does approach a minimum cost device for the desired performance goals. Reductions in machine size (the key cost driver) relative to the baseline are limited by volt-second requirements needed to maintain the plasma current and achieve acceptable burn time. To retain adequate performance margin, values of 1.3 m for the plasma radius and 5.0 m for the major radius were selected.
6. Startup. A number of startup options were considered for FED. Electron cyclotron resonance heating (ECRH) was selected for plasma initiation and appears to be the most efficient option; it may also prove to be the most relevant for reactors. Nevertheless, at this time, other rf options need to be retained for plasma startup in conjunction with the conventional approach using the ohmic heating (OH) system.
7. Bulk heating. Both rf and neutral beam heating were considered for the baseline design. Engineering design studies have confirmed that machine shielding, access, and reliability are significantly simplified by selection of rf as the primary bulk heating approach. The design studies indicate that the machine configuration can accommodate rf or beam heating. Therefore, neutral beam injection was retained as the alternative to rf which was selected as the baseline in FED.
8. Particle and impurity control. In the plasma engineering investigations, particular emphasis was directed to options in the area of particle and impurity control. The pump limiter was chosen for the baseline design because of apparent magnetic and structural simplicity The poloidal divertor was identified as the primary alternative to a mechanical pump limiter.

While iteration of a baseline design via system and trade studies served as the basis for many design decisions, a number of additional

considerations helped shape the general features of the device. These include the availability of technologies, the requirements for remote maintenance, considerations of system reliability, and the impact of the test program on machine access and operations. In addition, it is felt that flexibility is essential to accommodate both large uncertainties in plasma performance and potential improvements in physics and technology. This flexibility in the baseline design is reflected by a configuration that permits (1) either ICRH or neutral beam injection for bulk heating and (2) either a pump limiter or a poloidal divertor for particle and impurity control.

1.3 DESIGN DESCRIPTION

The following design description summarizes the plasma operation scenario, the approach for developing the overall machine configuration, and the major systems of FED including the facilities.

1.3.1 Plasma Operation Scenario

The FED plasma operation scenario involves the following phases: prefill of chamber, rf-assisted current initiation, current ramp, bulk heating, burn, shutdown, and pumpdown. Table 1-2 summarizes the features of each phase for operation at the 8-T level. At the 10-T level the features of the scenario are modified in the following manner:

- At the end of the current ramp-up phase the plasma current reaches 5.8 MA.
- At the end of the bulk heating phase the plasma density reaches $\sim 1.2 \times 10^{14}$ cm^{-3}, the plasma current reaches $\sim$6.5 MA, ignition is achieved, and the fusion output power reaches $\sim$450 MW.
- During burn the ICRH power is turned off because ignition is achieved.

Table 1-2. Plasma operation scenario
(8-T operations)

Phase	Interval (s)	Heating/fueling requirements	Plasma characteristics			
			Density ($\times 10^{13} cm^{-3}$)	Temperature (keV)	Current (MA)	Power (MW)
Prefill chamber	-	Pressure $<10^{-5}$ torr from $\sim 10^{-6}$ torr	-	-	-	-
Current initiation	0-0.8	ECRH power $\sim$1 MW	$\sim 10^{13}$	$\sim$0.1	0	0
Current ramp-up	0.8-6.0	ICRH power $\sim$5 MW Fuel	$\sim 3 \times 10^{13}$	$\sim$1.0	$\sim$4.8	0
Bulk heating	6-12	ICRH power $\leq$50 MW Fuel Pump limiter	$\sim 8 \times 10^{13}$	$\sim$10.0	$\sim$5.4	$\sim$180
Burn	12-112	ICRH power $\sim$36 MW Fuel Pump limiter	$\sim 8 \times 10^{13}$	$\sim$10.0	$\sim$5.4	$\sim$180
Shutdown	112-122	ICRH power off Fuel off Particle exhaust	$\sim 2 \times 10^{13}$	$\sim$1.0	0	0
Pumpdown	122-152	Pumpdown pressure	-	-	-	-

1.3.2 Machine Configuration

Elevation and plan views of the FED baseline configuration are given in Figs. 1-2 and 1-3. Table 1-3 lists the key parameters of the baseline for both the 8-T and 10-T operating modes.

Maintenance was a significant consideration in developing the FED configuration. The maintenance approach for FED consisted of the following key elements.

- Modularity — where possible, modularity has been a design goal for all components which are expected to require replacement or frequent maintenance; an example of this is the pump limiter blade.
- Accessibility — good access has been a central design consideration for the overall configuration and has strongly influenced the design of the TF coils (size and number) and the design of the torus.
- Hands-on capability — for all device components external to the shield, hands-on access appears to be a practical necessity for many operations and was adopted as a design requirement. Hands-on capability is available approximately one day after shutdown. Providing this capability has strongly influenced the design of the outboard shield.
- Component lifetime categories — two categories were established. Long-lifetime components are those that are expected to operate the lifetime of the device without replacement, e.g., the TF coils. Limited-lifetime components are expected to require replacement during the lifetime of the device, e.g., the pump limiter blade. This designation has been important in developing the FED maintenance needs including maintenance equipment.

Access was the dominant consideration in the selection of a 10-coil arrangement for the toroidal field (TF) coil system. The centering loads of the ten coils are reacted by a central bucking cylinder. The TF coils have a 7.4- by 10.9-m bore. Together they produce a 3.6-T field-on-axis when operating at 8 T and a 4.6-T field-on-axis when operating

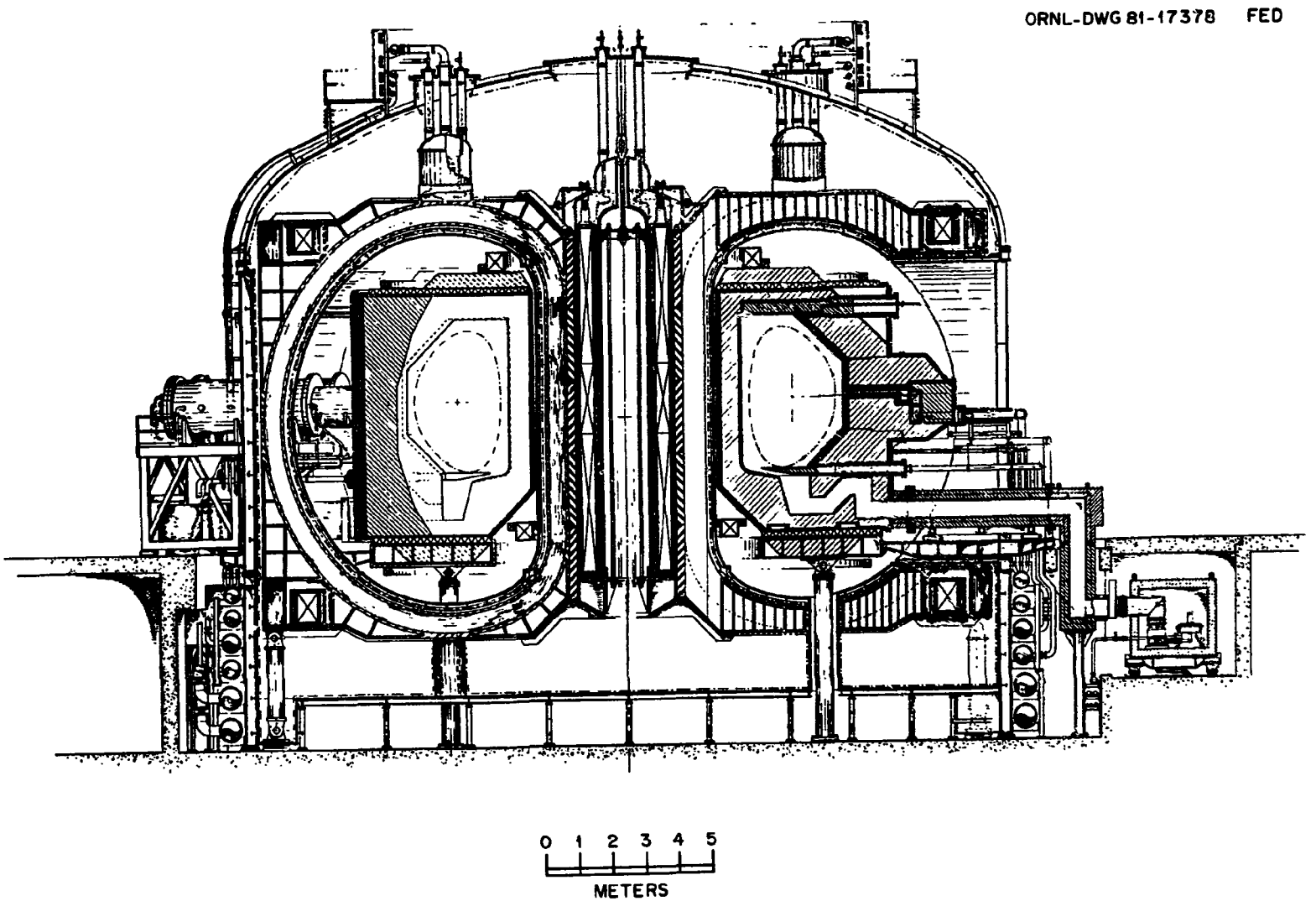

Fig. 1-2. FED reference configuration, elevation view.

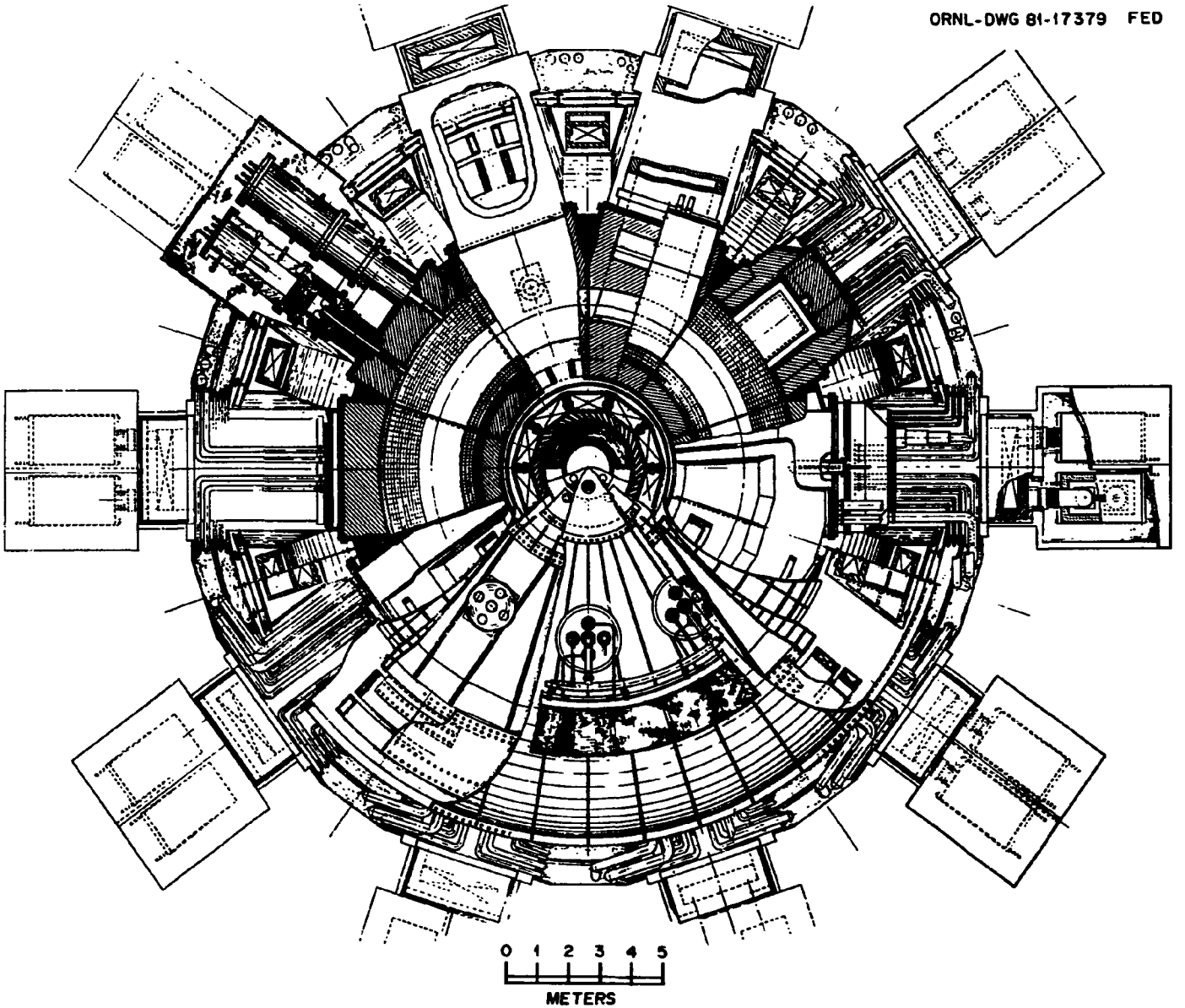

Fig. 1-3. FED reference configuration, plan view.

Table 1-3. Key parameters for the FED baseline

	8 T	10 T
Major radius (m)	5.0	
Plasma radius (m)	1.3	
Plasma elongation	1.6	
Fusion power (MW)	180	450
Neutron wall loading (MW/m^2)	0.4	1.0
Heating power (MW)		
Initial	50	
Burn	36	0
Q	5	Ignited
Burn time (s)	$\geq$100	$\sim$50
Duty factor	0.65	0.5
Average D-T density (m^{-3})	0.8×10^{20}	1.2×10^{20}
Average total beta (%)	5.2	
Plasma current (MA)	5.4	6.5
TF coil clear bore, width × height (m)	7.4 × 10.9	
Field on axis (T)	3.6	4.6
Number of full field pulses	2.5×10^5	2.5×10^4
Availability (%)[a]	10-20	10-20

[a]Defined as ratio of operating time to operating time plus downtime.

at 10 T. With this arrangement sufficient access is provided so that a torus sector comprising one-tenth of the torus can be either inserted or withdrawn solely by radial motion between the outer legs of the TF coils.

The plasma chamber consists of ten torus sectors inserted into a spool support structure. A schematic showing the details of the spool support structure is shown in Fig. 1-4. The outer edges of each shield sector are sealed with a bellows support frame of the spool structure and form the vacuum boundary for the plasma chamber. A typical torus assembly sequence is shown in Fig. 1-5. Note in this figure the modularity of several key components.

In addition to the above considerations, nuclear and electromagnetic criteria also influenced the development of the FED configuration. The nuclear criteria deal with issues such as radiation damage to materials, nuclear heat loads on components, and radiation exposure of personnel. Nuclear analyses were performed to determine optimal configurations and thicknesses for bulk and local shields. These analyses accounted for the effect of penetrations, gaps, and inhomogeneities. The electromagnetic criteria center around the engineering impact of transients such as plasma disruption, startup and shutdown, and plasma position control. These transients induce voltages, currents, and forces in the device components and therefore must be accounted for in the design. Analyses were performed to determine the magnitude and impact of the electromagnetic effects. It was found that plasma disruption is the dominant transient in design considerations. In order to mitigate the engineering impact of disruptions, the design approach used in FED ensures that acceptable toroidal current paths are achieved in the first wall panels, the pump limiter sectors, and the shield sectors.

1.3.3 Magnetic Systems Description

The magnetic system components consist of: the superconducting toroidal field (TF) coils; the poloidal field (PF) coils which include the superconducting ohmic heating (OH) solenoid, superconducting equilibrium field (EF) coils external to the TF coil bore, and normal copper

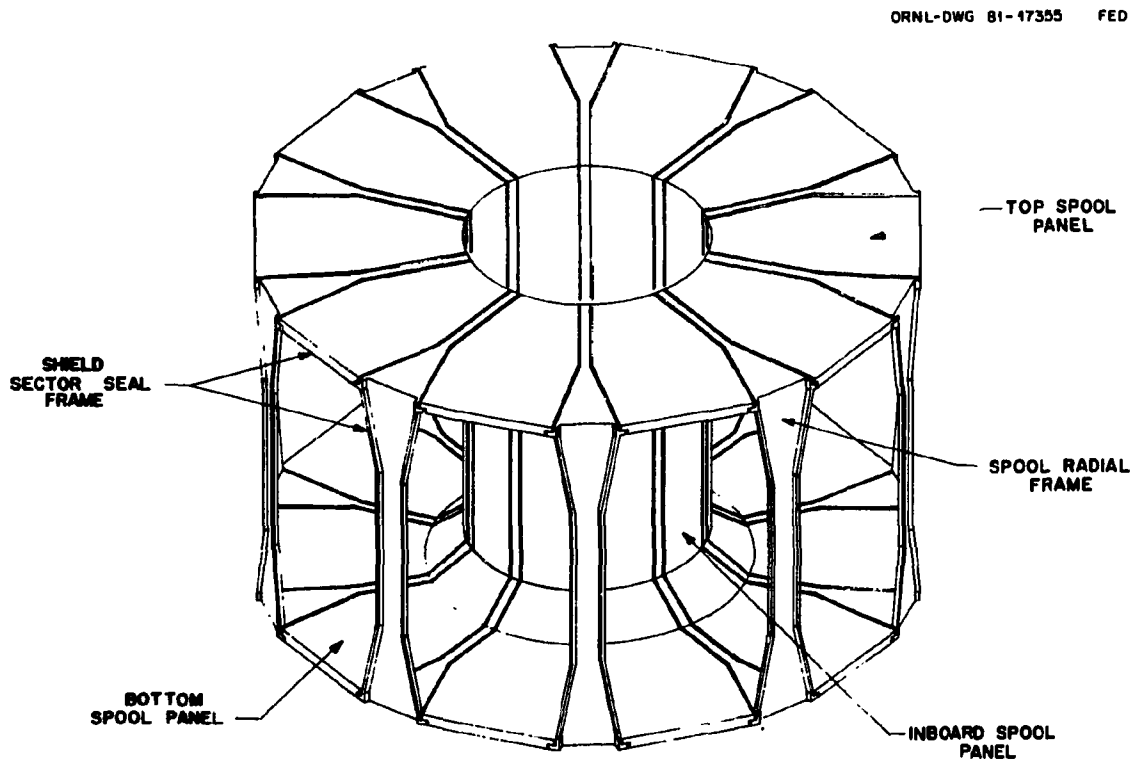

Fig. 1-4. Torus support spool.

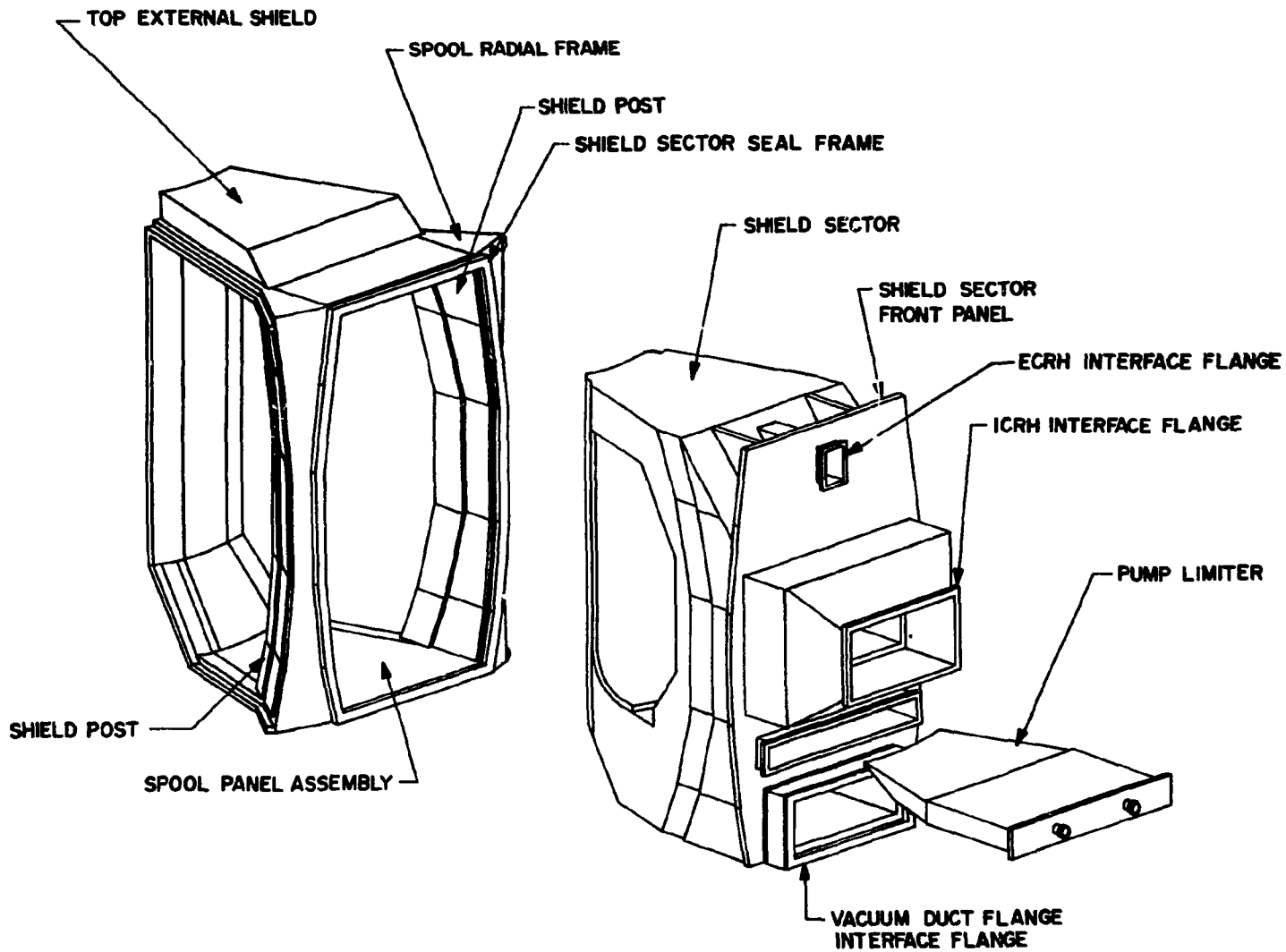

Fig. 1-5. Torus assembly.

EF and control field (CF) coils located internal to the TF coil bore; and the cryostat. The overall arrangment of the magnets is shown in Fig. 1-6.

TF coils

A conductor capable of operation to 10 T is required for the FED baseline. Three candidate coil technology approaches capable of achieving the required 10-T field were considered; these are NbTi pool-boiled superfluid-cooled to 1.8 K, NbTi forced-flow sub-cooled to 3 K, and a Nb_3Sn/NbTi combination cooled to 4.2 K. The basis for these coil technologies will be derived from the Large Coil Program (LCP) and 12-T coil technology development programs. At this time there is no clear technical basis for a preferred option. For purposes of illustrating design considerations, the NbTi forced-flow sub-cooled (3 K) option was selected as the FED baseline.

An overall winding current density of 2200 A/cm^2 was used in evaluating 10-T operation at 3 K. The coils are pancake wound with a total of 444 turns and use NbTi strands in a steel conduit cooled by supercritical forced-flow helium. The overturning moments are reacted by an intercoil support structure at the top and bottom of the TF coils. The dead weight of the TF coils is supported by a series of outboard pedestal supports designed to also withstand a 1 g seismic load laterally and vertically.

PF coils

The poloidal field (PF) coil system consists of a superconducting (NbTi) solenoid along with a combination of two normal copper ring coils located inside the bore of the toroidal field coils and two superconducting (NbTi) coils located external to the bore of the toroidal field coils. This combination and arrangement of ring coils were selected based on the results of trade studies which examined systems using: (1) all PF ring coils inside the TF coils; (2) all PF ring coils outside the TF coils; and (3) some PF ring coils inside and some outside the TF coils.

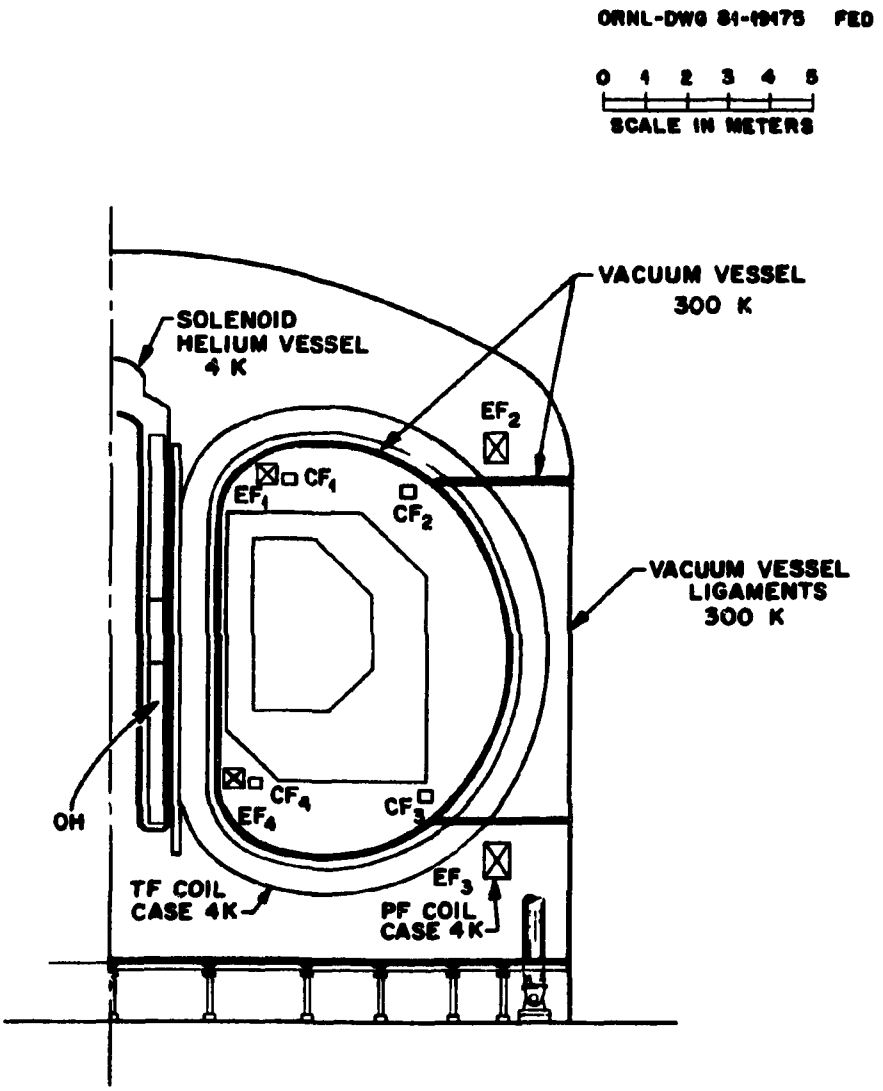

Fig. 1-6. FED magnetic system arrangement.

The results indicated that the combination of copper internal and superconducting external PF ring coils represents a configuration which satisfies the physics requirements and the engineering requirements at minimum cost. The external ring coils are located above and below the opening between the TF coil legs to preserve access for the torus sectors.

The design of the superconducting OH and EF coils is scaled from the Los Alamos National Laboratory (LANL) design for the 20 MJ Pulsed Coil Program. The design of the interior normal copper EF coils is dominated by the requirement for demountable mechanical joints to facilitate assembly and coil replacement. These coils are supported from the torus support spool

Cryostat

A common vacuum cryostat contains all of the superconducting coils. The cryostat has separate individual enclosures for the outboard legs of the TF coils. This approach maintains the good access between the TF coils and requires no penetration of the cryostat boundary for torus access. This approach also separates the warm and cold components of the FED configuration.

1.3.4 Nuclear Systems Description

The nuclear system components include the torus (spool assembly, shield sectors and support), the first wall (actively cooled outboard panels and passively cooled inboard armor) and the mechanical pump limiter.

Torus

The assembled torus constitutes the plasma vacuum chamber. It is made up of ten sectors which are inserted into a spool structure. Each sector is assembled into the spool solely by radial motion. Maintainability has been a dominant consideration in the design. The spool structure provides high vacuum integrity and high electrical resistance.

The shield sectors: attenuate nuclear radiation; convert neutron kinetic energy into heat; provide for the removal of this heat; and support the first wall and limiter components. The spool material is Inconel, selected because of its high electrical resistance. The shield sectors are constructed of Nitronic 33 which was selected because it is highly corrosion resistant, exhibits low levels of long-life radionuclides, and is commercially available. The shield is cooled with pressurized water. The shield is 60-cm thick on the inboard side and 120-cm thick on the top, outboard, and bottom sides. The shield limits radiation dose at the TF coil insulation to $<10^9$ rads and allows hands-on maintenance by limiting the activation level external to the shield to <2.5 mrem/h about one day after shutdown.

First wall

The FED first wall system (Fig. 1-7) consists of actively cooled stainless steel panels on the outboard wall and passively cooled graphite armor tiles on the inboard and top wall. This design has the capability of accommodating the nominal startup and burn heat loads and the anticipated disruption energy without replacement for the life of the device. The outboard first wall panels are 316 stainless steel. There are six panels on each torus sector. Each panel is about 2 m on a side and 7 cm thick. The vertical facet serves also as a startup limiter. The armor tiles are attached to the torus chamber with graphite bolts. Each tile is 5-cm thick and 15 cm on a side. About 6,300 tiles are required in the device. The tiles are coated with titanium carbide to limit chemical erosion.

Mechanical pump limiter

The FED baseline has a mechanical pump limiter for particle and impurity control (Fig. 1-7). The limiter is located at the bottom of the vacuum chamber and is continuous in the toroidal direction. The limiter establishes the plasma edge, pumps helium ash and hydrogen particles, and helps protect first wall components from large particle

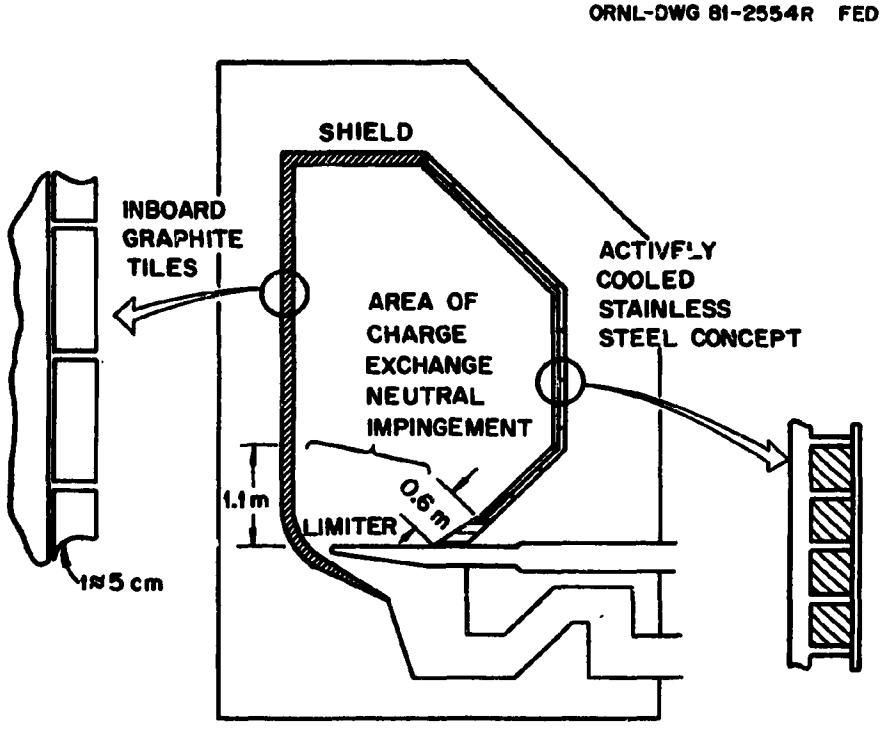

Fig. 1-7. FED first wall system.

and energy fluxes. The limiter is divided into ten removable segments, one in each torus sector of the device. Each limiter sector is removable independent of the shield sector. Each limiter segment has a reusable core structure (Nitronic 33) and a replaceable protective surface (armor tiles) attached to substrate copper. The segment is water cooled. Limiter segments are electrically connected with metal bellows and copper bus plates along one edge of each segment. Analysis indicates that the limiter will provide the desired particle pumping (at least 5% of the total ion flux leaving the plasma). Depending on the assumed plasma edge conditions (which are highly uncertain at present), the predicted erosion of the armor tiles varies from ∿0.3 cm/year to ∿7.0 cm/year. This results in a variation in predicted tile lifetime of from ∿2 months to ∿4 years.

1.3.5 Electrical Systems Description

The electrical systems include power handling and conversion, energy storage, and diagnostics, instrumentation, data acquisition, and control.

Power handling and conversion

The electrical power handling and conversion system includes the ac power system and the TF and PF coil power conversion systems. The ac power system provides both pulsed and steady-state power for the FED loads. The required ac power system capacity is 350 MVA for pulsed power loads. The TF coil power conversion provides for charging the ten TF coils (in about 4 hours with two 65 V power supplies) and for discharge through dump resistors (in about 2 hours). During a quench, the large stored energy (∿23 GJ for 10-T operation) is dissipated through external dump resistors with a time constant of ∿40 s and limits the maximum TF coil temperature to <200 K. The PF coil power convertors are used to take ac power from the motor-generator-flywheel (MGF) units (or utility line) and convert it to pulsed dc power needed for the PF coils during each operating cycle. The system also provides for PF coil protection in case a quench occurs.

Electrial energy storage

The electrical energy storage requirements are met in FED with a minimum of two MGF units. Energy storage is required for the PF coils and for the rf systems. A total of ∿6 GJ of energy is required during startup with a peak MVA load of ∿1850. The MGF units satisfy these requirements. Each is a wound-rotor induction motor of 15,000 hp. They provide variable frequency, 13.8 keV pulsed power. These units are safe, reliable, economical, and easy to control. Voltage can be regulated to within ±1% with conventional controls.

Diagnostics, instrumentation, data acquisition, and control systems

The diagnostics system features instrumentation for: developing physics understanding; machine performance verification and optimization; control; safety monitoring; and engineering testing. Diagnostics will dominate the use of three torus sectors of the machine. Additional diagnostic instruments will be present in other torus sectors as required. Separate sets of instruments will be required on FED once D-T operations commence. The information and control system for FED consists of the hardware and software to perform all programmable processes for the entire FED complex including control, monitoring, and data acquisition and processing, analyses, display, and archiving.

1.3.6 Plasma Heating Systems Description

Systems for plasma initiation and startup and for plasma bulk heating comprise the FED plasma heating systems. An rf system is used for initial heating of the plasma. This consists of ∿1 MW of ECRH (∿80 GHz at 8 T and ∿100 GHz at 10 T) launched through waveguides on the high field side of the plasma using the extraordinary mode of wave propagation. The FED bulk heating is based on ICRH. Second harmonic deuterium species used for majority heating is the baseline approach for both bulk heating and during burn (8 T). The frequencies required are ∿68 MHz (10 T) and ∿54 MHz (8 T). Minority heating is optional (either

He^3 or H) but only employed during the early phase of bulk heating ($T_e \leq 5$ keV). The frequencies are 45 MHz (10 T) and 36 MHz (8 T) for He^3 and ~68 MHz (10 T) and 54 MHz (8 T) for H. A total of 50 MW is provided for the bulk heating phase. The alternative to ICRH for bulk heating is 150-keV positive ion neutral beams. The baseline configuration accommodates a neutral beam injection system as well as the rf-heating system.

1.3.7 Auxiliary Systems Description

The reactor auxiliary systems consist of the following:

- Fueling
- Vacuum Pumping
- Tritium
- Cryogenics
- Remote Maintenance Equipment

Fueling systems

The FED fueling system consists of gas puffers and pellet injectors. Two independent gas puffing systems (one for redundancy) are available to provide fuel gas (deuterium, tritium, or a mixed species) to each of 10 inlet ports. The gas puffing is used to backfill the torus prior to startup and continues until a plasma temperature of 1 keV is established. Frozen deuterium and tritium pellets are then injected to control plasma density. Two pellet fuel injectors are located on one torus sector. Each can inject 4-mm pellets at a velocity of 2 km/s at an injection rate of up to 20 pellet/s. Either pneumatic or centrifugal pellet injectors, both of which are now being developed, can be used.

Vacuum pumping

Twenty large turbomolecular pumps, two at the end of each of the 10 vacuum ducts, backed by 20 first stage and one second stage scroll pumps, are used as the vacuum pumping system for FED. This system is used to

pump down the torus initially (to 10^{-7} torr) and between burns (from 3×10^{-4} torr to 10^{-5} torr) and to remove the gas load of 1.3×10^{22} s^{-1} from the pump limiter during the burn at 8-T conditions. The specified evacuation time between burns is 30 s. The conductance of the system, including the pump limiter entry slot, must be at least 60 m^3/s. The system was designed to handle the burn gas load requirement and can pump down the plasma chamber in somewhat less than the 30 seconds specified. The high vacuum turbomolecular pumps have a pump speed of 5.0 m^3/s. The scroll pumps are used to back the turbomolecular pumps and for rough pumping of the plasma chamber. These are sealed pumps which have no bearing lubricant in contact with the pumped gas. A first stage pump backs each turbomolecular pump and pumps at 33 ℓ/s exhausting at a pressure of 25 torr. The discharge of all 20 first stage pumps is combined and fed to a single small second stage pump that operates at ∿2 ℓ/s and discharges at about atmospheric pressure.

Tritium systems

The tritium systems must provide (1) fuel for the device, (2) tritium handling in a safe manner, and (3) an integrated test of tritium handling technology. The system is comprised of components to handle the primary fuel cycle requirements (fuel cleanup, isotope separation, and tritium analysis) and secondary systems to provide for safe operation of all systems involving deuterium and tritium (waste treatment, glovebox detritiation, and tritiated water recovery). The tritium system has a tritium inventory of 825 grams for continuous 8-T operation or 1470 grams for continuous 10-T operation. In addition, a building detritiation system provides for tritium handling and containment in the reactor building, hot cell facility, and tritium processing building. Finally, a data acquisition system is employed to monitor the tritium systems as a whole.

Cryogenic system

The cryogenic system for FED provides for an entropy generation rate which is several times larger than that of any existing or planned

cryogenic refrigeration system in the world. The system must be capable of performing 63 MW of work on helium at room temperature. This system must produce and transfer cryogens at a sufficient rate to sustain normal operations of the superconducting magnet systems of FED. The FED system consists of forced flow closed coolant loops for the TF coils, coil cases, and intercoil support structure, plus a separate loop for the PF coils.

Remote maintenance equipment

An extensive list of remote maintenance equipment required for FED has been developed. It includes both general purpose equipment, such as manipulators and cranes, and special purpose equipment for specific applications.

1.3.8 Facilities Description

A complete facility layout for FED was developed, including the reactor building, hot cell facilities, necessary additional support buildings, and a site layout.

The reactor building is a rectangular building approximately 60 × 50 × 40 m with small (3-5 psi) overpressure capability. The walls and roof are ∿2-m thick to provide for adequate shielding. The building was designed to reduce the consequences of postulated accident conditions. The hot cell facilities provide the capability to support the maintenance and operation of the reactor building and those other facilities involving radioactive operations. The hot cell facilities are of a controlled ventilation construction and require a size of ∿80 × 50 × 30 m. Walls and roof construction are of up to 2-m-thick concrete. The additional facilities required for the total FED complex were identified and a site layout developed (Fig. 1-8).

1.4 MODE OF OPERATIONS AND TEST PROGRAM

As presently envisioned, there will be four phases of device operation. These phases are delineated in Fig. 1-9: integrated systems

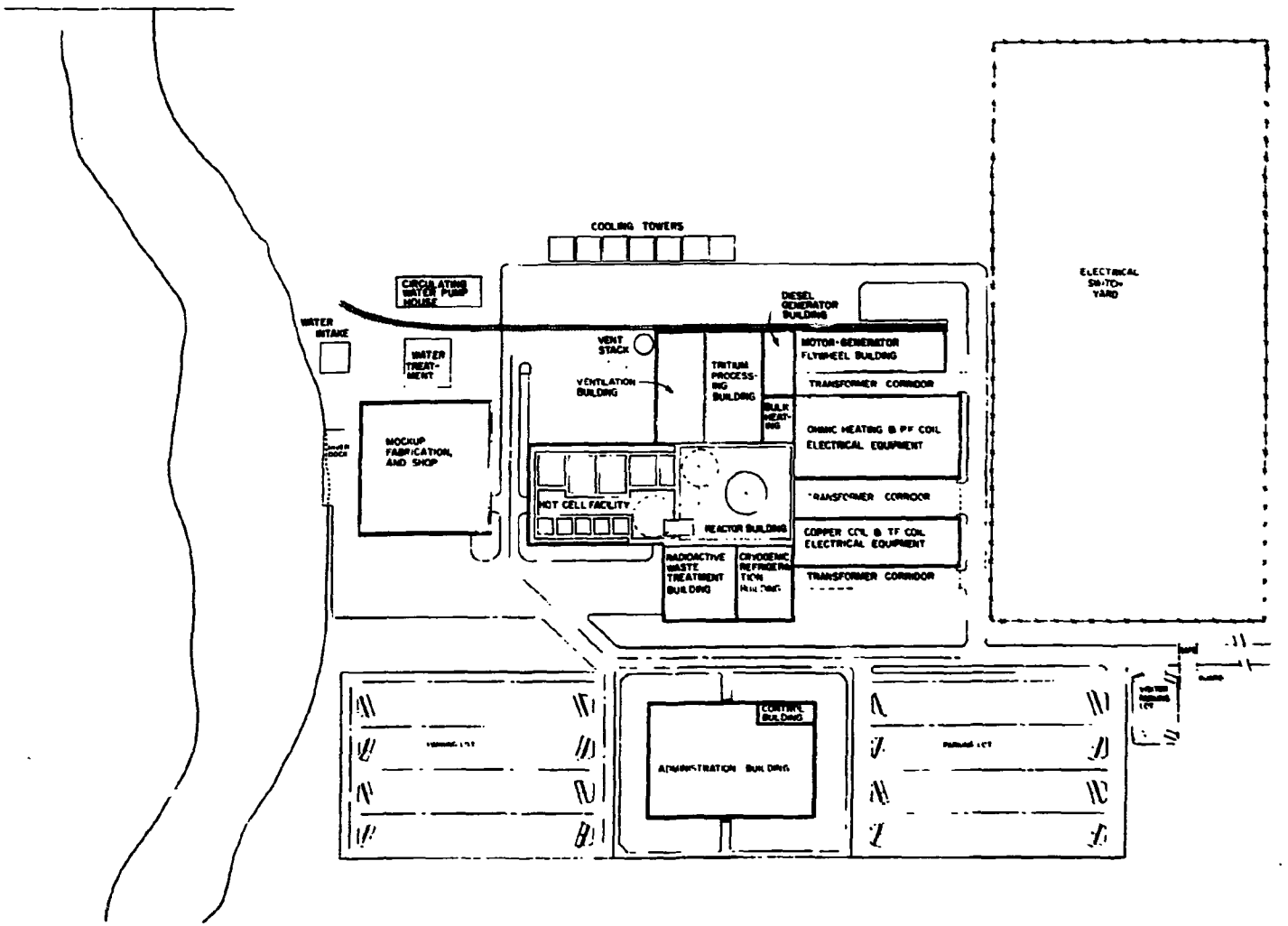

Fig. 1-8. FED facility site layout.

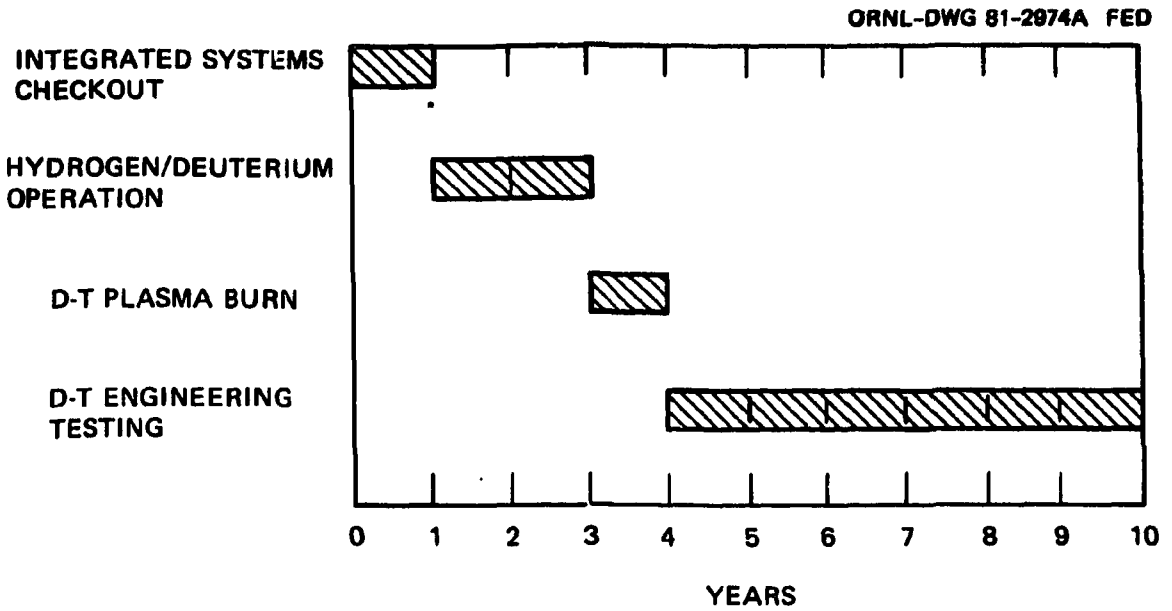

Fig. 1-9. FED operating phases.

checkout, occupying the first year of operation; a hydrogen or deuterium phase expected to require an additional two years; a D-T plasma burn phase of one-year duration; and the remainder of the presumed 10-year facility life devoted to D-T engineering testing. For a full discussion of the planned operation of the device, see Ref. 4. For this four-phase program, a preliminary test plan has been developed. The timetable for this test plan is presented in Fig. 1-10. A brief synopsis of each phase of the planned operation along with the elements of the test plan in that phase is contained below.

1.4.1 Integrated Systems Checkout

The first year of device operation will be devoted to verifying systems performance. Principal tasks during this phase include diagnostics shakedown and system and subsystem shakedown/integration. While there will be some hydrogen testing, it will be conducted predominantly at fields substantially below the peak device capability, and its main purpose is to demonstrate device operation rather than to explore plasma properties. However, some plasma related issues will be pursued as a prelude to later stages of device operation. These include achieving adequate plasma cleanliness, at least for low power density plasmas, and exploring the parameter space suitable for plasma discharge initiation. Relative to the test program, component verification is to be accomplished during pre-operational testing, and systems questions are to be addressed during the first year of operation.

Information on some aspects of full integrated facility operation will not be available until late in the operating life of the device. For example, the complete tritium reprocessing cycle will not be employed until a fairly substantial quantity of tritium has been bred and extracted from the blanket. On the other hand, data on reliability and maintenance will be accumulated throughout the machine life.

1.4.2 Tritium-Free Operation

A period of approximately two years will be dedicated to exploring the parameter space accessible to the plasma and to optimizing operating

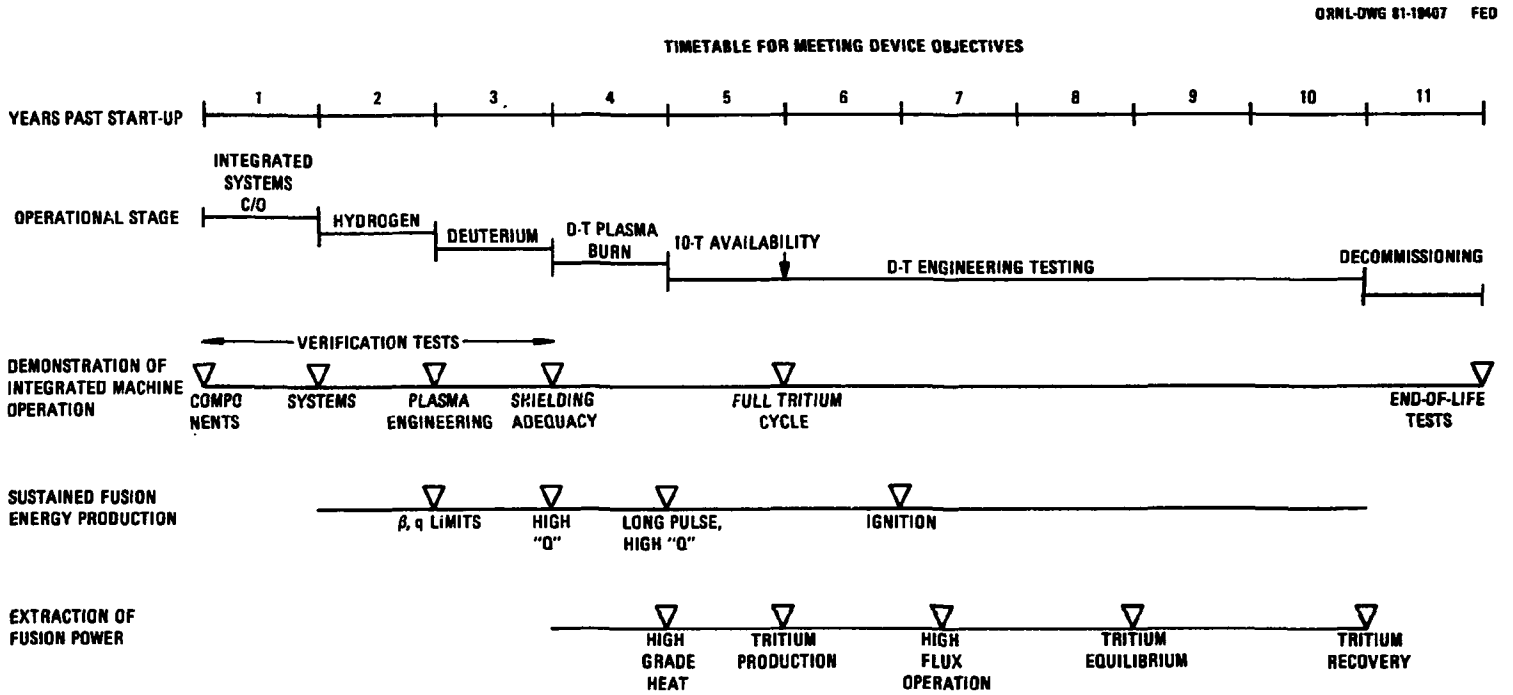

Fig. 1-10. Timetable for FED testing.

scenarios but without the complications of handling tritium and being forced into a fully remote mode of maintenance.

Initial experiments, perhaps extending a period of one year, will employ only hydrogen and will thus be compatible with full hands-on maintenance. The focus will be on plasma control with emphasis on plasma positioning, plasma shaping, density ramping, and current ramping. Since any damage to high heat flux surfaces would be far easier to repair during this period than in the fully remote handling phases to follow, this is the most logical point to map out the boundary of essentially disruption-free operation. As far as the test program is concerned, the year devoted to studying hydrogen plasmas will serve to qualify the plasma engineering, specifically the techniques required to produce, heat, and sustain clean, reproducible, reactor-grade plasmas. Operation with deuterium will provide important data regarding the adequacy of the shielding for personnel safety and component protection. A good indication of the operating point to be used in D-T testing can be obtained in the deuterium stage, where second harmonic ion cyclotron heating will be capable of achieving $n\tau T$ values comparable to those obtainable with alpha heating.

It is recognized that the phrase "tritium-free" is not strictly applicable to deuterium operation because D-D fusion produces tritium nuclei. However, tritium plays no part in the energetics of such operation, nor will it pose a serious environmental concern. The transitions from hydrogen operation to deuterium operation and from deuterium operation to tritium operation both represent major, irreversible commitments to accepting more limited experimental flexibility. It is expected that a several month shutdown will occur at some period during this phase, probably near the end of hydrogen operation, to perform a whole host of device modifications that would be far more time-consuming if done remotely. In particular, a substantial overhaul of the diagnostic systems is appropriate prior to moving into a high neutron flux mode of operation.

1.4.3 D-T Plasma Burn

The crux of the physics portion of the FED mission is the production of sustained fusion power, and this is the prime objective of the D-T plasma burn phase, which is slated to last approximately one year. Confinement, beta, impurity control, etc., must be reexamined in the $Q \geq 5$ regime. This is because all these properties depend to some degree on plasma profiles, and the profiles may be significantly modified when the energetics become dominated by alpha particle heating.

An additional issue that surfaces for $Q \geq 5$ is that of control of the operating point; under these conditions the dominant plasma heating is due to a source that is only indirectly under the control of the operator. Thus the demonstration of long pulse, high Q operation will represent a particularly significant milestone in the fusion program. The presence of significant plasma self-heating also adds to the difficulty of accomplishing a benign shutdown; so this phase offers an opportunity to demonstrate a shutdown procedure.

In order to be fully successful, however, the D-T plasma burn phase must go beyond such demonstrations. It must provide a catalog of reproducible, long pulse, high Q operating points for use in the engineering testing phase to follow.

1.4.4 D-T Engineering Testing

More than 80% of the full-field pulses during the life of the facility are planned for the engineering testing phase. Nuclear systems testing will be the primary focus of the D-T engineering testing phase. The bulk of the data will be accumulated during the planned 200,000 8-T shots with additional information to be gathered from 25,000 10-T shots. The 8-T tests will be adequate to demonstrate the critical elements of blanket operation. Extension of such tests to 10-T operation would provide another scaling point. Such an extension will also represent more challenging and more reactor-relevant modes of operation for many of the plasma engineering systems.

There will be a periodic need for continuous operation over a period of approximately one week. Such operations will be repeated a number of times as required by the test program (see Ref. 4). For example, in blanket tests, a large number of consecutive pulses is required for equilibrium tritium production and extraction.

A final phase of testing occurs at the end of the operating life of the facility. Although the operating life has been taken to be ten years, it should be recognized that this is by no means a firm date; rather, the total operating life will be determined by hardware status and by the appropriateness of the facility for meeting the needs of the fusion program at that time. The decommissioning itself is of great interest and may well be of importance in guiding design choices for commercial reactors.

The essential elements of demonstrating a reactor-relevant mode of extracting fusion power are the generation of high grade heat in a blanket and the verification of the feasibility of an essentially self-sufficient tritium cycle. High grade heat will emerge from the first sequence of D-T shots at a reasonable repetition rate. A more accurate simulation of the thermal/structural situation to be encountered in a Fusion Demonstration Plant (FDP) will take place at the higher wall loadings to be experienced after 10-T operation commences.

Tritium production in sufficient quantity to verify the physical modeling adopted in blanket design will be achieved early in the D-T engineering test phase. A test of recovery of the tritium retained in the blanket will also be possible during this time frame. These demonstrations will be adequate for FDP initiation. Further refinement of FDP blanket design will be made possible by more definitive tests later in the D-T engineering test phase: the attainment of equilibrium operation, which can be achieved via 10^3-10^4 consecutive 10-T shots, and a confirmation that sufficient tritium held up in the blanket can be removed at end-of-life. The key to this phase of testing is sufficient discharge control to generate a thoroughly reproducible neutron source.

1.5 COST AND CONSTRUCTION SCHEDULE PROJECTION

Cost and construction schedules were projected for the FED capital project. Such projections are important factors for future decisions on the project scope, and, therefore, it was deemed appropriate to begin to develop cost and schedule information at this early stage of the design process.

1.5.1 Cost Estimate

The cost estimate is given in Table 1-4. Based on constant 1981 dollars, the projected direct cost is $1044 million and the total capital cost (direct plus indirect) is estimated to be $2172 million. The estimated yearly cost and completion schedule for an eight-year construction project (see Section 1.5.2) are shown in Table 1-5. Note that escalation would increase the total cost relative to the constant dollar cost existing at the start of the project.

Not surprisingly, the estimated completion schedule shows the classic peak in the middle years of construction when most of the material and construction is required. The schedule also shows a large relative peak in the second year due to the cost of superconductor which must be purchased relatively early. The size of the peak stems directly from the assumption that a large fraction, on the order of 70%, of the superconductor material cost would have to be paid shortly after procurement is initiated.

Assumptions

The following assumptions were made in developing the cost projection:

- All costs are based on constant 1981 dollars.
- Direct capital costs include all costs associated with component procurement and fabrication including shipping to the construction site.

Table 1-4. FED cost projection summary (M$)

DIRECT COSTS	
• Magnet system	312
• Torus	162
• Cooling systems	38
• Tritium and fuel handling	54
• RF systems	89
• Electrical systems	99
• Vacuum pumping system	24
• Instrumentation and control	67
• Remote maintenance equipment	60
• Facilities	139
TOTAL Direct Cost	1044
INDIRECT COSTS	
• Engineering and management (45%)	470
• Installation (15%)	157
TOTAL (Direct + Indirect)	1671
• Contingency (30%)	501
TOTAL COST	2172

Table 1-5. Cost and completion schedule
(percent of constant cost at start of project)

	Schedule year[a]							
	1	2	3	4	5	6	7	8
I. Construction								
A. Buildings			30	40	20	10		
B. Special facilities								
1. Magnets		60	10	20	10			
2. Torus				30	30	30	10	
3. Cooling				50	50			
4. Tritium and fueling				20	40	40		
5. RF					50	50		
6. Electrical				20	60	15	5	
7. Vacuum pumping					50	50		
8. Instrumentation and control				30	60	10		
9. Maint. Eqpt.					30	30	40	
II. Engineering (45%)								
A. Design & Mgt.	20	25	25	6	6	6	6	6
III. Machine installation (15%)					10	30	30	30
IV. Percent of total project cost	6	18	11	16	22	15	7	5

[a]Each entry represents the percent cost expended in the indicated year. For each line, the sum of all entries is 100%.

- The indirect capital costs include engineering design and project management as well as all equipment installation and assembly at the construction site.
- A 30% contingency is included in the total cost.
- The estimate is only for the FED construction project and does not include any operating or maintenance costs, spare parts, fuel, associated research and development, transmission lines, or decommissioning.

Direct costs were estimated by applying unit cost values and cost algorithms that were developed as part of the FEDC systems code. The indirect costs for engineering (45%) and installation and assembly (15%) are based on fixed percentages of the direct costs and represent a best judgement based on recent large DOE projects.

1.5.2 Construction Schedule

An estimate of the construction schedule for FED was made and is summarized in Fig. 1-11. This effort was prompted by the need to identify potential impacts of construction and installation on design and to provide a basis for more detailed project planning. Both of these objectives are best satisfied by a success-oriented schedule that surfaces the schedule drivers and complexities. The resulting success-oriented schedule was useful in identifying the key drivers of the FED construction and installation process. It also was useful in relating the project needs to the proposed and current research and development activities. Finally, the schedule, together with cost estimates and design descriptions, served to scope the magnitude of the FED project and to define the sequencing of project activities.

The construction schedule is conveniently viewed as being made up of five distinct phases. In the *initial phase*, the site is prepared, design is started, safety review is completed, and construction approval is received. This preparatory phase is expected to take about 24 months.

The *second phase* starts with actual construction activities on the tokamak building. During this phase, the tokamak building construction

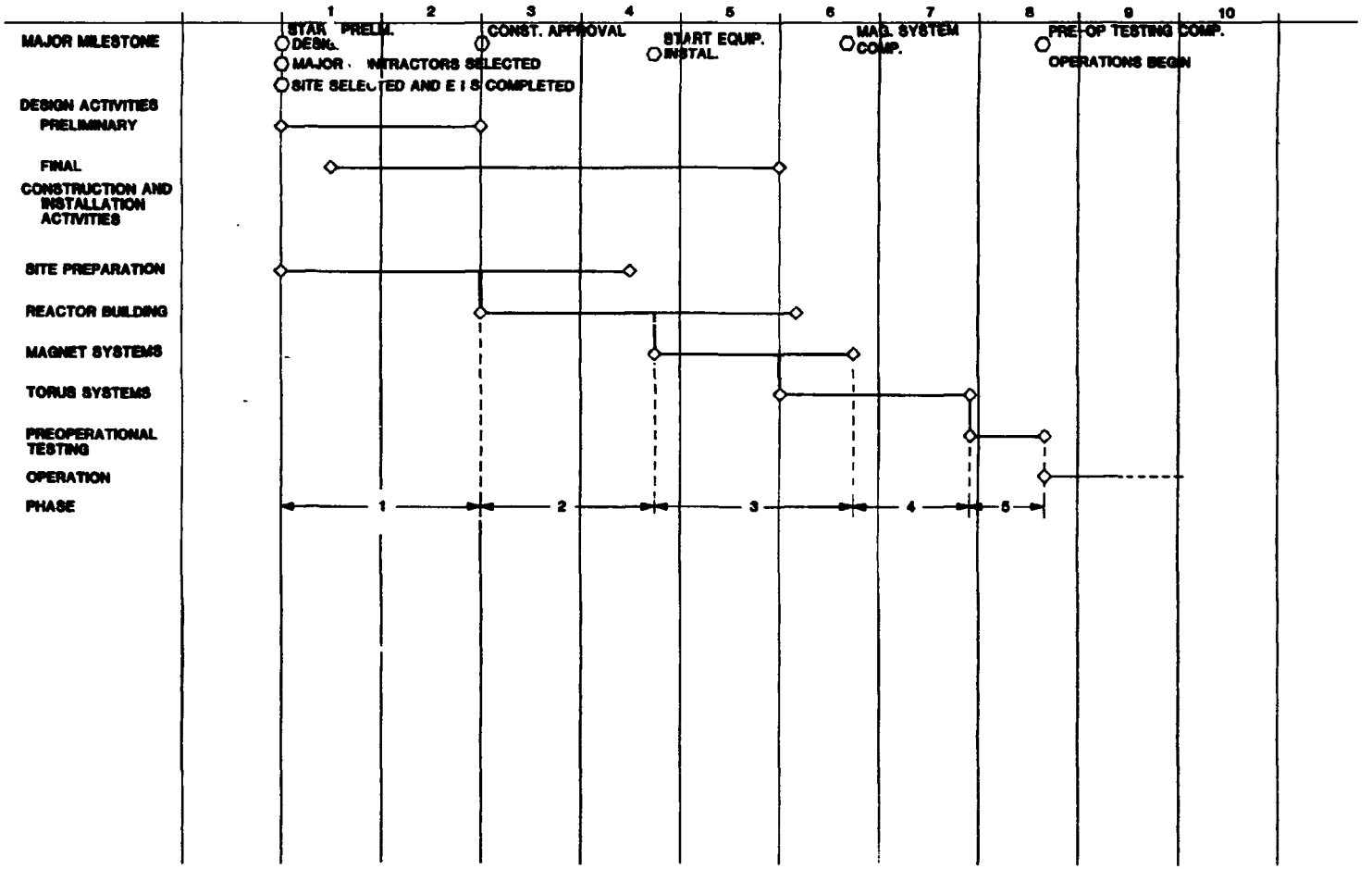

Fig. 1-11. FED summary construction schedule.

is taken to the point where device installation can begin. This tokamak building construction phase is expected to take about 21 months.

The *third phase* includes all the device installation through the completion of the magnet systems checkout. The installation logic has been worked out to give an estimate of the minimum installation time. This phase begins with the installation of the lower PF coils and ends with the completion of the cryostat. This is followed by a magnet systems checkout which will take two months. The magnet system installation and magnet check-out phase are expected to take about 23 months.

The *fourth phase* starts at the end of the magnet system test and goes through the end of mechanical and electrical equipment, piping, and cable installation. The torus spool structure, shield sectors, torus instruments, radio frequency (rf) heating, and fuel injectors are installed during this phase. The installation of the torus spool structure must start before the completion of the magnet test. The installation phase is estimated to take about 15 months.

The *final phase* is the pre-operational testing of the completed device. All construction and installation relative to initial FED operation must be completed prior to the beginning of this phase. A minimum of nine months was allowed for pre-operational testing.

The entire schedule from the beginning of preliminary design through the end of pre-operational testing is estimated to take seven years and eight months (92 months).

1.6 KEY DESIGN ISSUES FOR FUTURE INVESTIGATION

Although feasible solutions were developed for each of the major systems and subsystems of the FED baseline, further design effort is expected to yield significant improvement in the design. This section briefly summarizes some of the key design issues, identified during the FY 81 design effort, which if resolved could enhance the feasibility and/or reduce the cost of FED.

1.6.1 Configuration Engineering Design Issues

- Develop configuration approaches which can reduce the size of major components and/or the device and thereby reduce the cost while maintaining the FED performance. This includes such issues as: structural approach for the TF/PF coils; torus design and interface with the cryostat; and location of PF coils.
- Develop a maintenance approach for each FED major system, subsystem, and component with the intent of establishing *generic* maintenance methods applicable to the tokamak configuration.
- Determine major system, subsystem, and component support requirements. Establish replacement and/or likely repair requirements. From this identify needed support requirements such as required spares, repair stations, hot cell floor space, warehouse space, and maintenance equipment.
- Generate system reliability requirements necessary to satisfy *continuous operations* (e.g. ∿1000 back-to-back pulses) during the engineering testing. This information will assist in assessing the impact of the required FED testing on device system reliability and associated cost.
- Perform failure mode and effects analyses on the major reactor systems. The purpose is to determine potential modes of failure, the consequences of failure, the means of detection, and the appropriate corrective action.

1.6.2 Magnetic Systems Design Issues

- Investigate areas of design improvement for both the TF and PF coil systems including such aspects as alternate support structure concepts, alternate intercoil structure approaches, and alternate approaches for conductor, winding pack, insulation, eddy current losses, imposed loads, and fabrication methods.
- Develop alternate approaches to cryostat design to provide improved overhead access and to minimize the amount of cold shield in the cryostat.

- Develop in more depth a design for demountable normal copper PF ring coils.
- Investigate improvements that can be made in central solenoid design.

1.6.3 Nuclear Systems Design Issues

Torus

- Develop an improved design to ensure sector-to-sector electrical contact.
- Develop coolant flow system concepts for the shield.
- Develop dielectric break design for the torus spool
- Develop port designs (size and location) for performing in-vessel maintenance.
- Investigate design approaches to detect and minimize probability of vacuum leaks.
- Develop improved methods for sector removal and replacement.
- Investigate alternate techniques for handling torus structure loads.

First wall and limiter

- Develop further the first wall armor and stainless steel panel attachment design.
- Pursue joining methods for stainless steel first wall panels (e.g., welding and brazing).
- Develop remote methods for installing/removing armor tile and stainless steel panels.
- Develop methods of attaching the limiter to the shield and for remotely installing/removing limiter.
- Develop methods of limiter alignment.
- Develop improved electrical contact design for the limiter.
- Develop tile attachment technique on limiter blade.

1.6.4 Electrical Systems Design Issues

Electromagnetics

- Develop engineering designs of plasma feedback systems for vertical and horizontal plasma position control. Also investigate burn control engineering.
- Develop the engineering data and designs for sector electrical connections to provide for the conduction of disruption currents in sectors and first wall components.
- Develop an engineering analysis for disruptions to provide an improved basis for determining disruption characteristics that affect the torus design.
- Determine the volt-second requirements for startup and the control field requirements for providing the proper nul field for the low current stage of startup.

Power systems

- Develop improved methods of protecting superconducting coils based upon specification of protection requirements, developing protection instrumentation, developing fault logic diagrams, and defining trip-level threshold criteria.

Instrumentation and diagnostics

- Develop torus interface layouts for individual diagnostic instruments.
- Develop an integrated layout for the full set of instruments.
- Determine instrumentation required for facility control.
- Define nucleonics first wall instrumentation requirements.

1.6.5 Plasma Heating Systems Design Issues

- Develop an improved design of the interface of the ICRH and its shielding with the torus including such aspects as simplification of the shielding design, identification of location

for all service lines and routing pathways, and development of remotely actuated quick disconnects for service lines.

- Investigate alternate design approaches for providing current drive capability including identification of type of rf to provide current drive and method and type of launcher installation.

1.6.6 Facilities Design Issues

- Develop interface requirements between the device and the facility so as to evaluate the implications of facility equipment, piping/duct sizes and locations on device maintainability.
- Identify potential accidents and perform accident analysis to determine criteria for building and equipment with respect to issues such as overpressure, tritium release, and cryogenic release.
- Identify hot cell equipment and facility requirements for device operations including test program requirements.

1.7 RESEARCH AND DEVELOPMENT NEEDS

As part of the FY 81 FED activities, the critical technological research and development (R&D) required to perform the final design and to build the FED were identified. This effort was documented in Ref. 5. The critical physics issues which must be resolved for FED were documented in Ref. 6. This section provides a brief summary of the key technology R&D needed for FED. These needs are summarized in seven broad categories: magnetic systems, nuclear systems, plasma heating, plasma fueling, diagnostics, maintenance, and safety and environment.

1.7.1 Magnetic Systems R&D Needs

- There are several TF magnet concepts which will satisfy the FED requirements; however, there is varied opinion on which of the concepts offers the least risk. Because of the overwhelming impact of the TF coils on both cost and schedule, it is important

that R&D programs such as the Large Coil Program (LCP) and 12 tesla programs be pursued aggressively to allow designers to select the optimal concept.

- To minimize the risk of damage to the TF coils during abnormal operating conditions, it is vital that development work be initiated on a conductor of higher current than being planned for LCP. At the time LCP was originated it was widely believed that 10,000 amperes were not only pushing the technology, but would be adequate for a large tokamak. Today, system designers are less sanguine about being able to successfully dump the energy from a 10,000-ampere system. Fortunately, conductor designers and metallurgists are much more optimistic about being able to produce a high current conductor. Such a development program would also have a favorable impact on poloidal coil design, where large current conductors are already being designed for lower field.
- The data base on the behavior of high strength stainless steels for cryogenic service is inadequate for the cyclic loading expected in FED. The existing DOE-funded, National Bureau of Standards-managed program should be focused more sharply on the leading candidates. The number and size of test specimens should be greatly enlarged. Information on structural materials will have applicability to both TF and PF systems.
- The impact of nuclear radiation on the voltage breakdown in liquid helium is not well defined but is believed to have a significant deleterious effect. This phenomenon should be investigated promptly, otherwise excessive shielding will be required.
- Nuclear radiation is known to weaken currently popular polymeric insulations. Promising alternates exist and should be tested. Inadequate testing will result in either thicker shielding, or higher risk, or both.
- Because of the pulsed nature of the loads in both TF and PF coils, an investigation of fretting and wear in magnets under

cyclical operation should be initiated. There has been little experience with this type of magnet operation.

- The superconducting poloidal coils for FED require a concept to minimize eddy current heating of the coil support cases. One possibility is the use of a thin steel liner within a nonconducting structure. Another is the use of a nonconducting, vacuum-tight break in the structure. A program is required to bring at least one of these concepts to fruition.

1.7.2 Nuclear Systems R&D Needs

First wall and limiter

- Improved characterization and understanding of chemical sputtering of graphite armor material are required.
- Improved understanding is required of the behavior of stainless steel wall material in the melted condition, which is expected to occur under the influence of high energy deposition rates, electric currents, and magnetic fields corresponding to a disruption environment.
- Development and demonstration of the compatibility of substrate material with the proposed graphite surface material of the limiter are required. The program should include development of attachment techniques such as brazing and diffusion bonding.

Torus spool

- Either dielectric breaks or high resistivity structural techniques must be developed to allow the impressed electrical field to penetrate the shield structure and to induce the desired plasma currents.

Shield sectors

- A high current toroidal electric path near the plasma side of the shield is required for plasma stabilization. Such a path

must not complicate nor inhibit shield removal, and the path must be reliable. An appropriate solution, such as discrete electrical contacts, requires a development program.

- To minimize eddy currents in the shielding, laminations will be coated with a dielectric. The behavior of these coatings under the influence of radiation, stress, abrasion, and various coolant conditions must be investigated.
- Accelerated corrosion of stainless steels in water in the presence of a magnetic field has been observed and should be investigated. Corrosion inhibitors should be identified, if needed.

Vacuum pumping and tritium systems

- Development of backing and roughing pumps for tritium service with particular emphasis on seals and maintainability is required.
- Demonstration of performance and safety of an overall system (as will be accomplished at the Tritium Systems Test Assembly) is required.
- Basic data on tritium adsorption/desorption is needed for a wide range of surface materials at various temperatures.
- Generic research on the implantation and permeation of tritons in stainless steel is needed.
- Research in the development of tritium permeation barriers is needed and should be continued.

Nuclear analysis

- Advanced nuclear analysis techniques are required to allow less conservative shield designs which could reduce the overall cost of the device. An expanded materials nuclear data base is also needed.

1.7.3 Electrical Systems R&D Needs

Plasma heating

The baseline design for FED heating is rf. Ion cyclotron resonance heating (ICRH) is used for bulk heating. Electron cyclotron resonance heating (ECRH) is used for initiation of the plasma and for heating the plasma to approximately 100 eV. As a backup or alternate, neutral beam injection (NBI) at 150 keV is specified for bulk heating.

- The frequency range for gyrotrons is being extended as the experimental device fields are increased. At the present time, the development is in the 60 GHz range. Units with frequencies in the 100 GHz range will be required for FED. In addition to the gyrotron, development is required for auxiliaries such as: arc detectors, mode filters, directional couplers, and mode converters.
- The launchers for ECRH and ICRH require development. Radiation-hardened waveguides require development. Insulation breaks are needed that prevent induced currents and plasma disruptions from being conducted through the rf transmission lines.
- High-power, broad-band, tuneable amplifiers need development for ICRH technology.
- The NBI requires extension of the existing technology to 150 keV, 100-s pulses and requires development to assure reliable operation in a radiation environment. To obtain reasonable efficiency at the higher voltage (150 keV), direct recovery will have to be developed.

Fuel injectors

- Pellet injectors which are now being developed for existing machines require extended development for FED. The pellet speeds must be increased to 2000 m/s, which is near the maximum velocity obtainable, in order to drive the pellet deep enough

into the hot plasma to prevent excessive edge cooling and to get the fuel into the center region. The present hydrogen and deuterium pellet injectors will have to be converted to handle tritium and to provide a fast pellet injection rate.

Instrumentation and diagnostics

- Instrumentation for present fusion devices is frequently developed on the existing device. To provide the necessary reliability and availability for FED, a plasma instrumentation test facility becomes more of a necessity. This facility could be used to:
  1) Re-engineer instrumentation used on small devices, to provide for tritium and radiation environment and to provide improved reliability and accuracy.
  2) Develop remote maintenance instrumentation equipment and procedures including calibration and improved signal-to-noise ratios.
  3) Provide training, maintenance experience, calibration method development, and address other human-factor problems.

Control

The feedback control features on present machines are to a large degree developed on the machine after the machine is placed in operation. Because of the high temperature and long burn time of FED, as much development as possible off-line will provide the most economic development.

- Vertical and horizontal feedback control systems will be required.
- Location of the plasma separatrix on the limiter must be controlled and such capability must be developed.
- Burn control must be developed.

- Simulators must be developed for the various control systems.

1.7.4 Maintenance R&D Needs

- Neutron-induced activation of components weighing up to 400 tons will put special requirements on the FED maintenance system. Many other components which are smaller (e.g., diagnostics, test modules, pumps, and valves) will also require new techniques and equipment because of their relative frequency of replacement. Hence a development program on remote maintenance equipment is required.

1.7.5 Safety and Environment R&D Needs

- An FED plant will contain many potential hazards: cryogens, radioactive nuclides, high voltage, high currents, and massive-but-mobile shielding. Fortunately, most of these items can be addressed with existing and accepted practices. Certain features of FED related both to the handling of the tritium inventory and to the confinement of activation products must be addressed as part of the safety research program.
- Attention should be given to potential environmental concerns such as radiation exposure and magnetic fields.

1.8 CONCLUDING REMARKS

The baseline design developed for FED represents a workable tokamak design concept that satisfies the objectives established for FED. The physics analyses indicate that the device can achieve the plasma performance goals for a range of reasonable assumptions and eventualities. The design effort resulted in a feasible approach for all of the major device systems and components. The machine configuration incorporated features that reflect the importance of maintenance and access. Reactor support systems were developed to fully support the device and its planned operations. The needed facilities were identified and the

dominant features established. A site layout was developed. A preliminary cost projection and a construction schedule was developed.

The FY 81 FED activities focused on the development of a concept and supporting programs for moving ahead with the demonstration of engineering feasibility. The baseline design, along with the supporting information, constitute a basis upon which a full design effort can be initiated.

REFERENCES

1. *Final Report of the Ad Hoc Experts Group on Fusion*, DOE/ER-0008, Department of Energy (1978).
2. Fusion Engineering Design Center Staff (C. A. Flanagan, D. Steiner, G. E. Smith, eds.), *Initial Trade and Design studies for the Fusion Engineering Device*, ORNL/TM-7777, Oak Ridge National Laboratory (June 1981).
3. *Fusion Engineering Device*, Vol. I, *Mission and Program Summary*, DOE/TIC--11600 (to be published).
4. *Fusion Engineering Device*, Vol. III, *Test Plan*, DOE/TIC--11600 (to be published).
5. *Fusion Engineering Device*, Vol. V, *Technology R&D Requirements for FED Construction*, DOE/TIC--11600 (to be published).
6. *Fusion Engineering Device*, Vol. IV, *Physics R&D Requirements for the Fusion Engineering Device*, DOE/TIC--11600 (to be published).

2. PLASMA ENGINEERING

Y-K. M. Peng*
J. F. Lyon†
S. E. Attenberger†
S. K. Borowski‡
B. A. Carreras†
L. M. Hively‖
J. A. Holmes*
J. C. Hosea§
W. A. Houlberg†
H. C. Howe*
D. Q. Hwang§
D. Mikkelsen§
M. Petravic§
D. E. Post§
J. A. Rome†
J. A. Schmidt§
C. E. Singer§
D. J. Strickler*
M. Ulrickson§
J. Wesley††

This chapter addresses the performance and design requirements of FED as derived from our current understanding of fusion plasma physics. The FED physics basis in a number of crucial areas has recently been assessed by the FED Physics Group under the direction of P. H. Rutherford.[1] The areas considered there include: confinement, pump limiter operation and design concepts, low safety factor operation and plasma shaping, ion cyclotron resonance heating (ICRH), nonmagnetic impurity control, neutral beam injection heating, and poloidal divertor operation. In addition, FED-relevant physics results are generated by the fusion physics community on a continuing basis in areas such as startup, plasma modeling, neutral beam heating, high beta implications and limitations, plasma magnetics, plasma edge physics, and disruption characterization. This work has been incorporated into this chapter which comprises contributions from a number of experts in the tokamak community who were responsible for the main FED physics areas.

This chapter provides engineering-oriented interpretations of physics information cited above in support of the FED design studies. The plasma engineering analyses presented in this section are of three

*Fusion Engineering Design Center/Oak Ridge National Laboratory.
†Oak Ridge National Laboratory.
‡Fusion Engineering Design Center/University of Michigan.
‖Fusion Engineering Design Center/General Electric Company.
§Princeton Plasma Physics Laboratory.
††General Atomic Company.

general categories: (1) analyses that form the basis for the choice of the baseline parameters, (2) analyses that examine the possible range of plasma performance for the given baseline device, and (3) analyses that address potential options relative to the baseline configuration. These three types of analysis are woven through the subsequent discussions. This chapter updates and expands the plasma engineering analyses reported in an initial FED design study.[2] A summary of the studies can be found in the Design Summary.[3]

As discussed in Chapter 1, the FED mission includes the demonstration of controlled fusion burn over long pulses producing a neutron wall load of $\sim$0.5 MW/m^2. To achieve the plasma performance required for this mission, the FED is envisioned to have a major radius of 5 m and a minor radius of 1.3 m with an elongated D-shape plasma cross section. It is expected that this requires a clean ($Z_{eff} < 1.5$), long pulse ($\sim$100 s), high beta ($\langle\beta\rangle = 5.5\%$) plasma core dominated by fusion alpha particle heating. The baseline toroidal field on axis is chosen to be 3.6 T, corresponding to a maximum field of 8 T at the TF coils. With a plasma current of 5.4 MA, the fusion power during burn is calculated to be about 180 MW, driven at a fusion power amplification of $Q \geq 5$. To ensure against short-fall in the physics assumptions and to enhance the probability of fusion ignition in FED, a limited capability of 4.5 T in toroidal field on axis (10 T at the TF coils) and 6.5 MA in plasma current is also envisioned. The analyses to be discussed in this chapter deal primarily with the plasma design parameters, options, and sensitivities of the 8 T, $Q \sim 5$ operation. The option of enhanced field and performance will be discussed where appropriate.

Section 2.1 provides a description of the operating scenario of a typical FED discharge cycle. Section 2.2 deals with rf-assisted preionization and current startup. Sections 2.3 and 2.4 deal with modeling of plasma heating and burn by ion cyclotron resonance waves and neutral beams (backup), respectively. Section 2.5 examines beta implications and limitations. Section 2.6 considers issues associated with power, particle, and impurity handling via pump limiter and poloidal divertor (backup). Section 2.7 deals with the approach to, and the

requirements of, the poloidal field configuration. Section 2.8 deals with the characterization of and survival against plasma disruptions. Section 2.9 provides a summary of the major conclusions of the plasma engineering analyses. These assessments indicate that the current FED baseline design is appropriate for achieving the FED physics goals in spite of the significant uncertainties remaining in several physics areas.

2.1 OPERATING SCENARIO

Y-K. M. Peng — ORNL/FEDC

The FED plasma operating scenario describes the plasma behavior and the operational requirements through a typical plasma discharge cycle. The scenario serves as a reference to the engineering design trade analyses.

A typical FED plasma discharge cycle involves prefill and preionization, current initiation and rampup, bulk heating, burn plasma shutdown, and pumpdown. The proposed scenario of the plasma operation through these phases of a discharge cycle is discussed below, summarized in Table 2-1, and depicted in Fig. 2-1. The scenario should be consistent with the results of the plasma engineering studies presented in Sect. 2.2 through 2.8.

2.1.1 Prefill and Ionization ($-0.05\ s \leq t \leq 0.8\ s$)

Up to 2 MW of extraordinary mode, electron cyclotron resonant frequency (ECRF) wave at 90 GHz is launched from the high field side for a duration of 0.8 s to preionize and heat the electrons. The heated electrons ($T_e \sim 100$ eV, $n_e \sim 1 \times 10^{13}$ cm^{-3}) are expected to be located at R = 5.9 m (the upper hybrid resonance, UHR) over a radial width of about 0.4 m. This permits the application of a low toroidal loop voltage ($V_\ell < 25$ V) to initiate and ramp-up the plasma current, leading to dramatic engineering design advantages (see Sect. 2.2). An alternate preionization approach is to apply the ICRF bulk heating capability to obtain significant electron heating via mode conversion with a deliberately introduced minority species (see Sect. 2.3).

Before current initiation, the heated plasma (in the form of an axisymmetric, vertically extended belt) is estimated to occupy about 30 m^3 which is less than 1/10 of the chamber volume. A plasma electron density of 10^{13} cm^{-3} during this phase suggests that a prefill pressure of about 10^{-5} torr is required, in the absence of significant particle source or sinks on the chamber wall. The prefill and preionization approach should not be affected by 10-T operation except that the ECRH frequency then needs to be 113 GHz.

Table 2-1. Operation scenario assumed for the 8-T plasma baseline

Phase	Duration(s)	8-T operation	Plasma behavior
Prefill		$P_o \lesssim 10^{-5}$ torr	
Ionization, electron heating, and current initiation	0.9	P(ECRH) $\lesssim$ 2 MW f(ECRH) = 90 GHz $V_\ell \rightarrow$ 25 V $q_\psi \rightarrow 3.2$	$\langle n_e \rangle \sim 10^{13}$ cm^{-3} $\langle T_e \rangle \sim$ 100 eV Near R = 5.9 m (UHR) $I_p \rightarrow$ 0.17 MA, a = 0.4 m
Current ramp-up	5.2	V_ℓ = 25 V $\rightarrow$ 2 V P(ICRF) $\rightarrow$ 5 MW $q_\psi = 3.2$	$\langle n \rangle \rightarrow 3 \times 10^{13}$ cm^{-3} $\langle T \rangle \rightarrow$ 1 keV $I_p \rightarrow$ 4.8 MA, a $\rightarrow$ 1.3 m R $\rightarrow$ 5.0 m, $\kappa \rightarrow$ 1.6
Bulk heating	6	P(ICRF) $\leq$ 50 MW f(ICRF) = 54 MHz $q_\psi = 3.2$, $\varepsilon\beta_p \rightarrow 0.5$ Pump limiter, fueling (Impurity control)	$\langle n \rangle \rightarrow 8 \times 10^{13}$ cm^{-3} $\langle T \rangle \rightarrow$ 10 keV P(FUSION) $\rightarrow$ 180 MW $I_p \rightarrow$ 5.4 MA (FCT) $\langle \beta \rangle \rightarrow$ 5.5%
Burn	100	P(ICRF) = 36 MW	P(FUSION) = 180 MW $Z_{eff} \leq 1.5$
Shutdown	10	Fusion quench Particle exhaust Current quench $q_\psi = 3.2$	$\langle n \rangle \rightarrow 2 \times 10^{13}$ cm^{-3} $\langle T \rangle \rightarrow$ 1 keV $I_p \rightarrow$ 0.1 MA R $\rightarrow$ 5.9 m
Pumpdown	30	3×10^{-4} torr $\rightarrow 3 \times 10^{-6}$ torr	

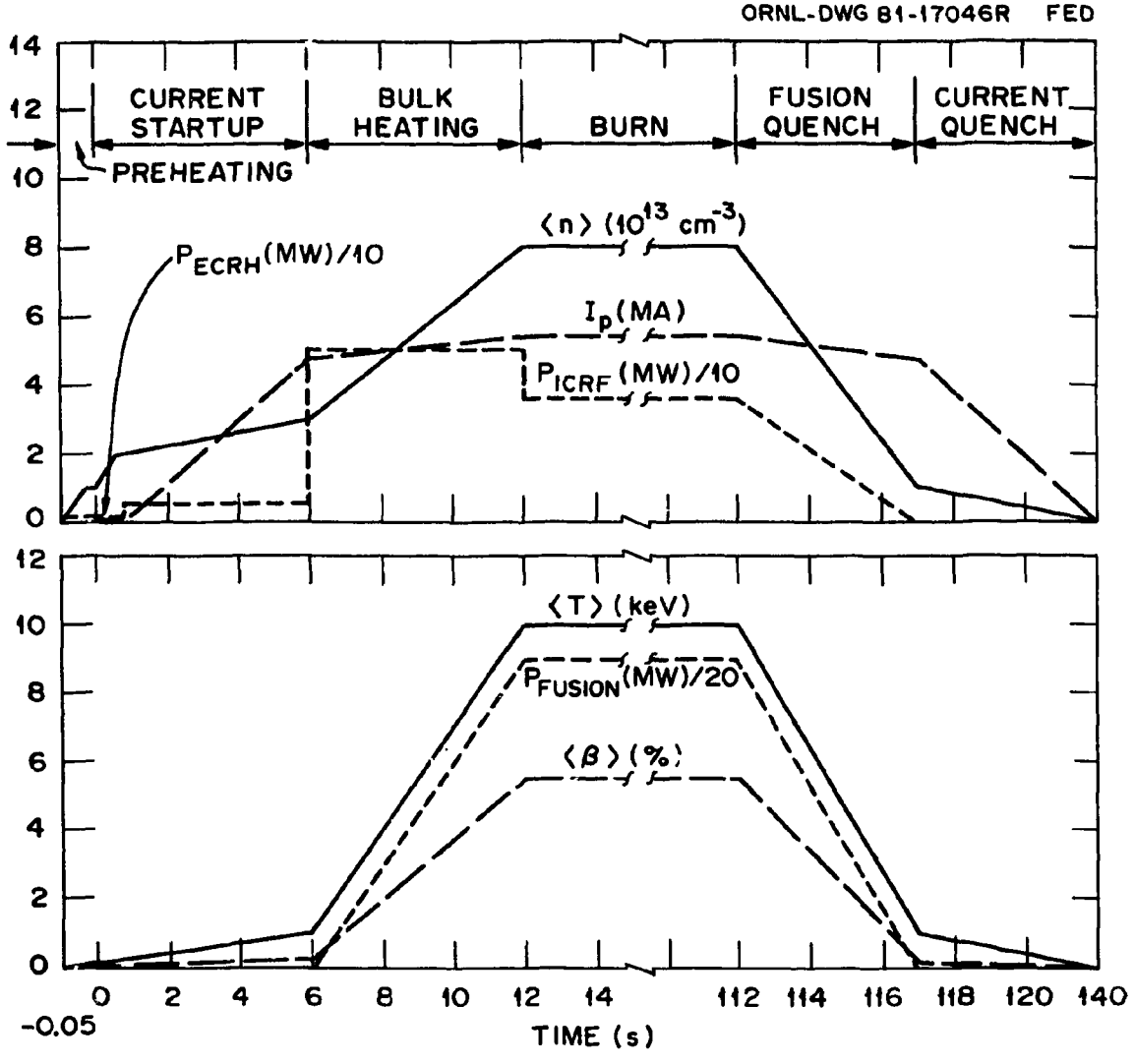

Fig. 2-1. Typical FED plasma behavior suggested for the 8-T operation.

2.1.2 Current Initiation and Ramp-up (0 s $\leq$ t $\leq$ 6 s)

During the first 0.8 s of this phase, a low loop voltage (V_ℓ < 25 V) is applied to initiate a current channel with a minor radius of about 0.4 m, defined by startup limiters on the midplane. The plasma current is slowly brought up to about 0.17 MA avoiding skin current formation and the associated instabilities. The safety factor at the plasma edge is also brought down to q_ψ = 3.2. The plasma volume would be reduced to about 15 m^3 during this time through formation of a nearly circular plasma cross section. Hence, n_e is expected to increase to 2×10^{13} cm^{-3} in the absence of particle sources or sinks.

The plasma minor radius is then increased from 0.4 m to 1.3 m by reducing the major radius and maintaining plasma contact with startup limiters on the midplane. The plasma elongation κ is raised to 1.6 to achieve full plasma contact with the pump limiter or the single-null poloidal divertor. The current is increased so that the safety factor q_ψ at the plasma edge remains constant in time, avoiding skin current formation. In the case of the poloidal divertor, q_ψ at the edge becomes undefined as the divertor separatrix is formed. Additional heating (e.g., by ICRF with proton minority) beyond 0.8 s can be used to reduce the volt-seconds expended via plasma resistance during this phase. The plasma reaches about 1 keV, 3×10^{13} cm^{-3}, and 4.8 MA at t = 6 s (see Sect. 2.2).

For 10-T operation, the plasma current reaches 0.2 MA at t = 0.8 s and 5.8 MA at t = 6 s.

2.1.3 Bulk Heating (6 s $\leq$ t $\leq$ 12 s)

Up to 50 MW of ICRF power is applied at a frequency of about 54 MHz for 6 s. The plasma reaches about 10 keV, 8×10^{13} cm^{-3}, and 5.4 MA via pellet fueling and gas puffing, maintaining nearly equal deuterium (D) and tritium (T) content. The contact between plasma and limiter is controlled to achieve adequate particle exhaust through the limiter channels without overheating the leading edge of the pump limiter (see Sect. 2.7). The value of q_ψ is maintained at 3.2 during this

phase. For the poloidal divertor option, the placement of the divertor separatrix configuration needs to be properly maintained to ensure proper divertor action.

An alternative to ICRF is neutral beam injection, in which about 50 MW of 150 keV (maximum) D^0 beam is coinjected in the quasi-tangential direction (at an angle of 35° toward parallel, measured at the outer plasma edge). The option of nearly perpendicular injection is retained because less access is required. For injection, an enhanced particle exhaust capability and tritium pellet injection are needed to maintain a nearly equal D-T plasma composition. The fusion power reaches about 180 MW at t = 12 s.

For 10-T operation, the plasma reaches 1.3×10^{14} cm^{-3} and 6.5 MA at t = 12 s. Under standard plasma beta and confinement assumptions, ignition is achieved and the fusion power is expected to reach 450 MW.

2.1.4 Burn (12 s $\leq$ t $\leq$ 112 s)

A steady-state heating power of about 36 MW is maintained to sustain a controlled fusion burn at $Q \sim 5$ while maintaining the plasma parameters. The pump limiter is estimated to adequately exhaust the helium and control the plasma edge, but auxiliary impurity control or reduction schemes may be needed. The maintenance of a radiation-cooled plasma edge is expected to minimize impurity production and ingestion at the plasma edge. This is an attractive possibility for use in conjunction with a pump limiter (Sect. 2.6). Assuming adequate helium exhaust and impurity control, the plasma burn time is limited either by the volt-second capability of the ohmic heating (OH) coils or by significant resistive diffusion of the plasma poloidal flux. With nearly classical toroidal plasma conductivity, the latter time scale is estimated to be a few hundred seconds.

The thermal power from the plasma is increased only mildly by the ignited plasma in the 10-T operation. However, the volt-second requirements and the fusion power handling requirements are increased, and, therefore, a reduced burn time of about 50 s is assumed for 10-T operation.

2.1.5 Shutdown (112 s $\leq$ t $\leq$ 122 s)

During shutdown, the fusion burn is quenched before the current is quenched. Under normal conditions, the fusion quench is initiated by termination of fueling while maintaining or possibly enhancing plasma exhaust through the pump limiter. Transport estimates have suggested a time scale of $\sim$5 s is required to return to the ohmic state. The supplementary heating is decreased in a fashion which avoids plasma disruption by staying within the modified Murakami density limit. A plasma density of $\sim 2 \times 10^{13}$ cm^{-3} may be assumed at the end of the fusion quench (at t $\simeq$ 117 s). Conceptually, the current shutdown is the reversal of the current ramp-up. The value of q_ψ at the plasma edge should be maintained or increased as the plasma radius decreases as much as possible during this phase to avoid disruptive termination of large plasma current.

2.1.6 Pumpdown (122 s $\leq$ t $\leq$ 152 s)

The neutral density in the chamber at the end of the current quench is expected to be about 3×10^{-4} torr. It is assumed that the residual gas is relatively clean, with only negligible amounts of helium and low Z impurities. Pumpdown to 3×10^{-6} torr in $\leq$30 s is assumed during this phase.

2.2 RF-ASSISTED CURRENT STARTUP

S. K. Borowski — UMI/FEDC, Y-K. M. Peng — ORNL/FEDC

Heating of electrons before and during current initiation and ramp-up in large tokamaks is expected to reduce the minimum required initiation loop voltage and the resistive flux expenditure during startup.[4] Reducing the loop voltage requirement to $\sim$25 V is expected to create significant engineering benefits in the FED design (see Chapters 5 and 7). Minimizing the loss of induction flux due to plasma resistance will maximize the plasma current and pulse length and hence enlarge the parameter space of FED operation (see Sect. 2.4). Potential

rf candidates include heating in the range of the electron cyclotron resonance (ECRH)[4] and fundamental heating of ion minorities (ICRF) (see Sect. 2.3). Studies of startup assist using the latter technique are being planned for the Princeton Large Torus (PLT), while experiments on the Impurity Study Experiment (ISX-B) have concentrated on ECRH.[5,6]

To date, the FED startup assessments have focused primarily on the use of ECRH.[7] The rf-assisted small-radius startup can be divided in three separate phases.

1. An extraordinary wave is first injected from the high field side to ionize and heat the electrons near the upper hybrid resonance (UHR) layer in the absence of toroidal current. The UHR layer, which is limited in volume, is deliberately placed toward the outboard side of the chamber to facilitate a small radius current initiation. Away from the UHR layer, a low temperature ($\sim$ a few eV) partially ionized plasma, produced by nonresonant rf breakdown of the prefill gas, is expected to fill the chamber (Sect. 2.2.1).

2. A low loop voltage is then applied to initiate the plasma current in the heated region over a relatively long time scale (0.2-0.8 s) to avoid the formation of plasma skin currents. The initial current channel is limited to $\lesssim$0.4 m in minor radius by a startup limiter at the outboard midplane until q_ψ reaches 3.2, the current baseline operating value (Sect. 2.2.2).

3. Additional supplementary heating (e.g., ICRF heating with a proton minority) is then introduced as the minor radius and the plasma current are increased while holding q_ψ = 3.2 and reducing the plasma major radius. This supplementary heating minimizes resistive loss of volt-seconds and allows a relatively slow current ramp-up in the remainder of the current startup phase (Sect. 2.2.2).

2.2.1 Electron Heating and Confinement Prior to Current Initiation

Extraordinary wave absorption and electron heating near the UHR region is particularly attractive because of its efficient energy transfer to the bulk electrons in a small volume. This mechanism relies on the condition:[8,9]

$$(\omega_{pe}^2/\omega_{ce}^2) \geq (kT_e/m_e c^2)^{1/2} \cos\theta ,$$

to avoid resonant interaction of the electrons at the cyclotron resonance. The extraordinary wave then accumulates near the UHR region and nonlinearly decays into electron Bernstein and ion-acoustic modes,[10] the former mode heating the electrons via Landau damping.[11] Experimental evidence of this highly efficient process in ISX-B has recently been obtained,[5] in consonance with earlier experimental indications.[12] Assuming an electron density of $n_e \simeq 10^{13}$ cm^{-3}, the UHR region can be located at R = 5.9 m if a frequency of 90 GHz is used for 8-T operation. The frequency scales to 113 GHz for 10-T operation.

Given an effective transfer of wave energy to the electrons near the UHR, a near classical electron and ion transport model is used to estimate the efficiency of electron heating[7] in the absence of plasma current. This UHR heating model contains the following elements:

1. Electrons are produced by ionization of neutrals and lost via curvature drift in the toroidal field and parallel drift in the poloidal error fields.
2. Electrons are heated by the rf power and cooled by losses due to ionization of neutrals, collisions with the ions, impurity radiation via corona radiation, and particle drift.
3. Ions are heated via collisions with the electrons and cooled by charge exchange and drift losses.
4. The radial extent of the heated electrons is estimated by the distance of Bohm diffusion in a drift time, given by the smaller of:

$$\Delta_H \simeq \begin{cases} 0.18\ (bR)^{1/2} \\ 0.43\ (b/\delta B)^{1/2} T_e^{1/4} \end{cases},$$

where cgs units are used with T_e in eV. Here b is the vertical half-height of the chamber at the radial location of the heated electrons and δB is the poloidal error field.

5. An ambipolar potential (with electric field $\vec{E}_{amb}$) at the conducting vacuum vessel, resulting from a preferential loss of the heated electrons, introduces an effective rotational transform via $\vec{E}_{amb} \times \vec{B}$ drift; this ambipolar potential and its benefits are tempered by the possibility of significant secondary electron emission at the vessel wall.

6. The plasma remains macroscopically quiescent.

The process of UHR heating and plasma sheath formation is depicted in Fig. 2-2. This generalized schematic shows a currentless tokamak plasma bounded by a continuous conducting poloidal limiter. The limiter provides a closed electrical path for the charge separation current and reduces the buildup of a large vertical electric field. In FED, the role of a conducting poloidal limiter is played by the conducting vacuum vessel itself, which provides the necessary circuit path.

The application of this model to the ISX-B conditions[5,7] has so far shown results consistent with the measurements of $n_e \sim 5 \times 10^{12}$ cm^{-3}, $P_{ECRH} \sim 80$ kW, T_e up to 50 eV, and a low level of impurity. This model has been applied to FED to assess the ECRH power requirement and its sensitivity to the uncertainties in temperature, error field δB, ambipolar potential Φ_{amb}, and the impurity content. The results are summarized in Table 2-2. It is apparent that low-Z impurity of a few percent can have a strong impact (a factor of 3) on the power requirement before the electron temperature is raised beyond the radiation barrier (at about $T_e \sim 20$ eV for oxygen). Furthermore, these results may be optimistic because of the assumption of the coronal radiation model.

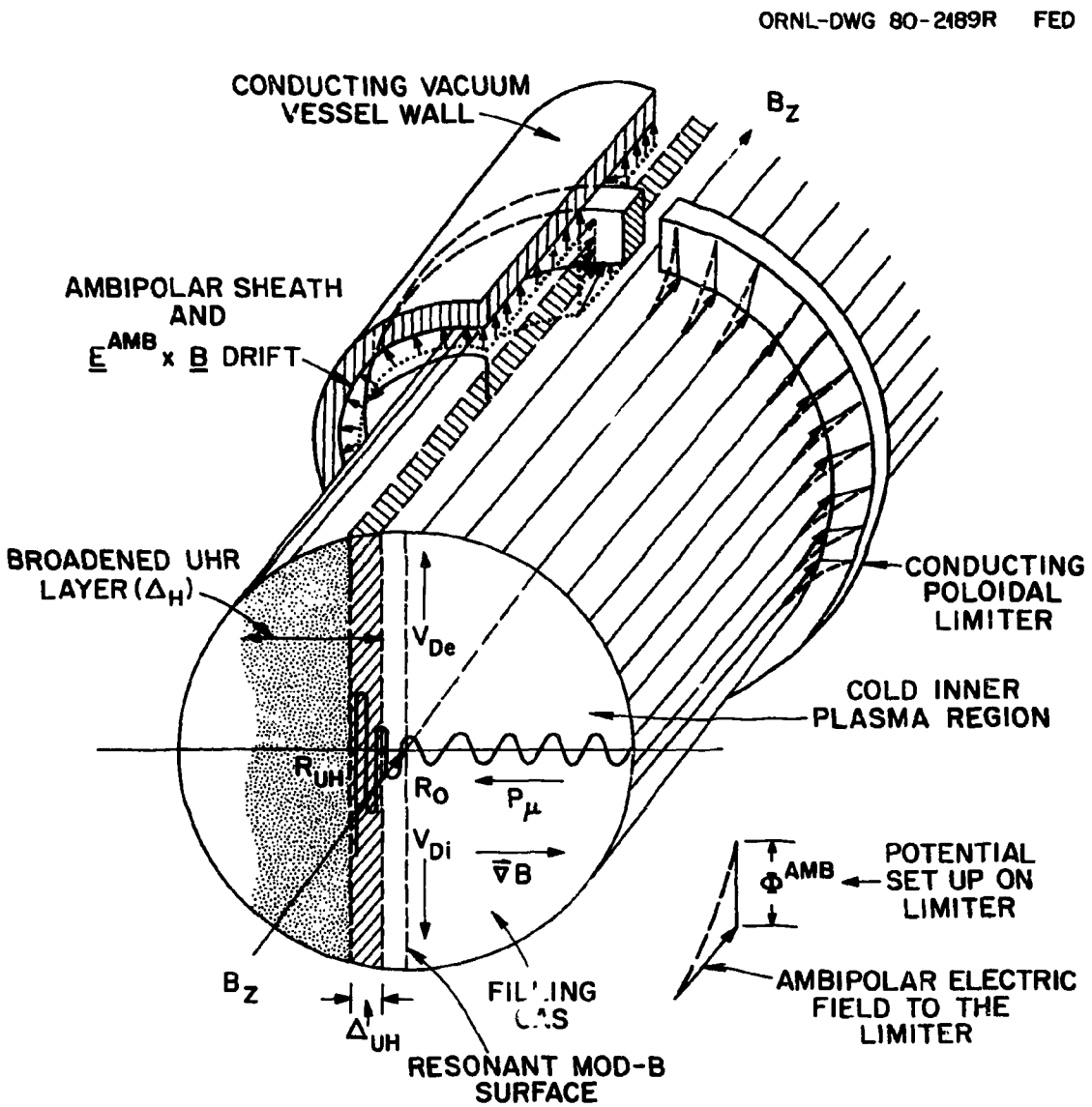

Fig. 2-2. Schematic illustration of electron heating near the UHR region prior to current initiation.

Table 2-2. Dependence of ECRH preheating power requirement P_{ECRH} on poloidal error field δB, T_e, the ambipolar potential ϕ_{amb}, and the impurity content in FED. The corresponding values for the electron parallel drift time, $\tau_{\delta e}$, curvature drift time, τ_{De}, and the radial extent Δ_H and volume V_H of the heated plasma are also indicated.

Parameters	Poloidal error field δB = 2G			Poloidal error field δB = 0		
T_e(eV)	20	100	200	20	100	200
T_i(eV)	∿20	92	144	∿20	94	154
$\tau_{\delta e}$(ms)	10	4.4	3.1	-	-	-
τ_{De}(ms)	430	87	43	430	87	43
Δ_H(cm)	6.5	10	12	42	42	42
V_H(m^3)	4.8	7.5	8.7	31	31	31
Φ_{amb}/T_e	-3.1→0	-2.7→0	-2.7→0	∿0	∿0	∿0
P_{ECRH}(MW)						
(1% oxygen)	0.44→0.46	0.15→0.50	0.48→1.65	2.8	0.31	0.98
(3% oxygen)	1.30→1.32	0.16→0.51	0.50→1.68	8.4	0.34	1.07

Once the radiation barrier is surpassed, the required P_{ECRH} is sharply reduced and is determined primarily by the collisional cooling of electrons with ions which in turn lose energy through charge exchange. The presence of a low error field can significantly reduce the confinement time ($\tau_{\delta e} << \tau_{De}$) and compete with cross field Bohm diffusion to bring about a large decrease in the heated volume. This results in only a modest decrease in loop voltage during current startup. Secondary electron emission from the walls can also lead to a deterioration of the ambipolar potential and an increase in P_{ECRH} by a factor of 2 to 3. With no error fields present, there is an improvement in confinement leading to $T_e \simeq T_i$, $\phi_{amb} \simeq 0$ and a factor of $\sim$4 increase in Δ_H. Because the volume of the heated plasma has increased by a factor of $\sim$6, oxygen losses can become quite prohibitive at $T_e \simeq 20$ eV. Finally, for $\phi_{amb} \sim 0$, a continuous conducting limiter or vacuum vessel becomes essential to prevent the buildup of a large vertical electric field.

These results suggest the following approach to electron heating prior to current initiation. In the presence of a low poloidal error field ($\sim$2 G), ECRH power up to 2 MW is injected to burn through the impurity radiation barrier in the UHR region, achieving $T_e \gtrsim 100$ eV. The initial heating volume, estimated to be about 5 m^3, would be produced in a time scale <50 ms. Then the error field would be eliminated near the heating zone to allow it to increase to about 30 m^3 in volume. The ECRH power can then be reduced to about 1 MW, sustaining T_e in the range of 100 eV to 200 eV at a density of about 10^{13} cm^{-3}.

2.2.2 Current Initiation and Ramp-up

The UHR electron heating just discussed leads naturally to the formation of a small radius current channel at the UHR layer. A relatively low voltage can be applied through programmed current ramps in the ohmic heating and the blip coils to raise the plasma current to 0.17 MA so that $q_\psi = 3.2$ at the plasma edge. During this process, the small radius (a = 0.4 m) is maintained at R = 5.9 m against startup limiters at the outboard midplane. For comparison, calculations have also been done for a smaller startup radius plasma (a = 0.2 m). The time duration

is approximately 0.8 s (0.2 s) for the a = 0.4 m (0.2 m) case. This time scale satisfies the constraint $\tau_I (= I_p/\dot{I}_p) > \tau_s$ (the plasma skin time = $\mu_o a^2/\eta \propto T_e^{3/2} a^2/Z_{eff}$) to avoid the formation of skin currents and the potential hazards of plasma disruption.[13] A power of about 1 MW is maintained (at 87 GHz for a = 20 cm and 90 GHz for a = 40 cm) to ensure proper electron temperature during current initiation.

Having achieved the initial current channel, the major radius is then compressed to permit an increasing minor radius and plasma current while maintaining a constant q_ψ. Additional supplementary heating ($\sim$4 MW) can be introduced to ensure adequate temperature and permit a relatively slow current rise process using only low voltage. It appears that ICRF at 54 MHz injected from the low field side to heat a deliberately introduced proton minority is a convenient option.

To assess the voltage and flux requirements during current initiation and ramp-up, the plasma temperature needs to be estimated. A relatively simple single-species power balance model has been used for this purpose.[7] In particular, we use the following relationship,

$$3n_e k\, T_e V_p/\tau_E = P_{oh} + P_{rf} - P_{ion} - P_{cx} - P_{rad} ,$$

with the following major assumptions:

1. The current rise time is much larger than the energy confinement time τ_E (based on Alcator scaling) to permit the use of the above steady-state equation.
2. Two times the Spitzer resistivity is used in the evaluation of plasma resistance and ohmic heating power P_{oh}.
3. The ECRH and ICRF power P_{rf} is completely absorbed.
4. The density buildup is limited to below the Murakami limit for plasma disruption avoidance.[14]
5. Radiation power loss P_{rad} is based on a uniform oxygen distribution and coronal radiation.

6. Charge exchange, ionization and radiation losses, P_{cx}, P_{ion}, and P_{rad}, are insignificant compared to transport losses with successful electron heating prior to current startup ($T_e \gtrsim T_i \sim 100$ eV, $n_e \sim 10^{13}$ cm^{-3}, and a = 20-40 cm).

In estimating the applied voltage requirements, the controllable parameters are assumed to be the ECRH/ICRF power and the plasma current, density, and elongation. By specifying the plasma current, rather than the applied voltage, the differential equation describing the current evolution is used to determine the time history of the plasma loop voltage. Specifically we have

$$V_\ell = R_p I_p + d/dt\ (L_p I_p) \ ,$$

where the plasma inductance is approximated by

$$L_p = \mu_o R[\ell n(8R/a\sqrt{\kappa}) + \ell_i/2 - 2] \ ,$$

and ℓ_i, determined from the flux-related definition of the internal inductance,[15] has a value of $\sim$1 for broad current profiles. The instantaneous major and minor radii during the constant q_I expansion phase are determined from the expression for the plasma current

$$I_p = \pi a^2 B_t (1 + \kappa^2)/\mu_o q_I R \ .$$

Other relations utilized in these calculations are (da/dt) = -(dR/dt), $R_{\ell im} = 6.3 = R(t) + a(t)$, and $B_t = B_t[R(t)]$. Starting from a reasonable $I_p(t)$, these equations can be used to determine T_e, P_{oh}, V_ℓ, V_{res}, and the resistive flux expenditure $\Delta\Phi_{res}$. The results are summarized in Table 2-3, showing the time-dependence of startup requirements on the oxygen impurity content, initial minor radius, and the electron requirements on the oxygen impurity content, initial minor radius, and the electron temperature prior to current initiation. Typical examples are also depicted in Figs. 2-3, 2-4, and 2-5.

Table 2-3. Dependence of startup requirements on initial plasma minor radius a_o, oxygen content n_{ox}/n_e, and electron temperature before current initiation $T_e(t \cong 0)$

Assumptions						
a_o (m)	0.4	0.2	0.2	0.2	0.2[a]	0.2[b]
$\xi = n_{ox}/n_e$ (%)	0	0	1	3	3	3
$T_e(t = 0)$ (eV)	100	100	100	100	20	10
Requirements						
Maximum V_ℓ (V)	10	18	20	25	70	130
at time (s)	2	0.2	0.2	0.2	0.04	0.01
Resistive induction flux loss $\Delta\Phi_{res}$ (Wb)	11.5	10	13.2	18.2	20	45

[a] Without successful electron heating prior to current initiation (T_e < 20 eV at t = 0.015) but with P_{ECRH} = 1 MW for $t \geq 0$.

[b] Without rf-assist prior to and throughout startup assuming an initial T_e of 10 eV at t = 0.01 s.

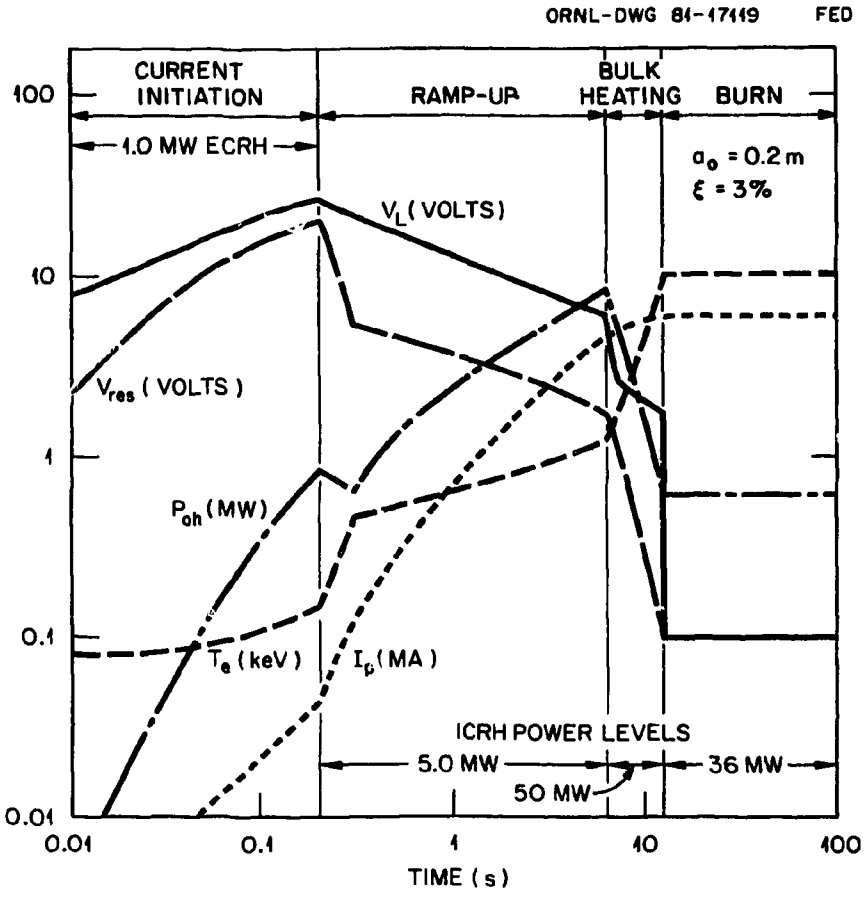

Fig. 2-3. Time behavior of I_p, T_e, P_{oh}, V_ℓ, and V_{res} in FED during an expanding radius startup (from a = 0.2 m) with electron preheating and rf assist for 3% oxygen impurity.

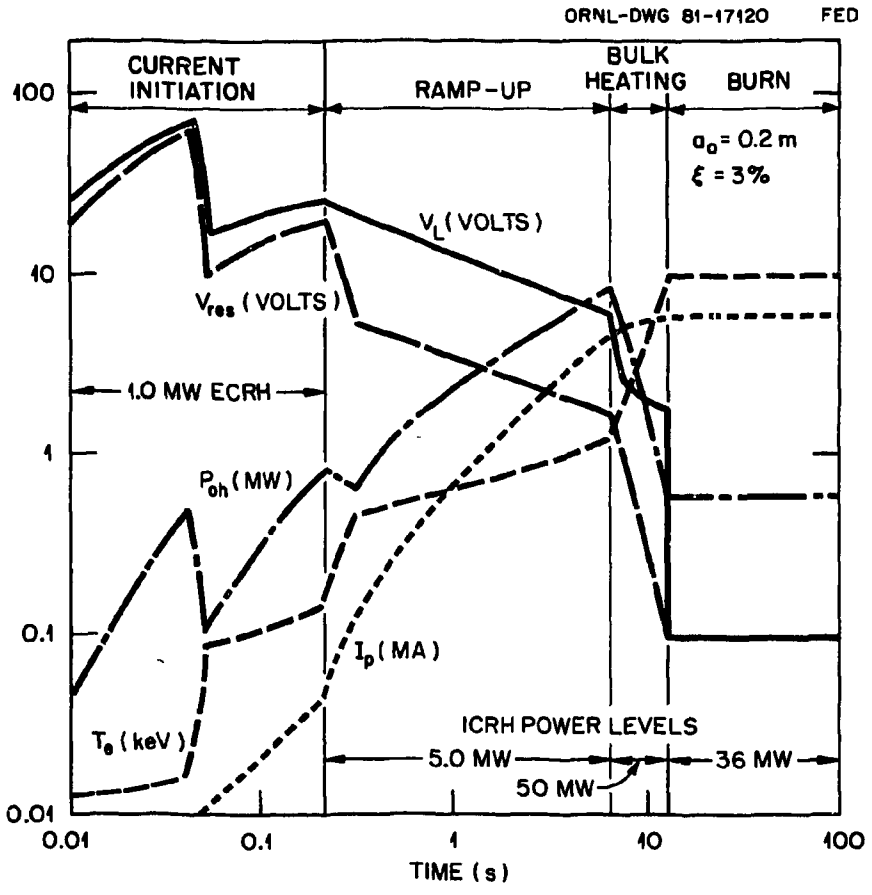

Fig. 2-4. Time behavior of I_p, T_e, P_{oh}, V_ℓ, and V_{res} in FED during an expanding radius startup as in Fig. 2-3 but without preheating. The behavior is identical to that shown in Fig. 2-3 after 50 ms.

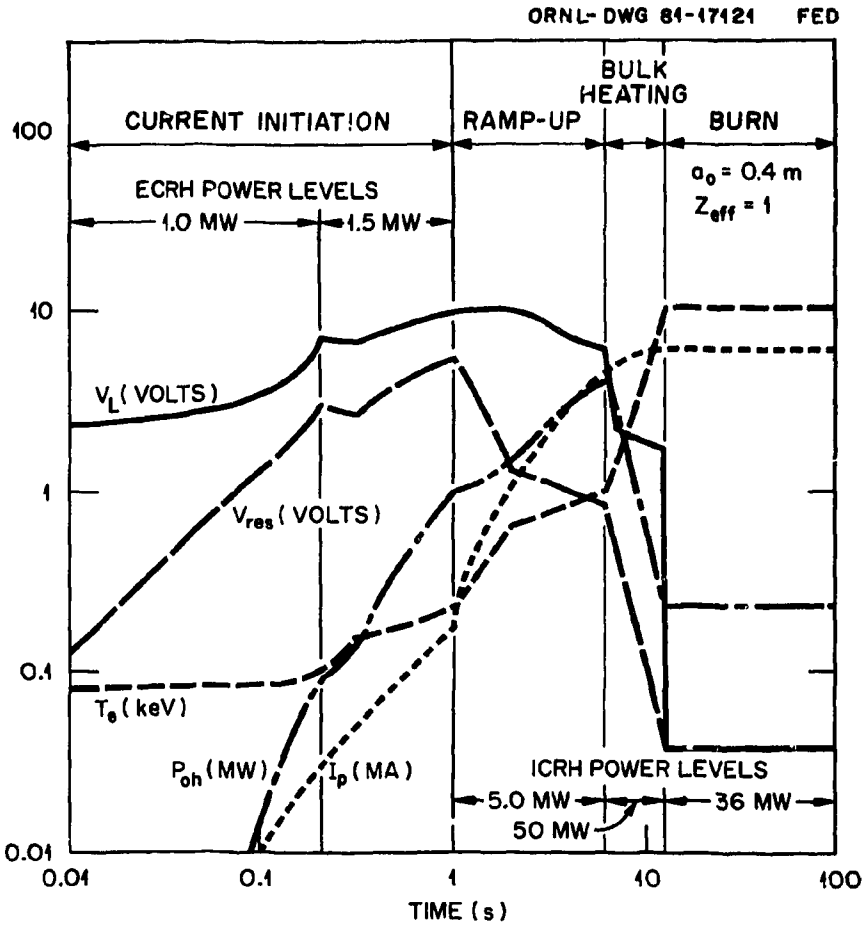

Fig. 2-5. Time behavior of I_p, T_e, P_{oh}, V_ℓ, and V_{res} in FED during an expanding radius startup as in Fig. 2-3 but with initial radius of 0.4 m and no oxygen impurity (Z_{eff} = 1).

The following conclusions can be drawn:

1. With electron heating prior to current initiation, the maximum V_ℓ during current startup remains below 25 V with up to 3% oxygen content.

2. With continued auxiliary heating at a level somewhat above P_{oh}, the resistive loss of induction flux $\Delta\Phi_{res}$ can be limited to below 20 Wb with up to 3% oxygen content. Given that the oxygen content can be limited to about 1%, $\Delta\Phi_{res}$ can be assumed to be 13 Wb for the baseline design.

3. Increasing the initial minor radius from 0.2 m to 0.4 m results in about a 50% reduction in the maximum V_ℓ and a small increase in $\Delta\Phi_{res}$.

4. The impact of not heating T_e beyond 20 eV (the impurity radiation barrier) prior to current initiation is to sharply increase the maximum V_ℓ requirement. An initiation voltage below 25 V would then fail to ramp up the plasma current, even in the presence of some rf-assist during current rise. The impact of no rf-assist prior to and during current rise is to raise the maximum V_ℓ above 100 V and more than double $\Delta\Phi_{res}$.

2.2.3 Summary

Our startup assessments suggest that the injection of extraordinary mode electron cyclotron waves from the high field side can be an effective method of electron heating in a small volume prior to current initiation. With $n_e \sim 10^{13}$ cm^{-3} and up to 3% oxygen content, no more than 2 MW of ECRH power at 90 GHz is needed to achieve $T_e \simeq$ 100-200 eV in a volume of about 5 m^3 near the UHR layer. A relatively low level of poloidal error field ($\sim$2 G) is required in the heating region.

The ECRH power can be reduced to about 1 MW during current initiation (with T_e maintained around 100 eV) without introducing serious skin currents. For an initial minor radius of 0.4 m, a time scale of about 0.8 s is required to reach I_p = 0.17 MA and q_ψ = 3.2. The auxiliary

heating power is then raised to about 5 MW (via ICRF) to assist the relatively slow buildup of the plasma cross section to a = 1.3 m, κ = 1.6, and the plasma current to 4.8 MA in about 5.2 s.

Although a maximum V_ℓ close to 10 V has been indicated under relatively ideal conditions, V_ℓ is specified to be 25 V to account for uncertainties in impurity content and the control of the initial minor radius. The resistive loss of induction flux has been estimated to be about 13 Wb to account for the slow current rise and a modest impurity content ($\sim$1% oxygen).

In view of its large impact on the design of FED, experimental and theoretical efforts are continuing to further elucidate the potential benefits of the rf-assisted startup process.

2.3 ICRF HEATING FOR FED

D. Q. Hwang, J. C. Hosea, D. Mikkelsen, D. E. Post, C. E. Singer — PPPL

The use of ICRF in FED for bulk ion and electron heating, as well as possibly for current drive, impurity control, and startup assist, offers several technological advantages over neutral beams. In the ion cyclotron range of frequencies (ICRF), typically from 10 to 200 MHz, high efficiency rf sources are commercially available. These sources can be placed away from the high radiation zone of FED, and the rf power can be delivered to the wave launcher through existing transmission systems.

Recent ICRF heating experiments on PLT,[16] TFR,[17] and JFT-2[18] have demonstrated both ion and electron heating with good efficiency for several heating schemes that are relevant to FED applications. In the minority ion regimes, where the charge to mass ratio of the minority species is greater than the majority species, strong ion heating is observed with rf power preferentially coupled to the minority ions which in turn heats the bulk plasma through collisions. Some electron heating has also been observed in these experiments. The minority heating scenario can be used on FED during both the startup phase of the discharge and the burn phase if a sufficiently high concentration of the particular minority is employed.

Once the plasma beta has reached an elevated level, harmonic heating can be employed. Fixed frequency systems can be used in FED for both minority and second harmonic heating schemes, given suitable control over the minority concentration. Efficient second harmonic heating has been demonstrated on PLT and on other tokamaks in hydrogen plasmas. Bulk ion heating efficiencies comparable to those for the hydrogen minority case have been achieved. Even higher harmonic heating is of considerable interest for FED since such heating becomes quite efficient at high beta and offers the possibility of using waveguide launchers due to the higher frequencies. In Sect. 2.3.1 the various possible heating scenarios for FED are discussed. Section 2.3.2 discusses the theoretical extrapolation of ICRF heating to FED based on experimentally compatible wave theories and FED baseline design transport models.

2.3.1 ICRF Heating Modes on FED

The FED ICRF task force[19] has suggested the following ICRF heating regimes based on promising experimental heating results and favorable launcher options.

The recommended ion heating mode for a driven FED at present using waveguide launchers is second harmonic deuterium (f = 54 MHz, $\lambda/2$ = 2.8 m for the 8-T operation) starting with fundamental proton minority. This regime is suitable for both second harmonic and minority cyclotron heating for the projected FED parameters. Secondary choices for 8-T operation using either waveguide or loop launchers which may be equally viable are:

- second harmonic tritium (f = 36 MHz, $\lambda/2$ = 4.2 m) with fundamental ^{3}He minority;
- third harmonic deuterium (f = 81 MHz, $\lambda/2$ = 1.9 m);
- fundamental deuterium (f = 27 MHz, $\lambda/2$ = 5.5 m); and
- second harmonic ^{3}He minority (f = 72 MHz, $\lambda/2$ = 2.1 m).

^{3}He minority heating could facilitate startup, current drive, and bulk heating whereas the higher harmonics allow the use of simple waveguides. Also it is generally preferred to heat the reacting species, and in particular, D and/or T, to optimize the fusion energy output for FED.

As to the wave launchers, the task force report recommended keeping the options of loop antennae, waveguide, and ridged waveguide open, pending further development and testing of the waveguide couplers. In addition, the various tasks envisioned for ICRF such as bulk heating, current drive, impurity control, etc., may require specialized launching structures.

2.3.2 Wave and Transport ICRF Modeling for FED

The theoretical treatment of the ICRF heating on FED is divided into five parts: (1) wave coupling from the launcher, (2) wave penetration in the plasma, (3) wave absorption by the various plasma species, (4) the energy distribution of the heated species, and (5) transport modeling of the plasma heating.

Wave coupling

The launcher coupling efficiency is estimated employing the cold plasma field model for the loop antennae used in present-day experiments. Coupling efficiency calculated for the assumed density profiles of FED is found to be over 95%. Similar coupling efficiency has also been found for a rectangular waveguide coupler using a single path wave absorption model. Since the coupling calculation is mainly critical to launcher design, it is assumed conservatively in these transport calculations that 80% of the power generated at the rf source is transmitted to the plasma.

Wave penetration

The dominant poloidal modes for the loop antennae are $m = 0, \pm 1$; the toroidal modes are centered around $N = 10$. The power spectrum of the antenna is calculated from the antenna current configuration. The path of the wave energy flow from the antennae and the amplitude of the electric field of various polarizations are obtained from cold plasma ray tracing theory. A tracing code using the finite temperature fluid model has been developed at Princeton;[20] however, the results have not been incorporated as yet into the transport calculations.

Wave absorption

The 1-D hot plasma WKB dispersion theory is used to calculate the effects of plasma temperature on the wave polarization and damping along the ray trajectory. So far only the minority heating scheme has been treated in the Baldur transport code[21] where it is assumed that the bulk D-T plasma contains a small concentration (<10%) of ^{3}He ions which absorbs nearly all the rf wave energy. The energy distribution of the minority ^{3}He ions is calculated using Fokker-Planck theory with the proper quasi-linear rf diffusion operator.

Energy deposition

Since the wave-particle interaction time is much shorter than any transport time in FED, the steady-state distribution of the minority ions is used to obtain the power exchange between the minority ions and the background ions and electrons. The power transfer between species is assumed to be time independent and calculated from the initial plasma temperature. This assumption is only meaningful when the minority distribution remains much hotter than the background plasma throughout the heating pulse. Moreover, the wave power deposition profile is more peaked for the initial cooler plasma than the rf heated plasma. Therefore, the power deposition profile used here is an average obtained between the initial and final plasma temperature profiles.

It should be emphasized that the results from these preliminary time independent calculations must be confirmed by the time dependent rf power deposition code which has been completed recently and will be interfaced with the Baldur transport code in the near future. With the steady-state assumption for the wave deposition, the heating results are generated from the one-dimensional transport code, Baldur.

A peaked rf power deposition profile for the fast magnetosonic wave in the minority regime is obtained from the wave theories as well as observed in recent PLT[16] and TFR[22] experiments. This peaked deposition profile results from the combined effects of the wave focusing and the wave damping profile. The direction of the wave energy flow in the plasma is determined by the focusing effects of the launchers and the

refractive properties of the plasma density profile. To obtain a peaked deposition profile in FED, it is essential to design launchers with strong poloidal focusing properties. The wave damping region is a vertical layer in the vicinity of the ion cyclotron layers and a function of the plasma temperature profile. For the FED baseline parameters and profiles, over 85% of the wave is absorbed for one pass of the wave through the damping zone. The centrally peaked deposition produces quite efficient plasma heating where the confinement is optimal; however, it should not be made so peaked that the power density in the central region is high enough to push the minority distribution into a quasi-linear plateau. To keep the ion and electron temperature within the limits of the steady-state approximation, i.e., the background plasma temperature is much lower than the effective temperature of the minority distribution, the input power is chosen to be 40 MW (or 32 MW into the plasma), and the deposition profile used is broader than that calculated from wave theory using the initial plasma profiles (Fig. 2-6).

Transport modeling for 10-T operation

The transport model used in the plasma heating simulation is applied to the assumed FED parameters for 10-T operation. The electron density is held constant at 1.3×10^{14} cm^{-3} (volume averaged) and the ion mixture is assumed to be 45% D, 45% T, and 10% ^3He by electron displacement. Particular contributions of the minority ^3He distribution to the plasma conditions such as the additional $<\beta>$ due to the 14.7 MeV protons resulting from D-^3He reactions are not included in the transport model. Moreover, impurity transport, ripple effects, and scrape-off models are not in the present calculation; however, all of these effects are presently being considered.

The electron thermal conductivity, χ_e, is taken to be $\sim 5 \times 10^{17}/n_e$ and $D_e = \chi_e/5$. The ion thermal conductivity is assumed to be twice neoclassical, and Z_{eff} is assumed to be 1.5. The Baldur code does not include ballooning limits, so $<\beta>$ is allowed to continually increase, but generally in these calculations $<\beta>$ is below $\sim 4\%$. At the projected FED density, the electron and ion coupling is sufficiently strong that their temperature remains roughly equal throughout the discharge.

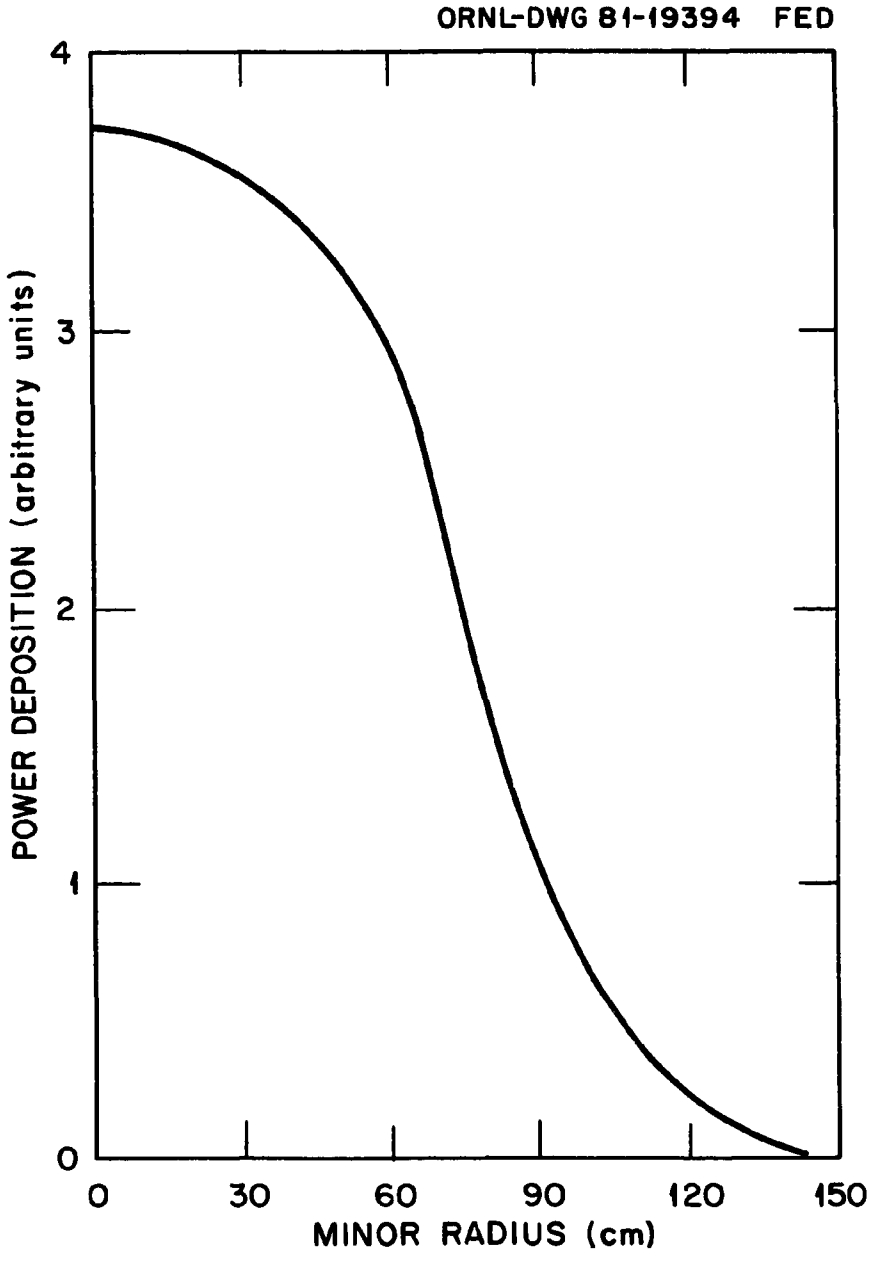

Fig. 2-6. RF power deposition profile obtained from wave theory and used in Baldur transport code. This profile corresponds to 45% D, 45% T, and 10% ^{3}He by electron displacement.

With the above assumptions, the results of the transport simulations for various rf power levels and pulse durations are shown in Figs. 2-7 through 2-11. The primary consideration addressed here is the rf requirement to bring FED to ignition. The ignition criterion used in these analyses is that the rate of increase in plasma energy exceeds the rf input power in the central half of the plasma volume.[23] Ignition can be approached from two directions, either through minimizing the rf pulse at fixed input power or minimizing the rf power at fixed pulse length. These two scenarios are studied using an rf power requirement of up to 40 MW (32 MW in plasma) corresponding approximately to the FED baseline level of up to 6 s.

Figures 2-7 and 2-8 show the heating results for a fixed input power of 32 MW with three different pulse lengths. Ignition, as defined above, is achieved with an rf pulse length of ∿4.25 s. At the ignition point, the volume averaged toroidal $\langle\beta\rangle$ is approximately 3.3% and the central electron and ion temperatures are about 17 keV.

To obtain the minimum rf power required to achieve ignition, a 6-s pulse is applied for various power levels from 24 MW to 28 MW into the plasma. Figure 2-9 shows the time evolution of the plasma β for three different power levels. The time evolution of the ion temperature profile for a subignition case (26 MW) is shown in Fig. 2-10. Ignition in Fig. 2-9 is reached with approximately 27 MW at $\langle\beta\rangle \sim 3.3\%$, and the central ion and electron temperature is again roughly 17 keV (Fig. 2-11).

It is emphasized that these results are obtained with a steady-state rf heating model and a conservatively broad deposition profile. More refined time-dependent wave and transport modeling is under way and should give more realistic predictions for FED. Moreover, a range of transport models will be studied to bound the rf requirements.

2.3.3 Discussion and Conclusions

The feasibility of eventual reactor application for ICRF will be determined by the physics of plasma heating, current drive, impurity control, and startup assist as well as the technological development of radiation hardened wave launchers. The major physics questions are

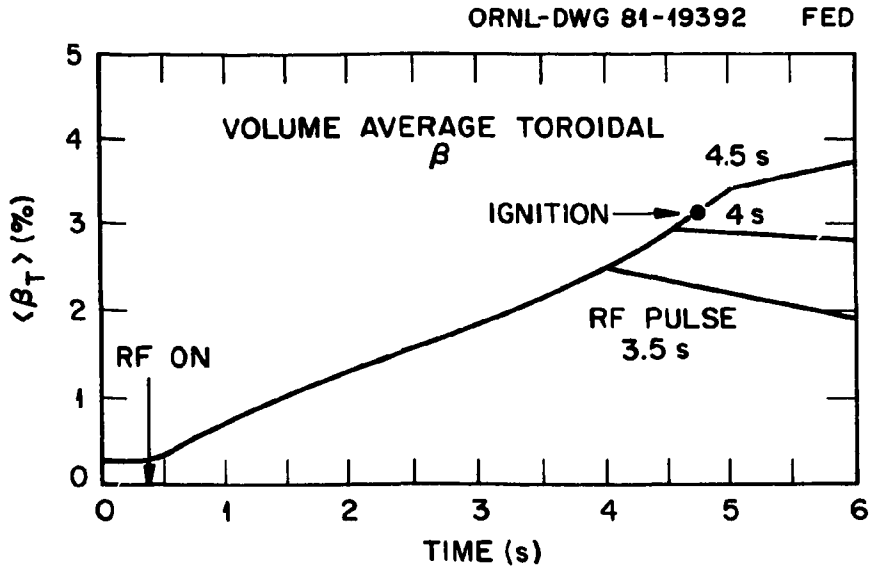

Fig. 2-7. Volume average β for 32 MW of rf power at various pulse length.

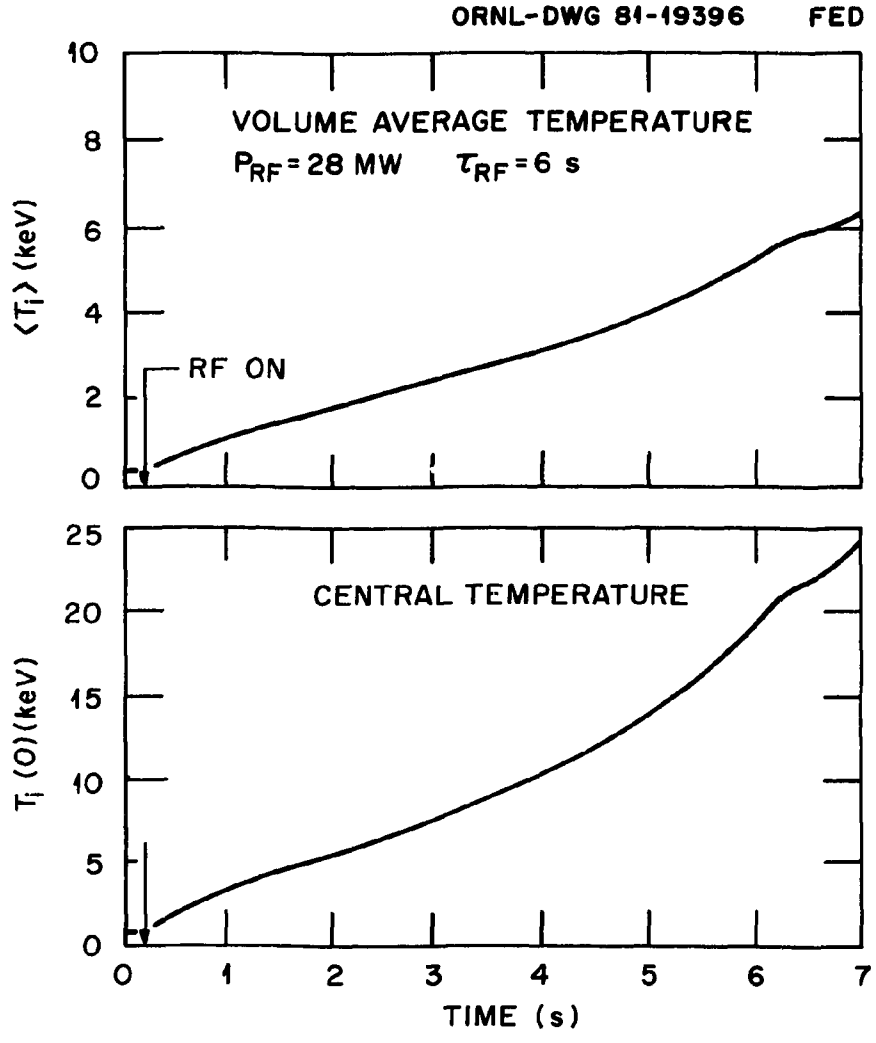

Fig. 2-8. Volume average and central ion temperature for 32 MW of rf power at 4.5 s pulse.

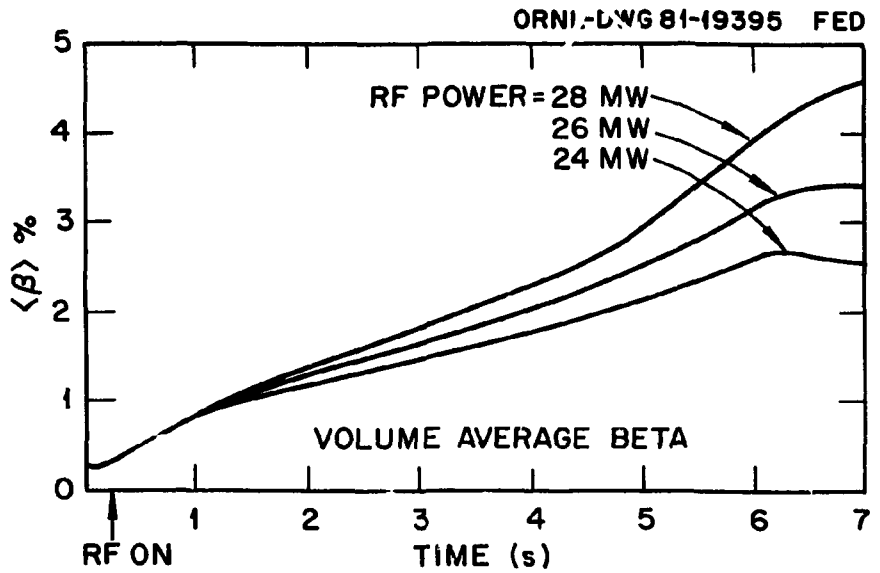

Fig. 2-9. Volume averaged β for a 6-s pulse at various power levels. Ignition is reached at approximately 27 MW.

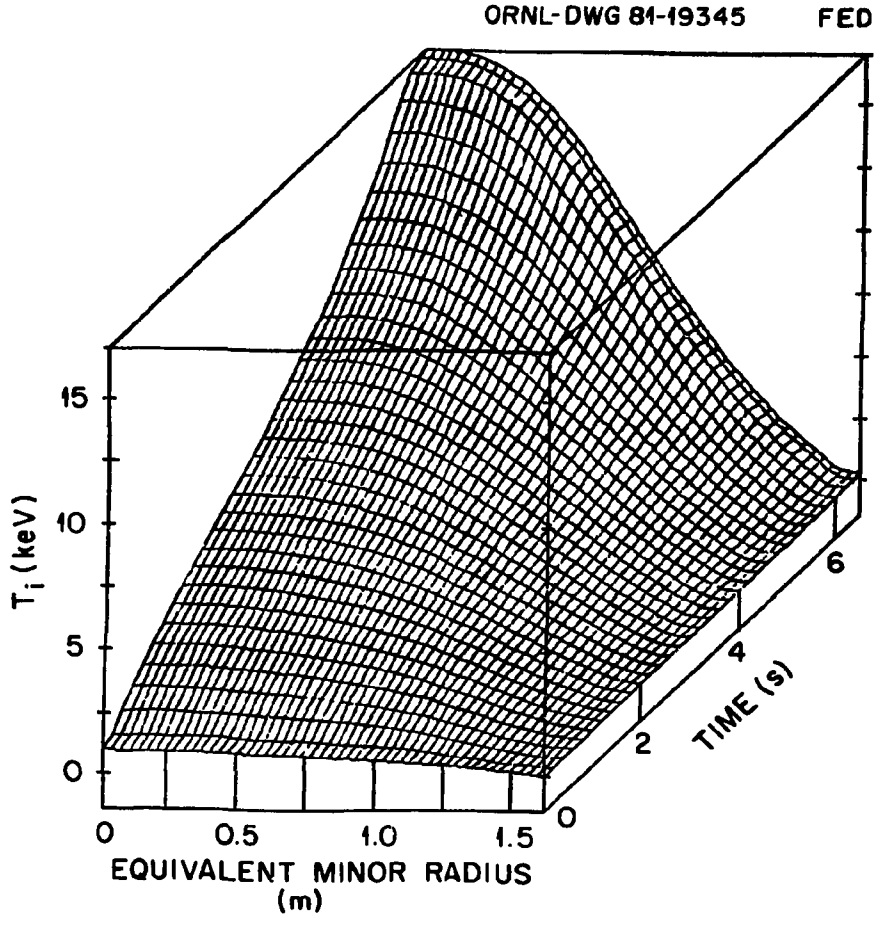

Fig. 2-10. Evolution of ion temperature profile for the 26-MW case shown in Fig. 2-9.

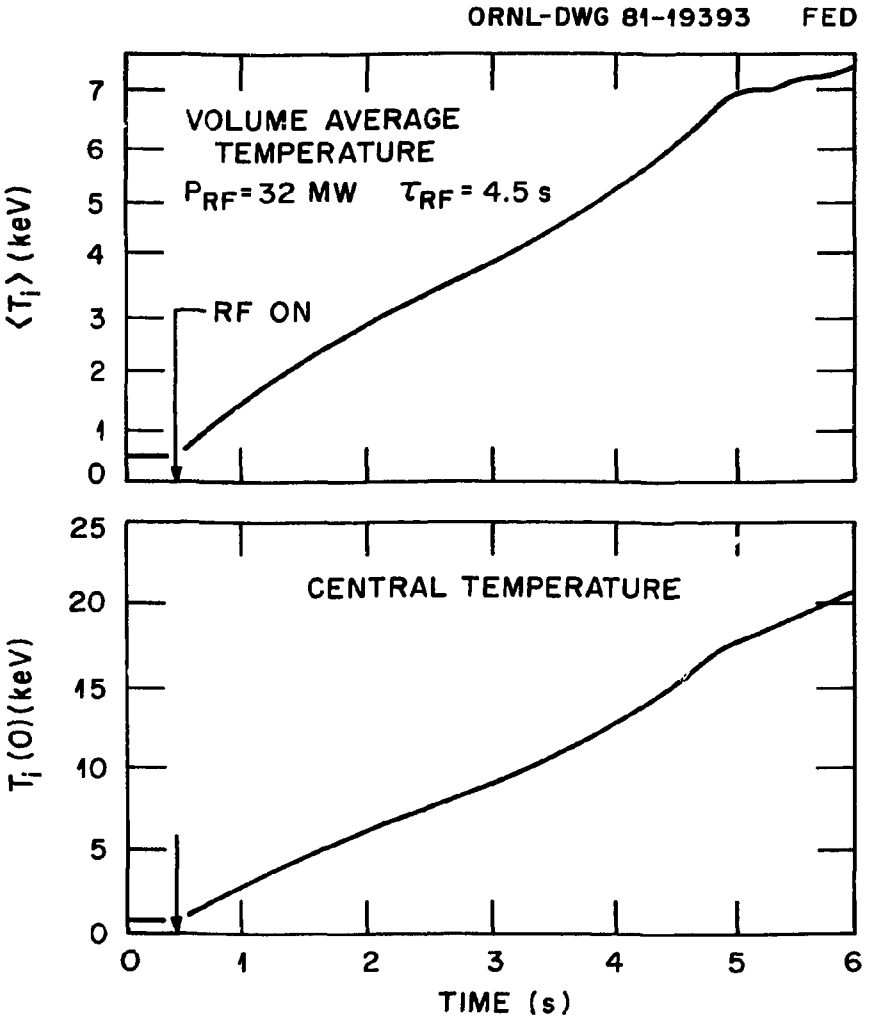

Fig. 2-11. Volume averaged and central ion temperature for a 6-s rf pulse at 28 MW.

currently being addressed on existing devices, notably PLT and TFR. The reactor technology development must be implemented on present-day devices (PLT, D-III, etc.) and near-term devices such as TFTR to provide a reliable ICRF heating option for the conditions in FED. Theoretical extrapolation of near-term experimental results will be used to choose the optimal ICRF heating scheme and wave coupler for FED.

2.4 PLASMA PERFORMANCE MODELING WITH NEUTRAL BEAM INJECTION

W. A. Houlberg — ORNL, S. E. Attenberger — ORNL/FEDC, and L. M. Hively — GE/FEDC

Relative to rf heating, neutral beam heating has a significantly more developed physics basis for application to FED, and hence remains a strong contender for bulk heating. Comprehensive beam heating calculations have therefore been performed for FED parameters which reveal not only the tradeoffs involved in determining beam energy and power requirements but also the sensitivity of FED performance to variations in the physics.

Determination of the supplementary heating power for steady-state operation of the plasma over a range of densities and temperatures with self-consistent profiles requires a level of detail that can only be obtained with 1-D or 1-1/2-D time dependent transport codes. Traditionally it has been difficult to extract enough information from such codes to make comprehensive parameter surveys worthwhile. A new method of analysis is presented below in Sect. 2.4.1 which simplifies comprehensive reactor physics studies using a 1-1/2-D transport code. This method is then applied to a reference FED case (Sect. 2.4.2) for the purpose of examining the physics of D-T operation and neutral beam heating. Optimization of neutral beam heating during startup is discussed (Sect. 2.4.3) along with issues concerning beam energy and species mix for positive ion based systems (Sect. 2.4.4). Finally, variations are made in the reference case to examine the sensitivity to uncertainties in the transport model (Sect. 2.4.5), the potential for 10-T operation (Sect. 2.4.6), the impact of pellet fueling coupled with low recycle poloidal divertor operation (Sect. 2.4.7), and heating requirements with an idealized heating source profile which may provide guidance for future rf heating studies (Sect. 2.4.8).

2.4.1 The POPCON Method of Analysis

A method has recently been developed which provides reactor design physics information in concise form from a set of 1-1/2-D time-dependent transport simulations.[24] Figure 2-12 illustrates the way the WHIST transport code[25] is forced to scan density and temperature space. Several time-dependent calculations are made, each at a constant volume-averaged density, and each with the average temperature defined in Fig. 2-12 slowly increasing in time through feedback on the supplementary heating. If the simulation time, t_{max}, is much longer than the particle and energy confinement time scales, the plasma profiles, and particle and energy loss terms remain at or near steady-state values at all times. A simulation of 40-80 s has been found to meet this criterion for typical FED conditions while the density-weighted average of the electron and ion temperatures is linearly ramped to 20 keV. At selected points in average density and average temperature space, we can then evaluate all the global parameters with self-consistent profiles and generate contours of constant supplementary beam power, plasma beta, fusion power output, etc., for comprehensive parameter surveys. We call this set of plots Plasma OPeration CONtour (POPCON) plots. These POPCON plots provide guidance for determining the potential operating regime for the plasma, the relationship between ignited and driven operation, and optimal startup sequences for supplementary heating by neutral beams with a given set of physics models. The effects of variations in the physics models and neutral injection parameters can also be examined.

2.4.2 The Reference Physics Model

The machine parameters and physics models for the reference FED case are summarized in Table 2-4. The neoclassical transport model is from Hinton and Hazeltine.[26] Anomalous contributions to electron energy confinement and particle diffusion dominate the neoclassical contributions using a model with $\chi_e = 5.0 \times 10^{17}/n_e(r)$ cm^2/s. This model has been chosen[27] because of its wide use in both INTOR and FED as a reference for various physics studies. At average ion temperatures

ORNL–DWG 81–3457 FED

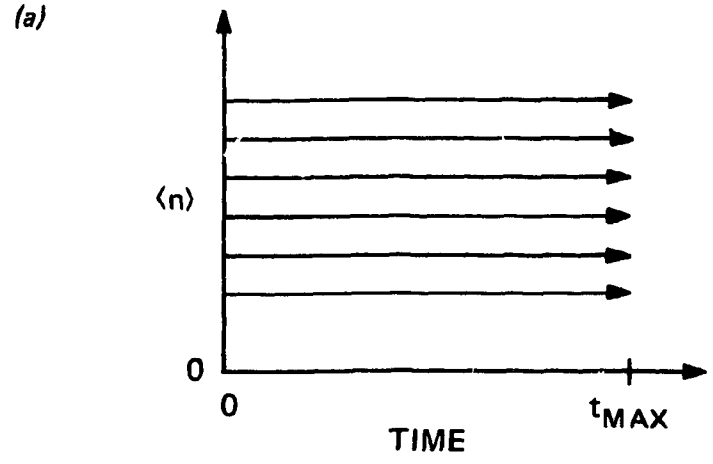

$$\langle n \rangle = \frac{\int n_e dV}{\int dV}$$

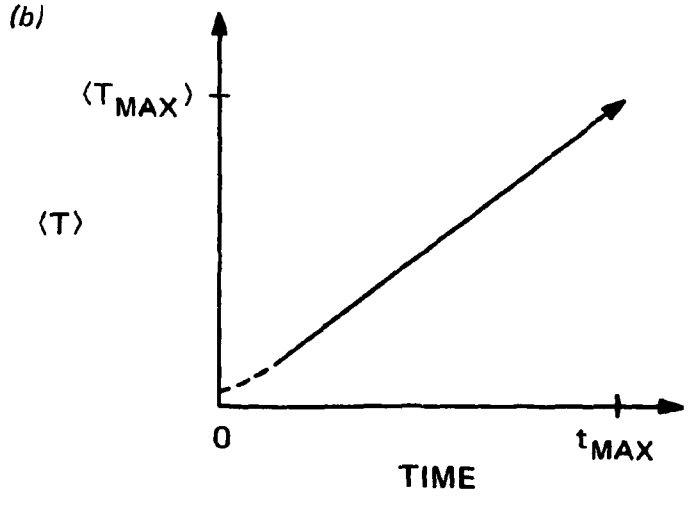

$$\langle T \rangle \equiv \frac{\int (n_e T_e + \sum_j n_j T_i) dV}{2 \int n_e dV}$$

Fig. 2-12. To force a 1-1/2-D time-dependent transport code to scan a prescribed range of <n>-<T> space, a) the average density for each sweep is maintained constant by feedback on the gas or pellet fueling source while b) the average temperature is linearly increased by feedback on the supplementary heating source.

Table 2-4. FED base parameters and models used in analysis

		Parameters
R_o	= 500 cm	— Major radius
a_o	= 130 cm	— Minor radius in midplane
a_{so}	= 10 cm	— Scrapeoff thickness in midplane
b_o/a_o	= 1.6	— Elongation
c_o/a_o	= 0.3	— Triangularity
B_{To}	= 3.6 T	— Vacuum toroidal field at R_o
$q_\psi(a_o)$	= 3.2	— Safety factor at a_o
$\delta(a_o)$	= 0.7%	— Peak-to-average ripple at a_o
N_c	= 10	— Number of TF coils
E_o	= 150 keV	— Deuterium beam energy
$P_1:P_{1/2}:P_{1/3}$	= 80:12:8	— Species mix by power at source
R_B	= 360 cm	— Beam tangency radius
		Models
Scrapeoff		— Toroidal limiter
Fueling		— Gas puffing and recycle at limiter
Electron energy confinement		— $\chi_e = 3.0\ \chi_e^{NC} + \chi_e^{ANOM}$
Ion energy confinement		— $\chi_i = 3.0\ \chi_i^{NC} + \chi_i^{RT} + \chi_i^{RP}$
Particle confinement		— $D = 3.0\ D^{NC} + 0.2\ \chi_e^{ANOM}$
Beam neutralization		— Ideal equilibrium fraction
Impurities		— None

$\langle T_i \rangle$ above 8 keV, ripple trapping[28] and ripple plateau[29,30] dominate the ion thermal conduction losses. The MHD equilibrium is solved with a variational moments method.[31] Increases in ripple conduction losses and improved neutral beam penetration due to an outward shift of the flux surfaces at high beta are included in the analysis. The species mix delivered to the plasma is obtained from the equilibrium neutralization fraction[32] for positive deuterium ions and is plotted in Fig. 2-13 and thus represents an idealization of the system. The rapid decrease in neutralization efficiency for deuterium between 100 keV and 200 keV (i.e., from ∿53% to ∿19%) is an important factor in the choice of beam energy which will be discussed later.

Figure 2-14 shows the supplementary beam power contours for the FED reference model. The anomalous electron conduction losses are dominant for $\langle T \rangle \lesssim 8$ keV. This electron conduction model, when applied to current experiments operating with low impurity levels and low beta, leads to losses which are high by about a factor of 2. These results can therefore be viewed as conservatively pessimistic regarding electron losses, although optimistic in the sense that there are no impurities and there is no degradation of confinement with increasing beta. At higher temperatures, ripple conduction losses dominate because of a combination of low collisionality and shift of the plasma to regions of higher ripple with increasing beta. Large amounts of power are required to maintain the plasma in the low density regime because of a lack of fusion heating. Boundary layer[33] and low collisionality corrections[34] to the neoclassical ripple losses could significantly change these contours, however. The relatively low current, high q(a) assumption leads to increased ion ripple conduction losses in the region $\langle T \rangle \gtrsim 8$ keV. At high density and low temperature, beam penetration is reduced leading to an increase in the beam power requirements. As the temperature increases at high density, fusion alpha heating takes over and ignition can be reached in this case at an average density of about 1.3×10^{14} cm^{-3}.

The saddle point and the local minima in density of the power contours of Fig. 2-14 outline the thermally unstable region, i.e., $\partial P_B / \partial T \,|_n < 0$.

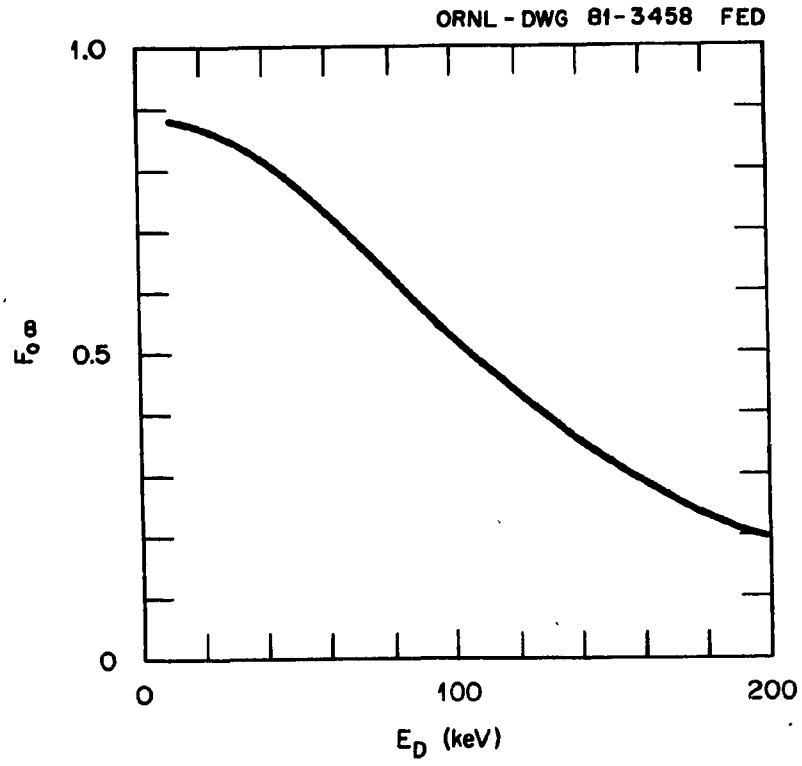

Fig. 2-13. Equilibrium neutral fraction for a deuterium beam in deuterium gas.

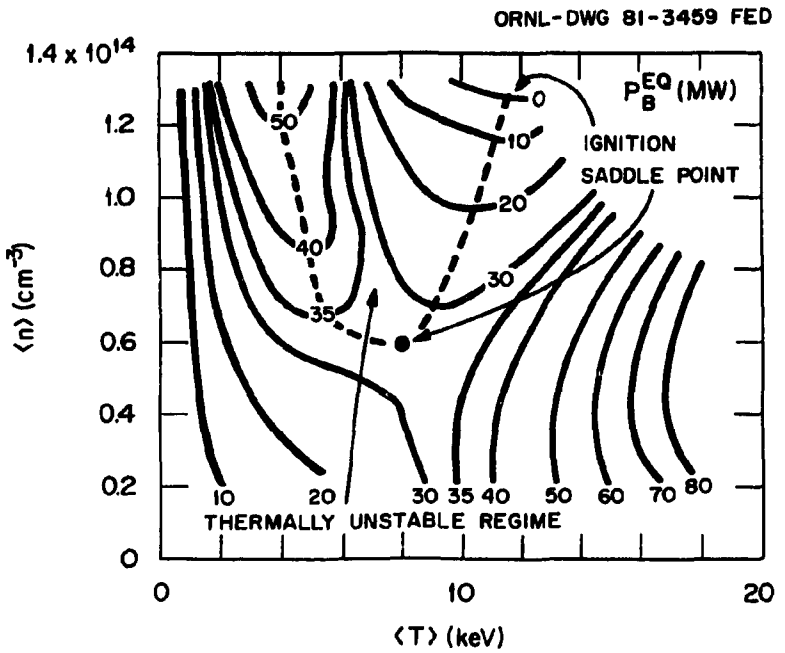

Fig. 2-14. Supplementary neutral beam power contours for steady-state operation for reference FED physics model.

Steady-state operation cannot be maintained in this region without feedback on the heating source (as was used to generate this plot). Allowing the plasma to move freely in major radius during a thermal excursion[35] moves the thermally unstable region slightly to the left. The ripple conduction losses at higher temperature tend to minimize the width of the unstable region; without ripple losses this region extends to $\langle T \rangle \simeq 30$ keV. The minimum in the ignition curve correspondingly drops to lower densities and higher temperatures as ripple losses are reduced.

Figure 2-15 shows the total fusion power output contours including beam/plasma reactions, while Fig. 2-16 shows the $Q = P_{fus}/P_B$ contours obtained from the data of Figs. 2-14 and -15. A given power output can be obtained over a wide range in plasma density and temperatures although the high-density, low-temperature end lies in the thermally unstable regime. Operation at $Q > 5$ can be obtained at about one-half to two-thirds the average density and beta required for ignition. The average toroidal and poloidal beta contours are shown in Figs. 2-17 and 2-18, respectively. Contributions from fast beam ions and fusion alphas have been included in the plasma pressure. The constant beta contours closely follow the constant fusion power contours.

Electrons and ions do not contribute equally to the pressure as shown in Fig. 2-19. Below a density of $\sim 8 \times 10^{13}$ cm^{-3} the central ion temperature is higher than the electron temperature even at high temperatures where ripple ion conduction losses dominate. In the high-temperature, low-density regime nearly all power flow is through the ions since the fast beam ions are the dominant heating source and predominantly heat the thermal ions. At higher densities, fusion alpha heating (which couples more directly to the electrons) drives $T_e(0)$ greater than $T_i(0)$. Ripple conduction losses then restrict the "hot ion mode"[36,37] to the low-density driven regime.

Using the contours in the preceding POPCON plots, an operating regime can be defined which meets physics and engineering design constraints. An example is shown in Fig. 2-20 where constraints of thermal stability, $Q > 5$, $\langle \beta_T \rangle < 5.5\%$, $P_{fus} < 180$ MW, and $P_B < 36$ MW have been

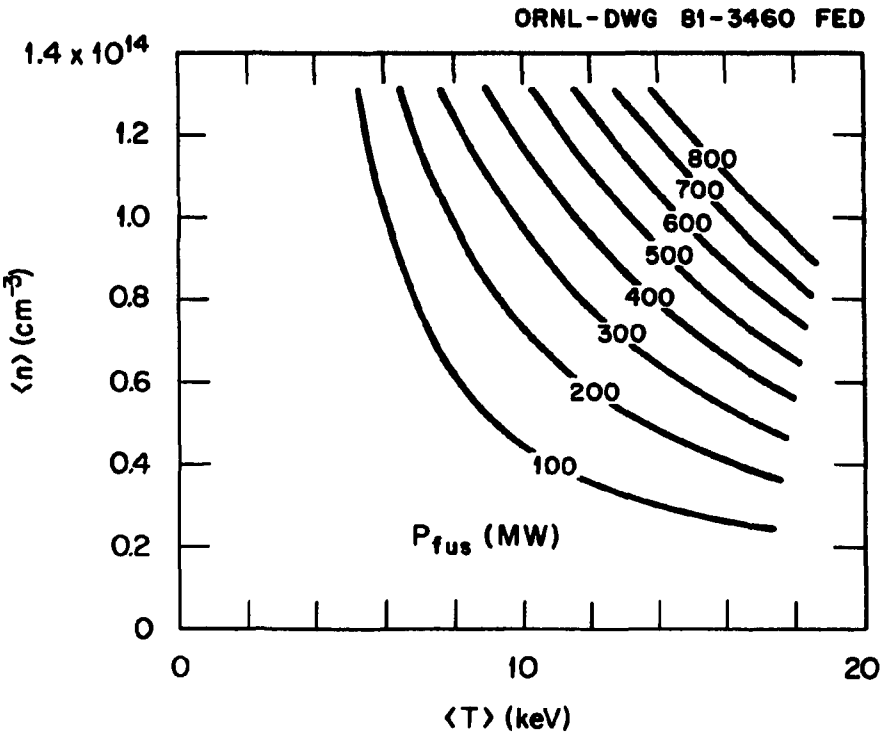

Fig. 2-15. Total fusion power output contours for steady-state operation for reference FED physics model.

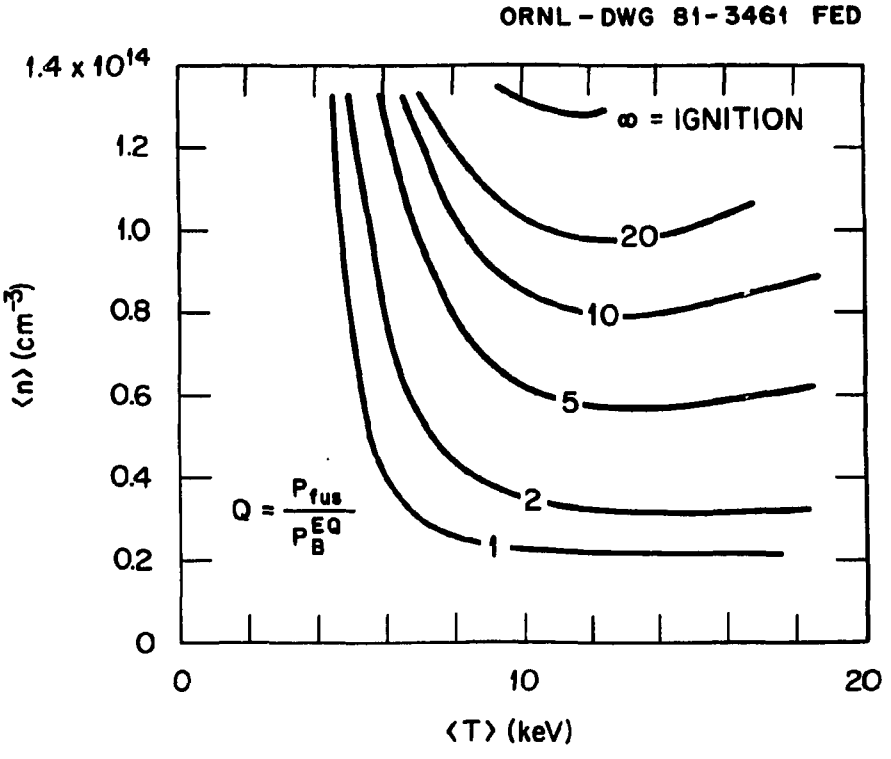

Fig. 2-16. Plasma energy multiplication factor, $Q = P_{fus}/P_B^{EQ}$, contours for steady-state operation for reference FED physics model.

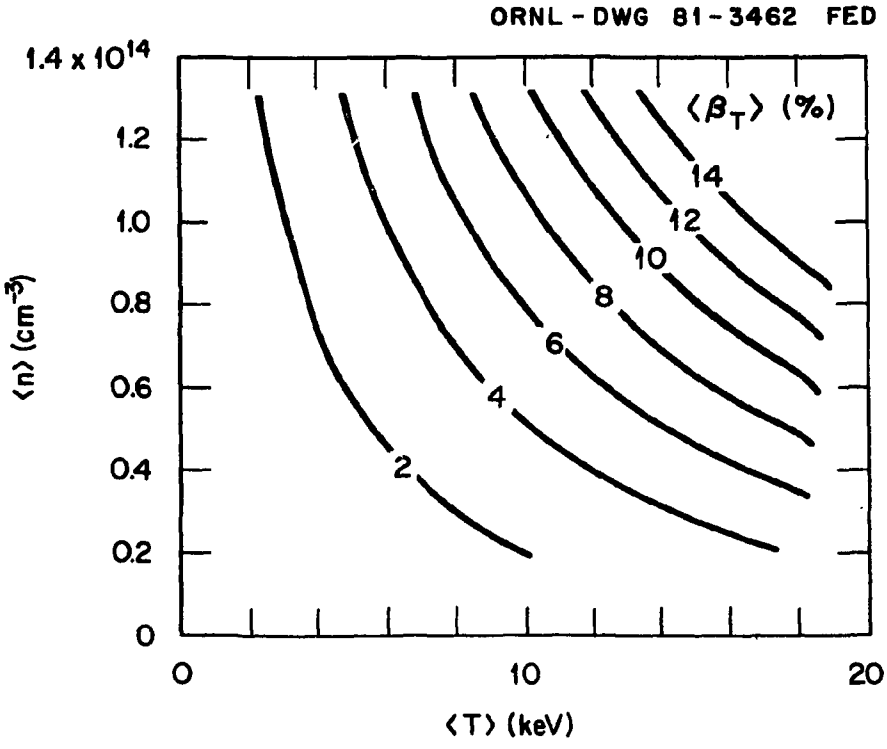

Fig. 2-17. Average toroidal beta contours, including fast beam ion and alpha pressure contributions, for steady-state operation for reference FED physics model.

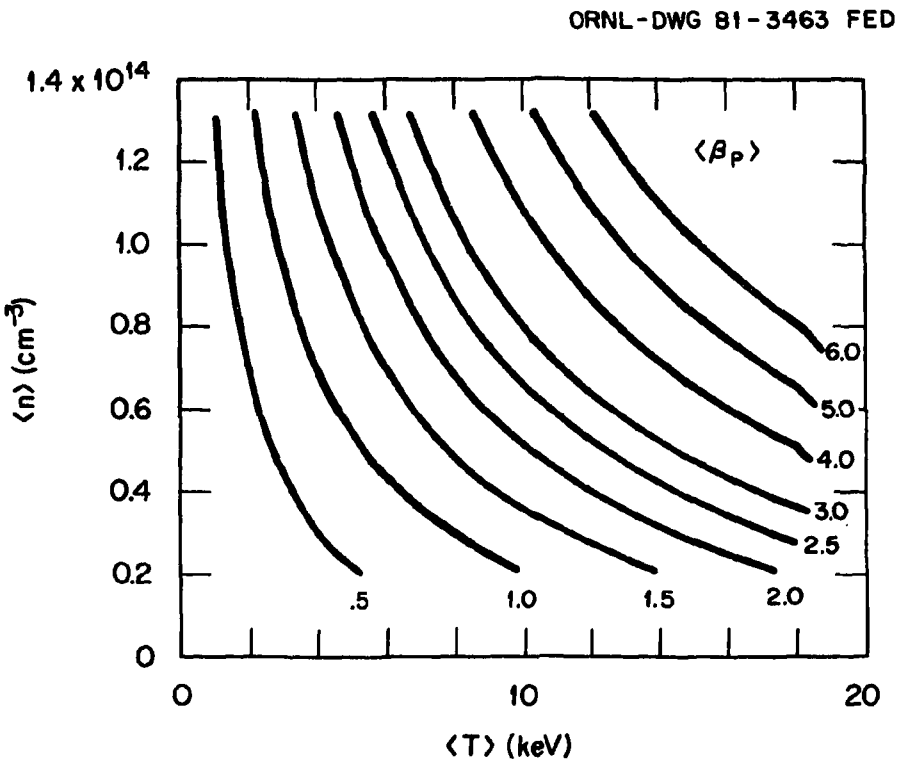

Fig. 2-18. Average poloidal beta contours, including fast beam ion and alpha pressure contributions, for steady-state operation for reference FED physics model.

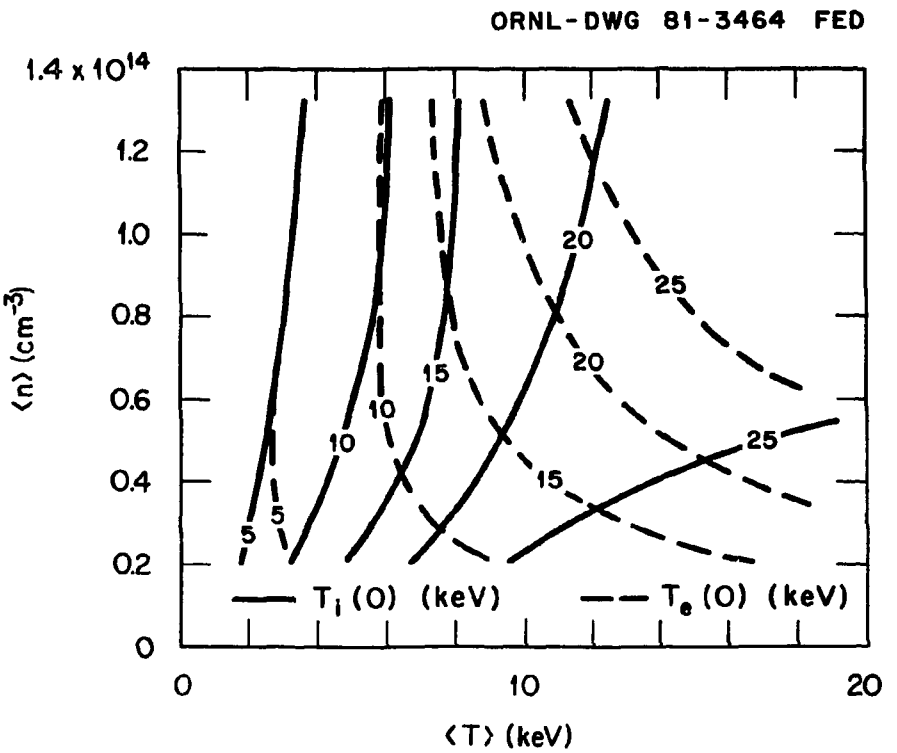

Fig. 2-19. Central electron and ion temperature contours for steady-state operation for the reference FED physics model.

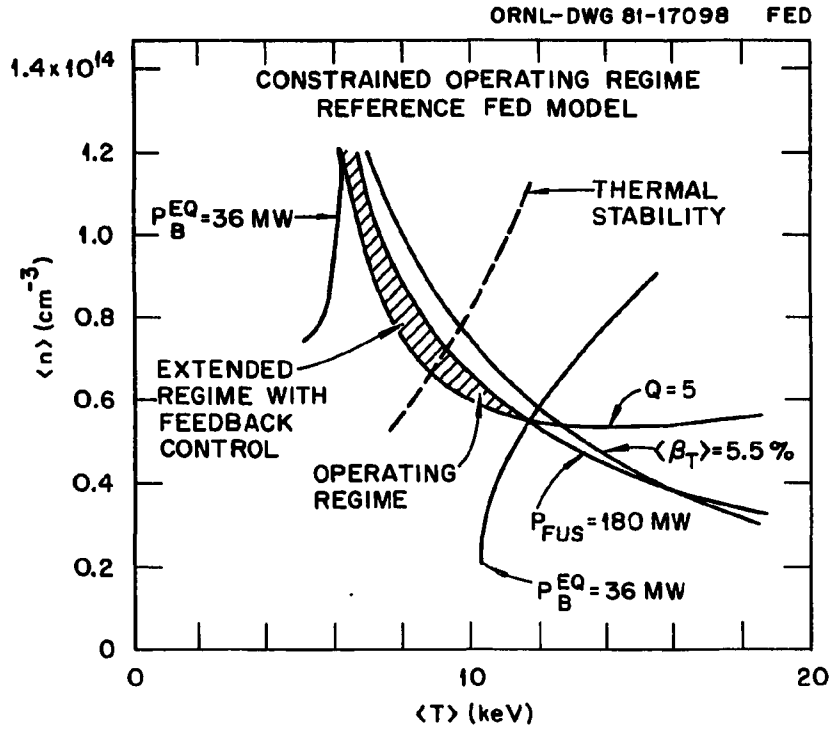

Fig. 2-20. Example of a steady-state operating regime which meets prescribed physics and engineering constraints for the reference FED physics model.

imposed. With the exception of the fusion power output curve, all of these contours represent relatively soft physics constraints which are subject to varying degrees of uncertainty in either direction. Relaxation of the 180-MW thermal fusion output constraint opens up the potential operating regime to even higher beta. Similarly, higher toroidal field, higher current operation may extend the regime for any potential beta limitations to higher densities and temperatures, as will be discussed later. The thermally stable operating regime is relatively small and confined to $6 \times 10^{13} \lesssim \langle n \rangle \lesssim 8 \times 10^{13}$ cm^{-3} with $\langle T \rangle \simeq$ 9-12 keV. Feedback on the supplementary beam heating source could extend this regime to lower temperatures and higher densities as shown in Fig. 2-20 although diagnostic limitations and the feedback response time would place further restrictions on the extended operating regime. Other means of extending the operating regime are discussed in later sections.

The evolution of the electron and ion temperature profiles for one of the POPCON sweeps at $\langle n_e \rangle = 7.0 \times 10^{13}$ cm^{-3} is shown in Fig. 2-21. Note that this does not represent a standard startup sequence since the supplementary beam power is being continuously varied to maintain a constant rate of temperature increase of 0.5 keV/s. The central ion temperature tends to be clamped after reaching about 20-25 keV due to ripple conduction losses while the electron temperature profile remains fairly peaked. The radial grid is major radius in the plasma midplane so the outward shift of the profiles at high beta can be seen. The electron, deuterium, and tritium density profiles are illustrated in Fig. 2-22. Significant beam fueling of deuterium is required to maintain the plasma thermal balance. The reference operating regime lies near the middle of the simulation where the deuterium profile is relatively broad and 20-25 MW of beam heating is necessary. The tritium profile is slightly hollow due to fusion burnup in the plasma center.

The normalized beam power deposition profiles, H(r), for the three components of the beam are shown in Fig. 2-23. As beta increases, the deposition profile for the 150-keV component becomes strongly peaked at the magnetic axis due to the outward plasma shift. Even the 75 keV component becomes centrally peaked, but only for $\langle \beta_T \rangle \gtrsim 10\%$. The 50-keV component always remains an edge heating source. The total beam heating

ORNL · DWG 81-3466R FED

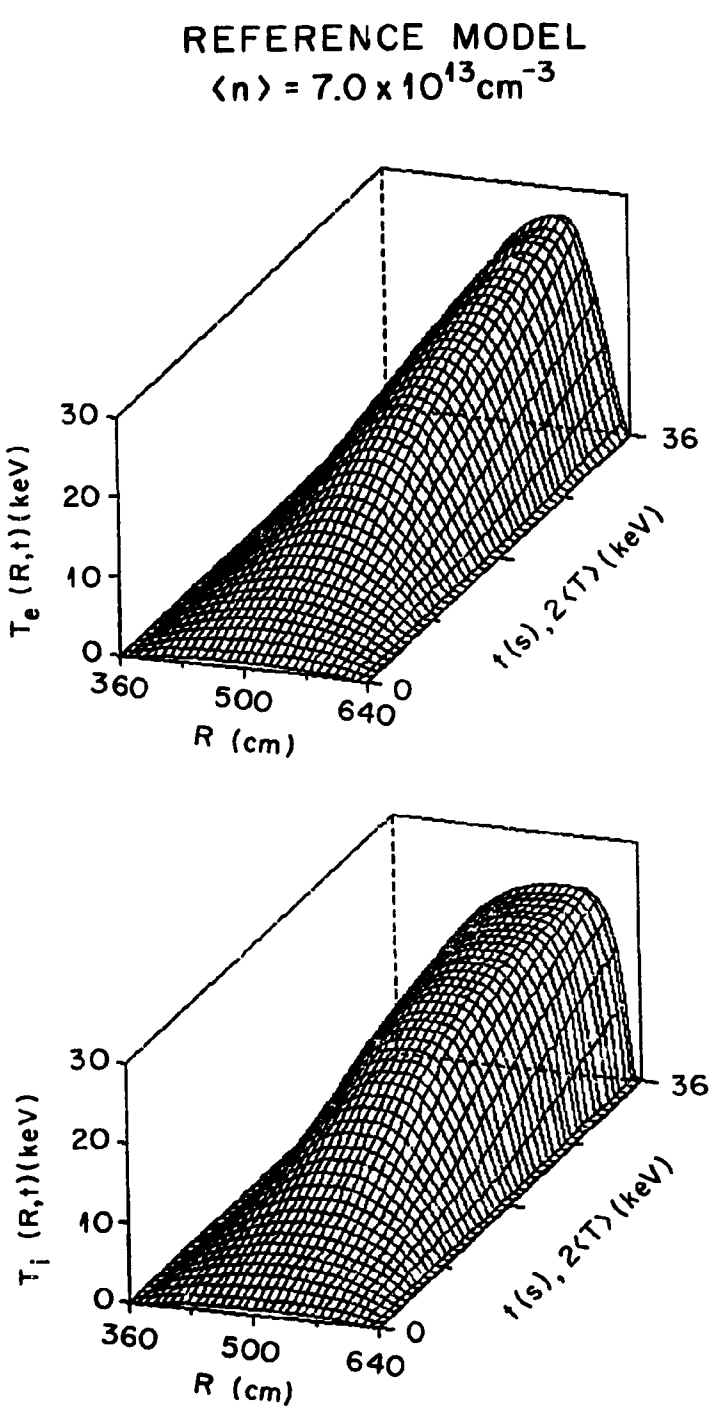

Fig. 2-21. Evolution of the electron and ion temperature profiles for a POPCON sweep at $\langle n_e \rangle = 7.0 \times 10^{13}$ cm^{-3}.

ORNL-DWG 81-3467R FED

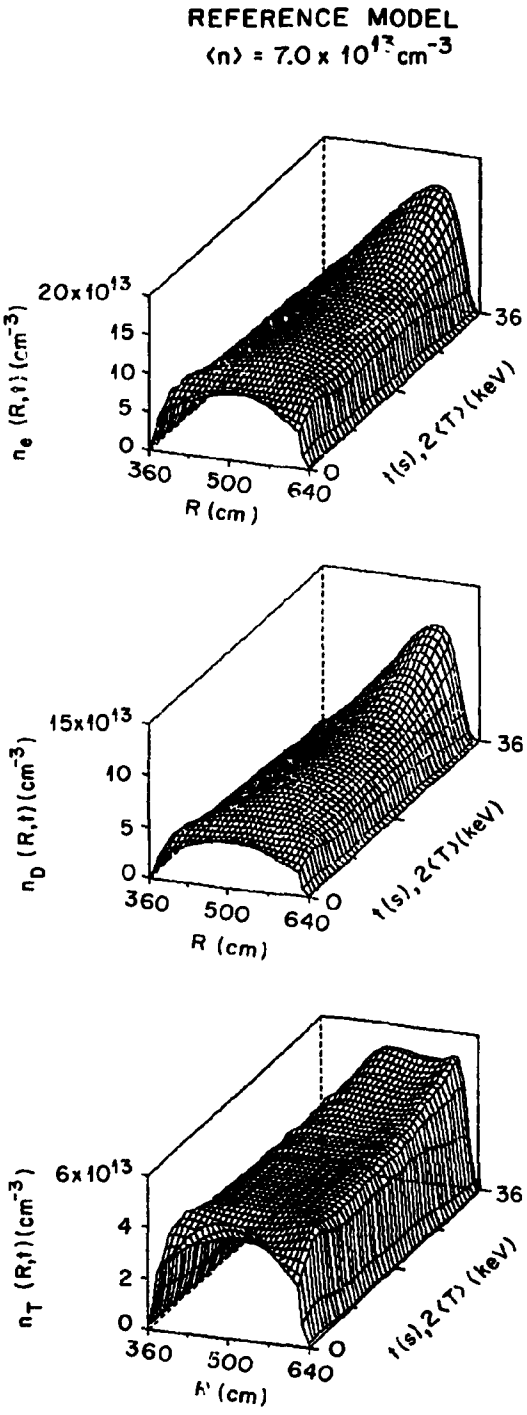

Fig. 2-22. Evolution of the electron, deuterium, and tritium density profiles for a POPCON sweep at $\langle n_e \rangle = 7.0 \times 10^{13}$ cm^{-3}.

ORNL-DWG 81-3468R FED

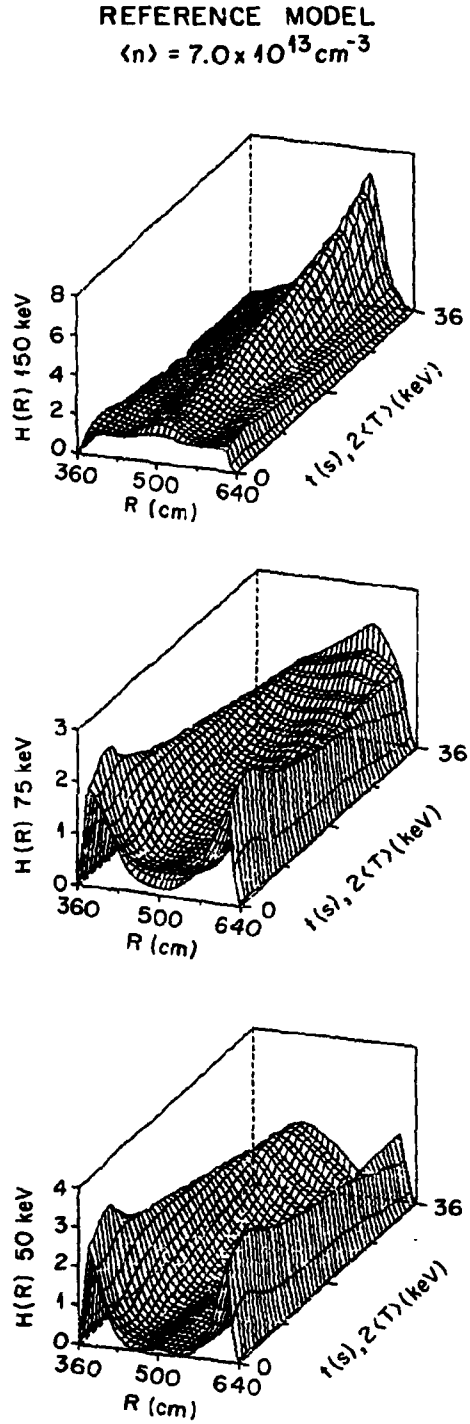

Fig. 2-23. Evolution of the normalized heating profiles for the 150-, 75-, and 50-keV neutral beam components for a POPCON sweep at $\langle n_e \rangle = 7.0 \times 10^{13}$ cm^{-3}.

profile, the fusion heating profile, and the total beam plus fusion heating profile all remain centrally peaked (Fig. 2-24). Lower initial densities followed by a density rise during the heating phase can be used to maintain strong central heating at all stages of a startup sequence[38] and lead to optimal use of the supplementary beam heating.

2.4.3 Optimal Heating During Startup

The information contained in the supplementary heating power contours (Fig. 2-14) can be used to derive an optimal heating path. A global energy balance can be written as

$$\frac{\partial E}{\partial t} = \frac{\partial (3nT)}{\partial T} = P_B - P_B^{EQ}(n,T) \qquad (2\text{-}1)$$

where n and T represent global averages as defined in Fig. 2-12, $P_B^{EQ}(n,T)$ is the supplementary power required for steady-state thermal balance as plotted in Fig. 2-14, and P_B is the constant supplementary heating power. As long as $P_B > P_B^{EQ}$, the plasma energy density will increase in time. Thus, the absolute minimum beam power requirement is determined by the maximum value of P_B^{EQ} for any given startup sequence. The above equation can be integrated over time and plasma energy density for a given constant applied beam power:

$$\int_o^{T_B} dt = \int_{E_1}^{E_2} \frac{dE}{P_B - P_B^{EQ}(n,T)} \qquad (2\text{-}2)$$

$$T_B = \int_{E_1}^{E_2} F(n,E)dE \ . \qquad (2\text{-}3)$$

We can minimize the time, T_B, to increase the plasma energy density from E_1 to E_2 by taking the variation of T_B with respect to n, i.e., by applying Euler's equation to F(n,E),

ORNL-DWG 81-3469R FED

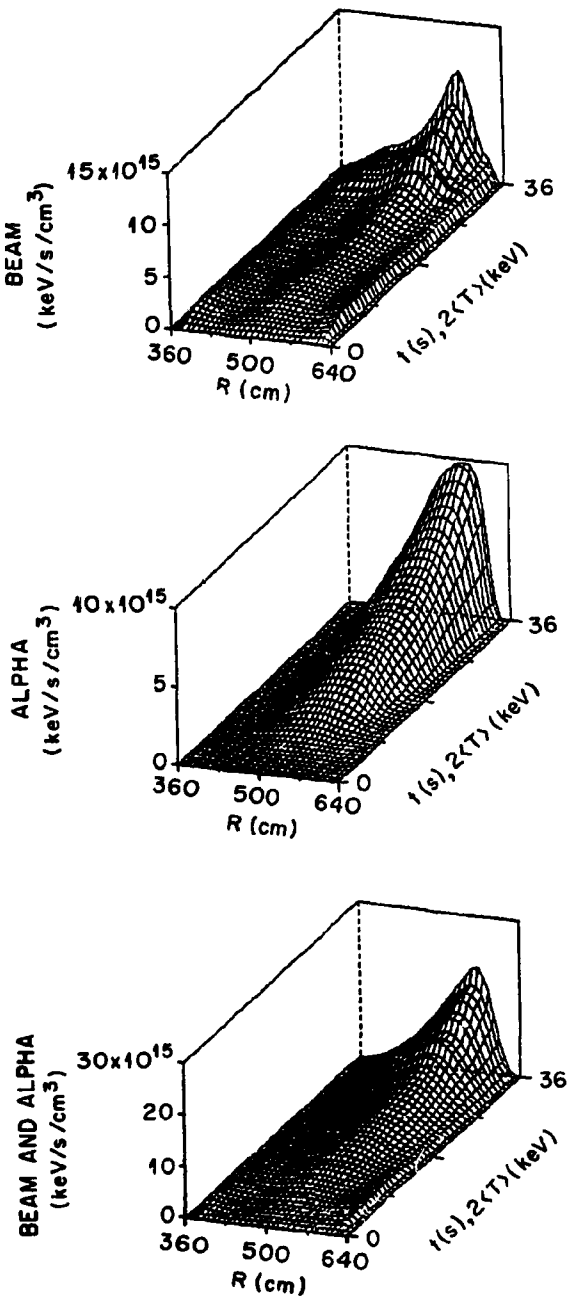

Fig. 2-24. Evolution of the total neutral beam, fusion, and beam plus fusion heating profiles for a POPCON sweep at $\langle n_e \rangle = 7.0 \times 10^{13}$ cm^{-3}.

$$\delta_n T_B = 0 \rightarrow \frac{\partial F}{\partial n} + \frac{\partial}{\partial E}\left(\frac{\partial F}{\partial n}\right) = 0 \ .$$

Then

$$\frac{\partial F}{\partial n}\Big|_E = \frac{\partial P_B^{EQ}}{\partial n}\Big|_E = 0$$

determines the path, n(T), over which the plasma energy density increases the fastest for any given applied beam power, P_B. This optimal path passes through the saddle point and intersects the supplementary beam power contours, P_B^{EQ}, at the points of minimum thermal energy content above the saddle point and maximum energy content below the saddle point; it is the path of steepest descent in energy and thus intersects the ignition contour at the lowest thermal plasma beta value. The optimal path for the reference FED base model is shown in Fig. 2-25. Since only points along the optimal path are connected, nonoptimal path must be taken from an assumed initial point to the optimal path and from the optimal path to the desired final operating point. We have chosen to make this connection at constant density, starting at $\langle n_e \rangle = 3.0 \times 10^{13}$ cm^{-3} in the ohmic state and ending with $\langle n_e \rangle = 8.0 \times 10^{13}$ cm^{-3} at the reference operating temperature of 10 keV.

Once the n(T) path is chosen, the time required for evolution from the initial to final operating point can be determined from Eq. (2-3) for a given supplementary power. The results for the data in Fig. 2-25 are shown in Fig. 2-26. The contributions to the total heating time along the constant density portions of the startup path are small since the beam power exceeds the equilibrium losses by a significant amount. The critical part of the path is the route through the saddle point since this represents an absolute minimum power requirement for an infinitely long startup time. Beam power requirements are not reduced much as the startup time is extended beyond about 6 s (which represents several total energy confinement times). Startup with a constant density of 8×10^{13} cm^{-3} would require a minimum of ∿38 MW for an infinitely long startup while the optimal path requires a minimum of ∿31 MW dictated by the saddle point (see Fig. 2-25).

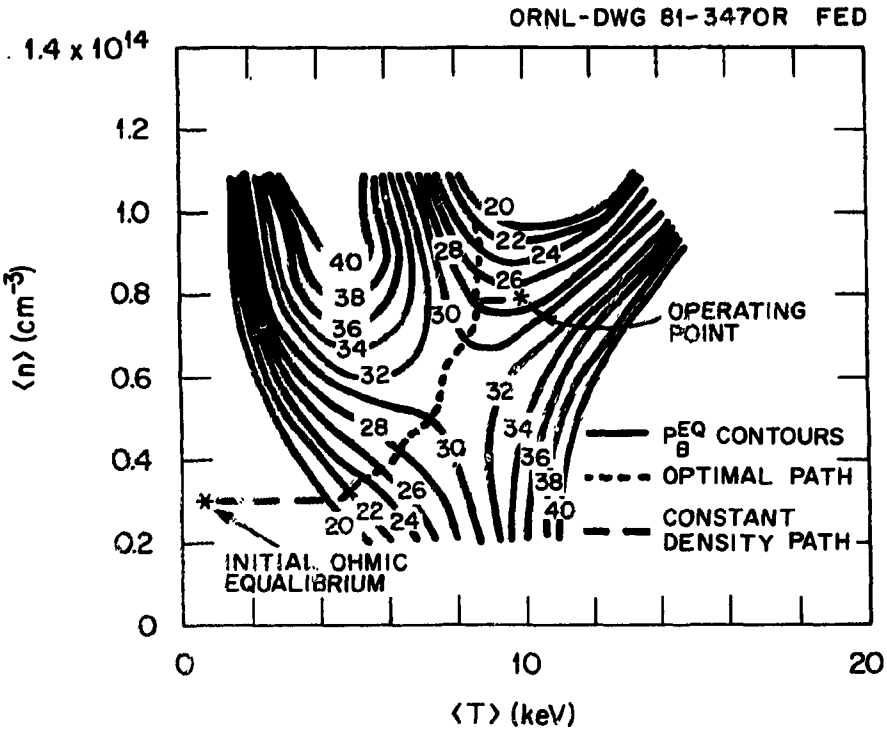

Fig. 2-25. Optimal heating path for startup. Constant density paths connect the initial and final operating points to the optimal path.

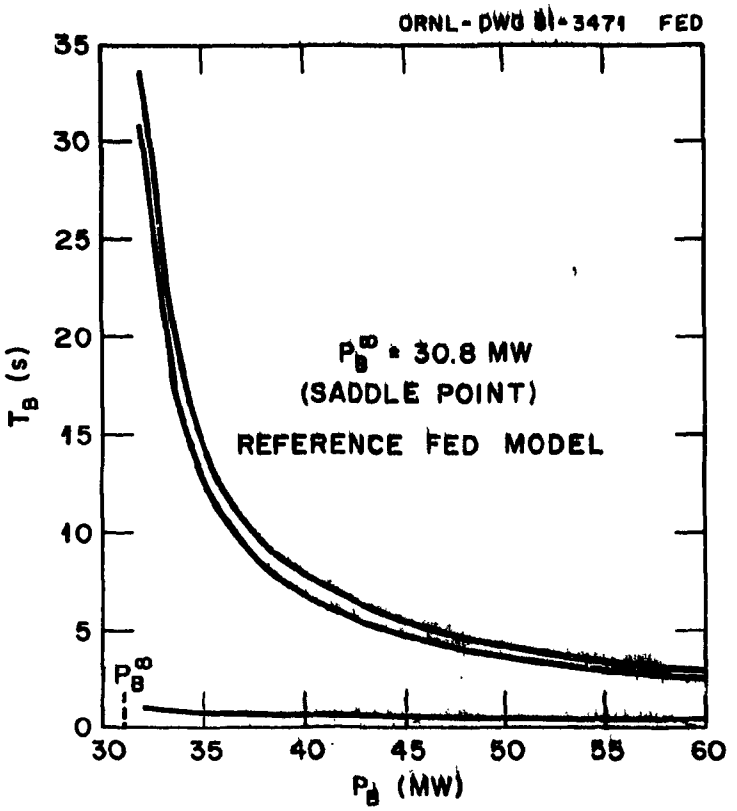

Fig. 2-26. Neutral beam heating time as a function of constant heating power. The top and bottom curves give the small contributions to T_B from the constant <n> portions of the heating path in Fig. 2-25 at high and low <n>, respectively.

2.4.4 Beam Energy and Species Mix

Any variation in the physics model, including beam species mix and energy, changes the optimal path and power requirements although the general features of the optimal path for beam heating remain the same. Beam energies in the range 100-200 keV have been examined for the FED reference parameters and models of Table 2-4 for three different source species mixes. The mix to the plasma is determined by the equilibrium neutral fractions of each component as plotted in Fig. 2-13. The resulting saddle point beam powers and 6-s startup powers are shown in Fig. 2-27. The optimal path prescription of the preceding section was used to uniquely determine the heating path for each case with the fixed end points shown in Fig. 2-25.

The power requirements of the plasma are not a very strong function of either beam energy or species mix but tradeoffs between energy and species mix can be made which allow the same net plasma heating requirements. For example, 100-keV beams with an ideal source species mix of 100:0:0 require the same total power to the plasma as 200-keV beams with a source species mix of 80:12:8 in power. Although beam penetration is reduced at lower energies, a greater fraction of the energy is transferred to the thermal ions which tends to reduce the dependence of power on beam energy. The overall system efficiency for the 100-keV beams is much greater than the 200-keV system with any of the species mixes considered due to poor neutralization efficiency at high energy as shown in Fig. 2-28. The powers plotted in this figure are idealized in the sense that they do not reflect any beamline losses or nonideal neutralization effects.

Other considerations in the tradeoffs between beam energy and power requirements are: injection angle, deuterium particle load on the plasma, edge heating and subsequent impurity production associated with lower energy beams or beam components, and trapping of beam ions and subsequent loss due to toroidal field ripple. Changing the beam orientation to fully perpendicular would provide the reduction in beam power shown in Fig. 2-27 for the 150-keV reference case. A compromise between perpendicular and tangential to the inside wall may avoid toroidal field ripple losses but would represent no more than a few percent savings in beam power.

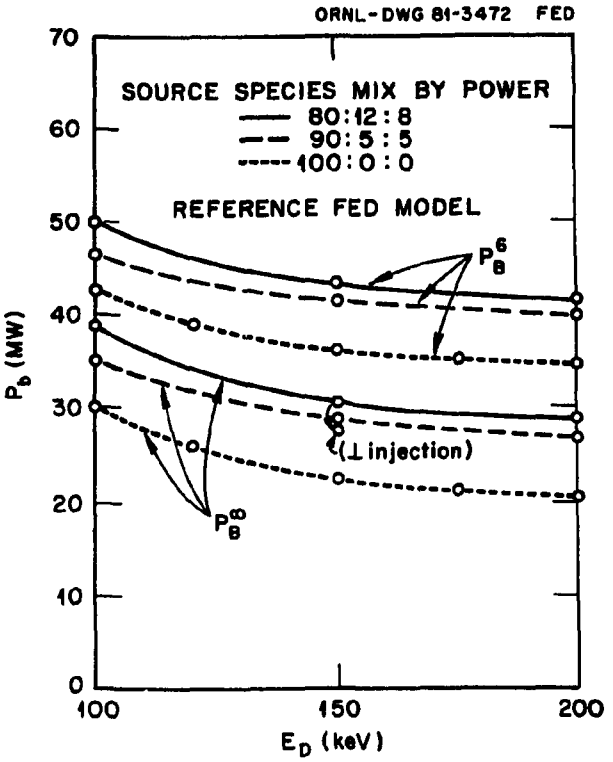

Fig. 2-27. Power requirements for an optimal 6-s startup, P_B^6, and saddle point powers, P_B^∞, as a function of beam source species mix and energy.

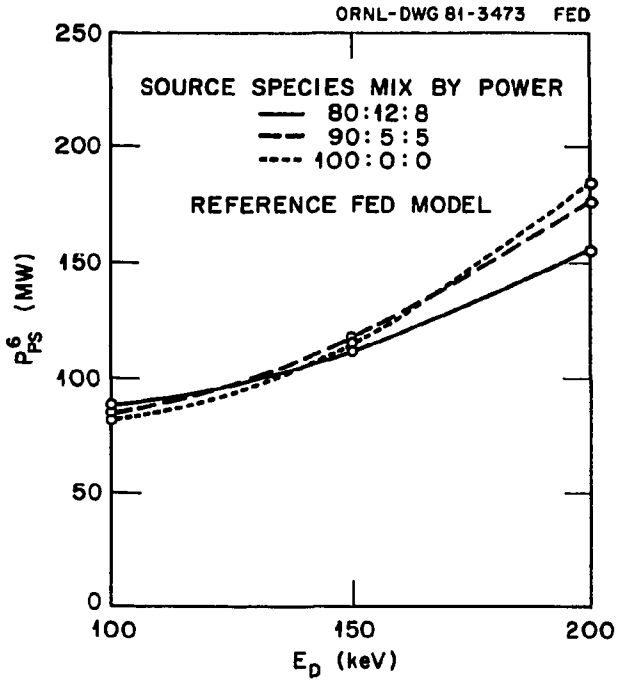

Fig. 2-28. Idealized source power requirements for a 6-s startup as a function of species mix and energy.

The deuterium particle source from the beams can cause the central deuterium density to be much greater than the central tritium density even if the average deuterium and tritium densities are equal, as shown in Fig. 2-22. This does not significantly degrade the fusion rate until the deuterium density exceeds about twice the tritium density. In the case of a high recycle limiter or divertor, however, control of the total deuterium density may be lost. Higher average energy per particle in the beam may help regain control of the deuterium density, but this problem is sensitive to the particle transport and recycling models.

The greatest physics uncertainty is the impact of edge heating on impurity production and confinement. If the total powers of Fig. 2-27 are broken down into components, we find that there is a strong decrease in the power in the full energy component with increasing energy for a given source species mix, while the power in the one-half and one-third energy components increases (Fig. 2-29). Even though the penetration of each component increases with energy, the increased power in the lower energy components may increase edge heating and potentially aggravate the impurity production problem. Two features of the physics of neutral beam heating tend to minimize the relationship between edge heating and impurity production. First, the neutral beam energy deposited at the edge is transferred primarily to the electrons which should reduce the potential for enhanced sputtering relative to direct ion heating at the edge. Also, beam ions lost before complete thermalization either due to charge exchange or ripple loss at the edge should not pose a severe problem since sputtering yields at incident energies greater than 10 keV are generally low. Nevertheless, a strong effort should be made to reduce the lower beam components (especially the one-third energy component) which are primarily responsible for edge heating either through source improvements or separating components before neutralization.

2.4.5 Variations in the Transport Model

The reference transport model[27] in the preceding discussions (Figs. 2-12 through 2-29), although popularly used as a reference in reactor design calculations, needs further examination because of uncertainties

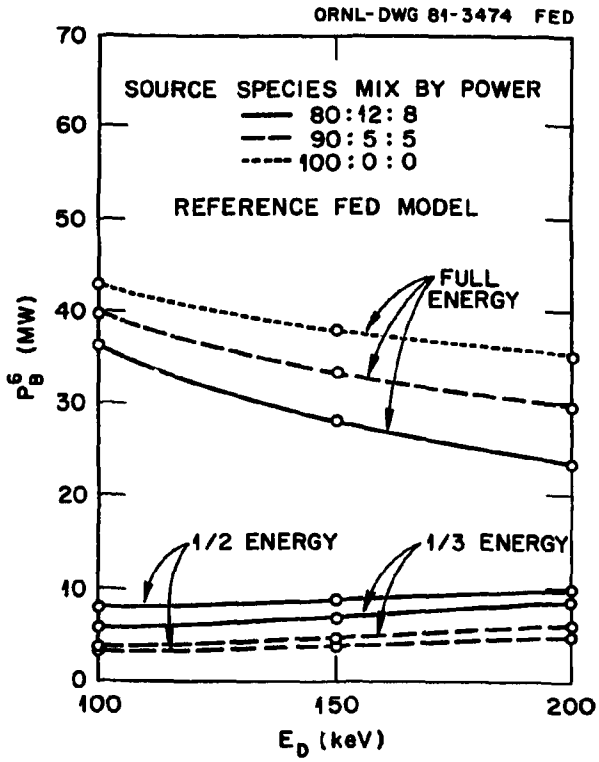

Fig. 2-29. Power delivered to the plasma, by energy component, as a function of beam energy and species mix.

in magnitude and scaling. In 1-D modeling of existing experiments with low impurity levels and low beta, this model leads to broader profiles and lower bulk electron temperatures than observed. A model which has $n_e\chi_e$ increasing with radius is required for more peaked electron temperature profiles.[39] Average values of χ_e should be about half as large as the reference model to match electron temperatures in many experiments under optimal conditions. An empirical 1-D model similar to those based on PLT data[39] also reproduces ISX-B and PDX results more reliably than the reference $n_e(r)\chi_e(r) = 5 \times 10^{17}$ cm^{-1} s^{-1} model, at least at low and modest beta values. If we then use a "PLT-like" model with

$$\chi_e^{PLT} = \frac{1.2 \times 10^{17}}{n_e(r)[1-0.4(r/a)^2]^{3.5}} \quad cm^2/s$$

and

$$D^{PLT} = \frac{1.5 \times 10^{17}}{n_e(r)} + 5000\left(\frac{r}{a}\right)^3 \quad cm^2/s$$

in place of the χ_e^{ANOM} and D^{ANOM} expressions in the calculations of the preceding sections, we obtain the supplementary beam heating contours shown in Fig. 2-30. Note that we have not included a temperature dependence in χ_e although the PLT data[39] tends to support such a model. Ignition now occurs in the vicinity of 7.5×10^{13} cm^{-3}, and $Q > 5$ operation is obtainable with densities as low as 4.5×10^{13} cm^{-3}. If the same physics and engineering constraints are used as in the reference model, the steady-state operating regime (Fig. 2-31) is much larger than that given in Fig. 2-20. The ignition curve lies slightly inside the thermally stable operating regime. The possibility of ignition could be further increased by operating with greater fusion power output and higher beta (or higher toroidal field). Lower toroidal field ripple losses would push the ignition curve even further into the operating regime.

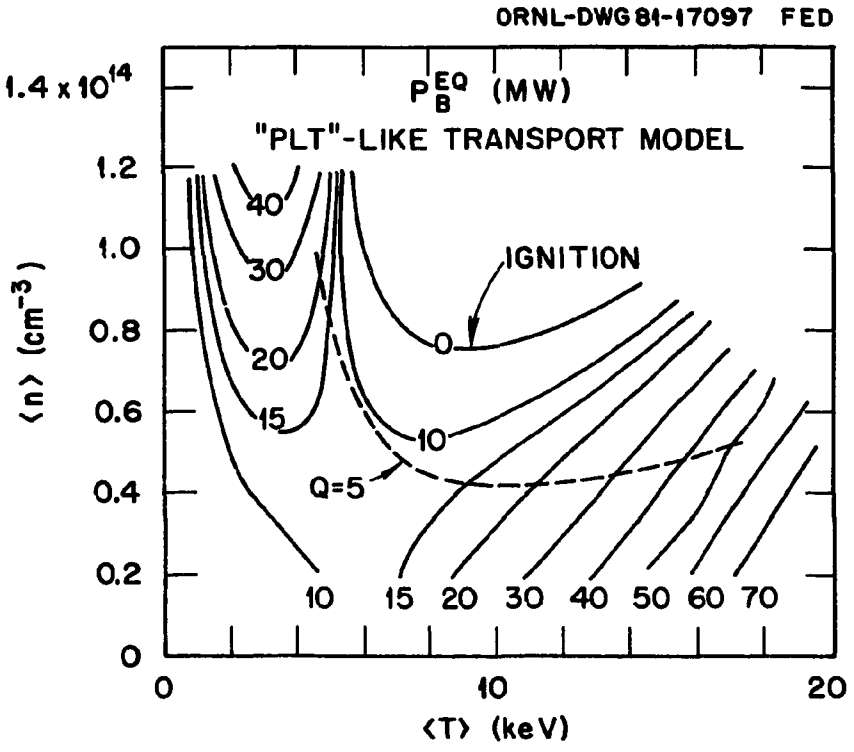

Fig. 2-30. Supplementary neutral beam power contours for steady-state operation using a PLT-like transport model for FED.

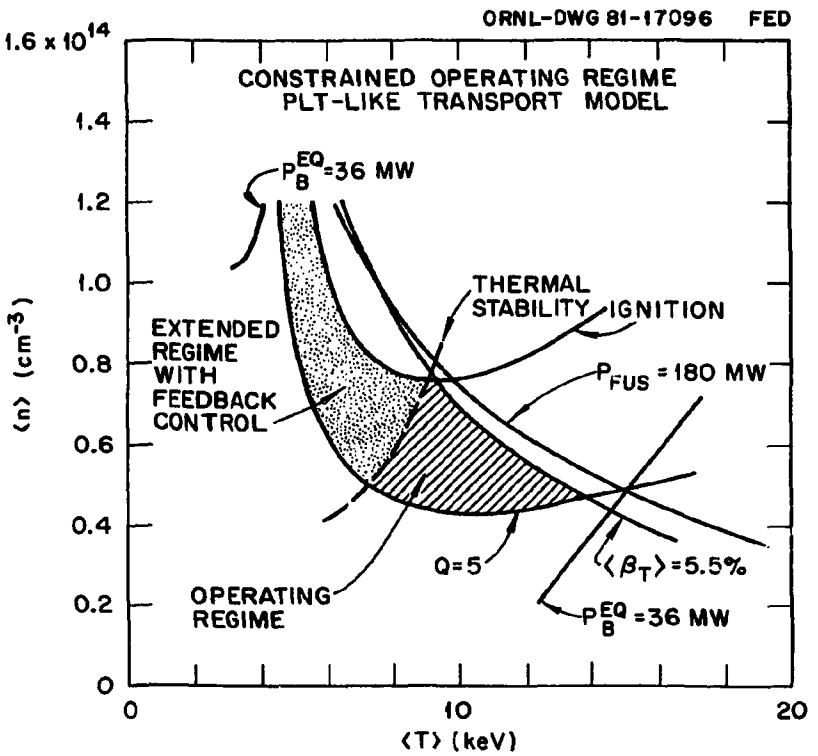

Fig. 2-31. Example of a steady-state operating regime for FED with a PLT-like transport model.

Since the radial variation of the PLT-like transport model should penalize poor beam penetration more severely than the reference model, a parameter scan of beam energies and species mix was also performed with this model. Figure 2-32 shows the saddle point powers and optimally determined total power requirements for a 6-s startup with the same end points as used for the reference case. The dependence on energy and species mix is essentially the same as shown earlier and the idealized power supply requirements still increase with beam energy as seen in Fig. 2-33. The powers in one-half and one-third energy components are nearly independent of energy (Fig. 2-34).

The differences between the power requirements and potential physics performance of the reference and PLT-like transport models are basically a reflection of a factor of two difference in the effective electron conduction losses. This sensitivity to the magnitude of the electron conduction losses also can be shown by simply changing the amplitude factor for χ_e while maintaining the remaining parameter dependence constant for a given model. Projections of startup power requirements and physics performance are clearly sensitive to the uncertainty in χ_e.

2.4.6 Projections for 10 T Operation

Higher toroidal field accompanied by an increase in the toroidal current to maintain the same safety factor q_ψ has the potential for extending the operating regime for any given limitation in either toroidal or poloidal plasma beta. Figure 2-35 shows the supplementary beam power contours with the toroidal field increased to B_t = 4.5 T (10 T at the magnet) while maintaining $q_\psi(a)$ = 3.2. All other conditions of Table 2-4 remain the same. Relaxing the P_{fus} = 180 MW constraint greatly extends the operating regime as shown in Fig. 2-36. The thermally stable operating regime lies very close to the ignition curve. Increasing the plasma current [reducing $q_\psi(a_o)$] would move the ignition curve inside the stable operating regime since ripple conduction losses would be reduced. The reduced supplementary power requirements (relative to Fig. 2-14) result from a decrease in ripple-induced ion thermal conduction losses: the Shafranov shift is reduced and the plasma is not

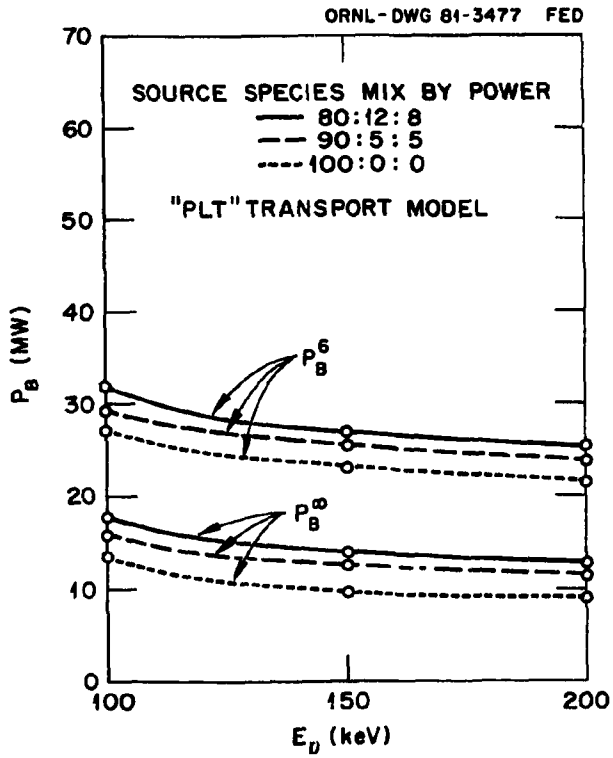

Fig. 2-32. Power requirement for an optimal 6-s startup, P_B^6, and saddle point powers, P_B^∞, as a function of beam source species mix and energy for FED with a PLT-like transport model.

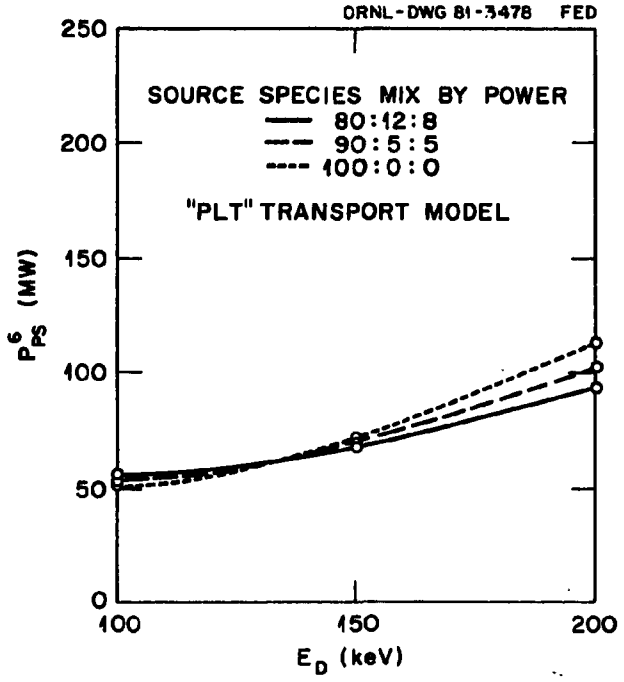

Fig. 2-33. Idealized source power requirements for a 6-s startup as a function of species mix and energy for FED with a PLT-like transport model.

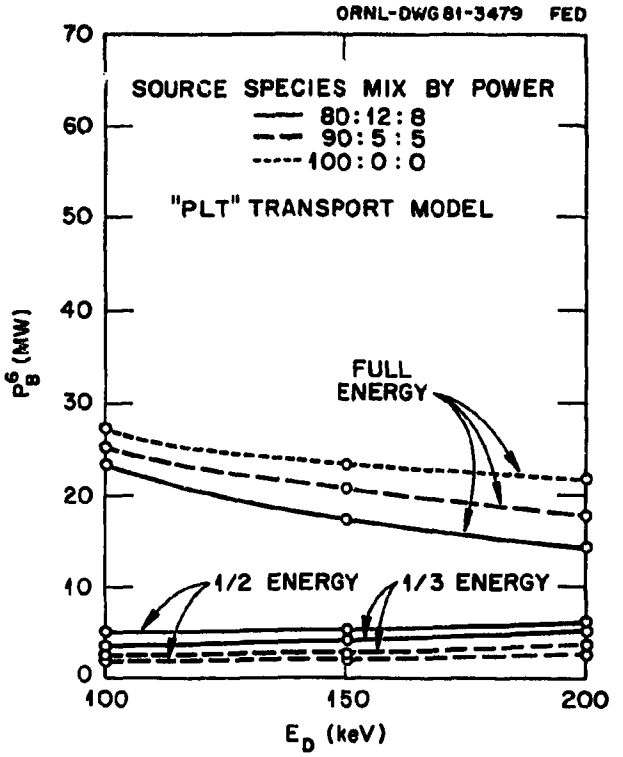

Fig. 2-34. Power delivered to the plasma, by energy component, as a function of beam energy and species mix for FED with a PLT-like transport model.

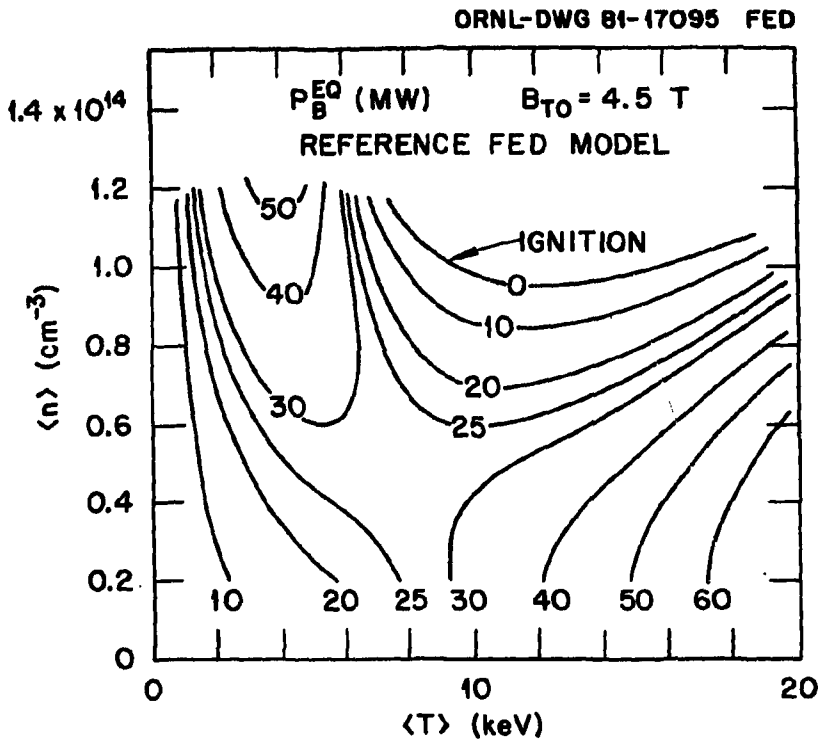

Fig. 2-35. Supplementary neutral beam power contours for steady-state operation using B_{To} = 4.5 T.

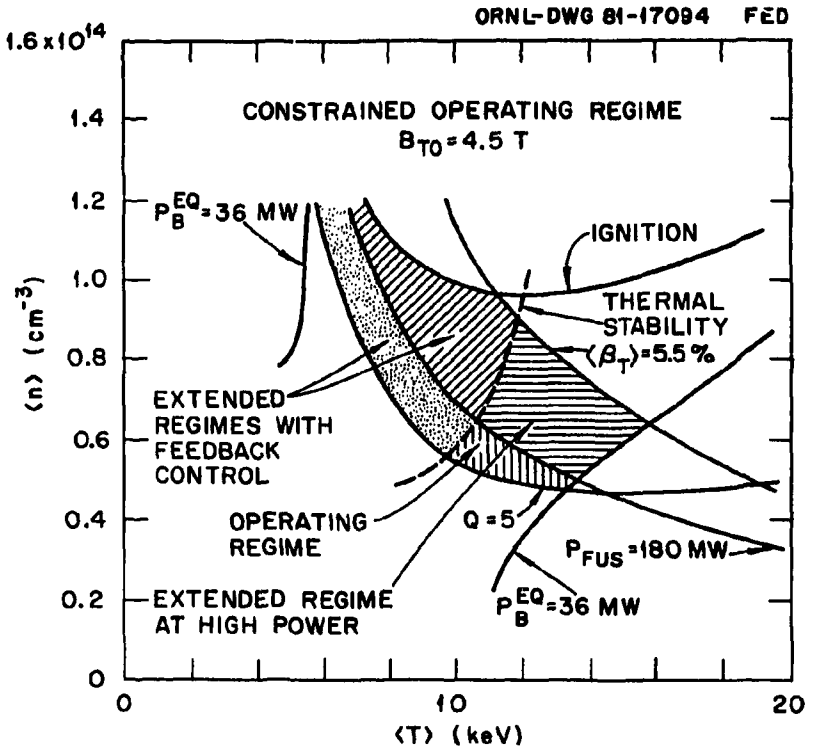

Fig. 2-36. Example of a steady-state operation regime with B_{To} = 4.5 T.

pushed as far into the higher ripple regions in this case. Since the ripple conduction losses dominate transport in the vicinity of the operating regime they deserve much greater theoretical and experimental attention. Significant modifications have been made in the theoretical ripple conduction models recently[33,34] and will be the subject of further investigation.

2.4.7 Control of the Density Profile

If the density profile is more centrally peaked, the fusion power output increases for a given volume averaged density. This tends to decrease the supplementary heating power requirements for startup and driven operation in addition to moving ignition to lower values of density and beta. Some measure of control of the density profile can be achieved by fueling more deeply into the plasma. However, this must be accompanied by a reduction in fueling associated with particle recycle at the plasma edge. A greater flexibility in the control of this recycle may be easier to accomplish with a poloidal divertor than with a toroidal limiter, perhaps by changing the openings to the pumping ports in the divertor chamber.

Neutral beams provide effective central fueling of the deuterium during startup and driven operation as shown earlier. However, if the neutral beam requirements are dictated by the energy balance, there is little independent control over the density. This is especially true with high particle recycle where all control over the deuterium density may be lost.

Pellet injection can increase the central peaking of both deuterium and tritium densities during either driven or ignited operation and thus offers the greatest potential for flexibility in density control. Calculations with relatively low velocity pellets (2 km/s) indicate that the average density and beta for ignition (or Q = 5 operation) can be reduced by about 20% below the typical values shown earlier for neutral gas fueling with high recycle. The net change in fuel handling requirements for this mode of operation is determined by a difference between two physics processes which have relatively large uncertainties. There

is an increase in the confinement time of the pellet injected particles and a decrease in the allowable level of internal recycling to maintain any given plasma density. A variety of theoretical and experimental studies is in progress, which should help define these tradeoffs in more detail.

2.4.8 The Heating Profile

Much of the structure in the steady-state heating contours of the preceding sections is dictated by the physics of neutral beam heating, i.e., beam penetration and the transfer of fast ion energy to thermal ions and electrons. A reference heating model has been constructed to examine this dependence and to serve as a guide for examination of rf heating methods such as ICRF.

A Gaussian heating profile of the form

$$H(r) \sim e^{-(2r/a)^2} ,$$

with 75% of the energy transfer to thermal ions, yields the power contours shown in Fig. 2-37 for the PLT-like transport model and other parameters given in Table 2-4. The structure of the contours in the low temperature, high density regime has vanished because the heating profile is assumed to be independent of density. In reality the heating profile of any rf heating technique would show some sensitivity to both density and temperature. With the structure shown in Fig. 2-37 there is no strong incentive for determining an optimal path since power requirements are equally low for all paths. The optimal path does progress from low density to high density as the temperature increases even though the valley is very broad.

The ignition contour, of course, is not affected by the choice of heating technique since the supplementary power requirements vanish there. In the vicinity of the driven operating point ($\langle n \rangle \sim 8 \times 10^{13}$ cm^{-3}, $\langle T \rangle \sim 10$ keV), the neutral beam power requirements are not significantly greater than those for the idealized Gaussian heating profile because of

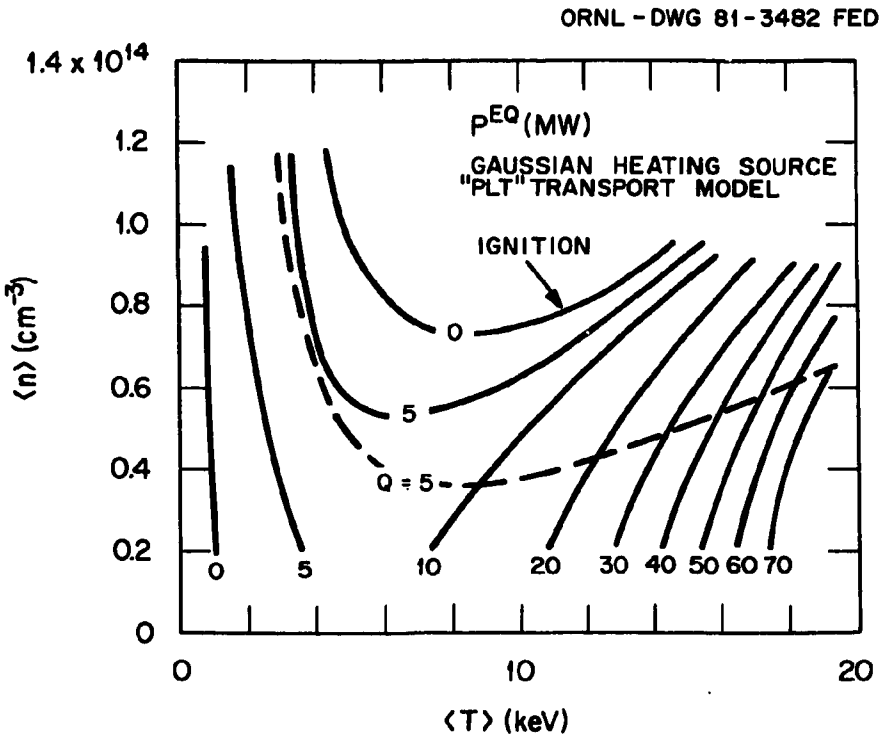

Fig. 2-37. Supplementary power requirements for steady-state operation using an idealized gaussian heating source which delivers 75% of its power to the ions using a PLT-like transport model for FED.

several advantageous effects of neutral beam heating. The shift of the magnetic axis makes the neutral beam heating profile strongly peaked on axis while energy transfer is primarily to the ions. On axis, over 90% of the power in the full energy component is transferred to the thermal ions. Power deposited at the edge is transferred mainly to the electrons. Deuterium fueling by the beams increases the density on axis and therefore the fusion production profile is more centrally peaked. Some benefit is also gained from beam-plasma fusion reactions. The idealized heating source does provide some reduction in the heating power requirements for all densities and temperatures and so slightly lowers the Q = 5 contour. This opens up the constrained operating space in the low density, low beta region.

More detailed physics models including launching, wave propagation, mode conversion, and absorption are currently under development for ICRF heating. These should form the basis of more comprehensive studies of ICRF heating needs.

2.4.9 Summary – Plasma Performance Modeling with Neutral Beam Injection

The potential operating regime of FED has been shown to be sensitive to the ion thermal conduction losses due to toroidal field ripple while startup power requirements are more dictated by electron energy confinement. Because of uncertainties in both ion and electron thermal losses and the roles of impurities, disruptions, and beta limits, fully optimal design choices cannot be made. It does appear, however, that a variety of modestly conservative physics models for the plasma thermal energy balance predict an acceptable operating regime consistent with the physics and design goals. Operation at higher fusion power output, higher plasma current, and higher toroidal field increases the possibility of ignition in FED.

The traditional argument of increased beam energy leading to increased central heating, and, therefore, greater heating efficiency in tokamaks is only one of many criteria which lead to a choice of beam energy. The shift of the magnetic axis improves heating at nonzero beta and relaxes the energy requirement, but even more criteria must be considered.

Source species mix, neutralization efficiency, and fractional energy transfer to electrons and ions all tend to push the beam energies to lower values. Physics arguments for greater penetration are aimed at reducing edge heating. Much greater emphasis should be placed on reducing the one-half and one-third energy components of the beam since those, and not the full energy component, are primarily responsible for edge heating.

2.5 BETA CONSIDERATIONS

Y-K. M. Peng, D. J. Strickler — ORNL/FEDC

Estimates of achievable beta ($\langle\beta\rangle = 2\mu_o\langle p\rangle/B_t^2$) in tokamak reactor studies[40] have typically been based on ideal MHD stability limits.[41-46] Recent ISX-B,[47,48] T-11,[49] JFT-2,[50] and DITE[51] results, however, have apparently suggested that these limits are not applicable. Nearly circular ISX-B plasmas have reached $\langle\beta\rangle \sim 2.5\%$ and exceeded the critical beta values established by Todd et al.[41] by about 50%. Equilibria obtained numerically in an attempt to model experimentally observed parameters have proven to be unstable to ideal MHD modes in computational studies.[45] The present assessments for beta in FED include a possible explanation for these apparent differences[52] and account for some of the latest work[53-56] that includes kinetic effects (Sect. 2.5.1). The implications of recent experimental results on achievable beta are summarized in Sect. 2.5.2 and used in Sect. 2.5.3 to suggest the best choices of poloidal beta, β_p, elongation, κ, and triangularity, δ, for FED.

2.5.1 Theoretical Assessments

Assuming a conducting surface near the plasma edge, ideal MHD stability studies indicate that for parameters roughly in the range of FED, beta is limited by the high-n ballooning modes.[43,44] Ballooning stability properties have been shown to improve with increased plasma elongation, κ, triangularity, δ, and with decreased aspect ratio, A, and safety factor, q_ψ.[41,45,46]

For a plasma with near FED parameters ($A = 3.7$, $\kappa = 1.6$, $\delta = 0.5$, $B_t = 3.6$ T at $R = 4.8$ m, and $q_\psi = 2.6$ at the plasma edge), and with pressure profiles such as have been used to model ISX-B plasmas,[57] a maximum stable average beta of $\sim$4.4% has been calculated using the General Atomic BLOON code.[58] This calculated value is about 20% below the design value of $\langle\beta\rangle = 5.5\%$.

Attempts to increase the MHD $\langle\beta\rangle$ limit calculated for ISX-B via only q-profile optimization have led to hollow plasma current profiles for $\langle\beta\rangle = 2.5\%$.[59] Therefore, it is of interest to determine if the pressure profiles of Ref. 57 can be improved to enhance stability. To improve the pressure profile, the region of unstable flux surfaces in the space of shear ($d\ell nq/d\ell n\rho$) and pressure derivative ($dp/d\psi$) of an FCT sequence of equilibria in FED can be calculated. As shown in Fig. 2-38, it becomes evident that the pressure profile can be improved by closely following the boundary of this instability region. For otherwise identical parameters [plasma shape, $q(\psi)$, B_t] such a profile is obtained (Fig. 2-39) and found to increase the stable beta to $\langle\beta\rangle \simeq 5.6\%$. This $\sim$20% increase in $\langle\beta\rangle$ has also been reproduced for an ISX-B like equilibrium, giving a calculated MHD $\langle\beta\rangle$ limit of 2.5%.[52] This suggests that the ideal MHD limits on $\langle\beta\rangle$ may not have been exceeded in present-day tokamaks. Using this improved pressure function, the critical beta values with respect to the $n = \infty$ ideal ballooning mode are given in Table 2-5 for typical FED configurations.

Table 2-5. Critical beta with respect to ideal MHD $n = \infty$ ballooning modes for some possible FED parameters using the improved pressure profiles

κ	δ	B_t(T)	I_p(MA)	q	$\langle\beta\rangle$(%)
1.6	0.5	3.6	6.2	2.6	5.6
1.6	0.3	3.6	4.8	3.2	3.8
1.6	0.5	3.6	8.0	2.0	7.5
1.6	0.3	4.5	6.0	3.2	3.8
1.5	0.2	4.5	5.2	3.2	3.3

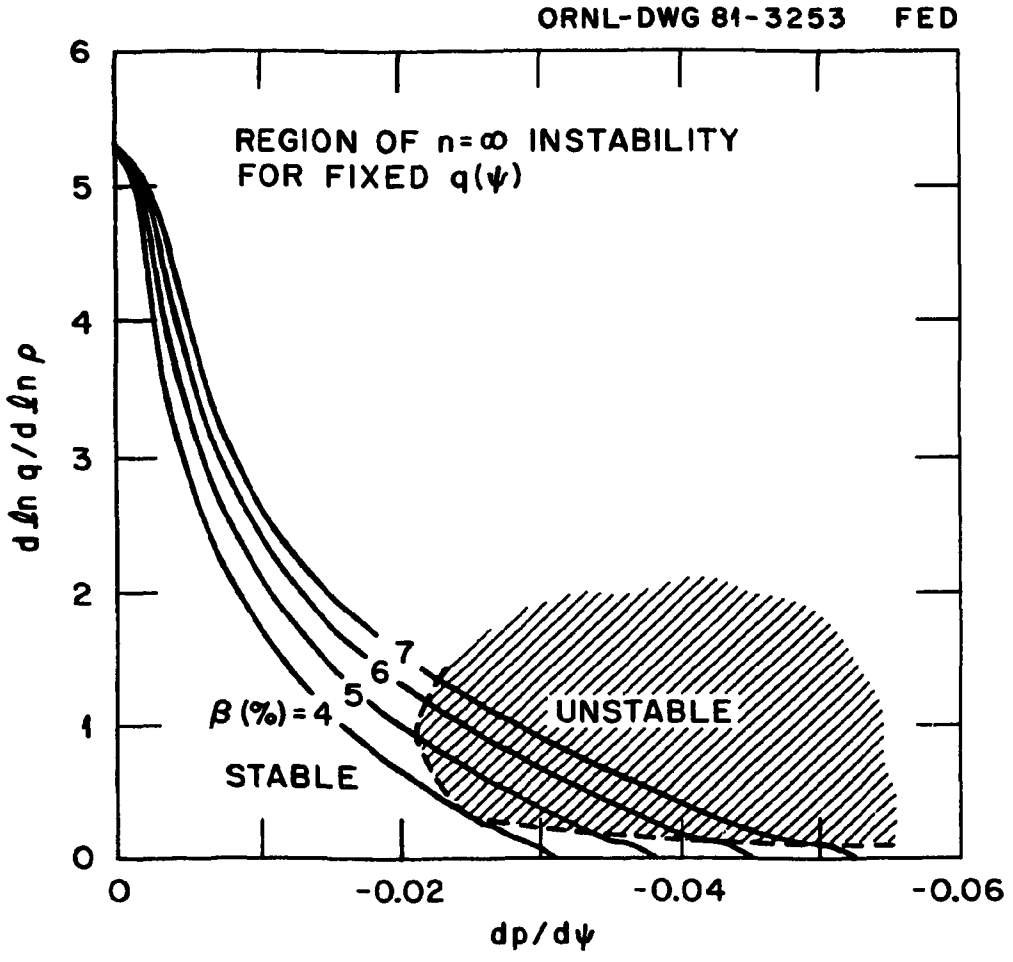

Fig. 2-38. Region of ballooning instability for fixed $q(\psi)$ as determined by a flux conserving family of FED-like MHD equilibria with pressure profile $p(\psi)$ given by Eq. 2-4. A $\langle\beta\rangle$ limit of 4% is obtained.

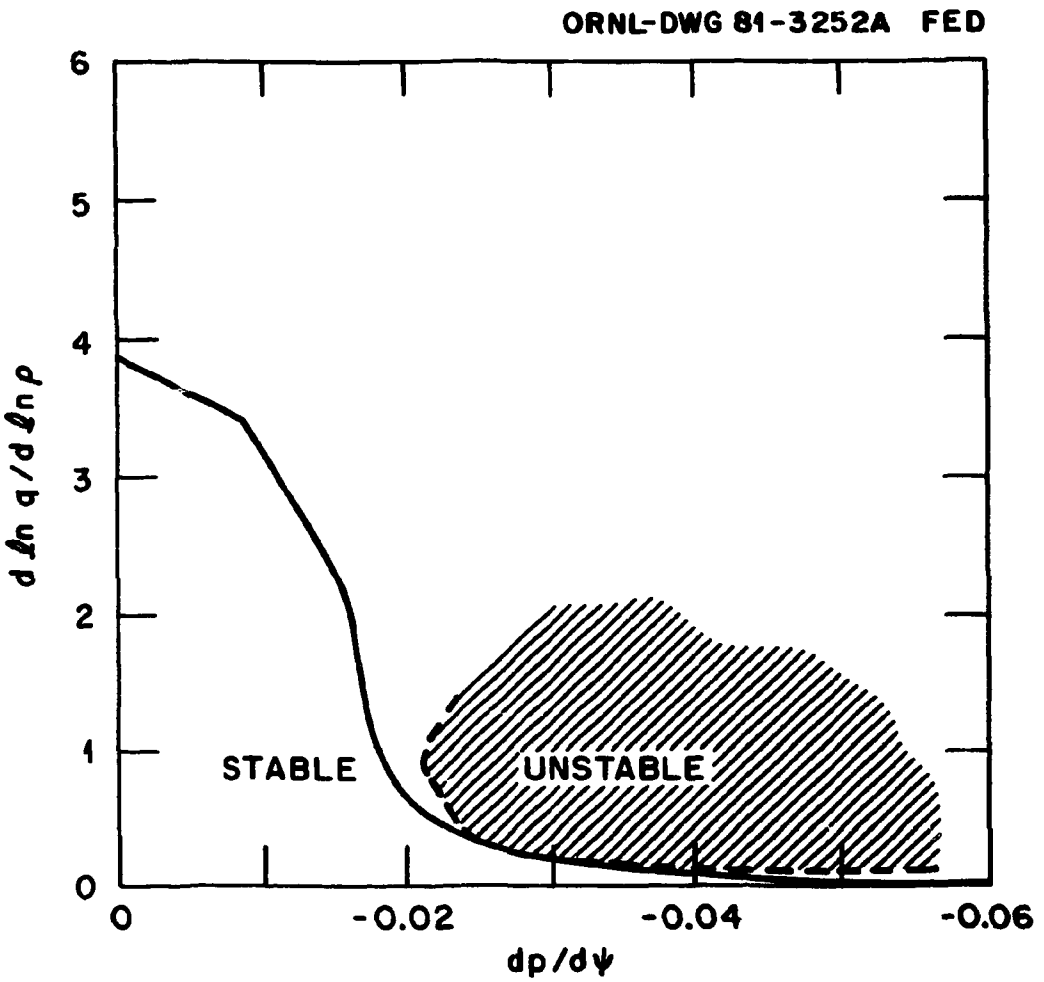

Fig. 2-39. The improved pressure function depicted in the shear ($d\ell nq/d\ell n\rho$) and pressure gradient ($dp/d\psi$) space. A ballooning mode $<\beta>$ limit of 5.5% for FED is obtained.

These numerical calculations indicate that the baseline FED beta value ($<\beta> \sim 5.5\%$) can be achieved for equilibria that are stable with respect to the ideal ballooning mode if pressure profiles are improved in a strongly D-shaped plasma with $q_\psi = 2.6$. Figure 2-39 suggests the pressure profile is far from being optimal and further $<\beta>$ increases are possible.

Several authors have examined the stabilizing influence of finite Larmor radius (FLR) effects on the ballooning mode in tokamaks, including the background and the energetic ions.[53-56] These investigations have shown consistently that the ballooning stability boundary is moved toward higher shear and pressure gradient as $(Nq\rho_i/a)$ is increased to order unity (N being the toroidal mode number and ρ_i being the ion gyroradius). Assuming $(Nq\rho_i/a) \sim 0.5$, the critically stable N_c is $\sim 40/\rho_i(\text{cm})$, above which all ballooning modes are stabilized for the FED parameters. For the 10-keV bulk ions in FED, N_c is found to be about 100, while for the energetic beam ions and fusion alpha particles, N_c in the range of 30 to 10 is estimated. Thus, the FLR effects would in effect remove the ballooning instability from the FED beta considerations. Under such an assumption, the achievable beta values are expected to be limited by other processes.

2.5.2 Experimental Indications

Because of the uncertainties in theoretical beta estimates based on stability criteria, it becomes of interest to assess FED beta based on recent experimental indications from ISX-B,[47,48] which are apparently consistent with results from DITE,[51] JFT-2,[50] and T-11.[49]

Three experimental observations from ISX-B[47,48] in nearly circular plasmas are of interest to beta considerations for FED:

1. Using power balance analysis, Murakami has suggested that the electron energy confinement time (normalized to density) decreases with increasing beam power.
2. Using magnetic pickup loop data, Swain has found that the quantity $(\beta_p I_p^{1/2})$ is a unique, empirical function of beam power and is satisfied over the typical operating range of ISX-B: $0.8\ T \leq B_t \leq 1.3$

$P_{beam} < 2.5$ MW, and 100 kA $\leq I_p \leq$ 180 kA. The results suggest a "soft" poloidal beta limit as the beam power is increased to 2.5 MW.

3. An examination of the $<\beta>$ and β_p values achieved shows that $<\beta>$ is bounded by two separate constraints. For high values of β_p, the $<\beta>$ value achieved appears limited by the impaired electron energy confinement. For low values of β_p, the $<\beta>$ value achieved follows the MHD equilibrium condition: $<\beta> \propto \beta_p/q^2$.
4. More recent observations[60] in ISX-B on elongated plasmas have indicated a similar degree of degradation of confinement as beam power is increased, so the plasma beta value has not increased beyond that obtained in circular plasmas with the same q_ψ.

With these observations, we propose the following basis for beta considerations in FED:

1. Figure 2-40 shows how the electron energy confinement time, τ_{Ee}, may vary with $\epsilon\beta_p$. The solid curve, not inconsistent with ISX-B results, is referred to as a "soft" limit. The dashed curve, referred to as a "stiff" limit, is included to reflect the degree of uncertainty in present results. Based on available data, it is not clear whether the decrease in τ_{Ee} is due to the high coinjected beam power density ($\sim$2 MW/m^3) or to the increasing value of β_p. Because the plasma heating power density in FED is about 0.25 MW/m^3 with much less momentum input, we choose the latter assumption for the current assessment.
2. Within the limits of power balance, the $<\beta>$ values achieved in ISX-B are consistent with MHD equilibria. It is assumed that this will also apply in FED. This means that the achievable $<\beta>$ values are limited either by disruption at low q (Sect. 2.8) or by the available current and size of the OH induction coils.

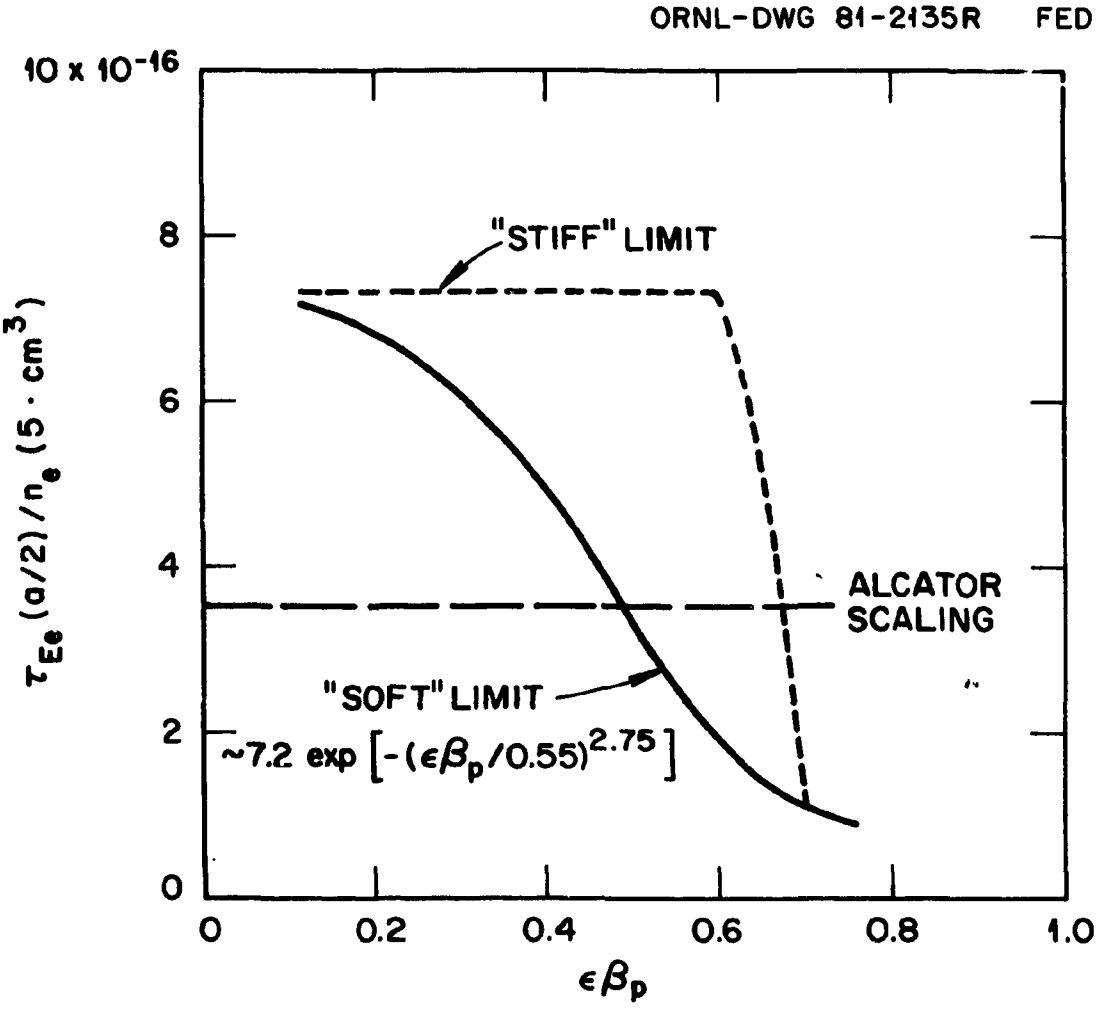

Fig. 2-40. Schematic dependences of τ_{Ee} in $\epsilon\beta_p$, reflecting a soft limit in β_p. The solid (dashed) line indicates a relatively soft (stiff) limit.

2.5.3 Choices of $\varepsilon\beta_p$, κ, and δ

The conditions that relate plasma equilibrium parameters, such as I, R, a, κ (elongation), δ (triangularity), $\langle\beta\rangle$, β_p, and q_ψ, are needed to assess the FED beta. A number of theoretical[61] and numerical[62] analyses of finite beta MHD equilibria in a flux-conserving tokamak (FCT) serve as the basis for the present formulation. It is convenient to start with an approximation[63] to the flux definition of safety factor q_ψ at the plasma boundary:

$$q_\psi \simeq 5C(\varepsilon\beta_p, q_\psi, \kappa, \delta)\ \frac{B_t a}{I_p}\ \frac{\varepsilon}{(1-\varepsilon^2)^2}\ \frac{1+\kappa^2}{2}\ , \qquad (2\text{-}4)$$

where $\varepsilon = a/R$ and $\kappa = b/a$. Here mks units are used with I_p in megamperes.

The coefficient C is somewhat greater than unity and increases as: (1) the magnetic axis shifts outward (with increasing $\varepsilon\beta_p$); (2) the current profile becomes more peaked (with increasing q_ψ); and (3) the cross section becomes more noncircular (with increasing κ and δ). At low values of $\varepsilon\beta_p$ and q_ψ ($\sim$2), the value of C is about 1.1 for a plasma with elongated D-shape.[63] A set of FCT equilibrium calculations was performed to determine C as a function of q_ψ (Fig. 2-41) and as a function of δ (Fig. 2-42) for $\varepsilon\beta_p$ up to 0.6.

A relatively convenient definition for β_p has been used in plotting Fig. 2-41

$$\beta_p \equiv 2\mu_o\langle p\rangle/\bar{B}_p^{\,2}\ ,$$

where the bar denotes the flux surface average at the plasma boundary. Under the approximation of an elliptical cross section, a relatively convenient and accurate relation linking $\langle\beta\rangle$ and β_p is obtained:

$$\langle\beta\rangle = \beta_p\ \left[\frac{C}{q_\psi}\ \frac{\varepsilon}{(1-\varepsilon^2)^2}\right]^2\ \frac{1+\kappa^2}{2} = \beta_p\ \left(\frac{I_p}{5aB_t}\right)^2\ \frac{2}{1+\kappa^2}\ . \qquad (2\text{-}5)$$

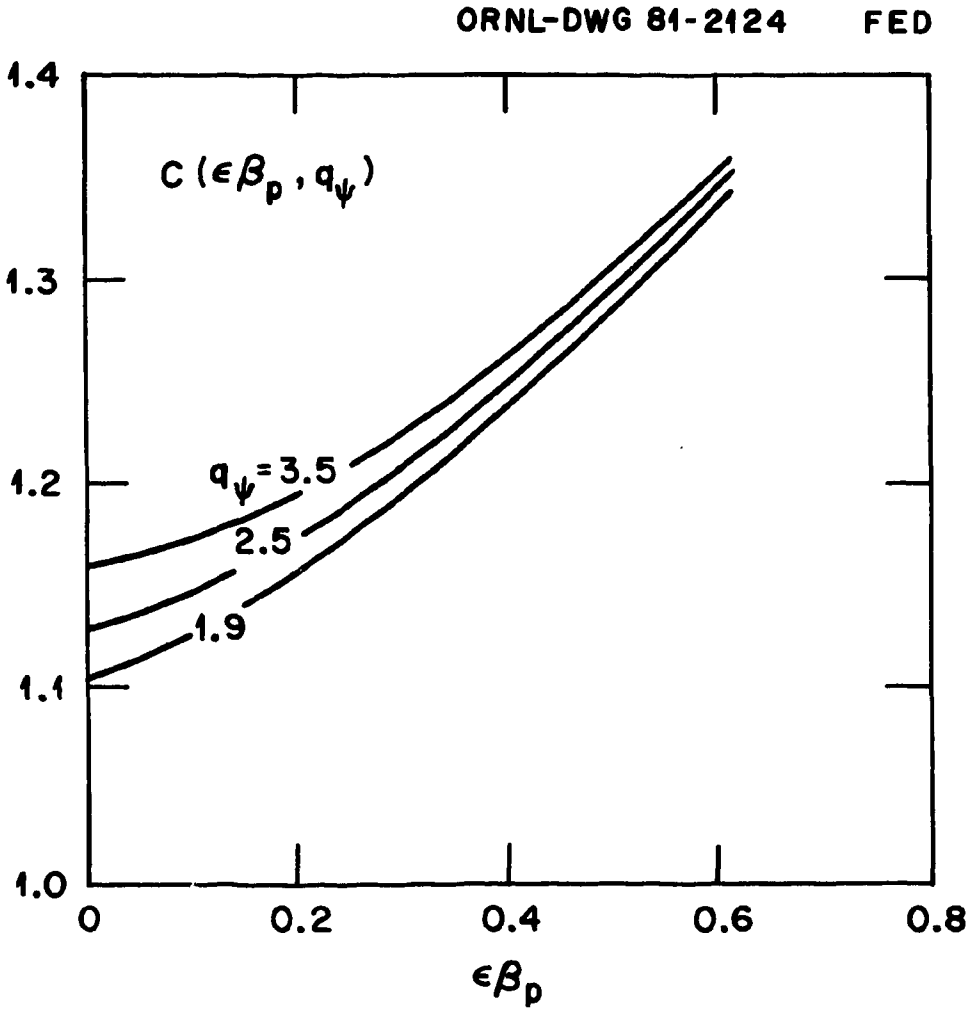

Fig. 2-41. The value of C in Eq. 2-5 as a function of $\varepsilon\beta_p$ and q_ψ for a FED-like flux-conserving tokamak where R = 4.80 m, a = 1.27 m, B_t = 3.62 T, κ = 1.6, and δ = 0.5.

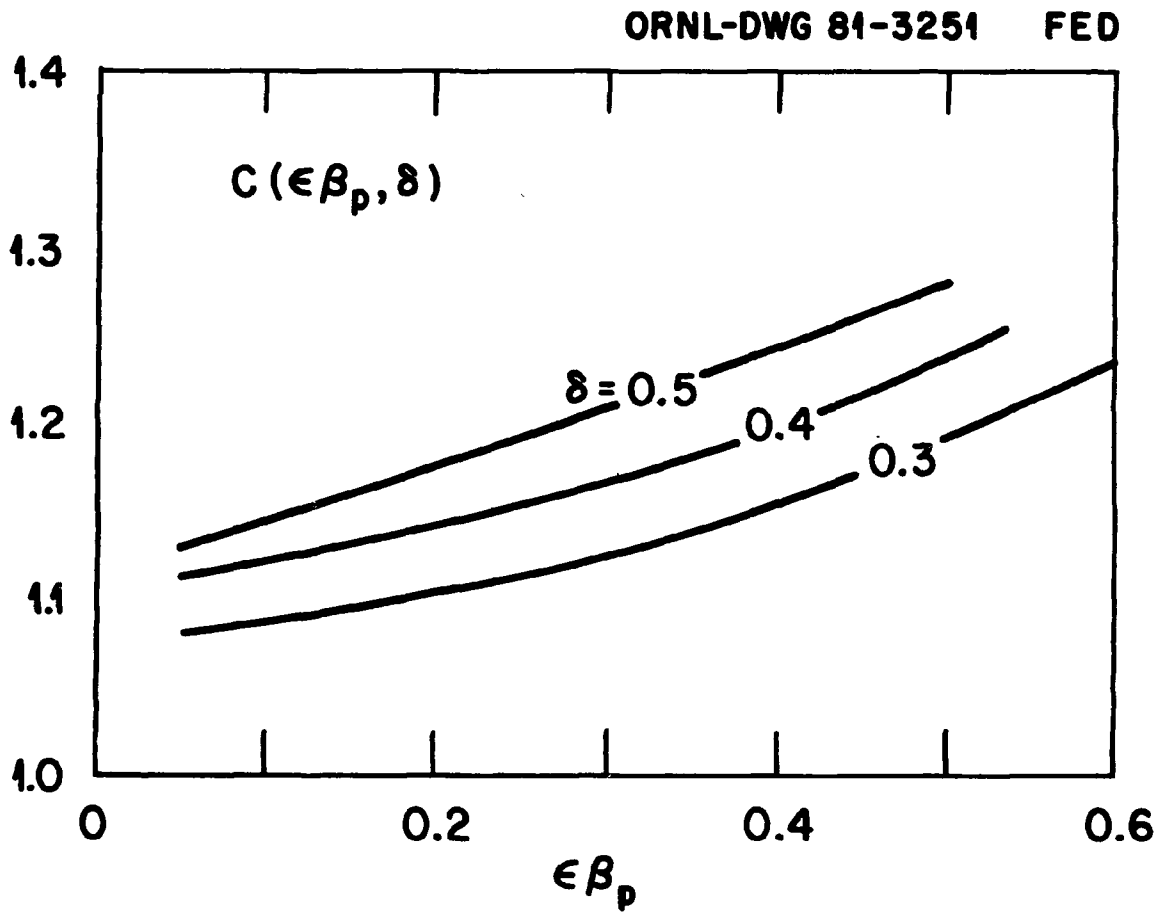

Fig. 2-42. The value of C in Eq. 2-5 as a function of $\epsilon\beta_p$ and the triangularity δ for a FED-like flux-conserving tokamak with R = 4.8 m, a = 1.3 m, B_t = 3.62 T, q_ψ = 3.2, and κ = 1.6.

The value of β_p as defined above is found to be within a few percent of the value of β_I[64] for $\beta_p < 2$.

To assess whether the baseline choices of $\varepsilon\beta_p \lesssim 0.6$, $\kappa = 1.6$, and $\delta = 0.3$ remain appropriate under these assumptions of achievable $<\beta>$, it is convenient to use $n\tau_{Ee}$ as a parameter to reflect potential plasma performance. A maximization of $n\tau_{Ee}$ is sought by appropriate choices of $\varepsilon\beta_p$ and κ, under typical choices of plasma temperature and density (Sect. 2.4).

Given the dependences of Fig. 2-40 and the uncertainties in the scaling of electron confinement,[1,2] a more general form of the empirical electron energy confinement time can be written as

$$\tau_{Ee} = C_\tau n_e a^s R^t q_\psi^u B_t^v \exp[-(\varepsilon\beta_p/\delta)^\gamma] \ , \qquad (2\text{-}6)$$

where $\delta \simeq 0.55$ and $\gamma \simeq 2.75$ have been chosen to represent a relatively soft β_p dependence. The values of s, t, u, and v can range from those for Alcator scaling[65] ($s = 2$, $t = v = 0$, $u = 0.5$) to those for Merezhkin scaling[66] ($s = 5/24$, $t = 21/8$, $u = 7/6$, $v = -1/3$). For fixed maximum toroidal field, B_m, at the coil, we have

$$B_t = B_m \left(1 - \varepsilon - \frac{\Delta_s}{R}\right) \ , \qquad (2\text{-}7)$$

where Δ_s is the distance between the inside TF coil leg and the plasma. Combining Eqs. 2-5 through 2-7 then gives:

$$n\tau_{Ee} = C_\tau \left(\frac{B_m^2}{4\mu_o T_o}\right)^2 B_m^v \alpha^2 q_\psi^{u-4} F(\varepsilon\beta_p) H(\kappa) G(R,a) \ ,$$

$$F(x) = x^2 C^4(x, q_\psi) \exp[-(x/0.55)^{2.75}] \ ,$$

$$H(\kappa) \simeq (1 + \kappa^2)^2/4 \ ,$$

$$G(R,a) = a^s R^t \varepsilon^2 \left(1 - \varepsilon \frac{\Delta_s}{R}\right)^{4+v} / (1 - \varepsilon^2)^8 \ , \qquad (2\text{-}8)$$

where T_o = 10 keV and α is the fraction of $<\beta>$ due to the thermal component of the D-T plasma.

In this equation, the dependence of $n\tau_{Ee}$ (i.e., the plasma performance) on $\varepsilon\beta_p$ and κ is contained solely in the functions $F(\varepsilon\beta_p)$ and $H(\kappa)$. As a result, uncertainties in the size scaling of electron energy confinement do not impact the choice of either $\varepsilon\beta_p$ or κ. Figure 2-43(a) gives $F(\varepsilon\beta_p)$ as a function of $\varepsilon\beta_p$. As indicated, a maximum occurs near $\varepsilon\beta_p = 0.55$ (soft limit), even though τ_{Ee} increases by a factor of 3 as $\varepsilon\beta_p$ increases from near zero to 0.55. For values of $\varepsilon\beta_p$ in the range of 0.4-0.7, it is seen that the function $F(\varepsilon\beta_p)$ remains within 20% of its peak.

Figure 2-43(b) gives the function $H(\kappa)$ versus κ. As indicated, there is more than a threefold increase in $H(\kappa)$ for an elongation of 1.6. This results from the increase in $<\beta>$ with increasing κ at constant $\varepsilon\beta_p$ and q_ψ. Thus, the role of elongation in increasing $<\beta>$ is via increases in I_p at constant β_p, a, and B_t [Eq. (2-5)]. This elongation enhancement is much more significant than, and in addition to, the currently perceived dependence of C_τ on κ.[67]

Figure 2-43(a) also shows that the value of $\varepsilon\beta_p$ that maximizes $n\tau_{Ee}$ is not sensitive to the uncertainty in the form of τ_{Ee} as long as a substantial decrease in τ_{Ee} occurs when the $\varepsilon\beta_p$ reaches values of 0.6-0.7. As indicated by the plot of the "stiff" limit in β_p in Fig. 2-43(a), a maximum value of $\varepsilon\beta_p$ of $\sim$0.6 remains appropriate.

As will be discussed in Sect. 2.7, a practical poloidal field coil configuration in FED calls for a reduction of triangularity to $\delta = 0.3$. Figure 2-42 shows that this will result in a reduction of the constant C by about 7%. The impact of this on the FED parameters can be assessed from Eqs. 2-4 and 2-5 and are summarized in Table 2-6. It shows that reducing δ to 0.3 leads to a lowered $<\beta>$ of 4.8%, an increased $\varepsilon\beta_p$ of 0.55, or a lowered q_ψ of 3.0. Lowering $<\beta>$ will lead to a significant reduction in FED performance. Increasing $\varepsilon\beta_p$ will potentially reduce τ_{Ee} and lead to increased plasma heating requirements. Lowering q_ψ will potentially enhance the probability of plasma disruption. However, the indicated variations in the latter two cases fall well within the uncertainties in current tokamak physics understanding. It is therefore

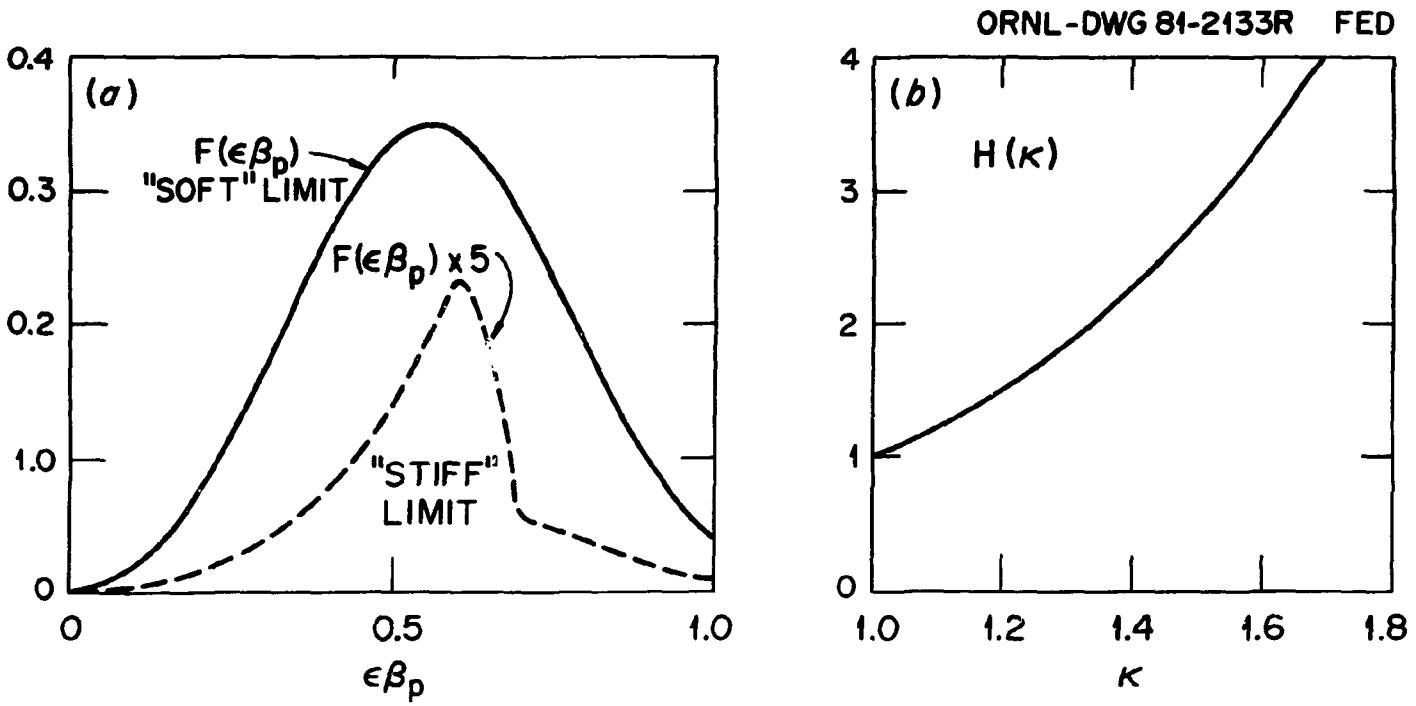

Fig. 2-43. The dependence of $n\tau_{Ee}$ on $\varepsilon\beta_p$ and κ with constant q_ψ as expressed in Eq. 2-9 through (a) $F(\varepsilon\beta_p)$ and (b) $H(\kappa)$. The variations of $F(\varepsilon\beta_p)$ assuming a relatively stiff limit in β_p as shown in Fig. 2-40 are also included.

recommended that the FED design values of I_p, $\varepsilon\beta_p$, and $\langle\beta\rangle$ remain unchanged while δ is reduced to 0.3. When δ is reduced further to 0.2, the table suggests that $q_\psi = 2.9$ is required.

Table 2-6. Impact of reducing δ to 0.3 on FED parameters

Parameters	Baseline	Lower $\langle\beta\rangle$	Higher $\varepsilon\beta_p$	Lower q_ψ	
δ	0.5	0.3	0.3	0.3	0.2
q_ψ	3.2	3.2	3.2	3.0	2.9
$\varepsilon\beta_p$	0.5	0.5	0.55	0.5	0.5
I_p (MA)	5.4	5.0	5.2	5.4	5.4
$\langle\beta\rangle$(%)	5.5	4.8	5.5	5.5	5.5

Finally, the impact of a possible soft β_p-dependence can be assessed by assuming

$$\chi_e = 0.5\ \chi_e^{ALC} \exp(2\varepsilon\beta_p)^2 + \chi_e^{NC} ,$$

in the transport calculations.[68] Here the superscripts label the Alcator scaling and neoclassical contributions to χ_e. The effect of degraded confinement with increasing β_p on the plasma operation regimes of Sect. 2.4 is that $Q \geq 5$ may still be achievable but that ignition at δ T must be regarded as highly improbable. However, since $\beta_p \propto I_p^{-2}$, this model depends on I_p as $\exp(I_p^{-4})$, and a small increase in I_p could substantially restore the confinement.

2.5.4 Conclusions and Future Work

Based on these assessments, and given the level of uncertainty in the MHD analysis, it becomes clear that the baseline value of $\varepsilon\beta_p = 0.5$ is relatively conservative but appropriate. The choice of

$q_\psi \lesssim 3.2$ is primarily based on concerns about major plasma disruptions (Sect. 2.8). Using Eqs. 2-4 and 2-5 we obtain for $q_\psi = 3.0$ the baseline FED plasma parameters of $\beta_p = 1.8$, $\langle\beta\rangle = 5.5\%$, $\delta = 0.3$, and $I_p = 4.8\text{-}5.4$ MA as $\langle\beta\rangle$ is increased from 0.2% to 5.5%.

With fixed q_ψ and B_m, the assumption of a "soft" limit in β_p leads to a strong maximization of $n\tau_{Ee}$ near $\varepsilon\beta_p = 0.55\text{-}0.6$, and a threefold enhancement of $n\tau_{Ee}$ by elongation to $\kappa = 1.6$. These results are found to be insensitive to uncertainties in the size scaling of τ_{Ee} and the "stiffness" of the β_p limit.

It is also seen that the plasma performance depends predominantly on B_m and q_ψ, as revealed in Eq. 2-8:

$$n\tau_{Ee} \propto B_m^{4+v}/q_\psi^{4-u} ,$$

with only a relatively weak dependence through $F(\varepsilon\beta_p)$. To achieve high plasma performance, it is, thus, just as effective to lower q_ψ as it is to raise B_m. Low B_m operation in FED can be offset by a lower q_ψ, as long as plasma disruptions can be avoided (Sect. 2.8). This is apparently consistent with the indications from varying B_t in ISX-B although the purported $\langle\beta\rangle$ benefit from plasma elongation is yet to be demonstrated.[60] This suggests that the disruption-free regime of $q_\psi < 2$ demonstrated in DIVA[69] if achievable in FED, would permit a highly cost-effective FED design.

The FED performance for a given cost is expected to depend strongly on the achievable $\langle\beta\rangle$ values. Means to maximize $\langle\beta\rangle$ should therefore continue to be explored.

2.6 POWER, PARTICLE, AND IMPURITY HANDLING

A critical area for FED is that of handling large fluxes of power, plasma particles, and fusion-produced helium ash at the plasma edge without excessive accumulation of impurities in the plasma or damage to the first wall. The main possibilities for accomplishing this function in FED are: (1) a pump limiter; (2) a poloidal divertor; (3) a bundle divertor; and (4) active impurity control schemes. The principal system considered for FED is the pump limiter with the poloidal divertor as the primary backup option. This section analyzes the first three options for power, particle, and impurity handling in FED. Potential active impurity control schemes are discussed in Ref. 1.

Section 2.6.1 discusses the general requirements for a FED pump limiter or poloidal divertor. Section 2.6.2 discusses pump limiter design considerations, and Section 2.6.3 analyzes pump limiter performance. Section 2.6.4 analyzes the cold plasma edge scenario which could ameliorate the potentially serious erosion problems for a pump limiter. Sections 2.7.5 and 2.7.6 discuss two magnetic divertor candidates for FED, the poloidal divertor, and the bundle divertor, respectively.

2.6.1 FED Pump Limiter/Divertor Requirements

M. Ulrickson — PPPL

The four primary functions needed for an effective FED power, particle, and impurity control system are: (1) heat removal, (2) helium ash removal, (3) minimization of impurity influx to the plasma core, and (4) minimization of first wall erosion. These functions may be combined as in a magnetic divertor (poloidal or bundle) or separated as in a pump limiter (heat and helium removal) and active control schemes (minimization of impurity influx).

The heat removal function requires that the thermal load be spread reasonably uniformly over an adequate area. This requirement can be satisfied with pump limiter or divertor plate areas of $\sim$60 m^2. This area can be provided with pump limiter or divertor plates which are about 2 m in poloidal extent and are toroidally continuous.

The helium removal function requires that $\sim 1.6 \times 10^{20}$ particles are exhausted per second of operation while maintaining the helium content below about 3%. This helium removal rate is small compared to the rate ($\sim 10^{22}$ s^{-1}) at which helium ions arrive at the pump limiter or divertor plate. For this reason the helium removal requirement can be satisfied with an acceptable ($\sim 10^5$ ℓ/s) pumping rate from the pump limiter or divertor region.

The impurity minimization requirement for the pump limiter or divertor is difficult to quantify with present understanding of plasma edge behavior. However, it is clear that divertors should be far superior to pump limiters in this role. Pump limiters may require a cold plasma edge to limit erosion and impurity production and/or an active impurity control scheme to inhibit impurity penetration into the plasma core. The next generation of tokamak experiments should provide a good test of impurity control with limiters. The outcome of these tests will strongly impact the choice of the impurity control option for FED.

The pump limiter/divertor system must minimize the erosion of the first wall. Large erosion rates would lead to excessively high impurity levels in the plasma center and require frequent replacement of first wall components. The large recycling near a pump limiter will increase the charge-exchange erosion in this region whereas the erosion associated with a divertor should be localized in the divertor channel.

Pump limiter systems are intrinsically easier and cheaper to design and fabricate than divertors and have less impact on the overall device performance. However, if design studies and experiments show that pump limiters cannot satisfy the impurity control and erosion requirements for FED, then a poloidal divertor appears to be an acceptable option.

Table 2-7 lists the heat load requirements and edge parameters for FED for 10-T operation. Twenty MW of the 90 MW of alpha heating power is assumed to be lost in the discharge by charge exchange and radiation. An additional 10 MW is assumed to be deposited on the divertor channel walls by the same mechanisms. Gas blanket effects inside the divertor channel could easily increase this load and reduce the divertor plate loading. The divertor should operate at higher edge densities than the

Table 2-7. FED edge parameters at 10-T operation

	Pump limiter	Divertor
Alpha power	90 MW	
Edge Load	70 MW	
Plate Load	70 MW	60 MW
Ion Power	54 MW	46 MW
Electron Power	16 MW	14 MW
Channel Charge Exchange		5 MW
Channel Radiation		5 MW
Ion Energy	300 eV	100 eV
λ_n	3 cm	
λ_T	6 cm	
λ_Q	2 cm	
λ_{nd}		9 cm
λ_{Td}		18 cm
λ_{Qd}		6 cm

pump limiter due to reduced flow into the divertor throat. This will reduce the edge temperature required to conduct the heat to the divertor plate. The electric sheath at the pump limiter or divertor plate will accelerate the ions and reduce the electron thermal load. The scrape-off widths which are listed in Table 2-7 are at the large major radius side of the discharge (λ) and inside the outer divertor channel (λ_d). The increased widths inside the channel are due to the expanded flux surfaces in this region. For the same reason, the scrape-off width at small major radius will be about 3λ, and inside the inner channel about $2\lambda_d$.

2.6.2 Pump Limiter Design

M. Ulrickson, D. E. Post, M. Petravic — PPPL

The design of the pump limiter for FED, which resulted from both the pump limiter task team study and from FED Design Center engineering studies, is shown in Figure 2-44. The limiter is flat in the poloidal and toroidal directions. The location at the bottom of the machine results in the lowest heat load on both the limiter surface and the leading edge for the case of a single toroidal belt. The pumping channel is formed between the back of the limiter and the inner surface of the shield wall. The plasma particles entering the pump channel are neutralized on the back face of the limiter. The fraction of the recycling plasma particles entering the channel is sufficient to remove the helium ash.

The location of the tip of the pump limiter on the small major radius side of the tangency point results in the lowest possible heat load on the tip. This is because of the expansion of the flux surfaces at the bottom of the elongated high beta plasma. The heat and particle loads along the top surface of the limiter are shown in Figure 2-45. The particle and energy scrape-off lengths were assumed to vary linearly with the spacing of the field lines. The particle and energy fluxes were determined from the radial distance from the tangent field line and the angle of incidence of the field line with the limiter surface. The results show that the heat flux is compatible with available steady-state cooling techniques. Location of the pump limiter as shown also

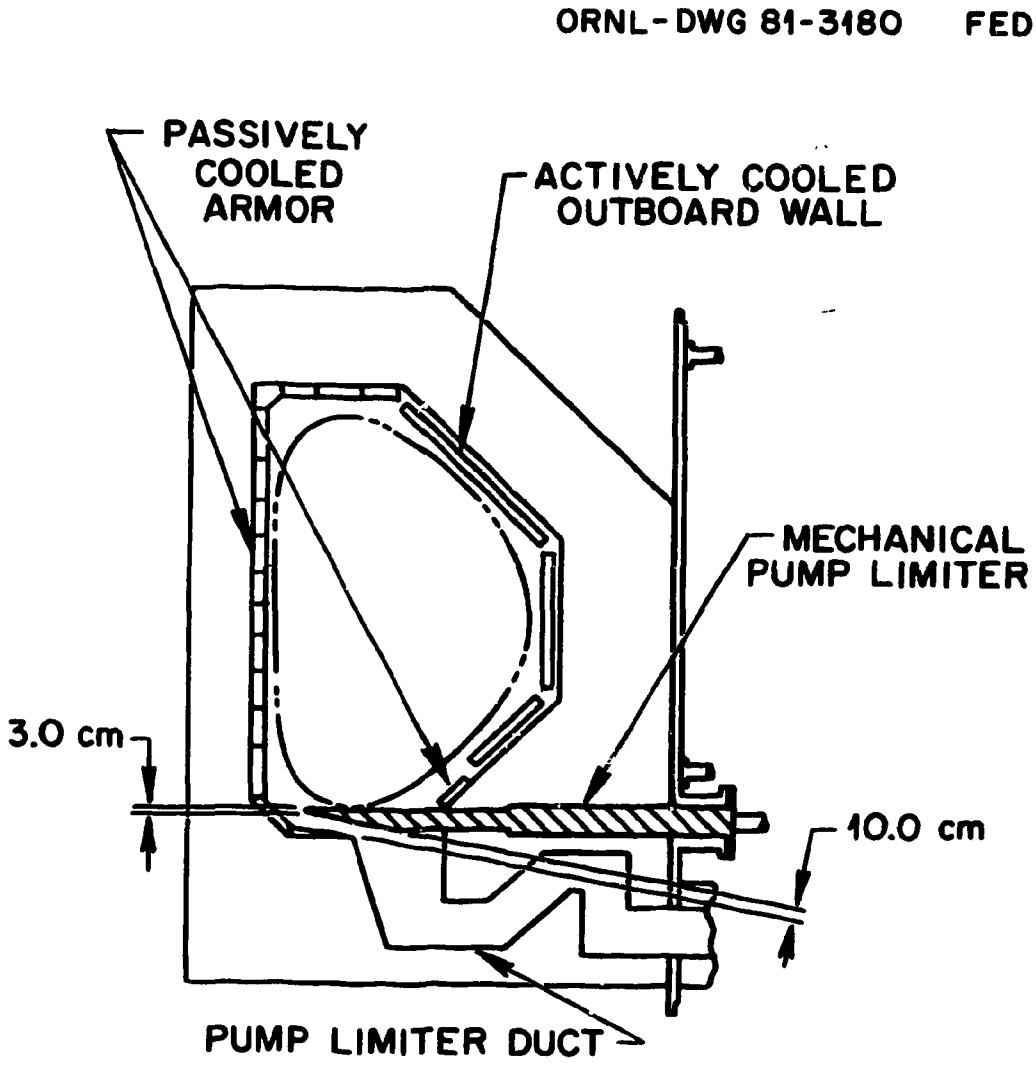

Fig. 2-44. The FED pump limiter configuration.

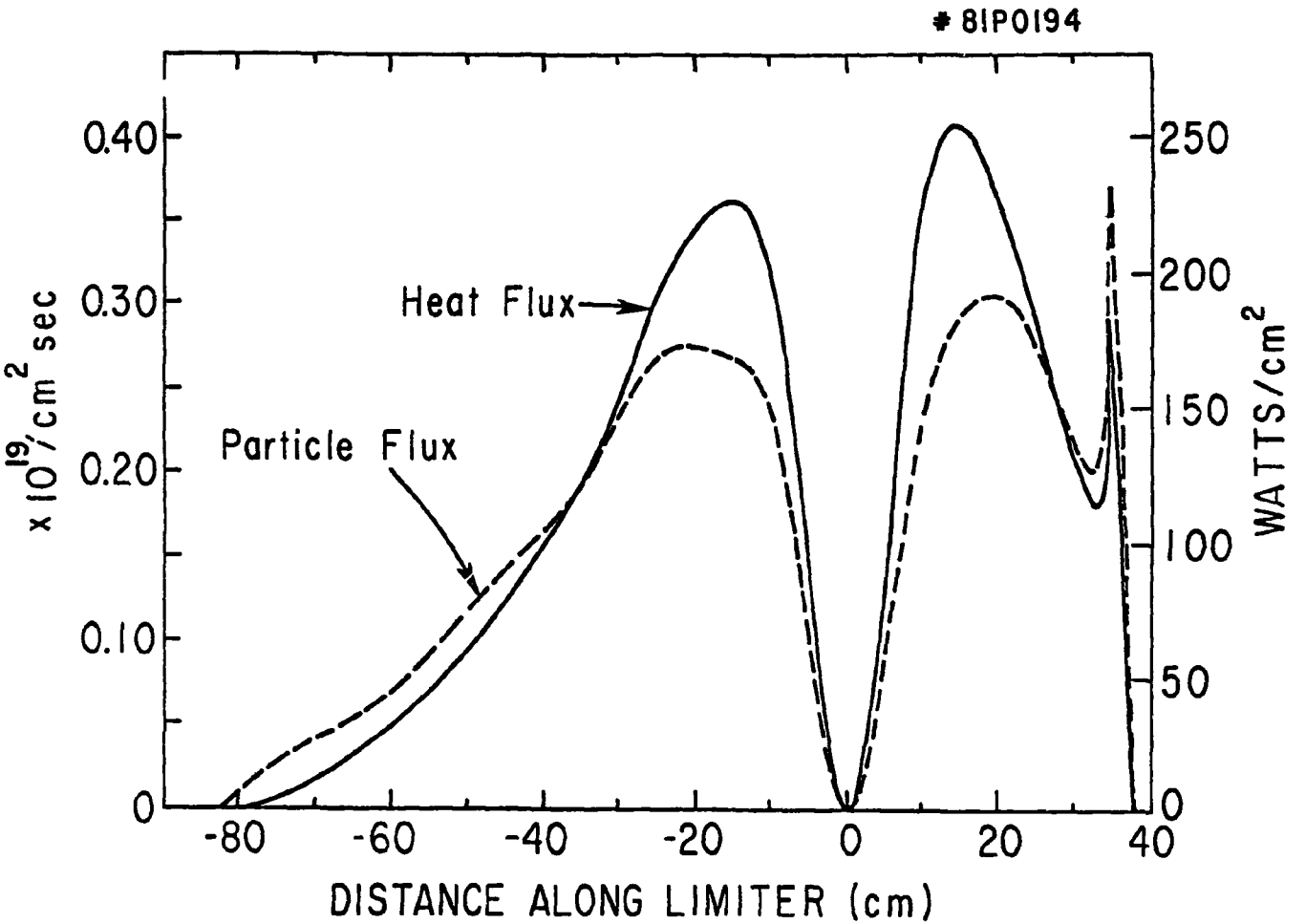

Fig. 2-45. The calculated heat and particle loads along the top surface of the FED pump limiter.

results in the least sensitivity of the tip heat load to changes in the plasma parameters, shape, and position.

The erosion of the limiter surface due to burn phase particle fluxes (shown in Figure 2-45) and due to disruption loads and other fault conditions is one of the major problems in pump-limiter design. The proximity of the eroding surface to the plasma requires the use of low Z materials, and the FED design is based on the use of graphite tiles. Graphite is the best of the low Z materials from a thermostructural viewpoint. However, in addition to the physical sputtering during normal discharges and evaporation and/or sublimation during disruptions, graphite exhibits chemical erosion through the formation of hydrocarbons. Since the chemical erosion rate is not well characterized and is temperature dependant, it was assumed equal to the physical sputtering. The disruption heat loads are also not well characterized at this time, and a safety factor of 5 was assumed in the analysis. The resultant erosion due to the sources listed above is 3.0×10^{-4} to 3.5×10^{-4} cm per pulse. The other major unresolved erosion question is how much of the eroded graphite actually enters the plasma.

With the pump limiter shown in Figure 2-44, about 5.5% of the recycling particle flux at the limiter enters the pump channel. A 2-D plasma particle and neutral transport code has been used to estimate the performance of the pump channel. The channel has been modeled as a 15 cm deep by 60 cm long rectangular slot with a pump duct of equivalent size near the neutralizer plate. The calculations have been performed using both a case for high edge flux, 5×10^{23}/s, and a case for low edge flux, 5×10^{22}/s. The results for the high flux case are shown in Figure 2-46 and the low flux case in Figure 2-47. The efficiency of the pump limiter is about 60% for the low edge flux case and 90% for the high flux case. Both are sufficient to pump the helium ash. In the high flux case the recycling at the neutralizer results in both a high neutral pressure which eases pumping and a lower electron temperature which reduces erosion of the neutralizer plate. Restriction of the pump in the low flux case can achieve the same result.

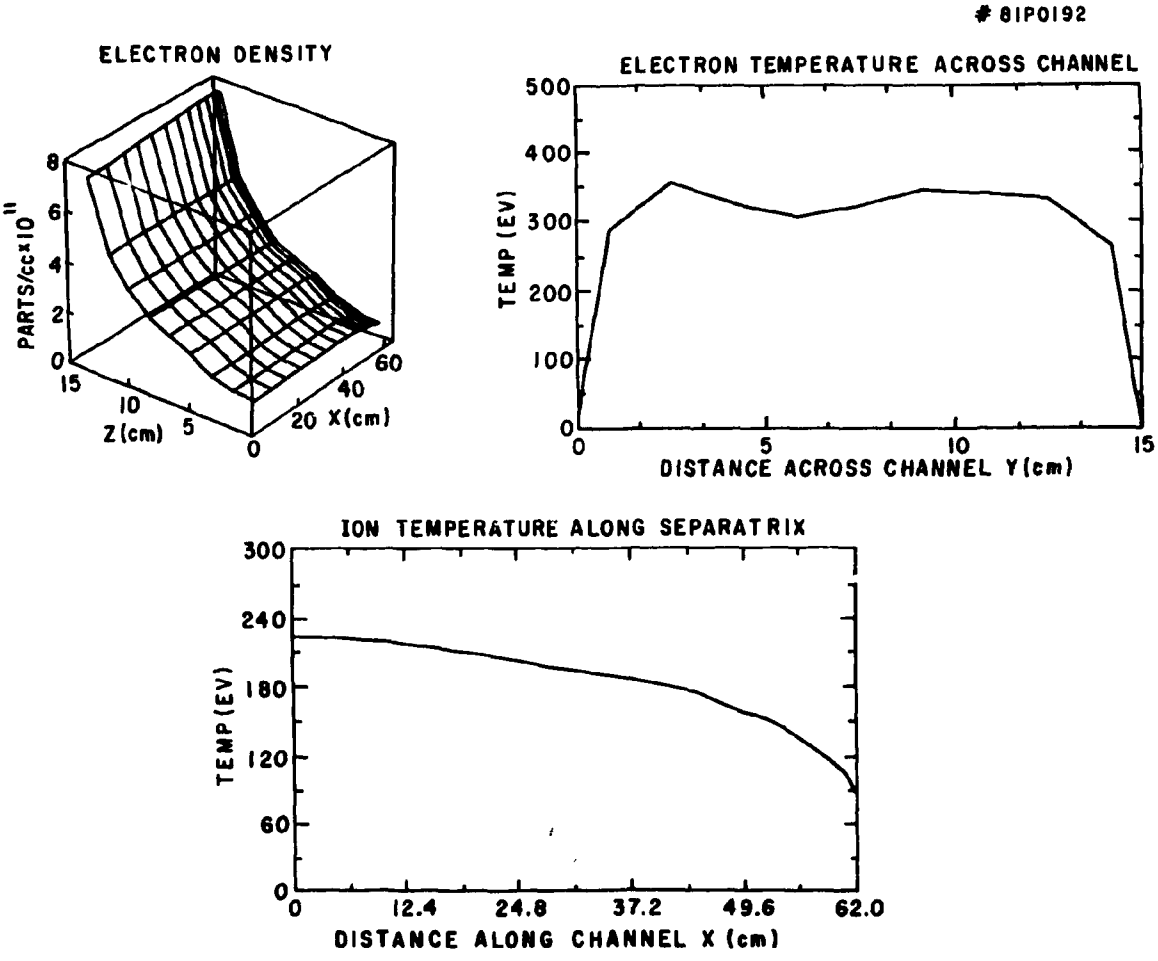

Fig. 2-46. Plasma parameters in the pump limiter duct for the high edge flux case (5×10^{23} s^{-1}): (a) density profile in the duct where Z is the distance across the duct and X is along the duct; (b) electron temperature profile across the duct assuming constant T_e along duct; and (c) ion temperature along the field for the center of the duct.

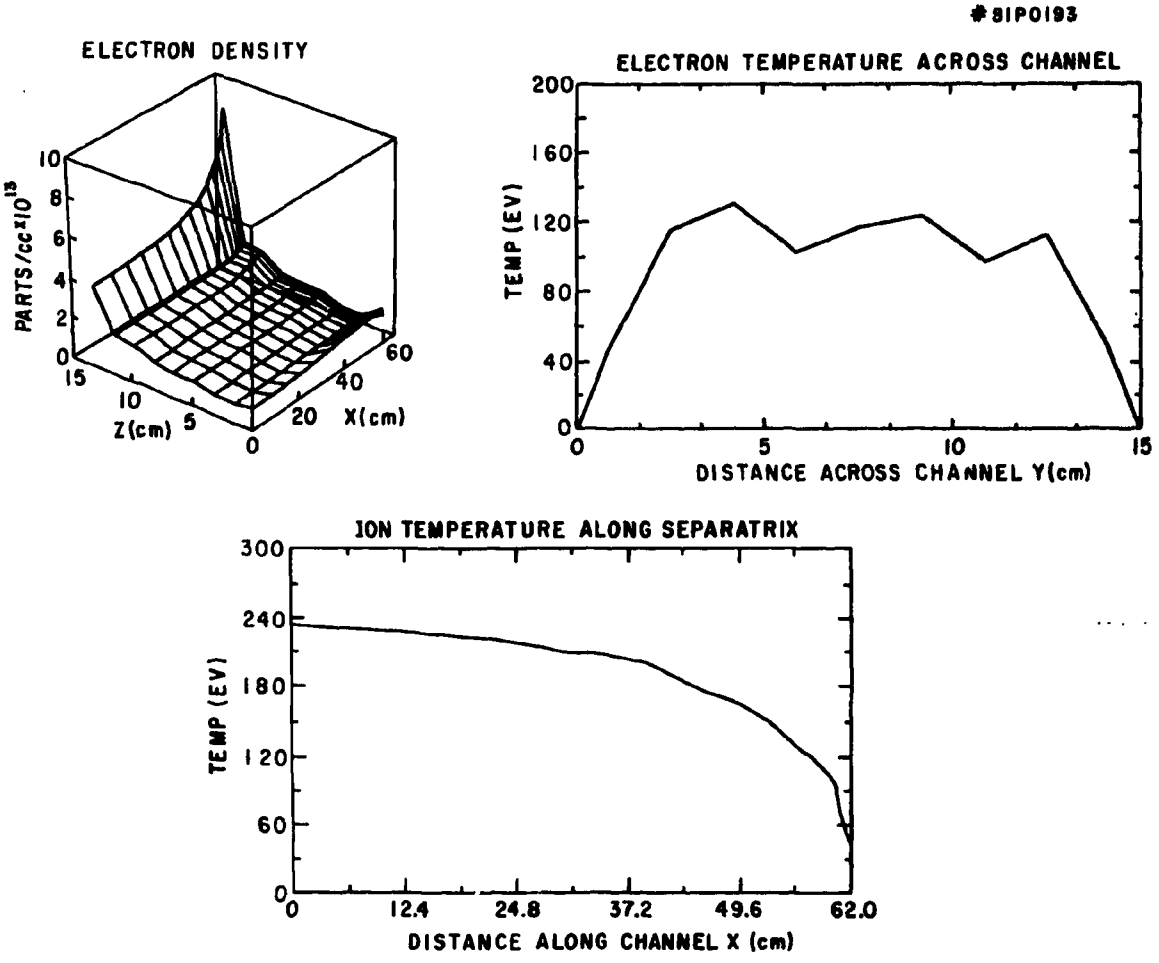

Fig. 2-47. Plasma parameters in the pump limiter duct for the low edge flux case (5×10^{22} s^{-1}). The corresponding high flux case is shown in Fig. 2-46.

The result is that a pump limiter can be designed which has a modest peak heat load and sufficient particle pumping to remove the helium ash. It also does not require accurate control of the separatrix position during start-up. The major uncertainties in the design involve erosion of the limiter surface, transport of the eroded material, and plasma contamination due to eroded material. Further experiments with pump limiters are required to resolve these issues.

2.6.3 Pump Limiter Analysis

H. C. Howe – ORNL/FEDC

In this section, we discuss several aspects of the pump design. Transport code estimates of the total particle and heat flows to the limiter are summarized and used as inputs to a simple analytic scrapeoff model. Uncertainty in the expected scrapeoff cross-field transport rates leads to a range of expected heat and particle flux profiles on the flat limiter surface. Within this range, the maximum heat flux on the flat surface appears acceptable. However, the high erosion rate on the graphite limiter surface (≈30 cm/year) is probably unacceptable and remains the major unsolved design problem. The ability to control the distance of the plasma from the limiter leading edge is necessary to maintain control of the leading edge heat flux and total particle pumping rate. This control is also needed to adjust for 1) the uncertainties in the plasma crossfield transport rate and resulting scrapeoff width and 2) temporal changes in the width or in the total power and particle limiter loads during a single burn. We discuss the feasibility of major radius motion of the entire plasma along the limiter surface to control the leading edge distance.

Before discussing transport code values for the total heat and particle flux incident on the limiter, we make the following simple estimates. The maximum total power incident on the limiter (P_T) in FED is mandated by the design. For 30 MW of auxiliary heating and Q = 5, the total thermal power flowing from the plasma is 60 MW. Allowing for some atomic losses, we assume a maximum of 50 MW flows to the limiter. The power to the limiter may be reduced substantially if edge radiation from impurities is significant, and so we also consider the case where only 5 MW reaches the limiter.

The total particle flow to the limiter may be approximated by a simple scaling from present-day experiments. If $\dot{N}_G$ is the external gas feed rate, $\dot{N}_T$ is the total fueling rate including recycling, and R is the total recycle rate, then in steady state, $\dot{N}_T = \dot{N}_G/(1 - R)$. For edge gas fueling with a constant penetration depth, the gas feed rate scales with plasma size as $\dot{N}_G \propto \kappa a^2$ (a = minor radius and κ = elongation). In ISX-B, $\dot{N}_G \simeq 10$ torr-liter/s for a = 26 cm, and we thus expect $\dot{N}_G \simeq 400$ torr-liter/s for FED where a = 130 cm and $\kappa = 1.6$. For 5% pumping, R = 0.95, and the total fueling rate is thus $\dot{N}_T \simeq 5 \times 10^{23}$ s^{-1} for FED.

These estimates of P_T and $\dot{N}_G$ are verified with detailed 1-1/2 D transport code calculations. Table 2-8 shows results from FED modeling using the transport code PROCTR[70] which includes the usual transport features. Three cases are considered: both ICRF and neutral beam driven operation with Q = 5 and 150 MW of neutron output, and ignited operation with 300 MW neutron output. The plasma density is varied between these three cases to obtain the desired total fusion neutron output. The impurity treated in these cases is carbon which does not radiate significantly. We see that the total power load on the limiter is similiar for the three cases and almost equal to the total thermal heating power. The total particle load is least for the case driven by neutral beams because the beams supply fuel directly to the plasma center and lower the required deuterium edge fueling rate. The particle load is highest for the ignited case because the extra fast α heating power required to replace the auxiliary heating requires higher plasma density and more fueling. These results lead us to consider two cases with total limiter particle loads of $\dot{N}_T = 3 \times 10^{23}$ and 10^{24} s^{-1}, respectively.

The third parameter needed for the analytic edge model is f, the fraction of the total gas fueling rate ($\dot{N}_T$) which is ionized in the plasma. The models in PROCTR include a detailed, spatially resolved scrapeoff model. Thus, an estimate of f may be obtained from the transport simulations. Values for f for the three cases described above are given in Table 2-8. Approximately 60% of the recycled and fueled gas is ionized in the scrapeoff, so we will assume that f is 0.4.

Table 2-8. Summary of transport simulations of FED

	Beam	ICRF	Ignited
P_T (MW)	48.2	59.9	54.0
$\dot{N}_T$ (s^{-1})	3.3×10^{23}	4.5×10^{23}	10^{24}
f	0.36	0.36	0.33
$\langle n_e \rangle$ (cm^{-3})	4.9×10^{13}	5.3×10^{13}	1.1×10^{14}
$\langle T_i \rangle$ (keV)	16.6	17.7	9.7
β_T (%)	5.1	5.9	6.9
β_p	1.8	2.1	2.4

The power and particle flux distributions on the limiter surface are estimated from the model discussed by Howe.[71] In this model, flow to the limiter at approximately the ion sound speed is balanced by cross-field transport from the main plasma. Several simplifying assumptions lead to the usual exponential decrease of plasma density and temperature with increasing distance into the scrapeoff layer. The model described by Howe[71] has been improved by the addition of 1) an elongated plasma and 2) ionization of some fraction (f) of the recycled gas in the plasma. The major unknown in the model is the rate of cross-field heat and particle transport and the resulting scrapeoff exponential widths. In present-day experiments, measurement of the scrapeoff plasma density and temperature profiles may be fit with a cross-field transport coefficient, D, of $\simeq 10^4$ cm^2/s. Since there is no model for this transport, we extrapolate to FED by assuming the same transport coefficient. The resulting scrapeoff widths are typically several centimeters and are given in Table 2-9 for the four cases described above.

One characteristic of a flat plate limiter which must be considered is the maximum heat flux on the flat part of the plate. This is particularly important because the heat flux is controlled only by the scrapeoff width and cannot be designed to a certain value. The heat flux distribution on the plate is easily derived from the model, and the maximum heat flux, Q_m, is given by

$$Q_m = \frac{P_T}{A}\,\pi e^{-1/2(a/\lambda_Q)^{1/2}},$$

where $A = (2\pi)^2 aR_o$ and λ_Q is the heat flux exponential falloff distance given by $\lambda_Q^{-1} = \lambda_n^{-1} + \lambda_T^{-1}$, where λ_n and λ_T are the plasma density and temperature falloff distances. The maximum heat flux occurs at a distance along the plate from the contact point (ℓ) of $\ell_Q = (a\lambda_Q)^{1/2}$. The dependence of Q_m on λ_Q for P_T = 50 MW in FED is shown in Figure 2-48. The maximum heat flux which can be handled on the flat face of the limiter is approximately 250 W/cm^2; thus, if $\lambda_Q > 2$ cm, the limiter should withstand the total thermal output of the plasma without damage.

Table 2-9. Scrapeoff parameters for four plasma conditions. The parameters are defined in the text. n_o and T_o are the plasma density and temperature at the plasma edge ($\ell = 0$).

P_T (MW)	50.0	50.0	5.0	5.0
$\dot{N}_T$ (s^{-1})	1.0×10^{24}	3.0×10^{23}	1.0×10^{24}	3.0×10^{23}
n_o (cm^{-3})	8.9×10^{13}	2.0×10^{13}	1.6×10^{14}	3.5×10^{13}
T_o (eV)	114.1	380.5	11.4	38.0
λ_n (cm)	5.5	4.1	9.8	7.2
λ_T (cm)	2.9	2.1	5.1	3.8
λ_Q (cm)	1.9	1.4	3.4	2.5
ℓ_Q (cm)	15.7	13.5	20.9	18.0
Q_m (w/cm^2)	321.2	373.3	24.1	28.0
ℓ_Γ (cm)	26.8	23.0	35.7	30.7
$T(\ell_\Gamma)$ (eV)	43.7	145.5	4.4	14.6
Γ_m ($cm^{-2}s^{-1}$)	3.8×10^{18}	1.3×10^{18}	2.8×10^{18}	9.8×10^{17}
t_{life} (months)	0.36	1.05	2.99	2.48

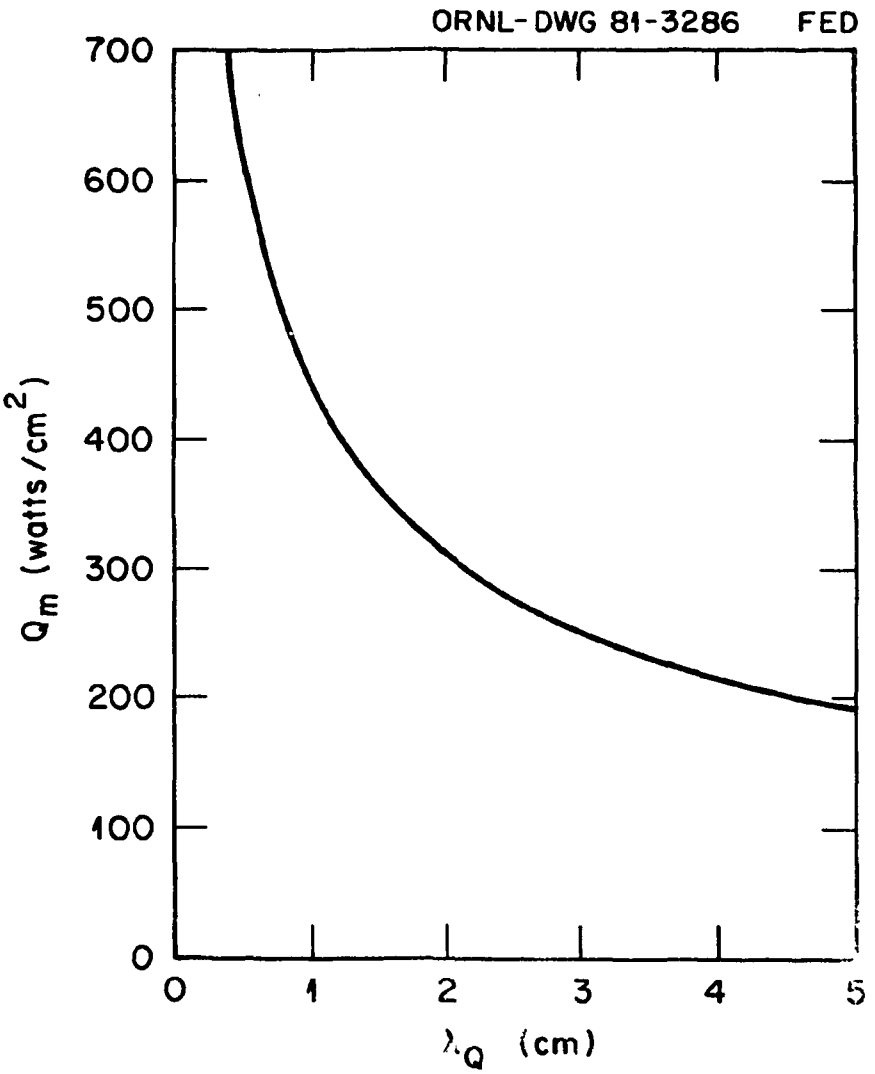

Fig. 2-48. Maximum heat flux (Q_m) incident on the flat surface of the FED limiter as a function of the heat-flux exponential decay length (λ_Q) for P_T = 50 MW.

Another consideration is the lifetime of the flat limiter face. A simple estimate of the lifetime may be made from the model by assuming that the maximum erosion occurs at the position of maximum particle flux. From the particle flux distribution given by the model, the maximum particle flux, Γ_m, is

$$\Gamma_m = \frac{\dot{N}_T}{A} \pi e^{-1/2(a/\lambda_n)^{1/2}}$$

and occurs at a distance $\ell_\Gamma = (a\lambda_n)^{1/2}$ from the contact point. The flux of limiter material eroded from the limiter at this point due to physical sputtering by the incident plasma ions is $\Gamma_z = \Gamma_m Y_s (E_n)$ where Y_s is the sputtering yield and E_n is the energy of the incident ions. We assume $E_n = 4T(\ell_\Gamma)$ to account for acceleration of the ions through the surface sheath potential, where $T(\ell_\Gamma)$ is the electron temperature at ℓ_Γ. If we define the lifetime (t_ℓ) to be the operating time required for a thickness (Δ) of material to be removed at ℓ_Γ, then $t_\ell = \Delta/v_s$ where $v_s = \Gamma_z/c$ is the maximum recession velocity of the surface and c is the limiter material concentration. The estimated lifetimes for the four plasma cases described above are given in Table 2-9 for Δ = 1 cm. For the high power and particle flux case, the lifetime is only several weeks of operating time. For the planned FED operating schedule, operating time is about 20% of calendar time. Therefore, several weeks of operating time would be equivalent to several months of calendar time. Lower heat and particle loads give longer operating lifetimes of up to several months. However, these lifetime estimates do not take into account chemical sputtering.

The distance from the plasma tangency point to the limiter leading edge (ℓ_s) is determined by two requirements. First, ℓ_s must be large enough to prevent excessive heating of the leading edge. Second, ℓ_s must be small enough to allow an acceptable flux of plasma and helium ions to flow behind the limiter for pumping. We now consider some of the factors which determine the value for ℓ_s.

A straightforward way to choose ℓ_s is to assume the leading edge heat flux must equal a design value, Q_d. If we assume we know that the heat flux falloff distance will be $\lambda_Q = \lambda_{Qd}$, then the design choice for ℓ_s is

$$\ell_{sd} = [2a\lambda_{Qd} \ln \beta_d]^{1/2}$$

where

$$\beta_d = \frac{P_T}{4\pi R_o \kappa \lambda_{Qd} Q_d} .$$

Typical values for these parameters are shown in Table 2-10. The problem with this approach is that the actual value of λ_Q cannot be predicted. The variation of the leading edge heat flux, $Q_{\ell e}$, from the design value due to variation of λ_Q is $Q_{\ell e}/Q_d = \lambda_{Qd}/\lambda_Q \; \beta_d(1-\lambda_{Qd}/\lambda_Q)$ and is plotted in Fig. 2-49(a). If $\lambda_Q > \lambda_{Qd}$, then $Q_{\ell e} > Q_d$. The maximum value of $Q_{\ell e}/Q_d$ occurs where $\lambda_Q/\lambda_{Qd} = \ln \beta_d$ and is plotted in Fig. 2-49(b). For the FED case with $P_T = 50$ MW, β_d is 25 for $\lambda_{Qd} = 2$ cm, and $Q_d = 100$ W/cm^2. Thus, heat fluxes of almost 300 W/cm^2 could occur on the leading edge for $\lambda_Q/\lambda_{Qd} = 3$. This could occur due to changes in λ_Q during a shot as well as to uncertainties in what λ_{Qd} will be.

Another way to choose ℓ_s is to set the value of the pumped fraction of the particle flux (g) equal to a desired design value (g_d). This criterion gives a design value for ℓ_s of

$$\ell_{sd} = [2a\lambda_n \ln (\frac{1}{2g_d})]^{1/2} . \qquad (2\text{-}9)$$

The criterion that this value for ℓ_{sd} be large enough to keep the leading edge heat flux below the design value (Q_d) is that

$$\beta_d \leq (\frac{1}{2g_d})^{\lambda_n/\lambda_Q} .$$

Table 2-10. Leading edge conditions for ℓ_s determined by leading edge heat flux [$Q(\ell_s) \equiv 100$ W/cm^2]

P_T (MW)	50.0	50.0	5.0	5.0
$\dot{N}_T$ (s^{-1})	1.0×10^{24}	3.0×10^{23}	1.0×10^{24}	3.0×10^{23}
β_d	27.5	37.1	1.5	2.1
g	0.16	0.15	0.43	0.39
ℓ_s (cm)	40.3	36.2	19.5	21.8
$t_{\ell e}$ (months)	0.58	0.85	0.55	0.69

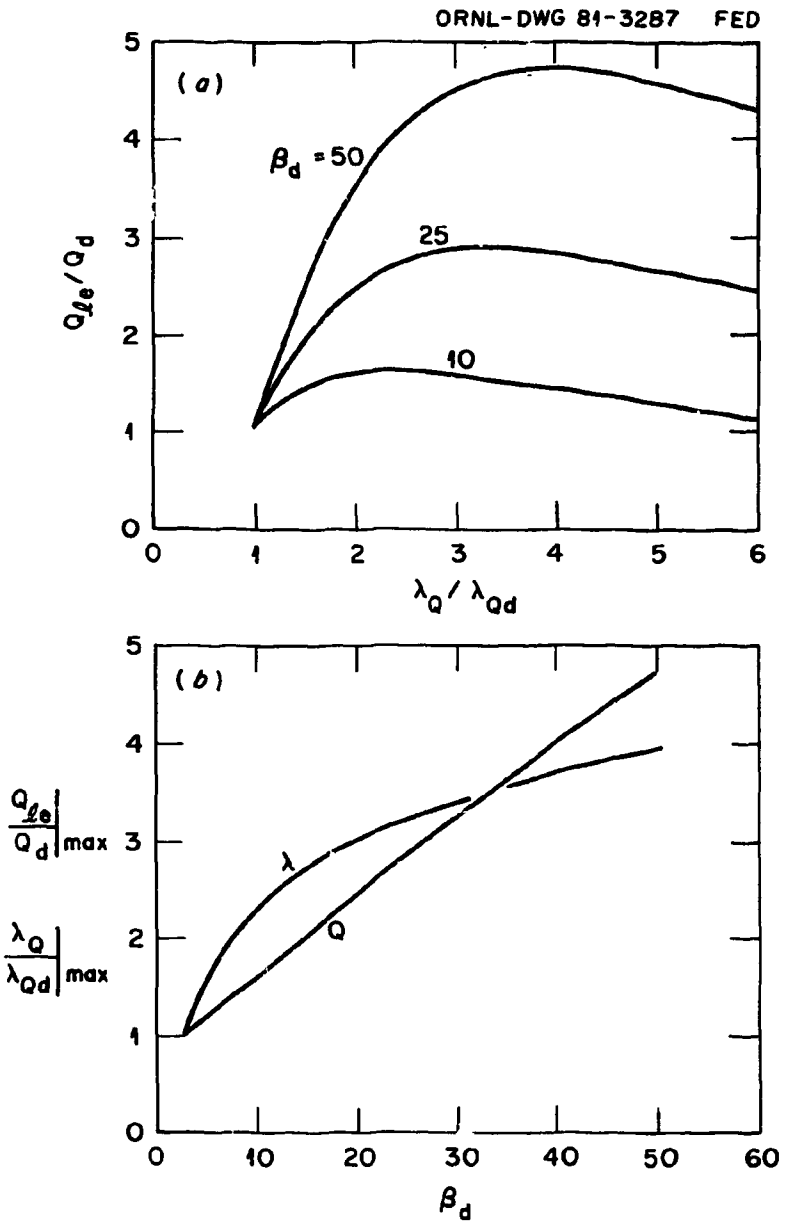

Fig. 2-49. (a) Ratio of the leading edge heat flux ($Q_{\ell e}$) to the design value (Q_d) as a function of the ratio of the actual scrapeoff width (λ_{Qd}). The parameter β_d is defined in the text and $\beta_d \approx 25$ for typical FED parameters. (b) Ratio of the maximum possible leading edge heat flux to the design value as a function of β_d. The value of λ_Q/λ_{Qd} at which the maximum possible heat flux occurs is also shown.

For FED, we anticipate that a pumping rate, g_d, of 5% will be sufficient, and this criterion should not be difficult to satisfy. Therefore, the leading edge heat flux may be maintained at or below the acceptable design value if the leading edge distance ℓ_s is chosen to give an acceptably small particle pumping rate. Values of the parameters for this case are shown in Table 2-11.

Values of the leading edge parameters for the four plasma conditions described above are shown in Tables 2-10 and 2-11. When the leading edge distance is determined by the heat flux condition, the pumping fraction (≃15% for the high power cases) is larger than necessary and the leading edge lifetime is short. Alternatively, when ℓ_s is increased to obtain 5% pumping, the plasma temperature at the leading edge is so low (≃ 1-5 ev) that flow of plasma into the pumping region is no longer assured. Therefore, a value of ℓ_s intermediate between these two cases is probably the optimum choice. This choice of ℓ_s gives an easily handled leading edge heat flux, a lifetime which is on the order of the lifetime of the flat surface of the limiter plate, and a pumping rate which is somewhat larger than needed but still acceptable.

The choice of ℓ_s, as we have seen, is uncertain because of our inability to predict the scrapeoff width. A further complication is that the scrapeoff width may change during a discharge due to changes in the crossfield transport rates or the total heat and particle flux to the limiter. Therefore, it may be necessary to vary ℓ_s during a discharge in order to control either the leading edge heat flux or the pumping rate. To obtain this control the limiter is placed at the bottom of the torus. The value of ℓ_s may be varied by simple in-out motion of the plasma along the major radius. For this application the bottom location is preferred over location at the 45° or vertical facets because: (1) in-out motion is more easily controlled than up-down motion; and (2) in-out motion does not change the plasma minor radius. The amount of motion required may be estimated, for example, from Eq. (2-9). Assuming constant pumping, a small change in λ_n results in a change in ℓ_s of $\delta\ell_s/\ell_s \simeq 1/2\ \delta\lambda_n/\lambda_n$. For ℓ_s = 50 cm and λ_n = 5 cm, a factor of two change in λ_n results in approximately a 50% change in ℓ_s. Thus, several

Table 2-11. Leading edge conditions for ℓ_s set by the requirement that the pumping fraction g ≡ 5%

P_T (MW)	50.0	50.0	5.0	5.0
$\dot{N}_T$ (s^{-1})	1.0×10^{24}	3.0×10^{23}	1.0×10^{24}	3.0×10^{23}
ℓ_s (cm)	57.4	49.4	76.6	65.9
$Q(\ell_s)$ (w/cm^2)	3.3	4.4	0.2	0.2
$T(\ell_s)$ (eV)	1.4	4.6	0.1	0.5

tens of centimeters of radial motion may be required. It may be impractical to leave this much extra space around the plasma. Another possibility is to vary ℓ_s by changing the plasma triangularity (which changes the position of the contact point). This may also prove to be difficult but should be studied further as the design proceeds.

2.6.4 Cold Plasma-Edge Analysis

H. C. Howe — ORNL/FEDC

The high heat and particle fluxes incident on the pump limiter in FED may lead to very short limiter lifetimes due to erosion by ion sputtering of the limiter. Subsequently, radiation from eroded material which enters the plasma reduces the heat load on the limiter and hence the erosion rate. The possibility exists that this process may come to an equilibrium where most of the power is radiated, resulting in a very cold plasma in contact with the limiter and a very low erosion rate. When the radiation is emitted primarily from the plasma edge, the hot burning core plasma is unaffected while the limiter is largely protected from damage due to high heat loads or erosion. Several authors [Hughes and Ashby,[72] Neuhauser,[73] and Neuhauser et al.[74,75]] have noted that this situation is automatically obtained in many transport simulations of burning plasmas when the limiter and wall materials are medium-Z (such as Fe) and impurity transport is assumed to be neoclassical [Hirschman and Sigmar[76]] with an anomalous spreading at a rate equal to the hydrogen anomalous diffusion rate. In this section, we review briefly simulations of FED which exhibit strong edge cooling due to sputtered wall and limiter materials.

The tokamak transport code PROCTR[70] uses a transport model similar to the INTOR model for the background plasma. The PROCTR model assumes central transport coefficients which extrapolate to more optimistic values in FED than do the INTOR coefficients. Impurity transport follows the models described above. Impurity radiation is given by coronal rates [Post et al.[77]] which include line radiation and bremsstrahlung. The impurity sources are sputtering from: (1) the wall by charge-exchange neutrals and (2) the limiter by plasma ions. Sputtering

yields are taken from the curve by Smith.[78] Charge-exchange neutral sputtering of the wall is calculated by the neutral transport model in PROCTR using the plasma profiles as they evolve in time. Ion sputtering of the limiter is assumed to be at the energy $E = T_i + 2T_e$ to account approximately for acceleration of the ions through the surface sheath potential. Since the limiter scrapeoff plasma is included explicitly in the plasma and neutral transport, lowering of both the wall and limiter sputtering rates due to cooling of the edge and scrapeoff plasmas is automatically included. Also included is shielding of the sputtered impurities by ionization in the scrapeoff and subsequent parallel loss to the limiter. It is assumed that there is no impurity recycling or self-sputtering.

The fusion neutron power for the simulations is 150 MW and is maintained as the temperature is lowered through radiation by feedback control of the external fueling rate and plasma density. An ICRF driven case for an iron limiter and wall is shown in Fig. 2-50. In steady state, the deuterium and tritium profiles are inverted due to the combination of edge fueling and central fusion burnup. The iron density builds up in the plasma until the iron radiation cools the plasma enough to reduce both the ion-limiter and neutral-wall sputtering impurity sources to levels compatible with a steady state. The primary source of impurities in steady state is ion sputtering of the limiter. The resulting radiation is from the plasma edge since the iron is peaked at the edge and is fully stripped in the hot core. The iron density is strongly peaked at the plasma edge due to 1) the neoclassical accumulation at the peak of the inverted hydrogen profiles and 2) a strong outward flux due to the ion temperature gradient. Almost all of the thermal power is radiated from this thin edge region and only 2 MW reaches the limiter by transport. This case illustrates the cold plasma edge condition. The same condition is obtained for an ignited plasma.

The same case driven by neutral beams is shown in Fig. 2-51. Due to central fueling by the injected beam ions, the deuterium profile is peaked on axis. The resulting inward neoclassical flux of the iron toward the deuterium peak partly overcomes the outward temperature screening and a larger central iron density results. The same accumulation

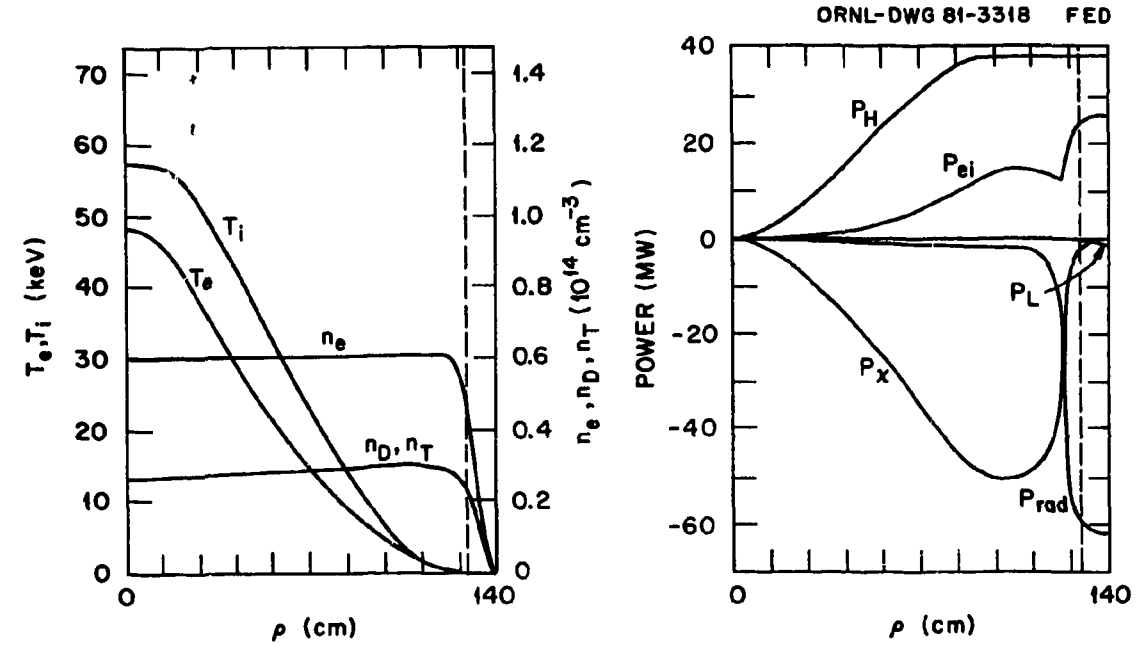

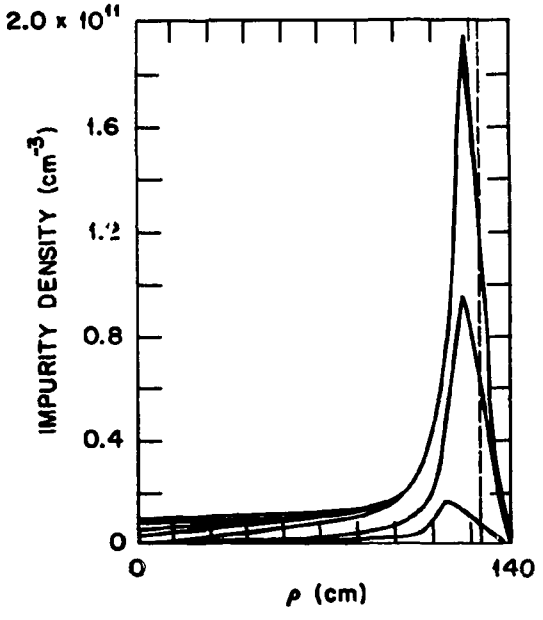

Fig. 2-50. ICRF-driven Q = 5 with Fe showing the cold plasma edge condition. Upper left: Steady-state plasma profiles for FED where n_D and n_T are the deuterium and tritium densities. The dashed line at ρ = 130 cm is the boundary between the main and scrapeoff plasmas. Upper right: Integrated electron energy balance. P_{rad} = total radiated power, P_{lim} = total power deposited on the limiter by both electrons and ions. Lower left: Time evolution of the impurity density profile for 15 s.

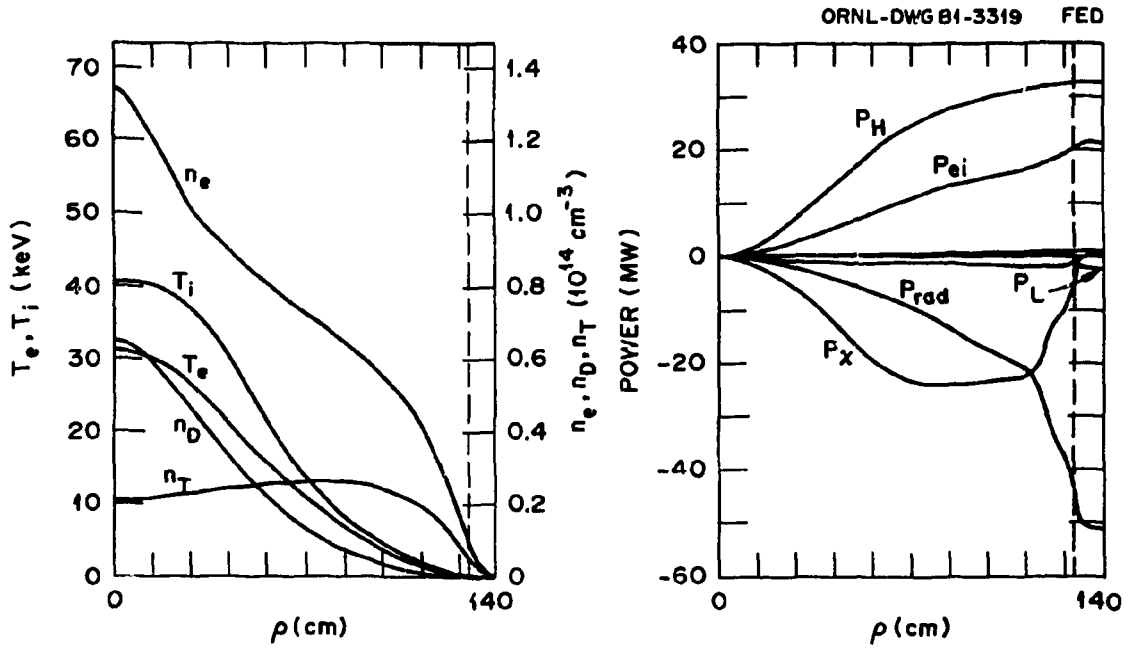

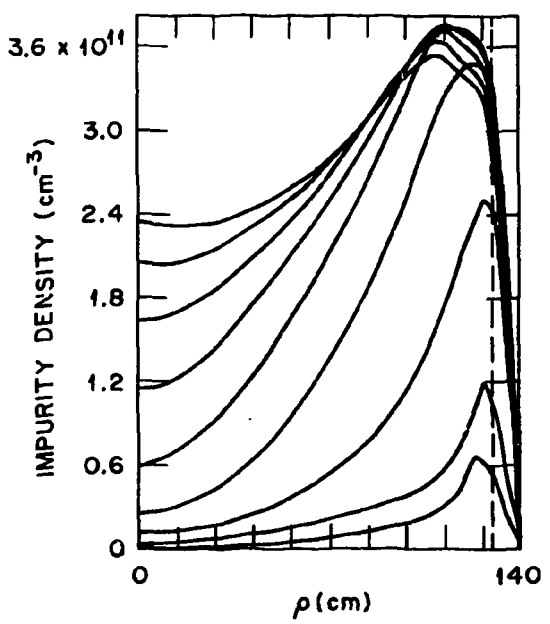

Fig. 2-51. Neutral beam driven Q = 5 with Fe. Impurity accumulation is caused by inward transport on the centrally peaked deuterium profile and loss of cold plasma edge. Upper left: Steady-state plasma profiles for FED where n_D and n_T are the deuterium and tritium densities. The dashed line at ρ = 130 cm is the boundary between the main and scrapeoff plasmas. Upper right: Integrated electron energy balance. P_{rad} = total radiated power, P_{lim} = total power deposited on the limiter by both electrons and ions. Lower left: Time evolution of the impurity density profile for 15 s.

occurs in simulations where the entire beam power is injected at the full energy. Thus, heating of the plasma edge by the fractional energy components does not cause the accumulation. More than 50% of the total radiation is now due to bremsstrahlung from the hot core. Because the radiating layer at the plasma edge is no longer as apparent, the edge plasma is not cooled as effectively as with ICRF heating and a large impurity accumulation occurs. This case approaches a steady state with a large Z_{eff} which is clearly an undesirable operating mode for a burning plasma. For example, if charge exchange between the injected neutrals and the impurities were included in the simulation, the resulting enhanced line radiation from the plasma center could quench the burn.

Although a radiating edge layer is obtained in some cases with a medium-Z impurity, the present FED design uses carbon for the limiter and for the part of the first wall exposed to charge-exchange neutrals. An ICRF-driven case which treats carbon instead of iron is shown in Fig. 2-52. As in the iron case, an inverted carbon density profile is obtained. However, very little radiation is produced in steady state because carbon is fully stripped at a lower temperature than iron and radiates at a much lower rate. Almost the entire thermal power from the plasma flows via particles to the limiter leading to the high power loads and short lifetimes which are the major problems with the present pump limiter design.

We conclude from these simulations that the presence of a radiating layer in FED is not certain enough to form the basis for the design. Simulations with carbon do not give the radiating layer although some improvement would result from a noncoronal simulation of the carbon transport. In present devices, there is clear evidence that large heat fluxes to limiters do not automatically produce enough impurities to radiate most of the power. As a result, melt damage on limiters is a problem in many beam heated tokamaks [Cohen et al.[79]].

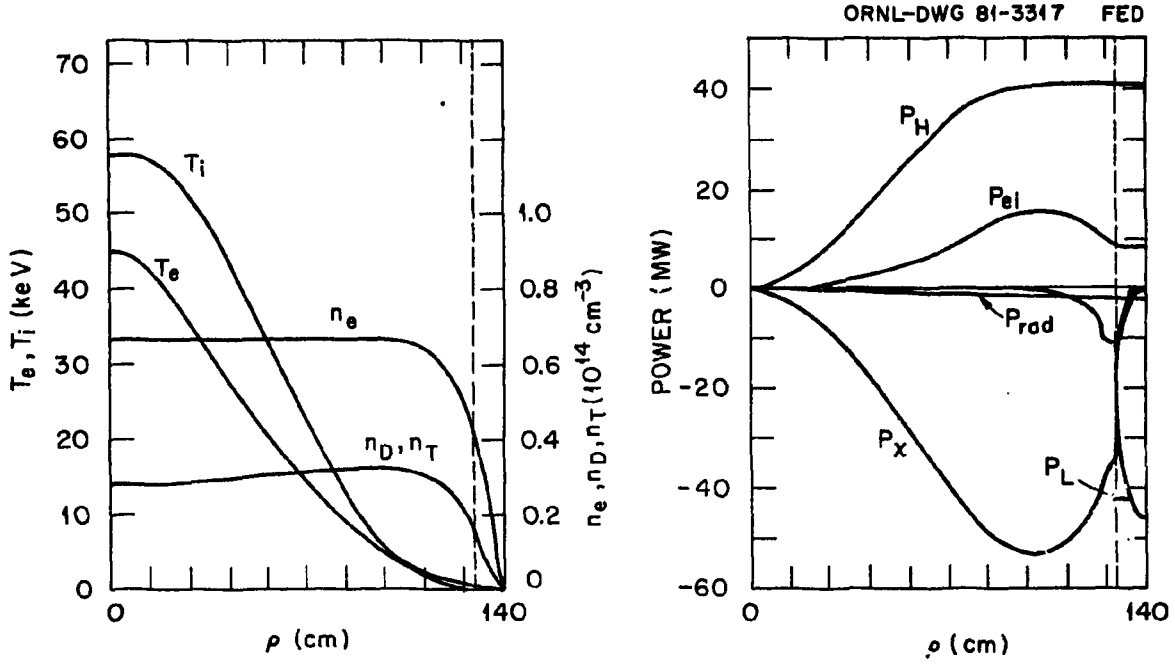

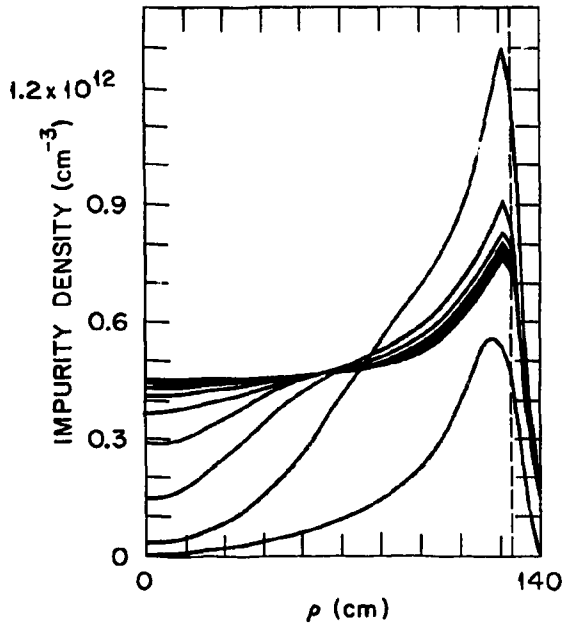

Fig. 2-52. ICRF driven Q = 5 with carbon. Due to low radiation levels from carbon, most of the thermal power is deposited on the limiter. Upper left: Steady-state plasma profiles for FED where n_D and n_T are the deuterium and tritium densities. The dashed line at ρ = 130 cm is the boundary between the main and scrapeoff plasmas. Upper right: Integrated electron energy balance. P_{rad} = total radiated power, P_{lim} = total power deposited on the limiter by both electrons and ions. Lower left: Time evolution of the impurity density profile for 15 s.

2.6.5 Poloidal Divertor

J. A. Schmidt, D. E. Post, M. Petravic — PPPL

Figure 2-53 shows the poloidal divertor mechanical configuration for FED. Also shown is the poloidal separatrix for the discharge. The divertor channels are very open due to the expanded flux surfaces in this region. The inner divertor plate is nearly vertical, and there is no pumping from the inner channel. Most of the recycled gas from the inner plate will refuel near the inner plate. The pumping duct from the outer channel will remove the helium ash.

The divertor plates are canted at a shallow angle to the poloidal flux surfaces so as to spread the heat and reduce the maximum thermal loads. The heat flux to the plates is shown in Fig. 2-54. The heat loads are acceptable and could be further reduced by contouring the divertor plates.

The divertor plate material is tungsten. The screening of the discharge from tungsten atoms has been studied. Very few tungsten neutrals will reach the main discharge due to their short mean free path for ionization. A qualitative analysis of the tungsten ion behavior has not been carried out; however, the parallel electric field and plasma flow should carry a large fraction of the impurities back to the divertor plate. This effect will provide impurity control and reduce the net erosion.

A two dimensional computational model was constructed to assess the divertor performance and to assist in the design of a poloidal divertor system for FED. The divertor channels were characterized by rectangular channels of 70 cm length and 30 cm width. The neutral gas transport is calculated using Monte Carlo techniques. The collisions of neutrals and ions with the walls were handled using experimental reflection data.[80] The relevant atomic collision processes for D°, T°, DD°, DT°, TT°, He°, D^+, T^+, DD^+, DT^+, TT^+, He^+, He^{++}, and e^- are included. The code is thus able to calculate ionization and charge exchange source terms for a plasma calculation. It also calculates the neutral gas flows and pressures and the heat loads and sputtering (erosion) rates.

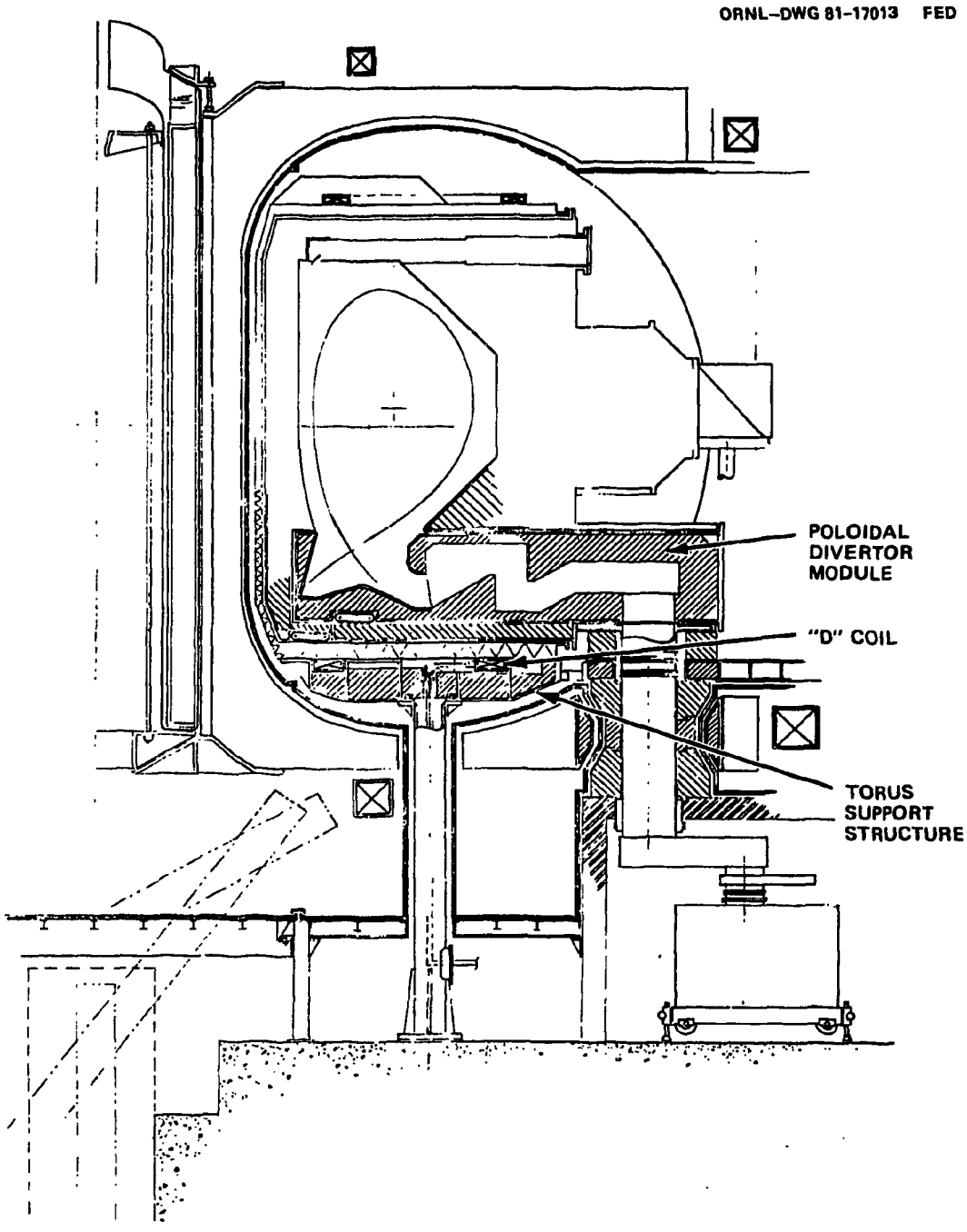

Fig. 2-53. Possible poloidal divertor configuration for FED.

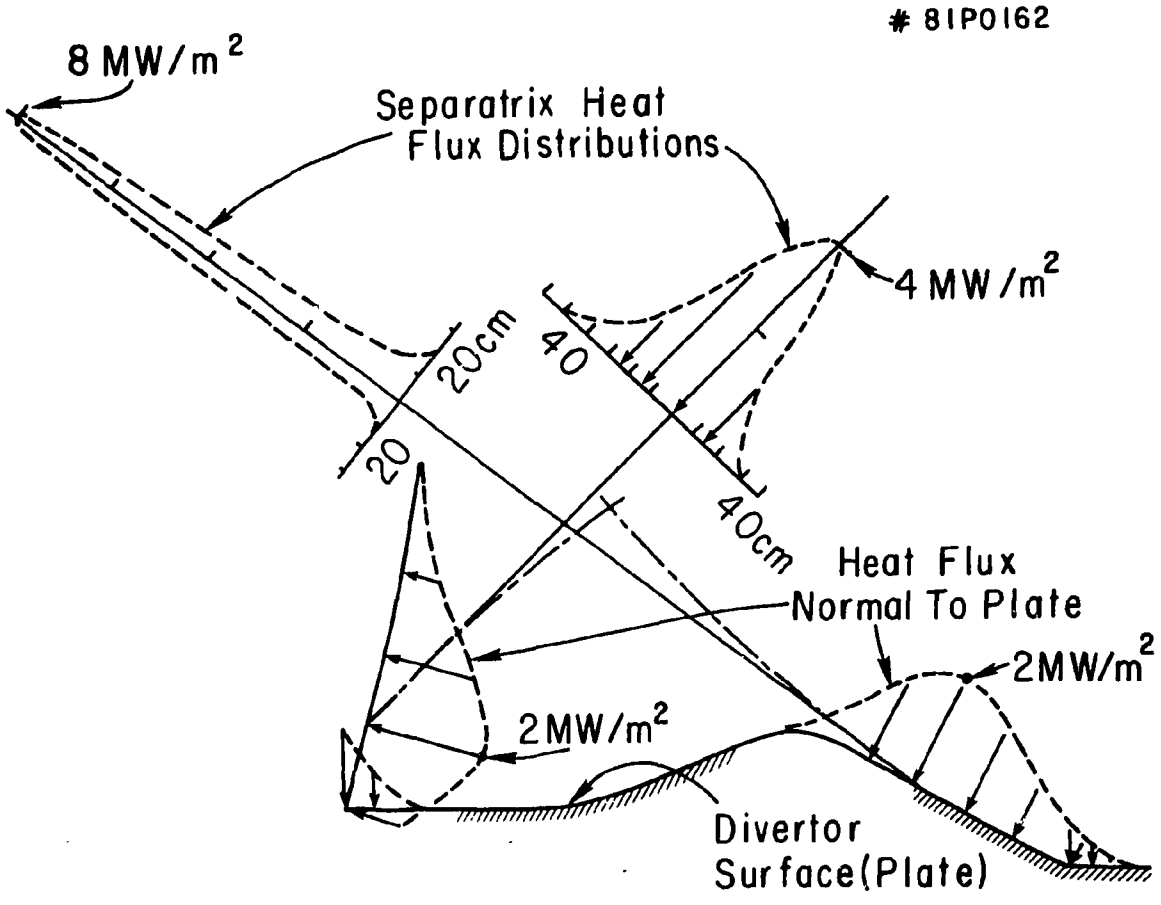

Fig. 2-54. Heat flux distributions of divertor plates for the configuration shown in Fig. 2-53.

The calculation of the plasma density (for one ion species), momentum, and energy transport is a two dimensional (along and across the magnetic field) steady-state fluid treatment.[81] For these studies it was assumed that the parallel electron thermal conduction is sufficiently high to maintain a constant electron temperature. The input particle and energy fluxes are specified at the divertor throat as boundary conditions. The other boundary conditions are that the electron heat flux at the plate is $Q_e = 2\lambda\ T_e n_e v_f$, where $v_f = (B_p/B_T)\ v_s$ and $1/2\ mv_s^2 = 5/6\ T_i + 1/2\ T_e$

The calculations were performed for conditions appropriate to a single null divertor with the heat flux of 40 MW and a particle flux of $3 \times 10^{22}\ s^{-1}$ into one divertor (Fig. 2-55). With these conditions, setting the neutral source terms to zero (no ionization or charge exchange) yields $T_e \sim 1500$ eV, $n_e \sim 2 \times 10^{11}\ cm^{-3}$, and $P_o \sim 10^{-5}$ torr at the neutralizer plate. Using the self-consistent source terms from the neutral gas computation lowers T_e to ~ 40 eV and raises n_e to $\sim 2.5 \times 10^{13}\ cm^{-3}$ and P_o to ~ 0.1 torr (Figs. 2-56 and 2-57). The ion temperature drops along the field line from $\sim$160 eV to 20 eV at the plate. The ionization source is localized near the plate. The particle flux increases by a factor of twenty from the throat to the plate. The particle flow velocity is about 10% of the sound speed at the throat and increases to the sound speed at the plate (Fig. 2-58).

The electron density rise is largest along the separatrix and near the corner away from the pump (Fig. 2-59). The ion temperature profile is flat at the throat (Fig. 2-60). The neutral pressure profile drops slightly near the pump but is still $\sim$30 millitorr at the pump opening. About 90% of the input power is still dumped on the neutralizer plate and the other 10% on the divertor walls. The total erosion rates of the neutralizer plate and divertor walls are about equal.

The high density operation is due to the rapid recycling of plasma and neutrals at the divertor plate. This can be understood from the continuity equation

$$\frac{\partial(nv)}{\partial x} = S_{ion} = n_o n_e \langle\sigma v\rangle_{ionization}$$

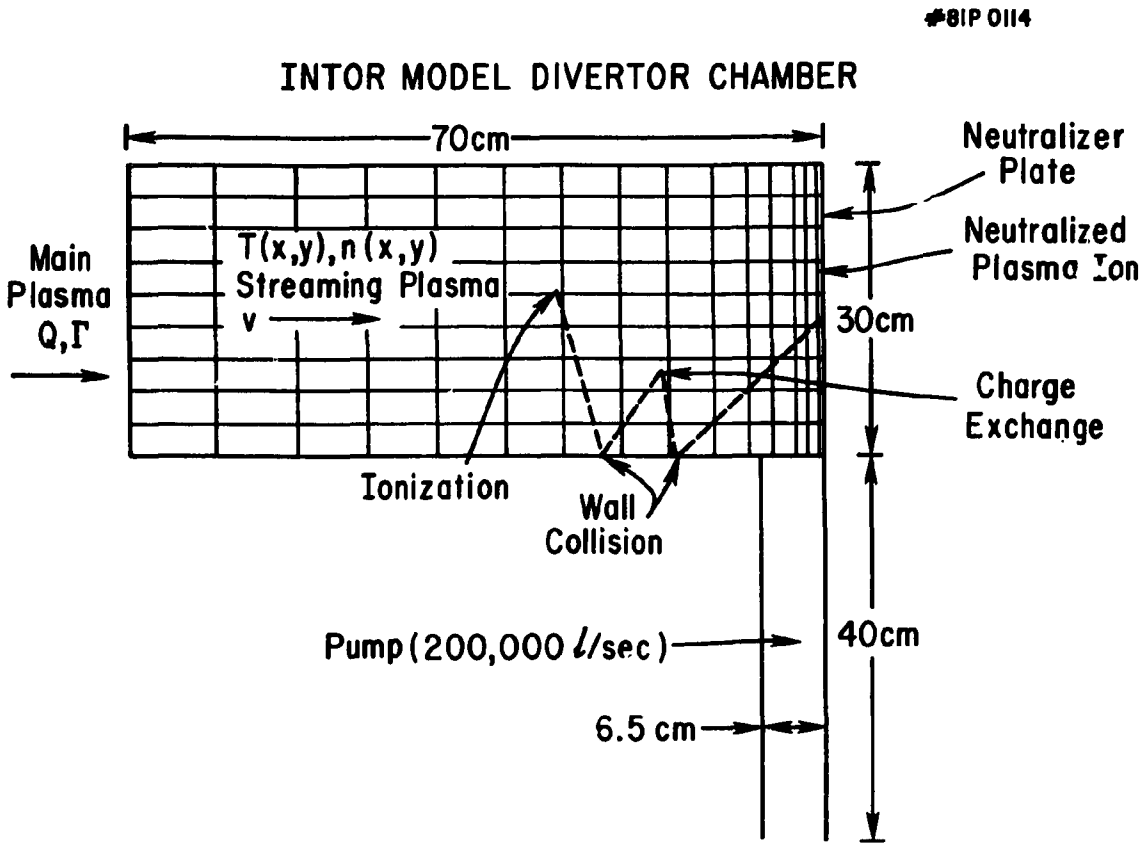

Fig. 2-55. Geometry for the FED poloidal divertor calculation.

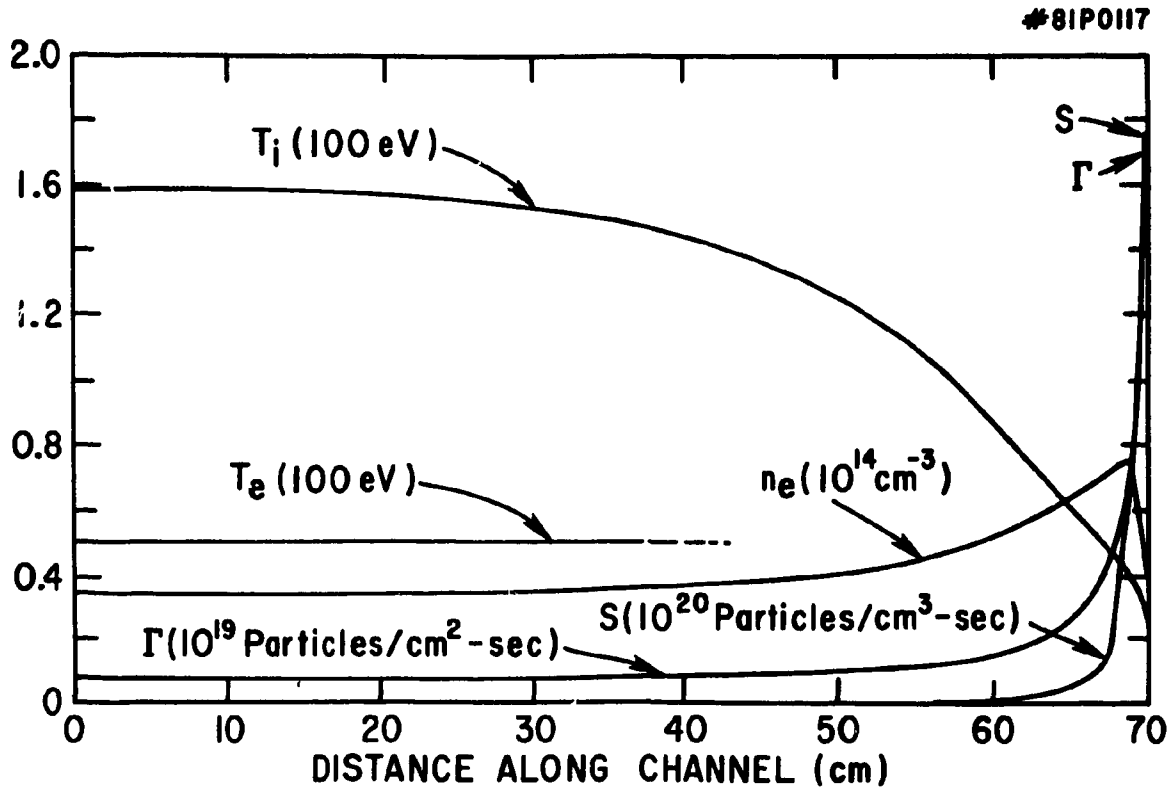

Fig. 2-56. Plasma conditions along the field line for the center of the poloidal divertor. The neutralizer plate is at x = 70 cm.

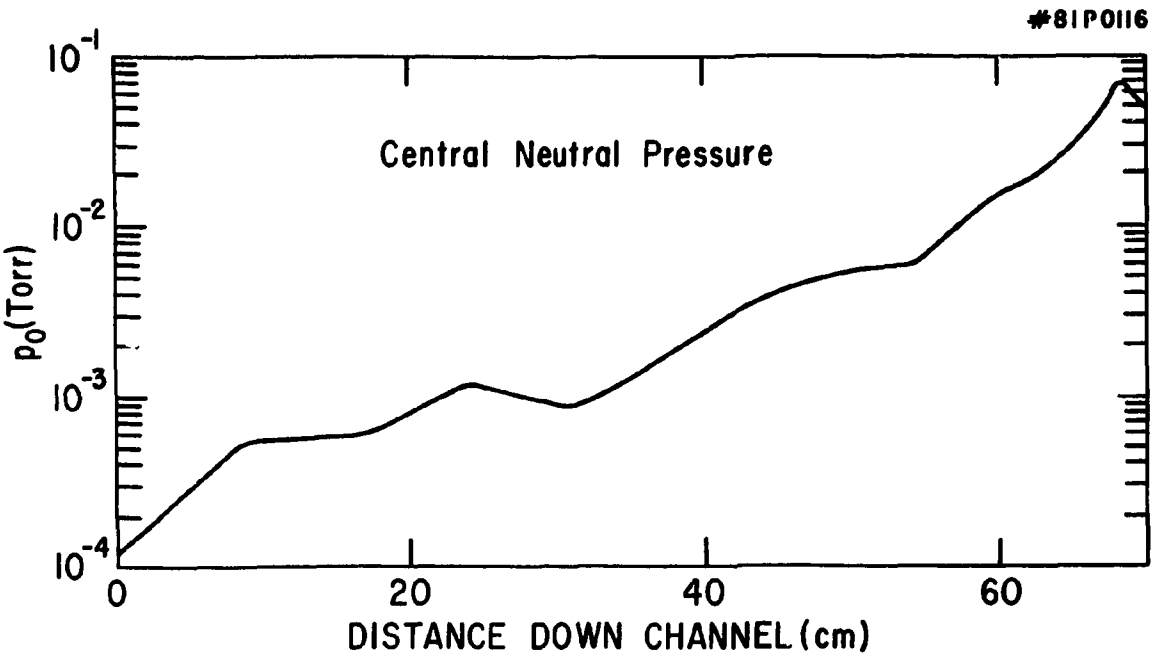

Fig. 2-57. Neutral pressure along the center of the poloidal divertor.

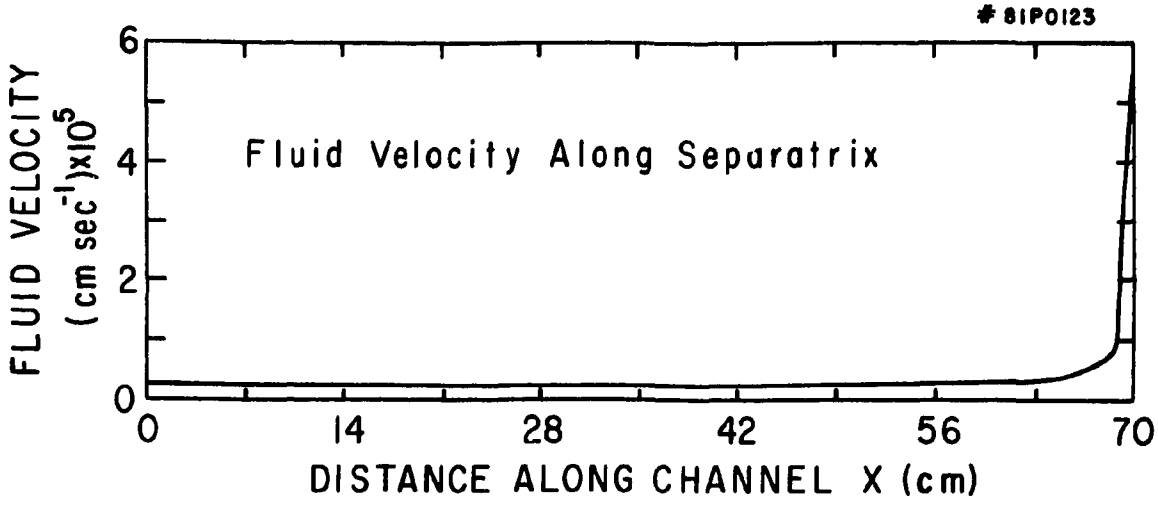

Fig. 2-58. Plasma flow velocity along the field line for the center of the poloidal divertor from the divertor throat (x = 0) to the neutralizer plate (x = 70 cm).

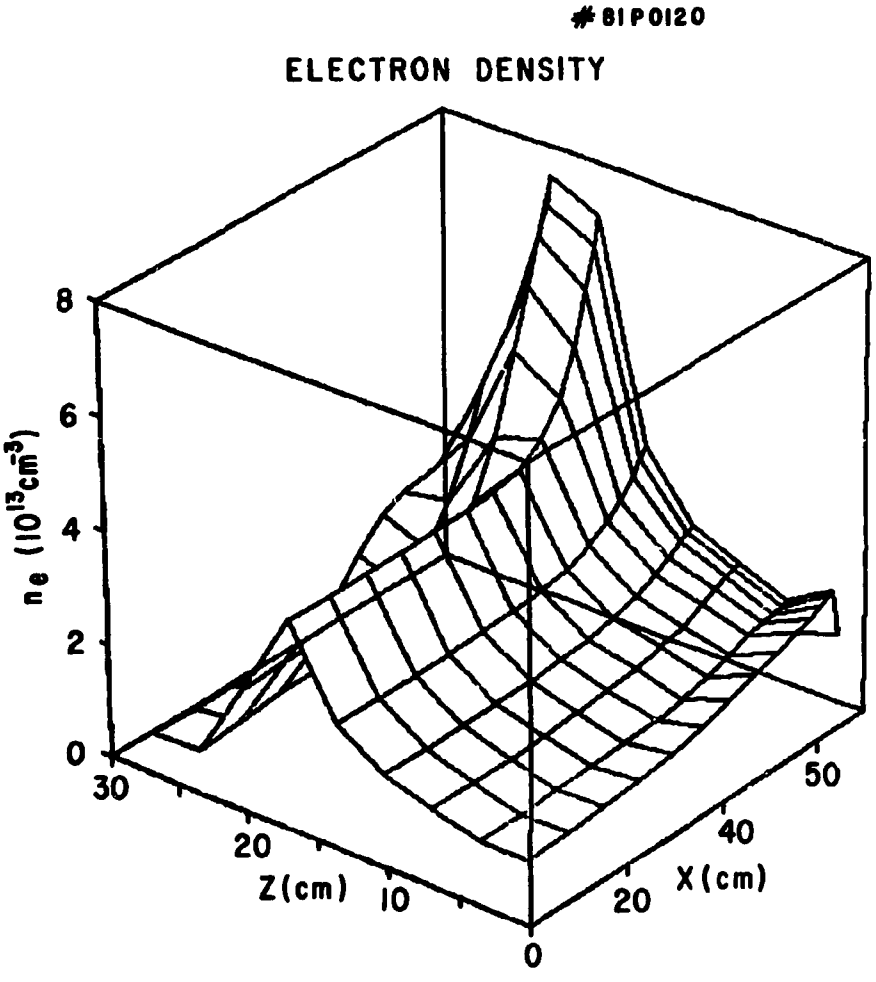

Fig. 2-59. Density profile in the poloidal divertor. Z is the distance across the divertor and x is along the channel.

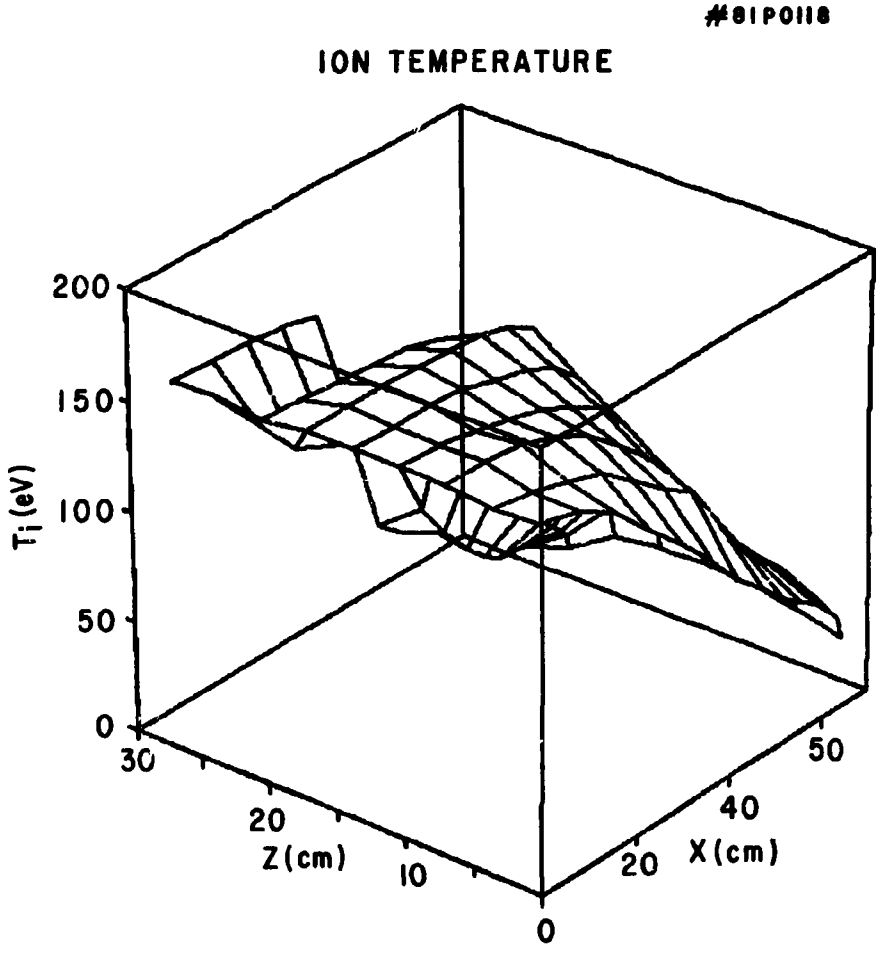

Fig. 2-60. Ion temperature profile in the FED poloidal divertor.

Since S_{ion} is positive, the flux will increase as the neutralizer plate is approached. If the neutrals cannot easily escape down the pump or return to the main plasma, they will recycle many times before escaping. In our case, the flux at the plate is 19 times the input flux (Fig. 2-56). Thus, the divertor acts as a "particle flux" amplifier. The temperature at the plate is reduced since $Q \propto Tnv$ which implies that T drops as F (= nv) rises. Since, at the plate $v \sim (T/m)^{1/2}$ and $Q \propto Tn\ (T/m)^{1/2} \propto T^{3/2}n$, $nT^{3/2}$ is a constant, and lowering T raises n. Thus, the large neutral pressure comes from the high recycling flux at the plate.

At the throat $v \sim 0.1\ v_s$ which is roughly consistent with the DIVA measurements.[82] The high neutral pressure is roughly consistent with the Alcator results,[83] PDX results,[84] and UCLA results.[85] Densities as high as $\sim 10^{14}$ cm^{-3} in a diverted plasma have been observed on D-III.[86] The particle flow rate down the pump is 3×10^{22} s^{-1}. With $n_{He}/n_e \sim 0.05$, the required pumping speed is only 4×10^{21} s^{-1}, so the geometric pumping speed of the duct could be reduced to $\sim$ 25,000 l/s.

Our calculations show no helium enrichment. Indeed, in some of the highest density cases, significant dilution is found which may raise the pumping requirements above the 25,000 l/s we calculate.

Lowering the electron temperature from 1500 ev to ~40 eV may allow the use of high-Z neutralizer plate materials such as tungsten. However, reducing T_e just a little farther would open up the use of medium-Z and even low-Z materials. The high-density divertor plasma will extend back to the edge of the main plasma and scrape-off layer, possibly providing a cool, dense, plasma blanket to shield the first wall from the plasma. Containing the neutrals near the neutralizer plate will reduce the erosion near the divertor throat. Since the neutral ionization and other effects are localized near the plate, the possibility exists that the divertor channel could be made shorter than 70 cm, perhaps as short as 30 cm.

In summary, the FED poloidal divertor should operate at high density, particularly near the divertor plate. The edge temperature and associated erosion should be reduced for this condition. The impurities sputtered from the divertor plate should be shielded from the discharge by the divertor action. The recycling and associated charge-exchange erosion should be localized inside the divertor channels away from the first wall

2.6.6 Optimization of a Compact Bundle Divertor for FED

L. M. Hively — FEDC/GE, J. A. Rome — ORNL

Previous design studies of bundle divertors had shown that divertor-created, on-axis, magnetic field ripple above 0.3% causes the loss of most banana-trapped fast ions.[87] These losses would be unacceptable in FED using quasi-perpendicular neutral beam injection of ICRF. In addition, these designs require large, expensive copper coils which would dissipate >100 MW of resistive power. Consequently, a bundle divertor is now considered only as a backup option to a poloidal divertor in FED. Here, the results of recent studies on optimization of the bundle divertor concept are presented.

Both fast ion and background plasma confinement may be degraded by divertor ripple. Nonaxisymmetry in a diverted tokamak causes fast ion losses due to particle trapping in localized magnetic field wells. In one resulting process, an ion can be collisionlessly trapped due to its finite orbit size when there is insufficient parallel velocity, $v_{\|}$, to escape from the ripple well. Such a ripple-trapped ion oscillates within the well, while drifting vertically into larger ripple, and is lost to the wall. Another process is collisional ripple trapping due to pitch-angle scattering as a large banana-width orbit traverses a B-field minimum with $v_{\|}/v \simeq 0$. Collisional detrapping can occur by the inverse process. There is also banana-drift diffusion because large banana-width orbits fail to close exactly. This arises from a ripple-induced "variable lingering period" as the $v_{\|}/v \simeq 0$ part of an orbit passes through a magnetic well. Usually the bundle divertor produces a local maximum in B on each side of the ripple well, yielding a new ripple-induced trapping process. In particular, a banana-trapped particle can become ripple-trapped between the divertor-created maximum and the usual 1/R increase in toroidal field, and then rapidly drifts out of the tokamak. These mechanisms cause outward radial transport and loss of fast ions, thus degrading plasma heating by neutral beams, fusion products, and ICRF.

Moreover, ripple degrades the background plasma confinement by enhancing the coefficients for ion heat conduction and spatial diffusion. A badly designed divertor may also ergodize the equilibrium field lines causing a further deterioration in plasma confinement or even major plasma disruptions. While these deleterious influences are not well-tested experimentally, it is prudent on theoretical grounds to assume that such effects are important. Consequently, minimizing divertor-induced ripple leads to a conservative set of optimization criteria.

Our studies have focused on divertor optimization to minimize the bad effects of localized ripple.[87] The objective is to minimize on-axis ripple, which also minimizes the overall magnetic field distortion. Present studies have concentrated on the double T-coil divertor (first proposed by T. Yang of MIT; see Fig. 2-61) because 2- or 4-coil designs appear unacceptable from an engineering viewpoint. Normal copper coils were selected due to space constraints and neutron damage considerations. Thus, the cross section of the coils is determined from the restrictions that power dissipation be $\leq$100 MW and current density be $\leq$6 kA/cm^2; nuclear shielding is included in the model. Ripple minimization is subject to several engineering constraints (see Fig. 2-61): (1) a magnetic scrapeoff thickness between 0.05-0.3 m; (2) horizontal and vertical clearances through the coil bore of $\geq$0.3 m and $\geq$0.4 m, respectively; (3) the front T-coil lying outside the plasma scrapeoff region; (4) no interference between the front and back T-coils; and (5) the innermost edge of the flux bundle lying beyond the back T-coil. The coil currents are chosen so that the separatrix joins the plasma edge far from the divertor. In our analysis, the total magnetic field is composed of the vacuum divertor field superimposed on an axisymmetric FED equilibrium. A single wire filament models each coil leg; TF ripple is presently excluded making the present results pessimistic. The resulting nonlinear minimization problem is characterized by nine design parameters (i.e., coil sizes and positions) subject to the above constraints, and must be solved numerically.[87]

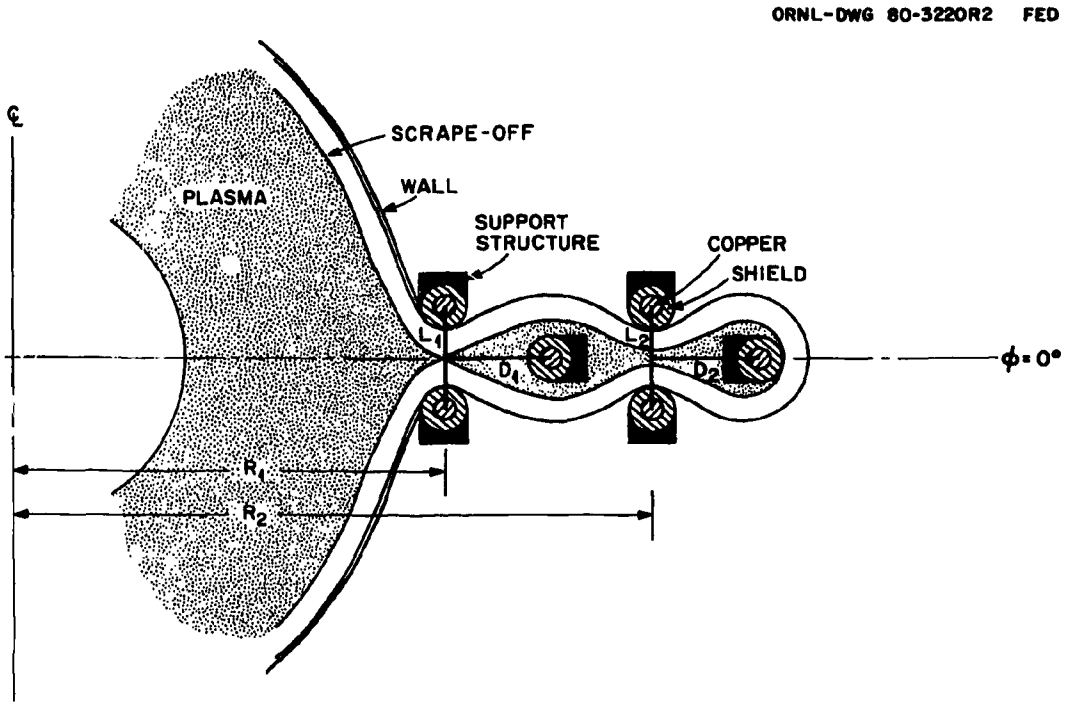

Fig. 2-61. Geometry of the double-T divertor labeled to show optimizable parameters. Not shown are H_1 and H_2, the heights of the front and back T-coils, respectively.

Acceptable results have been obtained for an unshielded divertor consisting of a small T-coil close to the plasma and a larger, nearly planar, T-coil behind it. This causes an unusual ripple distribution (Fig. 2-62) in which the contours of constant ripple are nearly vertical. Because the ripple decays quickly away from the divertor, only a small region of the plasma has significant ripple (e.g., over 0.4% for a scrape-off layer of 0.2 m). Furthermore, this example was computed for a high $\langle\beta\rangle$ (=6%) equilibrium so that the magnetic axis is shifted outward into the higher ripple region by about 0.2 m.

Our optimization studies have concentrated on the case with a 0.3-m-wide × 0.4-m-high hole. Figure 2-63 (Curve a) shows the ripple versus magnetic scrapeoff layer thickness, T_{so}, for this case. The power dissipated in the coils ranges from 30 MW for T_{so} = 0.05 m to >100 MW for T_{so} = 0.3 m. For such a compact divertor, it is relatively easy to obtain low on-axis ripple (<0.2%) for scrapeoff thicknesses up to 0.3 m.

Figure 2-63 (Curve b) is for a single-T divertor with a 0.5-m × 0.6-m hole (double-T studies are in progress). In this case, the design is more difficult, but the on-axis ripple can be maintained below 0.5%. A nuclear shielded, single-T divertor has excessive ripple (>0.3%), but such shielding is expected to be unnecessary for MgO-insulated coils at 8-T operation.[88]

The confinement of collisionless, 150-keV D^+ ions has been calculated[87] for an optimized, compact, double-T divertor with a 0.2-m scrape-off. For nonoptimized divertors with on-axis ripple ~0.5%, most of the bananas are lost. For the optimized case it is found that only those bananas with tips in the high ripple region ($\gtrsim$0.4%) are lost (see Figs. 2-62 and 2-64). These loss-orbits are usually D-shaped orbits or small bananas having tips outside the magnetic axis near the equator. Examination of the confinement of the ergodic orbits is in progress. Fast ions resulting from near tangential injection are expected to be well confined.

It is seen that significant improvements in low-ripple bundle divertor configurations have been obtained, yielding a much better design than previous efforts. Such designs are compact and can fit

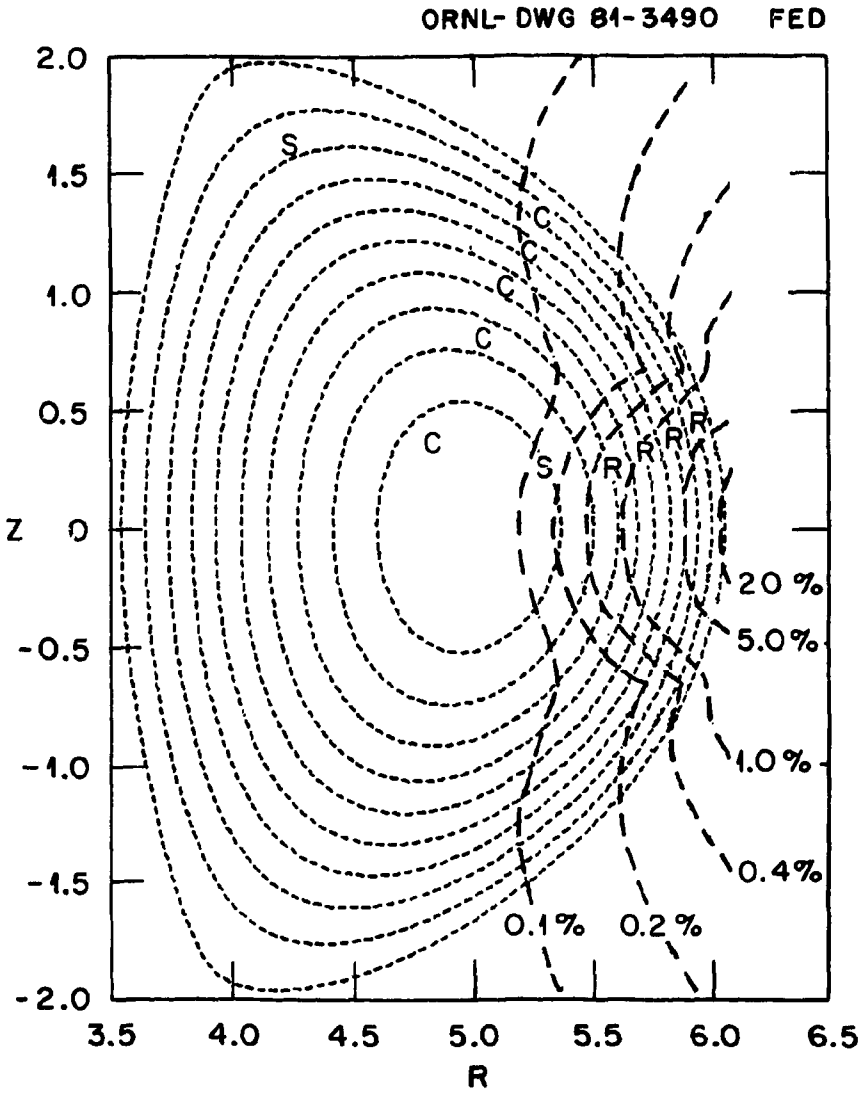

Fig. 2-62. Contours of constant ripple for the high-beta FED plasma with an optimized, double-T divertor without shielding and having T_{so} = 0.2 m. Letters indicate the locations of banana-orbit tips that are confined (C), ripple trapped and lost (R), and slightly ergodic but probably confined (S).

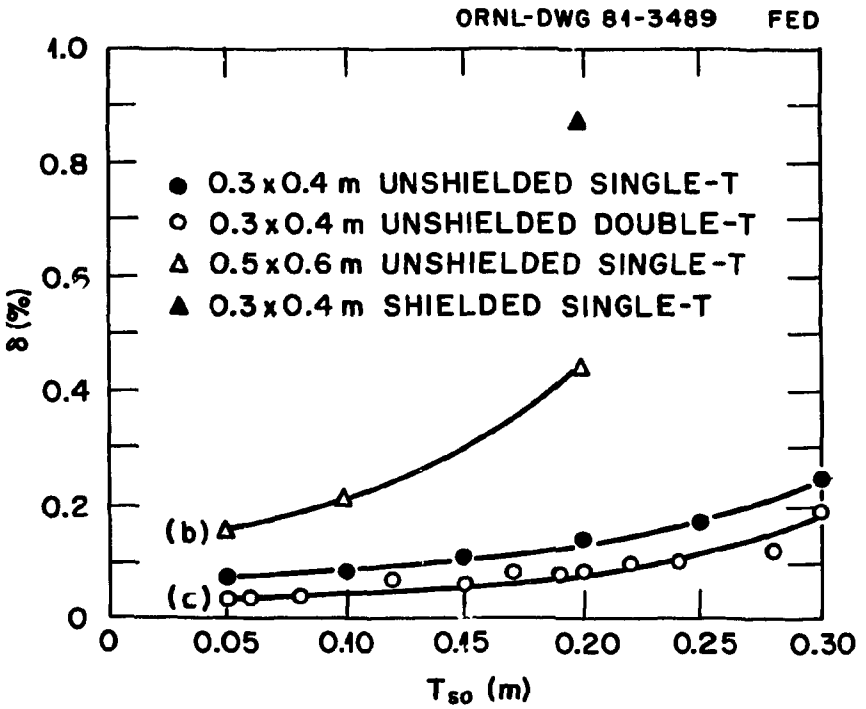

Fig. 2-63. On-axis ripple (δ) versus scrapeoff layer thickness (T_{so}) for various optimized diverters on FED.

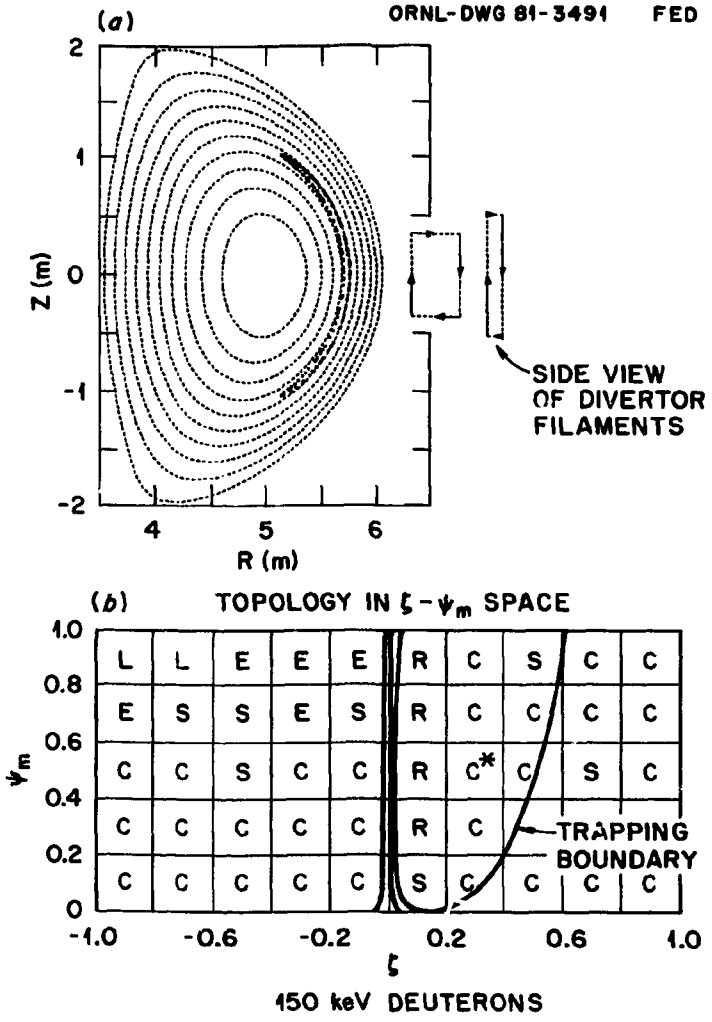

Fig. 2-64. (a) A puncture plot for a banana-trapped, collisionless 150-keV D^+ ion having constant of motion as designated by '*' in (b) for the FED plasma of Fig. 2-62. This figure was obtained by plotting where the guiding center orbit intersects a plane at a fixed toroidal angle in the course of 100 revolutions around the tokamak. (b) Summary of collisionless confinement of 150-keV D^+ ions for the FED plasma of Fig. 2-62 in the space defined by ψ_m (the maximum value of the poloidal flux function, ψ, along the guiding center orbit, where ψ is increasing from the magnetic axis and normalized to 1.0 at the plasma edge) and ζ [the cosine of the angle between the parallel component of plasma current and the ion velocity at ψ_m, i.e., $\zeta = \vec{J} \times \vec{v}/(|\vec{J} \times v)|_{\psi_m}$]. The letters indicate the fate of beam ions on orbits defined by ψ_m and ζ that are confined (C), ripple trapped and lost (R), slightly ergodic but probably contained (S), ergodic and probably lost (E), and lost to the wall (L).

between two adjacent TF coils. Additional back T-coils are needed to expand the diverted flux bundle near or beyond the outer legs of the TF coils. Experiments using high-ripple divertors on DITE and ISX-B will clarify the deleterious effects of ripple, but the present lack of definitive results on these devices should not prejudice the future of more advanced divertor designs.

2.7 POLOIDAL FIELD CONFIGURATION

D. J. Strickler, Y-K. M. Peng — ORNL/FEDC

The poloidal field (PF) configuration external to the plasma deals with the coil locations and currents that induce the plasma current and maintain the plasma shape and position over the ranges of plasma parameters of interest. The PF coils consist of equilibrium field (EF) and ohmic heating (OH) coil sets. Many engineering design issues are directly related to the configuration of these coil sets. Desirable coil locations (which minimize the total ampere-turns) must also satisfy the space, access, shielding, and maintenance requirements of FED. Moreover, the PF coil locations must mitigate the pulsed poloidal fields and out-of-plane forces on the TF coils and local fields in individual PF coils.

The concept of a PF coil system that is well coupled to high-beta, D-shaped plasmas[89,90,91] has been adopted for the FED concept. A decoupled PF coil system, such as that used in PDX, and a coil system with quasi-steady-state exterior superconducting coils have been assessed and found[92] to be less desirable because they require more interior copper coils giving a reduced induction flux capability.

In Section 2.7.1 we will discuss the choice of the baseline configuration. The PF coils and currents for pump limiter and for poloidal divertor designs will be characterized in Sections 2.7.2 and 2.7.3, respectively. The sensitivities of the configuration to variations in plasma equilibrium assumptions will then be assessed in Section 2.7.4.

2.7.1 Choice of Baseline Configuration

As discussed in Sect. 2.5, it is considered desirable for the plasma shape to be elongated ($\kappa = 1.6$) with a strong D shape ($\delta = 0.5$). These requirements in practice lead to rather stringent design conditions. For example, a triangularity of $\delta = 0.5$ leads to the necessity of equilibrium field coils on the inboard side of the torus carrying large ampere-turns ($\sim$10 MA).

Three possible arrangements to position these inboard EF coils in a hybrid coil system[90] have been examined. As shown in Fig. 2-65, option 1, with EF coils placed between the OH solenoid and the inner leg of the TF coil, superimposes the EF and the OH solenoid field at the end of a burn cycle. With the maximum ampere-turns specified by current drive and plasma equilibrium, a field of about 10 T is produced at the solenoid, exceeding the 8-T design limit assumed for NbTi operated at 4°K.

Option 2 then has a split OH solenoid, leaving space near the midplane for the inboard EF coils. This reduces the solenoid size and leads to additions of nulling coils with large opposing currents to the extent that the volt-second capability for startup was doubtful. Finally, Option 3 positioning inboard EF coils internal to the TF coils was rejected because of expected, severe maintenance problems. It is seen that none of these options appear acceptable.

By reducing the proposed plasma triangularity to about $\delta = 0.3$, inboard EF coils may be eliminated at the expense of larger shaping coil currents. Several feasible coil concepts were then identified (Fig. 2-66). These concepts were assessed by comparing the coil current requirements for the same degree of plasma shaping.

The external flux $\psi^{(e)}$ distribution of a high-beta ($<\beta> = 5.5\%$) FED plasma with triangularity $\delta = 0.3$ and elongation $\kappa = 1.6$ was first obtained assuming an idealized set of coils. For a given set of admissible coil locations, currents c_j can then be calculated by finding a minimum of the quantity

$$w = \sum_i [\psi_i^{(e)} - \psi_i(\vec{c})]^2 + \alpha \sum_j c_j^2$$

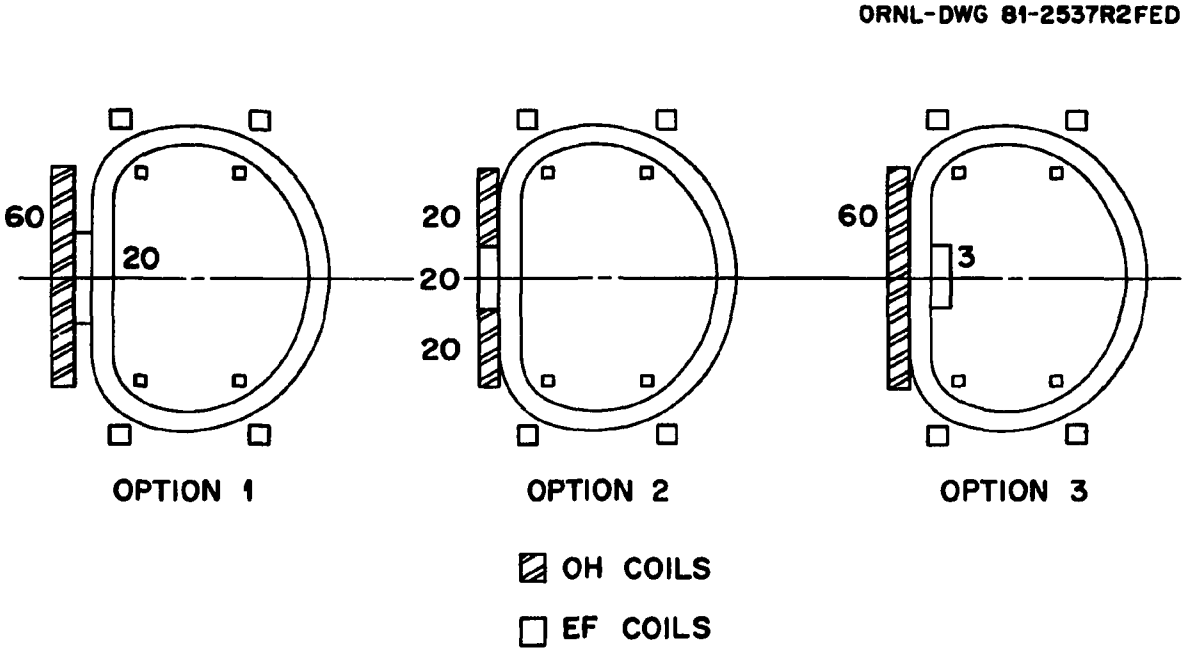

Fig. 2-65. Possible locations for inboard EF coils in the hybrid PF configurations. Coil ampere-turns at the end of a burn cycle are indicated.

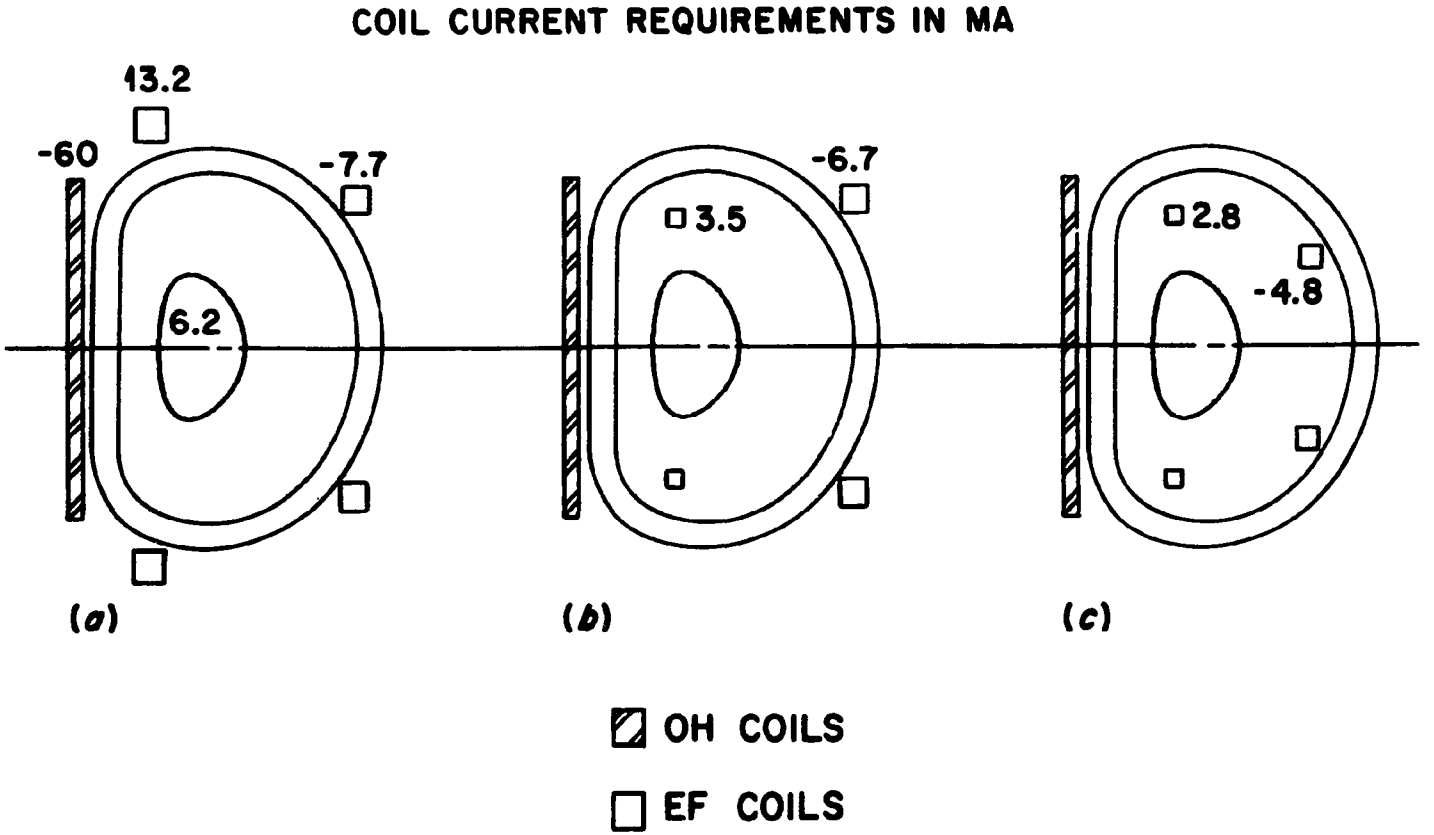

Fig. 2-66. PF coil concepts omitting the inboard EF coils: (a) all exterior superconducting coils, (b) interior normal shaping coils, and (c) all interior normal coils. Coil ampere-turns at the end of the burn pulse are indicated.

where the data $\psi_i^{(e)}$ are given on the plasma boundary and $\psi_i(\vec{c})$ are the corresponding values of poloidal flux created by the coil currents. Coil locations and the smoothing parameter α were varied until the field errors become acceptable.

$$\sum_i (\psi_i^{(e)} - \psi_i(\vec{c}))^2 / \sum_i \psi_i^{(e)2} < \varepsilon \ .$$

Approximate coil currents so obtained are given in Fig. 2-66 for $\varepsilon = 2.5 \times 10^{-4}$.

Based on analyses of cost (Sect. 4.3) and maintenance requirements (Sect. 3.3), the coil systems shown, the second option [Fig. 2-66(b)] consisting of normal internal shaping coils and superconducting external vertical field coils was chosen as the baseline concept. Allocations consistent with the device configuration were then chosen, using the above methods. Because of space and access considerations, they are asymetric with respect to the plasma midplane.

2.7.2 Poloidal Field Configurations for Pump Limiter

A sequence of equilibrium calculations were carried out to verify that the baseline coil configuration is appropriate in producing the field null required for startup, and to properly position and shape the plasma through the different stages of a typical discharge cycle during 8-T operation (see Fig. 2-67). The resulting coil currents from the equilibrium calculations are compiled to produce the current waveforms of the various coil groups (see Table 2-12 and Fig. 2-68).

As discussed in Sect. 2.2, a field null is required at time t = 0 to facilitate initiation of the plasma current channel in a minor radius of 0.4 m. Initial-field nulling currents are introduced in the EF coils for this purpose. A low-beta, circular plasma of minor radius $\sim$1 m is then produced at t = 2 s. The startup plasma is maintained in contact with startup limiters at the outboard midplane. At t = 6 s the primary OH current has swung from 60 MA to -30 MA, and an elongated, D-shape plasma in contact with the pump limiter is obtained. Plasma heating is assumed during the next six seconds, increasing beta, $\langle\beta\rangle$, to 5.5% followed by a 100-s burn.

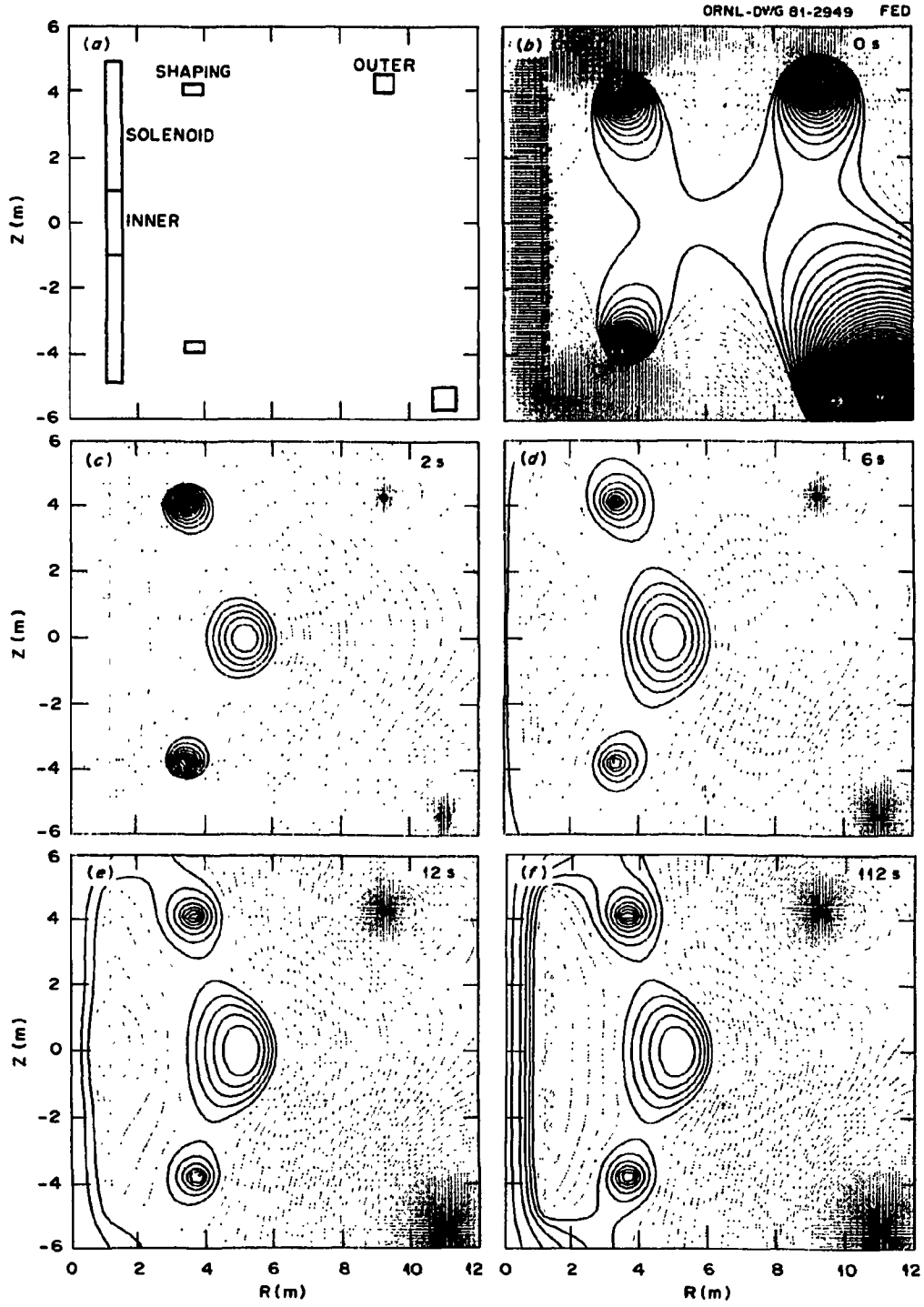

Fig. 2-67. (a) Baseline poloidal field coil configuration and a typical sequence of poloidal flux plots at (b) t = 0 s, (c) t = 2 s, (d) t = 6 s, (e) t = 12 s, and (f) t = 112 s with plasma parameters given in Table 2-12.

Table 2-12. Example plasma parameters and coil current requirements for 8-T operation (B_t = 3.6 T) with pumped limiter

Time into discharge(s)	0	2	6	12	112
Plasma shape					
Major radius (m)		5.1	4.8	4.8	4.8
Minor radius (m)		1.0	1.3	1.3	1.3
Elongation, κ		1.19	1.64	1.63	1.65
Triangularity, δ		0.07	0.28	0.43	0.36
Plasma parameters					
$<\beta>$ (%)		0.49	0.40	5.55	5.54
q_{axis}		1.0	1.0	0.9	0.9
q_{edge}		3.4	3.5	3.7	3.7
I_p (MA)		1.4	4.4	5.0	5.0
Coil currents (MA)					
OH solenoid (split)	48.0	24.0	-24.0	-25.0	-48.0
Inner coils	12.0	6.0	-12.0	-12.0	-12.0
Upper D-coil	1.8	2.9	2.9	2.6	3.0
Lower D-coil	2.0	2.5	2.6	2.3	2.6
Upper outer coil	0.6	-0.8	-3.1	-4.6	-4.8
Lower outer coil	1.0	-1.1	-4.5	-7.0	-7.3

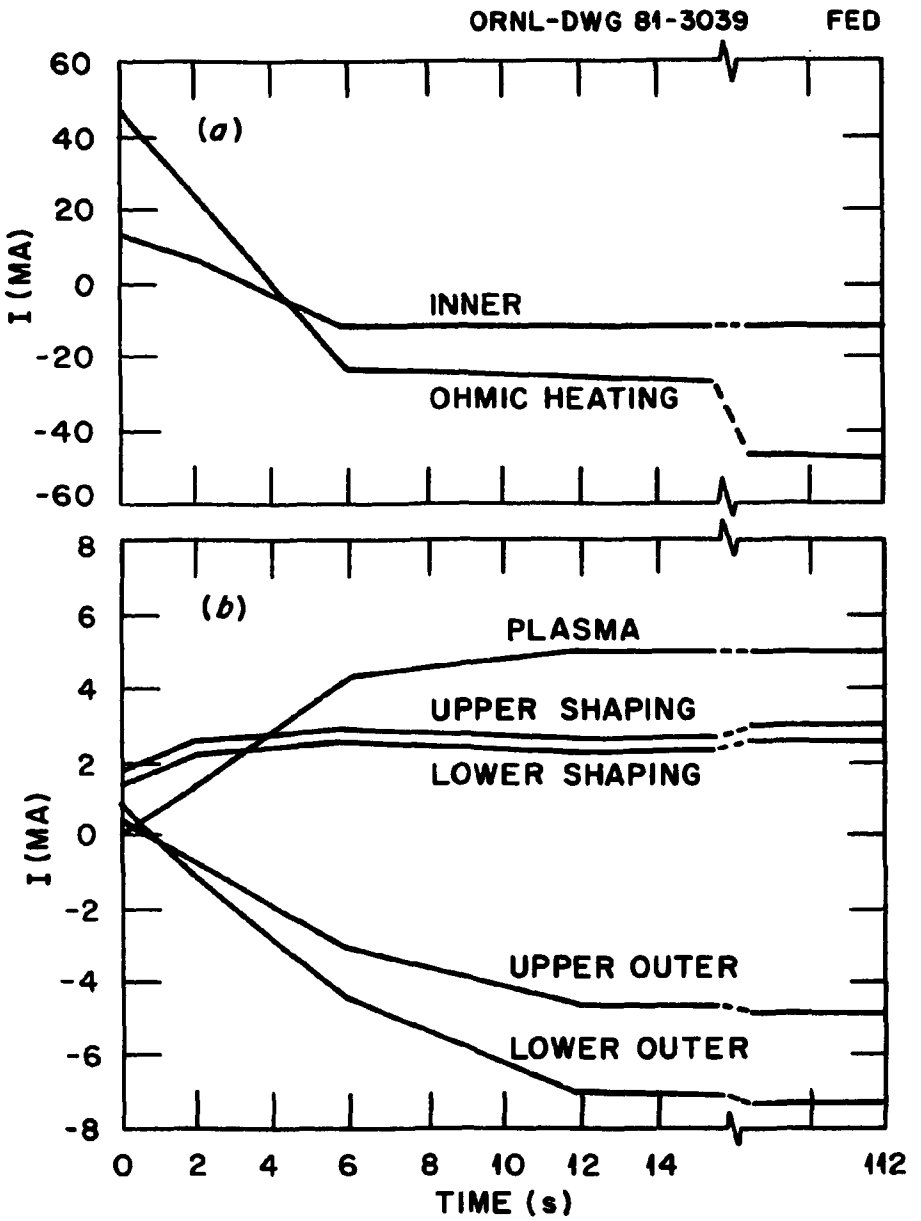

Fig. 2-68. Plasma and coil current waveforms for the 8-T operation with plasma parameters shown in Table 2-12.

The current swing in the center section of the solenoid is accelerated for 3 s $\leq$ t $\leq$ 6 s. This has the effect of a "split" solenoid (Sect. 2.7.1) without decreasing the volt-second capability. Small variations are introduced in the EF coil currents during burn to cancel the solenoid stray field. The maximum current in all EF coils is less than 20 MAT.

A similar analysis was carried out for 10-T operation, assuming the same current swing in the OH solenoid. The results are given in Table 2-13 and Fig. 2-69. It is seen that roughly a 25% increase in ET coil currents is needed for 10-T operation.

2.7.3 Poloidal Field Configurations for Poloidal Divertor

A single null poloidal divertor is proposed as the primary backup method of particle and impurity control for the FED (see Sect. 2.6). The poloidal field coil system in this case needs to be different from that of the baseline configuration because of somewhat increased access and separatrix control requirements. A sequence of plasma equilibria was computed to verify the coil system, model the plasma shapes, and determine the coil current waveforms of a discharge cycle. The results for 8-T operation are shown in Table 2-14 and Figs. 2-70 and 2-71.

The assumed discharge cycle scenario including startup, heating, and burn states is unchanged from that of the pump limiter case. The coil arrangement shown in Fig. 2-70(a) and Fig. 2-71 represents a compromise accounting for limited access to interior coils, the need to provide neutron shielding and some degree of separatrix control, and the avoidance of excessively large coil currents. The use of normal, internal window-frame coils carrying limited current ($\sim$1 MA, see Sect. 3.2) results in significant reduction in currents from those in an all external system such as the current INTOR concept.[93] The interior coils also help constrain the separatrix shift to $\lesssim$20 cm during plasma heatup. Note that the plasma elongation and triangularity above the midplane are reduced to $\kappa \simeq 1.5$ and $\delta \simeq 0.2$ in order to obtain a connected scrapeoff region, potentially leading to significant reductions in plasma performance (see Sect. 2.5). As compared with the baseline system, relatively

Table 2-13. Example plasma parameters and coil current requirements for 10-T operation (B_t = 4.5 T) with pumped limiter

Time into discharge(s)	0	2	6	12	112
Plasma shape					
Major radius (m)		5.09	4.80	4.80	4.80
Minor radius (m)		1.02	1.30	1.30	1.30
Elongation, κ		1.17	1.63	1.62	1.63
Triangularity, δ		0.10	0.28	0.36	0.36
Plasma parameters					
$\langle\beta\rangle$ (%)		0.51	0.49	5.38	5.38
q(axis)		0.9	1.0	0.9	0.9
q(edge)		3.4	3.4	3.6	3.6
I_p(MA)		1.8	5.5	6.2	6.2
Coil currents (MA)					
OH solenoid	48.0	24.0	-24.0	-25.4	-48.0
Inner coils	12.0	6.0	-12.0	-12.0	-12.0
Upper shaping	1.8	3.9	4.1	3.6	4.0
Lower shaping	1.5	3.4	3.6	3.2	3.5
Upper outer	0.5	-0.8	-3.8	-5.5	-5.8
Lower outer	0.9	-1.1	-5.5	-8.4	-8.7

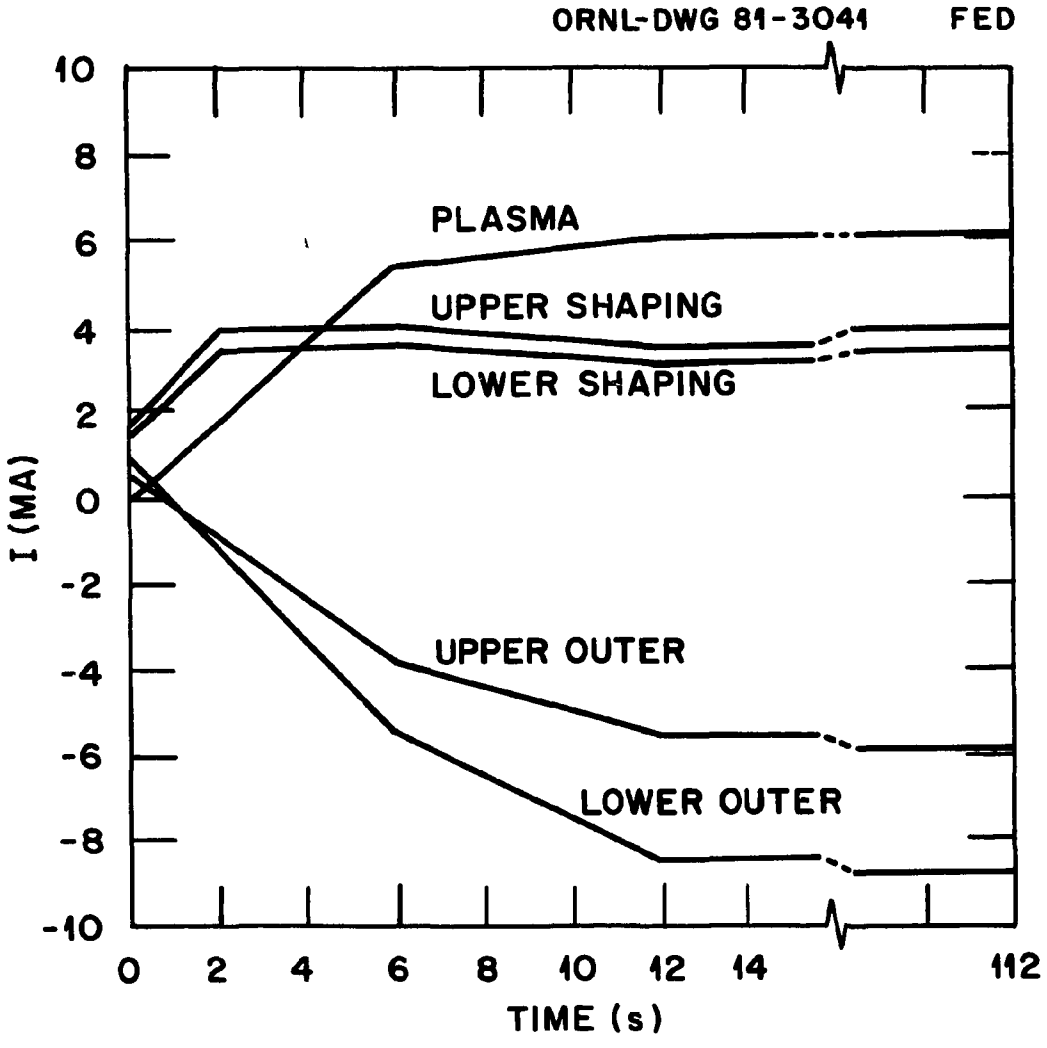

Fig. 2-69. Plasma and EF coil current waveforms for the 10-T operation with plasma parameters shown in Table 2-13.

Table 2-14. Example plasma parameters and current requirements for 8-T operation with poloidal divertor

Time into discharge (s)	0	2	6	12	112
Plasma shape					
Major radius (m)		5.09	4.80	4.85	4.85
Minor radius (m)		1.02	1.30	1.25	1.25
Elongation, κ		1.08	1.68	1.66	1.67
Plasma parameters					
$\langle\beta\rangle$ (%)		0.49	0.44	6.37	6.39
q(axis)		0.9	0.9	0.8	0.8
q(edge)		3.4	∞	∞	∞
I_p (MA)		1.4	4.4	5.0	5.0
Coil currents (MA)					
OH solenoid	48.0	24.0	-24.0	-25.4	-48.0
Inner coils	12.0	6.0	-12.0	-12.0	-12.0
Upper shaping (ext.)	2.4	2.6	1.3	2.4	2.5
Upper shaping (int.)	0.0	1.0	1.0	1.0	1.0
Lower shaping (ext.)	3.3	3.1	9.2	10.8	11.6
Lower shaping (int.)	0.0	1.0	1.0	1.0	1.0
Upper outer (ext.)	0.4	-0.6	-0.5	-2.6	-2.7
Upper outer (int.)	0.0	-1.0	-1.0	-1.0	-1.0
Lower outer (ext.)	0.2	-0.4	-7.9	-10.4	-11.1
Lower outer (int.)	0.0	-1.0	-1.0	-1.0	-1.0

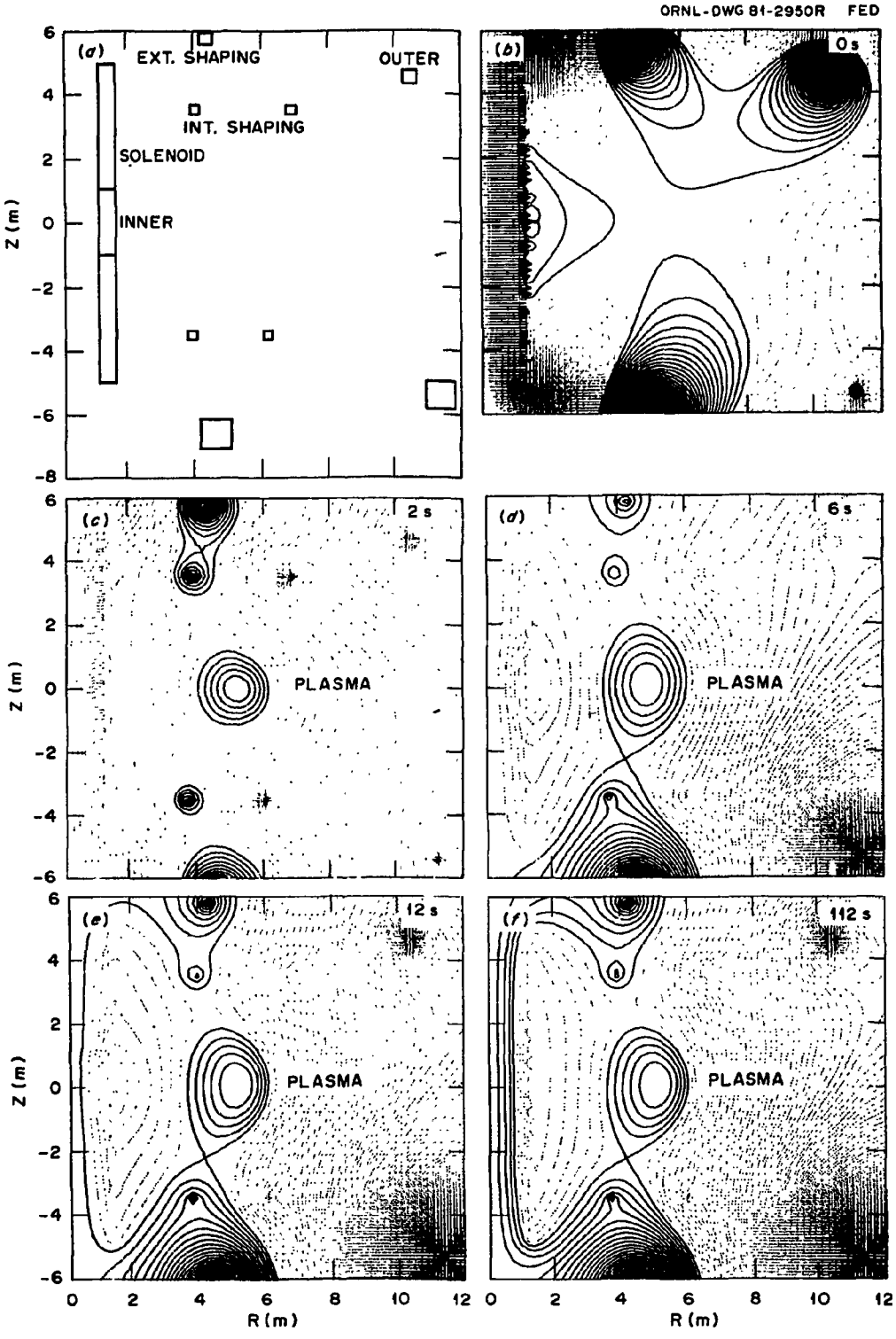

Fig. 2-70. (a) Poloidal field coil configuration for the poloidal divertor option and a typical sequence of poloidal flux plots at (b) t = 0 s, (c) t = 2 s, (d) t = 6 s, (e) t = 12 s, and (f) t = 112 s with plasma parameters given in Table 2-14.

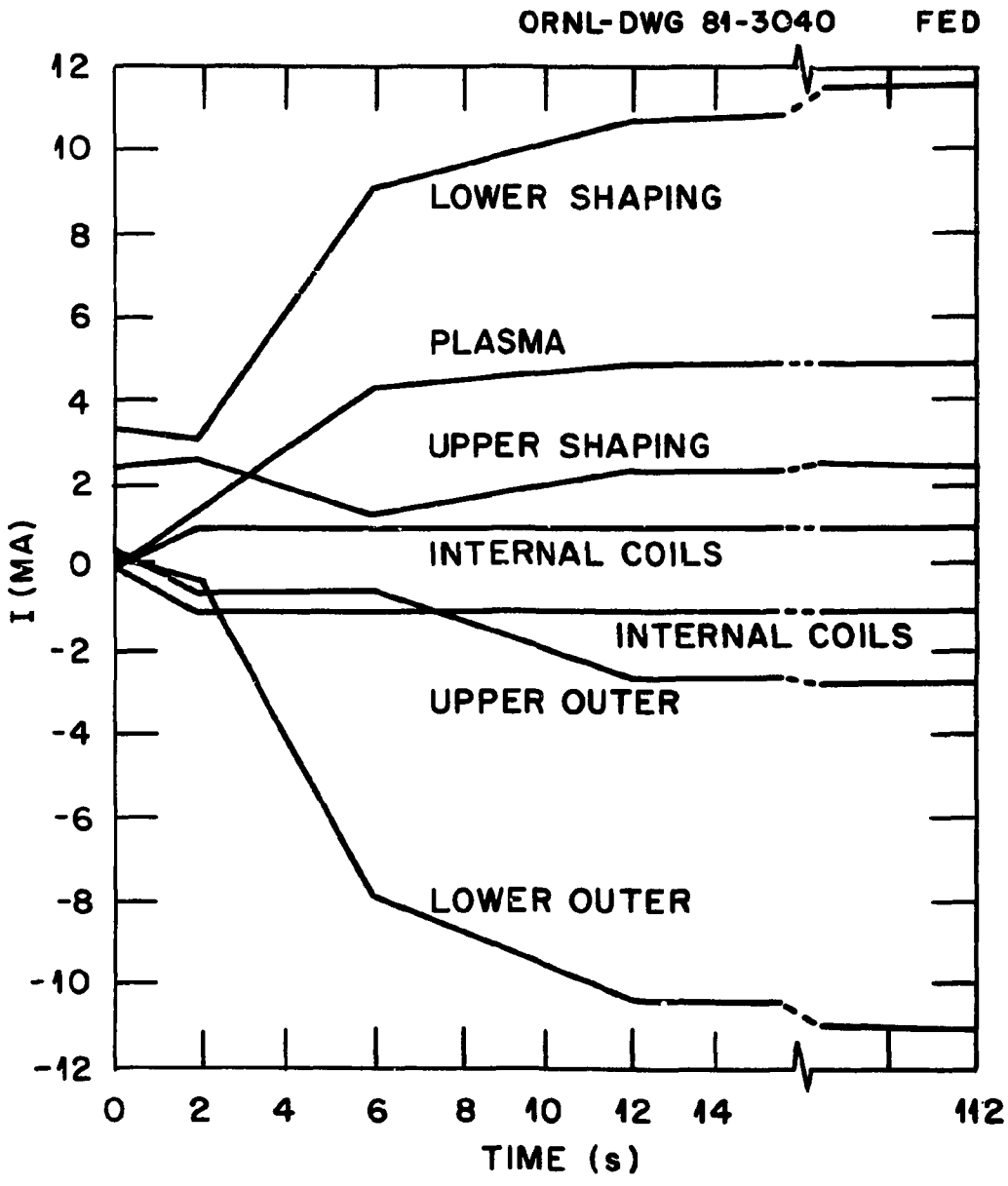

Fig. 2-71. Plasma and coil current waveforms for 8-T poloidal divertor operation with plasma parameters shown in Table 2-14.

large superconducting coils and currents are needed in this case, resulting in a total EF current of $\gtrsim$30 MAT.

2.7.4 Sensitivity to Plasma Variations

The baseline PF coil configuration [Fig. 2-67(a)] is unique in its relatively small total current ($\lesssim$20 MAT) in only 4 EF coil bundles. It is therefore of interest to assess its flexibility in handling uncertainties in plasma profiles and parameters. Also, the proximity of the poloidal separatrix to the plasma edge may disconnect the plasma scrapeoff and seriously degrade the effectiveness of the pump limiter. Thus, the dependence of separatrix location on the coil configuration and plasma parameters (e.g., κ and δ) needs to be clarified.

To ascertain this, an equilibrium code was used in which coil currents are iteratively adjusted in order to best reproduce a given plasma shape. The sensitivity of the flux lines in the scrapeoff region to the coil configuration, plasma parameters, and plasma shape are then examined. With the baseline coil concept, Fig. 2-72(a) shows that the separatrix for the near baseline plasma ($<\beta> = 5.7\%$, $B_t = 4.5$ MA, $q_{edge} = 3.3$, and $I_p = 6.3$ MA) is within the scrapeoff region of only 5-cm (15-cm) thickness at the plasma outboard (inboard). This diverts a larger portion of the scrapeoff before reaching the pump limiter. Using a broader plasma current profile [Fig. 2-72(b) with $I_p = 7.4$ MA and $q_\psi = 2.6$], this situation improves only slightly and the scrapeoff remains significantly disconnected.

Figure 2-73 exhibits the dependence of the separatrix and scrapeoff on the poloidal field coil system. The scrapeoff flux surfaces become fully connected [Fig. 2-73(a)] if the inboard EF coils are used. When these inboard coils are removed [Fig. 2-73(b)], however, the resulting coil current distribution produces a separatrix close to the plasma boundary. Since Figs. 2-73(b) and Figs. 2-72(a) are similar, the proximity of the separatrix is seen to depend primarily on the absence of inboard EF coils and not strongly on the number of EF coils or the plasma current profile. As a result, the poloidal flux lines are directed between the solenoid and the shaping coils, which carry current in an opposite

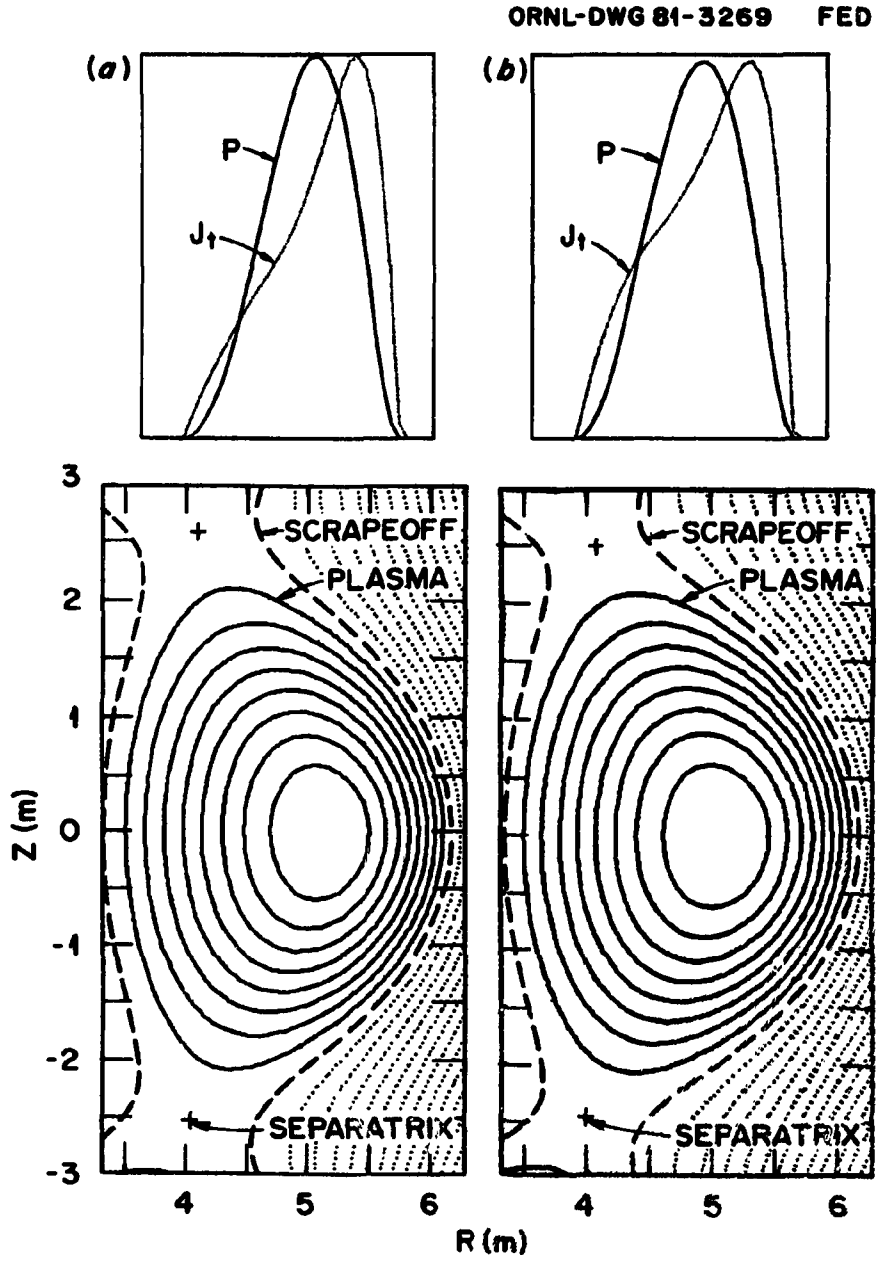

Fig. 2-72. Using the baseline EF coil concept, the plasma scrapeoff region is disconnected by the presence of a contained separatrix for (a) narrow and (b) broad plasma current profiles (J_t).

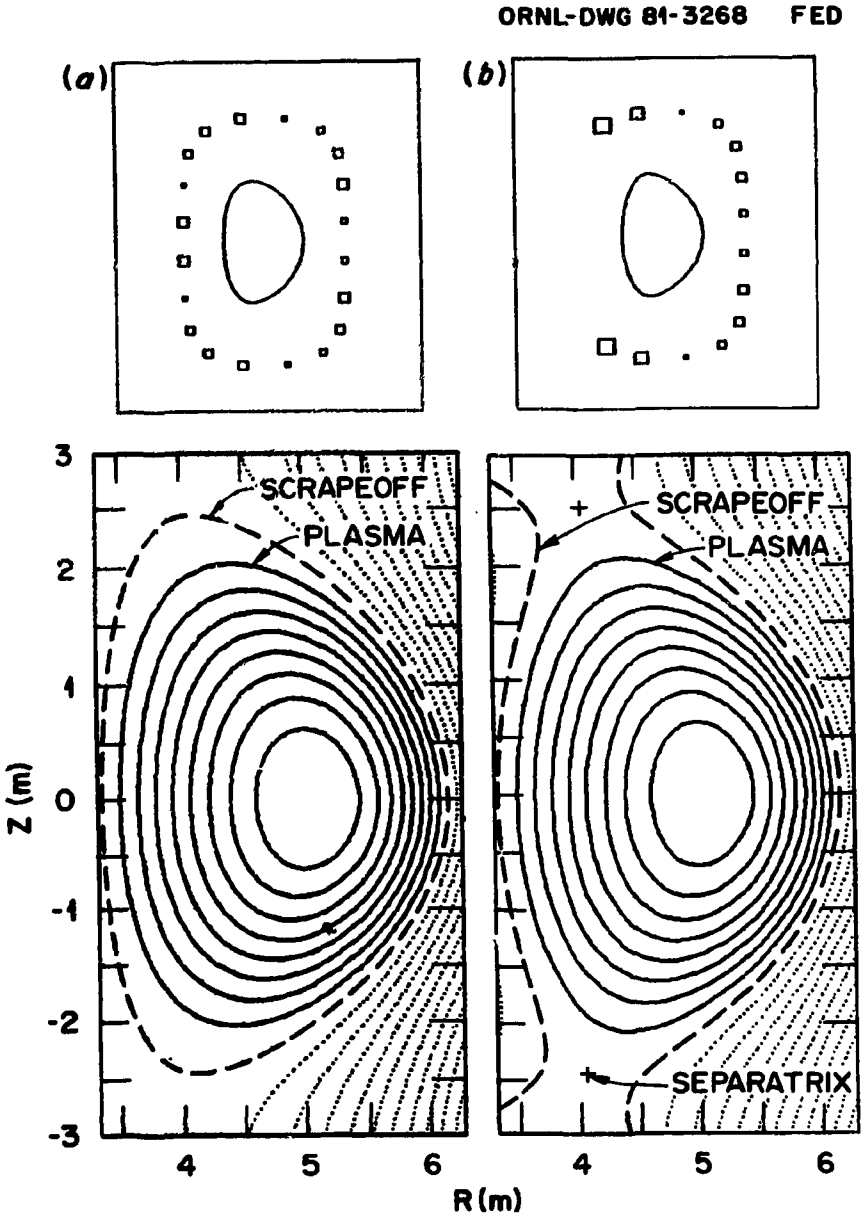

Fig. 2-73. The closure of the scrapeoff flux surface is (a) obtained by the use of inboard EF coils and (b) lost in their absence, despite the addition of several EF coils.

direction through most of the discharge, forcing the null point toward the plasma.

Since the OH solenoid is an indespensible component in the design configuration, and given the engineering restrictions on the use of inboard EF coils, the solution to the problem of maintaining nested flux surfaces in the limiter region appears to require a modification of the plasma shape. Figure 2-74 shows a case with a connected scrapeoff region with a plasma elongation of $\kappa = 1.5$ and triangularity $\delta = 0.2$, using the baseline coil concept. The potential impact of these relaxed plasma shapes is discussed in Sect. 2.5.

2.7.5 Conclusions and Future Work

A baseline coil concept [Fig. 2-67(a)] consisting of internal copper shaping coils and external, superconducting, vertical field coils has been selected for FED design studies, as a result of plasma equilibrium, engineering, and cost considerations. Numerical equilibrium calculations verify that this system is consistent with a baseline plasma shape of $\kappa = 1.6$ and $\delta = 0.3$. However, it is also shown that, in the absence of inboard EF coils, these shape parameters may be inconsistent with the impurity control configurations of the pump limiter and single null poloidal divertor. Reducing the elongation and triangularity to $\kappa = 1.5$ and $\delta = 0.2$, respectively, is shown to permit an adequate scrapeoff region for their operation. If, in fact, it is necessary to modify the baseline plasma shape, the positions of the shaping coils are expected to vary from the current baseline. These locations, together with the exact number of shaping coils, will need to be determined. Another area that should be explored is that of the physics implications of employing asymmetric coil locations.

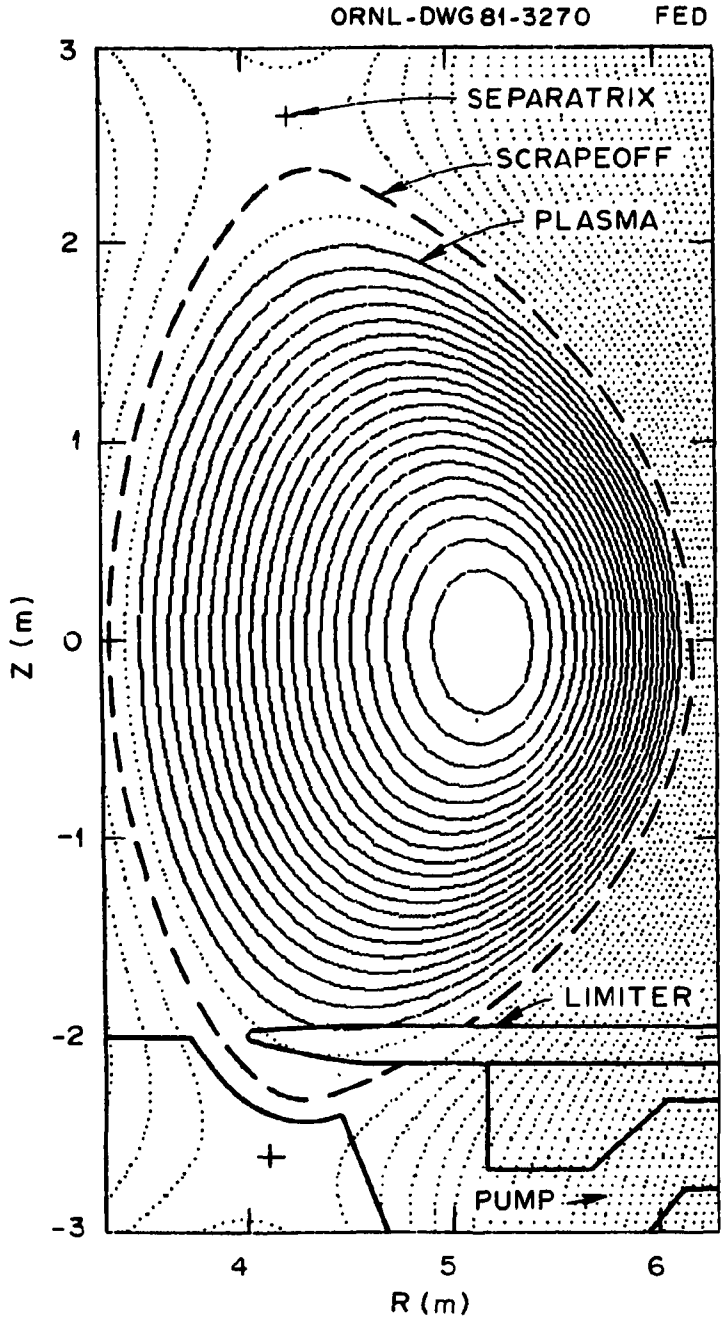

Fig. 2-74. Using the baseline coil configuration, the scrapeoff flux surface becomes closed by reducing the triangularity and elongation to $\delta = 0.2$ and $\kappa = 1.5$.

2.8 PLASMA DISRUPTIONS

The consequences of plasma disruptions can have a significant impact on the FED design. Major plasma disruptions limit the plasma current and density at which stable tokamak operation is possible. The abrupt termination of the tokamak discharge produces large electromagnetic and thermal loads on components of the device. It is therefore important to have as realistic an assessment as possible of disruption characteristics and their frequency over the operating range of the FED device. Section 2.8.1 describes the present characterization of plasma disruptions expected in FED and Sect. 2.8.2 discusses disruption avoidance and survival in FED.

2.8.1 FED Disruption Characterization

B. A. Carreras — ORNL, J. A. Holmes — ORNL/FEDC

There has been an increased effort in the fusion community to make a realistic assessment of disruptions in recent years. This effort is reflected in the documents produced by the Disruption Control Task Force,[94] the FED Low q/Shaping Team,[95] and several physics workshops for ETF[96] and FED. These documents also reflect the uncertainties involved in such an assessment due to the present limited knowledge of this subject.

The disruptive phenomena in a tokamak is quite varied. The consequences of disruptions to the plasma discharge vary from mild changes of plasma characteristics to abrupt termination (major disruptions). We limit our considerations here to this latter type of disruption because it can have the most severe impact on the FED design.

Disruptions are common during tokamak operation. However, due to the difficulty of appropriate experimental measurements, there are few fully documented cases of major disruptions, i.e., fully diagnosed measurements of the disruption precursor, the disruption process, and its consequences. Moreover, the available experimental information describes "typical" disruptions, those caused by some directly or indirectly controllable change of plasma parameters. There is no information on nontypical disruptions, i.e., those caused by accidental failures of the system during operation.

Present theoretical studies of major disruptions[97-99] are limited to low β and large aspect ratio tokamak plasmas. The thrust of these studies has been to identify the basic dynamic mechanism causing plasma disruptions. The effect of external conditions such as realistic power supply systems, cold plasma boundary, possible impurity influx, etc., has not been considered in a self-consistent way. Therefore, no present theoretical model can give a full account of the disruption process.

Comparisons between theory and experiment have been done for a very limited number of disruption events, and only for partial aspects of the disruptions. They show at most a qualitative agreement[100-102] between theoretical models and experiments.

Experimental observations

The main experimental features of major disruptions have been summarized in Refs. 94, 95, and 96. The most up-to-date summary is given in the Disruption Control Task Force Report:[94]

> "Disruption-free operation in circular or near-circular plasmas with q_a as low as 2.5 and at $\bar{n}_e R/B_T \sim 4 \times 10^{13}$ m•T^{-1}•cm^{-3} is now fairly routine in all of the major U.S. tokamaks. Here disruption-free means a disruption frequency in the range of 1-10%. Lower q_a (∿2.2) or high $\bar{n}_e/R/B_T$ (∿7) can be achieved with careful tuning, but the frequency of disruptions increases. So far, attempts to obtain $q_a < 2$ in PDX and D-III have resulted in 100% disruptions."

Major common features of disruptions in major U.S. tokamaks include an initial slight current increase, accompanied by a negative voltage spike, abrupt plasma cooling, and broadening of the current density profile. The plasma shifts radially inward and plasma-wall and plasma-limiter interaction increases dramatically. Typically, disruptions are preceded by a rapid growth of m = 2, n = 1 activity, although this is not observed in all cases, presumably due either to a lack of mode rotation (Alcator and PDX) or

the shielding effect of the vacuum wall (Doublet III). In PDX and Doublet III, major disruptions frequently result in a loss of vertical stability, with rapid (∿1 ms) vertical plasma motion. The magnitude of the negative voltage spike varies. In Doublet-III the spike is either small (<10 V/turn) or even unobservable, again due to the effect of the relatively thick vessel wall. In machines with thinner walls (e.g., PDX), much higher voltages (∿100 V/turn) are observed.

"The subsequent current decay after the onset of the disruption depends on a number of factors, including the wall conditions and the effectiveness of the radial and vertical position control systems. In machines with relatively fast feedback control (e.g., Doublet III) abrupt termination of the plasma current does not occur unless vertical stability is lost."

Recent experimental results[103] in Doublet III indicate that the plasma energy is mainly deposited on the limiter which was in contact with the plasma prior to the disruption. They show that the power going to other limiters or the wall is negligible. The energy deposition time in Doublet III is of the order of 250 μs or less. Earlier measurements in Alcator A[104] and PLT[105] gave similar values for the energy deposition time. The current decay is slower, being of the order of 1 ms for the fastest disruptions in these three devices.

Theoretical modeling of the disruption

We have already indicated the limitations in the present understanding of plasma disruptions. However, the available theoretical knowledge must be used to model the FED disruptions, even if the validity of the required extrapolation is questionable. We follow the model presented in Ref. 101 because it is the only one among those previously mentioned that allows an estimation of the different time scales of the process. This model, like most of the theoretical models, identifies the presence of an m = 2, n = 1 magnetic island in the plasma as the main cause of major tokamak disruptions. This magnetic island is generated by the m = 2, n = 1 tearing mode. Its interaction with some other

magnetic island, such as the m = 3, n = 2 island, triggers the disruption. The overlap of these islands destroys magnetic surfaces, and field lines become stochastic in a portion of the plasma volume. This leads to further destabilization of tearing modes and total destruction of the confinement. The plasma temperature decreases sharply with the corresponding energy loss and becomes uniform throughout the entire plasma volume. During this process the current profile broadens, reducing the plasma self-inductance. This explains the negative voltage spike observed in experiments. The equilibrium loss which accompanies the reduction in plasma energy probably causes the observed inward shift of the plasma. This whole process is followed by the decay of the toroidal current density.

This model shares many of the experimental features of a major disruption and is the result of three dimensional numerical calculations of the nonlinear interaction of tearing modes.[101] Figure 2-75 summarizes the results of one of these calculations for specific initial conditions which correspond to a major disruption (see Ref. 101). This calculation has been carried deeply into the nonlinear regime in order to understand the energy loss during the disruption. The mechanism for this loss is pure conduction.

As is indicated in Fig. 2-75 there are three phases in the disruption process. Each phase is characterized by a corresponding characteristic time:

1. The island overlap and nonlinear generation of high m and n modes constitute the first phase. The characteristic time, t_1, associated with this phase is proportional[101] to the inverse of the linear growth rate of the m = 2, n = 1 mode. The time, t_1, scales with the collisional resistivity as follows,

$$t_1 \simeq \gamma_{21}^{-1} \alpha \eta^{-3/5} .$$

2. When the level of fluid turbulence is large enough, the disruption proceeds with a time scale, t_2, faster than that of phase 1. The process becomes independent of the collisional resistivity. A

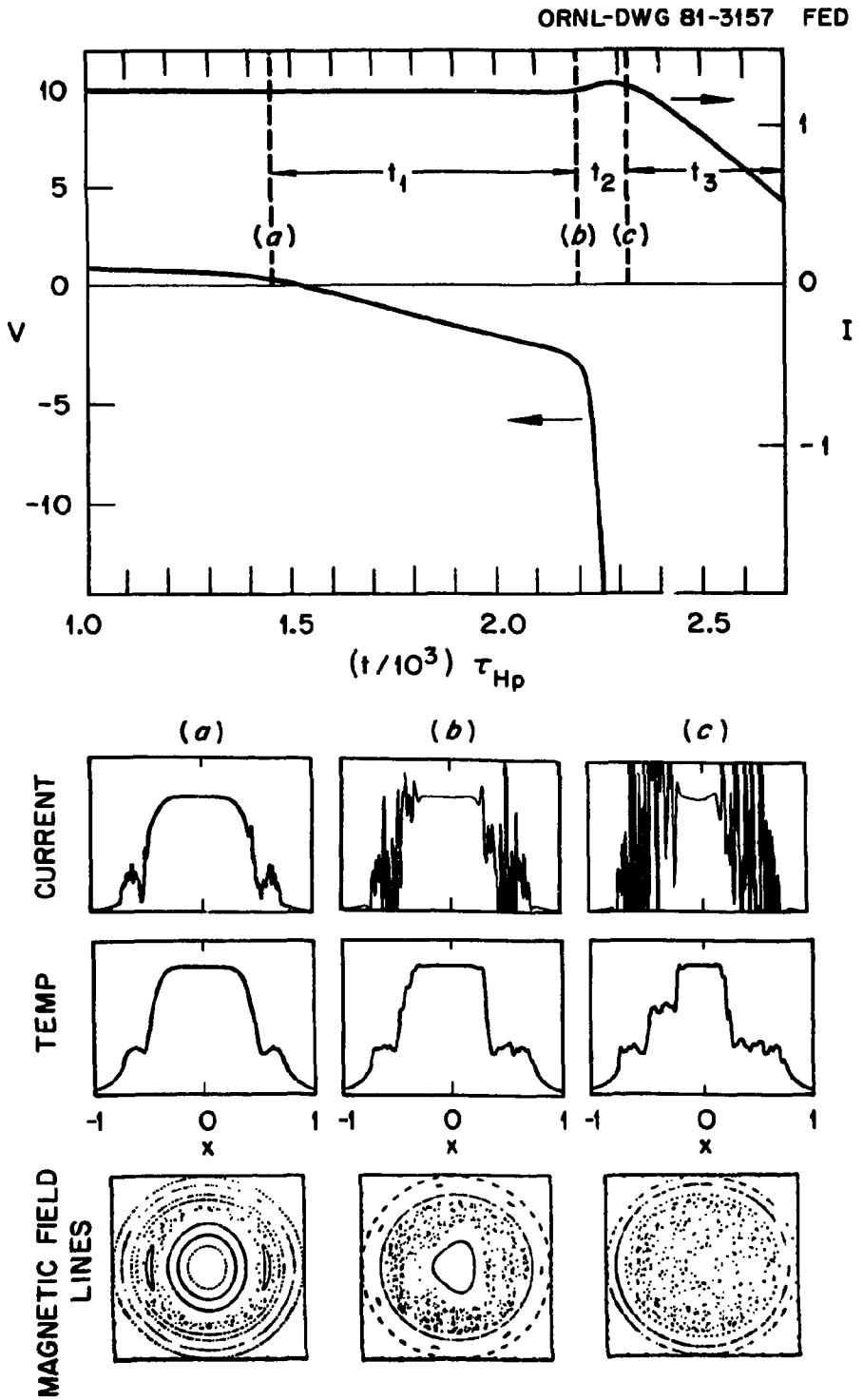

Fig. 2-75. Numerical results of a characteristic disruption process. The time evolution of the plasma current and loop voltage is shown at the top. The toroidal current and temperature profile and magnetic field line structure of three different times are given at the bottom.

detailed analysis[106] of this phase indicates that the faster growth of the low m modes is due to an anomalous resistivity η_A which increases with the level of fluid turbulence,

$$\eta_A = \sum_{m'n'} \frac{1}{\gamma} \left| \frac{\tilde{v}_{m'n'}}{V_A} \right|^2 \equiv \frac{1}{2\gamma} \hat{\eta}_A ,$$

where $\tilde{v}_{mn}$ is the fluid velocity associated with the mode (m,n) and v_A is the Alfven velocity. The time, t_2, scales like

$$t_2 \simeq \hat{\eta}_A^{-3/8} \tau_{Hp} ,$$

where τ_{Hp} is the poloidal Alfven time.

3. The final phase, which cannot be followed numerically, corresponds to the decay of the toroidal current. This decay is either a resistive decay (the collisional resistivity has increased due to the decrease in temperature) or a turbulent decay (due to the anomalous η_A). The most pessimistic prediction is given by the turbulent process. We will use the corresponding time scale here

$$t_3 \simeq \frac{a^2 \mu_s}{\eta_A} \propto \hat{\eta}_A^{-1/2} \tau_{Hp} .$$

The time scale t_1 is a direct result of the type of dynamical mechanism assumed in this model. However, the times t_2 and t_3 are related to the turbulence associated with the stochastization of field lines and they are probably less dependent on the specific mechanism which triggers the disruption process. For a device like PLT the values predicted for these time scales are $t_1 \simeq 400$ μs, $t_2 \simeq 100$ μs, and $t_3 \simeq 2$ ms.

Comparing with experiment, we see that the width of the negative voltage spike t_v is given by $t_1 + t_2$. Furthermore, since generally $t_2 << t_1$, one can set $t_v \simeq t_1$. This comparison was done in Ref. 107 for present-day tokamaks. During the time, t_1, the decrease in temperature

is slow and affects mainly the periphery of the plasma, near q = 2. During the time, t_2, the energy of the core of the plasma collapses. Since experimental observations are generally made using soft x-rays, this second phase is identified as the thermal energy quench. The quantity of interest is the energy quench time, which we take to be $t_2/(\Delta E/E)$, where $\Delta E/E$ is the fraction of energy remaining in the plasma after the first phase.

The values for t_1, t_2, and t_3 given above agree roughly with the time scales for the most severe disruptions observed in present-day tokamaks. Their extrapolation to FED parameters gives $t_1 \simeq 20$ ms, $t_2 \simeq 0.5$ ms, $t_E \simeq 2$ ms, and $t_3 \simeq 10$ ms. We will use these values as a basis for the FED disruption parameters. These proposed FED disruption parameters are given in Table 2-15.

The uncertainties encountered in the determination of the disruption parameters clearly indicate that they must be considered as rough estimates. It is necessary in planning a new device to study the sensitivity of the design characteristics to each of the parameters given in Table 2-15 over a reasonable range. This has been done for FED by J. R. Haines,[108] who has shown that the design is not sensitive to reasonable variations of the parameters. In this sense they can be adopted as baseline parameters for FED.

Table 2-15. Plasma disruption parameters

Parameter	Proposed value	Range
Thermal quench phase:		
Time scale t_E	2 ms	1-10 ms
Thermal energy deposition	80 MJ	60-100 MJ
via particles	75%	50-100%
via radiation	25%	50-0%
Current quench phase:		
Time scale t_J	10 ms	—
Thermal energy deposition	20 MJ	0-40 MJ
Region of plasma impact	Inboard, top, or bottom	

2.8.2 Disruption Avoidance and Survival in FED

J. Wesley – GA

Disruption avoidance

It will not be possible to avoid disruptions in FED. This conclusion is based on two principal factors:

1. Attainment of a disruption-free operating regime has not yet been demonstrated in a large-size tokamak.[94] In this context, the term disruption-free is defined to mean an operation regime which has a robust stability against major (current-terminating) disruptions. In such a regime, a major disruption will not occur, even if the plasma conditions (e.g., density, current, impurity content) are significantly perturbed. Such a mode has been observed in ohmically-heated DIVA and Wendelstein VIIA plasmas, but neither result can yet be convincingly extrapolated to FED.
2. Even if such a disruption-free operating regime is found, there is always the possibility that a hardware failure will result in a disruption.

Disruption frequency

Given that disruptions cannot be avoided completely, for design purposes it is necessary to know their anticipated frequency and characteristics. The guidelines for disruption frequency proposed in ORNL/TM-7777, Table 3.3, vary between 10^{-1} (per pulse) during the first year of system operation (Phase I) to 10^{-3} per pulse in the final 6 years of D-T engineering testing (Phase IV). These guidelines may be optimistic, especially during phases II and III (hydrogen and initial D-T operation, respectively). In these phases, the objective will be to bring up the plasma to design parameters, including in Phase III, appreciable α-particle heating and high beta. Operating experience in past experiments suggests that the frequency of disruptions encountered in exploring these new operating regimes may be higher than proposed, possibly as high or even higher than in Phase I (10^{-1}). Given that a stable operating mode with

low disruptivity is obtained by the end of Phase III, it is then not unreasonable to assume that the frequency of disruptions in Phase IV will drop to the level proposed, if the operating mode does not change. Indeed, identifying such modes of operation is a prime objective of the early experimentation on the device. This presumes that all plasma conditions (e.g., impurity levels) can be maintained constant during this period.

As a point of reference, a disruption frequency of 10^{-3} per pulse corresponds to approximately 10 days of continuous operation of a typical large present-day tokamak (e.g., Doublet III) with only one disruption. In most present-day machines, sustained operation of this type is the exception rather than the rule. It must also be recognized that the design guidelines must allow for disruptions caused by hardware failures as well as intrinsic plasma properties, and hence the intrinsic plasma disruptivity may have to be significantly less than the overall guideline of 10^{-3}, depending on the hardware reliability.

Magnitude and location of heat loads due to disruptions

Recent measurements[103] obtained in Doublet III show that more than 50% of the plasma thermal energy is deposited on the limiter area in contact with the plasma immediately prior to a major disruption, in a typical time of less than 250 μs. Although the plasma does move radially inward during the disruption, the motion prior to the completion of the thermal quench is relatively small ($\lesssim$2 cm) and appears (to first approximation) to be offset by a similar expansion of the magnetic flux surfaces. Although detailed interpretation of the data is continuing, these results suggest that:

1. an appreciable fraction ($\gtrsim$50%) of the plasma thermal energy will be deposited on the FED limiters (or divertor plates) on the same area which receives normal plasma thermal loading, and
2. the energy deposition time will be relatively short, and if, as appears to be the case, the deposition time is related to the parallel energy transport time for heat along the magnetic field

lines to the limiter, then the corresponding time in FED could be as short as 1 ms.

The implications of these results for FED need to be examined in more detail. One immediate conclusion is that an appreciable amount of limiter material will be sublimated by the disruption heat load. If 50% of the plasma thermal energy is uniformly deposited on 40 m^2 of limiter area, the average loading will be 120 J/cm^2. If the limiter material is graphite, this instantaneous energy flux would sublimate $\sim 10^{-2}$ g/cm^2, or about 0.1 mm per disruption. These figures are approximate and neglect the specific heat of the graphite, thermal conduction, and radiation, all of which will decrease the amount sublimated. The limiter surface would also be subjected to high mechanical stresses due to this thermal loading. These and other limiter-related problems need to be examined.

Concentration of the disruption energy on the limiter also implies a reduced heat load to the inner, top, and bottom portions of the first wall. While the accuracy of the Doublet III data is insufficient to unambiguously account for all of the plasma energy, there is no explicit evidence for a high heat flux to the inner wall when the plasma is normally positioned, i.e., more than 2 cm away from the inner wall. Apparently the inner wall is subject to a high load only if the plasma is positioned in contact with the wall, or if the radial movement of the plasma after the fast thermal quench has occurred results in contact with the inner wall. In FED, various scenarios resulting in energy deposition on the inner wall are possible, the worst-case being a loss of radial position control that drives a hot (maximum parameter) plasma into the inner wall, thereby precipitating a major disruption localized on the inner wall. A more probable scenario might be one in which the principal disruption is localized on the primary (pump) limiter, but after which the thermally degraded plasma moves radially inward and contacts the inner wall, precipitating a secondary disruption localized on the inner wall. Because of the size and energy content of the FED plasma, such a "secondary" disruption may have serious consequences.

Current decay

The proposed FED current decay time of 10 ms is a reasonable design guideline, provided (1) the presently proposed continuous low toroidal resistance vessel design is retained, and (2) sufficient plasma position control capability (power supply voltage and response speed) is provided to maintain control of the radial and vertical position after the disruption. There is a trade-off between requirements (1) and (2) in that a lower toroidal vessel resistance provides more effective passive position control during the disruption but increases the power necessary to restore the plasma position after the thermal quench is complete (significant active position during the thermal quench does not seem feasible). Again a careful design trade-off study is warranted; however, it should be recognized that the results of this study may be sensitive to the assumptions made about the plasma current decay. Since present theoretical understanding of this phase is poor and experimental results are varied, caution and sensitivity studies seem prudent. Also, it must be recognized that the plasma is the dominant circuit element in the current decay phase, and thus realistic modeling of the current decay must involve consideration of plasma effects such as magnetic stability, wall/limiter interaction, impurity influx, and plasma energy balance.

Survival measures

The ability of FED to withstand disruptions will be influenced by many design factors, but will be dominated by three principal aspects: electrical design of the poloidal system, electromechanical design of the torus and first wall, and design of internal projections within the torus. The electrical characteristics of the poloidal system during the current quench transient depend on the number and placement of the poloidal coils, their coupling to the plasma, and the shielding and/or loading effect of other nearby conductors, especially the vacuum vessel. General guidelines are to minimize the number of turns in the coil system, use parallel rather than series connections, and design all coils with voltage insulation well in excess of the maximum anticipated

levels. All power supplies should have low source impedance and should be provided with recoverable overvoltage protection (e.g., silicon carbide or magnesium oxide varistors).

As has been noted before, provision of a toroidally and poloidally continuous vacuum vessel with as low resistance as possible is perhaps the most important single factor in ensuring disruption survival. The present FED torus design seems to be adequate in this respect; however, the effect of penetrations and the means used to join the torus segments require careful study. The mechanical design must also afford adequate strength to withstand the magnetic forces produced by rapid plasma motion and/or current decay. Here again, realistic modeling of the current quench is required, and the design must be carefully reviewed for sensitivity to modeling assumptions.

Providing adequate protection for components projecting from the interior of the torus is again a matter of detailed design. The first guideline is to minimize the number and radial extent of the projections, which ideally should include only components such as limiters which must of necessity project beyond the torus wall. The problem of disruption heat load to the limiter and first wall has been previously discussed. In addition to the thermal loading, projections may also be subject to significant current flow and $\vec{J} \times \vec{B}$ force during plasma disruptions or position excursions. Because of the affect, it is important to provide either adequate electrical isolation to prevent current flow, or a low resistance electrical connection to the torus to avoid excessive joule heating, arcing, and/or material failure at contact points. Although limiters constitute the principal source of projecting components, diagnostic components may also present significant problems. It is essential that the design of such diagnostics be incorporated in the torus design from the beginning, rather than as later add-ons.

2.9 SUMMARY — FED PLASMA ENGINEERING

Y-K. M. Peng — ORNL/FEDC, J. F. Lyon — ORNL

The previous assessments indicate that the current FED baseline design is appropriate for achieving the stated physics goals in spite of the significant uncertainties remaining in several physics areas. In particular, the following conclusions can be made concerning the major issues in our study.

1. RF-Assisted Startup. One to two MW of 90 GHz ECRH power is expected to be sufficient for ionization and heating of the initial small-volume plasma to an electron temperature T_e = 100-200 eV, even with a few percent oxygen impurity concentration. This will permit current initiation in a small plasma radius with a maximum loop voltage less than 25 V on a slow time scale (0.2-0.8 s). Subsequent ICRF heating at a 5-MW level will permit a slow rise in plasma current in 5-6 s without excessive resistive volt-seconds requirements.
2. ICRF Bulk Heating. Second harmonic deuterium ICRF bulk heating at 68 MHz with about 30 MW power is shown to allow ignition to be reached for 10-T operation using optimistic transport assumptions and simplified power deposition models. For conservatism, a requirement of 50 MW power at 54 MHz over 6 s followed by a steady drive of 36 MW during burn is suggested for 8-T operation. More refined time dependent wave propagation and absorption modeling along with improved transport modeling is necessary to give more accurate predictions for FED.
3. Plasma Burn Performance. Transport simulation assuming 150 keV neutral deuterium injection reveals that the operating regime of 5.5×10^{13} cm$^{-3} \leq \langle n \rangle \leq 1.2 \times 10^{14}$ cm^{-3} and 6.5 keV $\leq \langle T \rangle \leq$ 12.5 keV satisfies the goals of $Q \sim 5$, $P_{beam} \leq 36$ MW, $\langle \beta_T \rangle \leq 5.5\%$, and P_{fusion} = 180 MW for 8-T operation. A broader operating regime, extending to ignition, is obtained for 10-T operation (with P_{fusion} = 450 MW), and for the 8-T operation (with P_{fusion} = 200 MW) if a more optimistic transport model is assumed.

4. Beta Considerations. The baseline plasma parameters of $\varepsilon\beta_p \simeq 0.5$, $\langle\beta\rangle \simeq 5.5\%$, $q_\psi \simeq 3$, $\kappa \simeq 1.6$, $\delta \simeq 0.3$, and $I_p \simeq 5.4$ MA remain appropriate despite uncertainties in the plasma-size and β_p dependence of electron energy confinement. If confinement decreases with increasing $\varepsilon\beta_p$ as suggested by preliminary indications in ISX-B, an acceptable operating regime in $\langle n \rangle$ and $\langle T \rangle$ still remains for 8-T operation. In this case, reducing q_ψ is as effective as raising B_t in enhancing the FED plasma performance.
5. Poloidal Field Configuration. A poloidal field coil system with no equilibrium field coils on the plasma inboard side is employed to shape and position the FED plasma, requiring only modest coil currents for a variety of possible plasma profiles. However, this configuration also shifts the poloidal field separatrix toward the plasma, potentially requiring reduced κ (to 1.5) and δ (to 0.2) to ensure closure of the plasma scrapeoff for proper operation of the pump limiter or the poloidal divertor.
6. Pump Limiter. A pump limiter at the chamber bottom that permits large adjustments to the plasma-limiter contact is chosen to adapt to the uncertainties in the plasma scrapeoff assumptions. Under the maximum heat load scenario, an acceptable heat load ($\sim$250 W/cm^2) and an adequate atomic particle pumping rate ($>2 \times 10^{22}$/s) can be obtained. However, a large surface erosion rate is also found, possibly reducing the limiter life to a few months and seriously enhancing the probability of impurity contamination of the plasma. Supplementary schemes such as maintaining a radiation-cooled plasma edge and impurity flow reversal could alleviate these problems but currently lack a reliable physics basis.
7. Poloidal Divertor. As an alternative to the pump limiter, a single-null poloidal divertor with short channels is estimated to be adequate in power, particle, and impurity handling, if the postulated high density divertor regime can be reliably achieved. An erosion problem at the divertor plate, similar to that at the limiter surface, is expected, but it may be mitigated by the use of high-Z material.

8. Disruption Considerations. It is assumed that plasma disruptions will not be avoidable in FED. Recent modeling work suggests a thermal energy quench time of ∿2 ms and a plasma current quench time of ∿10 ms during a full power major disruption. A toroidally and poloidally continuous vessel with low resistance is proposed to impede plasma current quench and reduce the impacts of disruption-induced arcing, heat deposition, and eddy currents.

REFERENCES

1. P. H. Rutherford et al., "FED Physics Basis and Physics R&D Requirements," Vol. IV, DOE/TIC--11600, to be published.
2. Fusion Engineering Design Center Staff (C. A. Flanagan, D. Steiner, G. E. Smith, eds.), "Initial Trade and Design Studies for the Fusion Engineering Device, Chapter 4, ORNL/TM-7777, June 1981.
3. Fusion Engineering Design Center Staff, "Fusion Engineering Device Design Summary," Vol. II, DOE/TIC--11600, to be published.
4. Y-K. M. Peng, S. K. Borowski, and T. Kammash, Nucl. Fusion 18, 1489 (1978).
5. R. M. Gilgenbach et al., Electron Cyclotron/Upper Hybrid Resonant Preionization in the ISX-B Tokamak, NRL Memorandum Report 4248, Naval Research Laboratory (June 1980); Nucl. Fusion 21, 319 (1981).
6. R. C. Isler et al., "Experiments in the ISX-B Tokamak: ECH, Ripple Studies, Pellet Fueling, Impurity Flow Reversal, and Surface Physics," paper IAEA-CN-38/A-5 in Plasma Physics and Controlled Nuclear Fusion Research 1980, to be published.
7. S. K. Borowski, Y-K. M. Peng, and T. Kammash, "RF-assisted Current Startup in Large Tokamak Plasmas," to be published.
8. V. V. Alikaev, Yu. N. Knestrovskii, V. V. Parail, G. V. Pereoerzev, Sov. J. Plasma Phys. 3, 127 (1977).
9. O. C. Eldridge, W. Namkung, A. C. England, "Electron Cyclotron Heating in Tokamaks," ORNL/TM-6052, Oak Ridge National Laboratory, Oak Ridge, Tennessee, November 1977.
10. B. Grek and M. Porkolab, Phys. Rev. Lett. 30, 836 (1973).
11. N. A. Krall and A. W. Trivelpiece, "Principles of Plasma Physics," McGraw-Hill Book Company, New York, NY, pp. 409 (1973).
12. A. I. Anisimov, N. I. Vinogradov, and B. P. Poloskin, Sov. Phys. Tech. Phys. 18, 459 (1973); 20, 626 (1976); 20, 629 (1976).
13. R. S. Granetz, I. H. Hutchinson, and D. O. Overskei, Nucl. Fusion 19, 1587 (1979).
14. M. M. Murakami, J. D. Callen, and L. A. Berry, Nucl. Fusion 16, 347 (1976).
15. R. J. Hawryluk, K. Bol, and D. Johnson, Nucl. Fusion 19, 1519 (1979).
16. J. C. Hosea et al., in 8th International Conference on Plasma Physics and Controlled Nuclear Fusion Research (Brussels, Belgium 1980) IAEA-CN-38/D-5-1.
17. J. C. Hosea et al., Plasma Physics and Controlled Nuclear Fusion Research, Vol. II, p. 95 (IAEA, Vienna 1981).
18. N. Suzuki et al., Plasma Physics and Controlled Nuclear Fusion Research, Vol. II, p. 525 (IAEA, Vienna 1981).

19. J. C. Hosea et al., "FED Ion Cyclotron Task Force Report," December 1980.

20. C. C. Karney, D. Q. Hwang, and J. Hovey, "Modeling of Ion Cyclotron Heating with Baldur," Bull. Am. Phys. Soc. 26, 929 (1981).

21. D. E. Post et al., "Computational Studies of Impurity Effects, Impurity Control, and Neutral-Beam Injection in Large Tokamaks," in Plasma Physics and Controlled Nuclear Fusion Research 1978, Vol. 1, p. 471 (IAEA, Vienna 1979).

22. J. Jacquinot, "ICRF Heating Experiments in TFR, paper 10A-3, International Conference on Plasma Physics, Nagoya, Japan, April 1980.

23. C. E. Singer, F. Seidl, D. E. Post, P. H. Rutherford, "Ignition in a Tokamak Reactor with INTOR-Like Parameters," PPPL Report 1693, July 1980.

24. W. A. Houlberg, S. E. Attenberger, and L. L. Lao, Proc. of the International Topical Meeting on Advances in Mathematical Methods for the Solution of Nuclear Engineering Problems, Munich, April 27-29, 1981, p. 425.

25. W. A. Houlberg et al., ibid.

26. F. L. Hinton and R. D. Hazeltine, Rev. Modern Phys. 48, 239 (1976).

27. Reference 1, Chapter 1, to be published.

28. R. J. Goldston and H. H. Towner, Nucl. Fusion 20, 781 (1980).

29. A. Boozer, Phys. Fluids 23, 2283 (1980).

30. R. J. Goldston and H. H. Towner, "Effects of Toroidal Field Ripple on Superthermal Ions in Tokamak Plasmas," Princeton Plasma Physics Report PPPL-1637 (1980).

31. L. L. Lao, S. P. Hirshman, and R. M. Wieland, Phys. Fluids 24, 1431 (1981).

32. C. F. Barnett, J. A. Ray, E. Ricci, M. I. Wilker, E. W. McDaniel, E. W. Thomas, and H. B. Gilbody, "Atomic Data for Controlled Fusion Research," Oak Ridge National Laboratory Report ORNL-5206 (1977).

33. K. C. Shaing and J. D. Callen, "Boundary Layer Corrections to Neoclassical Ripple Transport in Tokamaks," University of Wisconsin Fusion Design Memo UWFDM-410 (1981).

34. K. C. Shaing and J. D. Callen, "Neoclassical Ripple Transport in Tokamaks," University of Wisconsin Fusion Design Memo UWFDM-416 (1981).

35. L. Bromberg and D. R. Cohn, Nucl. Fusion 21, 110 (1981).

36. J. G. Cordey and F. A. Haas, in Plasma Physics and Controlled Nuclear Fusion Research (Proc. 6th Int. Conf. Berchtesgaden, 1976), Vol. II, IAEA, Vienna, 423 (1977).

37. J. F. Clarke, Nucl. Fusion 20, 503 (1980).

38. J. A. Holmes, J. A. Rome, W. A. Houlberg, Y-K. M. Peng, S. J. Lynch, Nucl. Fusion 20, 59 (1981).

39. D. E. Post, R. J. Goldston, R. C. Grimm, R. J. Hawryluk, S. P. Hirshman, et al., in Plasma Physics and Controlled Nuclear Fusion Research (Proc. 7th Int. Conf. Innsbruck, 1978), Vol. I, IAEA, Vienna, 471 (1979).

40. Recent examples include: D. Steiner et al., Oak Ridge TNS Program, Summary of FY 1978 Activities, ORNL/TM-6720, Oak Ridge National Laboratory (1979); ETF Interim Design Description Document, ETF Design Center (July 1980); International Tokamak Reactor: Zero Phase, International Atomic Energy Agency (1980).

41. A. M. M. Todd et al., Nucl. Fusion 19, 743 (1979).

42. L. A. Charlton et al., Phys. Rev. Lett. 43, 1395 (1979).

43. J. W. Conner, R. J. Hastie, and J. B. Taylor, Proc. Roy. Soc. A365, 1 (1979).

44. R. L. Dewer et al., PPPL-1587, Princeton Plasma Physics Laboratory Report, 1979.

45. M. Azumi et al., 8th International Conference on Plasma Physics and Controlled Nuclear Fusion Research (Brussels, Belgium 1980), IAEA-CN-38/K-1-1.

46. R. W. Moore et al., 8th International Conference on Plasma Physics and Controlled Nuclear Fusion Research (Brussels, Belgium 1980), IAEA-CN-38/J-5.

47. M. M. Murakami et al., "Neutral Injection Experiments in the ISX-B Tokamak," paper IAEA-CN-38/M-1 in Plasma Physics and Controlled Nuclear Fusion Research, 1980, to be published.

48. D. Swain, M. Murakami, et al., "High Power Neutral Beam Injection Experiments on the ISX-B Tokamak," to be published.

49. V. M. Leonov et al., Plasma Physics and Controlled Nuclear Fusion Research 1980, Vol. I, p. 393 (IAEA, Vienna 1981).

50. N. Suzuki et al., Plasma Physics and Controlled Nuclear Fusion Research 1980, Vol. II, p. 525 (IAEA, Vienna 1981).

51. K. B. Axon et al., Plasma Physics and Controlled Nuclear Fusion Research 1980, Vol. I, p. 413 (IAEA, Vienna 1981).

52. D. J. Strickler et al., "Pressure Profile Effects on Ballooning Mode Stability," Annual Controlled Fusion Theory Conference, 2C21, Austin, Texas, 1981, to be published.

53. W. M. Tang et al., "Finite Gyroradius Stabilization of Ballooning Modes in a Toroidal Geometry," to be published.

54. K. T. Tsang and D. J. Sigmar, "Stabilization of Ballooning Modes by Energetic Particles in Tokamaks," to be published; W. A. Cooper and K. T. Tsang, "Diamagnetic Drift Stabilization of Ballooning Modes in General Tokamak Geometry," to be published.

55. R. J. Hastie and K. W. Hesketh, Nucl. Fusion 21, 651 (1981).

56. M. S. Chu et al., Phys. Rev. Lett. 41, 247 (1978).

57. J. K. Munro et al., Bull. Am. Phys. Soc. 25, 14 (1980).

58. R. W. Moore, "BLOON User's Manual," General Atomic Report GA-A15353 (1979).

59. W. A. Cooper, "Safety Factor Profile Optimization of High-n Ballooning Mode Stability of Tokamaks," ORNL/TM-7807, Oak Ridge National Laboratory Report, Oak Ridge, Tennessee.

60. M. M. Murakami, private communication.

61. J. F. Clarke and D. J. Sigmar, Phys. Rev. Lett. 38, 70 (1977); D. J. Sigmar and G. Vahala, Phys. Fluids 21, 2280 (1978); T. Mizoguchi, T. Kammash, and D. J. Sigmar, Phys. Fluids 21, 2086 (1978).

62. R. A. Dory and Y-K. M. Peng, Nucl. Fusion 17, 21(1977); J. L. Johnson et al., J. Comput. Phys. 32, 212 (1979); J. A. Holmes, Y-K. M. Peng, and S. J. Lynch, J. Comput. Phys. 36, 35 (1980).

63. Section II.1.1 in JET Design Report, EUR5516e, Euratom (1976).

64. V. S. Mukhovatov and V. D. Shafranov, Nucl. Fusion 11, 605 (1971).

65. D. L. Jassby, D. R. Cohn, and R. R. Parker, Nucl. Fusion 16, 1045 (1976).

66. V. M. Leonov, V. G. Merezhkin, et al., "Ohmic-heating and Neutral-beam Injection Studies on the T-11 Tokamak," paper IAEA-CN-38/N-2 in Plasma Physics and Controlled Nuclear Fusion Research 1980, to be published.

67. J. C. Wesley et al., "Shaping and Characteristics of Ohmically Heated Noncircular Plasmas in Doublet III," paper IAEA-CN-38/A-3 in Plasma Physics and Controlled Nuclear Fusion Research 1980, to be published.

68. W. A. Houlberg and S. E. Attenberger, "Plasma Engineering Analyses of Tokamak Reactor Operating Space," presented at the IEEE 9th Symp. on Eng. Problems of Fusion Research, October 26-29, 1981, Chicago, Illinois, to be published.

69. DIVA Group, Nucl. Fusion 20, 271 (1980).

70. H. C. Howe, J. Nucl. Mater. 93&94, 17 (1980).

71. H. C. Howe, "Physics Considerations for the FED Limiter," ORNL/TM-7803, Oak Ridge National Laboratory Report, Oak Ridge, Tennessee (1981).

72. M. H. Hughes and DETF Ashby, "JET Calculations Using the HERMES Code," JET Workshop on 1-D Transport Codes and Scrape-off Layers, Culham, England (1981).

73. J. Neuhauser, "Characteristics of a Radiating Layer Near the Boundary of a Contaminated Plasma," Report IPP 1/182, Max-Planck-Institute for Plasma Physics, Garching (1980).

74. J. Neuhauser, K. Borrass, K. Lackner, and R. Wunderlich, "Conditions for the Existence of a Stable Photosphere at the Edge of a Hot Plasma," JET Workshop on 1-D Transport Codes and Scrape-off Layers, Culham, England (1981).

75. J. Neuhauser, K. Lackner, and R. Wunderlich, "Self-limitation of Impurity Production by Radiation Cooling at the Edge of a Fusion Plasma," ZEPHYR Report 23, Garching (1981).

76. S. P. Hirshman and D. J. Sigmar, "Neoclassical Transport of Impurities in Tokamak Plasmas," ORNL/TM-7588, Oak Ridge National Laboratory, Oak Ridge, Tennessee (1981).

77. D. E. Post, R. V. Jensen, C. B. Tarter, W. H. Grasberger, and W. A. Lokke, "Steady-state Radiative Cooling Rates for Low-density High-temperature Plasmas," Atomic Data and Nuclear Data Tables, 20, 397 (1977).

78. D. Smith, "Analytic Expressions: Physics Sputtering," Proc. of the Workshop on Sputtering, CONF-790775, Argonne (1980).

79. S. A. Cohen, R. Budney, G. M. McCracken, and M. Ulrickson, "Mechanisms Responsible for Topographical Changes in PLT Stainless-Steel and Graphite Limiter," Nucl. Fusion 21, 233 (1981).

80. D. Heifetz et al., "Monte Carlo Modeling of Neutral Particle Transport in Divertor Experiments," submitted to J. Comput. Phys.

81. M. Petravic et al., "A Cool High Density Regime for Poloidal Divertors," PPPL-1824, Princeton University (June 1981).

82. S. Sengoku and H. Ohtsuka, 4th Int. Conf. on Plasma-Surface Interaction on Controlled Fusion Devices, Garmisch, April 1980.

83. D. Overskei, Phys. Rev. Lett. 46, 177 (1981).

84. R. Jacobsen, "Preliminary Particle Scoop Limiter Measurements in PDX," submitted to Nuclear Fusion.

85. R. Taylor and S. Talmadge, private communication.

86. M. Mahdavi et al., "Particle Exhaust from Discharges with an Expanded Boundary Divertor," GA-A16334, General Atomic Company (1981).

87. L. M. Hively et al., "Constrained Ripple Optimization of Tokamak Bundle Divertors," Nuclear Technology/Fusion 2 (1982).

88. P. H. Sager, General Atomic Company, private communication, 1980.

89. D. Steiner et al., Oak Ridge TNS Program, Summary of FY 1978 Activities, ORNL/TM-6720, Oak Ridge National Laboratory (July 1979).

90. Y-K. M. Peng et al., in Proc. 7th Symp. on Eng. Prob. of Fusion Research, p. 186 (1977).

91. Fusion Energy Division Annual Progress Report Period Ending December 31, 1977, ORNL-5405, Oak Ridge National Laboratory (August 1978), p. 87.

92. T. G. Brown, private communication.

93. International Tokamak Reactor, Phase I, to be published by the International Atomic Energy Agency, Vienna.

94. J. Wesley, B. Carreras, H. Ikezi, B. Lipschultz, S. Luke, and K. McGuire, "Report of the Disruption Control Task Force," to be published.

95. J. T. Hogan, T. Brown, K. McGuire, M. Nagami, D. Overskei, A. Todd, and J. Wesley, "Report of the Physics Task Team on Low-q/Shaping Issues," to be published.

96. R. L. Miller, J. A. Holmes, G. M. Fuller, R. Hicks, Y-K. M. Peng, P. H. Sager, and S. Yoshikawa, "Plasma Disruption Characteristics and Protection Requirements in ETF/INTOR," Report prepared for ETF Design Center ETF-R-80-PS-025, Oak Ridge National Laboratory, Oak Ridge, Tennessee (July 1980).

97. R. B. White, D. A. Monticello, and M. N. Rosenbluth, Phys. Rev. Lett. 39, 1678 (1977).

98. B. V. Waddell, B. Carreras, H. R. Hicks, J. A. Holmes, and D. K. Lee, Phys. Rev. Lett. 41, 1386 (1978).

99. A. Sykes and J. A. Wesson, Phys. Rev. Lett. 44, 1215 (1980).

100. K. Toi, S. Itoh, K. Kadota, K. Kawahata, N. Noda, K. Sakwrai, K. Sato, S. Tanahashi, and S. Yasue, Nucl. Fusion 19, 1643 (1979).

101. B. Carreras, H. R. Hicks, J. A. Holmes, and B. V. Waddell, Phys. Fluids 23, 1811 (1980).

102. K. M. McGuire and D. C. Robinson, Phys. Rev. Lett. 44, 1666 (1980).

103. T. Taylor, "Limiter Heat Flux Measurement During Disruptions," presented by J. Wesley at the FED Physics Workshop at Princeton Plasma Physics Laboratory, Princeton, June 29, 1981.

104. D. Overskei, "Phenomenology of Disruptions in Alcator," in Ref. 3, p. 29.

105. N. Sauthoff, "Disruptions in PLT," in Ref. 3, p. 31.

106. R. D. Hazeltine, P. H. Diamond, B. A. Carreras, and H. R. Hicks, "Renormalized Tearing Mode Turbulence and Major Disruption," paper 3A2 presented at the Annual Controlled Fusion Theory Conference, Austin, Texas, April 1981.

107. J. D. Callen, B. V. Waddell, B. Carreras, M. Azumi, P. J. Catto, H. R. Hicks, J. A. Holmes, D. K. Lee, S. J. Lynch, J. Smith, M. Soler, and K. T. Tsang, Plasma Physics and Controlled Nuclear Fusion Research, Vol. I, p. 145 (1979).

108. J. R. Haines, FEDC, private communication, 1981.

3. SYSTEMS ENGINEERING

T. E. Shannon*

G. E. Smith[†] W. T. Reiersen[†]
R. J. Barrett[‡] P. T. Spampinato[†]
T. G. Brown[†] S. L. Thomson[§]
S. K. Ghose[§] K. F. Wu*
R. L. Reid*

The systems engineering effort ensures that the FED design satisfies overall engineering and physics guidelines and constraints, accommodates assembly and maintenance requirements, and provides a balanced integration of all subsystem elements. In addition, the systems engineering effort is responsible for developing FED project costs and a construction schedule for the device and its supporting facilities (see Chapter 9). Inherent in these tasks is the need for tradeoff studies and investigations aimed at optimizing the configuration and associated device cost. This chapter summarizes the following systems engineering topics:

- Configuration Design and Integration
- Assembly and Maintenance
- Availability
- System Trade Studies

The section on configuration design and integration begins with a brief summary of the device design requirements, followed by a description of the FED configuration and an outline of the significant configuration-related options in the areas of vacuum topology, torus sector removal, TF coil configuration, and impurity/particle control. The next section describes the impact of machine assembly/disassembly/maintenance requirements on configuration design; summarizes component replacement requirements in terms of physical characteristics (weights and dimensions) and

*Fusion Engineering Design Center/Oak Ridge National Laboratory.
[†]Fusion Engineering Design Center/Grumman Aerospace Corporation.
[‡]Fusion Engineering Design Center/Burns and Roe, Inc.
[§]Fusion Engineering Design Center/Bechtel Group, Inc.

estimated replacement time; and illustrates removal/replacement techniques for major components.

The section on availability describes FED availability requirements resulting from the proposed plan of operations. Results of a preliminary assessment of FED availability are presented based on our present understanding of the reliability, maintainability, and supportability characteristics of the design.

The final section summarizes the system trade studies which provided the basis for the FED concept selection. The studies include an evaluation of mission and device alternatives, toroidal and poloidal field coil configuration, an evaluation of copper vs superconducting TF coils, and a number of parametric studies to optimize the overall design and performance of the reactor. A complete discussion of all supporting trade studies is reported in ORNL/TM-7777.

A philosophy of "design for maintenance" has had a significant influence on the evolution of the FED concept. The resulting design features simplicity in assembly methods with modular design of components and a rather large TF coil system to provide access for maintenance of components in areas of high activation. Maintenance is the most critical uncertainty in the systems engineering area because of the strong cost sensitivity of tokamak size and shielding requirements. Future activities should be directed toward more detailed evaluation of the cost vs benefit and risk of maintenance design drivers.

3.1 CONFIGURATION DESIGN AND INTEGRATION

3.1.1 Design Requirements

Three major considerations have influenced the evolution of the device configuration: (1) the required operating parameters, (2) the maintenance criteria, and (3) the capital and operating costs. It was found that physics considerations impact the device configuration primarily in the particle and impurity control concept and in the PF system concept. On the other hand, the plasma ripple requirement was found to be less stringent in sizing the TF coils than the torus maintenance requirements.

Activation of components, the presence of tritium, and the general complexity of the electromagnetic features of the tokamak device significantly influence the maintenance and repair operations. Accordingly, maintenance considerations were established at the outset of the FED design study as a fundamental consideration in the development of the design configuration. Implementation of the FED maintenance approach (see Sect. 3.2) has led to a modularized design concept, and designing to achieve the required access has had a significant impact on the design of the tokamak systems.

Cost considerations have played a major role in forming component design and configuration decisions. The most notable areas include selecting a hybrid PF system configuration over an all-exterior PF system configuration and minimizing the overall device size while meeting the physics and engineering objectives.

3.1.2 FED Baseline Configuration

Figures 3-1 and 3-2 present the FED configuration in an elevation and plan view, and Table 3-1 summarizes its key features. The major systems and/or components which must be attached to the torus have been allocated dedicated bays (i.e., spaces between TF coils). This provides a straightforward interface between the tokamak device and the auxiliary systems. The dedicated sector allocations are shown in Fig. 3-3.

The radial build dimensions of the FED design are summarized in Fig. 3-4. The dimensions include space allocation for all components as well as for the required gaps for assembly tolerance.

The following sections summarize the main features of the FED design.

Magnetic system configuration

Cost and performance considerations influenced the selection of a hybrid system as the baseline PF coil arrangement. The PF system consists of two interior, water-cooled, copper equilibrium field (EF) coils; four interior, water-cooled, copper control coils; two exterior superconducting EF coils; and a superconducting ohmic heating (OH) solenoid.

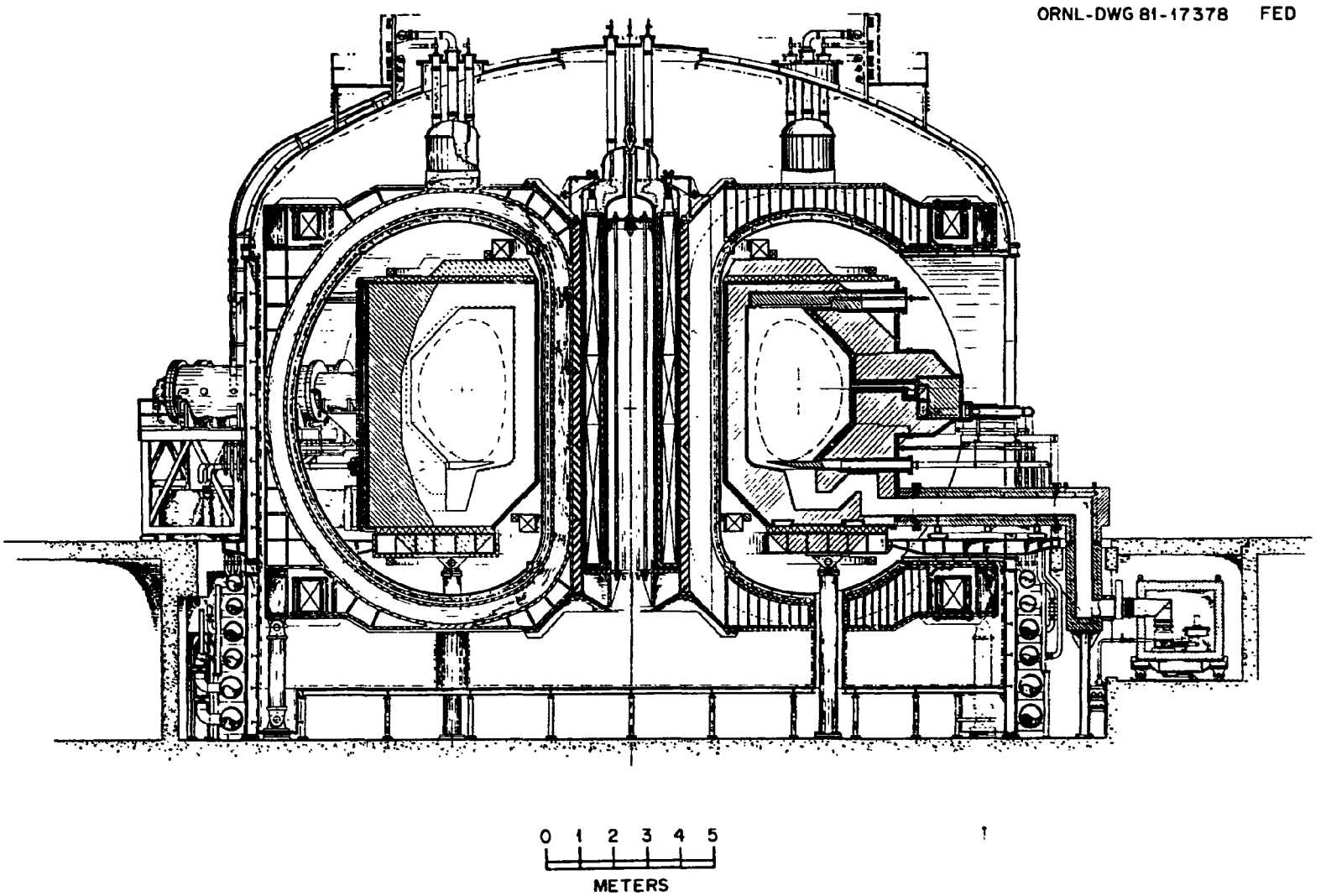

Fig. 3-1. FED elevation view.

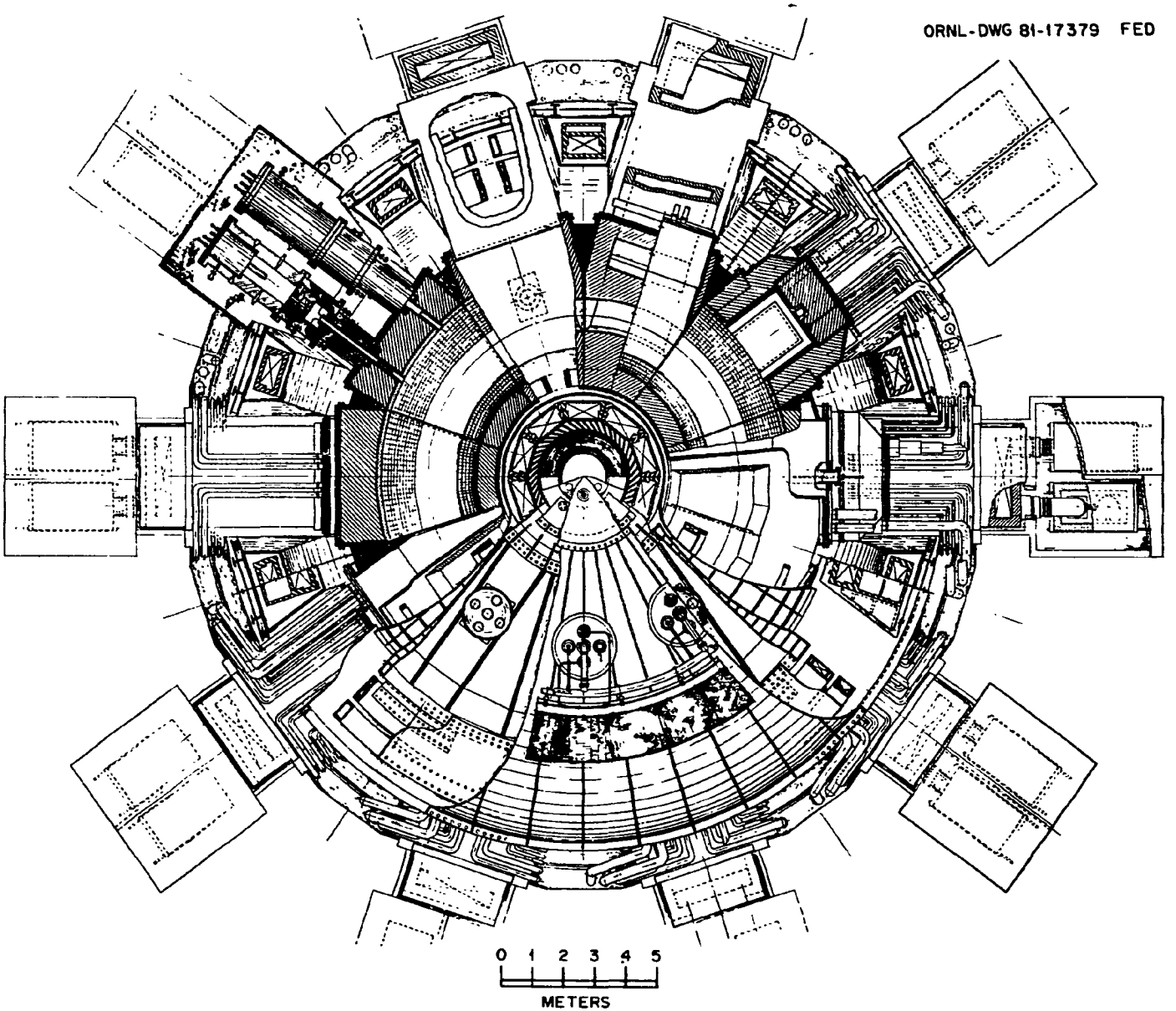

Fig. 3-2. FED plan view.

Table 3-1. Key features of FED configuration

Magnetics

- Poloidal field system consisting of both superconducting and normal copper coils
- All superconducting coils (PF and TF) contained in a common magnetic system vacuum vessel (cryostat)
- Gravity support trusses located beneath the outer leg of each TF coil support the coil dead weight
- A TF "window" maintained between adjacent TF coils to provide access to the torus
- TF coil centering force reacted by the bucking cylinder and by coil wedging
- TF coil overturning forces supported by contoured gusset plates added in the TF "window" area plus fitting attachments located at the top and bottom of the bucking cylinder

Torus

- Torus divided into ten sector modules each of which can be extracted through the TF "window" by straight-line motion
- Ten pump limiter modules located horizontally at the bottom of the plasma
- Torus rests on a circular platform supported by ten columns
- Ten rectangular vacuum ducts, each located below a pump limiter module, extend through the TF "window"

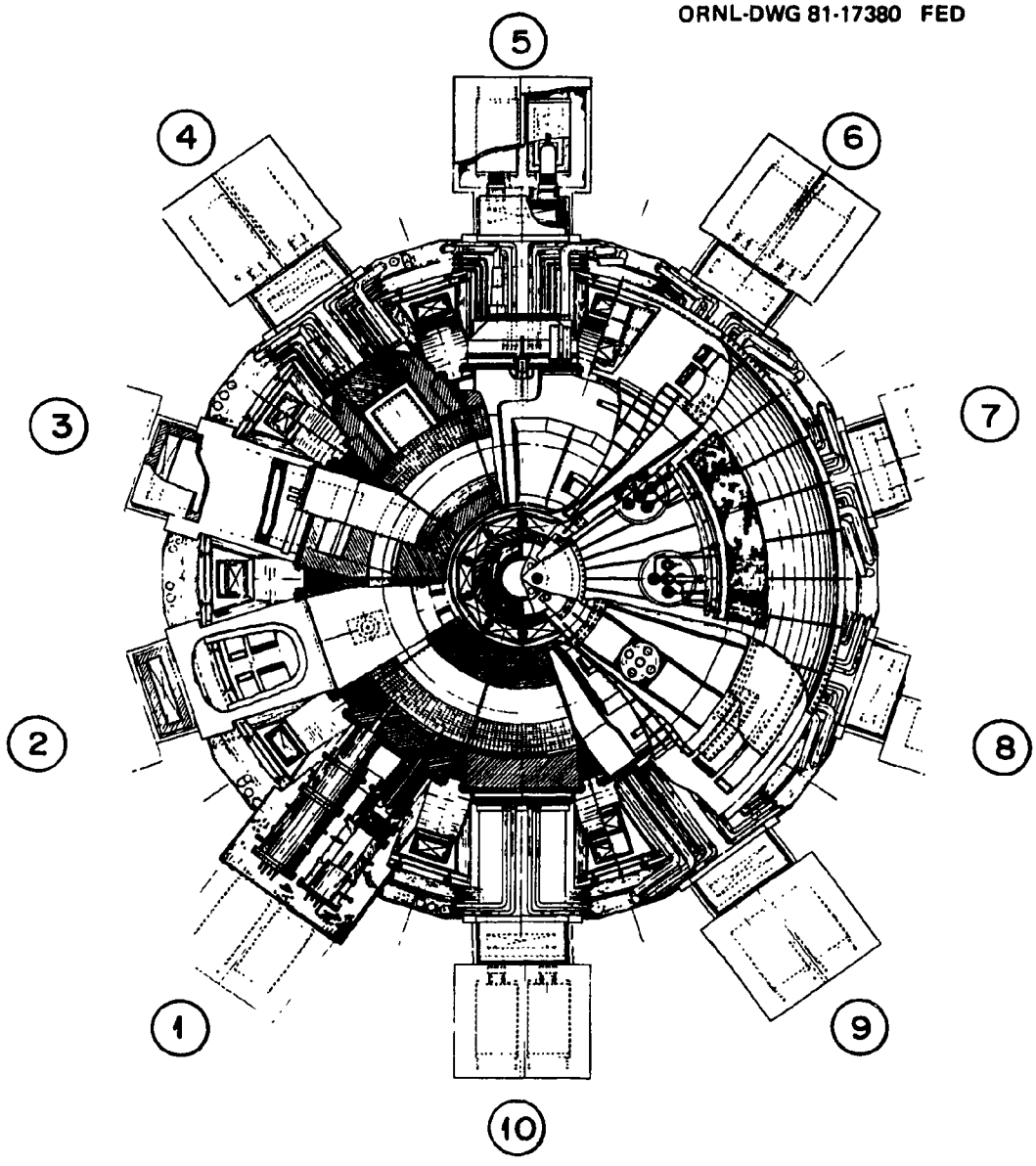

COMPONENT	SECTOR POSITION
HEATING	3, 4, 5, 6
FUELING	1
TESTING	2, 8, 10
DIAGNOSTICS, INSTRUMENTATION AND CONTROL	7, 8, 9

Fig. 3-3. Dedicated torus sectors.

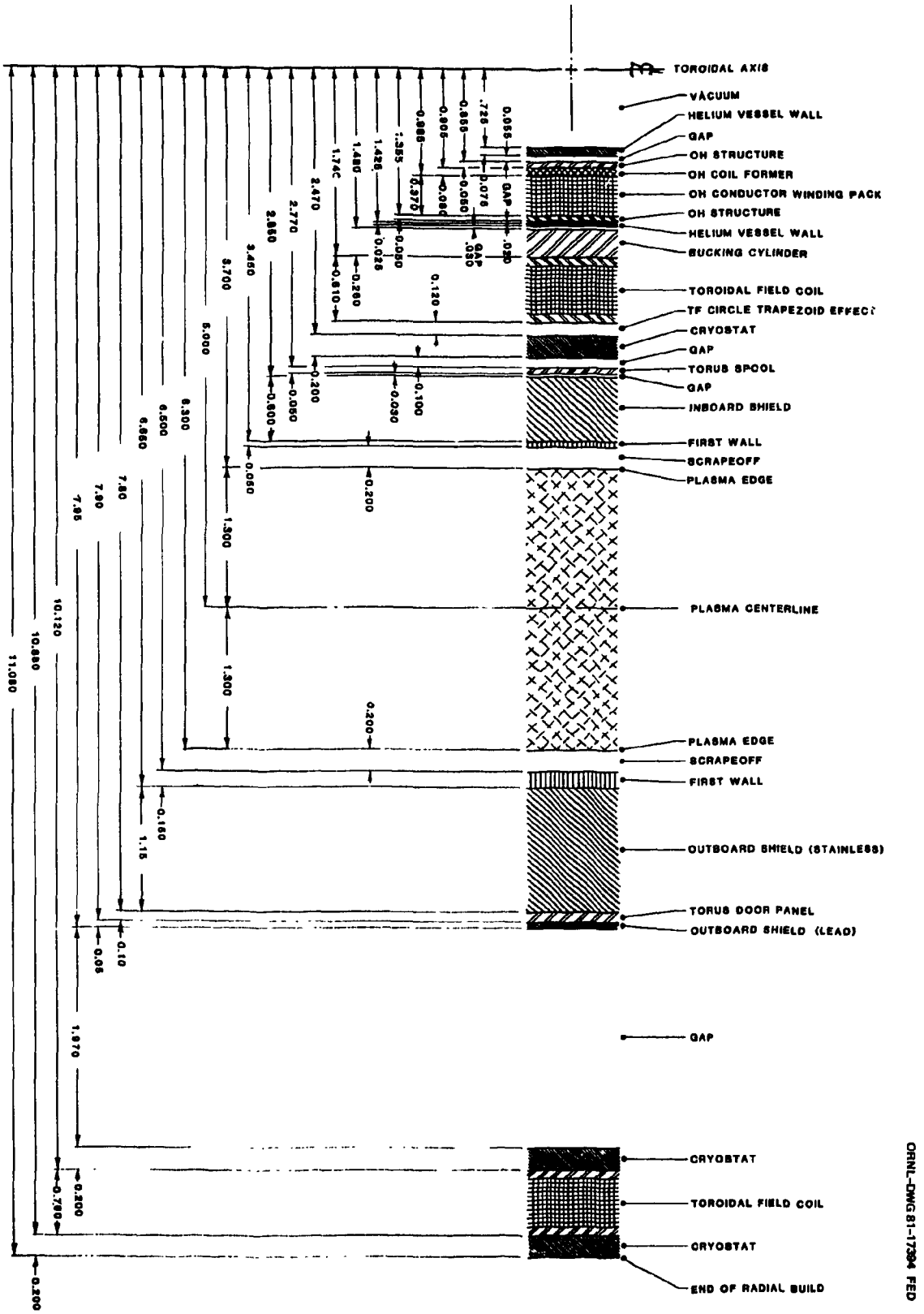

Fig. 3-4. FED device radial build.

The exterior poloidal field (PF) coils along with the TF coils are contained inside the magnetic system vacuum vessel (cryostat). This simplifies their structural support and provides thermal isolation of the warm and cold structure.

Gravity support trusses are located beneath the outer leg of each TF coil. This approach was adopted rather than that of supporting the dead weight of the magnetic components near the machine center. The approach selected provides clear access to the PF coil located under the tokamak device and also provides a broad foundation for support against seismic loads.

The elevation view shown in Fig. 3-1 illustrates that the structural design of the TF coil and intercoil structure uses a stiffened thin plate construction to support the local magnetic pressure loads. Shear ties to the bucking cylinder and contoured gusset plates are added in the TF "window" area to support the out-of-plane overturning moments. Centering forces are reacted by the bucking cylinder and coil wedging. An outer support ring provides a foundation for the gusset plates and ties them to the intercoil structure. A flanged interface between the TF coil and its intercoil structure permits a bolted connection and provides space for a fiberglass sheet to electrically isolate the TF coil and intercoil structure. A structural weld is located at mid-span between TF coils to simplify final installation (see Fig. 3-5).

Torus configuration

Figure 3-6 illustrates the torus configuration adopted for FED. The torus assembly consists of a spool structure (top, bottom, and inboard panels, plus a radial frame) and a seal frame which forms the sealing surface interface to a shield sector module. The shield contains the first wall, armor, and pump limiter, all of which must operate in a high neutron flux environment and which are subject to potential plasma disruptions. To provide for ready access to these components, the shield is divided into ten sector modules, each of which can be extracted by straight-line motion. Each module employs an integral door seal and rollers to simplify the maintenance operation. The potential for damage from thermal

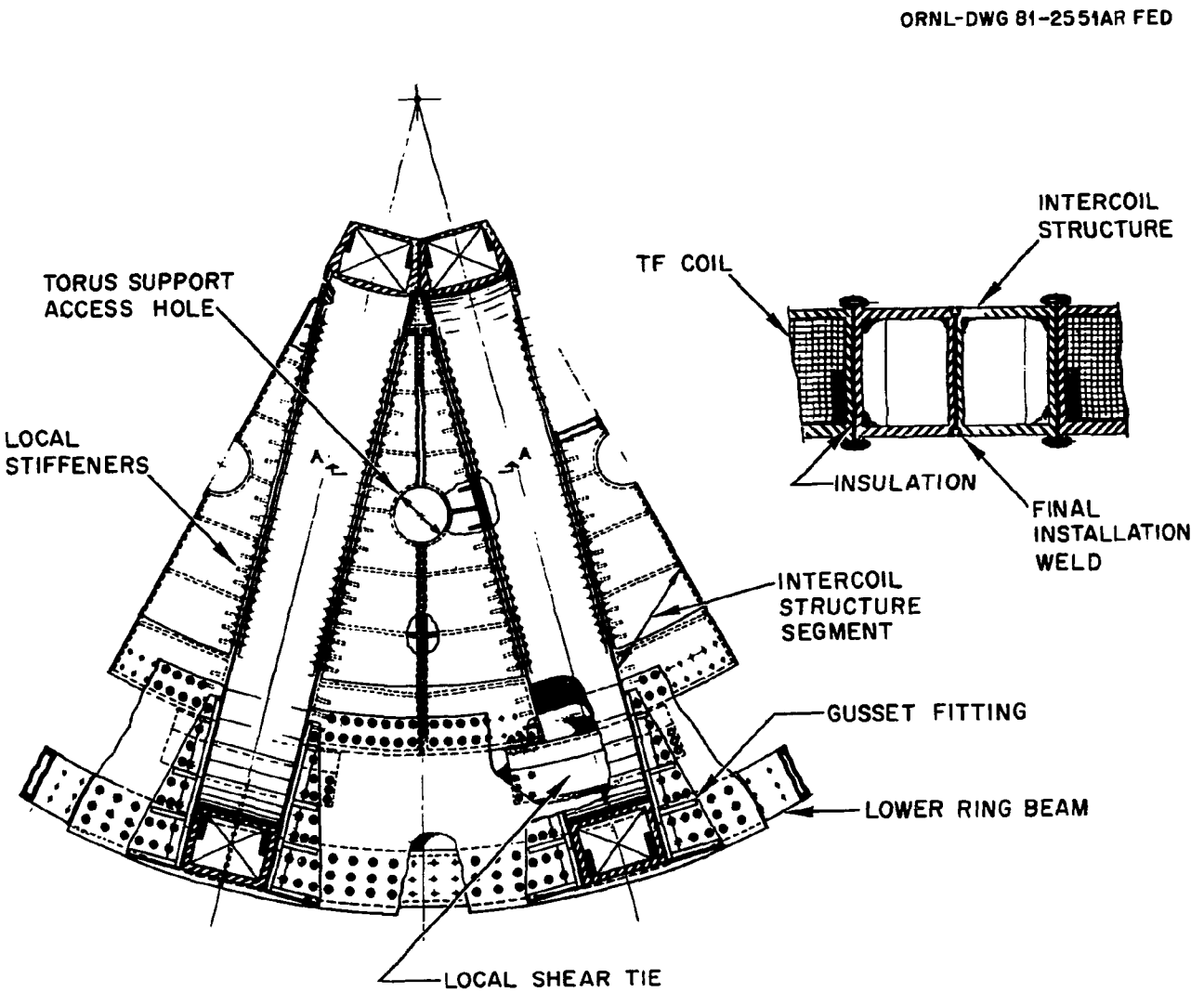

Fig. 3-5. Plan view of TF intercoil structure.

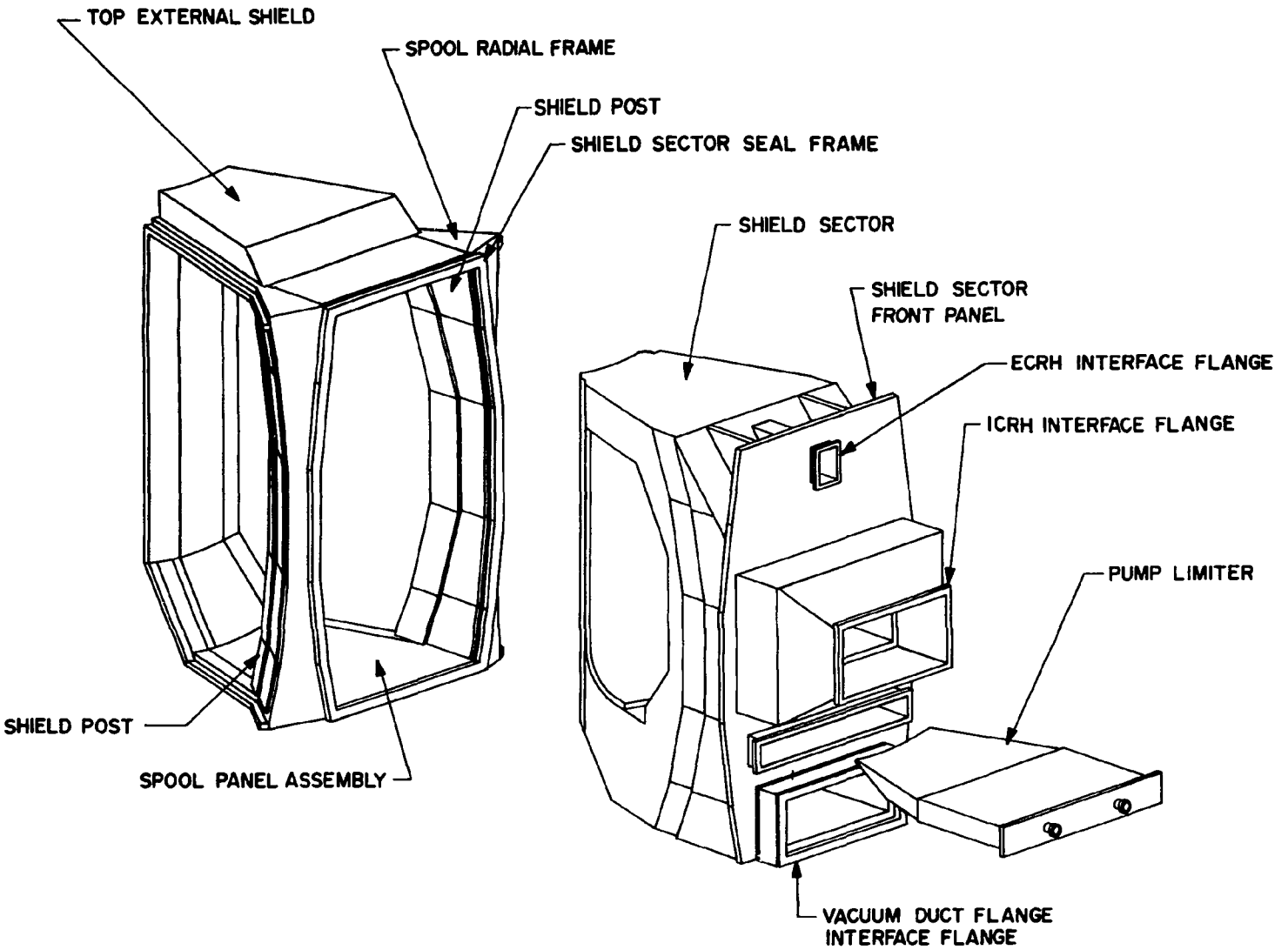

Fig. 3-6. FED torus assembly sequence.

and particle loads on the pump limiter is high and hence provisions are included in the design for frequent removal and replacement of the limiter blade. The limiter is divided into ten modules, the same number as the torus, to allow for removal of this component without removing the torus module itself. The support of the torus is provided by a platform supported by ten columns located under the torus. Another support platform providing lateral restraint runs through the TF "window" and is attached to the reactor building floor.

Peripheral torus systems

The width of each pump limiter module takes up nearly the full width of the shield sector module in which it is housed. The vacuum pump duct, located under each limiter module, runs horizontally through the TF "window" and connects with a vertical duct which penetrates the reactor building floor. A pair of vacuum pump modules, each consisting of a turbomolecular pump, scroll pump, and valves, is connected to the vacuum duct with an isolation valve. The peripheral equipment attached to the face of the torus is supported off the vacuum duct or by cantilever support off the shield sector module. Figure 3-1 illustrates the cantilever support of the ICRH launcher, service lines supported off the vacuum duct, and the bridge support of the pellet injector.

3.1.3 Configuration Options

The following options were considered:

Vacuum topology

High vacuum requirements for the plasma chamber are a source of design and operations difficulties. Design requirements for leak tightness and the various practices to minimize outgassing are well understood; however, the complexity of the tokamak configuration adds another dimension to the already difficult problem of locating the vacuum boundary. Maintenance considerations, especially in a radioactive environment,

require a very careful examination of options and overall systems impact. The vacuum requirement for the superconducting (SC) magnetic system is less stringent than for the torus; however, because of the configuration complexity, the magnetic system vacuum boundary was considered concurrently with the torus vacuum boundary. Figure 3-7 shows the three options considered. A vacuum seal at the torus was found to be required to isolate the high vacuum region (10^{-7} torr) and reduce the number of components and/or feed lines that would be subjected to outgassing and bakeout conditions. A separate vacuum boundary for the cryostat was selected for FED [option (a)].

Separate vacuum boundaries for the cryostat and plasma chamber yield the following advantages:

- Allows testing the superconducting magnet system before the torus is installed
- Allows inspection of the vacuum boundary of the superconducting system
- Allows repair of the spool without warming up the superconducting magnets
- Provides added reliability of superconducting magnet system
- Improves access for diagnostics

The principal disadvantages of the separate vacuum boundary are the need to provide additional void space (5-10 cm) on the inboard side for assembly tolerance and the higher impedance to startup associated with the separate cryostat.

Removable torus sector approaches

Two torus sector arrangements were considered: one option where the number of removable torus sectors equals the number of TF coils, and a second approach in which the number of removable torus sectors equals a multiple of the number of TF coils.

The torus sector approach in which the number of torus sectors equals the number of TF coils was chosen as the baseline concept. It offers the simplest maintenance concept since the removal of each torus sector from the

ORNL-DWG 81-17381 FED

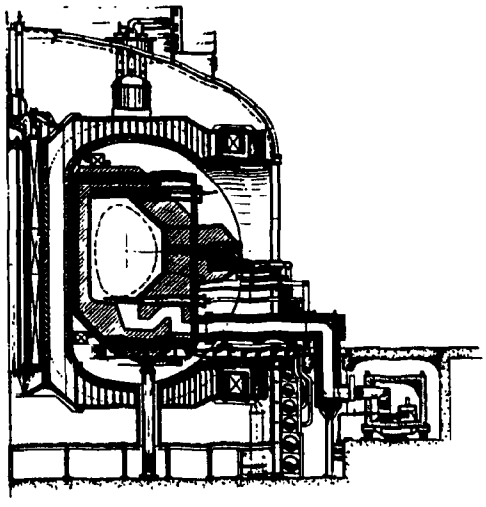

(a) PLASMA VACUUM BOUNDARY AT TORUS— SEPARATE VACUUM BOUNDARY FOR CRYOSTAT

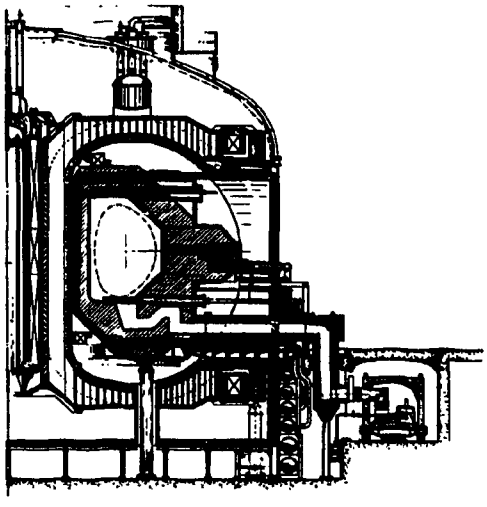

(b) PLASMA VACUUM BOUNDARY EXTENDED OUTBOARD OF TF COILS

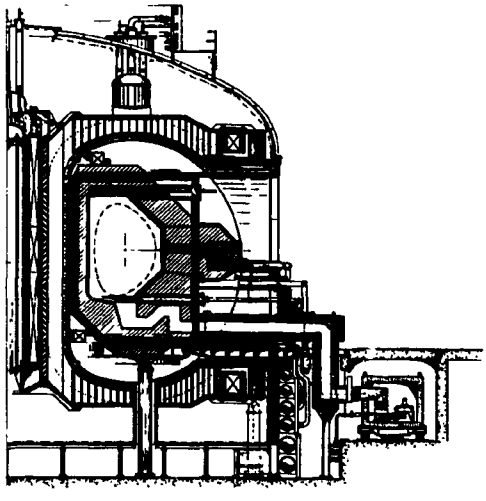

(c) PLASMA VACUUM BOUNDARY AT TORUS – CRYOSTAT VACUUM BOUNDARY COMBINED WITH TORUS

Fig. 3-7. Vacuum topology options.

device is accomplished using a single, straight line, radially outward motion between TF coils. Vertical posts inside the bore of each TF coil remain in place to form a seal and load bearing surface between each torus sector and the spool. From a component standpoint, this approach allows a single pump limiter module to be located in each torus sector, which simplifies the coolant feed line design and also simplifies module extraction.

TF coil configuration

The number and size of the TF coils in a tokamak play an important role in determining the device size, the access space between TF coils, and the total reactor cost. By using fewer/larger TF coils and by placing a restriction on the vertical location of the outboard PF coils, an access space (window) can be created between the outer legs of the TF coils to provide relatively easy access to all portions of the torus. Providing a "window" for torus access was considered essential in establishing a credible tokamak configuration which can be maintained. This approach was therefore adopted in the FED configuration.

Table 3-2 shows the impact of varying the number of TF coils from eight to ten based on a trapezoidal-shaped TF coil cross section whose outer leg is set by (1) a maximum plasma edge ripple limit of 2%, or (2) an access requirement which permits removal of a torus sector sized such that the total number of torus sectors is equal to the number of TF coils. Where the TF coils are sized for ripple (letting access vary), only the eight coil configuration satisfies the access requirement. When the coils are sized for access (letting ripple vary), the relative cost of the total device shows no significant variation while both ripple and midplane access decrease as the number of coils increases. To satisfy the FED maintenance criteria of straight-line radial motion of a torus sector through a TF "window," the ten coil, access-limited configuration was selected as the baseline design. The nine coil, access-limited arrangement was not chosen because its cost is the same as that of the ten coil system, and the associated ripple is higher than for the ten coil system.

Table 3-2. Effect of number of TF coils on configuration and cost

	Ripple Limited			Access Limited		
Number of TF coils	8	9	10	8	9	10
Ripple, %	2	2	2	2	1.4	0.8
Midplane access, m	6.8	5.5	4.6	6.8	5.8	5.2
Adequate access	Yes	No	No	Yes	Yes	Yes
Burn, sec	170	230	260	170	250	300
B_m, tesla	8.3	8.1	8.0	8.3	8.1	8.0
Relative cost	1.007	0.924	0.874	1.007	0.996	1.000

It is important that the structural load path which supports the out-of-plane magnetic loads acting on the TF coil is compatible with the torus design and maintenance approach. Ideally, the most effective approach is to form a shear tie between the outer TF coil legs by either truss members or shear panels. However, this approach results in additional torus access restrictions which require dismantling the intercoil structure for torus sector removal.

To retain a TF access "window" with sufficient clear width to accommodate removal of a torus sector requires a structural design which incorporates either a thick wall TF coil design or a built-up structure arrangement. The thick wall TF coil design approach results in a high level of eddy current heating associated with PF coil field changes. It also presents problems in fabrication and in void detection. The structural arrangement selected incorporates a built-up structure using relatively thin plates with stiffeners.

Pump limiter configuration

A mechanical pump limiter was adopted for particle control. Two locations for the pump limiter were considered: at the bottom of the shield sector module and on the lower 45° surface of the outboard wall. The bottom location was selected for the baseline design because of maintenance considerations. This location allows replacement of the limiter without removing the vacuum duct. Because the limiter is expected to experience substantial erosion from plasma interactions, it is important that it be located for ease of maintenance and repair. Location at the bottom of the plasma chamber achieves this goal.

3.1.4 Configuration Options for Future Considerations

Several configuration options were identified during the latter part of the FY 81 FED design effort. However, insufficient time was available to evaluate these concepts. None of them have been incorporated in the FED design, but each may prove attractive after additional investigation. Table 3-3 summarizes the design options that merit future evaluation. The following discussion describes the options in more detail.

Table 3-3. Configuration options investigated

Option	Potential Benefit
• Nonconstant tension TF coil	Reduces size of TF coil at no penalty to the TF structure
• Torus vacuum pump duct rerouted to pass through the TF intercoil structure	Reduces the duct length, improves access to the shield sector, and offers better access for the poloidal divertor option
• Inboard lower exterior coils removable via lower maintenance tunnel	Provides an improved maintenance scheme for the inboard lower EF coils
• Internal copper coils with maintenance access through the bottom of the torus	Improves the maintenance of interior coils, however requires the jointed copper coil to operate in a vacuum environment
• Saddle coils located at the bottom of the torus	Improves the maintenance of internal coils (independent saddle coils are not affected by the vacuum environment, however, their magnetic impact on the plasma must be defined)

Figure 3-8 illustrates the configuration options considered. In the current FED reference design (Fig. 3-1), the vacuum pump duct runs through the TF window and joins the vacuum pumps outside the superconducting system cryostat. There is no structural interference with the TF coils in this arrangement; however, it requires a longer duct than the option shown in Fig. 3-8. Running the vacuum duct down through the TF coil intercoil structure simplifies the maintenance of an optimal poloidal divertor configuration that serves as a backup to the pump limiter divertor approach; allows a pump limiter/poloidal divertor module to be incorporated in the FED design which enables either impurity control option to be investigated; plus enables the lower EF coil to be relocated outboard of the TF coil support to improve its maintenance. Figure 3-9 illustrates the configuration employing a poloidal divertor. This duct arrangement simplifies the maintenance of the divertor module, requiring only the removal of an end plate vacuum door to gain access to the divertor module plus substantially shortens the duct length. The main area for further investigation lies in determining the structural impact of placing a hole in the TF coil intercoil structure. A possible redesign of the TF intercoil structure to accommodate the vacuum pump duct is shown in Fig. 3-10. An isometric view of the pump limiter/poloidal divertor configuration is shown in Fig. 3-11. The space that allows the vacuum duct to pass through the TF intercoil structure was provided by relocating the lower outside PF coil further outboard of the TF structure. This modification reduces the local magnetic field and forces on the TF coil with little change in the EF current. This PF coil location was found to be in a more attractive position from the standpoint of maintenance compared to its present location shown in the reference drawing.

Maintenance of the inside copper EF coils is a difficult configurational issue. Limited space for maintenance of the lower coil is the major concern. Three configuration options have been identified that may ease this problem. One approach is to locate all PF coils exterior to the TF coils. Figure 3-8 shows the relative position of these coils. A lower coil maintenance tunnel is also shown that provides an access and maintenance scheme for the lower EF coil. The torus support was modified

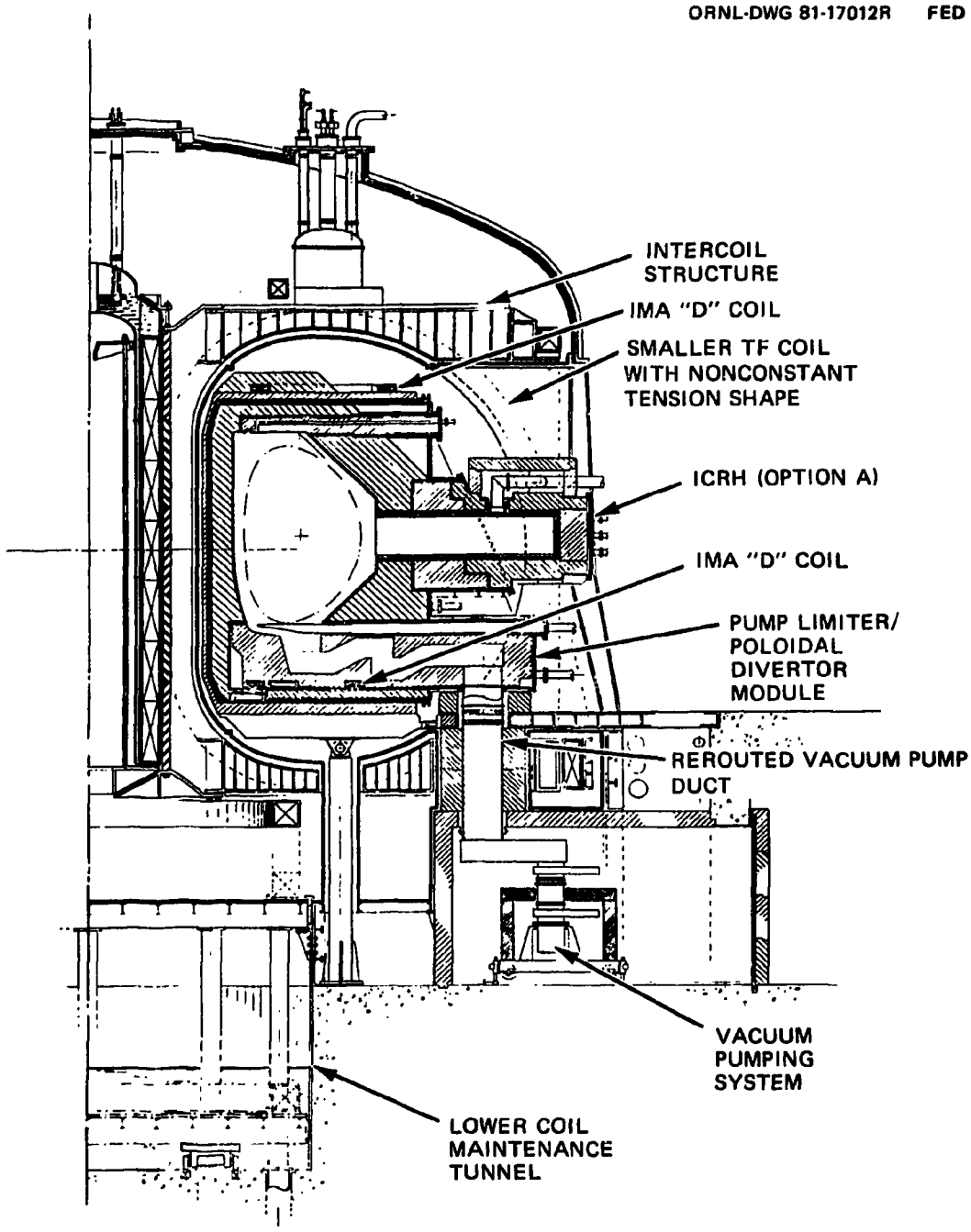

Fig. 3-8. FED configuration options.

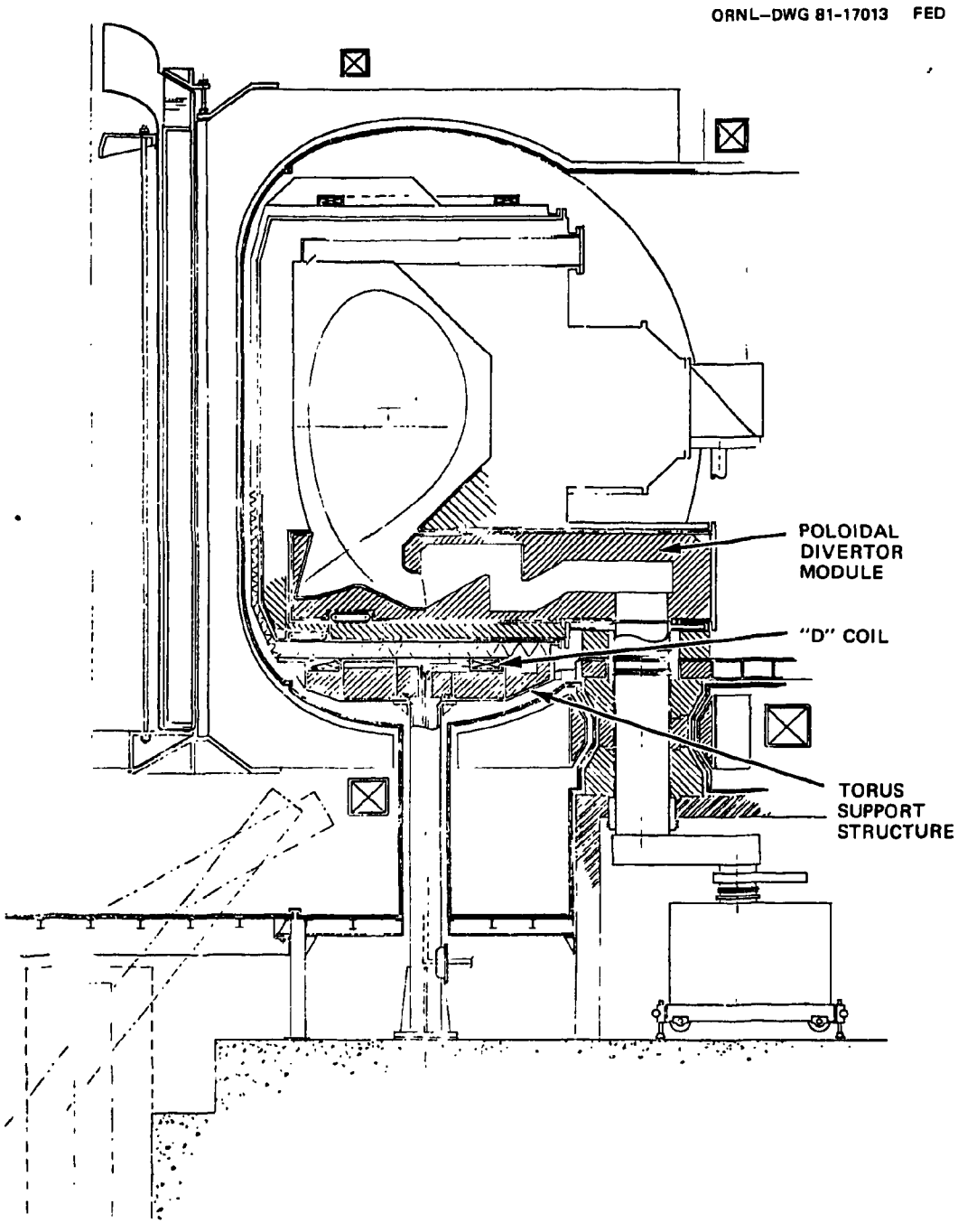

Fig. 3-9. FED configuration option to incorporate poloidal divertor.

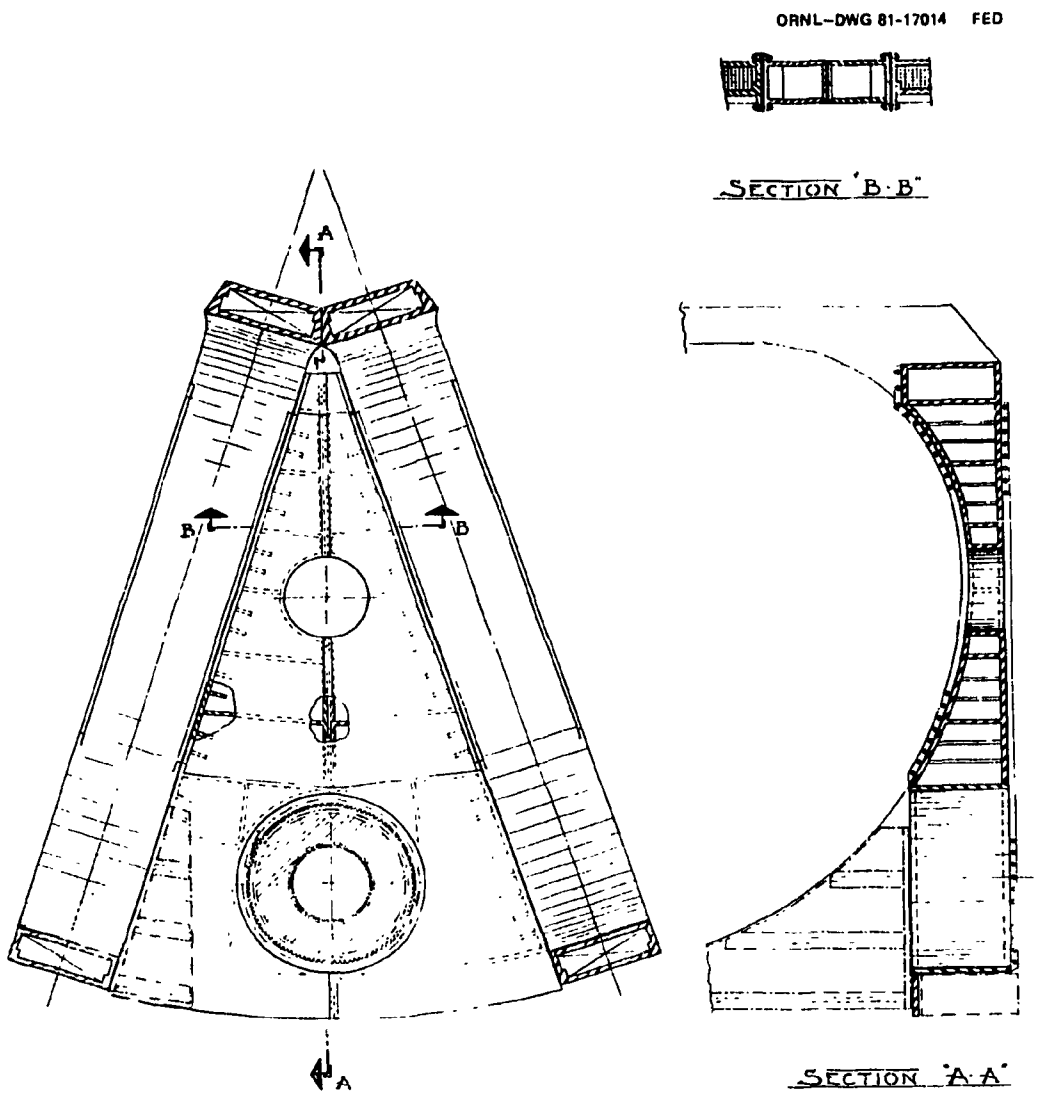

Fig. 3-10. FED configuration option which provides access space for vacuum pump duct through TF intercoil structure.

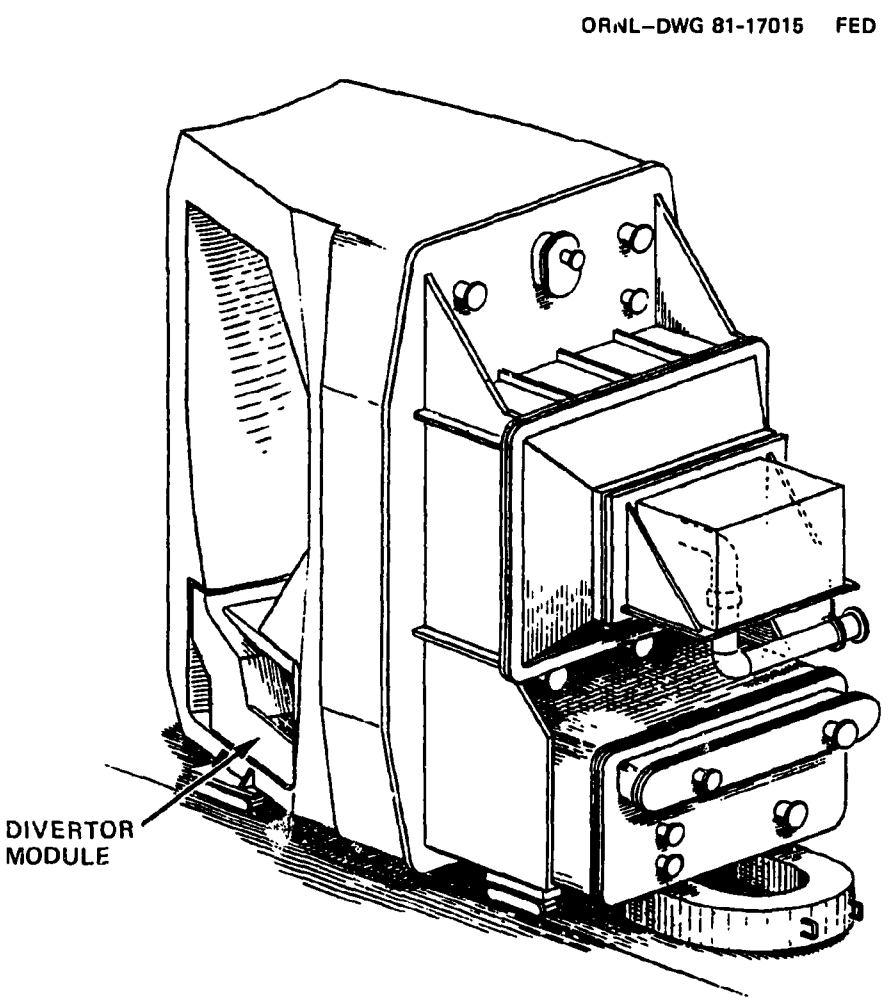

Fig. 3-11. FED isometric sketch of removable shield module option that accommodates either a pump limiter or a poloidal divertor.

to allow the TF coil vertical bore dimension to be reduced by approximately one meter over the current FED baseline design. The main disadvantage is that the current in a lower exterior superconducting coil would be higher than in an interior copper coil (10-15 MA vs 5 MA); however, it has the advantage that it can be maintained more easily.

Locating the lower inside copper coil inside the torus spool structure was also considered. Figure 3-12 shows an option with the EF coil located inside the torus spool structure with the coolant and electrical connections running through the torus gravity support columns. Coil maintenance for this option is provided by removing a shield module to gain access to the coil located beneath it. Figures 3-13 and 3-14 show a configuration option with the floor of the torus shield module removed to provide direct access to an internal EF coil, inside the spool structure, by removing only the divertor module in lieu of the full shield module.

A final option that was considered involved locating saddle (or "D" shaped) coils in either the bottom of the pump limiter module or in the torus support structure. Figures 3-15 and 3-16 show a plan view of the coils in the divertor module and in the torus support structure. This concept provides a modular design of the EF coil system, improving maintenance; however, there was insufficient time to determine the magnet implications of this coil configuration on the plasma.

3.2 ASSEMBLY AND MAINTENANCE

In the overall development of the FED configuration, the initial device assembly was considered as well as the subsequent disassembly required for component maintenance. A fully integrated configuration requires that initial assembly and subsequent disassembly be accommodated. Both operations must be investigated because much of the initial device assembly is different from the operations needed for component replacements. For example, the initial installation of the lower superconducting EF coil is independent of the torus and TF coil installations, but its subsequent replacement is very much affected by these components. In order to describe the considerations and design features for each operation,

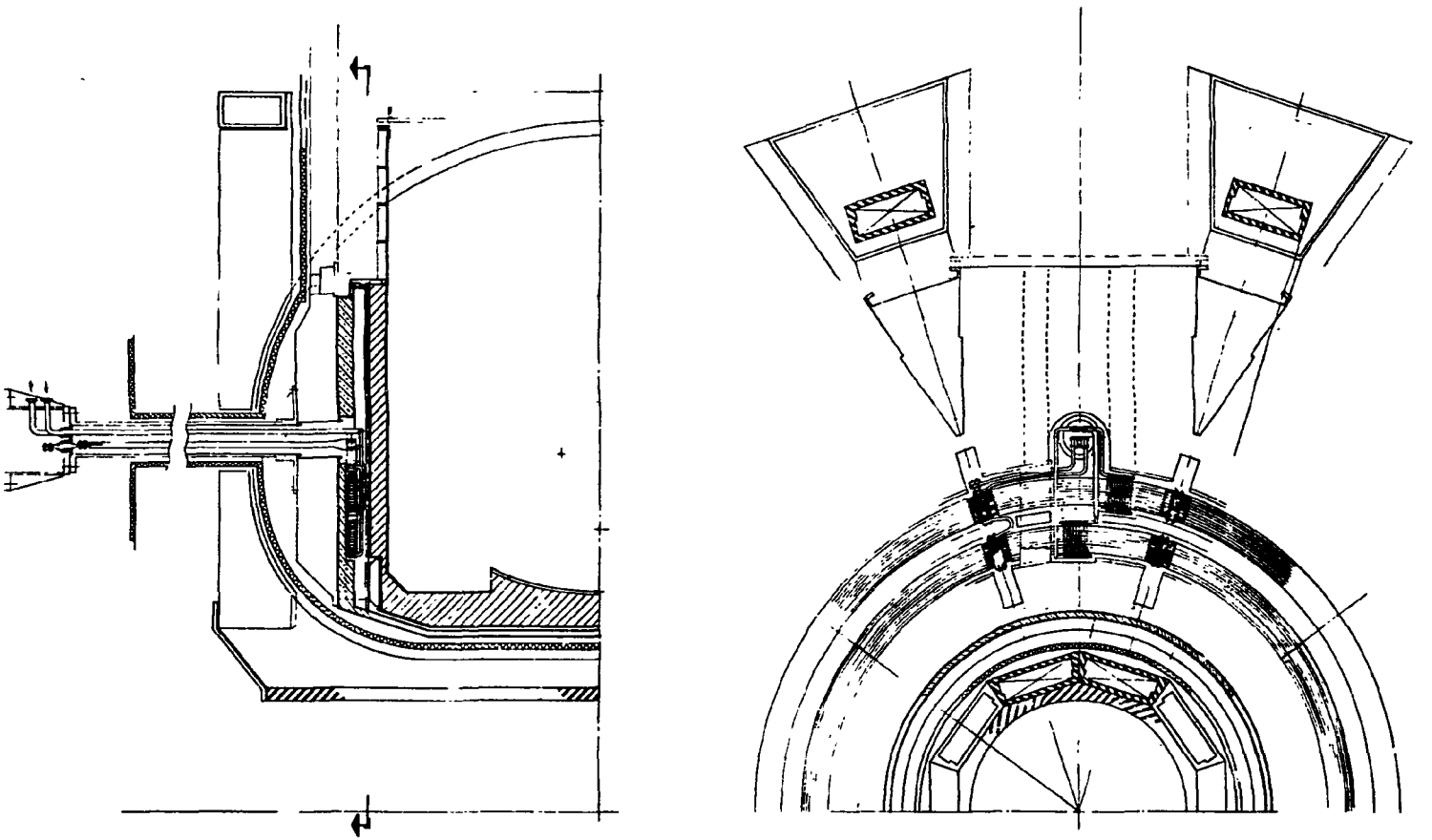

Fig. 3-12. Configuration option that locates lower internal EF coil inside torus spool structure.

ORNL–DWG 81-17017 FED

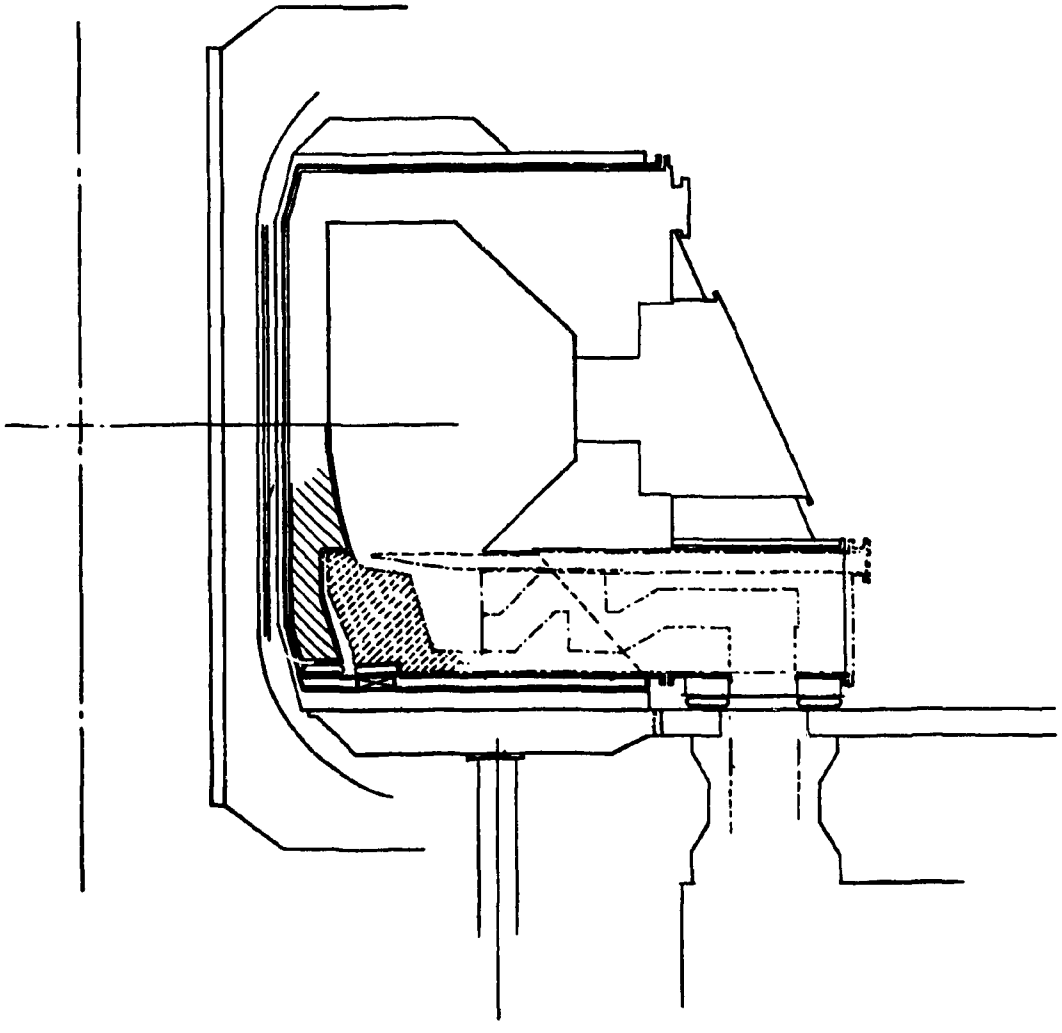

Fig. 3-13. FED configuration option that allows coil access through the divertor module.

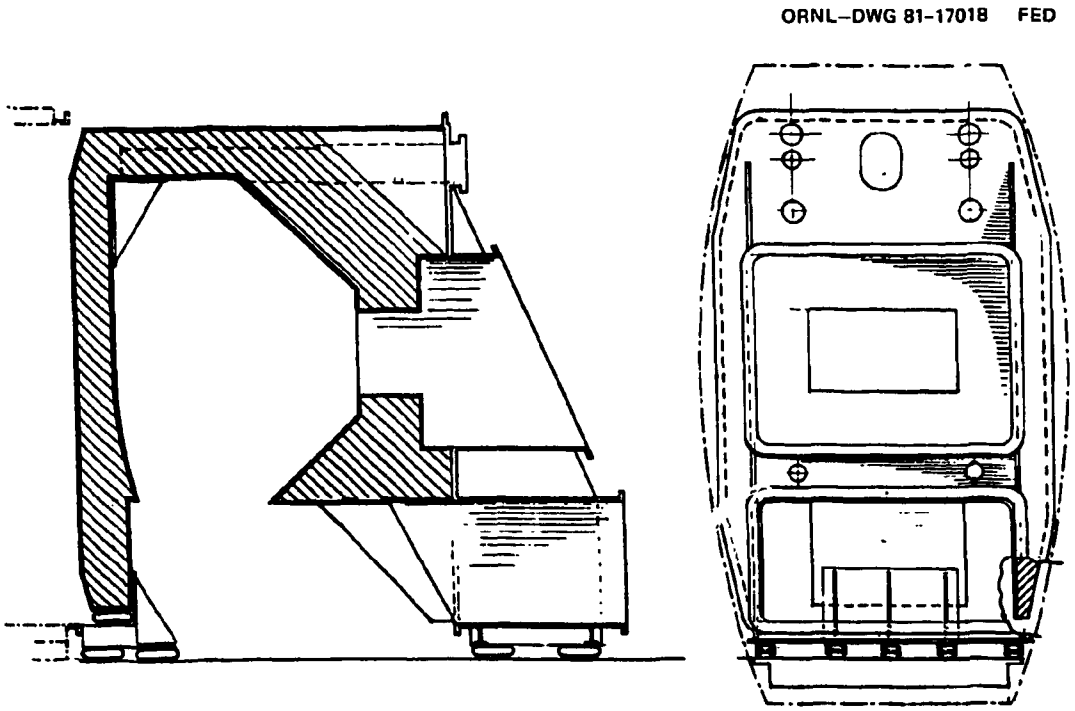

Fig. 3-14. FED configuration option with shield module design with floor removed.

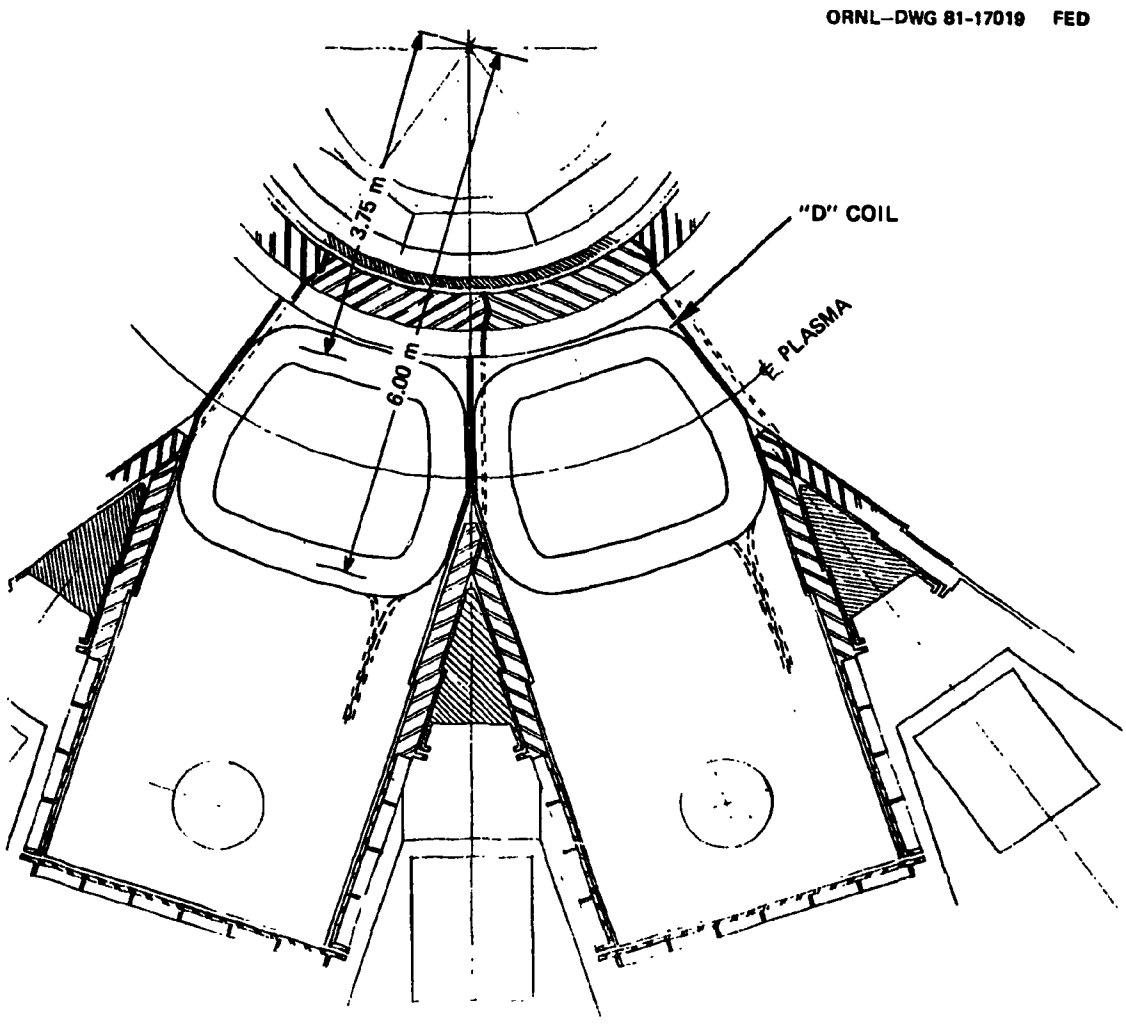

Fig. 3-15. FED configuration option with saddle coils located in divertor module.

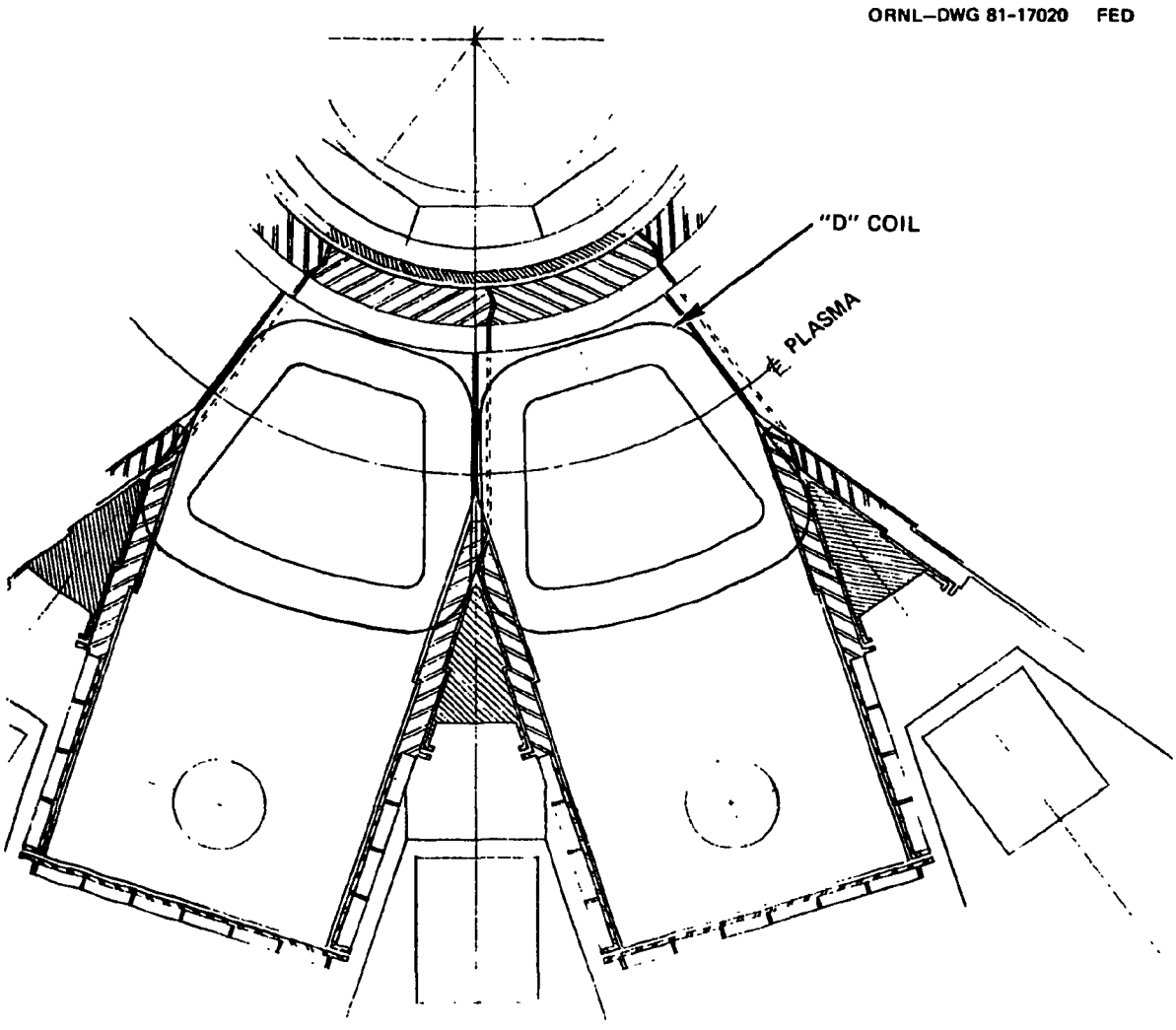

Fig. 3-16. FED configuration option with saddle coil located in torus support structure.

this section is divided into two parts. The first is a description of the basic assembly sequence of all major components. The second part is a description of the maintenance approach.

3.2.1 Assembly Sequence of the Device

The assembly sequence is divided into three phases. Phase I is primarily the installation and assembly of the magnet systems, Phase II is that of the plasma chamber systems, and Phase III addresses the assembly of the peripheral components. Table 3-4 shows the breakdown of major components by assembly phases. Figure 3-17 illustrates eight major steps in the assembly sequence described as follows.

The bucking cylinder is the first component to be assembled. It is placed on a temporary support structure which becomes redundant after the TF coils and the ring beams are in place. (At that time, the bucking cylinder is supported by the 10 TF coils.) EF coil #3 is then positioned into the reactor cell pit area along with the lower ring beam for subsequent installation onto the lower support structure of the TF coils. The 10 TF coils are then positioned and installed onto the support columns; the columns are configured as a truss to provide lateral restraint for the TF coil system. The upper and lower support structure between TF coils (the intercoil supports) are preassembled to the coils in half sections. The final shimming and joining of this structure are accomplished after the coils are in place. The final installation of the lower ring beam and the addition of the upper ring beam completes the TF coil support system. The temporary support under the bucking cylinder is removed at this time.

After the final installation of EF coil #3, the lower cryostat containment and the torus support columns are assembled. The cryostat vessel is also built up around the inner and upper legs of the TF coils. EF coil #2 is placed into the upper ring beam structure, although this can be done at a later stage. The same is true for the installation of the OH solenoid and the cryostat dome. Their assembly can be delayed if it is advantageous to do so. EF coil #1 is brought into the cryostat enclosure in two 180° segments through the window and temporarily

Table 3-4. Phased assembly of major components

Primary Device Components		Peripheral Components
Phase I	Phase II	Phase III
Bucking cylinder	Torus platform	RF heating
EF #3	Spool and frames	Limiter blades
TF coils	Torus sectors[a]	Pumps and ducts
Cryostat (less dome)	Solenoid[b]	Fuel injectors
EF #2	Cryostat dome[b]	Test modules
EF #1, 4		Diagnostics

[a]Many of the peripheral components may be preassembled to the torus prior to installation.

[b]May be installed at the end of Phase I or in Phase III.

ORNL-DWG 81-17035R FED

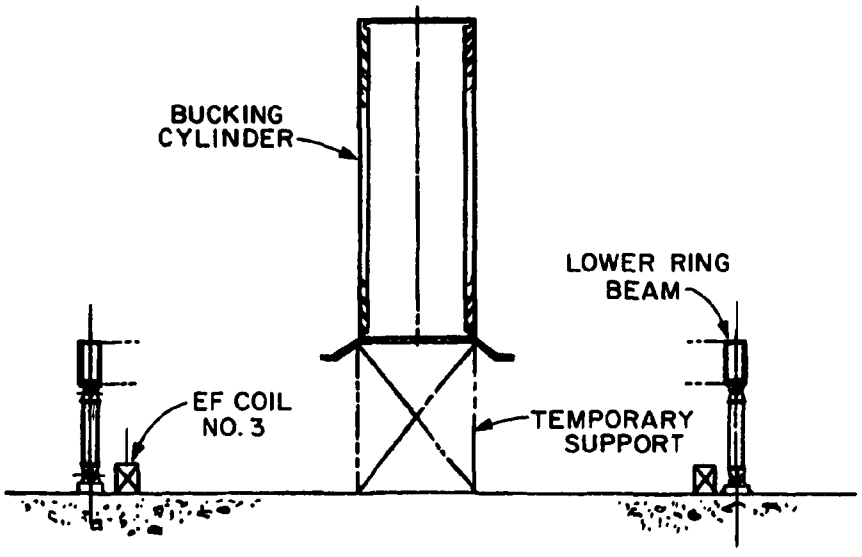

Fig. 3-17a. Initial assembly of the FED device — installation of temporary support bucking cylinder, EF coil #3, lower ring beam.

ORNL-DWG 81-17034R FED

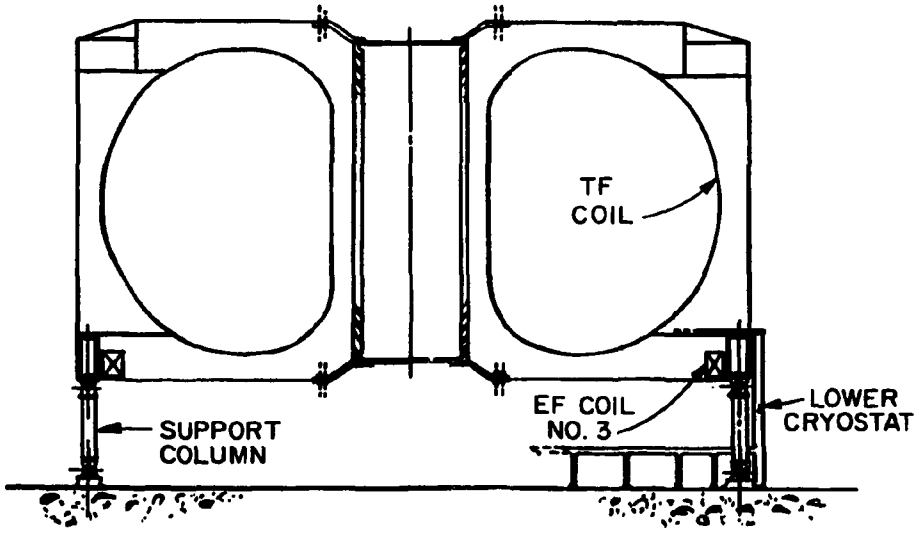

Fig. 3-17b. Initial assembly of the FED device — installation of TF coils, support columns, EF coil #3, lower cryostat.

ORNL-DWG 81-17033R FED

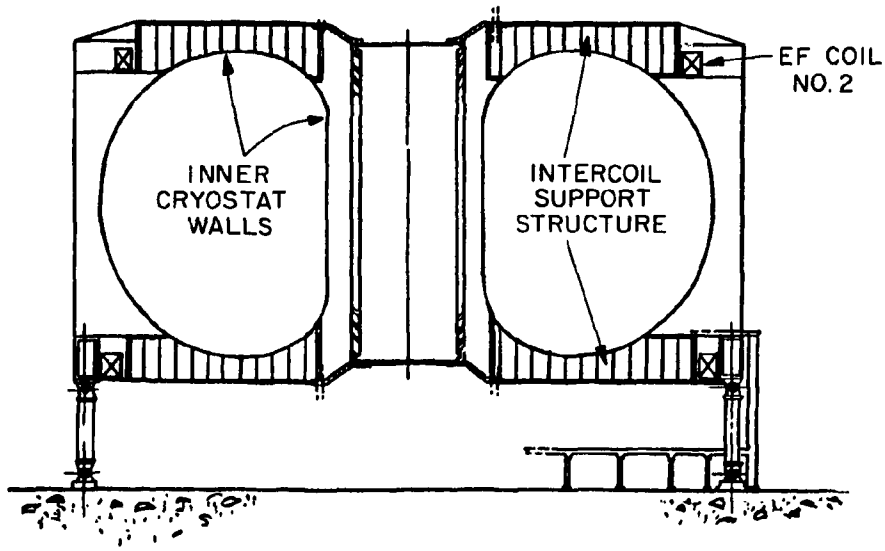

Fig. 3-17c. Initial assembly of the FED device — installation of intercoil supports, EF coil #2, inner cryostat walls.

ORNL-DWG 81-17031R FED

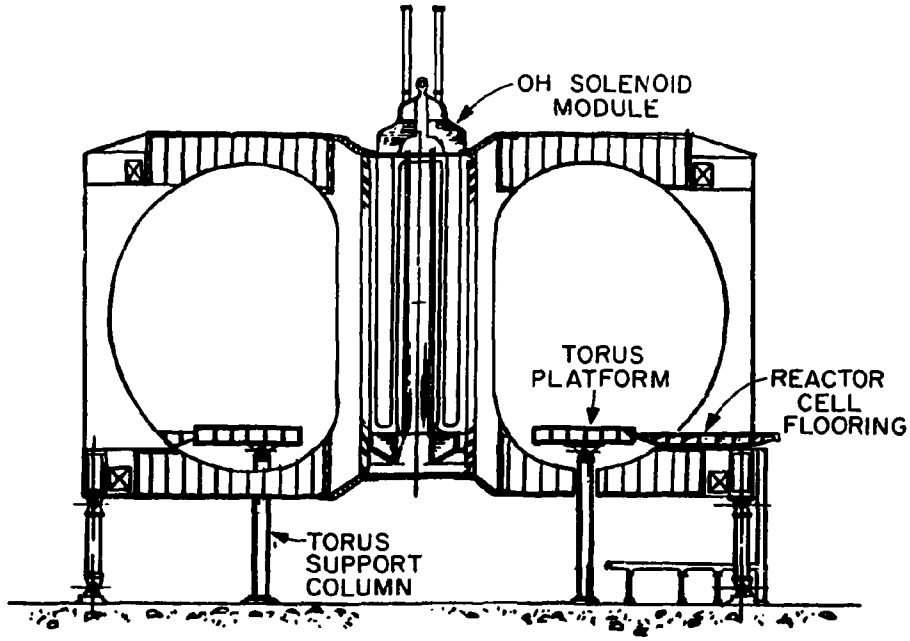

Fig. 3-17d. Initial assembly of the FED device — installation of torus supports, torus platform, OH solenoid module.

ORNL-DWG 81-17032R FED

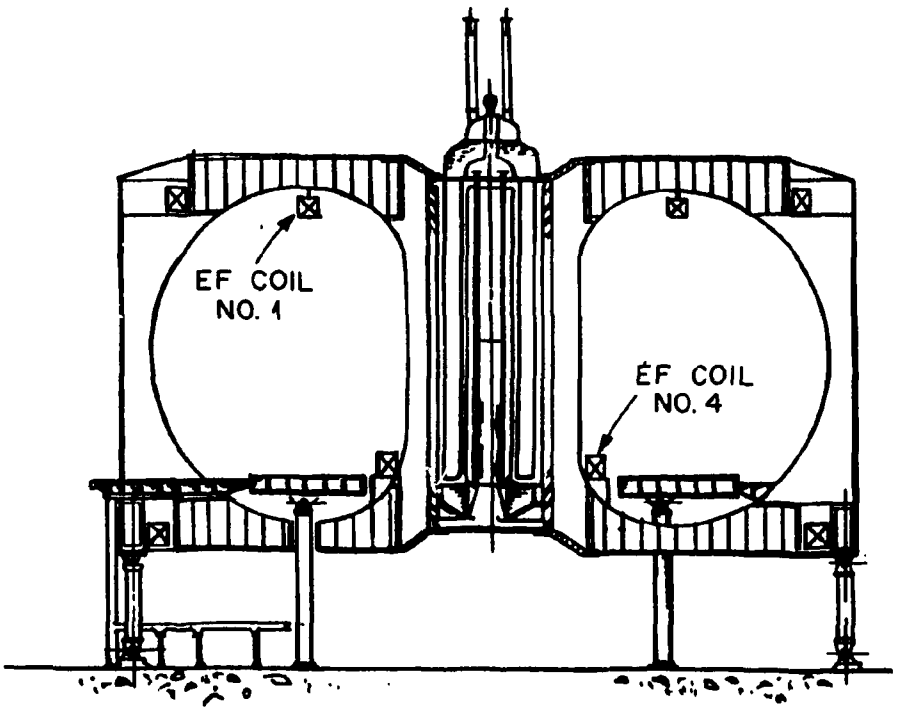

Fig. 3-17e. Initial assembly of the FED device — installation of jointed copper coils, EF #1 & #4.

ORNL-DWG 81-17030R FED

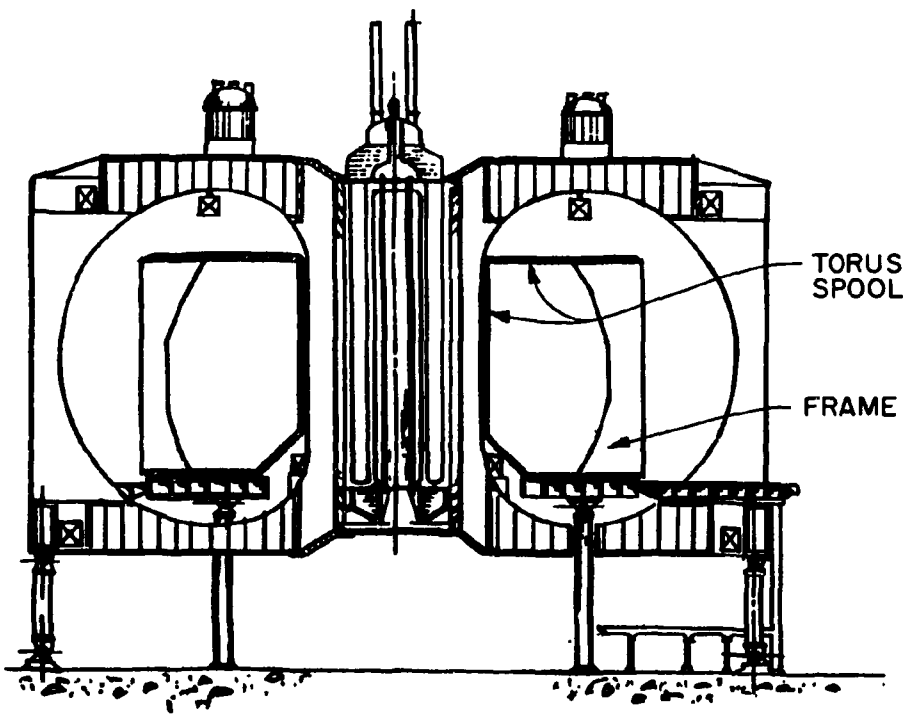

Fig. 3-17f. Initial assembly of the FED device — installation of torus spool and frame structure.

ORNL-DWG 81-1 '029R FED

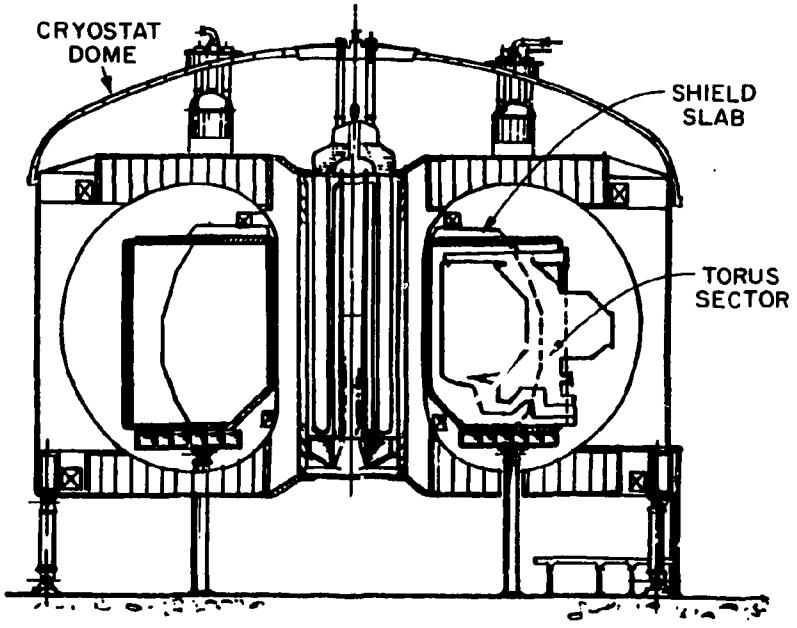

Fig. 3-17g. Initial assembly of the FED device — installation of torus sectors, shield slab, EF coils #1 & #4, cryostat dome.

ORNL-DWG 81-17028R FED

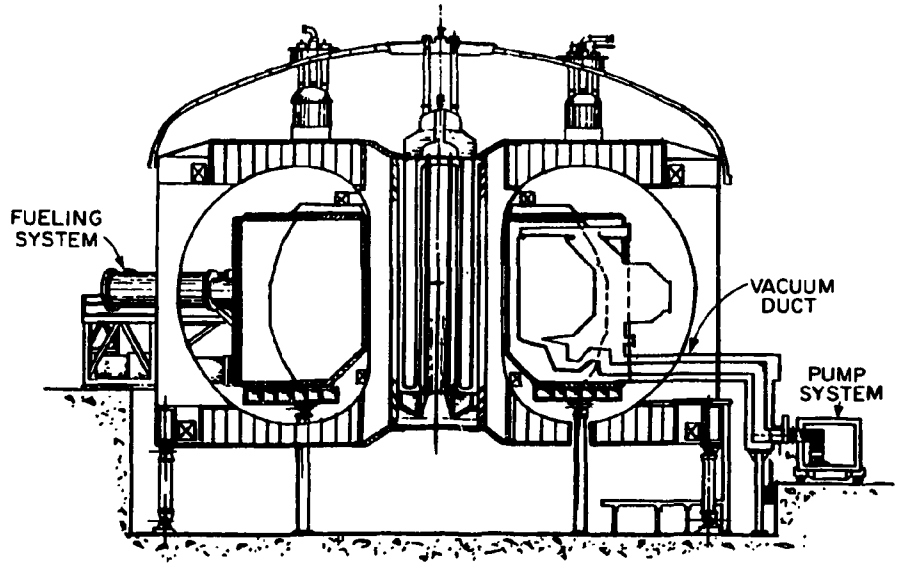

Fig. 3-17h. Initial assembly of the FED device — installation of peripheral components.

suspended from the upper intercoil structure. It remains in that position until the torus spool structure is completed. EF coil #4 is also introduced as two 180° segments through the window, but it is assembled into a ring coil and temporarily located on a support platform which is built into the lower cryostat surface. It remains there until the spool is completed.

The torus platform structure is introduced through each window in ten segments. Each is attached to a torus column support which is already in place and then joined to form a continuous platform for the torus. The flooring which bridges the torus platform and the reactor cell floor is next installed to aid the assembly of the spool structure. Ten spool pieces are then assembled on the platform after passing through the windows. They are joined to each other along with vertical frame supports to provide structural and vacuum integrity for the 10 sectors. EF coil #4 is then raised to its final position behind the truncated portion of the spool. The upper shield slab is passed through each window as a segment and installed on top of the spool structure. EF coil #1 is taken from its suspended position and joined into a ring coil on top of the slab.

The device is essentially complete at this stage except for the torus sectors and their peripheral components. Each of the 10 sectors is passed through its appropriate window opening for final installation into the spool. It is conceivable that each sector could be preassembled with its adjunct components, i.e., limiter blade modules, ICRH and ECRH systems, diagnostics, etc., although these could be the last items to be installed on the device prior to operational testing. After the sectors are in place, the pump limiter ducts, the 10 pairs of pump systems, and the fuel injector system are the last major components to be installed.

3.2.2 Maintenance

Maintenance and disassembly of the major FED components are prime drivers of the configuration evolution and have influenced both the design and the location of the major systems. The maintenance approach for the

FED is threefold and considers the mode of maintenance operations, the complex geometry of the tokamak, and available maintenance technology. This approach established the framework for developing the device configuration. It is briefly described below.

1. In general, all areas outside of the device shield can be maintained by contact operations about one day after shutdown if the plasma chamber is unopened and if torus penetrations are properly shielded. In addition, all systems are being designed with the ability to be remotely maintained for emergency situations when personnel entry into the reactor cell could be prohibited.
2. Those components whose replacement requires an extended device shutdown are classified as long-life and are designed to function normally without replacement for the life of the device. The capability to accommodate their unexpected repair or replacement, however, is one of the criteria guiding the configuration development.
3. All components are designed to be maintained using existing or near-term remote maintenance equipment and technology in the areas of manipulator systems, viewing systems, and transport systems.

In discussing tokamak maintenance, the tendency is to focus on remote operations because of their inherent difficulties, and likewise that is the thrust of this subsection. However, it is important to note the benefits of contact operations for routine inspection and maintenance while the device is fully assembled. The shield is designed to permit this flexibility. Even so, many of the maintenance activities will require remote operations, particularly the replacement of major components. This is true not only because of neutron-induced activation, but also because many of the components are large and heavy, thereby limiting contact procedures to inspection, supervision, and equipment setup.[1]

This subsection is divided into four parts. The first is a discussion of scheduled and unscheduled maintenance. The second part describes the influence of maintenance and disassembly on the device configuration, and the third part covers disassembly scenarios of the major components. The last is a discussion of future work.

Scheduled and unscheduled maintenance

Maintenance activities for the device fall into two broad categories: those which are scheduled or planned for and those which are unscheduled.

Scheduled repair (or replacement) is anticipated for components whose life is limited by mechanical wear or physical degradation resulting from operation in the reactor environment. The fuel injector is a rotating mechanical device which will require lubrication and bearing changes every 2 1/2 years. The limiter blades are expected to be changed periodically. Also included as scheduled operations are components which will be changed or added to the tokamak as its operating mission changes. These include instruments, diagnostics, and experiments.

Unscheduled events are not preplanned occurrences even though they have been anticipated in the configuration design. Even the most reliable components, those designed to last the life of the device, have a finite probability of at least one failure during the device lifetime requiring a replacement. In many cases, these will have a significant impact on the device downtime, particularly those classed as semipermanent installations. Some examples of components which may require unscheduled maintenance are: the ICRH and ECRH launchers and waveguides, PF coils, TF coils, vacuum and coolant containment systems, the torus spool, and possibly even primary and secondary support structure. Pumps, valves, and the like are also in this category but will not present serious maintenance problems because they are relatively small and accessible. These components will be designed for quick, remote changeouts.

A discussion of specific component replacements and the resulting downtime is presented later in this section.

Influence of maintenance on the configuration

Much of the overall configuration development is associated with the concern for maintenance and disassembly. Some of the maintenance considerations which have significantly affected the configuration include:

- Straight, radial translation for torus sector removal dictated that the number of sectors be equal to the number of TF coils.

- The required size of the window-like opening for sector removal established the minimum TF coil size and also provided access for torus penetrations.
- External vacuum sealing of the torus sectors led to the development of the fixed spool structure.
- The PF coils are positioned to provide clear access for sector removal.
- Major components which require periodic replacement are designed to be modular so they can be removed with a minimal impact to other components, e.g., the limiter blade.

The configuration description which follows is presented from the perspective of maintainability and disassembly of the device. Several major design iterations[2] led to the present FED reference configuration, and each of these was strongly influenced by maintenance requirements.

One of the most important maintenance operations influencing the development of the configuration is removal of the torus sectors. Earlier trade studies indicated that a minimum number of large sectors is the most efficient means of disassembling the plasma chamber. The minimum number of sectors which can be arranged for any tokamak configuration is simply equal to its number of TF coils. In such an arrangement, the access necessary for removing a sector is bounded by the outer TF coil leg (actually the cryostat) and the upper and lower cryostat enclosures. Figure 3-18 is a drawing of this "window concept." The window permits each sector to be removed in its simplest form of translation which is straight, radial motion.

The window also provides the maximum amount of clear space for penetrations into the torus. In the FED reference design, the major component penetrations are: 4 ICRH antenna launchers for bulk heating, 10 waveguides for ECRH heating, 2 fuel injectors, 10 pump limiter ducts, electrical and coolant lines for the internal PF coil system, and coolant piping for each of the 10 torus sectors. In addition to this required listing of components, there will be numerous penetrations for instrumentation and diagnostic equipment, as well as modular components for engineering testing.

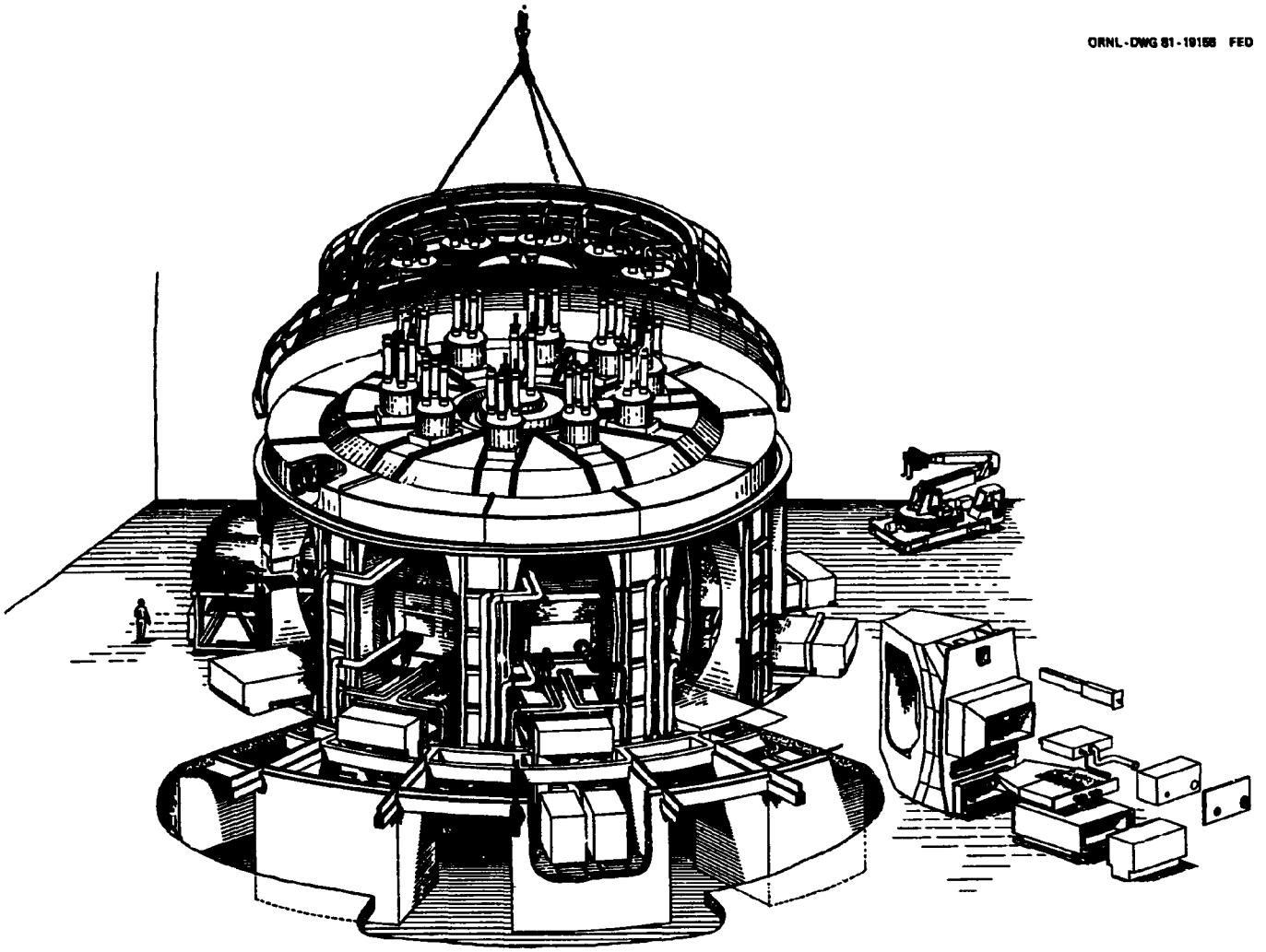

Fig. 3-18. The TF coil/cryostat window allows for radial extraction of the torus sectors.

One of the more significant tasks for sector removal is disengaging the vacuum closure of the torus seal. The flange is totally accessible through the window and is external to the plasma chamber. However, because of the compactness of the design (aspect ratio = 3.8), the clearance between the torus and the inner TF coil cryostat does not permit disassembly operations by contact or remote means. Therefore, there is no possibility of providing external sealing between adjacent sectors around each external interface. This design constraint led to the fixed-spool concept which is illustrated in Fig. 3-19. A portion of the plasma chamber is designed to be a semipermanent installation surrounding the common cryostat of the inner TF coil legs. It provides monolithic support for the individual torus sectors and also makes up three vacuum sealing surfaces of the plasma chamber. Each of the sectors is nested in this spool-like structure and rigidly attached to the outer edge of the spool and the vertical posts. These posts act to support the upper and lower spool flanges and are located in the plane of the TF coils.

Disassembly of the sector, including the vacuum closure, can therefore be accomplished by completely external operations. The operations which prepare the torus for removal can be accomplished "hands-on"

Adoption of the window concept influenced the location of PF coils. The FED design uses a hybrid system made up of internal and external EF coils. These coil positions are arranged to be compatible with clear access through the window for sector removal. The advantage of this configuration is the fixed location of the coils, unlike the earlier ETF design[2] which required raising and lowering of the inner EF coils. Fig. 3-20 illustrates the coil positioning around the open window.

The design of the limiter blade is another example of the influence of maintenance and disassembly on the configuration. It can be removed from the plasma chamber without disturbing the sector or other peripheral components (i.e., the ICRH launcher or the vacuum pump shielded duct). It is sized to fit within the boundary of the window and has an independent vacuum seal interface with the torus. Figure 3-19 also depicts the pump limiter module removal. This feature of independent removal is

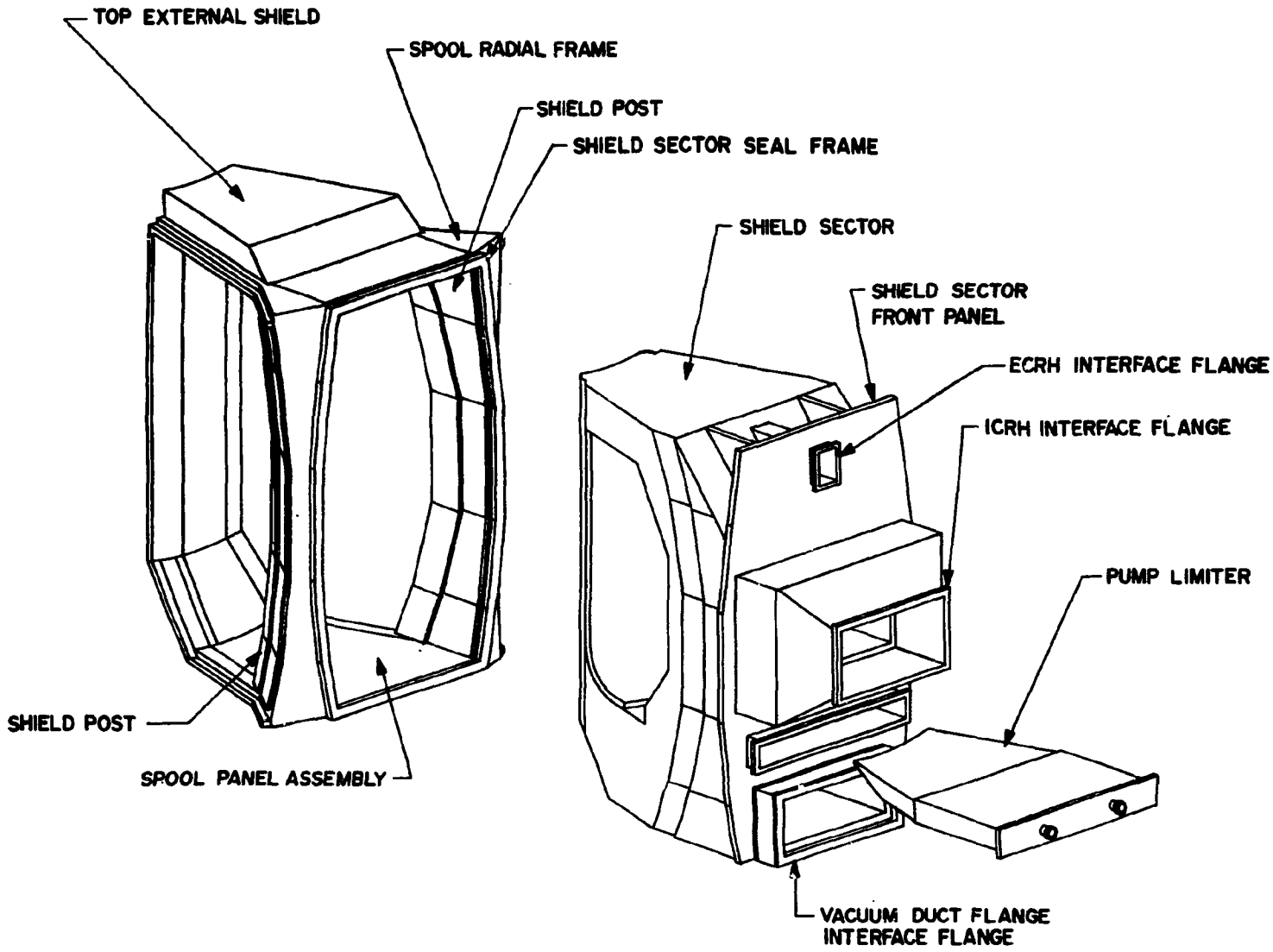

Fig. 3-19. The spool arrangement provides vacuum integrity and allows the torus seal to be totally accessible through the window.

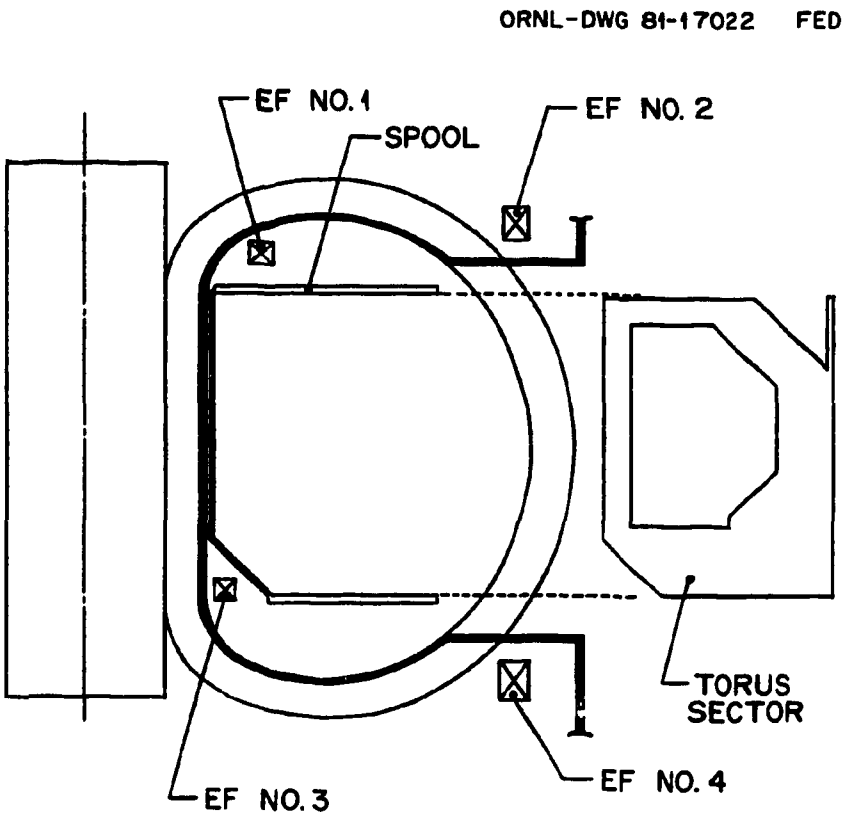

Fig. 3-20. The poloidal field coil locations are compatible with the window concept.

particularly attractive for this component because of its anticipated frequent replacement.

In-vessel operations

Generally speaking, all component repairs are accomplished outside of the reactor cell, and repaired components or spares are refitted into the device. This philosophy has led to component modularization as a means of increasing device availability. However, there are some situations where in-vessel operations offer a distinct advantage. The ability to have routine in-vessel inspection, without opening the plasma chamber is one example. Visual monitoring of the first wall, the limiters, and certain test modules, in situ, will provide valuable data without an adverse impact to availability. It is presently estimated that reconditioning the plasma chamber after it has been opened to the reactor cell may take one week. Consequently, viewing systems have been considered for each of the 10 sectors. One option is a modified periscope system which is built into the vacuum integrity of the plasma chamber.

The armor tiles of the first wall are designed for the life of the machine; however, it is expected that a finite number of tiles will fail and will require replacement. (A detailed discussion of this scenario can be found in Section 3.3.) Their replacement can be accomplished by removing the sector (or sectors) affected, with a potential downtime of many weeks, or they can be replaced in situ in perhaps half of the time. In order to accomplish this, four entry ports have been identified around the device for introducing a manipulator system. They are in bays I, IV, VI, and IX and are also penetrations common to other systems. Figure 3-21 shows the location of the bays and the locations for introducing a manipulator system to reach all surfaces in the first wall.

Disassembly scenarios

The disassembly scenarios discussed here generally do not reflect the routine maintenance operations, but instead describe major component changeouts which represent worst case occurrences. These are the scenarios

ORNL-DWG 81-17027R FED

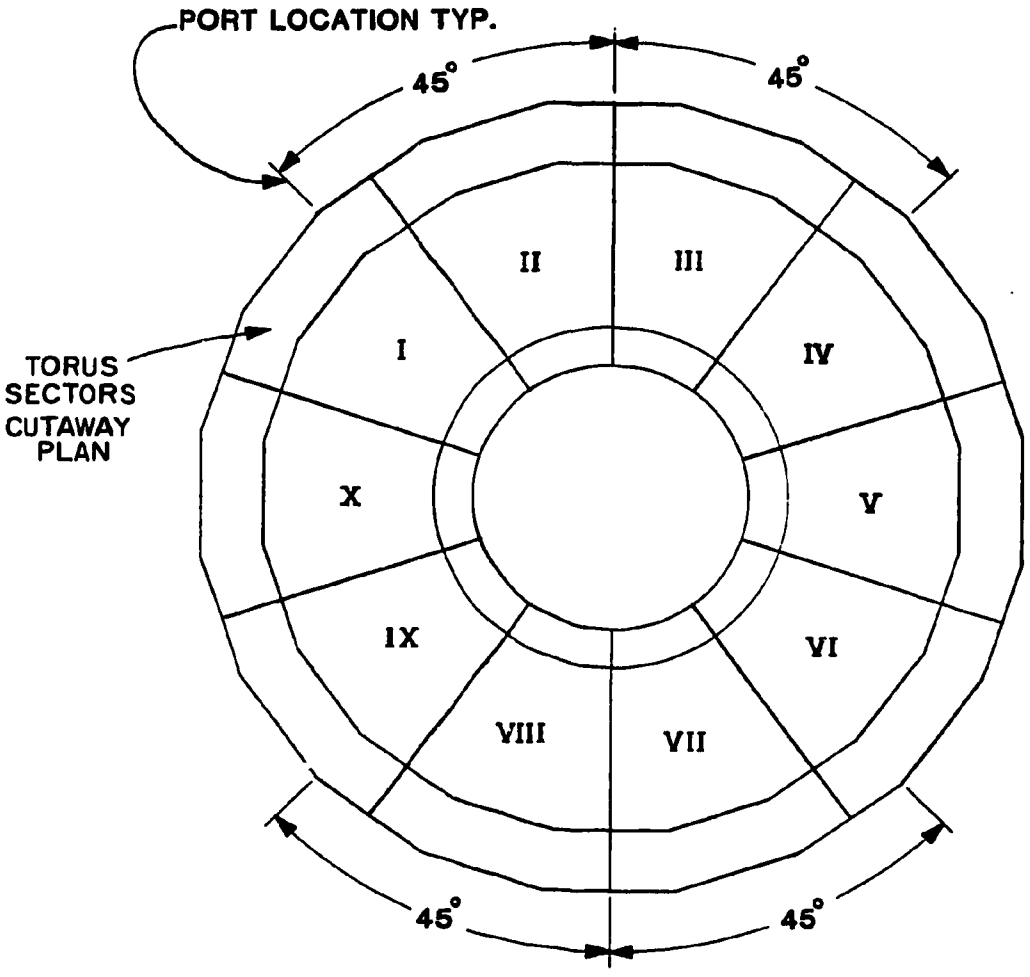

Fig. 3-21. In-vessel manipulator operations are accomplished through four ports.

upon which the configuration is based. A summary of the component replacement times is given in Table 3-5.

The time estimates assume that maintenance and disassembly operations occur in three full shifts, seven days per week. Figure 3-22 shows the components which are discussed in this section.

Torus sector

The plasma chamber is made up of 10 sectors which are fitted into the spool structure. They are externally sealed to the upper and lower spool pieces and the vertical support frames. Their removal is through the TF coil/cryostat window. The removal of a sector may be required for any of several reasons: an internal coolant or vacuum leak, severe erosion of the first wall and armor, or the replacement of a TF coil. While none of these are scheduled occurrences during the device lifetime, they must nevertheless be accounted for. A tabular summary of the major steps necessary for sector removal is shown in Table 3-6. Two things should be noted: 1) the first twenty-four hours after device shutdown, a "cooldown" period is required to permit personnel access into the reactor cell; 2) the cryostat maintains all of the superconducting coils and their structure at liquid helium temperature during this scenario.

It is assumed that the components which are installed on the torus are not disassembled but remain in place, i.e., ICRH launcher, ECRH waveguide, diagnostics, and limiter. The additional downtime required for the repair or replacement of the failure in the torus is not included in the total elapsed time; it is assumed that a spare sector is available.

Limiter module

The pump limiter is a modular component which is positioned in each of the ten torus sectors. It is a blade-like component which is made up of a replaceable sleeve and a reuseable core, and its scheduled changeout is on the order of once per year. Because of the relative frequency of these operations, this component is designed to be removed independently of the torus sector and the shielded ducting.

Table 3-5. Summary of component replacements

Component	Quantity	Physical Characteristics (per unit)	Replacement Time (days)[a]
Torus sector	10	375 tonnes 7 × 5 × 4 m	11
Limiter module	10	30 tn 4 × 3 × 0.5 m	10
Pump system	20	<10 tn 2.5 × 2 × 1.5 m	2
ICRH launcher	4	<10 tn 3.3 × 2.5 × 1.3 m	9
ECRH, diagnostics	10	--	8
OH solenoid	1	350 tn 12 × 3 dia. m	44
EF coil #2	1	350 tn 19 dia. m	45
EF coil #3	1	450 tn 19 dia. m	209
EF coils #1, 4	1	90 tn 3.9 dia., 3.1 dia. m	43
TF coil	10	235 tn 7.4 × 10.9 m clear bore	168
Fuel injector	2	<20 tn 6 × 3 dia. m	<2
Valves, pumps, etc.	--	--	<2

[a]The times listed are for one individual component; it does not follow that removal of all components is a multiple of the time shown; also assumes around-the-clock operations.

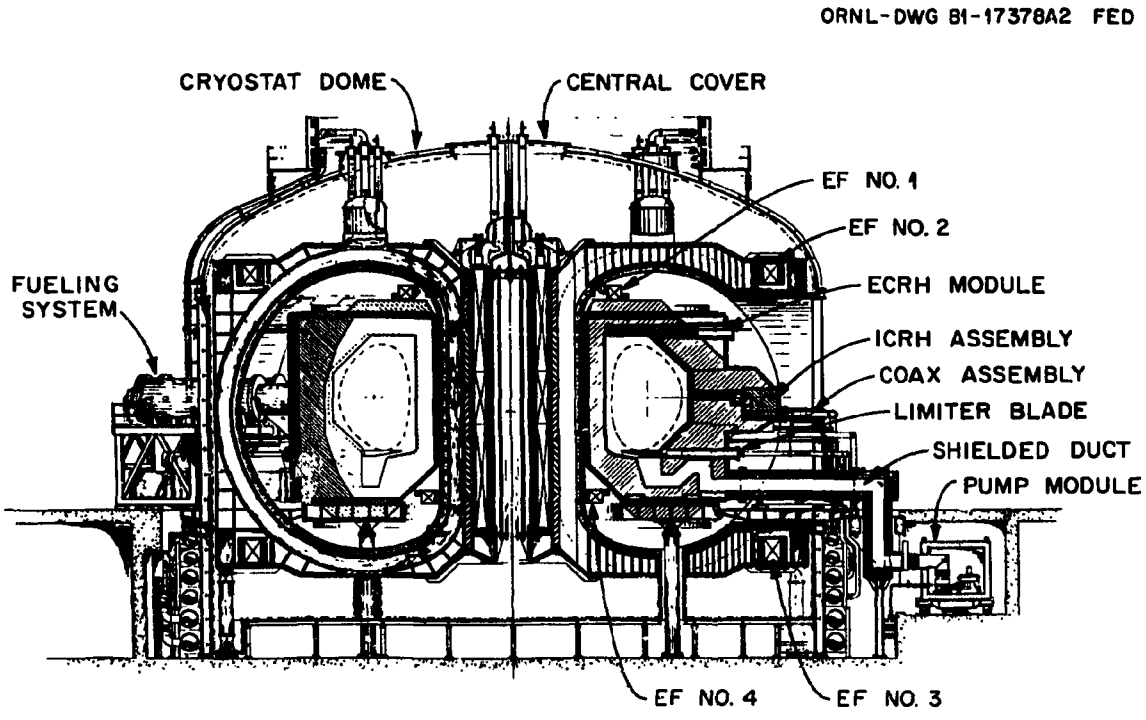

Fig. 3-22. The disassembly of major components influenced the configuration design.

Table 3-6. Torus sector replacement

	Steps	Mode of Operation[a]	Duration (hrs)
1.	General device shutdown	A	
	Magnetic coils discharged	A	
	Torus sector drained of coolant	A	
	Maintenance equipment is readied	-	
	Bakeout at elevated temperature	A	24
2.	Disconnect electrical and coolant lines including those of adjunct components	C	8
	Cut torus vacuum seal and limiter duct seals	C/R	8
3.	Extract limiter duct; install shield plugs to all duct openings	R	4
	Remove sector through window	R	
	Transport to hot cell	R	4
4.	Decontaminate area	R	4
5.	Install sector through window	R	4
	Remove shield plugs; install duct	R	4
6.	Weld torus vacuum seal and duct seals	R	16
7.	Connect electrical and coolant lines	C	8
8.	Recondition plasma chamber	A	168
9.	Refill coolant, energize coils	A	4
	TOTAL		256 hrs (10.7 days)

[a] A = automated operation
C = contact operation
R = remote operation

The primary maintenance equipment needed for this removal is a transporter device which is used to extract the module after the flange attachments to the sector have been disassembled. This operation utilizes the shielded duct as a platform to support both the transporter and the engaged limiter module. It is assumed that 10 spare modules are available for the sequential changeout of the entire limiter system, and that contact maintenance procedures are possible before the extraction of a blade.

A summary of the major steps necessary for limiter replacement is shown in Table 3-7. The time required to replace one limiter blade is 9.4 days; it can be shown that replacing 10 modules in a sequential operation is approximately 13 days.[3]

Vacuum pump system

The 10 pairs of vacuum pump systems are located below the reactor cell floor. This arrangement conserves valuable space around the reactor and allows the pumps to be maintained with minimal impact to other device systems. Scheduled maintenance for the turbomolecular pumps (TMP) is expected after 25,000 hours of operation for bearing replacements, and after 6 months of operation for oil changeout. The replacement steps and time estimates are given in Table 3-8. The secondary pumps in this system are assumed to be repaired within these same periods.

The pump system is enclosed in a magnetic shield which could serve as a secondary containment for tritium if required. Therefore, the pump and shielding system is treated as a modular component. Its removal requires closing the isolation valve at each TMP in order to maintain vacuum integrity in the plasma chamber. After separating the duct interfaces with the module, the pump system is lifted out of the pit to the hot cell. The single most important feature in this system design is its isolation from the plasma vacuum. This increases device availability since the one week of plasma chamber reconditioning is not required.

Table 3-7. Limiter blade replacement

	Steps	Mode of Operation	Duration (hrs)
1.	General device shutdown	A	
	Limiters drained of coolant	A	
	Maintenance equipment is readied	-	
	Bakeout at elevated temperature	A	24
2.	Disconnect coolant lines	C	4.5
	Disassemble mechanical seal and install extractor	C/R	9
	Remove module to hot cell	R	2.5
3.	Install replacement module	R	4
	Assemble mechanical seal	R	8.5
	Test seal integrity	C/R	1.5
4.	Connect coolant lines	C	4.5
	Recondition plasma chamber	A	168
	TOTAL		226.5 hrs (9.4 days)

Table 3-8. Vacuum pump system replacement

	Steps	Mode of Operation	Duration (hrs)
1.	General device shutdown	A	
	Discharge coils	A	
	Close isolation valves	A	
	Remove floor over pit	R	24
2.	Cut vacuum seals	C/R	4
	Lift out pump system module	R	1
3.	Install and align pump system module	R	2
	Weld vacuum seals	R	6
4.	General device startup	A	4
	TOTAL		41 hrs (1.7 days)

ICRH launcher

The launcher system is essentially an integral part of the torus and is located in 4 sectors. It is made up of 4 subassemblies which can be sequentially removed from the sector. They are: the coax assembly, the cover plate, the shield plug, and the waveguide sleeve. Replacement of the waveguide sleeve requires a complete disassembly of the launcher system. Assuming that spares are readily available, a waveguide sleeve can be replaced in about 9 days – without removing the torus sector (see Table 3-9).

ECRH, diagnostics, test modules

These components are discussed as a group because of their common relationship with the torus interface. They penetrate the torus in a plug-like or drawer-like manner, and they are of a size which is relatively manageable. The ECRH waveguide assembly shown in the elevation drawing (Fig. 3-22) is also representative of many of the diagnostic assemblies; they can be removed and replaced like a drawer in a cabinet.

Removal of the waveguide assembly requires simple tasks in a totally accessible region within the TF coil window. A mechanical or welded structural seal must be opened prior to disassembly of the waveguide coupling and inlet and outlet coolant lines. It is estimated that each of these components can be replaced within a 16-24 hour period after device shutdown. The dominant downtime penalty for these changeouts is the reconditioning required for the plasma chamber, estimated to be one week. Total replacement time for these components is 192 hours (8 days).

PF coil system

Maintenance and disassembly of the poloidal field coil system has been a major concern in the design of tokamak reactors. The poloidal coils, because of their interlocking relationship with the rest of the device, require a systematic design process for integration into the

Table 3-9. ICRH launcher replacement

	Steps	Mode of Operation	Duration (hrs)
1.	General device shutdown	A	
	Magnetic coils discharged	A	
	Maintenance equipment readied	-	
	Bakeout at elevated temperature	A	24
2.	Remove all electrical and coolant connections	C	4
	Remove coax assembly	C	2
	Remove cover plate	C/R	1
3.	Remove shield plug	R	2
	Remove waveguide sleeve	R	2
4.	Replace waveguide sleeve	R	2
	Replace shield plug	R	2
	Replace cover plate	R	1
5.	Install coax assembly	C	2
	Connect electrical and coolant lines	C	4
6.	Recondition plasma chamber	A	168
	TOTAL		214 hrs (8.9 days)

overall reactor system. Among the early work on PF coils was the hybrid system proposed at ORNL by Peng.[4] It was a mix of copper resistive and superconducting coils, respectively, located inside and outside of the TF coil bore. This system was adopted for the Oak Ridge TNS Study,[4] which incorporated movable resistive coils to permit sector removal. It did not address coil replacements. The present FED design embodies a hybrid system without movable coils and it also has fewer coils than the previous studies.

The options for coil replaceability were: 1) installing redundant coils during initial device assembly; 2) winding coils in situ; and 3) removing failed coils and replacing them with jointed copper coils for the inside coils and continuous superconducting coils for the outside coils. The third option was chosen.

The PF coil system which evolved from combining the requirements of plasma stability (startup, position, and control) and coil replacement has not yet yielded a totally acceptable coil configuration. After numerous trials using variations ranging from all-exterior to various mixes of hybrid coils, it can be concluded that the PF system should not drive the device configuration. It is the configuration which must drive the coil design. Nevertheless, much has been learned about PF coil replacement in developing the present configuration, and new options are available for future work (see Sect. 3.1.4).

The present PF system design consists of the ohmic heating solenoid, two interior copper resistive coils denoted as EF #1 and #4, and two exterior superconducting coils, EF #2 and #3. EF #1, #3, and #4 are the most difficult to replace as illustrated in the following discussions.

OH solenoid

The OH solenoid is concentrically located within the bucking cylinder, in a cryogenic environment. It is designed to be removed by access only through the cryostat dome. A ring flange which is bolted to the upper TF coil support structure locks the solenoid assembly into a cradle support. The cradle ties the lower TF structure together. Table 3-10 is a summary of the solenoid disassembly/reassembly scenario. It can be

Table 3-10. OH solenoid replacement

	Steps	Mode of Operation	Duration (hrs)
1.	General device shutdown	A	
	Cryostat warmup	A	336
2.	Disconnect He lines and electrical leads	C	
	Remove central dome cover	C	
	Remove support ring structure	C	
	Engage lifting hook	C	12
	Lift out solenoid assembly	R	
	Transport to hot cell	R	4
3.	Transport from hot cell	R	
	Lower solenoid assembly into bucking cylinder	R	4
4.	Install support ring	C	
	Install dome cover	C	
	Connect He lines and electrical leads	C	12
5.	Cryostat cooldown	A	672
	General device startup	A	4
	TOTAL		1044 hrs (43.5 days)

seen that the major contributor to device downtime for these operations is the cryogenic thermal cycling time. Figure 3-23 shows the sequence of operations. The total time shown only accounts for the disassembly and subsequent reassembly. The time needed in the hot cell for repairs or the time required to obtain replacement components has not been estimated.

EF coil #2

EF coil #2 is readily accessed and replaced after removal of the cryostat dome. Like the OH solenoid, its replacement time is significantly affected by cryostat cycling. Figures 3-24 and 3-25 show the disassembly sequence. The maintenance steps and time estimates are given in Table 3-11.

The total time shown only includes disassembly and replacement assuming that a spare coil is available. A detailed economic evaluation is required to trade off the cost of spares vs the impact of downtime while waiting for repair or fabrication of a new coil (see Sect. 3.3.4).

EF coil #3

The detailed steps of the disassembly of this coil along with a discussion on the impact to the surrounding structure and components are summarized here. The sequence shown in Fig. 3-26 shows four stages of the coil removal (or replacement) along with the support structure impacted. A major change incorporated into the device configuration, was to move the TF support columns to the outside diameter of the machine (Earlier designs located a support under the bucking cylinder and within the diameter of EF #3). This reduces the number of affected TF coil support columns to four instead of ten and provides a relatively clear space under the center of the machine.

Three adjacent vacuum pump systems require removal along with their shielded ducts. In order to maintain contact operations in the reactor cell, the three open ducts just outboard of the window are closed with shield plugs. The reactor cell flooring beyond these pumps is then

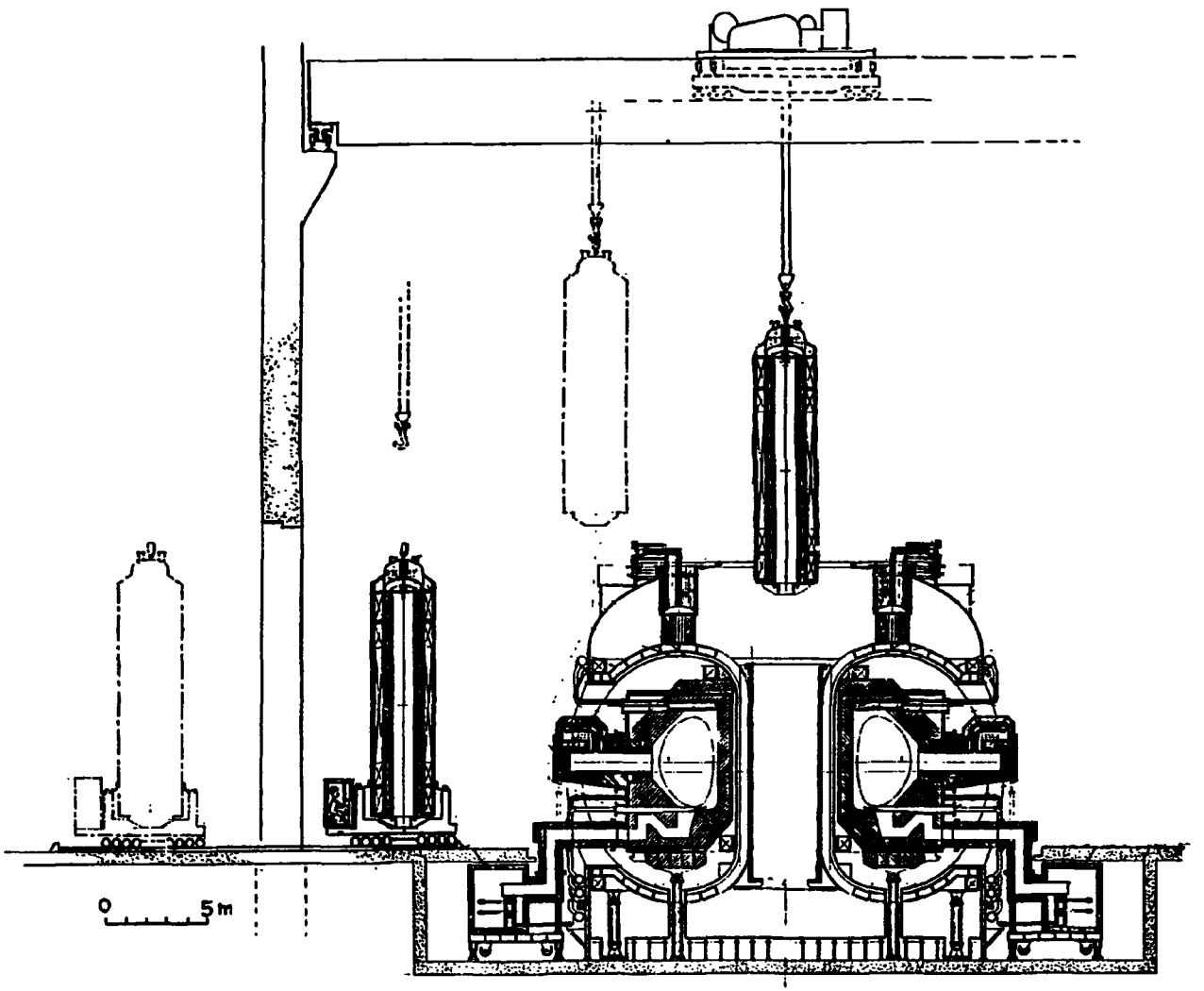

Fig. 3-23. OH solenoid removal.

ORNL-DWG 81-17021 FED

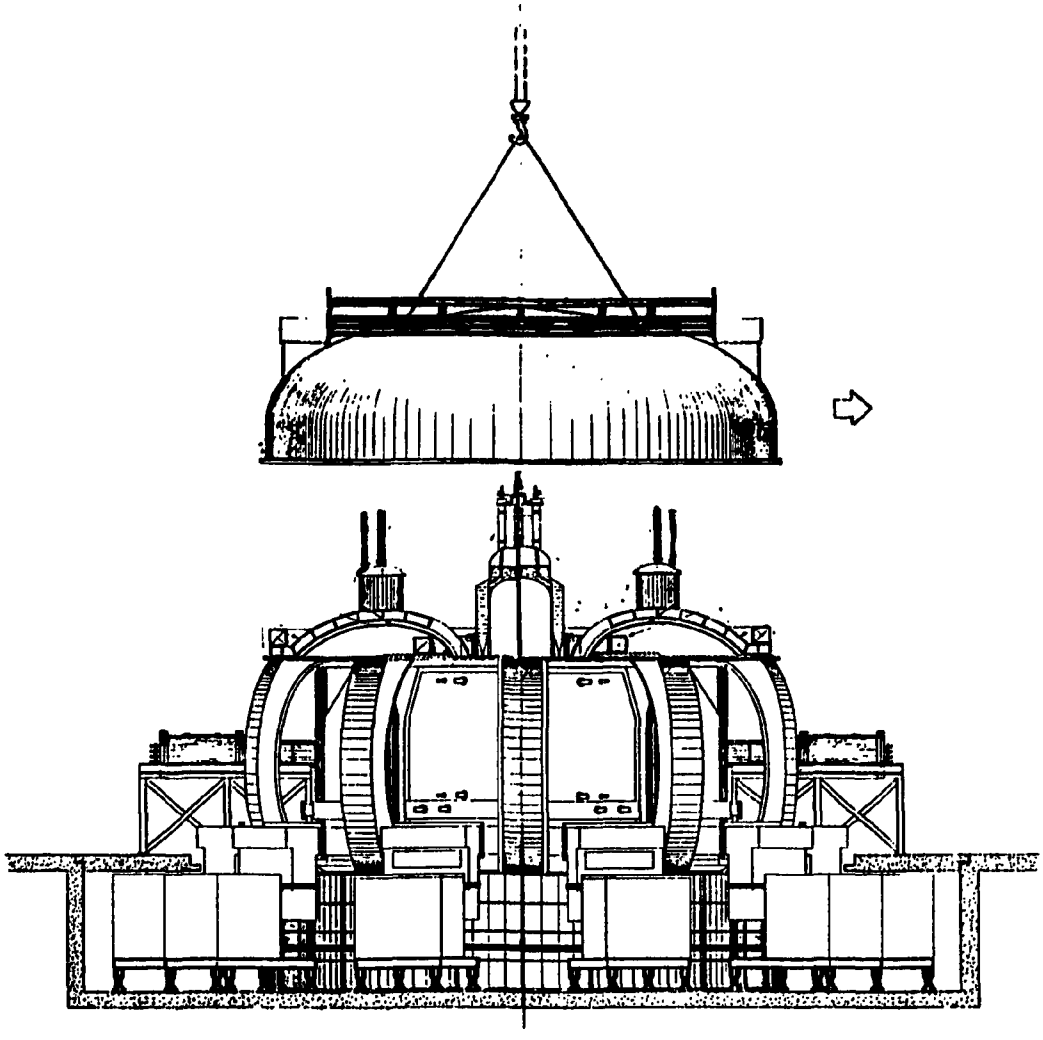

Fig. 3-24. Removal of the cryostat dome.

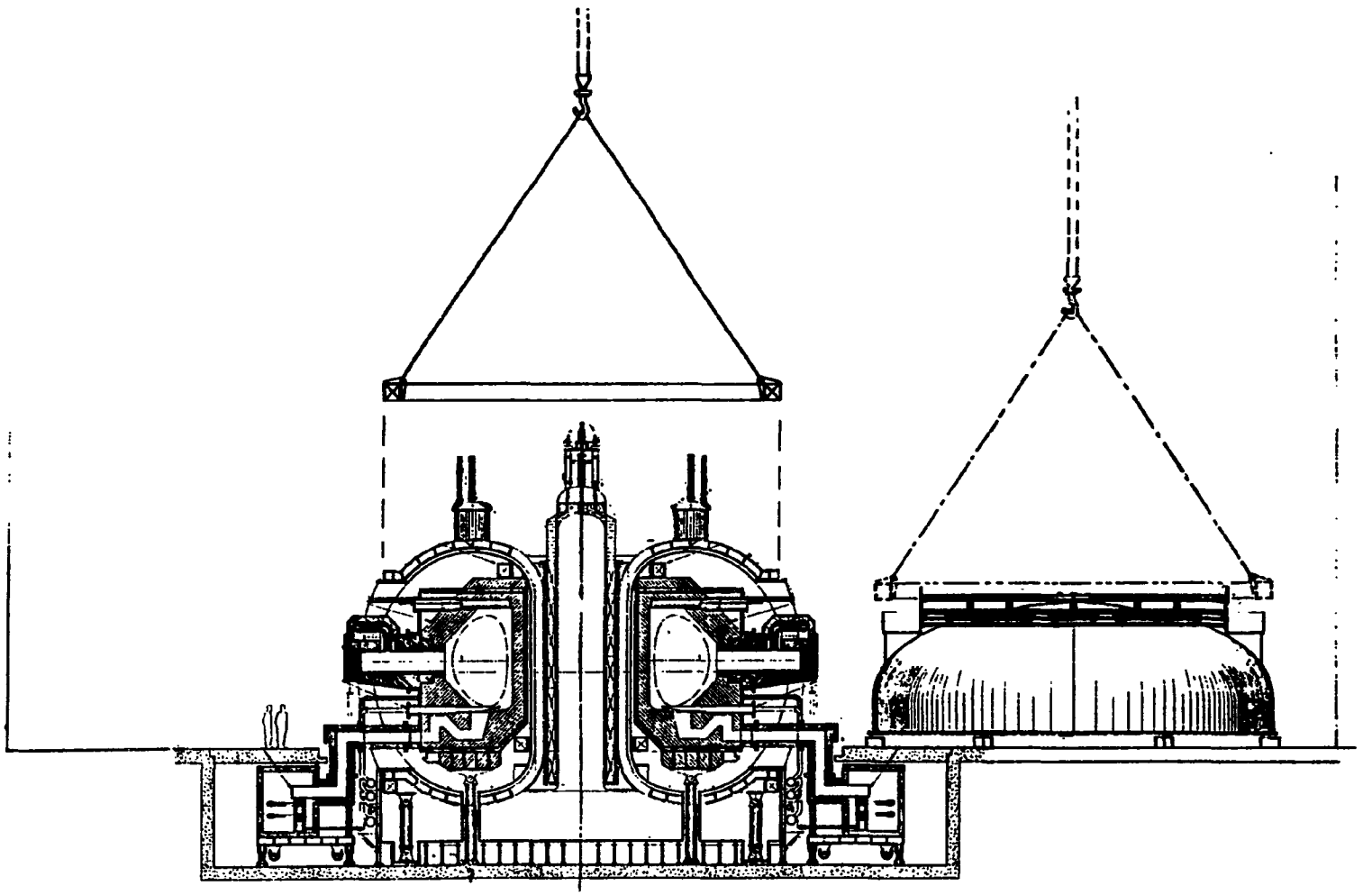

Fig. 3-25. EF coil #2 is stored in the laydown area on top of the dome.

Table 3-11. EF coil #2 replacement

	Steps	Mode of Operation	Duration (hrs)
1.	General device shutdown	A	
	Cryostat warmup	A	336
2.	Disconnect lines to solenoid	C	
	Remove central cover	R	
	Disconnect He and electrical lines of EF coil #2	C	
	Disconnect He reservoirs to TF coils (if pool boiling)	C	
	Remove cryostat dome bolts	C	
	Remove dome to laydown area	R	24
3.	Remove plate structure over coil	C	
	Install hoist fittings	C	
	Engage sling and lifting hook	C	
	Remove coil to laydown area	R	16
4.	Replace coil into device	R	
	Install plate structure	C	12
5.	Install dome and attaching bolts	R/C	
	Connect He reservoirs	C	
	Connect He and electrical lines of coil	C	
	Install central cover	R	
	Connect solenoid lines	C	24
6.	Cryostat cooldown	A	672
	General device startup	A	4
	TOTAL		1088 hrs (45.3 days)

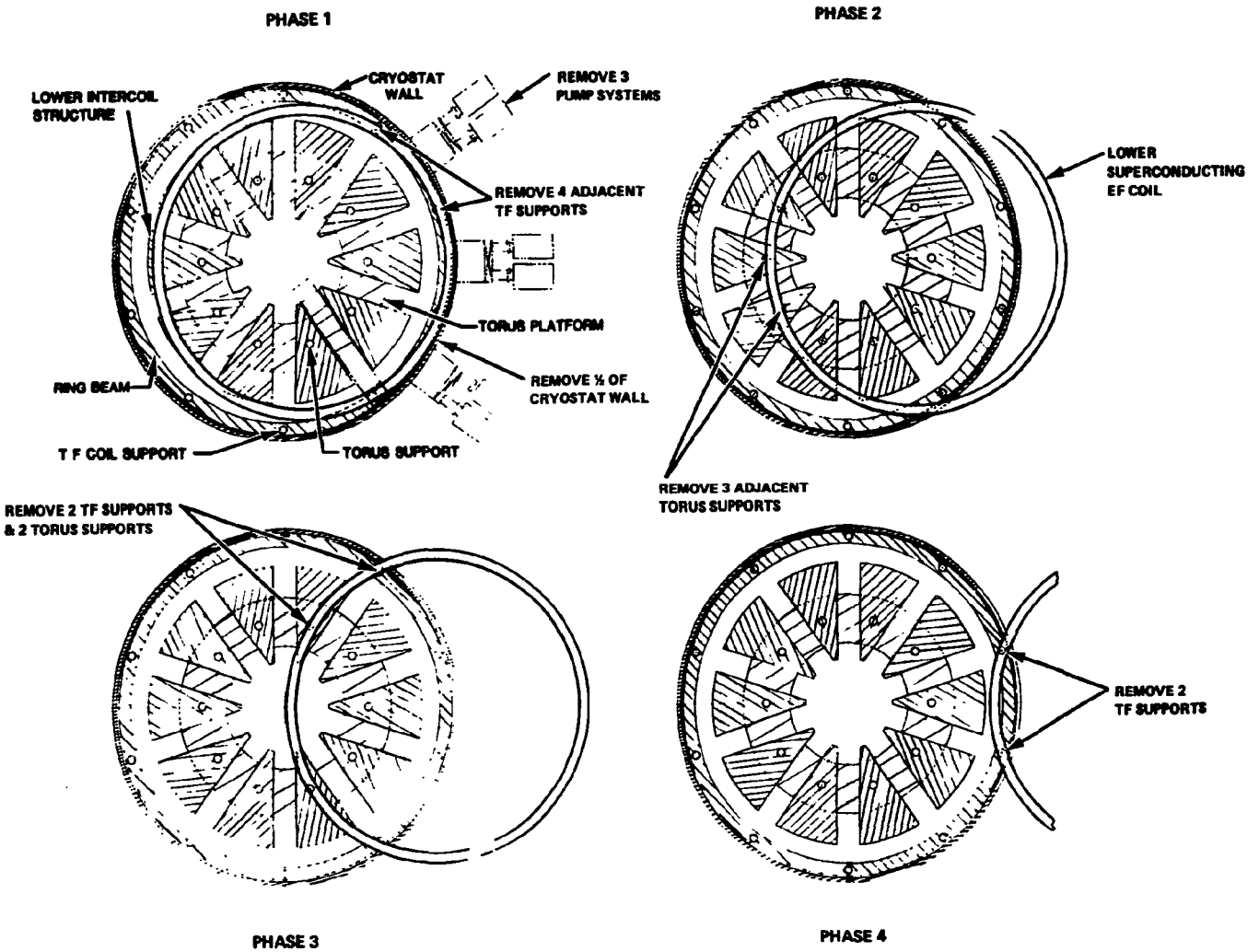

Fig. 3-26. Removal of EF coil #3 is a four-phase operation.

removed to create the pit area into which the coil is moved. One hundred and eighty degrees of the lower cryostat wall is disassembled next to provide access under the device. Mobile stands with jacks are then placed under the coil at 20 locations. They are used to lower the coil from its support in the lower TF structure and provide the means for moving it into the pit area.

In Fig. 3-26 it can be seen that the initial coil translation has the most significant impact on the support structure. Four adjacent TF columns require removal and consequently, the installation of at least two temporary supports under the intercoil structure. As the coil is moved outward, the supports are intermittently removed and replaced. The same procedure is followed when the coil intersects the torus support columns. When the coil is finally positioned in the pit area, it is removed with the overhead crane.

The reverse procedure is required for the installation of the replacement coil. The impact of this replacement operation on machine availability is severe considering the duration time of 7 months (see Table 3-12). It is obvious that a high degree of reliability for fail safe operation of the superconducting coils is essential.

EF coils #1 and #4

These are the two interior copper coils located above and below the plasma chamber. Locating the equilibrium field coil system close to the plasma has distinct performance advantages and results in a relatively simple coil system. It was originally thought that the vertical opening of the TF coil/cryostat window would provide the necessary access for coil replacement. As it turned out, the structural requirements for reacting the out-of-plane TF coil loads would not permit a large enough opening. Consequently, removal of these coils, particularly EF coil #4, is made extremely difficult because of limited access.

This problem is further compounded by the need for mechanical joints in the coils. Each turn is spirally wound so that disassembling a coil requires removing individual turns, layer by layer between joints. The coils are jointed at 180° to permit their initial installation as two

Table 3-12. EF coil #3 replacement

	Steps	Mode of operation	Duration (days)
1.	General device shutdown	A	1
	Cryostat warmup		14
	Remove pump systems	C/R	2
	Remove ducts and install shield plugs	R	1
2.	Remove reactor cell floor	C	21
	Remove lower cryostat wall	C	30
3.	Install mobile jacks	C	6
	Lower the coil assembly	C	1
4.	Remove (and replace) column supports as required	C	
	Install (and remove) temporary supports as required	C	
	Translate coil into pit	C	16
5.	Translate coil under device	C	
	Add and remove support structure as required	C	16
6.	Install coil	C	1
	Remove jacks	C	3
7.	Reassemble cryostat wall	C	45
	Install reactor cell floor	C	21
8.	Install ducts	R	1
	Install pump systems	R	2
	Cryostat cooldown	A	28
	TOTAL		209 days (7 months)

prefabricated segments. It has been assumed that the failed coil is cut up in place and removed, and the replacement coil installed in many layered pieces. This arrangement can require as many as several hundred joints for a 3-5 megamp coil.

A special-purpose manipulator system such as that shown in Fig. 3-27 may be required for disassembly of the mechanical joints. The figure shows the device positioned under EF coil #4. A summary schedule for the disassembly of these coils is presented in Table 3-13.

Fuel injector

The fuel injector system is a modular component consisting of the mechanical injector (either centrifugal or pneumatic) and a series of shielded duct sections. These can be separated from the plasma chamber by activating an isolation valve. The modules are track mounted on a support platform. The most likely module to experience failures is the mechanical injector which is located with abundant overhead and horizontal access. Like the pump system, it can be replaced without disturbing the vacuum integrity of the plasma chamber. It is estimated that a modular changeout of the injector system can be accomplished with contact operations, within one day after personnel entry into the reactor cell. Therefore, the total downtime will be less than two days, assuming spares are available.

Valves, pumps, ancillary equipment

The components in this category fit into the same mode of replacement as the fuel injector. If contact operations are an advantage, then <2 days of downtime can be expected. Many of these replacements may actually be done by remote means within the twenty-four hour shutdown period normally required for safe reactor cell access. This presumes that the components are designed to be efficiently handled by remote means.

ORNL-DWG 81-17023A FED

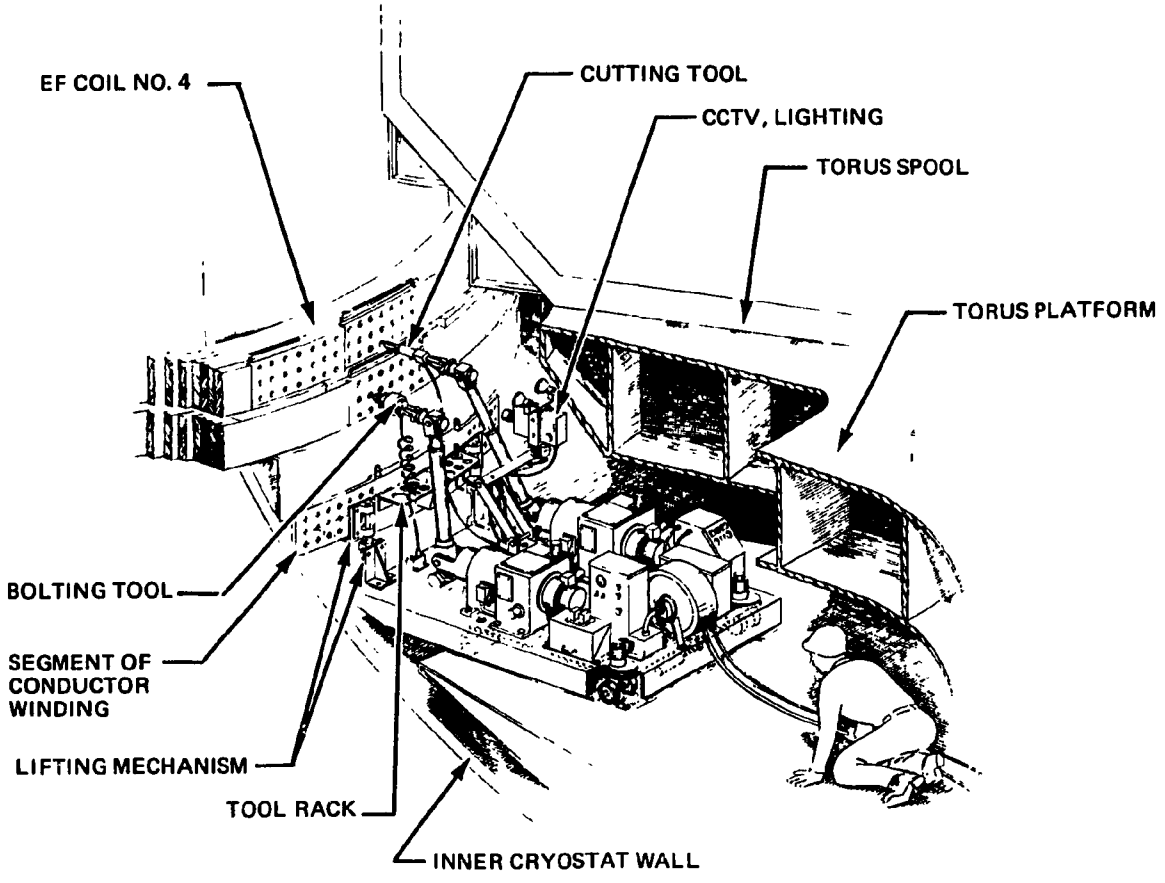

Fig. 3-27. Remote disassembly of EF coil #4.

Table 3-13. EF coil #4 replacement

	Steps	Mode of Operation[a]	Duration (hrs)
1.	General device shutdown	A	24
	Deenergize coils		
	Drain EF #4 of coolant		
	Activation decay to safe level		
2.	Remove limiter ducts (10)	C/R	40
	Install shield plugs (20)	R	40
	Lower coil onto platform	C/A	--
	Install tracks, hoists, disassembly tools; provide bay access as required	C	168
3.	Cut coil into segments and remove (300)	C	200
4.	Assemble and install jointed segments (300)	C	100
	Install bolts (3600)	C	100
	Braze coolant tubes (300)	C	25
	Insulate joints (300)	C	100
5.	Test completed system	C	48
	Remove tools and equipment	C	48
	Raise coil into position	A	--
	Remove shield plugs	R	20
	Install ducts	R/C	40
	Replace components cleared away for access	C	96
	TOTAL		1049 Hrs (43.7 Days)

TF coil

Replacement of a TF coil has a significant impact on device availability because it involves disassembling a large portion of the semi-permanent structure. The replacement scenario is presented in summary form as follows (refer to Table 3-14).

The two torus sectors adjacent to the failed TF coil are first removed. The open plasma chamber and the open vacuum ducts must then be covered with shield plugs in order to restore contact operations in the reactor cell for the remaining disassembly tasks. Removal of the cryostat dome is the next major disassembly and requires several intermediate steps (see Fig. 3-24):

1. Electrical and coolant leads to all PF and TF coils which emerge through the dome central cover are disconnected.
2. The dome central cover is removed using the overhead crane.
3. The ten helium reservoir interfaces on the dome are disassembled and removed (for pool boiling TF coils).
4. The circumferential interface of the dome flange to the cryostat is disassembled and the dome is moved to its laydown area using the overhead crane.

Removal of the upper external PF coil (EF #2) is accomplished using the overhead crane and is shown in Fig. 3-25. The laydown area for this large diameter coil is on top of the cryostat dome. Repositioning the lower external PF (EF #3) coil downward, clear of the TF coils, is the next major operation. This is accomplished using mechanical jacks. The exposed spool structure in the two adjacent open bays is the next major disassembly, and it is assumed that only half of each adjacent spool sector needs to be removed. An operation such as this will require extensive cutting of large, heavy structure and may also require the emplacement of temporary platforms and tracks to extract these components clear of the TF coil for overhead hoisting. At this stage, the disassembly and removal of a quadrant of each of the jointed interior coils, EF #1 and #4, are assumed. Each piece will weigh on the order of 20 tons and requires the use of boom-type cranes. The vertical frame support in the shadow

Table 3-14. TF coil replacement

	Steps	Mode of Operation	Duration (days)
1.	General device shutdown	A	1
	Cryostat warmup	A	14
	Remove two torus sectors and vacuum ducts	R	3
	Install shield plugs		1
2.	Remove cryostat dome	C	1
	Remove EF coil #2	C	1
	Lower EF coil #3	C	7
3.	Remove two half sectors of spool structure	C/R	12
	Remove EF coils #1 and 4	C/R	4
	Remove the vertical frame support	C	2
4.	Remove cryostat surfaces	C/R	10
	Remove a portion of the torus platform	C	2
	Disassemble the intercoil structure	C	4
	Unfasten the bucking cylinder interface	C	1
	Translate the coil outward and up using the overhead crane	C	1
5.	Replacement of the TF coil is assumed to take 50% longer than disassembly	C/R	75
6.	Cryostat cooldown	A	28
	TOTAL		168 days (5.5 mos)

of the TF coil is the next component to be removed. Because of the relative instability of this unsupported structure, large holding fixtures will be required during and after spool removal. Partial extraction is accomplished using the temporary platforms in order to clear the plane of the TF coil. Overhead hoisting then removes the frame because the cryostat dome (and hence the coil window) is not a constraint in this partially disassembled configuration. The inner cryostat surfaces which are also in the shadow of the TF coil are disassembled next. The cryostat containment around the outer leg of the coil can be left in place and removed as part of the TF coil assembly. (It may also be part of the initial TF coil assembly.) Disassembly of the inner cryostat wall and the spool requires extensive cutting of welded structure and therefore their joints must allow for the requirements of automated, remote equipment for both cutting and rewelding. Removal of all of these cut segments is through vertical access using the overhead crane. Removal of the torus platform structure in the plane of the TF coil is the last operation prior to removing the TF coil. The final step is to provide lateral and vertical support to the TF coil when unfastening the shear and moment connections to the bucking cylinder and the intercoil structure, and this is accomplished using the overhead crane. The crane then moves the coil outward and up after its outer leg support is unfastened.

The total time estimate for the TF coil replacement assumes that a spare coil is available.

3.2.3 Conclusions

The FED configuration is the result of the integration of component designs for all of the major systems and components. The changes from earlier design studies were derived from a better understanding of performance and cost, guided by the need to improve maintainability. Without the influence of maintenance considerations, each of the systems would have been developed around its own particular needs, and it is likely that the configuration would lack reasonable access and disassembly capability. Hence, configuration development must go hand in hand with device maintainability.

The purpose of this study was to gain a better understanding of the relationship between maintenance and availability, or more specifically, to determine the impact of maintenance tasks on downtime. One fact that clearly emerges from studying the replacement scenarios for the major systems is that the unscheduled occurrences dominate the potential downtime of the device. Perhaps that should not be surprising, except that most of these components, even though they are high-reliability, lifetime designs, do have a small probability of failure. The results then, for this first level of study, indicate that further improvements in the configuration must be developed to lessen the possible impact of component replacements on the operating lifetime.

Future work should include not only configuration changes related to the above discussion, but also more in-depth studies of disassembly which will further define the steps involved, their required time, and the maintenance equipment and concepts required. In addition, concepts for in-vessel inspection and operations should be investigated. These include routine inspection systems which do not impact device availability and a manipulator concept which can operate in the plasma chamber.

3.3 AVAILABILITY

A fundamental consideration in the design of FED is that the availability* which FED is capable of achieving be commensurate with the availability required by the plan of operations. The availability which FED is capable of achieving is determined by the reliability, maintainability, and supportability characteristics of the design and by scheduled maintenance requirements. The following sections describe FED availability requirements stemming from the proposed plan of operations and the results of a preliminary assessment of FED availability.

---

*Availability is defined by the ratio of operating time to operating time plus downtime. For the purpose of this analysis, all nonoperating periods were assumed to be downtime periods wherein essential maintenance would be accomplished.

3.3.1 Availability Requirements

A plan has been proposed which integrates FED testing requirements into sequenced phases of operation and establishes guidelines for operation in each phase. Table 3-15 summarizes the phases of operation, operating guidelines, and the estimated number of pulses associated with each phase. The availability shown is that associated with accomplishing the indicated number of pulses in the time allotted.

The lower level of availability requirements shown in earlier phases is consistent with the operational constraints which are expected to impact initial FED operation. These operational constraints include:

- Hardware checkout and software debugging
- "Infant mortality" failures due to deficiencies in initial design fabrication and assembly
- Initial unfamiliarity with maintenance procedures
- Incorporation of design upgrades for improved performance

During Phase IV, there will be a period of 10-T operation for which a year has been allotted. Due to uncertainties about operational constraints in earlier phases (as enumerated above) and the impact of 10-T operation on availability, an availability assessment was made for Phase IV 8-T operation only. It should be noted that Phase IV 8-T operation includes 65% of FED operating time and, hence, is most critical with respect to availability.

Phase IV 8-T operation has been estimated to involve approximately 200,000 pulses in a five-year period. Assuming a pulse length of 152 s, FED would have to achieve an availability greater than 19% in order to complete the indicated operations in the time allotted. Nominal operation will be for six days per week with two (eight hour) operating shifts per day. (Maintenance crews were assumed available around-the-clock, seven days per week.) A two-week period every other month has been identified for scheduled maintenance and reconfiguration activities. FED would have to operate 45% of the scheduled operating time in order to achieve an availability of 19%.

Table 3-15. FED plan of operations

Phase	Duration (years)	Description	Operating Guidelines[a]	Number of Pulses	Average Availability[b]
I	0-1.0	Integrated system checkout	6 days/week 2 shifts/day Downtime of 2 weeks/month	15,000 (≤8 T)	0.07
II	1.0-3.0	Hydrogen (deuterium) operation	6 days/week 2 shifts/day Downtime of 2 weeks/2 mos.	50,000 (≤8 T)	0.12
III	3.0-4.0	D-T plasma burn	Same as Phase II	25,000 (8 T)	0.12
IV	4.0-10.0	D-T engineering testing	Same as Phase II	200,000 (8 T) 25,000 (10 T)	0.19 0.08

[a]The assumptions of operations 6 days/week, 2 shifts/day and the indicated periods of downtime per month are used solely to estimate the number of expected pulses in each phase of FED operations. It is not meant to imply the manner in which the device may actually be operated in any given week or month. Once available to operate, the device may actually run 7 days/week, 3 shifts/day and the actual frequency of pulses will be governed by the testing requirements; some testing will require continuous operation at the reference duty cycle of repeated pulses every 152 s.

[b]Pulse lengths of 152 s for 8-T operation and 102 s for 10-T operation were assumed.

3.3.2 Availability Assessment

FED availability and operating characteristics were assessed using a computer model which simulates machine operation from a reliability, availability, maintainability standpoint. Primary inputs to the model comprise equipment failure rates and repair times. Outputs for each item of equipment include: number of maintenance activities; operating time, down time, and idle time; and availability. Outputs are provided at four levels ranging from individual items of equipment (level 3) to the complete machine (level 0).

Numerous sources of failure rate data exist for conventional equipment such as might be found in a nuclear or fossil fuel plant. Estimating failure rates of equipment peculiar to fusion applications is more difficult. Records which would be useful in quantitatively characterizing the reliability of equipment peculiar to fusion devices are not currently available. In the absence of historical information, failure rates were generated by examining component design, noting similarities to conventional equipment, and estimating failure rates accordingly. Repair rates were generated by performing task time analyses for the repair procedures. Considerable work remains to be done in the generation of failure and repair rates before high confidence can be placed in FED availability assessments.

For the baseline availability assessment, it was assumed there would be no delays due to lack of spares or unavailability of maintenance equipment or technical expertise. These factors, coupled with the lack of detail in the reference design, tend to make the baseline availability assessment somewhat optimistic.

Analysis indicated that FED could operate 48% of the time it was scheduled to operate, demonstrating an availability of 21%. Failures requiring suspension of operation can be expected on the average every 43 operating hours ($\sim 10^3$ pulses). The majority (67%) of these failures should be minor, requiring less than a day to effect repair. However, due to the influence of failures requiring extended downtimes (>1 week), the mean time to repair failures is $\sim$3.5 days.

Table 3-16 shows typical availabilities for some of the major FED systems. This table indicates that the prime availability drivers are the coil system and torus system.

Table 3-16. FED system availabilities

System	Availability
Coil systems	0.51
Torus system	0.62
RF heating system	0.84
Fueling system	0.99
Vacuum pumping system	0.99
Reactor control system	0.75
Ex-reactor systems	0.72
FED TOTAL	0.21

Scheduled maintenance activities also have a major impact on FED availability. Under the proposed plan of operation, FED is scheduled to operate only 43% of the time. Recognized scheduled maintenance operations include:

- pump limiter replacement,
- test module changeout,
- tritium inventory,
- turbomolecular pump oil changes and bearing replacements.

Two-week periods have been allotted for scheduled maintenance because much of the scheduled maintenance activity will require letting the torus up to air, e.g., pump limiter replacement and unpocketed test module changeout. Once the torus is let up to air, a week is required for pumpdown/bakeout to the desired pressure. The actual maintenance would be performed in the first week. The availability characteristics of select FED systems are discussed in the following section.

3.3.3 FED System Availabilities

Coil systems

FED coil systems rank as the foremost availability driver on FED with an availability of ∿51%. Coil systems include all FED coils, cryostat, and associated equipment, e.g., leads, plumbing, and instrumentation. Coil power supplies were considered with balance of plant systems. The FED coil configuration is shown in Fig. 3-28.

A key factor determining coil system availability is the time required to warm up superconducting coils to room temperature for maintenance and subsequently cooling the coils down to cryogenic temperature for operation. For this analysis, it was assumed that the combined warmup/cooldown time would be six weeks. For most superconducting coil related maintenance, this period is substantially longer than the active repair time. Figure 3-29 shows the sensitivity of coil system availability and Phase IV 8-T mission time to warmup/cooldown time.

The coil system availability drivers and associated availability parameters are listed in Table 3-17. In terms of generic equipment, vapor-cooled leads appeared to have the greatest impact on availability. The current FED configuration features 34 vapor-cooled leads. A failure rate of 5×10^{-6}/lead-hour was assumed which, although better than past experience, seems reasonably achievable. During 5 years of Phase IV 8-T operation, 3.3 vapor-cooled lead failures would be expected. Allowing 6.5-7.0 weeks to repair a lead failure (including a 6 week warmup/cooldown period), approximately 5 months of downtime would be accrued to lead failures.

Two important assumptions made in assessing the impact of vapor-cooled leads on FED availability were:

1. A lead failure would require warming the superconducting coils up to room temperature to effect repair.
2. Expected lead failure modes, e.g., vapor channel blockage, would not precipitate coil failures.

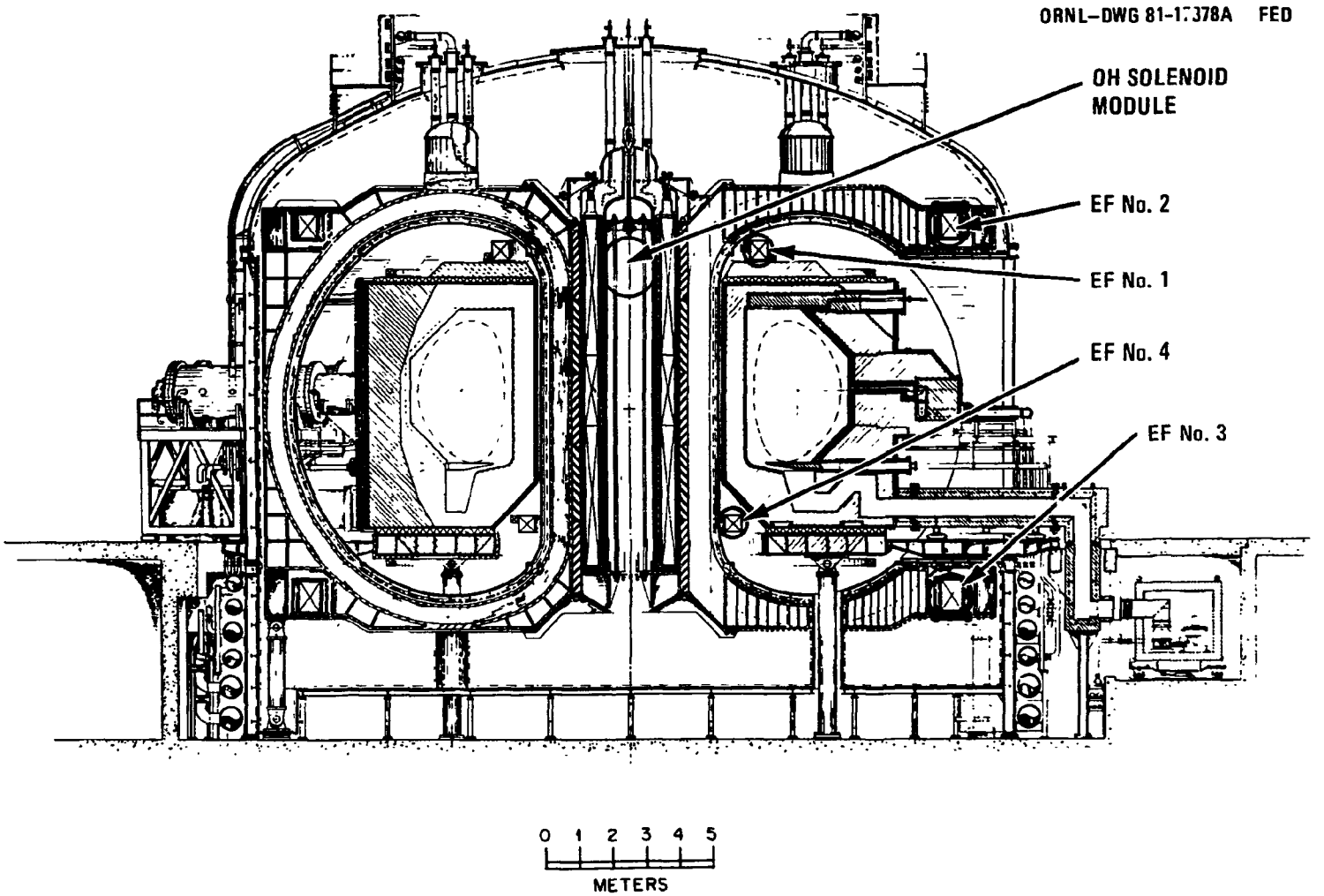

Fig. 3-28. FED coil system configuration.

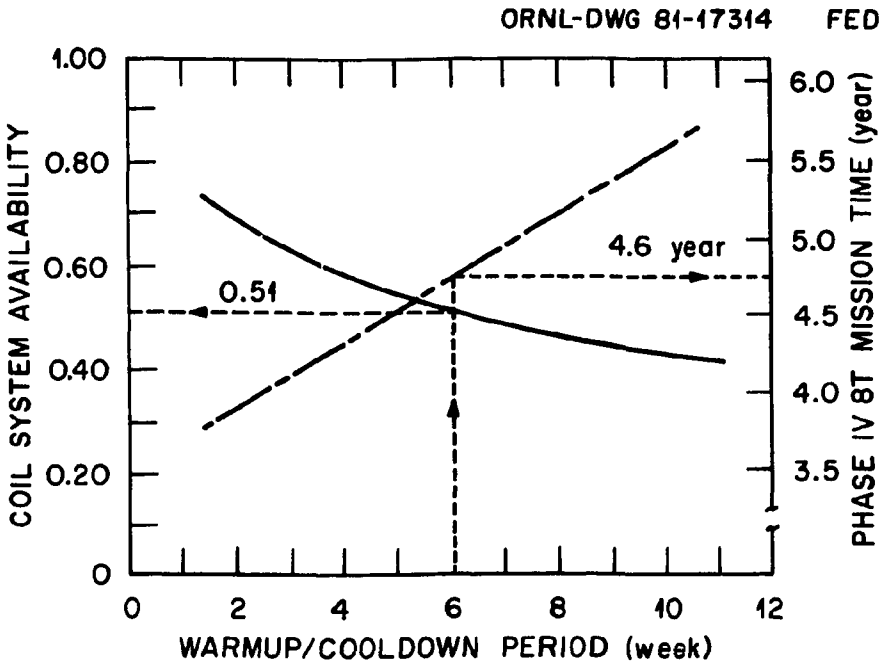

Fig. 3-29. Coil system availability and FED mission time are sensitive to the warmup and cooldown time for superconducting coils.

Table 3-17. Coil system availability drivers

Equipment	Failure Rate			Downtime	
	$\lambda \times 10^6/h$[a]	DF[b]	N[c]	T[d]	N×T
Vapor-cooled leads (34)	5.0	0.1-0.5	3.3	6.5-7.0 w	5.0 m
LN2 shielding (1000 $2m^2$ panels)	0.04[e]	1.0	1.7	2-6 m	4.2 m
TF coils (10)	2.8	0.2	0.4	6 m	2.5 m
PF solenoid	8.8	0.1	0.10	8 w	5.8 d
EF1	8.5	0.1	0.10	5 w	3.5 d
EF2	7.9	0.1	0.09	8 w	4.9 d
EF3	11.4	0.1	0.13	7 m	4.0 w
EF4	7.5	0.1	0.09	6 w	3.9 d

[a]Failure rate for an individual module (failures/hr).

[b]Failure rate multiplier during nonoperating periods.

[c]Expected number of failures for all modules.
$N = Q\lambda(8,444 + DF[31,429])$

[d]Downtime per failure (hrs).

[e]Failure rate per panel.

Among FED coils, TF coils were found to have the greatest impact on FED availability. It is difficult to accurately predict FED coil reliability. Existing experience is too limited and application and technology too different to predict superconducting coil reliability on the basis of the sketchy historical data which exists. While copper coils have had more widespread application, no systematic quantitative compilation of copper coil failure rates appears to have been made.

For the purpose of this analysis, coil failure rates were assumed to scale directly with conductor length (L). The failure rates used are listed in Table 3-18. It may be seen that the base failure rate (λ_o) assumed for TF coils is an order of magnitude less than for the superconducting PF coils. One reason for this is that TF coils should be more tolerant of turn-to-turn shorts. Turn-to-turn shorts can be accommodated by controlling the charge and discharge time on TF coils. On PF coils, turn-to-turn voltages are fixed by the current waveforms. The conductor used for TF coils (10 kA vs 50 kA) should also exhibit a lower failure rate on a per length basis.

Table 3-18. FED coil failure rates

Coil	Type	$\lambda_o \times 10^6$/km-h	L(km)	$\lambda \times 10^6$/h
TF	S/C	0.1	28.3	2.8
EF1	N	0.5	0.97	8.5[a]
EF2	S/C	1.0	6.9	7.9[b]
EF3	S/C	1.0	10.4	11.4[b]
EF4	N	0.5	0.67	7.5[a]
Blip	N	0.5	0.18	0.8[a]
Solenoid	S/C	1.0	8.8	8.8

[a]Overall failure rate increased by 0.1×10^{-6}/h per joint-turn.

[b]Overall failure rate increased by 1.0×10^{-6}/h to account for helium leaks through nonmetallic case.

It may also be seen that the base failure rate for normal PF coils is half that of the superconducting PF coils. This assumption was based on qualitative consideration of coil failure mechanisms. Aside from the inert nature of LHe as a coolant, it seemed that superconducting coils would be comparable to or more sensitive than normal PF coils to postulated failure mechanisms.

Because of the lengthy downtimes associated with superconducting coil failures (especially TF coil failures), coil reliability is a key determinant of FED availability. Coil reliability must be "designed in" on a theoretical and historical basis and "built in" through extensive testing of materials and processes involved in coil construction. At this stage of design evolution, serious consideration should be given to evaluating superconducting coil design alternatives on the basis of reliability characteristics. These design alternatives include:

- conductor material (NbTi or Nb_3Sn)
- heat transfer mechanism [forced flow or pool boiling (natural convection)]
- voltage capability
- internal construction

By actively seeking to optimize coil reliability on a theoretical basis and incorporate lessons learned from past experience, the probability of successful FED operation is enhanced.

One potential coil system availability driver which had not been highlighted in previous availability studies of devices similar to FED is the LN2 shielding on the inner wall of the cryostat. There is >2000 m^2 of LN2 shielding area required on the inner wall of the cryostat. On the Large Coil Project, this shielding is in the form of panels having an area of about 2 m^2. Each panel has six LN2 ports. Assuming a similar configuration for FED, this corresponds to >1000 LN2 panels and considerable associated plumbing. Because of the benign environment (very low stress, relatively inert coolant), leaks should be an infrequent occurrence notwithstanding the size of the system once the system has been thoroughly leak tested. With an assumed failure rate of 0.04

failures per million panel-hours, 1.7 failures would be expected over the period of 8-T Phase IV operation.

For this analysis, it was assumed that a leak would have to be repaired. The superconducting coils would be warmed up to room temperature and the cryostat brought to atmospheric pressure. The procedure for isolating LN2 leaks (and cryostat vacuum and coil LHe leaks) has not yet been established. However, some potential failure locations, e.g., the central cylindrical and toroidal shells, promise to be especially problematic for repair as well as fault isolation. If leaks would not have to be repaired, i.e., panel sections could be valved off, the potential impact on availability would be greatly reduced.

Torus system

The torus system ranks behind the coil systems as an FED availability driver with an availability of 62%. The torus system includes the spool assembly, first wall, pump limiter, bulk shielding, and associated equipment. The system configuration is shown in Fig. 3-30.

A key factor in determining torus system availability and overall FED availability is the time required to pump the torus down to an initial base pressure of 10^{-7} torr prior to resuming operation once the torus has been let up to air. In order to accomplish pumpdown in a reasonable period of time, the inner surface of the torus must be kept at an elevated temperature. The current scheme for pumpdown/bakeout calls for circulating hot N2 gas through the coolant passages to elevate surface temperatures. For this analysis, pumpdown/bakeout was assumed to require one week once the vacuum integrity of the torus system has been restored.

There are many maintenance actions for which the torus might be let up to air. These include:

- pump limiter, first wall panel, armor, and shield sector module removal;
- removal of unpocketed materials test modules and blanket modules;

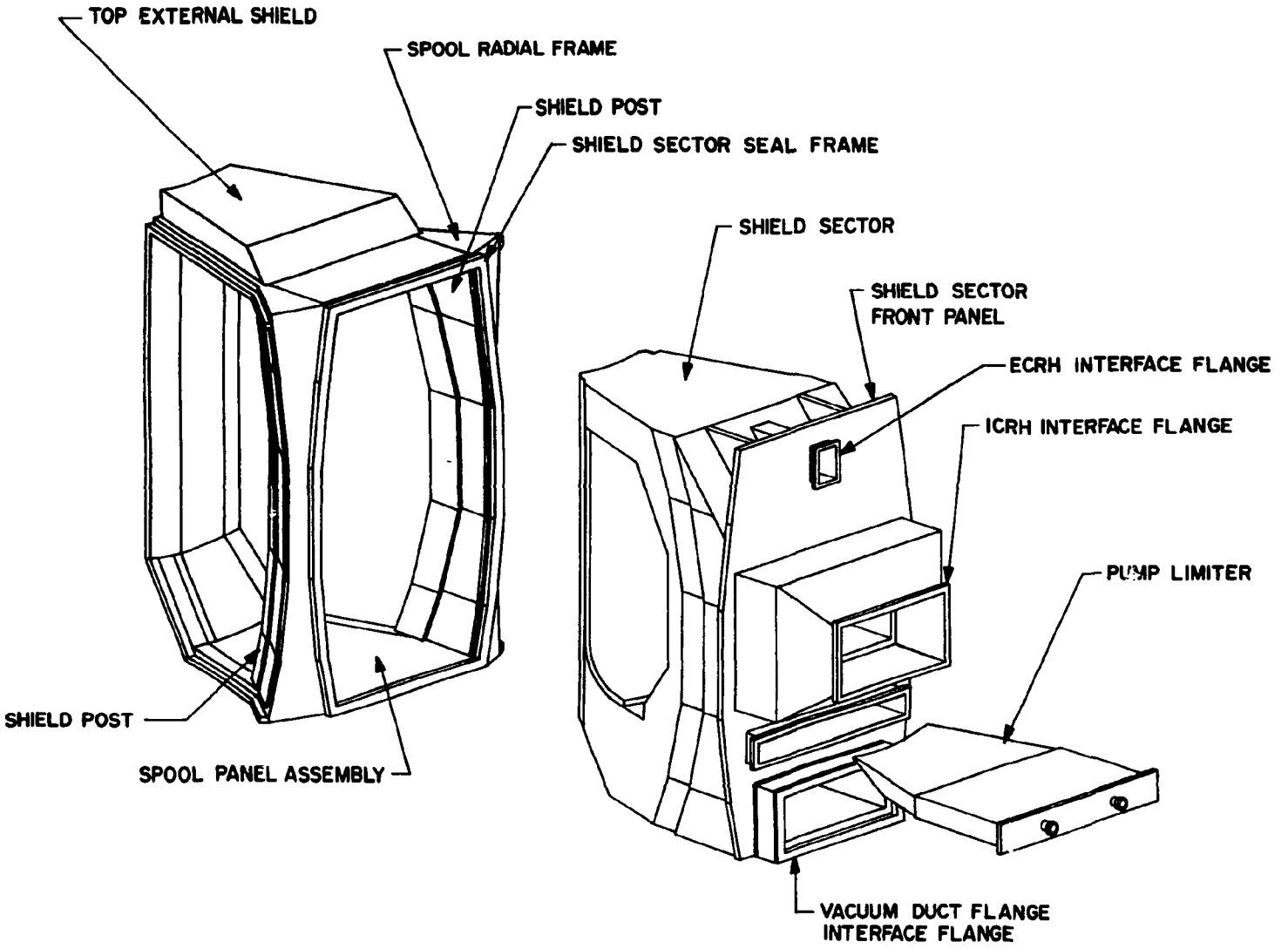

Fig. 3-30. FED torus system components.

- removal of diagnostics requiring direct access to the plasma chamber;
- ICRH/ECRH launcher maintenance;
- in-chamber inspection;
- vacuum pumping duct/valve maintenance.

Figure 3-31 shows the sensitivity of torus system availability and Phase IV 8-T mission time to pumpdown/bakeout time.

Torus system availability drivers and associated parameters are listed in Table 3-19. All of the components listed as availability drivers operate in an extremely harsh environment. Environmental considerations include:

- prolonged exposure to a pulsed surface heat load and high energy neutron flux;
- exposure to off-normal conditions such as disruptions, runaway electrons, arcing, and mechanical shock from dislocated tile fragments;
- plasma requirements for high vacuum and low impurity concentrations means the system will be sensitive to minute coolant leaks and other seemingly minor failures.

Repair times are necessarily long because of the extended period required for pumpdown/bakeout of the torus (1 week). As more depth is added to the design, a better understanding of the peripheral equipment impeding torus system maintainability and of remote maintenance equipment limitations will increase. This is likely to result in longer repair time estimates.

The spool assembly did not appear as an availability driver. Spool panel assemblies and panel/frame seals were assumed to have a secondary vacuum boundary with a differentially pumped region in between. Under these assumptions, spool panel assembly failures requiring repair should be a very infrequent occurrence on FED.

Table 3-19 reflects the impact of limiter modules on availability for unscheduled maintenance only. Limiter modules are life limited components which must be replaced on a scheduled basis. Lifetime estimates

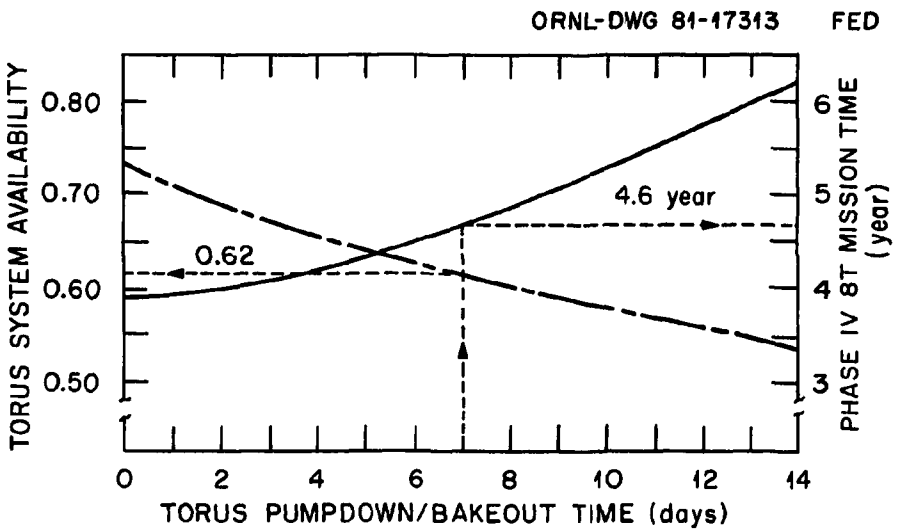

Fig. 3-31. Torus system availability and mission time are sensitive to torus pumpdown/bakeout time.

Table 3-19. Torus system availability drivers

	Failure Rate			Downtime	
	$\lambda \times 10^6/h^a$	DF^b	N^c	T^d	N×T
First wall panels (60)	10.0	0.0	5.1	3.1 w	3.7 m
Armor tiles (6500)	0.05	0.0	2.7	1.7 w	4.7 w
Limiter modules (10)[e]	30.0	0.0	2.5	1.4 w	3.6 w
Sector modules (10)	9.0	0.0	0.8	3.1 w	2.4 w

[a]Failure rate for an individual module.

[b]Failure rate multiplier during nonoperating periods.

[c]Expected number of failures for all modules

$$N = Q\lambda[8,444 + DF(31,429)] .$$

[d]Downtime per failure.

[e]Not including scheduled replacements.

range from 6,600-170,000 pulses during Phase IV 8-T operation. This corresponds to replacement periods of two months to four years, assuming FED operates 48% of the time scheduled for operation. The two-week period every other month which has been assumed for scheduled maintenance can readily accommodate scheduled limiter replacement. Scheduled limiter replacement impacts availability only to the extent that it drives the frequency or duration of scheduled maintenance periods. The impact of scheduled limiter replacement on availability is thus indeterminate until other scheduled maintenance requirements, e.g., test module changeout, become better defined.

Vacuum pumping system

The vacuum pumping system features 20 pumping stations located beneath removable sections of reactor cell floor. The pumping stations are connected to the torus in pairs through 10 pumping ducts (one per bay). Each pumping station includes a turbomolecular pump backed by a first stage scroll pump, isolation valves and valve operators, and bellows. The pumping stations will be encased in magnetic shielding.

The combined failure rate for pumping station components was assessed to be $\sim 100 \times 10^{-6}$/station-h. Recognizing that the vacuum pumping system will often be operating when FED is inoperative, it was estimated that $\sim$50 pumping station failures will occur during Phase IV 8-T operation. The availability impact of these failures is mitigated by the fact that not all pumping stations need be operating to sustain FED operation. For the purpose of this analysis, it was assumed that 16 pumping stations would be required to sustain FED operation and that for virtually all pumping station failures, the failed station could be isolated and operations continued without interruption.

The vacuum pumping system is being designed in such a way that backstreaming of bearing lubricant does not pose a serious problem. Also, the potential for multiple pump failures due to a single event, e.g., sudden pressurization of the torus, will be safeguarded in pump design or protection provisions.

The turbomolecular pumps will require periodic maintenance for oil change (six months) and bearing replacement (three years). Under the assumed schedule of operations, both maintenance requirements can be readily accommodated.

Other system components include a second stage backing pump and a master controller. Neither should significantly impact availability. Overall, vacuum pumping system availability was assessed to be 99%.

Fueling system

Fueling is accomplished via pellet injection and gas puffing. Pellet injection requirements for 8-T operation are for 4-mm-diameter pellets to be injected at velocities up to 2 km/s at rates of 16/s during startup and 8/s during burn. Two pellet injectors are featured in the present FED design. Each injector has an injection rate capability of 20/s. FED operation could thus be sustained in the event of a single injector failure.

Pellet injectors capable of satisfying FED requirements have yet to be developed. It is not clear whether they will be of pneumatic or centrifugal design or what degree of reliability can be achieved. For this analysis, a failure rate of 200×10^{-16}/h was used per pellet injector assembly.* Six injector assembly failures would be expected during the period of 8-T Phase IV operation. However, due to the fault tolerant nature of the system and the frequent maintenance opportunities for restoring failed injector assemblies, the impact of injector assemblies on availability was not significant.

The gas puffing system provides the initial gas charge after torus evacuation and a means of plasma edge control during startup and burn. The gas puffers are essentially selector valves and nozzles located around the torus. Gas flow to the puffers is controlled by pulsed control valves. The proposed configuration features adequate fault tolerance to preclude a significant impact on availability.

The availability of the fueling system was assessed to be 99%.

*Pellet injector plus pellet formers.

RF heating system

The proposed FED design features both ICRH and ECRH microwave heating systems. Fifty megawatts of ICRH is required during startup with 36 MW required during burn. One megawatt of ECRH is required during startup only.

ICRH power is transmitted to the plasma through four ridge-loaded launchers. The launchers have envelope dimensions of 0.3 m height, 2.0 m width, and 2.0 m depth. Power is supplied to the launchers through coaxial waveguides. Failure of a launcher or coaxial waveguide would constitute a system failure since the 50 MW startup requirement could no longer be met and since, in the event of a launcher failure, operation would likely be precluded due to coolant leakage.

On the other hand, the equipment required for ICRH generation (amplifiers, oscillators, power supplies, et al.) is configured with back-up capability. Most failures can be accommodated by increasing the power level in remaining channels. A "bottoms-up" assessment of ICRH generating equipment availability has not yet been made. However, an availability of 96% should be readily achievable if the system is designed to be fault tolerant.

A greater impact on availability can be anticipated from the ICRH launchers. The launchers are passive components but channel considerable power. A prime concern about launcher reliability is the occurrence of arcing in the presence of debris eroded or fragmented from the first wall. For this analysis, a failure rate of 75×10^{-6}/h was assumed per launcher. Over the period of 8-T Phase IV operation, 2.5 failures would be expected. System downtime accrued due to launcher failures would be ∿3.6 weeks. Launcher availability would be 93%. The availability of the ICRH system was assessed to be 88%.

ECRH power is transmitted to the plasma through 10 tubular (∿6.5 cm ID) waveguides with a step reflector. The waveguides are pressurized with SF_6 gas. The gas is contained by a window which is optically hidden from the plasma. The current configuration is capable of delivering 1.2 MW although the requirment is only 1.0 MW. Considerable fault tolerance is thus provided, at least for the ECRH generating equipment. The ECRH

system should be capable of demonstrating an availability of 95%. Overall, the availability of the rf heating system was assessed to be 84%.

Reactor control system

In order to achieve repeatable, long pulse operation on FED, a multifunction integrated control system is required. In the language of control theory, the systems discussed thus far have been effectors. For this analysis, "reactor control system" refers to all control system elements except the effectors. These elements can be grouped in two categories: sensors (diagnostics) and signal conditioning/data processing equipment.

Numerous diagnostics are required for control. Table 3-20 lists some control diagnostics, quantity required, and monitored parameters. While the diagnostics requirements have been defined, the diagnostics have not yet been integrated into FED design. It is therefore not yet possible to make a "bottoms up" assessment of the availability parameters characterizing each of the control diagnostics.

In general, sensitive instruments operating in a harsh environment (such as a D-T fusion plasma) are prone to failure. Diagnostic maintainability will be less than desired in many cases because the torus may have to be let up to air to effect repair. If in the period of 8-T Phase IV operation there are 10 diagnostic failures, each requiring ∿10 d to repair (1 d for cooldown, 2 d for active repair, and 7 d for pumpdown/bakeout), diagnostics availability would be 78%. For this analysis, such an availability was considered a reasonable allocation.

The signal conditioning/data processing elements of the reactor control system has not yet been defined. Based on specifications for other large signal conditioning/data processing systems, an availability of 96% was allocated for signal conditions/data processing elements.

Overall, the allocation for reactor control system availability was 75%.

Table 3-20. FED control diagnostics

Diagnostic	Quantity	Parameter
$\dot{B}$ loops	2 sets of 30	Plasma shape
Rogowski loop	2	Plasma current (I_p)
Saddle coils	4	Plasma position
FIR interferometer array	10 vertical	Electron density (n_e)
2 ω_{ce} detector array	10 horizontal	Electron temperature (T_e)
Charge exchange	10	D-T density (n_o, n_T)
Bolometers, radiometers	2 arrays	Radiated power (P_r)
Spectrometers	8 systems	Impurity composition and concentration
Neutron collimators	10 vertical 7 horizontal	Counters and collimation for space and time resolution of neutron production
Soft x-ray array	2 arrays	--
Faraday rotation	1	Current density distribution

Ex-reactor systems

Ex-reactor systems include those systems whose elements are not integral to reactor device. The focus of FED design to date has been reactor design. Relatively little emphasis has been placed on the design of ex-reactor systems.

For this analysis, availability allocations rather than "bottoms up" assessments were made for ex-reactor systems. Some ex-reactor systems are renowned "bad actors" on currently operating fusion devices, notably PF power supply systems and cryogenic systems. The availability allocations for these systems may seem insufficient based on past experience. However, the allocations are intended to reflect reasonably achievable availabilities when greater economic incentive exists for availability and a higher level of support is provided than on currently operating fusion devices.

Table 3-21 lists the ex-reactor systems and their respective availability allocations. The collective availability allocation for ex-reactor systems is 72%.

Table 3-21. Ex-reactor system availabilities

System	Availability
Heat transport system	0.96
Electrical power distribution system	0.99
PF power supply system	0.96
TF power supply system	0.99 +
Fuel processing system	0.98
Cryogenic systems	0.90
Testing systems	0.90
Facilities systems	0.98

3.3.4 Reliability, Maintainability, and Supportability

Reliability

FED reliability has been a concern to date only insofar that availability would be impacted by poor reliability. There may be reliability requirements that are divorced from the availability requirements previously discussed. The FED test program features tritium breeding blanket module testing as an important goal. Any follow-on to FED would be responsible for supplying the bulk of its tritium requirement. In order to assess blanket module performance on FED, long periods ($>10^3$ cycles) of continuous operation are required. FED reliability was found to be consistent with this requirement.

Maintainability

Maintainability is a measure of ability to restore a device to an operational condition. A maintainable design is essential to satisfying FED availability requirements. FED configuration has been driven by maintainability considerations. The establishment of a window for sector removal, an equal number of torus segments and TF coils, and a bottom limiter which can be removed independently of the vacuum ducting are good examples. However, much design work is yet required to assure adequate maintainability, especially in the areas of fault detection and isolation and remote maintenance system design and integration.

Supportability

A device such as FED will be subject to scheduled and unscheduled maintenance. In order to perform maintenance in a routine and efficient manner, provisions must be made for:

- Spares
- Maintenance equipment
- Facilities accommodations for maintenance

Supportability is a term which describes the cost and feasibility of making these provisions.

Spare components would be required to avoid excessive downtimes associated with waiting for a failed component to be repaired or waiting for a replacement component to be fabricated when the failed component is beyond the limits of economical or feasible repair. On FED, the question of spares is critical because many reactor components will be custom made rather than off-the-shelf items. There will often not be any vendors or other facilities from whom a spare could be procured on short notice.

Table 3-22 lists FED spares costs (for full initial coverage) and associated parameters for several major FED components. One indicator of supportability is the ratio of the cost of procuring initial spares to the cost of components installed (C_S/C_I). A high ratio indicates poor supportability. Components in Table 3-22 exhibiting high ratios include the superconducting EF coils, sector modules, and first wall panels. Supportability can be improved by increasing commonality in design. For the superconducting EF coils, for example, this could be accomplished by dividing each coil into several identical smaller coils which would be vertically stacked. There are at least five and perhaps as many as ten noninterchangeable sector modules. Variations between sector modules appear confined to the outboard leg. If the portion of the outboard leg where variations occur was made a separate module, supportability would be greatly enhanced. A similar lack of commonality exists for first wall panels. However, it is not clear what options are available to improve supportability of first wall panels.

In Table 3-22, a distinction is made between the cost of procuring initial spares (C_3) and the cost of providing initial spares (C_3'). For components beyond feasible or economical repair (such as those shown in Table 3-22), the cost of providing initial spares is simply the cost of procurement multiplied by the probability that the procured item would not be used (neglecting the time value of money). Consider for example, a component which is sure to fail in the life of FED. The cost of providing initial spares would be nil because a replacement item would have to be procured upon the first failure if not procured initially.

Table 3-22. FED spares costs and associated parameters for selected components

Component	Unit Cost	Installed[a]		Spares[b]		C_s/C_I[c]	P_o[d]	C_s'[e]	T_s[f]	T_s'[g]	C_s'/T_s'[h]	Resource Priority
		N_I	C_I	N_S	C_S							
TF Coil	$12M	10	$120M	1	$12M	0.10	0.67	$8M	1Y	4M	$2,700/h	6
TF V-C Lead	$5K	20	$100K	1	$5K	0.05	0.14	$700	1M	3.7W	$1/h	1
EF2 Coil	$20M	1	$20M	1	$20M	1.00	0.91	$18.2M	6M	2.3W	$47,000/h	10
EF3 Coil	$30M	1	$30M	1	$30M	1.00	0.88	$26.4M	8M	4.2W	$37,000/h	9
EF2/3 V-C Lead	$10K	4	$40K	1	$10K	0.25	0.67	$6.7K	1M	10d	$28/h	4
Solenoid Pancake	$300K	60	$18M	1	$300K	0.02	0.90	$270K	2M	6d	$1,850/h	5
Solenoid V-C Lead	$10K	10	$100K	1	$10K	0.10	0.37	$3.7K	1M	2.7W	$8/h	2
First Wall Panel	$90K	60	$5.4M	30	$2.7M	0.50	0.01	$2.3M	1M	1M	$3,150/h	7
Sector Module	$8M	10	$80M	7	$56M	0.70	0.45	$48M	6M	3.3M	$19,900/h	8
ICRH Launcher	$100K	4	$400K	1	$100K	0.25	0.08	$8K	1M	4.0W	$12/h	3

[a] Number and cost of components procured for installation.

[b] Number and cost of components initially procured for full spares coverage.

[c] One indicator of supportability; a high ratio indicates poor supportability.

[d] Probability of no failures, i.e., probability that spare would not be utilized, in Phase IV 8-T operation.

[e] Cost of providing initial spares; $C_s' = P_o \times C_s$ for nonrepairable components (neglecting the time value of money).

[f] Downtime saved by initially providing a spare given a failure.

[g] Downtime saved by initially providing a spare; $T_s' = (1-P_o)T_s$.

[h] Figure of merit for allocating resources.

The figure of merit for allocating resources is the ratio of the cost of providing initial spares to the downtime saved by initially providing a spare (C_s'/T_s'). The dimensions would be \$/h. In order to determine a cost effective level of spares support, a determination has to be made for the rate at which FED costs accrue during downtime periods (\$/h). Initial spares would be provided for those components whose figure of merit was less than that rate. For example, if FED costs accrued at \$1,000/h during downtime periods, initial spares would not be procured for TF coils, PF coils, sector modules, or first wall panel sections (under the assumptions of this analysis). The availability impact of not sparing those items alone would be to reduce FED availability from 21% to 18%. The expected time required to complete 8-T Phase IV operations would be extended by approximately ten months.

For components with limited lifetimes or high failure rates, support costs can exceed initial installation costs. The prime example is limiter modules. Limiter life will be determined by yet uncertain plasma conditions. Lifetime estimates range from 6,600-170,000 pulses during 8-T Phase IV operation. If a log mean lifetime of 33,500 pulses is assumed, six limiter module replacements would be required during 8-T Phase IV operation alone. The cost of replacement limiter sheaths would be ∿\$12 M as compared to a \$2 M initial installation cost.

Support costs are not limited to spares costs. Maintenance equipment costs must also be included. On FED, the cost of maintenance equipment is expected to be ∿\$33 M for the reactor cell and \$27 M for the hot cell. Facilities accommodations for maintenance also impact support costs.

On FED, it is imperative that the reactor design be supportable to make most efficient use of the resources which will be provided to support FED and minimize the impact of support on availability.

3.3.5 Conclusions

The availability characteristic of the present FED design appears consistent with the availability required by the FED plan of operation.

Considerable work remains to be done in improving availability assessments, evaluating the availability impact of design alternatives, and promoting cost effective availability improvements for FED design.

3.4 SYSTEM TRADE STUDIES

In order to help define and interpret the Fusion Engineering Device (FED), the trade studies listed in Table 3-23 were conducted using the FEDC system code.[6] The results of many of the trade studies have been used in other sections of this document or have been reported in ORNL/TM-7777.[7] This section summarizes the results of the studies listed in Table 3-23.

3.4.1 Comparison of FED Mission and Device Alternatives

A key ingredient in the program to achieve engineering feasibility of magnetic fusion is the definition of the role of FED. Consistent with the goal of demonstrating engineering feasibility, it is possible to define several different fusion engineering devices, each representing a differing role in terms of mission, cost, complexity, and risk. Each device will necessarily require differing levels of complementary facilities in order to achieve the overall goal of engineering feasibility. A study was performed at the outset of the FY 81 design activities to consider various FED mission and device alternatives.

Three mission alternatives were defined in terms of test objectives with increasing levels of achievement. These alternatives are designated Levels I, II, and III and are summarized in Table 3-24. Note that each subsequent level (i.e., mission) includes a more ambitious test objective as well as those of the previous level. Thus, the Level II mission includes nuclear engineering as well as the Level I mission (plasma engineering and engineering operations). The Level III mission includes component and materials qualification as well as plasma engineering, engineering operations, and nuclear engineering. The Level II mission is that currently envisioned for the FED.[8]

Table 3-23. Trade studies conducted for FED

1. Comparison of FED mission and device alternatives.
2. Number of TF coils, ripple, access study.
3. Copper TF coil evaluation for FED.
4. The effect of TF coils sized for 8/10-T operation on FED performance and cost.
5. The effects of PF coil configuration on FED performance and cost.
6. Variation of capital cost and fusion power as a function of neutron wall loading.
7. Plasma minor radius variation.
8. Device size and cost sensitivity to number of pulses.
9. Impact of $\varepsilon\beta_p$ and q on FED performance.
10. Inboard shield thickness trade study for FED.
11. Variation in fusion power.
12. Circular plasma and no OH solenoid.

Table 3-24. Mission alternatives for the FED

- Level I = Plasma engineering + engineering operations
  - Demonstrate long-pulse capability of components to control reactor-grade plasma
  - Demonstrate systems integration based on reactor-relevant technologies
  - Demonstrate maintenance operations in a radioactive environment
  - Demonstrate safety of operations
- Level II = Level I + nuclear engineering
  - Demonstrate performance of blanket with significant fusion power
  - Demonstrate total tritium fuel cycle
- Level III = Level II + component and materials qualification
  - Establish high fluence performance
  - Develop reliability data base

The essential features and requirements of the devices necessary to achieve the alternate missions defined in Table 3-24 are summarized in Table 3-25. Here the Level I device represents a base case and the Level II and Level III device features and requirements are presented as incremental characteristics. The Level I device operates with a catalyzed deuterium-deuterium-tritium (D-D-T) fuel, which provides low fusion power and tritium consumption while at the same time providing a radioactive environment. Thus, neutron shielding, tritium handling equipment, and reactor-relevant maintenance operations are required for the Level I device. The Level II device is that currently envisioned for the FED baseline. The features and requirements of the Level III device are similar to those of ETF/INTOR.[9]

In order to generate a set of consistent device parameters and also to provide relative cost estimates, the FEDC systems code was employed. In order to ensure a common basis for analysis, a number of ground rules were established. These ground rules are summarized below.

- Beta was held constant at ∿6% for all devices and plasma elongation was held constant at 1.6.
- The toroidal field (TF) coils were assumed to be NbTi operating at a maximum field of 8 T.
- The pulse length was held constant at ∿100 s.
- The outboard shield was sized to allow hands-on maintenance 24 h after shutdown.
- Reactor-relevant maintenance assumes that only straight-line radial movement of bulk-shield sectors outward from the device is allowed.

Table 3-26 summarizes the key parameters which characterize the devices associated with each alternate FED mission. Note that the devices characterized in this table do not represent optimizations for each level of mission; rather, they represent devices that nominally satisfy the features and requirements described in Table 3-25. The choice of plasma radius for the Level I device was made on the basis that a reactor-grade plasma should be no smaller in radius than the

Table 3-25. Features and requirements of devices associated with the FED mission alternatives

	Level I (base)		Level II (incremental)	Level III (incremental)
Features	• Long pulse (∿100 s) • Reactor-grade plasma • Reactor technology • Availability ∿ 10-20%	• Remote maintenance • Radioactive environment • Low power and tritium • D-D-T fuel	• Substantial fusion power ∿ 200 MW • L_n ∿ 0.5 MW/m^2 • Availability ∿ 10-20% • ∿1 kg tritium/ year	• $L_n \geq 1$ MW/m^2 • Availability ∿ 50% • ∿10 kg tritium/ year
Plasma requirements	• Control • $\beta \geq 5\%$ • $n\tau$ ∿ few × 10^{13}	• $\bar{T}$ ∿ 5-10 keV • L_p ∿ 20-30 W/cm^2	• Enhanced a, B_t, or β • Burn control	• Enhanced a, B_t, or β
Eng/tech requirements	• Steady-state systems: First wall Armor Limiter Heating • Superconducting TF coils	• Access for maintenance • Neutron shielding • RM equipment • Tritium handling equipment	• Neutron shielding • Blanket test capability • Access for tests • Heat dissipation	• Tritium breeding • Redundancy • Reliability • Shielding

NOTES: L_p is the plasma thermal flux to the wall, L_n is the neutron wall loading, and RM stands for remote maintenance.

Table 3-26. Device parameters for alternative FED missions

	Level I	Level II	Level III
Plasma radius (m)	0.8	1.3	1.5
Major radius (m)	3.5	4.8	6.0
Aspect ratio	4.4	3.7	4.0
Field on axis (T)	4.3	3.6	4.1
Plasma current (MA)	3.2	5.4	6.4
Number of coils	10	10	10
Bore (m × m)	4.5 × 6.4	7.5 × 10.9	8.9 × 12.6
Fusion power (MW)	0.5	180	485
Neutron wall loading (MW/m^2)	0.0025	0.4	0.8
Shield thickness (inner/outer) (cm)	20/80	70/115	80/120
Heating power (MW)	46	36	35

TFTR. The major radius of the Level I device is dictated primarily by the volt-seconds required to start up and achieve the 100-s pulse.

The Level II device is similar to the current FED baseline. The Level III device was sized to achieve about twice the neutron wall loading of the Level II device. The Level I and Level II devices operate in a driven mode. The Level III device would achieve ignition with the physics models employed.

Relative capital costs for the three devices were generated by the FEDC systems code. If the Level II device capital cost is normalized to a value of 1.0, then the Level I device relative capital cost is 0.6 and the Level III device relative capital cost is 1.4. It is noted that the key cost drivers in moving from the Level I device to the Level III device are the increases in (1) shielding, (2) size of the TF coils, (3) requirements on the poloidal field (PF) coils and the associated electrical equipment, and (4) building sizes.

The capital costs generated by the FEDC systems code do not reflect the costs associated with availability requirements. Because of the high availability required for component and materials qualification, it is expected that the relative cost of the Level III device will, in fact, be greater than the value of 1.4 derived from the systems code. Also, it is noted that the Level III device has a high tritium consumption rate, $\sim$10 kg/year, and, therefore, will require some level of tritium breeding. This requirement, coupled with the need for some component redundancy (high availability), increases the relative complexity and technological risk of the Level III device.

On the bases of capital cost, complexity, and risk, it appears that the Level III device (similar to ETF/INTOR) may be too ambitious a step for FED. The Level I device offers attractive capital cost, complexity, and risk. However, it does not provide a demonstration of either blanket performance or the total tritium fuel cycle. These demonstrations are currently considered to be essential parts of the FED mission.[8] Therefore, it was recommended that the Level II mission and device be retained as the context for the FED mission and FED baseline concept.

3.4.2 Toroidal Field Coil Configuration

This study examined the impact of varying the number of toroidal field (TF) coils from 8 to 12 on (1) access for torus maintenance, (2) magnetic field ripple at the plasma edge, and (3) capital cost. In this study the following key parameters were held fixed.

- Major radius = 4.8 m
- Aspect ratio = 3.7
- Minor radius = 1.3 m
- Magnetic field on axis = 3.6 T

The FED maintenance approach requires that the number of torus sectors be equal to the number of TF coils so that sector removal and replacement can be accomplished by straight-line motion. This requirement results in an access limit on the midplane clearance between adjacent TF coils. Table 3-27 shows the impact of varying the number of TF coils from 8 to 12 when the TF outer leg dimension is set by the access requirement (straight-line motion of torus sectors and the number of sectors equal the number of TF coils). Under this limit, cost is seen to be essentially invariant while both ripple and midplane access decrease with increased number of coils. The 10 TF coil configuration was chosen for FED. This configuration allows adequate access for peripheral equipment such as RF injectors and fuel injectors while maintaining a relatively low value of ripple, i.e., less than 1%.

It is also of interest to examine the impact of varying the number of coils from 8 to 12 when the TF coil outer leg dimension is set by a fixed ripple limit rather than an access limit. Table 3-28 shows the results of such a study for a fixed ripple limit at the plasma edge of 2%. For this limit a 17% reduction in total capital cost is achieved for a 12-coil TF configuration relative to an 8-coil configuration. Note that the relative cost values in Tables 3-27 and 3-28 are referenced to the 10-coil access limited configuration.

Table 3-27. Effects of number of TF coils on configuration and cost (access limited)

Number of TF coils	8	9	10	12
Ripple, %	2.6	1.5	0.8	0.3
Midplane access, m	5.2	4.6	4.2	3.5
Burn, s	250	320	370	430
B_m, T	8.3	8.1	8.0	7.9
Relative cost	1.00	1.00	1.00	1.00

Table 3-28. Effect of number of TF coils on configuration and cost (2% ripple)

Number of TF coils	8	9	10	12
Midplane access, m	5.5	4.4	3.7	2.7
Is midplane access adequate for straight-line sector removal?[a]	Yes	No	No	No
Burn, s	250	300	310	300
B_m, T	8.3	8.1	8.0	7.9
Relative cost	1.03	0.97	0.92	0.86

[a]Assuming torus sector equal in number to the number of TF coils.

3.4.3 Copper TF Coil Evaluation

The purpose of this study was to compare the life cycle costs of the FED with a device of equivalent plasma performance but using resistive copper TF coils instead of superconducting TF coils. The current density and void fraction of the copper winding, 1300 amps/cm^2 and 0.13, respectively, were determined so as to be consistent with a continuous coolant path through the inboard leg of the TF coil and a 200°F (93°C) maximum temperature in the copper. The minimum inboard shield thickness for the copper TF coil device was set by radiation dose (10^9 rads) to the coil insulation. By contrast, the minimum inboard shield thickness in FED was set by refrigeration limitations associated with nuclear heating in the coil.

A comparison of parameters for the copper TF coil device and the FED is presented in Table 3-29. Note that the plasma performance is the same. The copper TF coil device has a lower maximum field due to the somewhat smaller shield and the absence of a cryostat for this device. The copper TF coil has a resistive loss of 800 MW compared to 25 MW refrigeration power for the FED.

Relative capital cost for the copper TF coil device is compared to that of the FED in Table 3-30. It is noted that the capital costs are essentially equivalent. The copper TF coil device has a lower cost for the TF coils but higher costs associated with systems handling the 800 MW of resistive losses, namely the TF electrical (power supplies), the ac power (transformer and circuit breakers), and the heat transport system.

The yearly operating costs of the copper TF coil device, requiring 800 MW, are substantial as shown in Table 3-31. The operating cost is comprised of two portions: a demand charge of $5.70/kW per month and an energy charge of 2.2 cents per kilowatt hour. At a typical availability figure for the FED of 25%, these operating costs amount to $91 M a year or $910 M over the proposed 10-year life of the FED.

It could be argued that reducing the current density in the copper TF coil would be advantageous in that the resistive losses would be reduced. In so doing, the radial build of the TF coil would increase,

Table 3-29. Selected parameters for a copper TF device compared to FED

Parameter	Units	Copper device	Common	FED
Plasma radius	m		1.3	
Aspect ratio	-		3.7	
Major radius	m		4.8	
Field on axis	T		3.6	
Fusion power	MW		180	
Plasma current	MA		5.4	
OH solenoid field	T		7.0	
Number TF coils	-		10	
% ripple	-		0.8	
TF megamp turns	-		87	
Burn time	s	410		375
Inboard shield thickness	m	0.53		0.60
Max TF field	T	7.2		8.0
Winding pack current density	amps/cm^2	1300		2500
Overall current density	amps/cm^2	1000		1600
Void fraction	-	0.13		0.15
OH bore	m	2.6		2.5
TF resistive losses	MW	800		0
TF refrigeration power	MW	0		25

Table 3-30. Relative capital costs for a copper TF coil device compared to FED

	Copper device	FED
Shield	0.124	0.126
TF	0.103	0.149
PF	0.093	0.098
Heating	0.119	0.119
PF electrical	0.083	0.087
TF electrical	0.039	0.007
AC power (transformers)	0.041	0.021
Refrigeration	0	0.018
Heat transport	0.056	0.021
Buildings	0.217	0.222
Other	0.132	0.132
Total (relative)	1.007	1.000

Table 3-31. Electrical power cost for 800 MW

Facility availability	Monthly cost: Demand charge[a] $Million	Monthly cost: Energy charge[b] $Million	Monthly cost: Total $Million	Yearly cost / Total
2.4	4.54	0.30	4.84	58
25	4.54	3.08	7.62	91
50	4.54	6.16	10.70	128
90	4.54	11.09	15.63	188

[a]Based on $5.70/kW per month.

[b]Based on 2.2¢/kWh.

and the ohmic heating solenoid bore (thus the volt-second capability of the OH solenoid) would consequently decrease for a tokamak with constant major and minor radii. To determine the impact of this alternative, the winding pack current density in the copper TF device was reduced from 1300 to 725 amps/cm^2 and the plasma burn time was consequently reduced from 410 s to 25 s. Even for this case, the TF coil resistive losses are substantial, ∿450 MW, which translates into a yearly operating cost of $52 M at 25% availability.

It was concluded that superconducting TF coils should be retained on the FED based on capital and operating costs.

3.4.4 Effect of TF Coils Designed for 8/10-Tesla Operation on FED Performance and Cost

The impact on performance and cost of designing FED to operate over an 8- to 10-T range of magnetic field strength was determined using the FEDC Systems Code. The 8- to 10-T device was compared with a device capable of only 8-T operation.

In principle, the capability for operating the TF coils at 10 T can be achieved by any of the three following conductor designs:

- NbTi forced flow design at 3 K
- NbTi superfluid design at 1.8 K
- Nb_3Sn/NbTi hybrid design at 4.2 K

The study was conducted based on the following constraints:

- Plasma radius = 1.3 m
- Burn time ∿ 100 s
- Operating life = 3×10^5 [100-s shots] 8 T only

  2.5×10^5 [100-s shots]

  2.5×10^4 [50-s shots] 8 to 10 T

A comparison of characteristics for FED devices designed for 10-T operation versus the characteristics of a machine designed for 8-T operation is shown in Table 3-32. Note that the winding pack and overall current densities are lower for the TF coil designed for 8/10 T

Table 3-32. Performance and cost of candidate FED configuration

	8 T only (NbTi)	8 to 10 T forced flow (NbTi)	8 to 10 T superfluid (NbTi)	8 to 10 T hybrid (NbTi/Nb_3Sn)
TF coil temp, °K	4.2	3.0	1.8	4.2
Overall coil current density, A/cm^2	1600	1400	1400	1400
Winding pack current density, A/cm^2	2500	2200	2200	2200
Major radius, m	4.81	5.0	5.0	5.0
Field on axis, T	3.62	4.64	4.64	4.64
β, %	5.5	5.2	5.2	5.2
Fusion power, MW	180	450	450	450
Neutron wall loading, MW/m^2	0.45	1.0	1.0	1.0
Power amplification, Q	5	∞	∞	∞
Plasma current, MA	5.4	6.5	6.5	6.5
Cost, relative	1.0	1.18	1.18	1.24

than for the coils designed for only 8-T operation. The lower current density and higher peak TF field requires that the major radius of the FED be increased to 5.0 m to accommodate the TF coils sized for 8/10 T operation.

As indicated in Table 3-32, sizing the TF coil for some limited operation at 10 T does allow ignition to be achieved at a modest increase in capital cost, 18-24%. Of the conductor designs considered for limited 10-T operation, the least expensive is the forced-flow NbTi or the superfluid NbTi designs. The hybrid TF coil design is the most expensive due to the increased cost of Nb_3Sn winding compared to NbTi winding, i.e., \$255/kg vs \$90/kg.

A detailed study of the magnetic system required to accomplish 8/10-T operation was conducted by the Magnetics Branch and is reported in Chapter 4 of this document.

3.4.5 Effects of PF Coil Configuration on FED Performance and Capital Cost

Three poloidal field (PF) coil configurations were evaluated for the FED. These configurations are shown schematically in Fig. 3-32 and are defined as follows:

Concept 1	
External/SC	All external superconducting EF coils.
Concept 2	
Hybrid/Hybrid	Internal copper EF coils, external superconducting EF coils.
Concept 3	
Internal/Normal	All internal copper EF coils.

Figure 3-32 also shows the required EF coil currents consistent with a plasma current of 5.2 MA. In addition to the EF coil currents, each configuration utilizes a superconducting ohmic heating coil system of approximately 70 MAT.

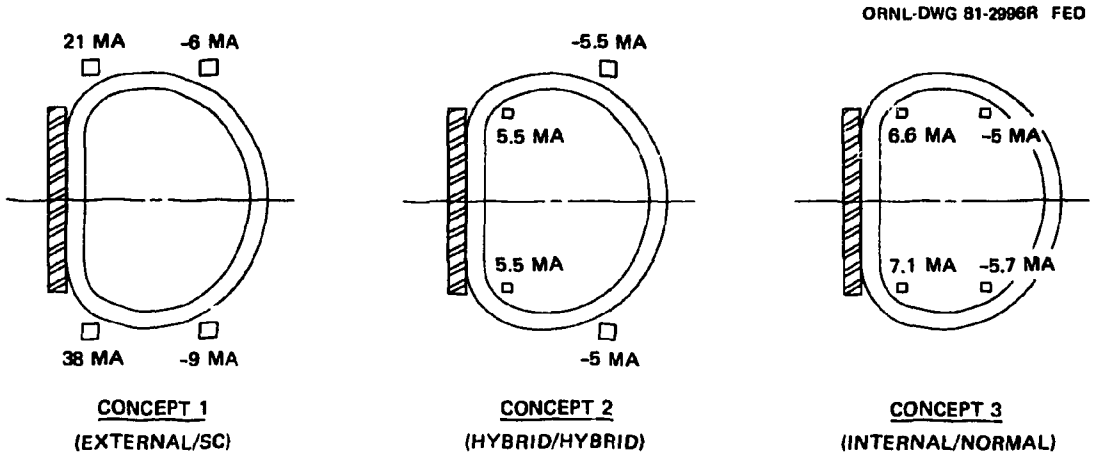

Fig. 3-32. Candidate PF configurations evaluated for FED application.

This study was based on the following fixed parameters:

- Major radius = 4.8 m
- Minor radius = 1.3 m
- Plasma current = 5.2 MA
- TF max field = 8 T
- Current density in copper EF coils and SC OH solenoid = 1500 amps/cm^2
- Current density in SC EF coils = 1400 amps/cm^2

The results of this study are shown in Table 3-33. The volt-seconds supplied by the PF system to the plasma are 20% less for the external/SC concept compared to either the hybrid/hybrid or internal/normal concepts. This results in a shorter plasma burn for FED with an external/SC configuration. Resistive losses in the PF coil are highest, 265 MW, for the internal/normal configuration compared to 72 MW for the hybrid/hybrid and only 2 MW for the external/SC configurations. Total capital costs are 30% higher for the external/SC configuration compared to either alternative.

Based on consideration of capital and operating costs, the recommended EF system for FED is the hybrid/hybrid configuration. This configuration is 30% less expensive than the external/SC configuration and has a factor of ∿3 lower operating costs (72 MW compared to 265 MW) than does the internal/normal configuration.

A detailed study of the PF system alternatives was conducted by the Magnetics Branch and is included in Section 4.2 of this document.

3.4.6 Variation of Capital Cost and Fusion Power as a Function of Neutron Wall Loading[7]

The purpose of this study was to determine the impact of neutron wall loading on FED performance and cost. The study was conducted based on the following assumptions:

- Beta = 6%
- Max TF field = 8 T
- Aspect ratio = 3.7
- Burn time ∿ 100 s

Table 3-33. Cost and performance for alternate PF configurations

	External/SC	Hybrid/Hybrid	Internal/Normal
Volt-second,	73	90	91
PF system resistive losses, inc. buss, MW	2	72	265
PF coil capital cost, relative	3.20	1.0	0.63
PF electrical system cost, relative	1.56	1.0	1.42
Total capital cost, relative	1.30	1.0	1.03

The results of this study show that capital cost varies almost linearly with neutron wall loading. A change of ±20% in neutron wall loading results in a ±10% change in cost. At each value of wall loading, the plasma minor radius and the field on axis were determined consistent with constant values of aspect ratio and maximum toroidal field. The field in the OH solenoid was selected consistent with a burn time of approximately 100 s but was not allowed to exceed 7.0 T. As previously indicated, cost decreases with decreasing values of neutron wall loading. However, fusion power also decreases, while plasma heating power increases, resulting in lower values of Q. The minimum value of neutron wall loading consistent with the constraints of this study is approximately 0.3 MW/m^2, imposed by limitations on the volt-second capability of the OH coil. As wall loading decreases to this value, the self-consistent plasma minor radius is 1.16 m. When coupled with the fixed aspect ratio of 3.7, this value produced just enough volt-seconds to provide 100 s of burn. A further reduction in wall loading and plasma minor radius at this fixed aspect ratio of 3.7 would result in a tokamak configuration that would burn for less than 100 s.

The capital cost and performance of FED are dependent on the selected value of neutron wall loading. The minimum-cost FED is therefore dependent on the minimum neutron wall loading and the lowest value of Q deemed necessary to achieve the goals of FED.

3.4.7 Plasma Minor Radius Variation[7]

The purpose of this study was to investigate the impact of variation in plasma minor radius on performance and cost when the baseline value of neutron wall loading (0.44 MW/m^2) is held constant. The constraints imposed on this study are as follows:

- Neutron wall loading = 0.44 MW/m^2
- Beta α 1/aspect ratio
- Max TF field = 8 T
- Inboard shield thickness = 0.7 m
- Max OH field = 7 T

Note that imposing the requirements of both fixed neutron wall loading and fixed field at the TF coil yields a unique combination of values for aspect ratio and field on axis for a given plasma minor radius.

Decreasing the plasma minor radius from the base value of 1.3 m to 1.1 m (with an associated increase in both field on axis and aspect ratio) yields an increase in burn time to approximately 1000 s for a 6% increase in cost. Performance is degraded in that Q decreases from 5.3 to 4.0. In essence, enhanced burn time is traded for lower Q. Increasing the minor radius from 1.3 m to 1.4 m (with an associated decrease in both field on axis and aspect ratio) results in a tokamak configuration that has insufficient volt-seconds to achieve current startup. Disregarding the startup limitation, this configuration achieves a slight increase in performance (Q increases from 5.3 to 6.2) for a 4% increase in cost.

For the constraints considered in this trade study, it is concluded that reducing the plasma minor radius from 1.3 m to 1.2 m (with an associated increase in aspect ratio and field on axis to 4.2 and 3.9 T, respectively) has some positive cost benefit impact. This configuration would achieve an increase in burn time of approximately 400 s for essentially the same cost but at a reduction in Q of ∿15%.

3.4.8 Device Size and Cost Sensitivity to Number of Pulses[7]

The purpose of this study was to examine the sensitivity of device size and cost to the number of pulses applied over the lifetime of the machine. Specifically, sensitivity was determined for pulse levels of 5×10^4, 1×10^5, 5×10^5, and 1×10^6. The study was conducted holding the following parameters fixed:

- Plasma radius = 1.3 m
- Field on axis = 3.62 T
- Average beta = 6%
- TF ripple = 0.83%
- Safety factor, q = 2.5
- Neutron wall loading = 0.44 MW/m^2
- Burn time = 100 s

In varying the design life from 5×10^4 to 1×10^6 pulses, while holding performance constant, the FEDC systems code indicated a required increase in machine size (major radius) of ∿4% and an attendant increase in capital cost of ∿5%. It should be noted that characteristic parameters and capital cost estimates did not change appreciably between 5×10^4 and 1×10^5 pulses; such changes only became significant between 1×10^5 and 1×10^6 pulses. The changes in total capital cost were largely attributable to changes in the costs of the TF coil system, the shield, the refrigeration system, the building, and the fuel processing system.

The change in TF coil system cost is directly related to TF coil structural requirements. Over the range of 5×10^4 to 1×10^6 pulses, TF coil case weight doubled and TF coil system costs increased by 22%.

The mechanical properties of TF coil conductor insulation and the resistivity of the copper stabilizer are affected by the fluence to the TF coils. A maximum exposure of 10^9 rad was assumed for the insulating material. For the copper stabilizer, exposure was limited to 2.4×10^{-4} displacements per atom (dpa). However, two anneals were allowed over the life of FED, which effectively eliminated constraints due to displacement damage of the copper stabilizer.

Fluence to the TF coils (inboard leg) is limited by the thickness of the inboard shield. At 1×10^6 pulses, a shield thickness of 0.66 m is required to limit the fluence to 10^9 rad; at 5×10^5 pulses, the required shield thickness is 0.62 m. Reducing the shield thickness results in a smaller device in a smaller building, with attendant cost benefits. Below 10^5 pulses, however, the benefits of further reducing the inboard shield thickness tend to be offset by increased refrigeration requirements due to increased nuclear heating of the TF coils. The outboard shield is sized for a biological dose rate of ∿2 mR/h, 24 h after shutdown and was found to be relatively insensitive to number of pulses.

Another system that appeared sensitive to the number of pulses is the fuel processing system. Increased utilization is required with an increased number of pulses. Conceptually, increased utilization requires

that fuel be processed at a faster rate, resulting in increased capital costs. However, this would not necessarily be true if the fuel processing system was sized for a specified period of sustained operation at lower levels of utilization. In order to accurately assess the impact of number of pulses on fuel processing system costs, more detailed specifications are required.

The capital cost analyses do not reflect the cost of availability enhancements that would be required in order to achieve the utilization required at an increased number of pulses. The availability characteristics of FED have not yet been established. However, based on previous analyses performed on similar tokamak designs [ETF and the International Tokamak Reactor (INTOR)],[5] the cost of availability enhancements should not be appreciable below 1×10^5 pulses. However, as the number of pulses approaches 1×10^6, the cost of availability enhancements can be expected to become increasingly substantial. The general conclusion derived from this study is that FED operations at up to $2\text{-}4 \times 10^5$ pulses can be accomplished in a reasonable period of time (<15 years) without major capital cost impact.

3.4.9 Impact of $\varepsilon\beta_p$ and q_ψ on FED Performance[7]

The purpose of this study was to determine the impact of variations in $\varepsilon\beta_p$ and q_ψ on FED performance. The study was conducted about the FED baseline configuration. As can be seen from the following, the assumed values of $\varepsilon\beta_p$ and q_ψ have a dominating effect on the performance of the FED plasma:

$$\langle\beta\rangle = \beta_p \left[\frac{C}{q_\psi} \frac{\varepsilon}{(1-\varepsilon^2)^2}\right]^2 \frac{1+\kappa^2}{2} \tag{1}$$

$$= \beta_p \left(\frac{I_p}{5aB_t}\right)^2 \frac{2}{1+\kappa^2} .$$

where

$\langle\beta\rangle$ = volume average beta,
β_p = beta poloidal,
ϵ = 1/aspect ratio,
q_ψ = safety factor of the plasma edge,
κ = plasma elongation,
a = plasma radius,
B_t = field on axis,
C = coefficient which increases with $\epsilon\beta_p$,
I_p = plasma current.

The impact of $\epsilon\beta_p$ and q_ψ on the average beta ($\langle\beta\rangle$), fusion power (P_{fusion}), neutron wall load (L_w), plasma current (I_p), burn pulse length (t_{burn}), and fusion energy production per pulse (W_{fusion}) was determined using the FEDC Systems Code. At a low value of $q_\psi \simeq 2.3$, a fusion power of $\sim$1000 MW and a neutron wall loading of $\sim$2.5 MW/m^2 can be produced by the plasma if $\epsilon\beta_p = 0.6$ is assumed. However, the plasma current is near the limit of the OH flux capability, so only a negligible t_{burn} is obtained, producing little W_{fusion} per pulse. As q_ψ is increased, W_{fusion} rises sharply, reaches a maximum near $q_\psi \simeq 3$, then falls off relatively slowly. Similar behavior is seen if $\epsilon\beta_p = 0.4$ is assumed, except that the maxima of P_{fusion} and L_w are 300 MW and 0.8 MW/m^2, respectively.

This analysis concludes that a design limit of $P_{fusion} \lesssim 200$ MW will determine a lower bound of q_ψ as a function of $\epsilon\beta_p$. This bound occurs at $q_\psi = 2.6$ for $\epsilon\beta_p = 0.4$ and at $q_\psi = 3.5$ for $\epsilon\beta_p = 0.6$.

3.4.10 Inboard Shield Thickness Trade Study for FED[7]

The purpose of this study was to determine the effect of varying inboard shield thickness on capital cost, TF coil dose rate, and performance. The study was conducted subject to the following constraints:

- Plasma minor radius = 1.3 m
- Maximum TF field = 8 T
- Beta = 6%

- Burn time = 100 s
- OH field = ±7 T
- Number of cycles = 3.5×10^5

The results of varying the inboard shield thickness from 0.5 m to 0.8 m on capital cost is slight, approximately 1.0% relative to the base FED cost at a shield thickness of 0.7 m. The capital cost decreases with decreasing shield thickness down to ∿0.6 m and then increases as shield thickness is further decreased. The minimum in capital cost as a function of shield thickness occurs when cost associated with decreased tokamak size is compensated for by increased TF coil refrigeration cost due to the thinner shields.

Instantaneous refrigeration requirements and radiation dose to the TF coils increase as the shield thickness is decreased. At a shield thickness of 0.5 m, the nuclear heating in the TF coil is approximately 200 kW, which appears excessive and suggests that a shield thickness greater than 0.5 m should be used. The radiation dose to the TF coil insulation exceeds the imposed limit of 1×10^9 rad for a shield thickness of 0.5 m. The dose is dependent on accumulated burn time. A substantial margin for increased number of cycles exists for the thicker shields (i.e., 0.7 m and 0.8 m), but little margin on dose is available for the 0.6-m shield configuration.

For the constraints of this study it is concluded that inboard shield thickness has a minimal influence on FED cost. A value of shield thickness of at least 0.6 m is required to avoid radiation damage to the TF coil insulation and to maintain reasonable TF coil refrigeration loads. While this conclusion is valid for FED where minimized capital cost is a goal, it is not necessarily valid for reactor consideration. Fusion power and neutron wall loading increase as shield thickness decreases. This result is a decrease in unit cost [$/kW(t)] and an increase in Q with decreasing shield thickness. Increased Q and decreased unit cost are important considerations for fusion reactors but are of less significance for FED as it is currently envisioned.

3.4.11 Variation in Fusion Power[7]

The incentive for this study was the recognition that the fusion power produced by a fixed FED device could be greater or less than the FED baseline value of 180 MW because of the uncertainties associated with the physics performance of the plasma (confinement, beta, safety factor, etc.). A study was performed using the FEDC systems code to determine which systems are most impacted by such considerations and to determine the associated capital cost impact for postulated ranges of fusion power output.

This study was performed using the following fixed parameters:

- Minor radius = 1.3
- Major radius = 4.8
- Max TF field = 8.0
- Field on axis = 3.6

Two basic options were considered — either enhanced performance (resulting from postulated improved energy confinement or enhanced beta) or degraded performance (resulting from postulated degraded energy confinement or lower beta). The postulated enhanced performance could result in ignition, and for this circumstance two situations were examined: in the first case the fusion power remains at the baseline value (resulting from improved confinement) and in the second case, the fusion power is assumed to be twice the baseline value (resulting from increased beta). The postulated degraded performance leads to a requirement that the device must be operated in a driven mode, and again two situations were examined: in the first case the fusion power is equal to the baseline (impared confinement is assumed) and in the second case, a doubling of the baseline power is postulated (increased beta and impared confinement is assumed). For each of these four cases the following points are noteworthy.

Case 1

This case achieves ignition. It results from a postulated improvement in confinement by a factor of 2 and assumes the average beta is

held constant at 6%. In this case, the sustaining auxiliary heating power requirement is reduced to zero, but auxiliary heating is required to achieve ignition. As a consequence, there is a net reduction in the particle and heat flux to the first wall components (first wall, armor, and limiter). Otherwise, there are no engineering implications, since the fusion power remains the same and the auxiliary power required is similar to the baseline case.

Case 2

This case is driven, with the total fusion power equal to the baseline case. Confinement is assumed to be only half as good as the baseline case and the value of Q decreases from 5 to 2. To maintain the same total fusion power requires a significant increase in auxiliary heating. Average beta is held at 6%. The systems most affected are the bulk heating systems, the first wall and limiter (to handle the increased surface heat loads), the ac power systems, the heat dissipation sytems, and the tritium processing systems.

Case 3

This case assumes that the total fusion power is doubled. To achieve this, the average value of beta increases from 6% to 8.5% and ignition is achieved. The systems most affected are the first wall and limiter (to handle the increased surface heat load), the shield (to handle the increased neutron power), the heat dissipation system, the refrigeration system, and the tritium processing system.

Case 4

This case also assumes that the fusion power is doubled but that relative to Case 3 the energy confinement is decreased by 50%. The result is Q = 10 at an average beta of 8.5%. The systems most affected are the same as those in Case 3.

The systems code was employed to examine the associated capital cost impact. If the range of variations indicated for these four cases were to be accommodated in one design, the total capital cost would be approximately 15% greater than the baseline. The results of the present study suggest that considerable engineering flexibility can be provided at modest cost ($\leq$15%) by designing selected systems to accommodate a range of device performance.

3.4.12 Effects of a Circular Plasma and the Elimination of the OH Solenoid

Trade studies were conducted to investigate the first order impacts on FED of: (1) assuming a circular plasma rather than an elongated plasma, and (2) assuming a viable current drive mechanism which eliminates the need for an OH solenoid. These studies were conducted subject to the following constraints:

- Power amplification = 5
- Inboard shield thickness = 0.7 m
- Max TF field = 8 T (NbTi)
- Neutron wall loading = $\sim$0.5 MW/m^2
- Burn time = $\sim$100 s

The specified values of power amplification and wall loading were held constant in order to ascertain the first order cost effects of removing the OH solenoid or assuming a circular plasma. The fusion power was calculated by multiplying the fixed neutron wall loading by the calculated plasma surface area and adjusting for the alpha power contribution. Auxiliary heating was determined from these values of fusion power and the fixed value of power amplification. For the circular case, the PF system currents were not adjusted for the relaxed plasma shaping requirement.

The results of these studies are presented in Table 3-34. The FED configuration without an OH solenoid achieves the lowest cost (57% of the baseline) but achieves poor utilization of the TF magnetic field, 1.65 T on axis as opposed to 8 T at the coil inner leg. At this lower field, a very high value of beta, $\sim$30%, is necessary in order to achieve

Table 3-34. Trade study results

Parameter	FED baseline	FED baseline circular	FED baseline no OH solenoid
Plasma radius, a (m)	1.3	1.3	1.3
Aspect ratio, A	3.85	3.45	2.5
Major radius, R (m)	5.0	4.48	3.25
Elongation, σ	1.6	1.0	1.6
Field on axis, B_T (T)	3.75	3.34	1.65
Beta, β	0.06	0.08	0.31
TF bore (m)	6.6 × 10.2	6.3 × 10.3	5.7 × 9.3
Safety factor, q	2.5	2.5	2.5
Plasma current, I_p (MA)	7.0	4.0	5.8
Volt-seconds	82	45	--
DT power (MW)	250	170	160
Heating power, P_{aux} (MW)	50	34	32
Relative capital cost	1.00	0.74	0.57

the assumed neutron wall loading of 0.5 MW/m^2. The circular plasma FED achieves the next lowest cost (74% baseline). Part of this cost reduction is due to the lower plasma current, 4.0 MA, which requires less volt-seconds from the poloidal field system. This configuration would require a value of beta of $\sim$8% to achieve the neutron wall loading of 0.5 MW/m^2.

REFERENCES

1. P. T. Spampinato, personal communication, FEDC-M-81-SE-011 (January 1981).
2. Fusion Engineering Design Center, *ETF Interim Design Description Document*, Oak Ridge National Laboratory, July 1980.
3. W. T. Reiersen, personal communication, FEDC-M-81-SE-132 (July 1981.
4. D. Steiner et al., *Oak Ridge TNS Program: Summary of FY 1978 Activities*, ORNL/TM-6720, July 1979.
5. IAEA, Vienna, Austria, *INTOR, International Tokamak Reactor Phase One Conceptual Design*, to be published.
6. R. L. Reid et al., "ETF Systems Code — Composition and Application," paper presented at the Fourth ANS Topical Conference on the Technology of Controlled Nuclear Fusion, King of Prussia, Pennsylvania, October 14-17, 1980.
7. Fusion Engineering Design Center Staff (C. A. Flanagan, D. Steiner, and G. E. Smith, eds.), *Initial Trade and Design Studies for the Fusion Engineering Device*, ORNL/TM-7777, Oak Ridge National Laboratory (June 1981).
8. ETF Design Center Team, *ETF Mission Statement Document*, ORNL/TM-6733, Oak Ridge National Laboratory (April 1980).
9. W. M. Stacey, Jr., et al., *The U.S. Contribution to the International Tokamak Reactor Phase-1 Workshop, Conceptual Design*, June 1981.

4. MAGNETIC SYSTEMS

R. W. Derby*

S. S. Kalsi† R. J. Hooper†

B. L. Hunter† V. C. Srivastava†

S. Kim‡ L. Turner‡

The magnetic systems represent the core of the device, providing both plasma confinement and control functions. Both the structural design and the overall configuration of FED are dominated by the requirements of the magnetic systems. Moreover, these systems constitute a substantial portion (~30%) of the FED capital costs. Thus it is essential that the magnetic systems be designed for high reliability. Accordingly, the design approach has been somewhat conservative, which is prudent in view of the scale of the FED magnetic systems and their critical role.

The magnetic systems consist of the toroidal field (TF) coils, the poloidal field (PF) coils [including the equilibrium field (EF) coils and the ohmic heating (OH) solenoid], the associated support structure, and the cryostat. The cryogenic system, including refrigerators, is discussed in Chapter 8. For each of these components, a variety of options was considered and a baseline option was selected and developed in sufficient detail to demonstrate feasibility and allow a cost estimate to be made.

The FED magnets are designed to provide 3.6-T field on the plasma axis during the bulk of device operation (250,000 pulses) and 4.6-T field during a limited portion of device operation (25,000 pulses). In order to achieve the specified on-axis fields, the TF coils are designed to develop 8-T and 10-T peak field, respectively, at the TF coil windings. The PF coils are designed to operate up to a peak field of 7 T at the winding.

---

*Fusion Engineering Design Center/Massachusetts Institute of Technology.

†Fusion Engineering Design Center/General Electric Company.

‡Argonne National Laboratory

The configuration of TF coils and PF coils is shown in Fig. 4-1. The major design and performance parameters are summarized in Table 4-1. There are 10 superconducting TF coils which are capable of operation at fields up to 10 T. The OH solenoid is located inside the bucking cylinder (not shown). The PF system uses a combination of superconducting and normal coils. The PF coils which lie outside the TF coil bore are superconducting, and use a NbTi pool boiling conductor, while the PF coils inside the TF coil bore are water cooled copper resistive coils. The PF coil configuration was selected on the basis of cost, plasma shape, dynamic control requirements, and access requirements for remote maintenance. The EF coils, which are a subset of the PF coil system, also serve as trim coils for shaping the OH solenoid flux lines.

The cryostat provides a cryogenic environment for the TF coils, the bucking cylinder, the intercoil support structure, and the superconducting PF coils (including the OH solenoid).

The mechanical pump limiter has been selected as the means of impurity control in the FED baseline. Magnetic divertors are considered the prime alternate. Since magnetic divertors are not part of the FED baseline, no significant effort was devoted to this concept. It will receive further attention only if the pump limiter appears unworkable.

A variety of conductor and cooling concepts was considered for use in the TF coil as a means of achieving 10-T peak field. These options include the following:

- NbTi pool boiling conductor cooled by 4.2 K liquid helium during 8 T operation, cooled by 1.8 K superfluid helium during 10 T operation.
- NbTi forced flow conductor cooled by 4.5 K supercritical helium at 8 T, cooled by 3.1 K supercritical helium at 10 T.
- Nb_3Sn/NbTi pool boiled hybrid conductor, cooled by 4.2 K liquid helium. Nb_3Sn conductor is used only in the portion of the winding which operates at a field above 8 T.
- Two concentric TF coils, each with its own conductor type, cooling environment, and structural support. The outer coil operates at fields up to 8 T and uses an LCP-type conductor. The inner coil, which is energized only when the device is

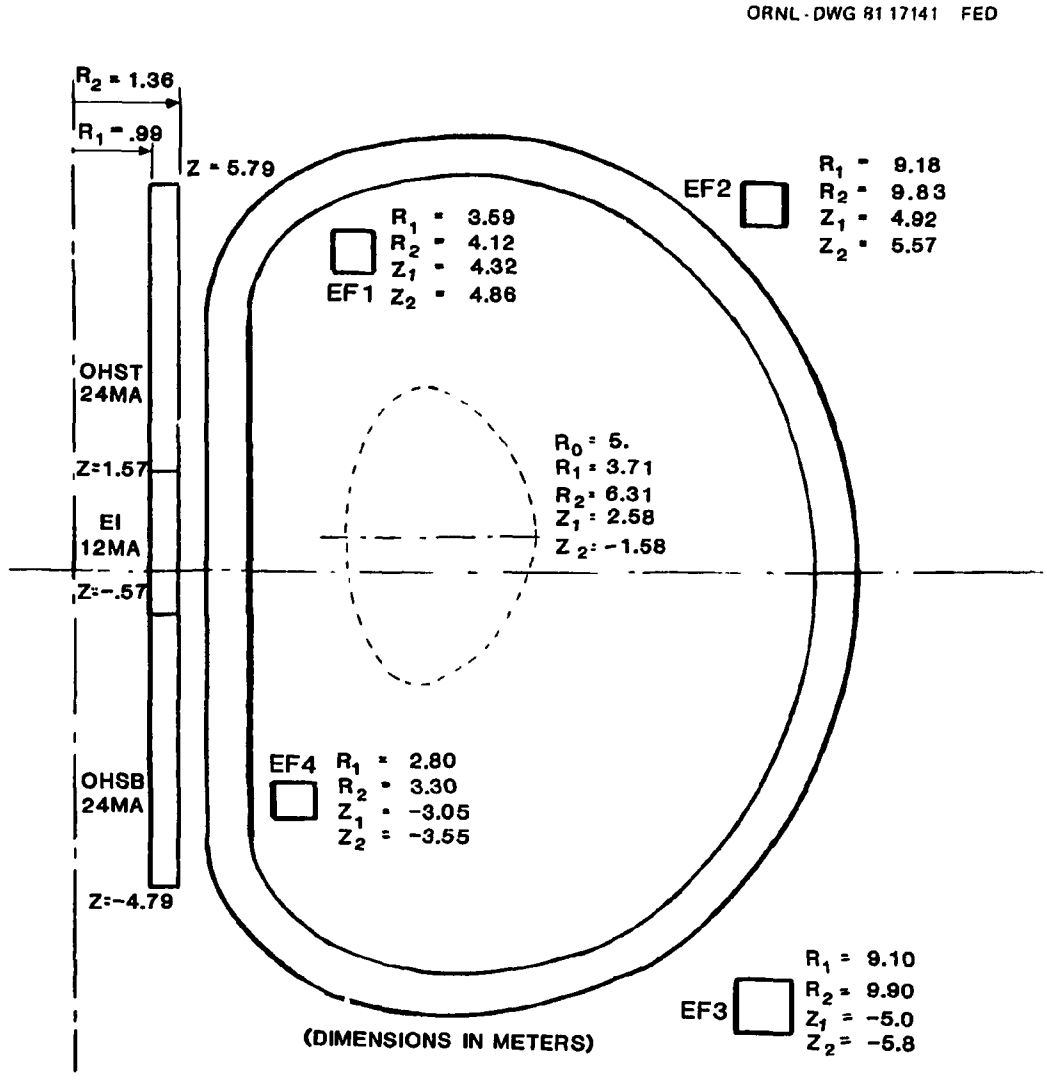

Fig. 4-1. FED 8-T/10-T baseline magnetic system.

Table 4-1. FED magnetic system parameters

Description	Unit	At 8 T	Common value	At 10 T
Major axis	m		5	
Field on axis	T	3.6		4.6
Number of pulses		250,000		25,000
TF coils				
Number			10	
Conductor			NbTi forced flow	
Design field at winding	T	8		10
Winding bore	m		7.4 × 10.0	
Maximum permissible radiation dose	rads		10^9	
Ampere-turns per coil	MAT	9		11.5
Overall current density	A/cm^2	1150		1470
Operating current	kA	20		25.5
Stored energy/coil	GJ	1.5		2.3
Coil mean perimeter	m		34.6	
Bucking post — outside radius	m		1.74	
— inside radius	m		1.48	
OH coil				
Volt-seconds	Wb	44		44
Conductor			NbTi	
Maximum field at coil	T	7		7
Charging time	s	30		30
Discharge time (+7 to -7 T)	s	6		6
Length of central solenoid	m		10.6	
Winding current density	A/cm^2		1500	
Stored energy in the solenoid	GJ		1.0	
Voltage per turn	V		8.3	
EF coils				
Volt-seconds	Wb	43		47[a]
Conductor — superconducting coils			NbTi	
— normal coils			Cu	
Field at EF coils	T		<7	
Charging time	s		6	
Discharging time	s		10	
Winding current density	A/cm^2			
— superconducting coils		1370		1500
— normal		915		1000
Voltage per turn	V	16.5		18

[a]The 47 V-s is provided by the EF coils during a normal pulse; the normal EF coils provide an additional 11 V-s during preionization.

being operated at 10 T, operates at fields between 8 T and 10 T and uses an advanced cryogenic conductor of the type being developed in the 12-T program, or as an alternative, a resistive copper conductor cooled by water or liquid nitrogen.

All of these options are capable of providing the required performance, although none is clearly superior to the others on technical grounds. The superfluid options and the forced flow options appear less costly than the others, but do not differ significantly in cost between themselves. The forced flow option was selected for the baseline for illustrative purposes. This selection of conductor type is by no means final.

To the maximum extent practical, the design of the superconducting coils, both toroidal and poloidal, is based on on-going superconducting coil development programs designed to support the FED program. These include the DOE Large Coil Program (LCP) in the area of large toroidal field coils and the Los Alamos National Laboratory (LANL) 20-MJ Coil Program, instituted to develop the technology of a large pulsed solenoid. Although the LCP and LANL programs represent large efforts in terms of coil size, application to FED represents a large extrapolation in size. This is illustrated in Fig. 4-2, in which an LCP coil, the LANL solenoid, and FED coils (a TF coil, a PF ring coil, and the solenoid) are drawn to scale, with coil weights in tons also indicated.

While the design of the toroidal field (TF) coils will draw on the experience gained in LCP and the 12-Tesla Conductor Development Program, the design and development of the TF coils present additional questions beyond those that can be easily answered in the above programs. As may be seen in Fig. 4-2, the FED TF coils are approximately three times as large as the LCP coils; accordingly, scaling of this technology must be well understood. Another important unresolved issue is the degree to which eddy current losses drive the design and the degree to which they can be studied in LCP. In addition, fatigue and fracture mechanics play a more prominent role in FED structural design than in LCP, since cyclic out-of-plane loads in FED are much higher than those in the LCP coils. These subjects have received careful attention during the design studies.

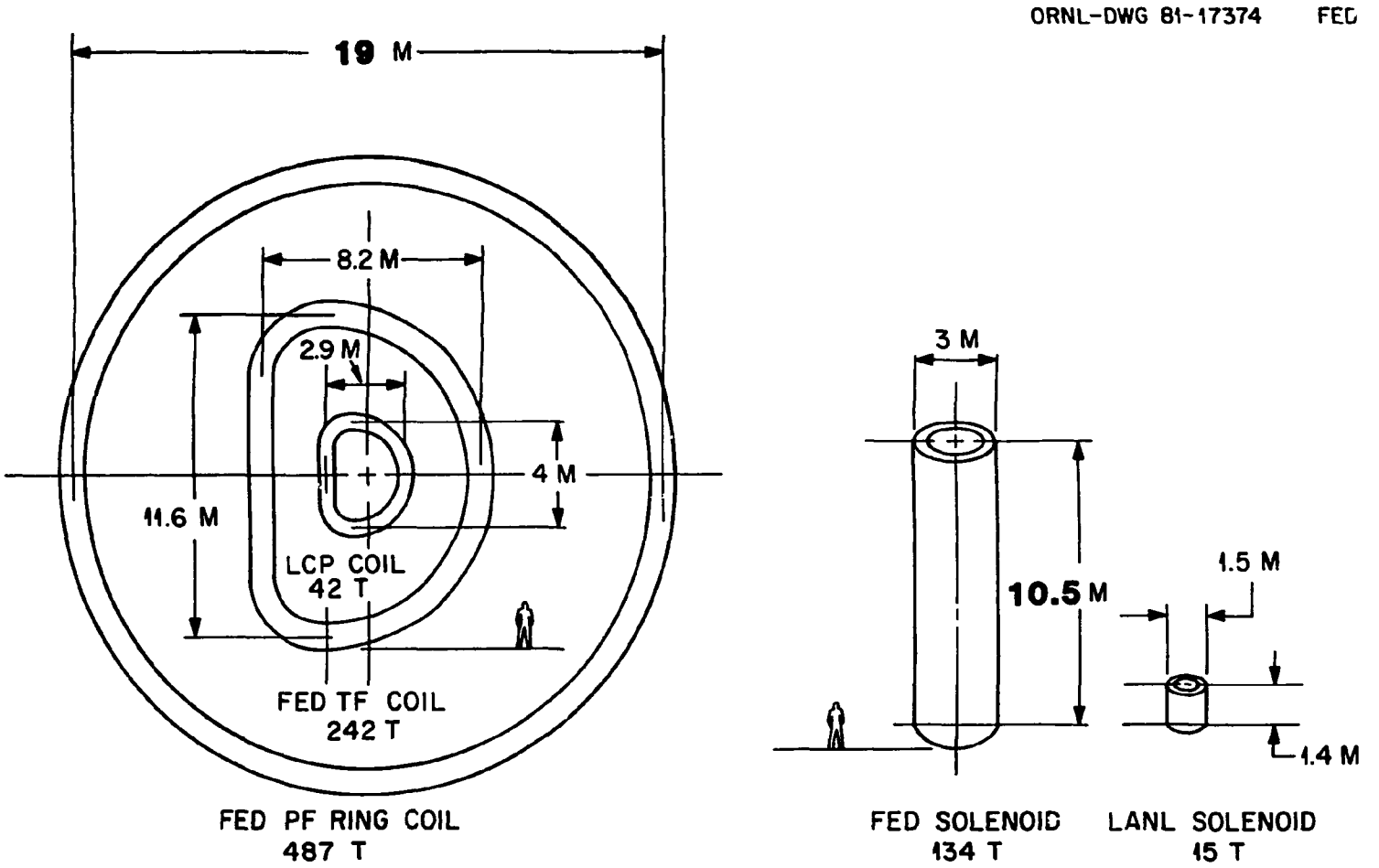

Fig. 4-2. Comparison of FED superconducting size/weight with on-going DOE coil development programs.

The design of the poloidal field (PF) system also presents technical challanges. The PF system performs a variety of functions – plasma initiation and plasma equilibrium through equilibrium field (EF) coils, plasma heating through ohmic heating (OH) coils, and plasma control through control field (CF) coils. Each of the above functions is provided by a combination of currents in different coils of the PF system. The superconducting PF coils are considerably larger than similar coils in any previous or on-going program. As is evident from Fig. 4-2, the EF coils for FED are approximately five times as large (in perimeter) as the LCP TF coils, and the FED solenoid is approximately seven times as long and twice the diameter of the pulsed solenoid in the LANL 20-MJ Coil Program. The location of the superconducting EF coils places them where the fringing effects of the TF coils produce very large circumferential bending loads which, combined with the proportions of these coils, makes structural design a very challenging task.

4.1 TOROIDAL FIELD COIL SYSTEM

This section describes the toroidal field (TF) coil system. The major design considerations, including a system function summary and a summary of requirements and design features, are presented first. A description of the TF coil layout and of the principal components in the system follows. The process by which the present design concept was selected is next described, followed by a discussion of the alternate concepts which were considered. The results of the winding design analysis and the structural design analysis are then discussed. The section concludes with a brief discussion of important needs and plans for future work.

4.1.1 TF Coil Major Design Considerations

This section presents a system function summary, addressing such issues as the TF coil geometry, number of coils, and conductor concept selection.

A summary of requirements and design features is then presented and discusses the forces which the coils are designed to withstand, the heat loads on the TF coil system, the credible fault conditions which are considered, and the structural design criteria upon which the design is based.

System function summary

The FED baseline design has ten toroidal field (TF) coils; each coil has a clear bore height and width of 10.9 m and 7.4 m, respectively. The number and size of the coils have been selected on the basis of extensive trade-off studies involving physics, vacuum vessel geometry, and maintainability constraints. The TF coils are designed primarily for operation at a peak field of 8 T, but they are to be operable for a limited number of cycles at 10-T peak field. The specified combination of 250,000 8-T pulses plus 25,000 10-T pulses is equivalent from a fatigue damage standpoint to 350,000 8-T pulses alone, or to 80,000 10-T pulses alone.

Several conductor concepts being developed in the Large Coil Program (LCP) and the 12-Tesla Program can be used in the FED TF coils (see Sect. 4.1.3 for more information). There is no clear basis for a preferred option at this time. However, for the purpose of design discussions and component costing, a NbTi forced flow conductor design has been selected. The final winding configuration will be selected in the conceptual design phase on the basis of cost, availability, and relative performance of various conductor concepts.

Summary of requirements and design features

The major requirements and parameters of the TF coils are summarized in Table 4-2. A variety of TF coil designs meet the requirements. The number, size, and shape of the TF coils in the baseline design were selected on the basis of tradeoff studies that considered physical requirements, vacuum vessel geometry, and maintainability. The TF coils are a modified pure tension D-shape, although introduction of intercoil

Table 4-2. FED TF coil requirements and parameters

- Plasma major radius: 5.0 m
- Field on plasma axis: 3.6 T (8-T operation); 4.6 T (10-T operation)
- TF coils must withstand the following loads:
  - In-plane Lorentz force (steady state)
  - Out-of-plane loads due to PF coil interaction (pulsed)
    - 250,000 pulses (8-T operation)
    - 25,000 pulses (10-T operation)
  - Out-of-plane loads due to unequal currents in TF coils
  - Dead weight of TF coils plus dead weight of components supported off the TF coils
  - 1 g horizontal and/or vertical seismic load
- Winding insulation must withstand 10^9 rads neutron fluence, accumulated over the lifetime of the machine.
- Winding bore size, m: 7.4 × 10.9
- Mean coil perimeter, m: 34.6
- Number of TF coils: 10

	8-T operation	10-T operation
Overall current density, A/cm^2	1150	1470
Winding current density, A/cm^2	1720	2200
Conductor current, A	20,000	25,500
Number of turns	444	444
Outlet Coolant temperature, K	4.5	3.1

structure to react overturning loads leads to departure from the constant tension condition. The conductor is designed for 20,000 A at 8-T operation and is cooled by pressurized forced flow helium. The 10-T field is achieved by increasing the conductor current to 25,500 A and using supercritical helium coolant which exits the winding at a temperature of 3.1 K. The winding is designed to remain superconducting during normal pulsed operation. Following a plasma disruption, a temporary excursion into the resistive state is acceptable, provided the winding returns to the superconducting state. Analysis indicates that the present winding design remains superconducting during and after a plasma disruption.

During normal pulsed operation at 10 T, time-varying currents in the PF coils produce eddy current heating in the TF coil case and in the intercoil support structure. Nuclear radiation causes additional heating of the coil case in the inboard leg of the case. These heat loads are beyond the heat removal capability of the coolant in the conductor conduits. To prevent this heat from reaching the winding, additional liquid helium coolant tubes are embedded between the winding and the inside surface of the coil case and in the intercoil support structure.

Each TF coil is subjected to in-plane forces due to interaction of the coil current with the toroidal field. Similarly, out-of-plane loads are caused by interaction of the TF coil current with the radial field component of the poloidal fields. The force containment structure must provide support for the winding while allowing minimum slipping movement and keeping conductor strain within allowable limits. The coil support structure must support the coils against

- centering forces tending to push each TF coil to the torus centerline
- out-of-plane forces tending to tip the coils sideways during pulsing action
- out-of-plane forces tending to bring two adjacent coils together if TF coil currents are unbalanced during an abnormal condition
- gravity loads
- horizontal and/or vertical seismic loads.

The coil case would also act as a helium vessel if a pool boiling winding were used.

Loads are categorized as normal and abnormal. The normal category includes loads occurring in the course of the device performing its intended function. It also includes loads which are expected to occur, albeit not by design (e.g., plasma disruption, quench). The stress limits are selected to provide reasonable assurance that there will be no equipment damage. Although there may be localized yielding at stress concentrations, there will be no significant yielding. The abnormal category includes loads which may occur during service but which are not expected during normal operation of the device (e.g., a seismic event, loads due to unbalanced TF coil currents). The stress limits for this category permit yielding at structural discontinuities but prevent gross yielding. The component must remain functional.

Structural support members are designed according to structural design criteria which are similar to those used in other large superconducting magnet programs such as the Large Coil Program (LCP), the Component Development and Integration Facility (CDIF), and the Mirror Fusion Test Facility (MFTF). The criteria, which are summarized in Table 4-3, provide a safe margin against failure due to gross overloading of a structural member, as well as providing a margin against growth of an undetected flaw due to cyclic loading and potential subsequent fracture in the vicinity of the flaw. Given the number of cycles for which FED must be designed, the fracture mechanics allowable stresses are generally more restrictive than the design allowable stresses which would apply to a steady state device. In view of the high cyclic loads which exist in the baseline design, many structural components are sized by fatigue and fracture mechanics considerations.

4.1.2 TF Coil Layout and Principal Components

This section describes the configuration of the TF coils and their supporting structure. Many of the design features were selected on the basis of tradeoff studies in which the advantages and disadvantages of two or more potentially workable concepts were compared.

Table 4-3. FED structural design criteria

- PRIMARY STRESS LIMITS

  Limits are defined as multiples of S_m, defined as follows:

  Metals S_m = the lesser of 2/3 yield strength or 1/3 ultimate strength at operating temperature

  Non-metallics S_m = 1/3 ultimate strength at operating temperature

  - Normal operating conditions

    Primary membrane stress intensity $\leq S_m$

    Primary membrane plus bending stress intensity $\leq 1.5\ S_m$

    Average shear stress $\leq 0.6\ S_m$ (metals)

  - Abnormal operating conditions

    Each of the above limits is multiplied by 1.5

  - If buckling is a potential failure mode, a margin of 5 against elastic buckling is required

- FATIGUE AND FRACTURE MECHANICS LIMITS

  An allowable peak tensile stress is derived from the Paris crack growth law and from fundamental fracture mechanics principles. For 316 LN stainless steel (used in FED) and a fully cyclic load, the allowable stress σ and required number of cycles N are related by the approximate expression

$$\frac{\sigma}{\sigma_o} = \left(\frac{N}{N_o}\right)^{-0.307}$$

  where

  σ_o = 16.6 ksi and N_o = 350,000 cycles.

The coils are pancake-wound and consist of 28 pancakes of 15 turns plus 4 pancakes of 6 turns each, for a total of 444 turns. The conductor utilizes NbTi strands in a steel conduit, and is cooled by supercritical forced flow helium. At 8-T peak field operation, the liquid helium outlet temperature is 4.5 K, while at 10-T peak field operation the outlet temperature is reduced to 3.1 K. A U-shaped steel channel is co-wound with the conductor to provide a direct load path to the case for the accumulated magnetic loads in the winding that would otherwise crush the conductor conduit. Without the channel, the magnetic loads would have to be transmitted through successive conduits in bending action (because of the rounded conduit corners), which would result in an unacceptable conduit wall thickness. The conductor-in-channel is wrapped with kapton and fiberglass tape for electrical insulation. The assembled winding is then vacuum-impregnated with an epoxy potting compound which provides additional electrical insulation and also eliminates interturn conductor slippage and slippage of the conductor in the channel, which is a potential mode of heat generation.

During normal operation, there are distributed forces acting along the periphery of the coil, both in and normal to the plane of the coil. The resultant of the in-plane forces is a net radially inward centering force. This centering load is reacted principally by the bucking post, which supports the TF coil radially along the straight leg of the D-shaped coil. Analysis shows that a portion of the net centering load ($\sim$40%) is reacted by wedging of the TF coil cases adjacent to the bucking post. A small portion of the net centering load is also reacted by wedging of the intercoil support structure.

The out-of-plane forces on the TF coil, which result from interaction with the field created by the poloidal field (PF) coils, are such that there is no net force normal to the plane of the TF coil but a large overturning moment which tends to tip the TF coils about their horizontal axis of symmetry. The overturning moment is reacted by intercoil support structure (ISS) which joins adjacent TF coils at the top and bottom. Figure 4-3 is a sketch of a TF coil showing the cross

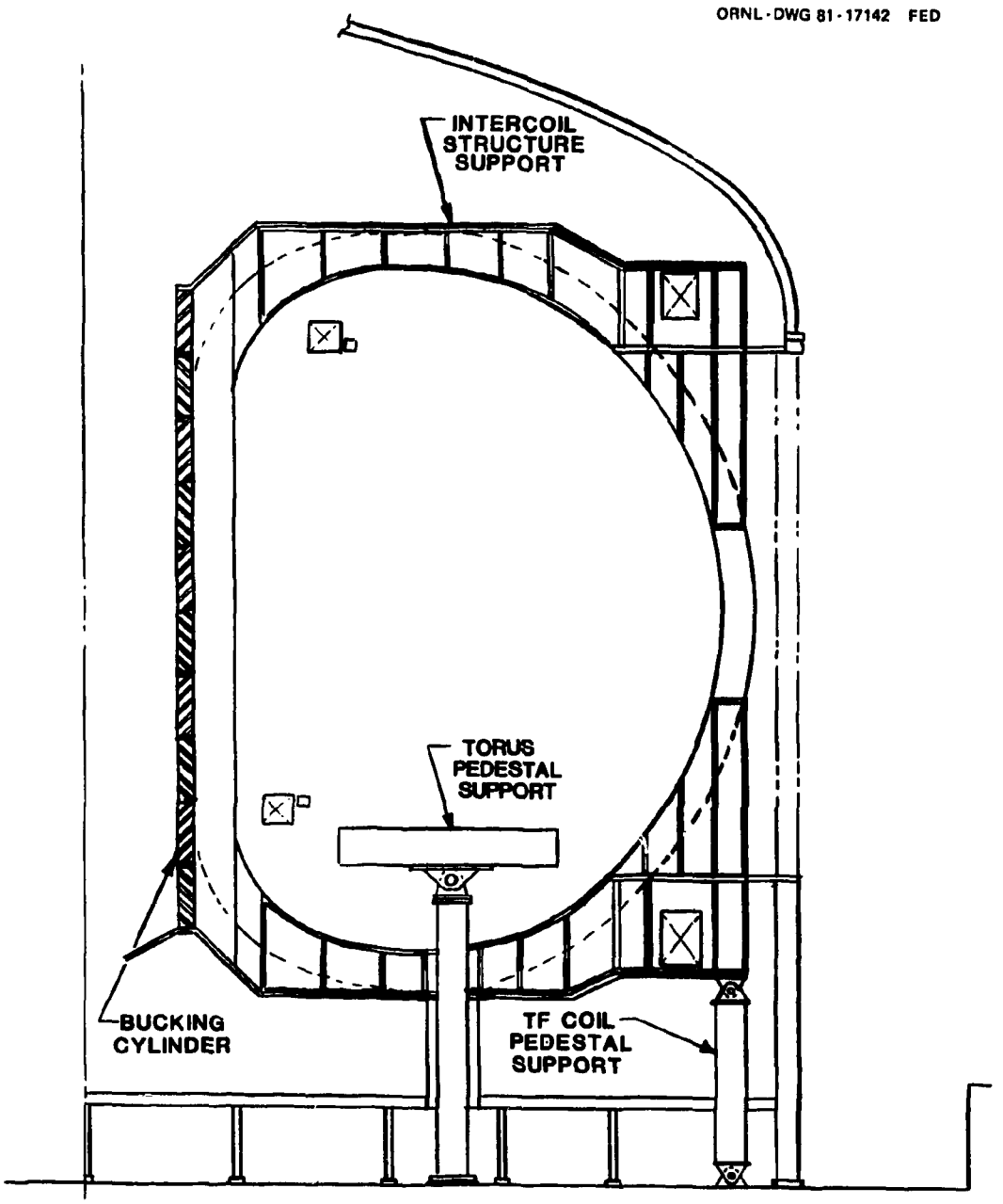

Fig. 4-3. FED TF coil, intercoil support structure, bucking cylinder and pedestal support.

section of the ISS. The ISS consists of box-type modules having an inner and outer shell plus circumferential stiffening ribs.

In order to permit removal of torus sectors, there is an open window region between adjacent TF coils extending to approximately $\pm$4.5 m from the horizontal midplane of the TF coils. The upper and lower portions of the TF coils, which are joined to the ISS modules, behave approximately as two rigid umbrellas joined by ten relatively flexible beams (the outboard portions of the TF coils). Because of the near-antisymmetry of the out-of-plane forces about the horizontal midplane, the two rigid umbrellas tend to rotate in opposite directions, leading to shear and bending loads on the 9 m midspan of the TF coils. The two ends of this span of TF coil case are reinforced by triangular gusset plate modules which are designed to lend additional stiffness to the two ends of the span while not interfering with torus sector removal. Figure 4-4 shows a sketch of a portion of a TF coil, along with one ISS module and some of the gusset plates. Support of the open window region of the TF coils against out-of-plane loads is one of the more difficult TF coil design problems. The need to maintain the open window rules out the use of shear panels or cross-bracing between TF coils in the midspan region. The problem is intensified by the pulsed nature of the out-of-plane loads, which leads to a comparatively low design stress level because of flaw growth and fracture mechanics considerations (see Section 4.1.1).

The ten TF coils are contained within a common vacuum vessel. The vacuum vessel is designed to enclose the open window region of each TF coil in a manner resembling the fingers of a glove. In this way, the open access region between TF coils is preserved.

The dead weight of the TF coils is supported by a series of outboard pedestal supports, as indicated in Fig. 4-3. The pedestal supports are designed to withstand 1 g horizontal and vertical seismic load, and are a negligibly small heat load on the TF coil system.

In the remainder of this section, the design of the principal components of the TF system is discussed in greater detail.

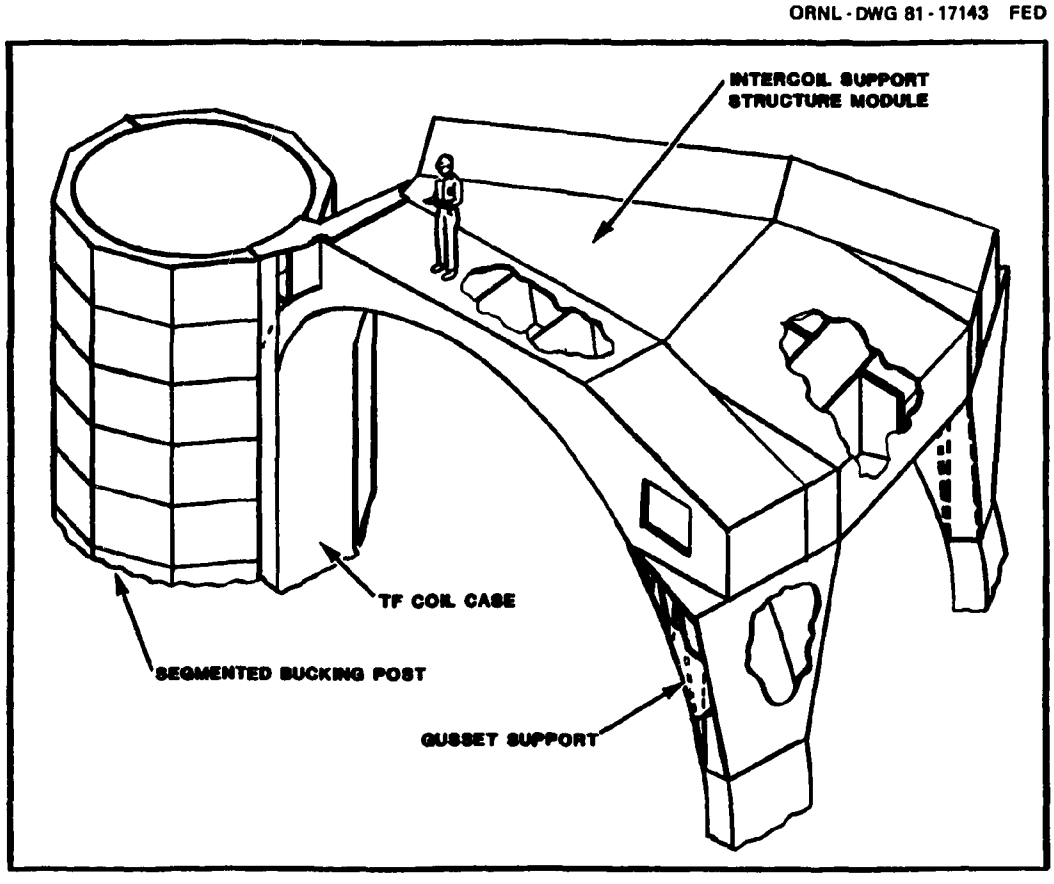

Fig. 4-4. Perspective cutaway view of TF coil, intercoil support structure and bucking cylinder.

Coil case

The TF coil case is welded from 316 LN plate stock. The case has a variable cross section, as shown in Fig. 4-5. In the inboard region, adjacent to the bucking post, the cross section is modified trapezoidal. The cross section is rectangular around the remainder of the coil, with a smooth transition between trapezoidal and rectangular cross sections. The winding cross section is constant around the coil.

The coil case sidewall thickness is sized to carry the distributed load which results from the winding being thrust against the sidewall by the out-of-plane pulsed field forces. Because this load is highly non-uniform around the coil periphery, the coil case thickness is zoned, with the thickness in each zone based on the maximum running load in that zone. The three zones are 1) the inboard zone, adjacent to the bucking post, 2) the ISS zone, the portion of the coil case between ISS modules, and 3) the outboard zone, the unsupported midspan of the case in the open window region. The sidewall thicknesses are based on a fracture mechanics working stress of 16.6 ksi, and are as indicated in Table 4-4.

Table 4-4. TF coil case wall thicknesses

Inboard region	5.4 cm (side), 8.0 cm (inside, outside)[a]
ISS region	10.7 cm (all around)
Outboard region	12.0 cm (all around)

[a]See Fig. 4-5.

In addition to the plate bending stress in the sidewall, the case develops in-plane membrane and bending stresses as the coil is dilated by the in-plane Lorentz forces. The membrane component is shared between the case wall and the structural steel in the winding (conductor conduits, co-wound channels). Since the case wall is sized for a 16.6 ksi working stress, it can easily accommodate the in-plane dilational stresses, the allowable for which is much higher (see Sect. 4.1.1). It is, therefore,

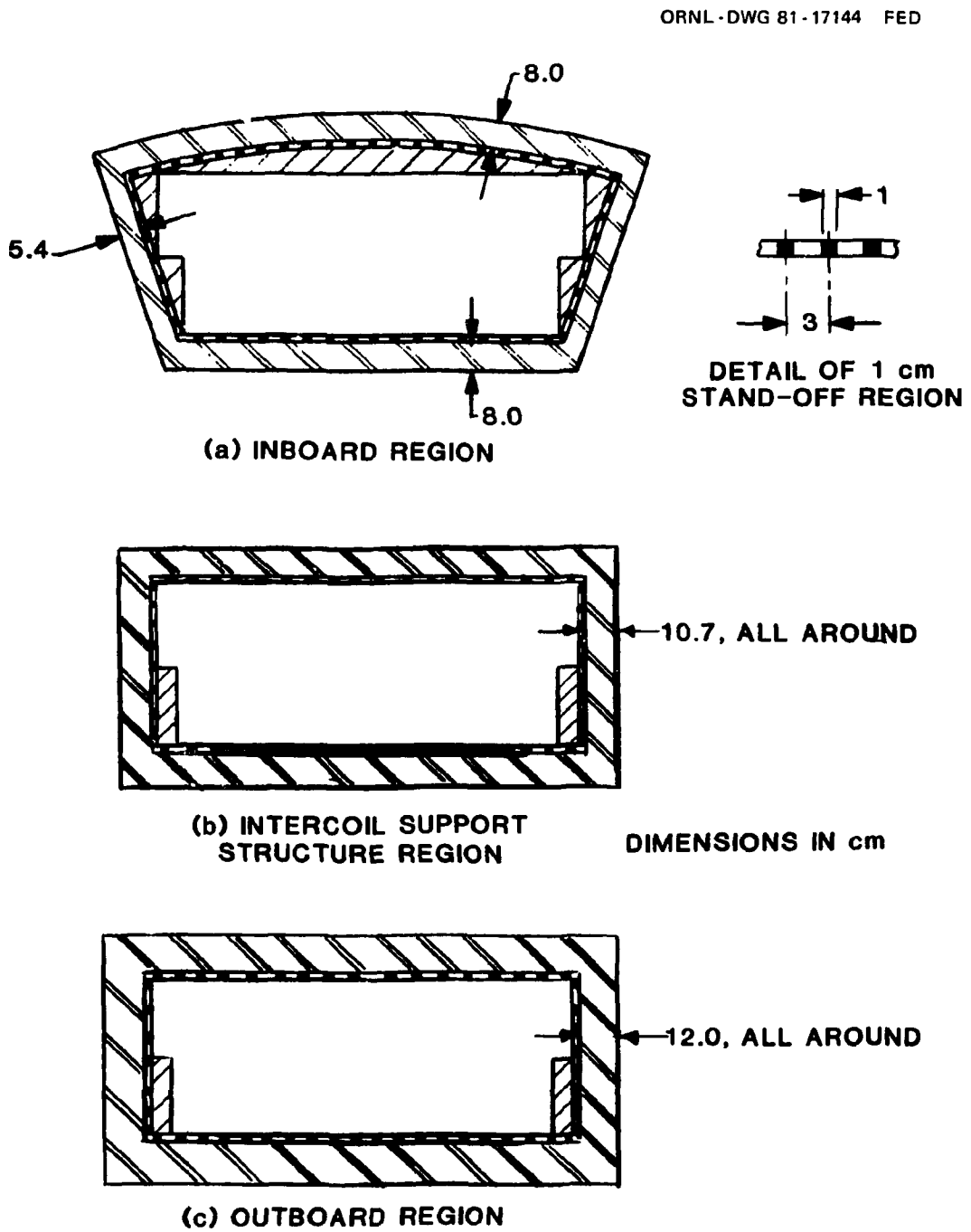

Fig. 4-5. TF coil case cross section.

not necessary to leave a gap between the winding and the coil case to enable the winding to carry the full dilational force.

Gusset support modules

In view of the near-antisymmetry of the out-of-plane forces about the horizontal axis of the TF coil, the top and bottom TF coil-ISS assemblages rotate in opposite directions, causing the outboard region of the TF coil case to behave as a beam, rigidly clamped at both ends, in which one end deflects relative to the other. This type of loading is cyclic, so that the resulting beam bending stresses in the case are subject to a 16.6 ksi allowable per fracture mechanics considerations. The coil case cross section, whose wall thickness is sized to carry the plate bending load exerted directly by the winding, does not have sufficient section modulus to meet the 16.6 ksi allowable on beam bending stress. Straightforward thickening of the case wall to develop the required section modulus leads to unreasonable wall thicknesses. Consequently, reinforcement of the ends of the beam is provided in the form of gusset plates. These members are designed to increase the section modulus of the beam cross section without encroaching on the window space needed for torus sector removal.

Figure 4-6 shows the construction of the gusset support modules. Four vertical triangular rib-like plates are welded to a backing plate whose shape matches an extension of the TF coil case sidewall. An additional triangular plate is placed across the top of the four vertical ribs, in a horizontal plane. This subassembly is then bolted to the extension of the TF coil case sidewall and also to the overhead intercoil support structure. Finally, an exterior cover plate is bolted to the outside of the subassembly. The fully assembled gusset support module is shown in place in Fig. 4-4. The vertical ribs and external cover plate are fabricated from 7.5 cm thick 316 LN plate stock, while the backing plate and the triangular plate across the top of the four ribs is made from 5 cm thick 316 LN.

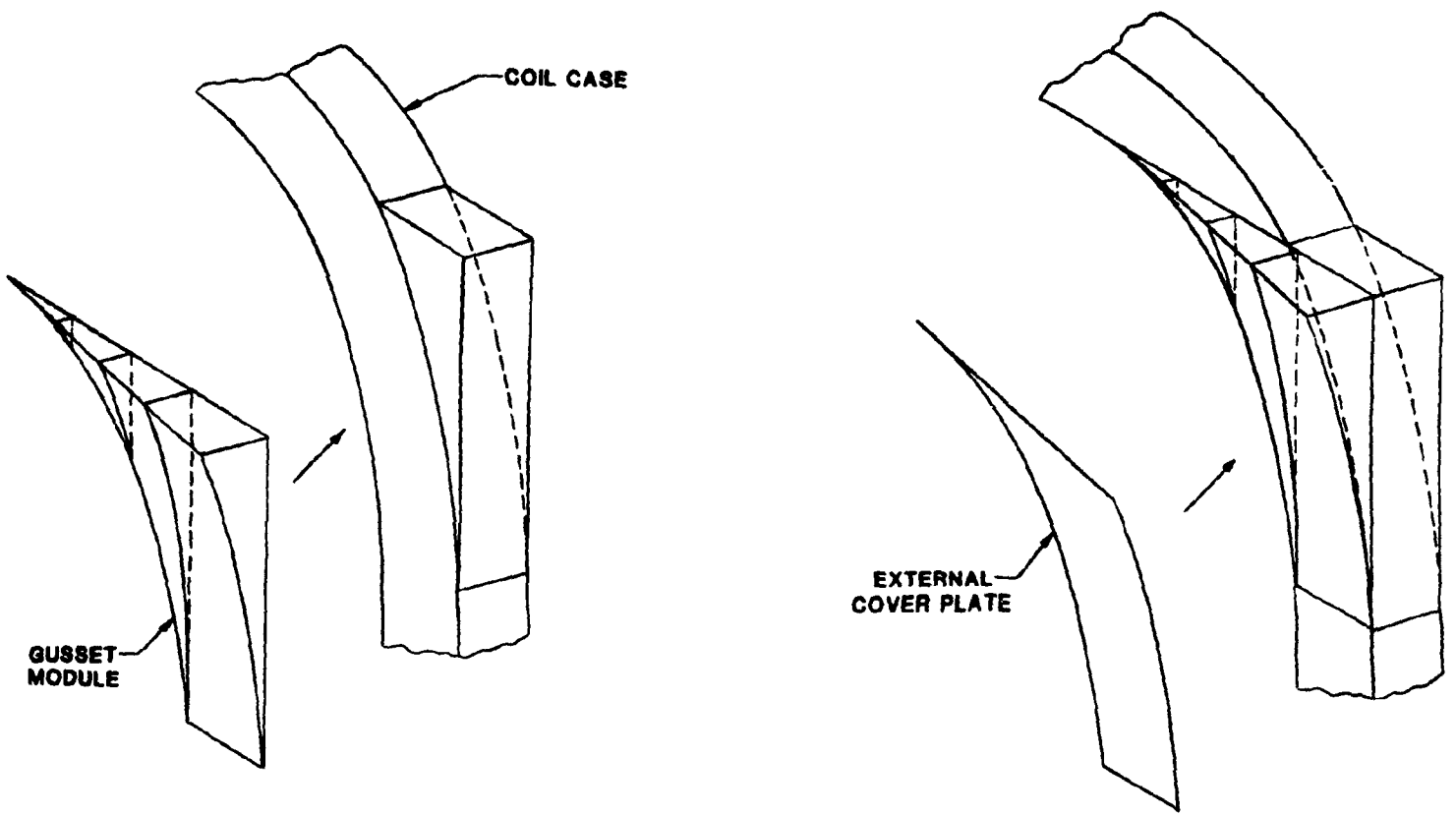

Fig. 4-6. TF coil gusset support modules.

Intercoil support structure

The purpose of the intercoil support structure (ISS) is to equilibrate the overturning moment on the TF coils. The ISS is fabricated in the form of box-type modules which are bolted to the TF coils. The ISS modules have an inner and outer shell plus internal stiffening panels running in the circumferential direction. Figure 4-7 shows the cross section of the ISS modules, while Fig. 4-8 shows a plan view.

The ISS is welded up from 316 LN plate stock, most of which is 5 cm thick. Each ISS module is composed of two subassemblies, which extend from the TF coil sidewall to the midplane between adjacent TF coils. The TF coil case sidewall is extended to match the overall depth of the ISS subassemblies. The subassemblies are bolted to the extended TF coil case; adjacent subassemblies are then joined to form an ISS module by a weld along their common boundary. Because of dimensional tolerance fit-up problems, which are virtually certain to occur with large structures, shims may be inserted, if needed, along the boundary between the subassemblies prior to performing the closure weld. When all of the ISS modules are in place, the assemblage of TF coils and ISS modules form two very rigid umbrella-like structures which are connected by the inboard and outboard legs of the TF coils.

The configuration of stiffening panels within the ISS modules is chosen to allow room for two superconducting ring coils, as shown in Figs. 4-3 and 4-7. These ring coils (top and bottom) produce sharp peaks in the out-of-plane force distribution. Consequently, a heavy-wall ring girder (box beam) is used just outboard of the ring coils to react the load peak and to provide rigid support to the ends of the mid-span of the TF coil case; the walls of this ring girder are 10 cm thick.

There are penetrations in the lower ISS modules which allow the torus pedestal supports to pass through the ISS midway between TF coils.

When the TF coils are operated at 10-T peak field, the eddy current losses in the ISS are about 46 kW during normal pulsing operation. To shield the TF windings from this heat load, a layer of low thermal conductivity dielectric material is inserted between the TF coil sidewall and the ISS subassemblies at the time the subassemblies are placed in

ORNL-DWG 81-17362 FED

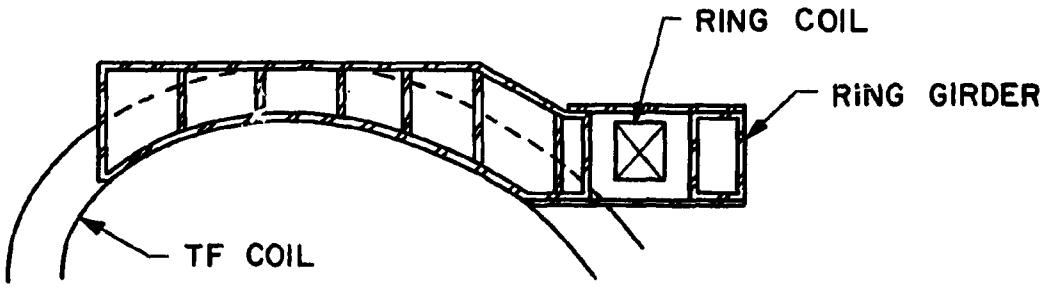

(a) UPPER PORTION

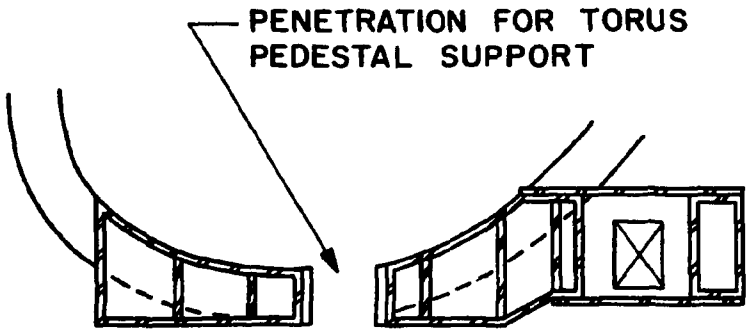

(b) LOWER PORTION

Fig. 4-7. Intercoil support structure, cross section.

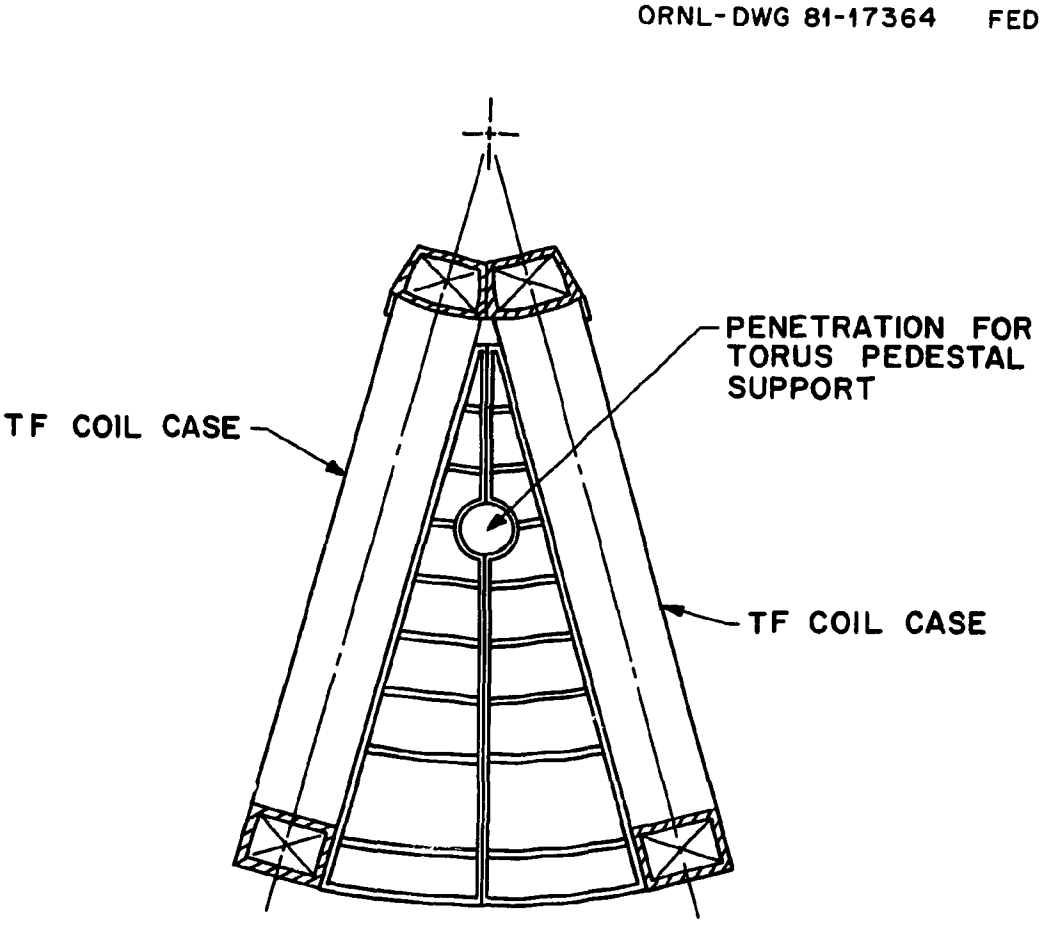

Fig. 4-8. Intercoil support structure, plan view.

position. Besides serving as a thermal barrier, the insert prevents ISS eddy current losses due to toroidal current flow in the ISS umbrellas.

Coolant channels

Time varying poloidal fields induce eddy current losses in the TF coil case and the intercoil support structure (ISS). The eddy current losses in the TF coil case and ISS during normal pulsed operation at 10-T are 3.2 kW and 4.6 kW per coil, respectively (averaged over 152 s cycle); during plasma disruption, the case losses are about 5.8 kW (averaged over 152 s) per coil, with a comparable loss in the ISS.

These losses are the dominant heat load and are much larger than the losses which occur directly in the winding. The helium coolant flow in the winding is sufficient to remove the losses which occur in the winding, but cannot handle the higher losses in the coil case and ISS. In the present design, supplementary coolant channels are provided between the inside surface of the TF coil case and the exterior of the winding. Liquid helium flows through these channels and intercepts the case heat before returning to the refrigerator, as described in Sect. 8.4. Similar coolant channels are embedded in the ISS to intercept the ISS losses.

Ground supports

The TF coils are vertically supported by a series of outboard pedestal supports. The supports are in the form of a hollow cylinder fabricated from concentrically wrapped layers of fiberglass cloth and epoxy (such as G-10). The two ends of the cylinder fit over steel fittings which permit attachment to the underside of the TF coils and provide a pinned support at each end (see Fig. 4-9). The supports penetrate the vacuum vessel, so that one end is at cryogenic temperature and the other at room temperature. The heat leak through the pedestal supports is only about 35 W, which is negligible compared to the eddy current losses in the coil structure; consequently, a liquid nitrogen heat intercept for the supports was dismissed as unnecessary.

ORNL-DWG 81-17146 FED

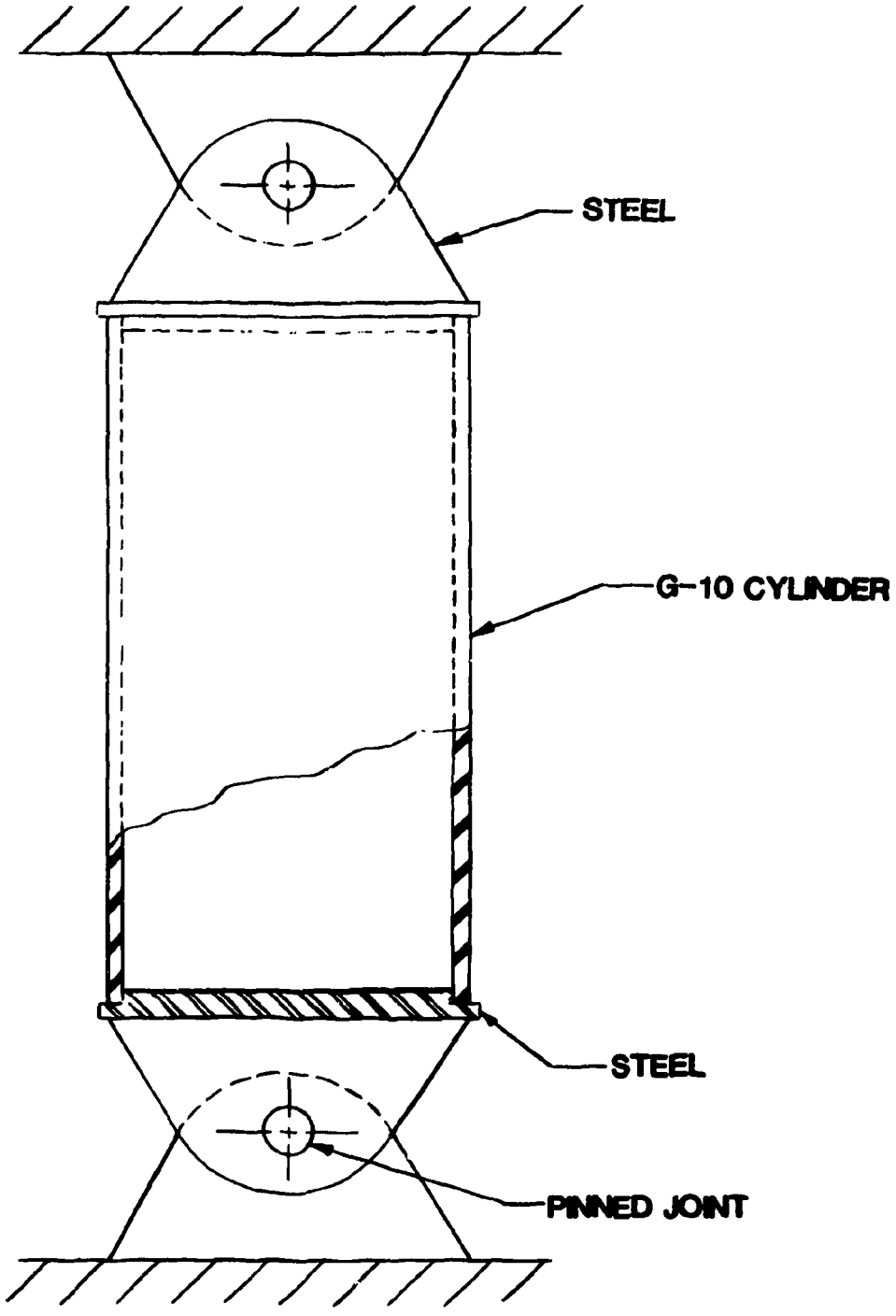

Fig. 4-9. TF coil pedestal support.

The mean diameter of each pedestal support is 1 m and the wall thickness of the cylinder is 3.8 cm. The pedestal supports are sized to accommodate the dead weight of the TF coils, intercoil support structure, bucking cylinder and other equipment which is supported off the TF coils (most notably the two outboard superconducting EF coils), as well as to withstand horizontal and vertical seismic loadings of 1 g. This seismic loading is the design value ground acceleration of 0.25 g multiplied by an amplification factor of 4, which results from a simple vibration analysis.

Bucking post

The bucking post equilibrates most of the net centering force on the TF coils. It is a right cylinder of length 10 m and has a cross section which is a 10-sided regular polygon with a circular central hole. The distance across flats of the polygon is 3.48 m, while the diameter of the central hole is 2.96 m. In addition to the compressive radial loading on the bucking post, there are small torsional loads due to the out-of-plane loads on the TF coils; however, the torsional stresses have been shown by analysis to be very low.

The bucking post is fabricated from 316 LN forgings in 10 axial segments, each 1 m long. The axial segments are designed to fit together by means of a male-female joint, as indicated in Fig. 4-10. The segments are joined by a series of recessed bolts which fit into tapped holes, thereby providing stability against torsional loads and axial tensile loads (which could arise during a vertical seismic event).

Each of the axial segments of the bucking post contains a single thin radial insert of G-10 dielectric whose function is to suppress eddy currents. This insert is in the direction of a line between the center of the interior hole and a corner of the polygonal outside cross section. Since the mechanical strength of the dielectric is less than that of the metal, the inserts of the various axial segments are azimuthally staggered in order to avoid any significant local structural weakening. Because of the staggered position of the radial inserts, adjacent axial segments

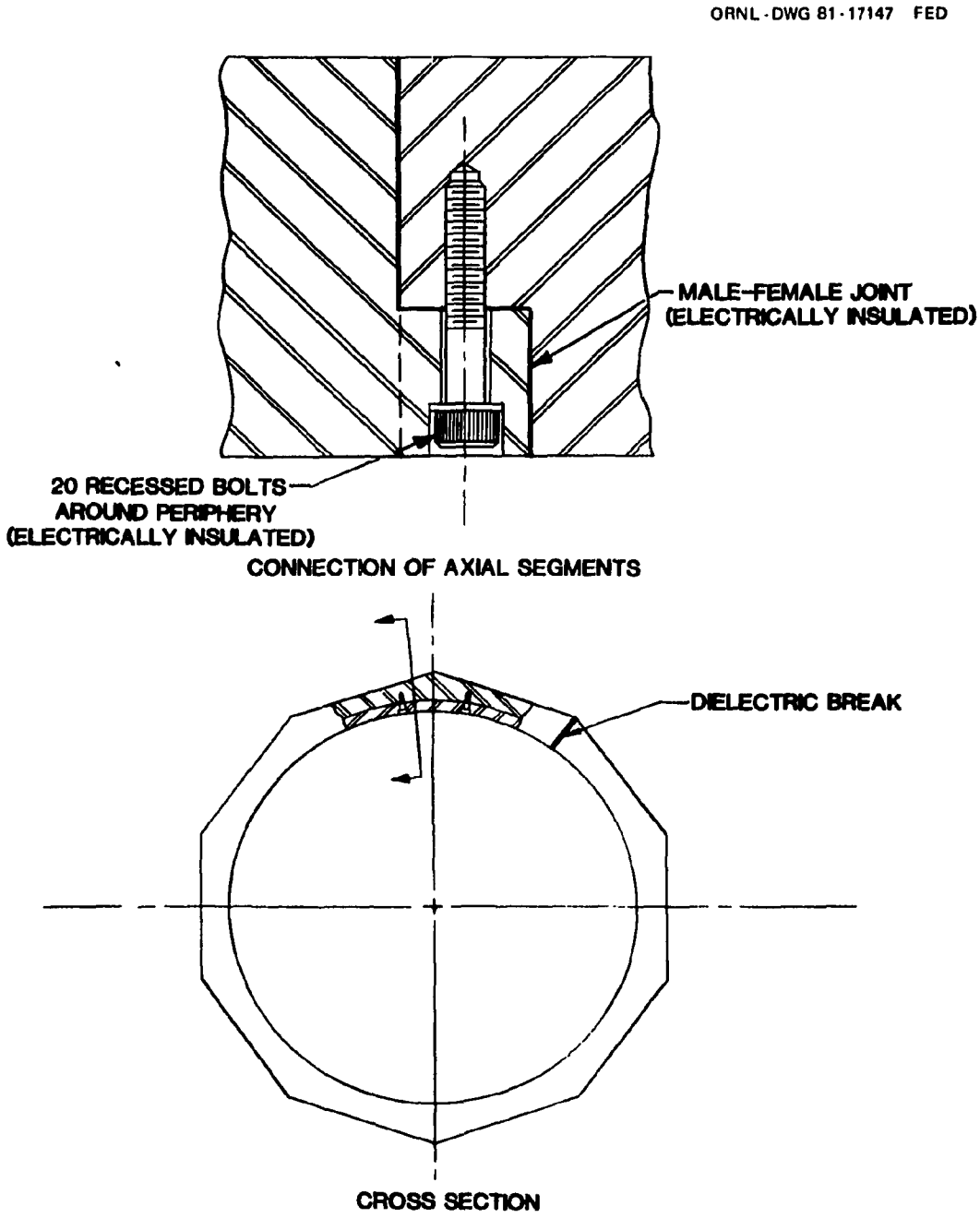

Fig. 4-10. Bucking post design.

of the bucking post must also be separated by a G-10 dielectric layer; in addition, the recessed bolts which join the axial segments must be electrically insulated.

The dead weight of the bucking post and that of the ohmic heating (OH) solenoid are supported off the TF coil intercoil support structure by means of a collar joining the lower end of the bucking post to the intercoil support structure. A similar collar joins the upper end of the bucking post to the intercoil support structure. The collar configuration is shown in Fig. 4-11. Besides supporting the dead weight of the bucking cylinder and OH coil, the collars contribute some additional stiffness against the TF coil out-of-plane overturning loads.

The 10 axial segments of the bucking post together weigh 230×10^3 kg. The two collars together weigh about 30×10^3 kg.

Winding and insulation

The TF winding must operate reliably under normal operating conditions while withstanding both steady state and pulsed magnetic loads, as well as eddy current and nuclear heat loads. The winding is designed to be cryostable. Various conductor concepts were considered (Sect. 4.1.3); although there is no clear basis at this time for a preferred concept, the internally cooled cabled superconductor (ICCS) was selected for illustrative purposes in this report. A winding design, based on ICCS, which meets the system requirements, is described in the following sections.

Conductor

The overall conductor dimensions are shown in Fig. 4-12 and its relevant parameters are given in Table 4-5. The conductor design is based on an ICCS successfully used in a small test magnet at ORNL[1,2]. The two European LCP coils and the Westinghouse LCP coil are also based on a similar ICCS.

The number and diameter of the insulated strands and filaments in the conductor are chosen to obtain low ac losses in the winding. The

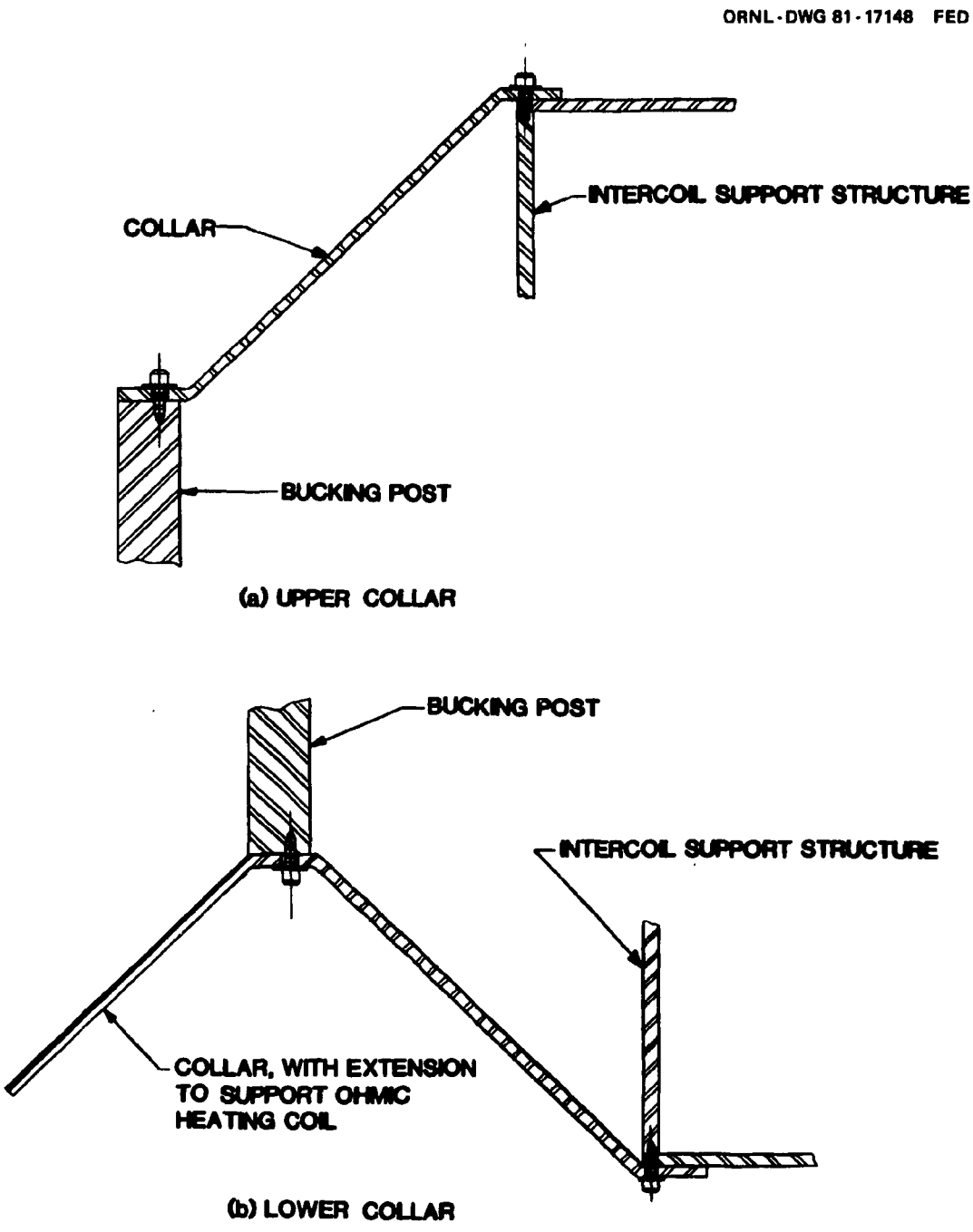

Fig. 4-11. Attachment collars on bucking post.

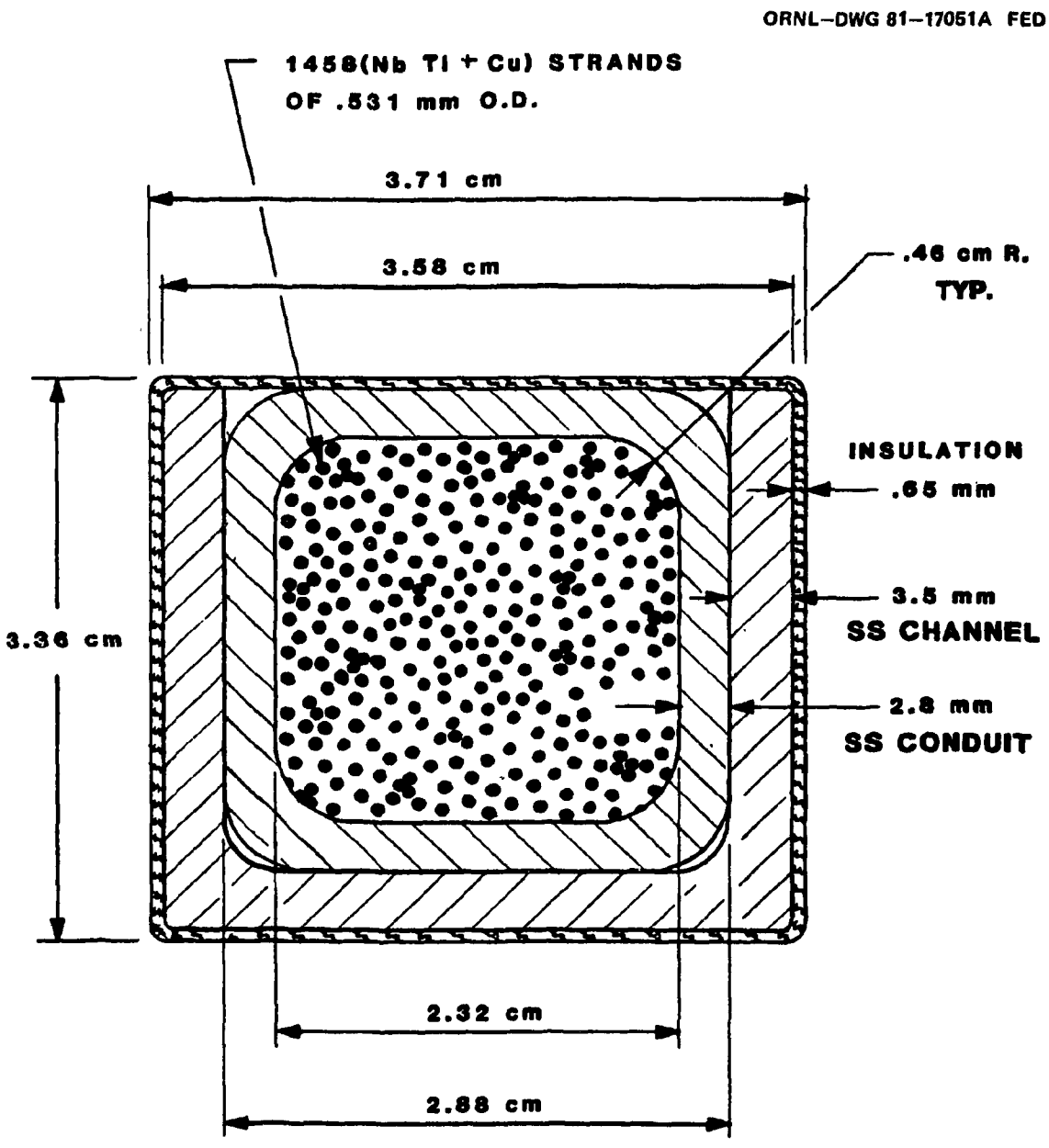

Fig. 4-12. ICCS conductor dimensions for TF coils.

Table 4-5. Internally cooled cable superconductor (ICCS) parameters

Overall dimensions	3.58 cm × 3.23 cm
Unit cell volume (He + Cu + NbTi) (cm^3/cm)	5.385
Metal volume (NbTi + Cu) (cm^3/cm)	3.231
NbTi volume (cm^3/cm)	0.588
Cu volume (cm^3/cm)	2.643
Helium volume (cm^3/cm) [40% of unit cell]	2.154
Cu/SC Ratio	4.5:1
Cooled perimeter (cm^2/cm)	203.0
Number of strands	$6 \times 3^5 = 1458$
Strand diameter (mm)	0.531
Hydraulic diameter D_{hf} (mm)	0.406
Number of filaments in each strand	114
Filament diameter (μ m)	21.2
Strand twist length L_s (mm)	3.9
Operating current I_o at 8 T, 4.5 K (kA)	20
Operating current at 10.2 T, 3.1 K (kA)	25.5
I_o/I_c (at 8 T, 4.5 K)	0.555
I_o/I_c (at 10 T, 3.1 K)	0.528
Limiting current density (J_{Limit}) (at 8 T, 4.5 K) (kA/cm^2)	10.2
Limiting current density (J_{Limit}) (at 10 T, 3.1 K) (kA/cm^2)	11.4
Thermal Capacity ΔH (mJ/cm^3) (at 8 T, 4.5 K and 10 T, 3.1 K)	200

conductor is cooled by forced-flow pressurized helium with an outlet temperature of 4.5 K and 3.1 K at 8-T and 10-T operation, respectively. The conductor has a thermal capacity of about 200 MJ/cc both at 8-T and 10-T operation without reverting to the normal (resistive) state. Stability and protection considerations are discussed in Sect. 4.2.4.

Winding

The cross section of the TF coil in the inboard region is shown in Fig. 4-13. The design parameters are listed in Tables 4-5 and 4-6. The coils are pancake wound and consist of 28 pancakes of 15 turns plus 4 pancakes of 6 turns, for a total of 444 turns. Each pancake is wound with 3 conductors in parallel, so that a full coolant channel consists of 5 complete turns. Electrical connections (current leads and splices) are in the top region of the coil. As illustrated schematically in Fig. 4-14, the turns are electrically connected in series but have three parallel cooling circuits. Helium enters through headers inside the coil bore and exits through headers outside the coils. The length of each cooling path is about 173 m; this path length results in a pressure drop of about 1 atm during 10-T operation.

A header is fabricated at each electrical joint (between terminals of the conductors from adjacent pancakes) using the Westinghouse LCP coil concept shown in Fig. 4-15. The supercritical helium exits the conductor through these headers. Joints are made by inserting the cable (superconducting strands) into a copper collar which is compacted to remove all the voids between strands. Two adjacent conductor joint sections are then resistance welded together and supported as shown in Fig. 4-15. Low resistance ($\sim 2 \times 10^{-9}$ ohm) mechanically rugged joints have been achieved in the Westinghouse LCP coil using this technique.

The temperature and pressure conditions shown in Table 4-6 for the inlet and outlet helium are based on an estimate of the heat load occurring in the hottest channel. This heat load consists of the average ac loss heat load plus the nuclear heating which results from attenuation of nuclear radiation in the turn closest to the shield. The heat leak from the case to the winding has been calculated and found to be negligible.

Table 4-6. TF coil data for 8-T and 10-T operation

Parameter	Unit	8-T Operation	10-T Operation
Field on plasma axis	T	3.6	4.6
Peak field at the winding	T	8.0	10.2
Ampere-turns/coil	MAT	9	11.5
Operating current	kA	20	25.5
Winding current density	A/cm^2	1720	2200
Number of turns		444	444
Number of full pancakes		28	28
Number of partial pancakes		4	4
Superconductor operating current density	A/cm^2	34,200	43,500
Ratio operating/critical current density	A/cm^2	0.555	0.521
Helium inlet temperature	K	4	2.2
Helium outlet temperature	K	4.5	3.1
Helium inlet pressure	Atm	5	5
Helium outlet pressure	Atm	4.3	4
Helium flow rate per coil	g/s	250	400
Maximum quench pressure	Atm	135	218
Maximum temperature rise during quench	K	200	200
Maximum discharge voltage	kV	5	6
Stored energy/coil	GJ	1.5	2.4

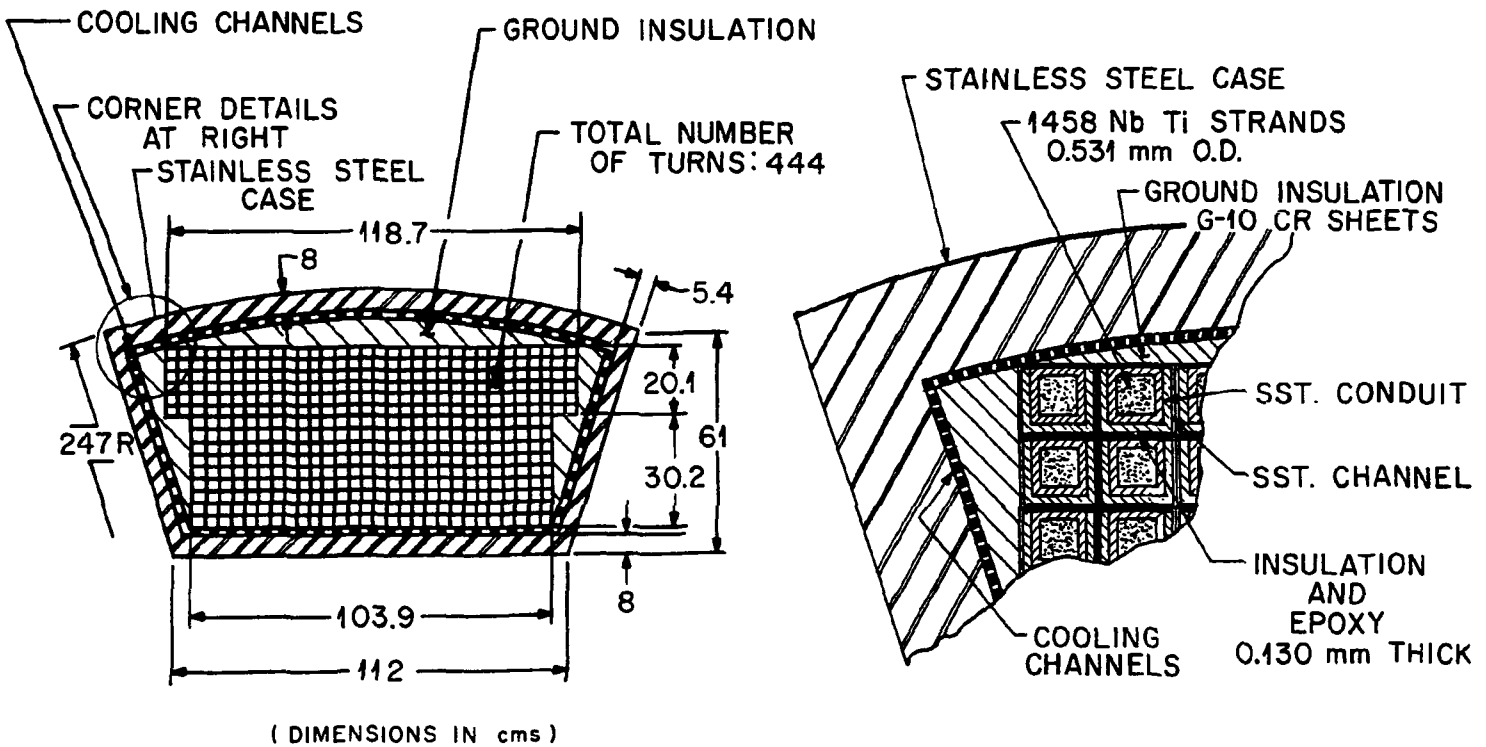

Fig. 4-13. Winding pack configuration.

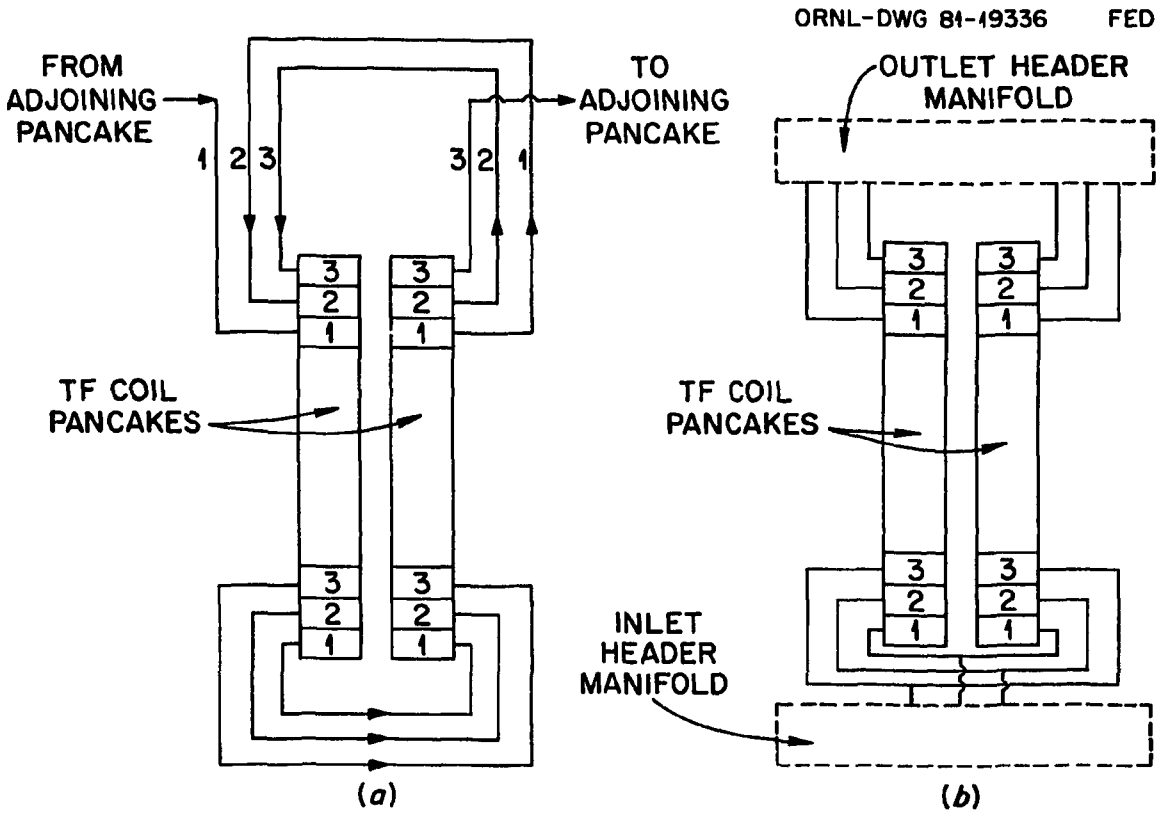

Fig. 4-14. Winding of TF coil pancakes with three conductors in parallel: (a) Schematic of electrical connections, and (b) schematic of coolant connections.

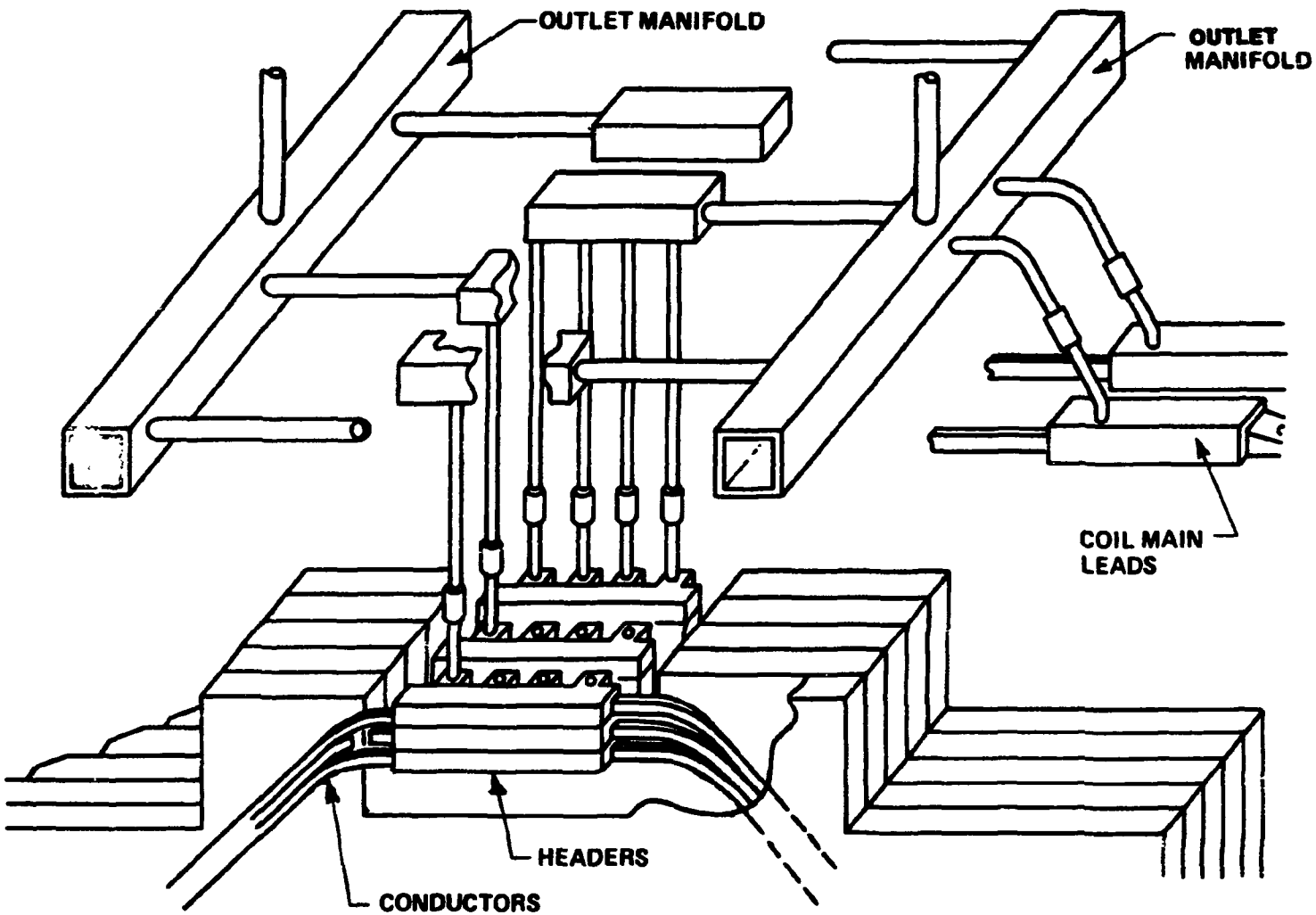

Fig. 4-15. Schematic of coil header region.

The average channel heat load is 6 W. The refrigeration design discussed in Section 8.4 assumes a hot channel heat load of 18 W and concludes that the inlet helium must be in a superfluid state. The calculations in this section use a 7 W hot channel heat load and conclude that at 10 T, the inlet helium temperature is 2.2 K, just barely above the λ-point temperature.

Furthermore, the present calculations are based upon a 152 s pulse length at 10 T. For the shorter pulse length presently being considered for 10-T operation (102 s per the FED parameter list), the average heat load would increase by 50% and the need for superfluid inlet helium would be certain. Use of superfluid helium increases the complexity and cost of the refrigeration equipment so that it would be prudent to maintain the cycle time of 152 s at 10 T as well as at 8 T.

Even with a 152 s pulse length, however, the ability to avoid the use of superfluid helium is marginal, at best. Considering the uncertainties in the present thermodynamic analysis, and the great increase in refrigeration system complexity and cost if superfluid is required, a more precise identification of the inlet helium conditions remains an unresolved issue which will be addressed during the conceptual phase.

Insulation

As shown in Fig. 4-12, the conductor is insulated before winding the pancakes. Primary insulation is provided by wrapping six layers of 0.025 mm (0.001") thick Kapton H tapes (butt lapped). Kapton has excellent dielectric strength and good radiation resistance. Two layers of glass tape are then applied during the winding. A total insulation thickness of 0.025" is applied to each side of the conductor. After all the pancakes are wound and connected together, the winding is covered on all sides by thin (2 mm thick) G-10 CR sheets. These G-10 sheets provide the ground insulation and thermal barrier between the winding and the coil case. Finally, the winding is vacuum impregnated using an epoxy potting compound. The potted winding is housed inside a stainless steel casing as shown in Fig. 4-13. The cooling channels between the winding and the case are provided to intercept the heat leak from the coil case

to the winding. The helium returning from the winding is circulated through these cooling channels in the coil case before being sent back to the refrigerator.

Current leads

The current leads are designed for 25,000 amperes for 10-T operation. The lead design concept is similar to the Westinghouse LCP leads.[3] A schematic of the lead routing is shown in Fig. 4-16. The transition region between the conductor and the lead is shown in Fig. 4-17. The leads are connected to the winding through a header. This header consists of a jacket collar entrance, cable support shock collar, swaged joint cover, jacket adaptor, and lead jacket. A length of the superconductor swaged down inside a copper sleeve (the same as the conductor ends) is brazed into the opposite end of the copper lead. The stainless steel sleeve is also brazed into the end of copper lead for welding to the header that encloses the joint between the lead and the winding. The main lead assemblies are supported by the protective header box sidewall and bolted to the coil structure with eight 0.5 in. bolts as shown in Fig. 4-17.

Thus from the coil side, the lead would be cooled by supercritical helium at 3.1 K. The copper leads will be cooled by circulating supercritical helium ($\sim$4.0 K) through the internal cooling channels (not shown in Fig. 4-17).

The copper lead will be electrically isolated from the top flange with a G-10 insert and epoxy bushing. The leads would be insulated with sixteen layers of Kapton H (0.001 in. thick) tape butt lapped and four layers of dry glass tape. It is also proposed to vacuum impregnate the copper leads as much as possible before attaching to the coil. Also, the leads would be adequately supported all along their length for the Lorentz forces on them. It may be possible to react these forces against each other if the two copper leads could be placed in close proximity to each other with adequate insulation.

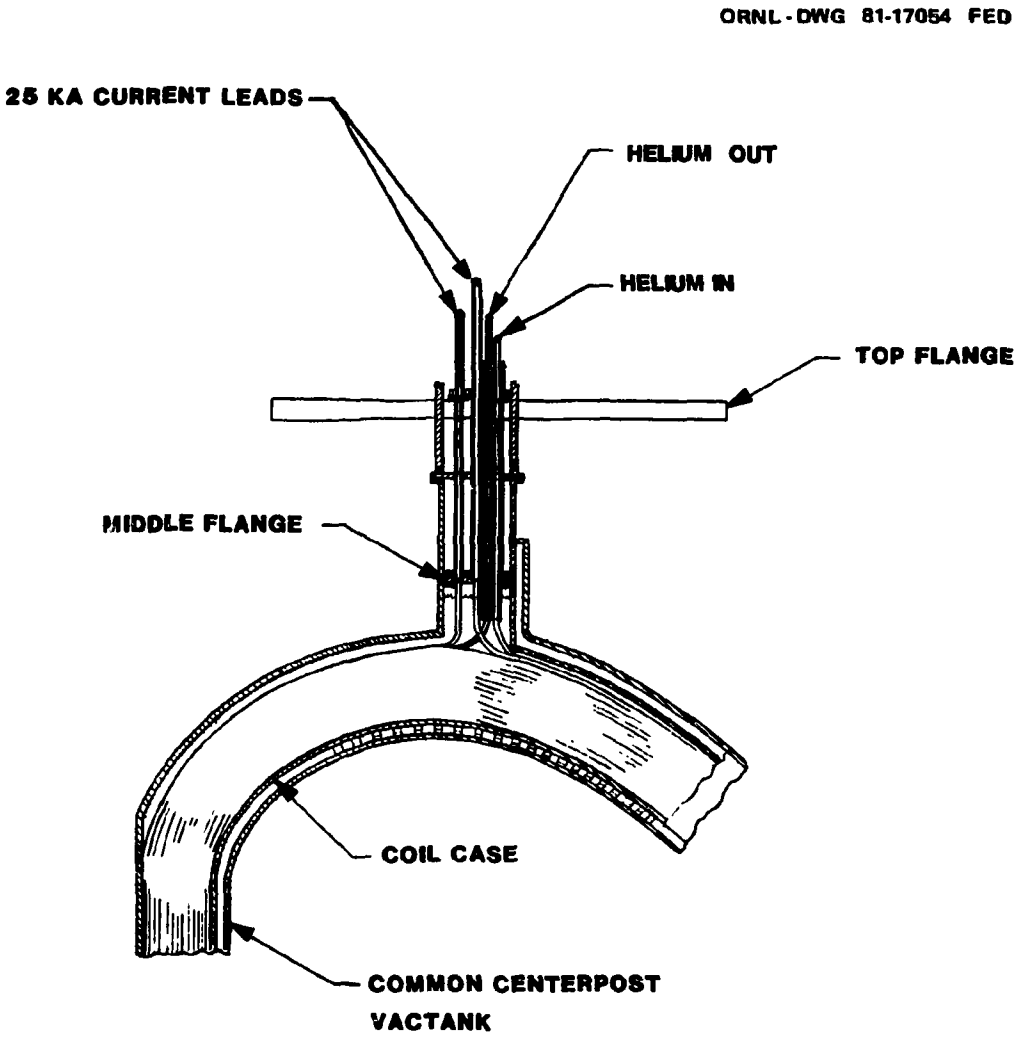

Fig. 4-16. Schematic of current leads routing.

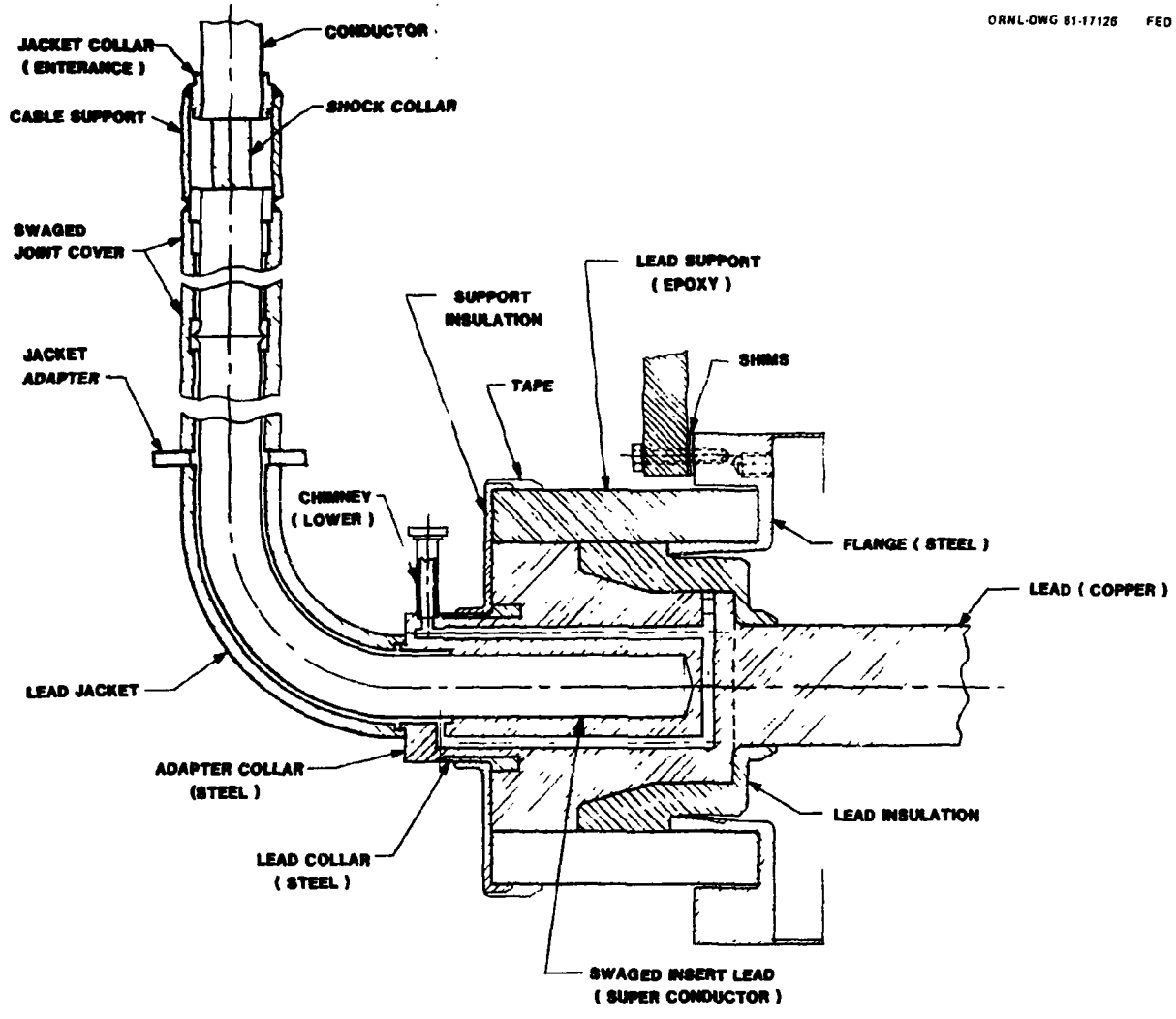

Fig. 4-17. Main lead assembly.

4.1.3 TF Coil Design Selection

The procedure leading to the selection of the TF coil winding baseline concept is discussed in this section. Several options were explored, all of which require a machine major radius of ∿5.0 m and a deviation from the LCP technology in at least the high-field portion of the winding. There are at least three options for winding and cooling concepts, each of which fit in the same envelope, and each has its advantages and disadvantages. The overall magnet community supports the credibility of reaching 10 T with one or another of the options and agrees that an adequate base can be developed to support construction of a selected option.

A winding cavity configuration consistent with 5 m major radius is shown in Fig. 4-18. The winding cavity is sized on the basis of an overall winding current density of ∿2,200 amps/cm^2 at 10 T. This compares with 2500 A/cm^2 at 8 T in LCP and 2000 A/cm^2 at 11 T in INTOR.

Structural design (sizing of case thicknesses, etc.) is consistent with 250,000 8 T-pulses plus 25,000 10-T pulses. Implementation of fatigue and fracture mechanics structural design criteria for this combination of cycles is accomplished by assuming 350,000 8-T pulses and no 10-T pulses; from a fatigue damage standpoint, the two loading conditions are equivalent.

A NbTi winding cooled with forced flow helium has been selected as a baseline for the purpose of design discussions in this report.

Common structural considerations

Five of the six 8-T LCP coils, the MFTF coil, and the FED 8-T design utilize an external case for structural support and transfer all the loads (except for the in-plane load carried by hoop tension of the conductor) from the conductor to the case by compression. At fields above 8 T, this becomes increasingly difficult as the cumulative compressive stress in the conductor exceeds the allowable, independent of the strength of the case. It becomes necessary to add distributed structure, generally in the form of a steel ribbon or channels incorporated into

ORNL-DWG 81-1734 FED

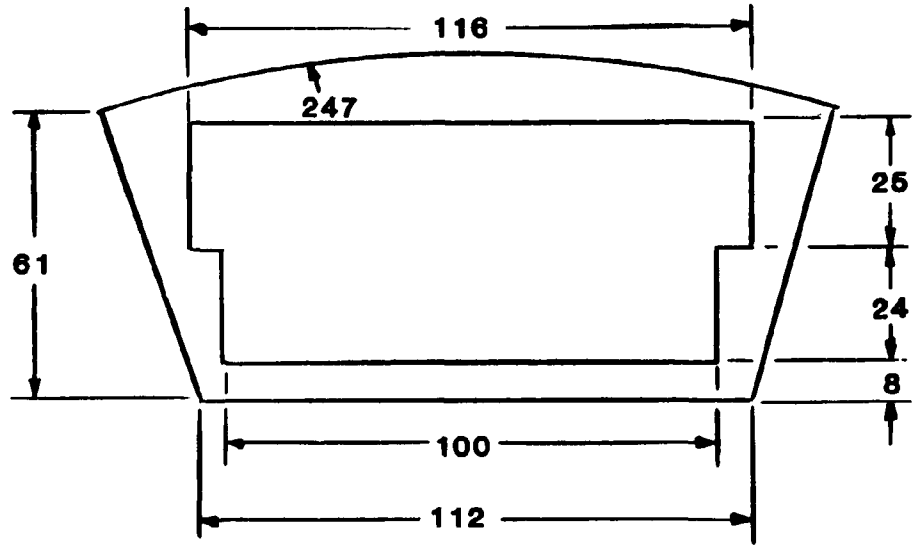

DIMENSIONS IN cm

WINDING CURRENT DENSITY - 2200 amps/cm^2

AMPERE-TURNS REQUIRED AT 10 T - 11.5 MA

COIL CASE STRUCTURE SIZED FOR 350,000 PULSES AT 8 T

Fig. 4-18. Baseline cavity configuration with R_o = 5 m.

the winding. The amount of the steel can vary throughout the winding, depending on the hoop and compressive in-plane loading. This results in a reduced current density in the coil. This need to add distributed structure is independent of the cooling or conductor option chosen for the coil and is treated as a common requirement in the options examined.

Two structural concepts are examined — one in which the distributed structure is added entirely to the conductor and a second in which the coil pack is regionalized. The overall envelope requirements are similar, but each option has its advantages.

Superfluid-cooled NbTi option

This option appeals to many designers because to them it represents the minimum perturbation from the pool-boiling, 4.2 K, NbTi coils for which the largest data base exists. To first order, simply reducing the helium temperature to 1.8 K increases the critical current more than sufficiently to reach 10 T, while the improved heat-transfer capability from the conductor to fluid easily handles the increase in joule heating heat flux. Refrigeration systems at 1.8 K up to 200 W have been built, though they typically require about three times as much power per watt removed as an equivalent unit at 4.2 K.

No large magnets have been built at 1.8 K and only the TORE SUPRA tokamak design team has examined the technology in any detail. There are certain limitations of superfluid which must be evaluated. For example, the need to maintain the coolant in the superfluid state places limitations on the passage cross-sections and passage lengths. This limit influences the amount of ac loss which can be transported out of the winding pack, and influences the length of normal conductor from which recovery can be guaranteed. Within the superfluid limits, however, heat transport is extremely effective.

Stability in superfluid magnets has been treated by the TORE SUPRA group. Subcooled helium at 1.8 K can absorb approximately 300 mJ/cm^3 between 1.8 K and 2.16 K (the limit of superfluid) and still remain superfluid. In view of the high thermal conductivity of superfluid helium, a winding pack which is 25% helium by volume can, therefore,

absorb approximately 75 mJ/cm^3 from a transient disturbance without a local hot spot developing. Superfluid subcooled magnets are therefore expected to be very stable against transient disturbances up to a point, although their ability to transport heat away from a steady-state normality is limited.

This heat transport limit also applies to the ability to handle ac losses. A winding whose cross section is 25% helium can withstand about 1,600 W per coil up through the 10 m center leg. Use of cable conductors would reduce the losses, but because of the lower current density, the overall envelope requirements remain approximately the same.

Superfluid cooled coils will require temperature guard to prevent excessive heat leak from the 4.5 K case to the 1.8 K winding. This could be treated as in the TORE SUPRA design with low conductivity compression blocks for load transfer between the temperature stages, and with all structure and lead losses taken at 4.5 K. The barrier requirements result in a 10 to 15% loss in overall current density.

The coil envelope requirements for a superfluid cooled coil are compatible with the baseline winding dimensions, as shown in Fig. 4-19. The overall current density in the winding pack, which includes the thermal barrier is 2,200 A/cm^2. Coil losses are summarized in Table 4-7. Losses due to neutronic heating in the conductor and helium vessel appear to dominate the total winding losses. The losses in the outer casing would have to be removed through separate cooling tubes embedded in the casing.

If a superfluid option is used for the FED coils, heavy dependence must be placed on the 12-T project and on the TORE SUPRA project. Consideration should also be given to either operation of one of the LCP coils at 1.8 K or construction of a major demonstration coil approaching LCP scale.

Internally cooled NbTi option

This option is based on the high level of stability that appears to be associated with internally cooled coils which are cooled by supercritical helium. In the supercritical state helium does not boil, and

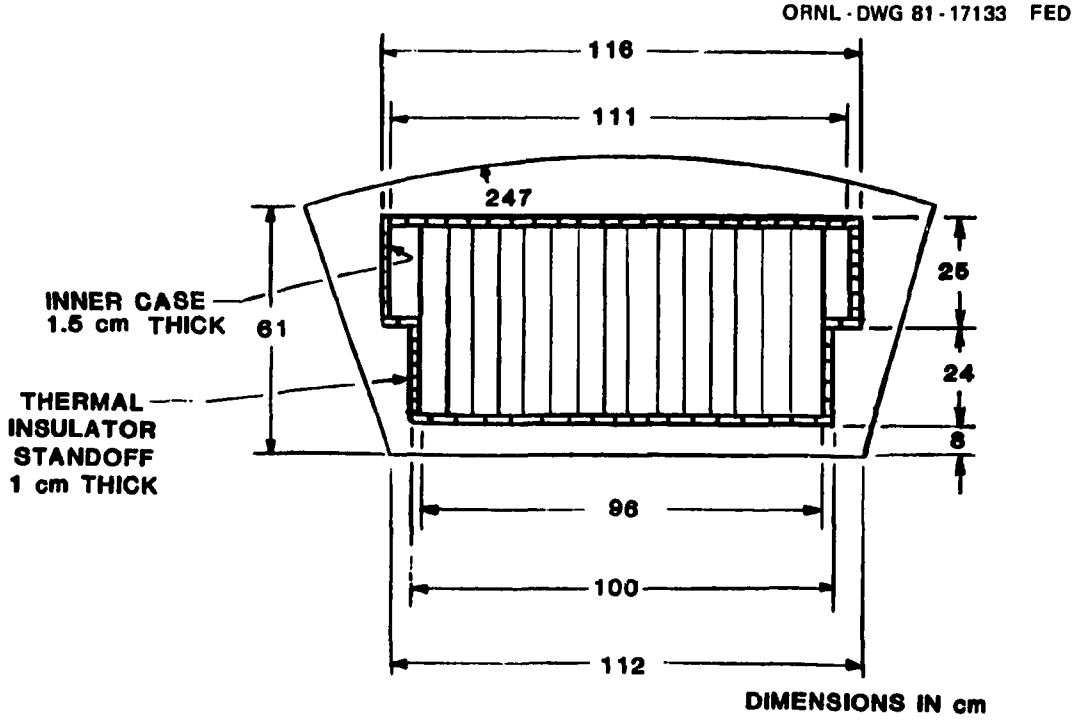

WINDING CAVITY CURRENT DENSITY AT 10 T		
INCLUDING THERMAL BARRIER	-	2200 A/cm^2
WINDING PACK ONLY	-	2500 A/cm^2
AMPERE-TURN REQUIRED AT 10 T	-	11.5 MA
HEAT LEAK INTO THE WINDING FROM THE 4.5 K OUTER CASING	-	40 W/COIL

Fig. 4-19. NbTi winding cooled with superfluid helium pool.

Table 4-7. Summary of losses[a] in alternate TF coil concepts
(Losses averaged over one cycle period)

Description	Losses (W) @8 T, 4.2 K	@10 T, 1.8 K
Winding pack losses		
Winding	70	110
Neutronic heating	350	350[b]
Splices	50	80
Helium vessel (inner casing wall)	350	550
Heat leak from the outer 4.2 K casing	0	40
Total winding losses	820	1130
Other losses		
Casing	2200	3440
Intercoil structure	2120	3300
Neutronic heating	700	700[b]
Terminals	100	160
Service penetrations	40	40
Miscellaneous (thermal radiation instrumentation, cold mass support, etc.)	10	10
Total casing loss	5170	7650

[a]All loss calculations are approximate (based on an earlier design).
[b]Boron shielding is assumed.

recovery from local disturbances appears to result instead from high local velocities produced by the change in the temperature-dependent properties of the single phase fluid. If the inlet temperature of the conductor is reduced to ∿2.5 K, a NbTi conductor is suitable for operation at 10 T. This option avoids the requirement of reducing the temperature into the superfluid range, which the open bath technique requires to obtain adequate heat transfer characteristics. Advocates also argue that internally cooled conductors offer certain advantages for integral insulation and monolithic coil construction, although requiring manifolding.

As shown in Fig. 4-20, the winding envelope requirements for this option are also compatible with the baseline winding envelope. A thermal barrier is also provided for this option partly because the internally cooled conductors have a limited ability to absorb steady-state heat inputs and partly to limit the overall refrigeration load. The thermal barrier is provided by lining the inside wall of the winding cavity using 1 cm thick insulating material developed by TORE SUPRA Project. The heat leak into the winding at an average winding temperature of 3 K would be 100 W per coil from the warm coil casing at 4.5 K. The overall winding pack current density, including the barrier, is 2,200 A/cm^2.

If this concept were chosen for the FED coils, it would be based on the 12-T Program and on the two European LCP coils. Those LCP coils do not use as finely stranded a conductor as that used in the U.S. experiments on flow-induced stability, and they will operate only down to 3.8 K. Another major demonstration coil may, therefore, be required. Small coils have demonstrated exceptional stability at 8 T and will soon be run at a reduced temperature to illustrate 10-T capacity.

Nb_3Sn coil option

Niobium-tin does not require a reduction in operating temperature to achieve 10 T, and advocates argue that the higher current sharing temperature gives a significantly greater temperature margin for stability.

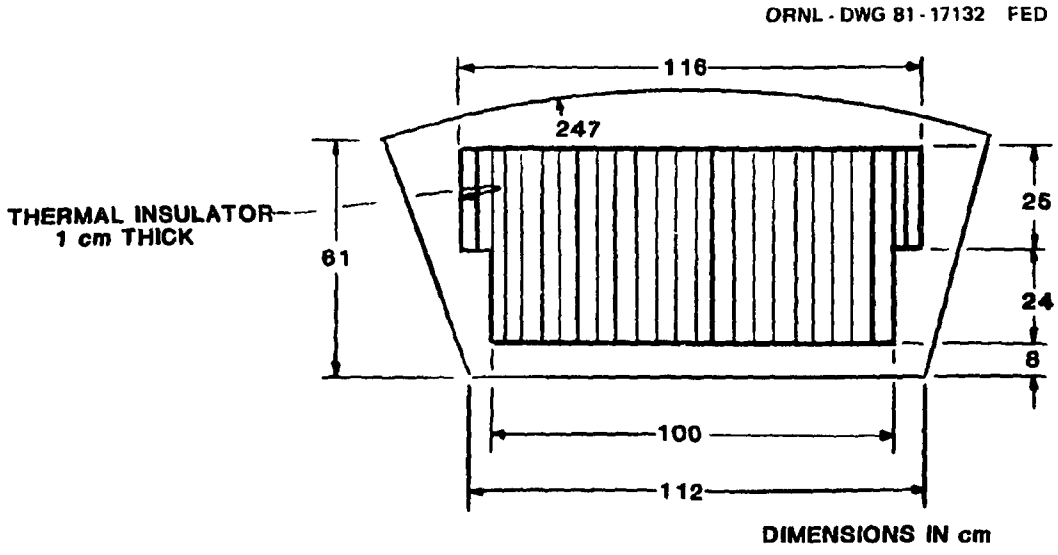

WINDING CAVITY CURRENT DENSITY AT 10 T		
INCLUDING THERMAL BARRIER	—	2200 A/cm^2
WINDING PACK	—	2300 A/cm^2
AMPERE-TURNS REQUIRED AT 10 T	—	11.5 MA
HEAT LEAK INTO THE WINDING PACK FROM THE 4.5K OUTER CASING	—	30 W/COIL

Fig. 4-20. NbTi winding internally cooled.

Advocates also argue that Nb_3Sn is more likely to be the long-range choice in the tokamak and mirror program when fields beyond 10 T are required.

At present, Nb_3Sn has two disadvantages: cost and concern over mechanical properties. Advocates believe that both problems can be solved, but agree that the data base for choice of Nb_3Sn as the FED option is weak. The Westinghouse LCP coil uses Nb_3Sn, and successful operation of that coil will certainly add greatly to the data base.

The coil envelope for the Nb_3Sn option, shown in Fig. 4-21, will fit into the winding envelope for the baseline configuration. The winding is based on a hybrid concept with that portion of the winding below 8 T utilizing NbTi. The overall winding pack current density is 2,200 A/cm^2. In this option, no space is provided for the thermal barrier but additional copper area is provided to assure cryostability of the conductor at 10 T; hence, the overall current density is equivalent to the previous options.

Insert coil options

There are several potential advantages to adding the 2-T increment to the 8-T baseline as an actual incremental coil, following the insert coil concept suggested in Ref. 4. The insert coil would be independent in the sense of having its own structure and cooling environment. It would ideally utilize the inner surface of the 8-T coil to carry the net centering load forces, and an extension of the intercoil structure to react the out-of-plane loads, but would be self supporting for in-plane dilation loads. This would circumvent the need for a perfect fit between the nested coils.

High field magnets generally use a regionalized approach to allow a variation in construction approaches, or materials, as a function of build. It is often advantageous to prevent the accumulation of radial load by using intermediate structures or by actually subdividing the winding into modular sections. Recent modular examples include HFTF and the Japan 12-T Cluster. All existing Nb_3Sn/NbTi coils have in fact been regionalized into independent sections.

ORNL-DWG 81-1734 FED

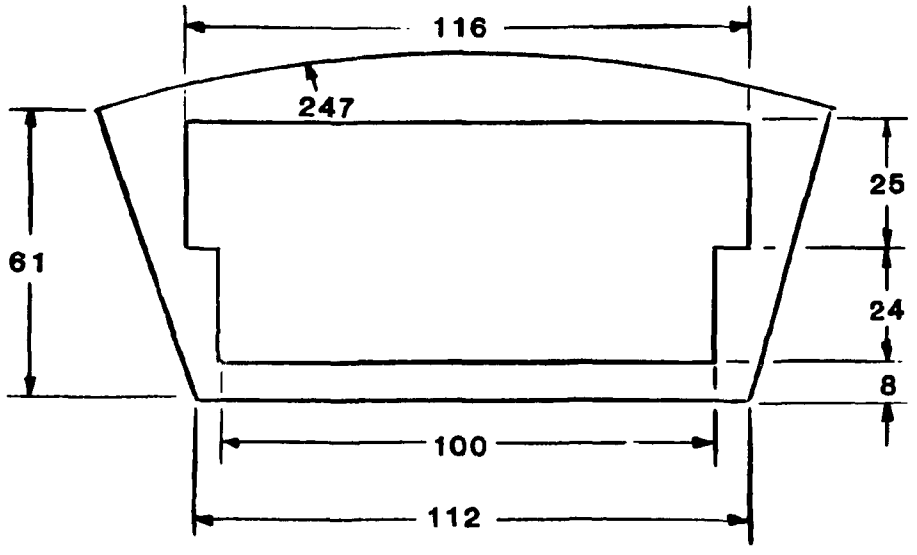

DIMENSIONS IN cm

WINDING CURRENT DENSITY - 2200 amps/cm^2

AMPERE-TURNS REQUIRED AT 10 T - 11.5 MA

Fig. 4-21. Nb_3Sn winding cooled with helium pool.

Use of dual coils, which are joined just prior to installation, has several potential advantages:

- The outer coil remains a baseline coil whose design is based on LCP technology and is not compromised by choice of an advanced conductor or cooling technique.
- The advanced conductor is limited to an independent insert coil which can accommodate any of the three advanced options. Any risk associated with the 10-T operation would be limited to the independent section.
- The smaller volume insert modules could begin production fabrication independently, and be delayed (if need be) from the main production coils, allowing a longer period of development.
- The regionalized insert concept could be tested in LCP by adding an insert to one or more of the existing coils. Conductors and cooling concepts would first be developed in the HFTF 12-T facility.
- Most of neutron heating (and potential insulation damage) will be restricted to the inner coil module, allowing special cooling or special materials to be restricted to that region, thereby isolating failures.

There are, of course, arguments for a single coil (regionalized or not) rather than independent coils. There are complications associated with independence such as extra leads and cryogenic connections and the requirements for fit-up between the sections. On the other hand, independence does offer isolation of potential faults, and could substantially affect long-term overall reliability.

The coil envelope for a two coil concept is shown in Fig. 4-22. The inner coil envelope is compatible with any of the single coil options previously discussed, including the baseline. The overall winding pack current density, including any barrier required, is chosen at 2,200 A/cm^2. The outer coil is based on LCP.

As a design alternative, the inner coil of the dual coil design could be a nitrogen-cooled copper insert. A nitrogen-cooled insert in

ORNL-DWG 81-17140 FED

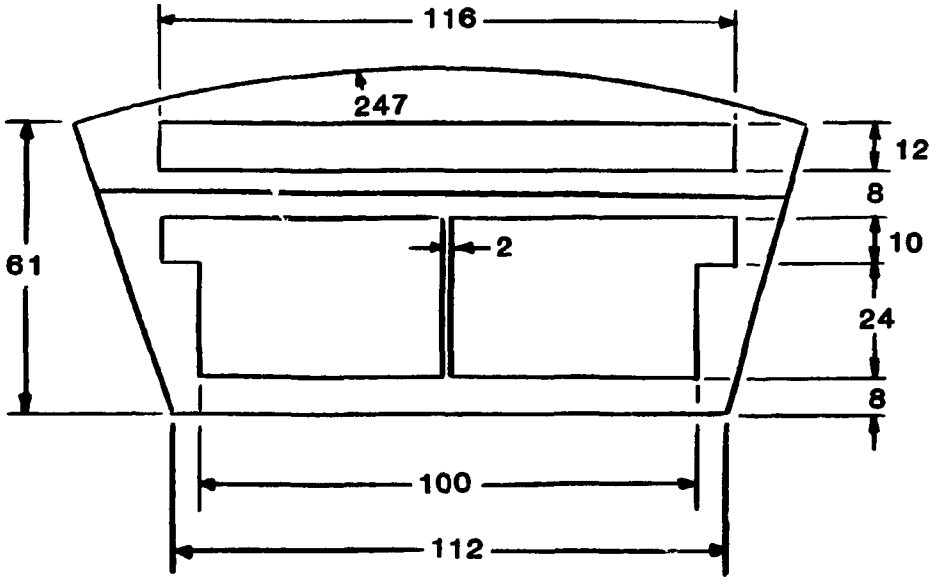

DIMENSIONS IN cm

OVERALL WINDING PACK CURRENT DENSITY	- 2200 A/cm^2
8 TESLA WINDING PACK CURRENT	- 2500 A/cm^2
10 TESLA WINDING PACK CURRENT DENSITY	- 2000 A/cm^2
AMPERE-TURNS REQUIRED IN THE 8 TESLA CAVITY	- 9 MA
AMPERE-TURNS REQUIRED IN THE 10 TESLA CAVITY	- 2.5 MA

Fig. 4-22. Two coil concept.

the same envelope would require 3.6 MW for each coil at 10-T peak field. Such a coil could operate as a "pulsed coil" and be energized prior to each 10-T shot. The charging supply would need to be 125 MW if the insert coils were charged in 60 seconds. The coils are of sufficiently low current density that they would experience only a 25% resistance increase during a 30-second flat top pulse, even if no cooling were provided. This pulse mode would only be suitable for very low duty cycle operation. While the heat could be removed in steady-state operation, the refrigerator power to supply the LN_2 would be approximately 270 MW.

It would be necessary to provide a thermal barrier between the LN_2 cooled coil and 4.2 K structure of the main coil. Assuming this barrier to be 1 cm thick Kerimid insulation, the heat leak into the 4.2 K zone would be 700 W.

If a nitrogen-cooled insert were chosen, it is likely that the major radius of the machine could remain at 4.8 m. The copper coil could serve as a shield for the superconducting outer magnet and hence could replace the outer 20 cm of the inner shield.

Relative cost of the 10-T options

Before considering the overall magnetic system cost, it would be prudent to evaluate the relative cost of the structure for (1) the baseline 8-T design for 350,000 pulses, (2) upgrade 8-T coil structure to 10 T for 80,000 pulses, and (3) 10-T design for 350,000 pulses. The comparative costs for the three alternatives are summarized in Table 4-8. Additional assumptions made in these cost calculations are summarized below.

1. Loads on the TF coils at 10-T operation are $(10/8)^2 = 1.56$ times those on the FED 8-T baseline coils.
2. The cost of support structure is \$26 per kg (\$12 per pound) except for the inner wall and thermal insulators associated with the double-wall concept in the up-grade design. The combined cost of the inner wall and thermal insulators is taken at \$52 per kg of inner wall weight.

Table 4-8. Weight and cost estimates for three configurations

Component	FED 8 T Baseline 350,000 pulses		8 T with upgrade to 10 T		10 T Design 350,000 pulses	
	Weight, 10^3 kg	Cost,$\$10^6$	Weight,10^3 kg	Cost,$\$10^6$	Weight,10^3 kg	Cost,$\$10^6$
TF Coil Outer Case (10 coils)	666	17.3	866	22.5	1290	33.7
Bucking Post	210	5.4	262	6.8	262	6.8
Intercoil Support Structure	1300	33.8	1300	33.8	2030	52.7
Total	2176	56.5	2428	63.1	3582	93.2

The incremental cost of structure of a 10-T device is $37 M with respect to the baseline 8-T design, the number of pulses in both cases being 350,000. However, if the 8-T design is upgraded to 10 T, the incremental cost would be $7 M.

The overall cost of the toroidal field magnetic system is shown in Table 4-9 for the baseline 8-T FED TF coils and for the three alternate winding concepts. The following assumptions were made in the cost calculations:

- All NbTi conductors cost the same per-unit basis, i.e., no differentiation is made with respect to the conductor configuration.
- Structural cost is based on upgrading an 8-T baseline structure to 10 T.
- In the double-walled casing concept, the cost per unit weight of inner wall is twice the cost of ordinary structural steel.
- The refrigerator costs are calculated using the empirical cost formula [Cost ($) = 5430 $(kW)^{0.741}$]. The cost calculated by this formula is then doubled to allow for the cost of the auxiliary equipment.
- The refrigeration ratio of 1,500 watts per watt is used for superfluid helium at 1.8 K. Similarly, 1,000 watts per watt is used for 2.5 K supercritical helium.
- Additional cryogenic component cost is added to superfluid and 2.5 K forced flow systems to account for non-typical equipment that is not standard on 4.2 K refrigeration system.

The overall assessment of the three concepts is summarized in Table 4-10. Since none of the above concepts is clearly technically superior to the others, the NbTi forced flow option has been selected for illustrative purposes as a baseline configuration for the present design and costing study.

Table 4-9. Cost comparison among various FED TF coil concepts

Parameter	8 T baseline design	NbTi superfluid design	NbTi forced flow design	Nb_3Sn/NbTi hybrid winding design
1. Cooling	Pool boiling	Pool boiling	Forced flow	Pool boiling
2. Coolant conditions	4.2 K helium	4.2 K for 8 T 1.8 K for 10 T	4.5 K for 8 T 3 K for 10 T	4.2 K for 10 T
3. Cost of winding (M$)	93	116	116	193
4. Cost of structure (M$)	57	69	63	63
5. Cost of refrigerator (M$)	25	35	33	30
6. Cost additional cryogenic equipment (M$)		5	2	
7. TOTAL COST of magnet system (M$)	175	225	214	286
8. Percent cost (%)	100	129	122	163

Table 4-10. Alternate design options

	Parameter	8 T baseline design	NbTi superfluid design	NbTi forced flow design	Nb_3Sn/NbTi hybrid winding design
1.	Conductor	NbTi monolith (GD-LCP)	NbTi cable in SS channel	NbTi cable in conduit	Nb_3Sn & NbTi cable in SS channel
2.	Cooling	Pool boiling	Pool boiling	Forced flow	Pool boiling
3.	Coolant conditions	4.2 K helium	4.2 K for 8 T 1.8 K for 10 T	4.2 K for 8 T 3.0 K for 10 T	4.2 K for 10 T
4.	Coil casing	Single wall	Double wall	Single wall	Single wall
5.	Overall current density (A/cm^2)	1600 @ 8 T	1100 @ 8 T	1100 @ 8 T	1100 @ 8 T
6.	Winding current density (A/cm^2)	2500 @ 8 T	2200 @ 10 T	2200 @ 10 T	2200 @ 10 T
7.	Refrigeration equipment needs	Normal 4.2 K system	Most complex Extra heat exchangers	Complex Extra heat exchangers and pumps	Normal 4.2 K system
8.	Cryogenic piping	Normal	Complex - bulky	Complex manifolding	Normal
9.	Conductor fabricability	Current technology	Current technology	Minor change in the current technology	Nb_3Sn technology to be proven
10.	R & D - on going	LCP	12 T program at GA	Successful ORNL small scale tests and European LCP coils.	MIT/W LCP & 12 T programs will demonstrate fabrication of Nb_3Sn strands
	– Needs		Demonstration on large coil	Conductor scaleup to 20 kA	Pool boiling Nb_3Sn cable conductor development

4.1.4 TF Coil Alternate Structural Concepts

In the course of arriving at the baseline design, a variety of structural alternates were considered. These structural alternates include the following:

- Interleaving of the bucking cylinder with the ohmic heating coil, so that the bucking cylinder supports the TF coils at discrete intervals instead of continuously.
- Elimination of the bucking post.
- TF coil case fabricated from thinner plate stock, but with welded stiffening ribs at intervals.
- Single central support spindle for all TF coils.
- Reacting overturning loads by shear panels or crossbracing between adjacent TF coils.
- Compartmentalized TF coil case to transfer compressive winding loads to the case.
- Leaving a gap between the TF winding and the case, so that the in-plane TF coil load is reacted by dilation of the winding without any dilation of the case.

The advantages and disadvantages of these structural alternatives are summarized in Table 4-11 and are discussed more fully below.

1. The present baseline design shows a bucking post radially supporting the inboard section of the TF coils, with the ohmic heating solenoid inside the bucking post. One alternative concept which was considered involves a bucking post which supports the TF coils only at discrete intervals. Between the discrete support points, portions of the OH solenoid are recessed into the outside surface of the bucking post. This concept has the advantage of locating the OH coils closer to the plasma, thereby making them more effective. However, this concept was rejected because of adverse structural consequences to the TF coil case and the OH solenoid. Between the discrete support points, in the absence of direct support from the bucking post, the back wall of the TF coil case must carry the Lorentz force in plate bending action, and the case as a whole must carry

Table 4-11. Comparison of structural alternatives

Option	Advantages	Disadvantages	Comments
Interleaving of bucking cylinder with ohmic heating solenoid	• Locates ohmic heating coils closer to plasma, increases mutual inductance.	• Thickness of TF coil case must be increased in the inboard region to react centering load between discrete support points. • Separate helium vessel is required for each ohmic heating coil module.	
Elimination of bucking post	• Locates ohmic heating coils closer to plasma, increases mutual inductance. • Saves expense of bucking post.	• Thickness of TF coil case must be increased in the inboard region to react centering load by wedging action. • Requires close fit-up tolerances to avoid dimensional misalignment of adjacent TF coils.	• Little, if any, net saving of material.
Use of thinner plate stock plus stiffening ribs in TF coil case.	• Reduction in overall weight. • Easier to weld thin plate stock. • Reduced eddy current losses in case wall.	• Greatly increased amount of welding and inspection.	• Present TF coil case wall thickness ($\leq$12 cm) is manageable.

Table 4-11. Comparison of structural alternatives (continued)

Option	Advantages	Disadvantages	Comments
Single central support spindle.		• Poor stability against horizontal seismic loads.	• This support concept was a carryover from TNS program.
Intercoil support structure in form of truss-like beams.	• Slight reduction in overall weight of intercoil support structure. • Lower eddy current losses in intercoil support structure. • Better access between TF coils (from above) for diagnostics and instrumentation.	• Poorer support against shear and bending loads in coil case due to out-of-plane loads.	
Use of shear panels or crossbracing between TF coils.	• Supports outboard window region of TF coil case against out-of-plane loads.	• Impedes torus sector changeout. • Inconsistent with design objective of the device. • Very heavy members required to achieve worthwhile results. • Difficult to design structural interface between warm and cold structure.	• STARFIRE uses shear panels; panel thickness is 30 cm.

Table 4-11. Comparison of structural alternatives (continued)

Option	Advantages	Disadvantages	Comments
Compartmentalized TF coil case.	• Eliminates need for channel co-wound with conductor-in-conduit. • May permit some walls of the coil case to be thinner, depending upon arrangement of compartments.	• Requires precise fitting corner joints in case. • Great increase in the amount of case machining. • Coil winding operation more complex.	• Effect on overall current density about the same as for baseline configuration.
Gap between winding and case.	• Reduces stress level in the case.	• Increased potential for motion of winding and subsequent heat generation. • More steel is needed in the winding if the winding must react the dilational load; winding space needed for conductor.	• With case wall thickness sized to carry cyclic out-of-plane loads, there is ample case steel to also carry in-plane dilational load.

the force in beam bending action. The result is a large increase in the required thickness of the back wall of the TF coil case, in which case much of the advantage of the concept is lost.

A second alternative involves dispensing with the bucking post entirely. Again, this concept permits the OH solenoid to be located closer to the plasma and saves the expense of the bucking post. In this case, the net centering load on the TF coils is reacted by wedging of adjacent TF coil cases in the inboard region. This necessitates a thickening of the coil case back wall and bobbin ring to accommodate the hoop load that would otherwise be taken by the bucking post. Also, as before, the back wall of the coil case becomes unreasonably thick in order to carry the Lorentz force from the winding in plate bending action. A further drawback of this concept results from dimensional fit-up tolerances in large structures. If the design must depend upon precise fit-up of adjacent TF coil cases to achieve the necessary wedging action, very close dimensional tolerances must be observed in the fabrication of the cases, driving up the cost. If precise fit-up is not demanded, load path uncertainties can result, which in turn can lead to either unanticipated local overstress conditions or misalignment of the coils and resulting unequal loads on the TF coils.

2. The present baseline design shows a TF coil case whose thickness is zoned but is uniform along the coil perimeter within each zone. In some earlier designs, particularly those involving operation of the TF coils for their full design life at 11-12-T peak field, this method of coil case sizing led to unacceptable wall thicknesses and excessive TF coil eddy current losses. An alternate concept involves use of thinner plate stock (e.g., ~5 cm) for the case and the addition of welded-on stiffening ribs at intervals along the coil perimeter; this concept has been adopted in INTOR. Use of this concept eliminates the need to fabricate material in very thick sections, leading to easier inspection (flaw detection) and reduced overall weight. However, the overall fabrication cost is not necessarily less, in view of the increased number of welds. While

the use of the welded-on stiffener concept solves an otherwise intractable problem in INTOR, the uniform thickness approach has been retained for FED because the required wall thickness ($\leq$12 cm) is not unreasonable to fabricate.

3. The present baseline design shows the TF coils vertically supported by outboard pedestal supports. An alternate concept which was considered earlier involved support of all of the TF coils off a single support spindle at the center of the machine. The present concept has superior stability against rocking motion which could result from a horizontal seismic event.
4. The present baseline design shows intercoil support structure in the form of modules having an inner and outer shell, plus circumferential stiffening panels. An alternate concept which was considered involved substitution of a truss-like arrangement of beams between adjacent TF coils. While the truss arrangement appeared to offer the potential of an overall reduction in ISS weight and increased access between coils for diagnostic equipment, it was found that the present concept provides better support with no penalty in overall ISS weight.
5. In view of the difficulty of supporting the outboard midspan region of the TF coils against out-of-plane loads, some consideration was given to compromising the objective of maintaining open windows between all TF coils and closing off some bays by use of diagonal stiffening beams or solid panels; the latter approach is used in STARFIRE. This concept was dismissed not only because it is inconsistent with the design objectives of the device, but because very heavy members are required to achieve worthwhile results. For example, if diagonal crossbracing beams are provided in every other bay, the cross sectional area of the crossbraces must be about half that of the TF coil case in order to limit the beam bending stresses in the open window region of the coil case to the allowable. Similarly, STARFIRE uses 30 cm thick anti-shear panels. An additional disadvantage of using support structure across bays between TF coils is that the support structure is at room temperature but must be attached to components at cryogenic temperature. The

structural interface between room temperature and cryogenic temperature appears difficult to achieve, in view of the pulsed nature of the loading.

6. The present baseline design shows a U-shaped channel which is co-wound with the TF coil conductor. This channel provides a load path to transfer the accumulated winding loads to the coil case without crushing the conductor. An alternate concept involves dividing the coil case winding cavity into compartments and using the interior ribs to intercept a portion of the accumulated load and transfer it directly to the case. Although the compartmentalized case eliminates the need to wind a stiff steel-reinforced conductor, the case manufacture and coil winding operation are greatly complicated by the presence of the ribs. Depending upon the manner in which the ribs are secured to the case, the manufacturing process can involve many precise fitting corner joints and a large amount of additional case machining. Several options for adding structural material have been considered. They all involve comparable amounts of additional structure, so the effect on overall winding current density is similar in each case. However, the manufacturing problems appear simpler if the additional structure is in the form of steel co-wound with the conductor.

7. The TF coil winding dilates in the plane of the coil under the action of the in-plane Lorentz forces. The present baseline design shows the winding fitting snugly inside the case so, as dilation occurs, the resulting hoop load is shared between case and winding steel (conductor conduit, co-wound channel). An alternate design involves allowing a gap between the winding and the outer wall of the case. In this concept, as the coil dilates, the full radial load is borne in the winding before the gap is taken up. The snug-fit concept has been selected for FED because winding space is at a premium, and it is desired to minimize the amount of winding steel so that the required number of turns of the conductor can be fitted into the available winding cavity. Furthermore, with the case wall thickness sized on the basis of a fracture mechanics allowable

stress of 16.6 ksi, there is ample case steel available to carry the steady-state radial loads.

4.1.5 TF Coil Winding Design Analysis

The TF coil winding is designed primarily for operation at 8 T but will be operated at 10 T for short periods of time. The windings are designed for the NbTi forced flow conductor concept discussed in Sect. 4.1.3. For 8-T operation, the winding is cooled with 4.5 K helium, while for 10-T operation, 3.1 K helium is used. The coil winding is held together with epoxy and the winding pack is supported by the coil case structure. The discharge voltage can reach 8,000 V without exceeding the allowable hot spot temperature of 200 K.

Loss calculations have been made for the winding and the structure both during a normal pulse and following a plasma disruption. The major portion of the losses occurs in the coil casing; this heat is removed through tubes embedded between the winding and the structure. Losses occurring in the winding, however, must be removed through the conductor coolant.

Field and force analysis

Each TF coil is subjected to a varying field due to the poloidal field (PF) system and a steady toroidal field due to TF coil currents. The winding must be designed to withstand the peak field at any instant during a pulse. Interaction of TF coil current with the toroidal and poloidal fields results in in-plane and out-of-plane forces on each TF coil. The TF coil structure must be able to withstand these forces.

The whole magnetic system is shown in Fig. 4-23. It consists of TF and PF coils. The time variation of currents in the PF coils is shown in Fig. 4-24. The PF coils achieve 80% of their peak current in 6 s and achieve peak current in 12 s. The poloidal coils maintain their peak current until the end of the plasma burn phase. All PF coils are discharged to zero in 10 s at the end of the burn phase. The magnetic field due to the poloidal field currents is shown in Fig. 4-25 along

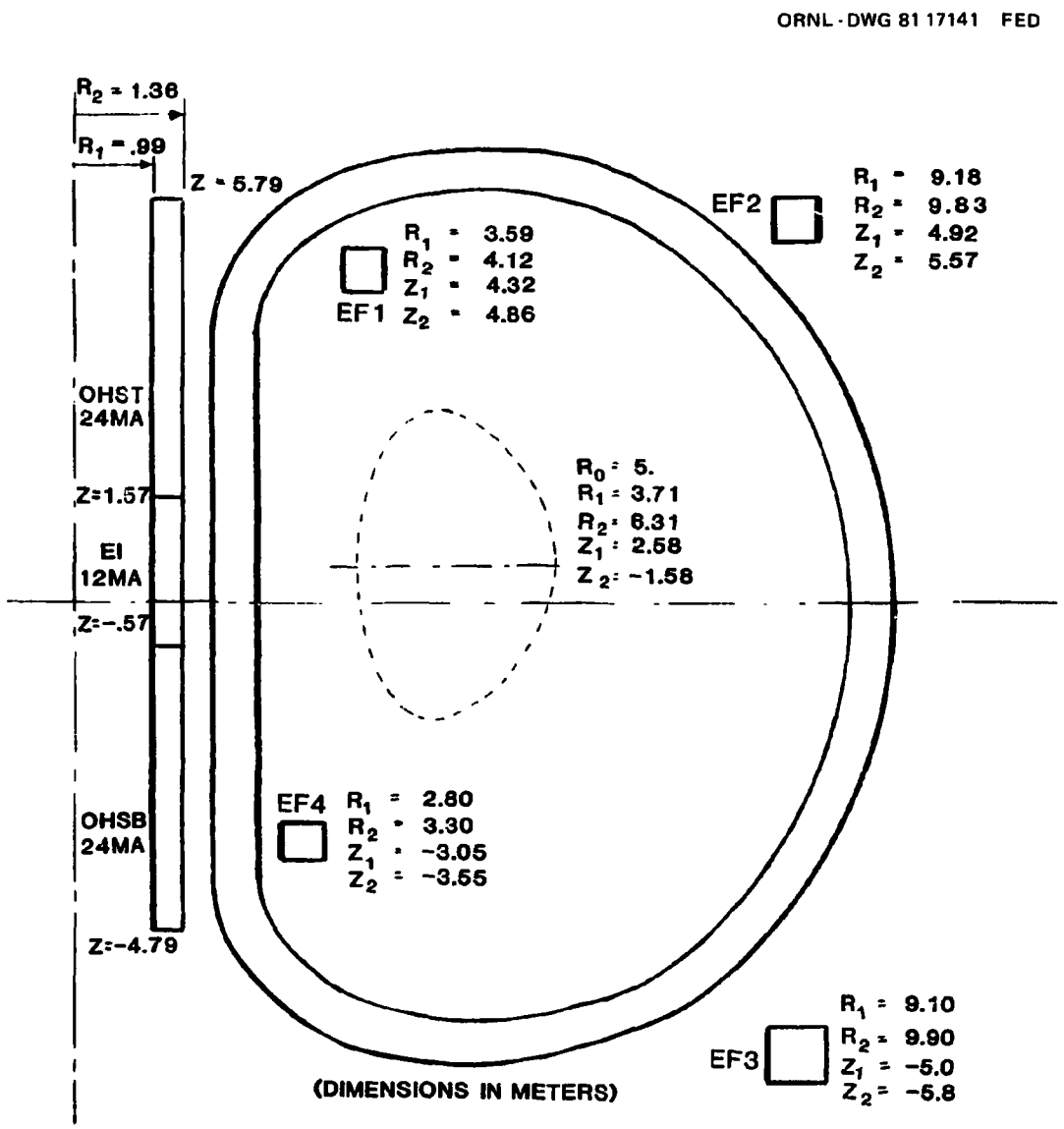

Fig. 4-23. FED 8-T/10-T baseline magnet system concept.

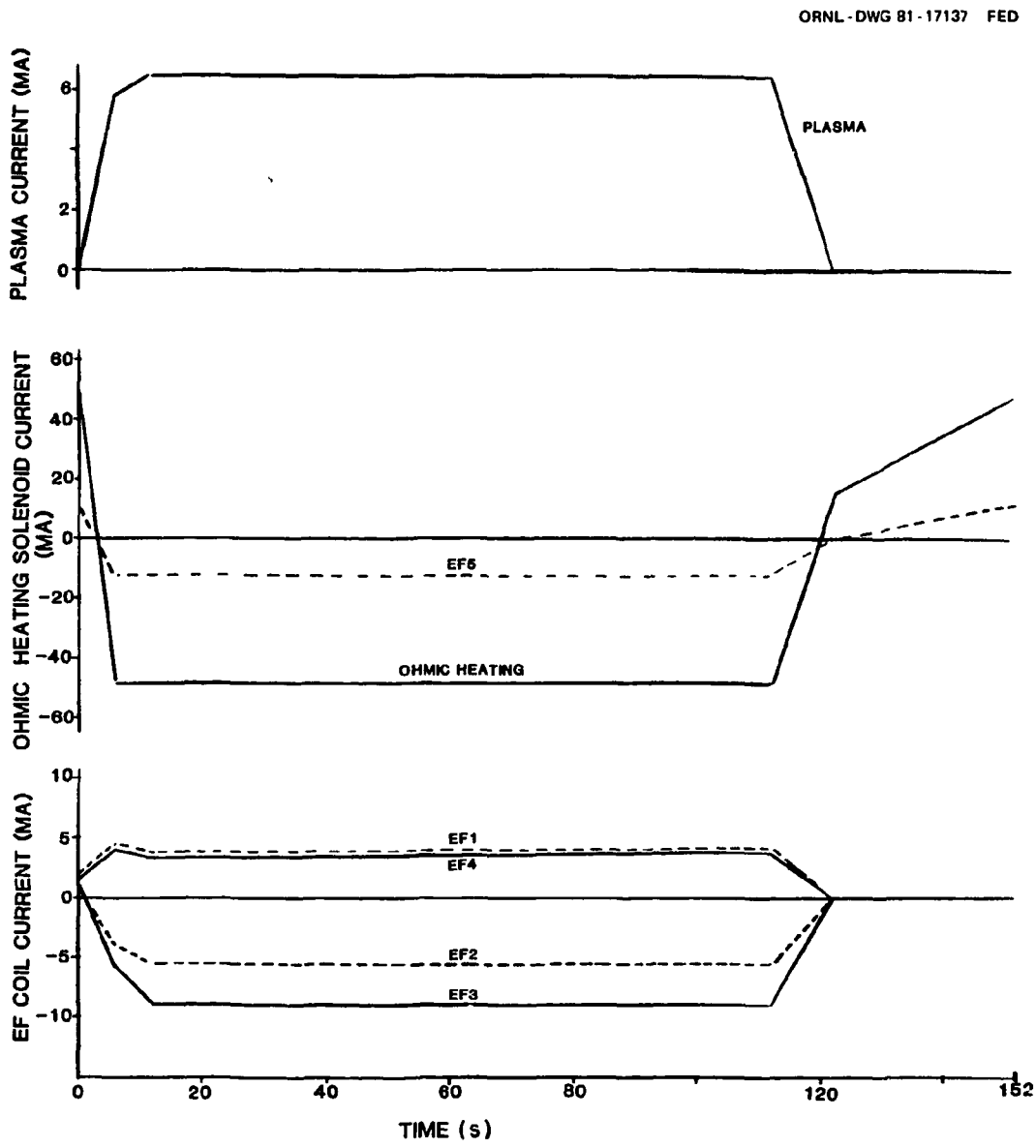

Fig. 4-24. Poloidal field coil current variation (10-T operation).

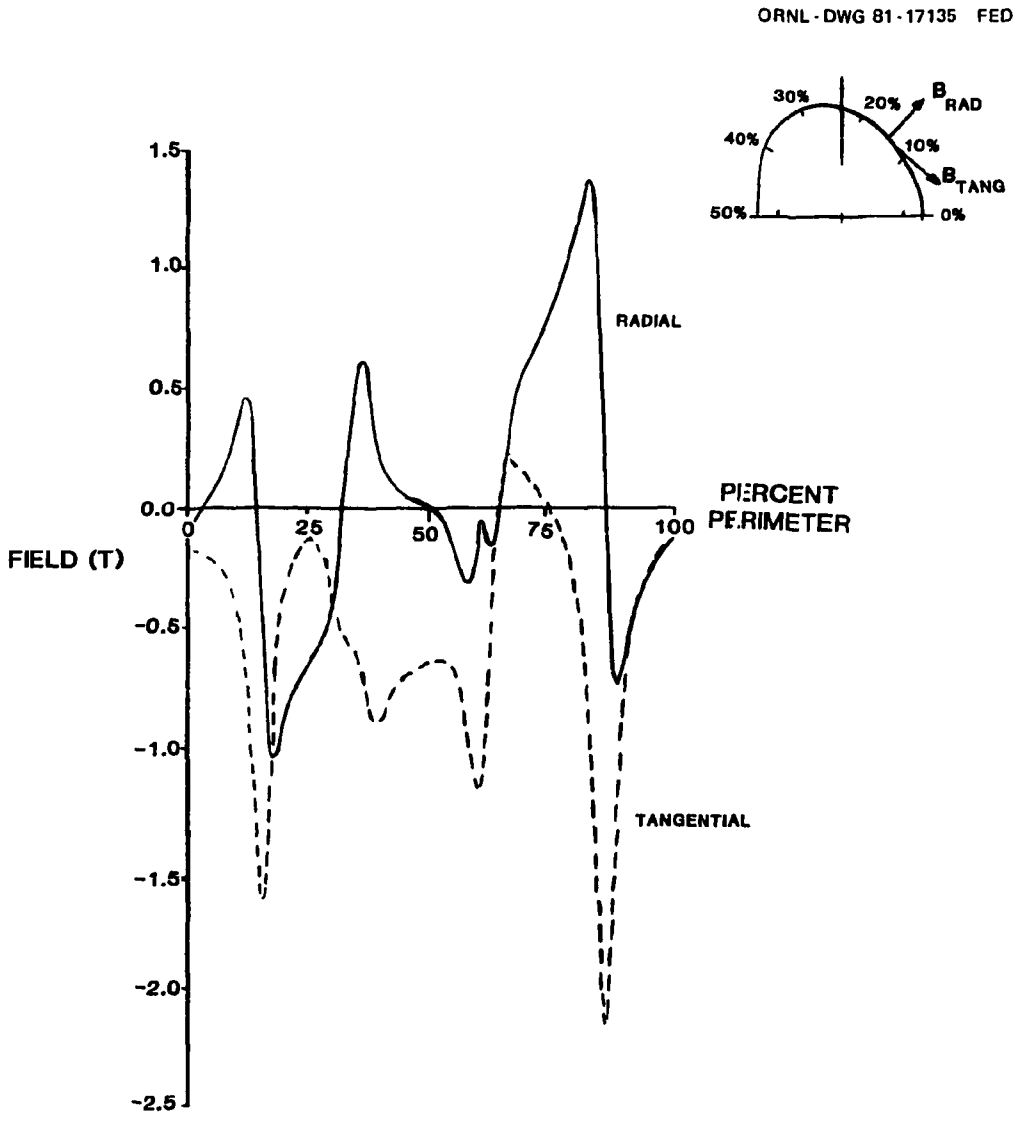

Fig. 4-25. Field distribution at TF coil midsurface at 10 T.

the TF coil mid-surface. The magnetic field due to plasma current alone is shown in Fig 4-26. These magnetic field values, coupled with charging/discharging times, are used for calculating eddy current losses in the winding and coil structure.

Following a plasma disruption, the field due to the plasma (Fig. 4-26) is assumed to decay to zero in 0.1 s (as seen at the TF coils). This field decay is also used for calculating losses in the windings and the coil structure. The time decay effect of the torus structure has been deliberately underestimated so as to result in a conservative estimate of the losses due to a disruption; in reality the field due the plasma will decay less rapidly than assumed.

Each TF coil is subjected to in-plane loading caused by interaction of TF coil current with the toroidal field. Similarly, out-of-plane loading is the result of interaction between the TF coil current and radial component of the poloidal field. The in-plane and out-of-plane loads are shown in Fig. 4-27. Peak out-of-plane loads appear in the vicinity of the upper and lower superconducting PF coils (EF_2 and EF_3). The largest peak is due to EF_3; for an optimum PF configuration the two peaks should be about equal. Forces on the TF coil due to EF_3 are high because the current in EF_3 is higher than required by plasma equilibrium considerations. Additional analysis is needed to determine the optimum currents in the PF coils.

Heat loads

The TF coils are subjected to eddy current heating due to pulsed poloidal fields and nuclear radiation heating in the inboard region. The pulsed poloidal field produces losses in the coil case, intercoil supporting structure, and winding. These heat loads must be removed effectively to ensure that the TF coils remain operational in the superconducting mode during normal pulse operation and following a plasma disruption. A summary of heat loads is given in Table 4-12. The ac losses in the winding and eddy current losses in the coil case and intercoil support structure occur during the startup (6 s) and shutdown (10 s) phases of a normal pulse. The inboard region of the coil is also

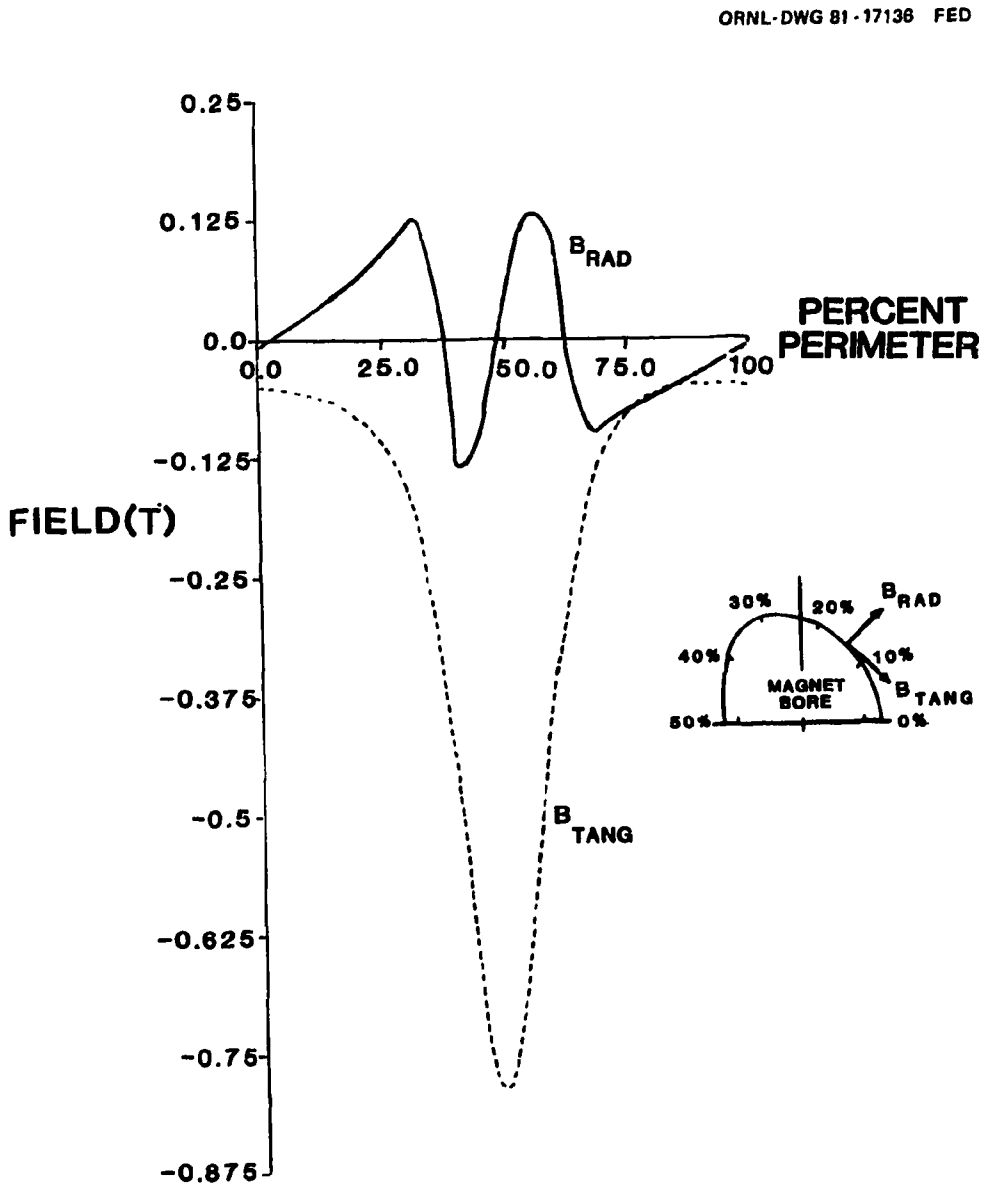

Fig. 4-26. Plasma field contribution at TF coil mid-surface at 10 T.

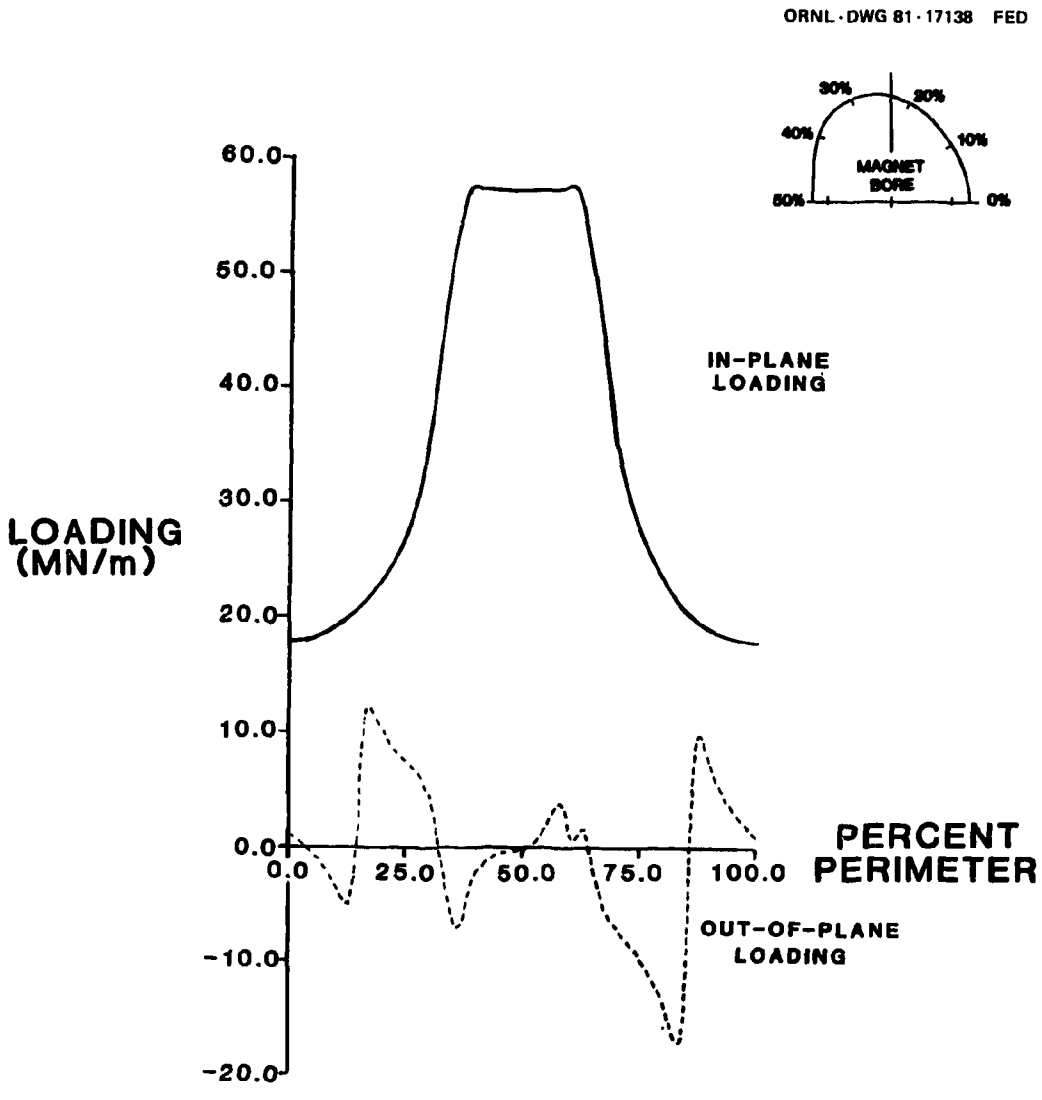

Fig. 4-27. Load distribution on TF coils at 10 T, at the end of burn phase.

Table 4-12. Summary of TF coil heat loads
(Time averaged over 152 s pulse period)

	8-T operation (W)	10-T operation (W)
Winding ac losses	30	45
Splice losses (I^2R)	30	45
Winding nuclear heating in the inboard region	225	280
Coil case eddy current losses	2030	3175
Intercoil structure eddy current losses	2960	4625
Coil case nuclear heating in the inboard region	700	875
Coil leads	30	50
Miscellaneous (thermal radiation, cold mass support leakage, molecular heat flow, instrumentation leads, service penetration)	30	30
Total for each coil	6035	9125

subjected to nuclear heating during the plasma burn period (100 s at 8 T, 50 s at 10 T).

Calculation of the eddy current losses in the TF coil cases was performed for the 6 s startup phase, the 10 s shutdown phase at the end of burn, and following plasma disruption. The calculations were based on the equations developed in Ref. 5. Eddy current loss distribution along the TF coil perimeter is shown in Fig. 4-28 for the startup and in Fig. 4-29 following plasma disruption; both Figs. 4-28 and 4-29 are for 10-T operation, the corresponding losses for 8-T operation may be calculated by multiplying by the square of the ratio of field or 0.64. The losses during the 10 s shutdown, although not plotted, may be obtained by multiplying the Fig. 4-29 6 s startup data by 0.6. The coil case eddy current losses, integrated over the coil and averaged over the 152 s cycle, are 3.2 kW per coil due to normal startup and shutdown and 5.8 kW per coil for disruption.

Eddy currents are also induced in the ISS during startup and shutdown. Losses were calculated separately for the radial and tangential pulsed field components, with the radial component being more significant. The averaged radial field component in the ISS is $\sim$0.6 T at the end of startup and the total eddy current loss for all the ISS is 46.2 kW averaged over the 152 s cycle, with 97.5% of the total due to the radial field component.

The time-varying pulsed poloidal field leads to coupling losses, eddy current losses and hysteresis losses in the TF winding. The winding ac losses are summarized in Table 4-13, they are calculated using formulae developed in Ref. 8. To reduce ac losses, the conductor strands are electrically insulated. As in the Westinghouse LCP coil, which uses internally cooled cabled superconductor, the predominant winding losses are due to hysteresis.

Joule heating (I^2R) losses occur in splices during steady state operation. The splice resistance is taken as 1.4×10^{-9} ohm (based on the splice resistance achieved in the Westinghouse coil at 2 T).

Other miscellaneous heat loads (see Table 4-12), including heat conduction along the structural supports, current leads thermal radiation,

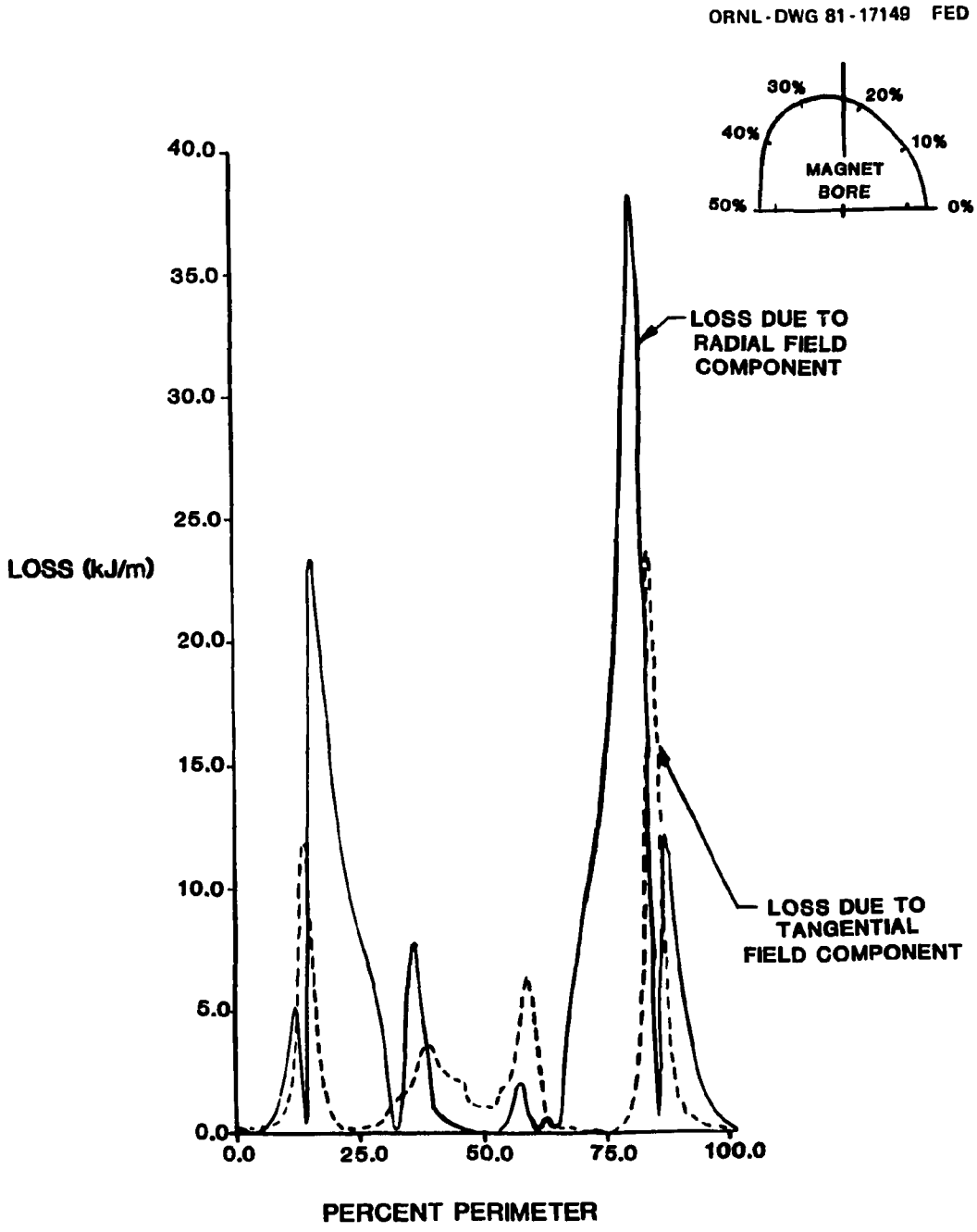

Fig. 4-28. Coil case losses during startup phase (6 s).

ORNL-DWG 81-17150 FED

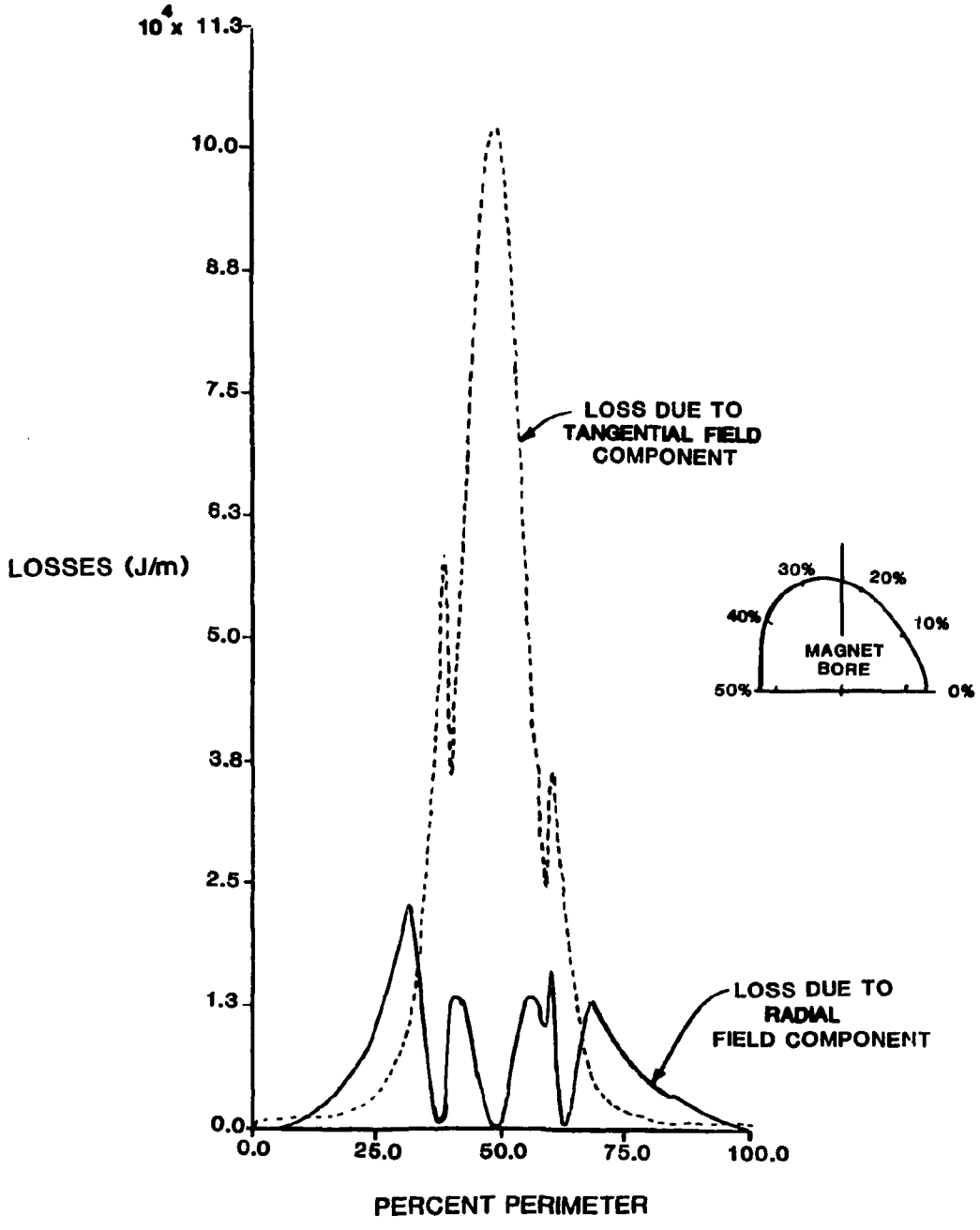

Fig. 4-29. Plasma disruption loss profile at 10 T (Field decay time ∿0.1 s).

Table 4-13. Winding ac losses
(Time averaged over 152 s pulse period)

Parameter	Losses for 8-T operation (W)	Losses for 10-T operation (W)
Perpendicular		
Coupling	6	9
Eddy current	<1	<1
Hysteresis	11	17
Parallel		
Coupling	5	8
Eddy current	<1	<1
Hysteresis	8	11
Total winding ac losses	30	45

instrumentation leads, service penerations, etc., together account for less than 0.5% of the total heat load.

Protection

The TF coil protection scheme is based on controlled dissipation of the stored energy through an external dump resistor as shown in Fig. 4-30. The value of the external dump resistance is determined by the maximum permissible conductor temperature and peak discharge voltage. A peak conductor temperature rise of 200 K is used for the TF coils employing forced flow conductors. The corresponding pressure rise in the conductor conduit is approximately 220 atmospheres; the thickness of the stainless steel conduit for the conductor (see Fig. 4-12) is sized to withstand this pressure. The discharge data for the TF coils is listed in Table 4-14, and the basis for the tabulated values is discussed below.

Temperature rise

The peak temperature rise for the winding is estimated using the TASS (Thermal Analysis for Safety and Stability) code[9] with stagnant helium at atmospheric pressure. The peak conductor temperature, as a function of discharge voltage, is shown in Fig. 4-31 for 8-T and 10-T operation. The temperature rise calculation may be conservative because the thermal capacity of the stainless steel conduit is not included in the calculations. The normal zone is assumed to propagate only along the length of the conductor. In this analysis, one quarter of a turn is modeled and the heat conduction to neighboring turns is ignored. The effect of radiation dose (10^9 rads) is incorporated by appropriate changes in the resistivity of the copper stabilizer. The normal zone is created by initially raising the temperature of the turn to 30 K and then discharging the coil through an external dump resistor. The temperature rise of the normal zone as a function of time calculated under these conditions is shown in Fig. 4-32 for the 8-T and 10-T operations. The discharge voltage of 6 kV ($\Delta T \sim 200$ K) is considered acceptable for epoxy potted forced flow conductors.

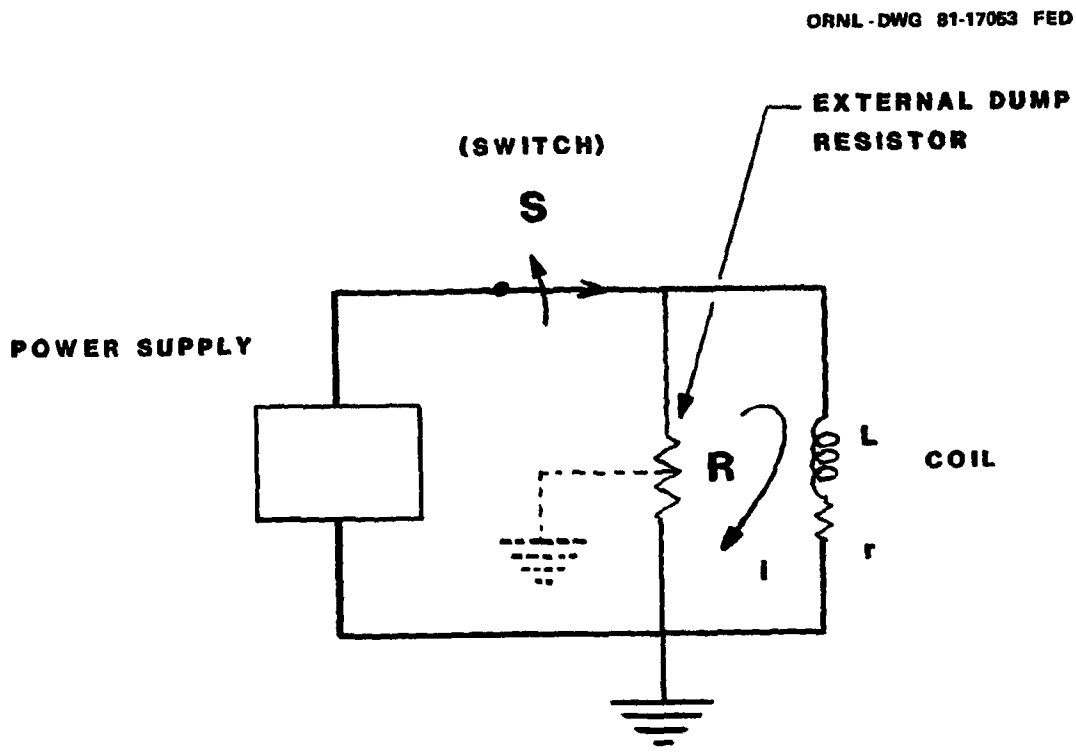

Fig. 4-30. Protection circuit.

Table 4-14. TF coil discharge data

Parameter	Unit	8-T operation	10-T operation
Operating current	Amp	20,000	25,500
Copper cross section in the conductor	cm^2	2.644	2.644
Initial current density in copper (J_{cu})	A/cm^2	7565	9665
Maximum copper resistivity	ohm-cm	6.9×10^{-8}	7.7×10^{-8}
Self-inductance of each coil	H	7.53	7.53
Stored energy for each coil	GJ	1.5	2.5
Current decay time constant(τ)	s	30	32
Peak temperature rise	K	120	200
Peak discharge voltage	kV	5.0	6.0
Hydraulic diameter D_h	mm	0.406	0.406
Maximum quench pressure	atm	135	218

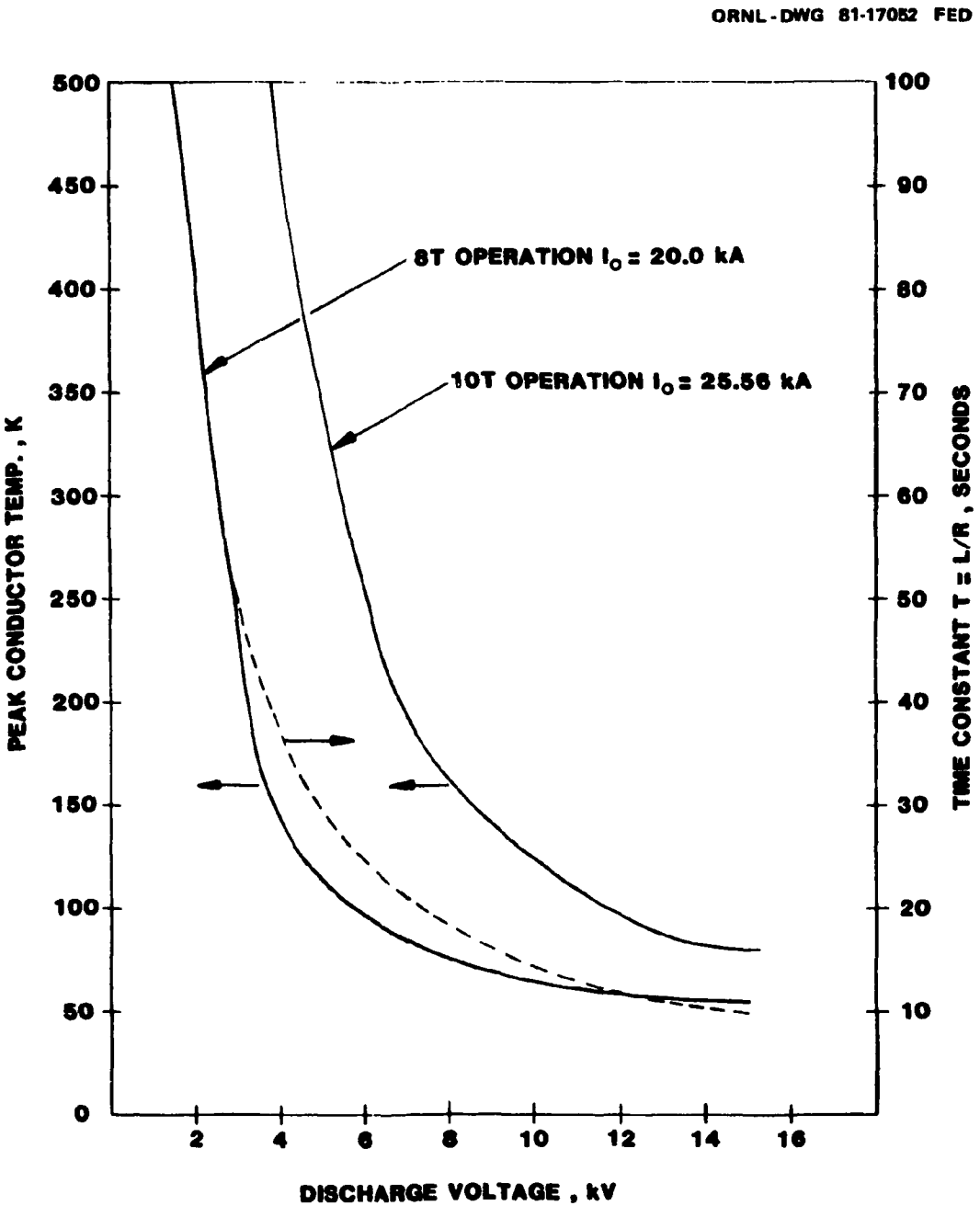

Fig. 4-31. Winding performance during quench.

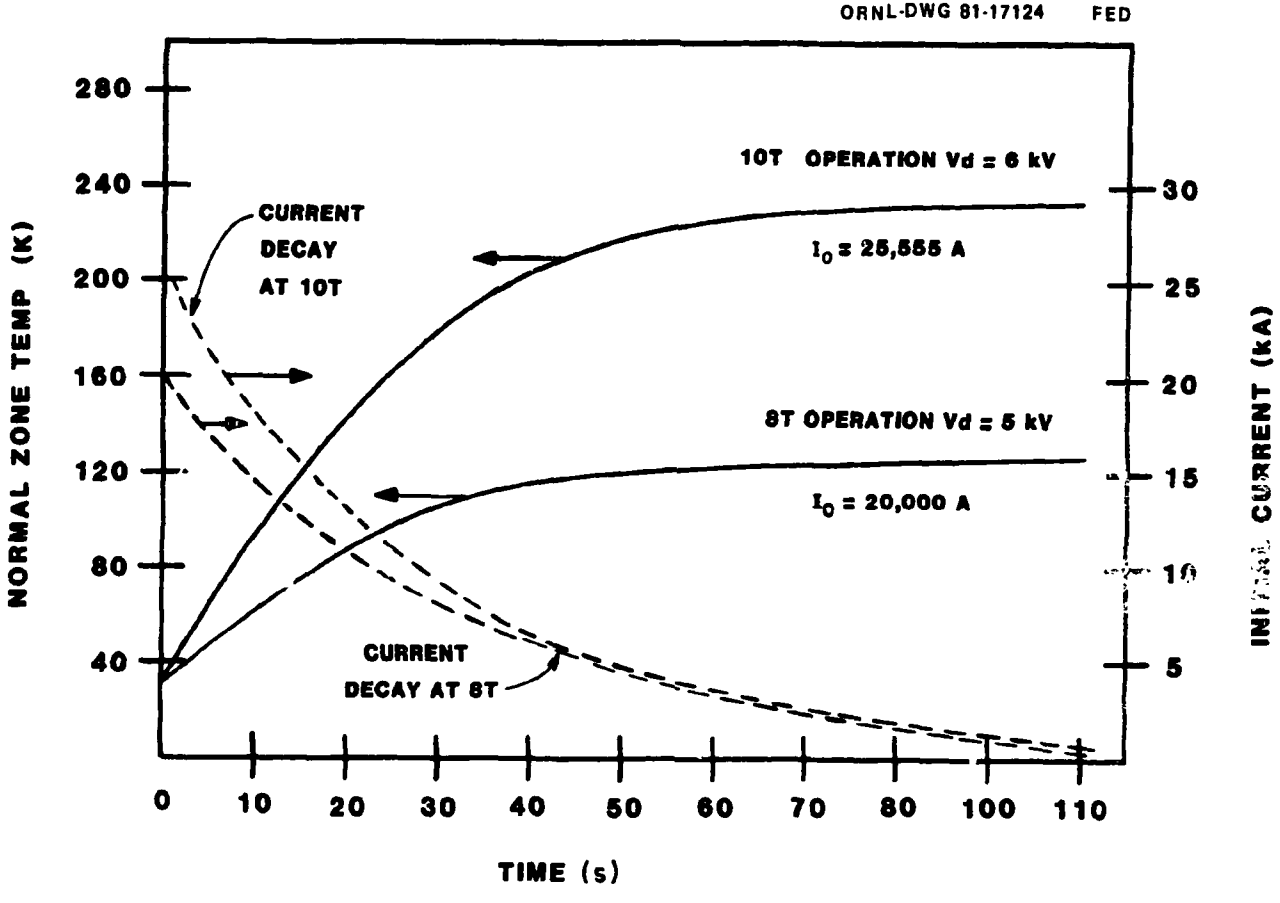

Fig. 4-32. Quench characteristics of TF coils for 10-T and 8-T operation.

Quench pressure

The maximum pressure P_{max} expected in the event of a quench of the entire coil, is estimated[1] using the empirical relationship (mks units)

$$P_{max} = 0.1 \left[\frac{Q^2 \ell^3}{D_h}\right]^{0.36}$$

where $Q = \frac{J_{cu}^2 \times \rho_{cu} \times A_{cu}}{A_{He}}$ is the initial heating rate per unit volume of helium.

D_h = hydraulic diameter of the conductor,

$\ell = \frac{\ell_p}{2}$, where ℓ_p is the cooling flow path length,

ρ_{cu} = the resistivity of copper,

A_{cu}, A_{He} = the cross section area of copper and helium in the conductor, respectively, and

J_{cu} = the initial current density in copper.

If the entire coil is assumed to quench instantaneously, the quench pressure is estimated to be ∿135 atm and 220 atm for 8-T and 10-T operation, respectively. However, since the whole coil cannot go normal instantaneously, the quench pressures would be less than calculated above. Comparable quench pressures are calculated in Ref. 3 for the Westinghouse LCP coil.

Stability considerations

The TF coils are required to remain in the superconducting mode during normal operation and following plasma disruption. To meet this requirement, adequate helium flow must be maintained in the winding to effectively remove steady state heat loads and to ensure recovery to

the superconducting mode after localized heat inputs (e.g., due to strand or conductor movements, localized ac losses, nuclear heating, etc.).

The winding stability is evaluated for normal pulse operation at 10 T. A summary of heat loads is given in Table 4-15. The peak ac losses occur in the vicinity of the EF_3 ring coil. The ac losses are calculated using the peak pulsed poloidal field components during the startup period. The peak nuclear heating occurs in the inboard region during the burn phase. The heat leak from the coil case is neglected.

The thermal capacity of helium between bath temperature (T_B) and the conductor current sharing temperature (T_{cs}) is given as

$$\Delta H_u \geq \frac{A_{He}}{A_{cond}} \int_{T_B}^{T_{cs}} \rho C_p dT$$

where A_{He} and A_{cond} are the areas of helium and conductor, respectively, in the winding. The thermal capacity of helium between temperatures T_{cs} and T_B (the integral above) is shown in Fig. 4-33 for different bath temperatures. At 8-T operation, the bath temperature is 4.5 K and $(T_{cs} - T_B)$ for the conductor is 0.5 K; the helium thermal capacity for this condition is ∿300 mJ/cc. The area ratio A_{He}/A_{cond} is 2/3, and, therefore, the effective thermal capacity is 200 mJ/cc. Likewise, the bath temperature at 10-T operation is 3.1 K and $(T_{cs}-T_B)$ is 0.8 K; for these conditions, the effective helium thermal capacity is also ∿200 mJ/cc.

Since the heat loads in the winding for both conditions are less than the thermal capacity (∿200 mJ/cc) available in the helium within the winding cavity, it is concluded that the winding will recover to the superconducting state. Analysis indicates that the winding is stable both during a normal pulse and following a plasma disruption; additional analysis is needed to confirm that the effects of eddy currents induced by the control coils are negligible. Future stability analysis will include heat loads neglected here, e.g., the heat leak from the coil casing, etc. Detailed heat balance calculations will also be made to more accurately determine helium condition along the flow path.

Table 4-15. TF coil winding stability data

Normal pulse — 6 s startup period and 50 s burn period at 10 tesla

Parameter	Instantaneous Heat Load (W/m length of conductor)	Load Density (J/m length of conductor)
• Peak ac loss during 6 s startup	0.2	0.62 mJ/cc
• Nuclear heating during the burn phase (50 s)	22.1	68.4 mJ/cc
• Joule heating in a normal zone	1	3.1 mJ/cc

Abrupt plasma disruption — 0.1 s decay time constant at TF coils

Parameter	Integrated Heat Load (J/m length of conductor)	Load Density (J/m length of conductor)
• Peak ac loss	4.5	14
• Joule heating in a normal zone	0.1	0.3
Thermal capacity available between bath temperature and conductor current sharing temperature	∿200 mJ/cc	∿200 mJ/cc

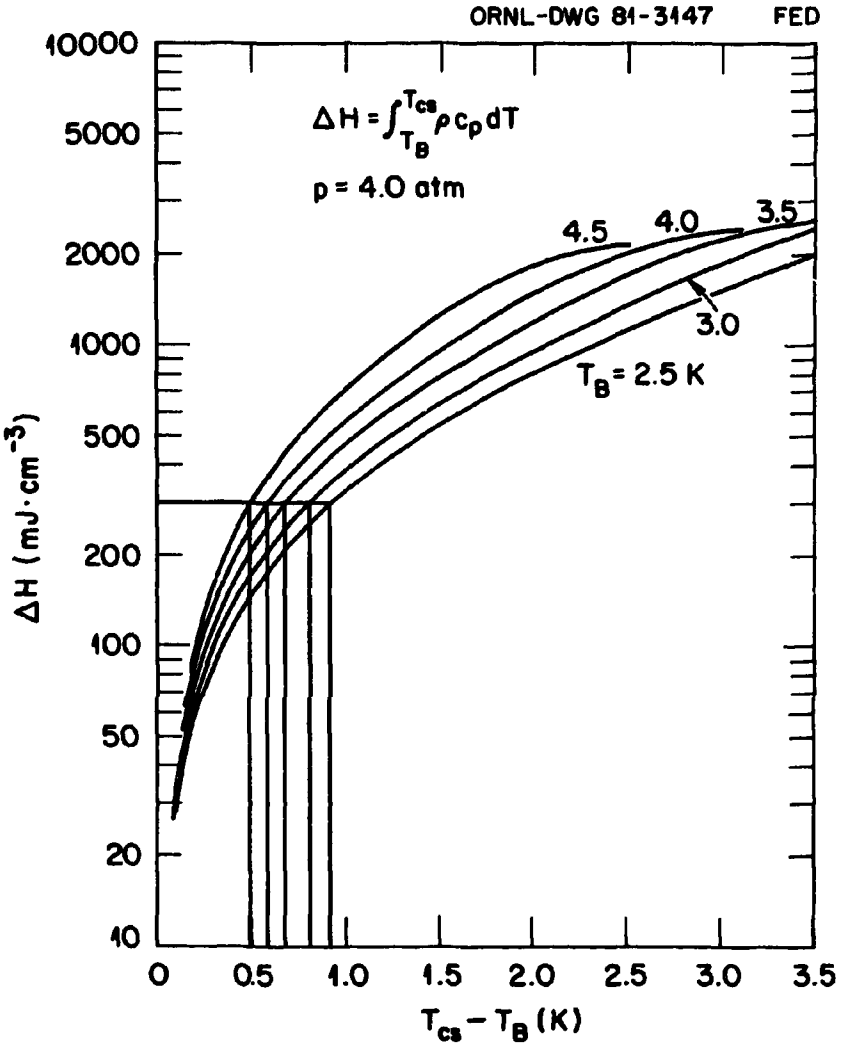

Fig. 4-33. Helium thermal capacity.

4.1.6 TF Coil Structural Design Analysis

This section describes the structural design analyses which have been performed for the TF coil components. Many of the analyses required for preconceptual design may be performed by hand, using well-known handbook solutions.[6] On the other hand, some components, notably the intercoil support structure, require machine-aided computation using finite element techniques.

The design allowable stresses are based on structural design limits discussed in Section 4.1.1, and include both conventional primary stress limits based upon maintaining a satisfactory margin against large-scale yielding or rupture due to gross overloading and limits on peak tensile stress based upon fatigue and fracture mechanics concepts. There is not an abundant amount of data available to characterize material behavior at cryogenic temperature, particularly the fatigue life of organic composites such as G-10. However, based on available data, it is clear that for the load levels and number of pulses typical of FED, components which are subjected to pulsed loads are sized by fatigue and fracture mechanics stress limits, which tend to be more restrictive than the conventional primary stress limits.

Tables 4-16 and 4-17 list the mechanical properties of the structural materials used in the present design. The primary stress limits are defined as multiples of S_m, as discussed in Section 4.1.1. Fracture mechanics limits used in the analysis of 316 LN structural components involve the assumed initial flaw size. Figure 4-34 shows the fracture mechanics stress limit evaluated using the 316 LN base metal properties in Table 4-16, as a function of assumed initial flaw size, assuming the applied load is fully cyclic. Similar curves can be drawn when the applied load is a superposition of a cyclic component plus a steady component; when the load is not fully cyclic, the stress limits become higher.

A machine requirement is to withstand 250,000 pulses at 8-T operation plus 25,000 pulses at 10-T operation. For components which are fracture mechanics limited, the above requirement is equivalent to withstanding 350,000 pulses, all at 8 T, with no additional cycles at 10 T. Therefore,

Table 4-16. Mechanical properties of TF coil structural metals

	Temp. (K)	316 LN plate (thick sections)	316 LN plate (thin sections)	316 LN (weld)	310 s (rod)
Modulus, 10^6 psi	293	30	30	30	26.5
	4	33	33	33	28.5
Yield strength,	293	30	33	30	130
ksi	4	125	140	100	200
Ultimate strength,	293	75	84	70	155
ksi	4	200	225	161	260
S_m, ksi	293	20	22	20	51.7
	4	66.7	75	53.7	86.7
Fracture toughness					
ksi $\sqrt{\text{in.}}$	4	150	150	100	—
$C_o{}^a$	4	4.5×10^{-11}	4.15×10^{-11}	7.6×10^{-11}	—
n^a	4	3.26	3.26	3.36	—

$^a\frac{da}{dN} = C_o(\Delta K)^n$; $\frac{da}{dN}$ in inches/cycles, ΔK in ksi$\sqrt{\text{in.}}$

Table 4-17. Mechanical properties and fatigue stress limit for G-10 epoxy fiberglass at 4 K

Properties	
Modulus, 10^6 psi	4.5
Ultimate strength, compression (thin sheets)	120
Ultimate strength, compression (thick sheets)	80
S_m, ksi (thin sheets)	40
S_m, ksi (thick sheets)	26.7

Fatigue Limit

For thin sheets loaded cyclically in compression, after a neutron fluence $\leq 10^{11}$ rads, the allowable cycles N at stress σ (ksi) is $N = (\sigma/75)^{16}$.

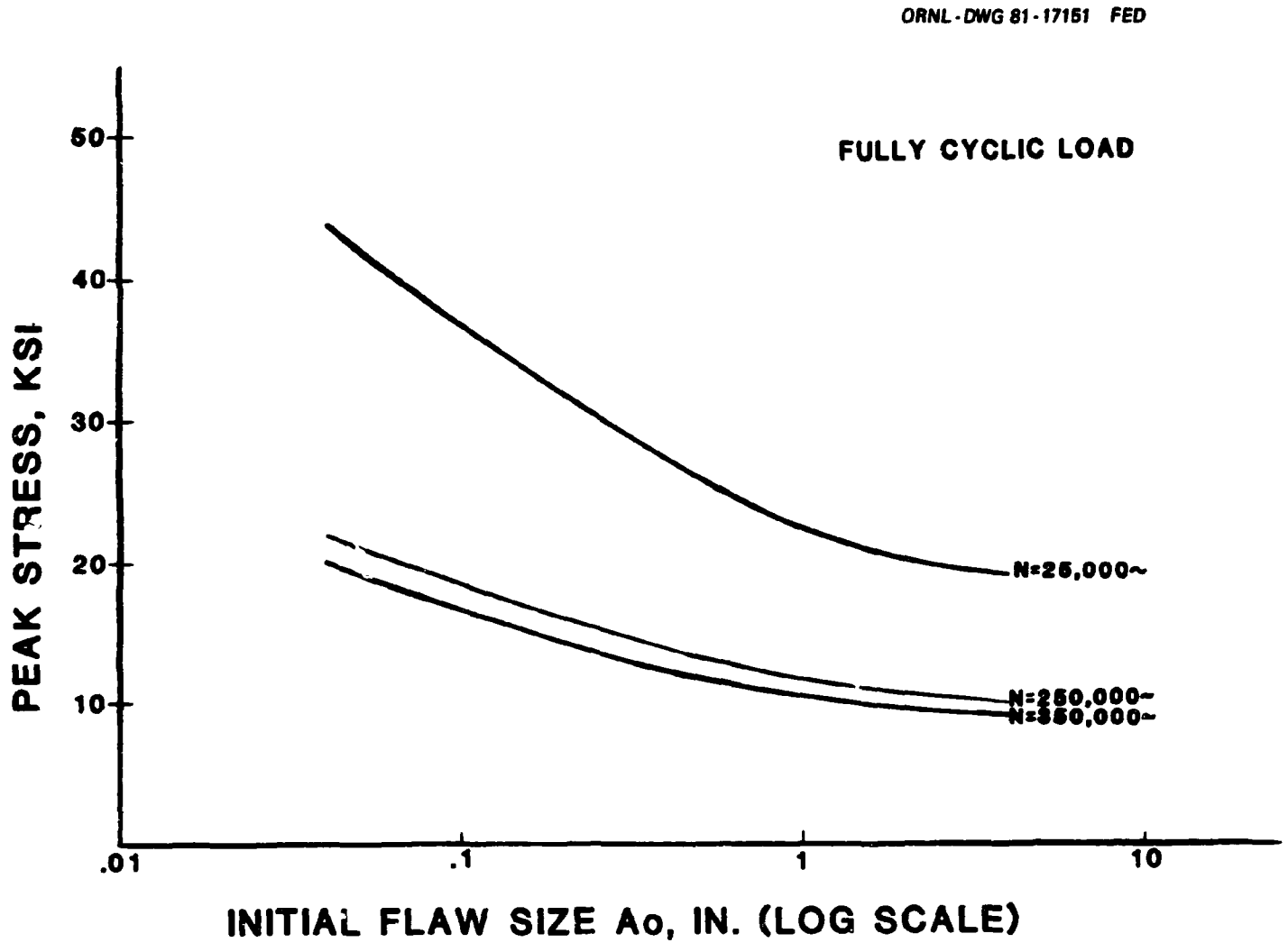

Fig. 4-34. Fracture mechanics allowable stress for 316 LN.

these components are analyzed using an allowable stress based on 350,000 cycles and loads representative of 8-T operation. On the other hand, components which are sized by loads which are steady with time (e.g., the bucking post) are analyzed on the basis of loads characteristic of 10-T operations, since the primary stress limits must be satisfied regardless of how many (or few) times the load is applied.

For thick sections of steel (e.g., the TF coil case, with a thickness up to 12 cm), an initial flaw size of 0.1 in. has been assumed. This choice of flaw size reflects the assumption that the material will be ultrasonically inspected; in the TF coil case, for example, the final case closure welds cannot be radiographed. The assumed flaw size reflects consultation with several persons conversant in inspection techniques, and represents the average of several estimates of the maximum size flaw which can escape detection. A flaw size of 0.1 in. is considered an aggressive, but not unreasonable, quality control goal.

For thinner sections, such as the 3.5 mm thick U-shaped steel channel which is co-wound with the conductor, an initial flaw size of 0.040 in. is assumed. Considering that the channels can be radiographed, this flaw size is regarded as a reasonably conservative value.

Designing for overly conservative flaw sizes leads to unnecessarily low working stresses and, therefore, heavier structure. On the other hand, basing design on overly optimistic flaw sizes can greatly increase manufacturing costs, since the assumption of a given flaw size implies the requirement to grind out and weld repair any indication exceeding the assumed size.

The remainder of this section briefly describes the structural analysis of the major TF coil components, and reports the stresses which have been calculated.

Winding pack

Figure 4-12 shows the cross section of a typical conductor. The conductor-in-channel is wrapped in Kapton and fiberglass tape for inter-turn insulation. The conductor force exerted in the plane of the TF coil is transferred through the insulation and the legs of the channel

to adjacent channels and ultimately to the case. In like manner, the conductor force exerted normal to the plane of the TF coil is transferred through the insulation and the web of the channel to adjacent channels and ultimately to the sidewall of the case. In evaluating the compressive stresses on the insulation, it is conservatively assumed that only the portion of the insulation directly in the load path, i.e., directly in line with the legs or web of the channel, is effective in transmitting load.

Based on maximum running loads (force per unit length of coil periphery) at 10-T peak field operation, the compressive stresses on the insulation are 39.5 ksi due to in-plane loads and 36.2 ksi due to out-of-plane loads; these are both within the allowable of S_m = 40 ksi per Table 4-17. Since the out-of-plane compressive loading is cyclic, the fatigue life of the insulation must also be considered. Table 4-18 considers the 8-T shots and 10-T shots as two separate duty cycles and calculates an allowable number of cycles for each per Table 4-17 and a corresponding fatigue usage factor for each cycle. It is required that the sum of the usage factors be less than unity, and it is evident from Table 4-18 that this requirement is met.

Table 4-18. Fatigue life of winding insulation

	Cycle 1 (8-T shots)	Cycle 2 (10-T shots)
Compressive stress, ksi	22.2	36.2
Required number of cycles	250,000	25,000
Allowable number of cycles	2.9×10^8	115,000
Fatigue usage factor (Required cycles/allowable cycles)	0.009	0.22

The steel channel which supports the conductor experiences compressive stresses in two orthogonal directions, as well as a tensile stress (due to coil dilation by the in-plane loads) in the third direction.

The maximum stress intensity resulting from this combined loading at 10-T peak field operation is 52.4 ksi, which is well within the allowable of S_m = 75 ksi. The vertical legs of the channel are also subject to a cyclic bending stress, due to the pulsed out-of-plane conductor load. If an initial flaw size of 1 mm (0.040 in.) is assumed for the 3.5 mm thick channel material, a peak allowable stress of 20 ksi is found from Fig. 4-34. The nominal bending stress at the root of the fillet, based on the peak out-of-plane load at 8-T peak field operation, is 9.1 ksi, so that the fillet must have a stress concentration factor not exceeding 2.2. For the present geometry, the stress concentration factor is about 1.6,[7] so the channel wall is amply sized to withstand the cyclic pushoff load.

The conduit wall must be capable of withstanding a quench pressure of 218 atm at 10-T operation. For the conduit dimensions shown in Fig. 4-12, the combined membrane-plus-bending stress for 218 atm internal pressure loading is 115 ksi, which slightly exceeds the allowable 1.5 S_m = 112.5 ksi. Considering the preconceptual stage of the design, the degree of non-compliance is considered insignificant.

Coil case

The coil case thickness is sized to carry the out-of-plane load of the winding pressing against the sidewall of the case. This is a cyclic load, so that the fracture mechanics stress limit (16.6 ksi, based on an assumed initial flaw size of 0.1") is the design driver which sizes the wall thickness.

A unit length of the coil case cross section is modeled as a frame in which one leg is subjected to a uniformly distributed load. The expression for the maximum bending moment is a function of the aspect ratio of the frame and varies between the extremes corresponding to a simply supported beam and a clamped-clamped beam.

The coil case thickness is sized separately in the inboard region (adjacent to the bucking post), in the intercoil support structure (ISS) region (where the case sidewall is directly supported by the ISS modules), and in the outboard region of the coil. In the inboard region, where

the TF coils nest together, the sidewall load is reacted by two sidewalls bending back-to-back. Similarly, in the ISS region, the case sidewall is backed up by the wall of the ISS module. In each case, the available support is taken into account in sizing the wall thickness.

In each zone, the coil case thickness is sized to limit the sidewall plate bending stress to 16.6 ksi, based on the maximum out-of-plane running load in that zone per Fig. 4-27 (scaled to 8-T level). The wall thickness obtained in this manner is used in all four walls of the case, except in the inboard region, where the inner and outer wall thickness must be increased to limit the hoop stress which results from wedging of the coils.

In addition to the plate bending load in the sidewall, a similar plate bending load exists on the outside wall of the coil case due to expansion of the winding by the in-plane Lorentz forces. Since the resulting stress is steady in time, flaw growth is not a problem, and the limit on primary bending stress is slightly more restrictive than the fracture mechanics limit. Based on in-plane loads at 10-T peak field operation, the plate bending stress in the outer wall is 88 ksi, which is within the allowable 1.5 S_m = 100 ksi.

The in-plane Lorentz force causes the TF coil to dilate in the plane of the coil, the load being shared between the case and the structural steel in the winding. In evaluating coil case stresses due to this loading, it is assumed that the winding fits tightly in the case, and that the case immediately picks up load as soon as the winding begins to dilate. The resulting longitudinal stress in the case is 17.2 ksi, well within the allowable S_m = 66.7 ksi.

Bucking post

The cross section of the bucking post is a 10-sided regular polygon with a central hole. Each of the flats is loaded normal to the surface by a load which is approximately uniformly distributed.

For purposes of analysis, the cross section is modeled as a cylinder whose outside surface is the circle inscribed in the regular polygon. The loading is approximated as a uniform external pressure loading. The

net centering force on the TF coils is shared between the bucking post and wedging of the TF coil cases. It has been shown by finite element calculations (using the model described under Intercoil Support Structure) that about 55% of the net centering force on the TF coils is reacted by the bucking post. Therefore, in analyzing the bucking post, it is assumed that the bucking post carries 60% of the net centering force.

Given an inside radius of 1.48 m and an outside radius (one-half the distance across flats) of 1.74 m, it is found that 60% of the net centering force on the TF coils leads to an average compressive hoop stress of 31 ksi, which is within the allowable S_m (66.7 ksi for the metal, 40 ksi for the dielectric insert material). If it were conservatively assumed that the bucking post takes the full centering load, the hoop stress would rise to 51.7 ksi.

Since the bucking cylinder is loaded in compression, ring buckling is a potential failure mechanism. The design criterion is that the margin against elastic buckling be at least 5. For the present bucking cylinder dimensions, the critical elastic buckling pressure is 6.9 times the pressure resulting from 60% of the net TF coil centering force, so the buckling criterion is satisfied. It is to be noted, however, that the hoop stress in the cylinder corresponding to the critical elastic buckling load is 216 ksi, and since this stress is above the proportional limit, the actual margin against buckling is smaller than 6.9. A more refined buckling analysis, which accounts for the decrease in modulus with increasing stress level, shows that the actual margin on buckling is 3.3. This margin is considered ample; note, for example that commonly used primary stress limits (including those used in the present design) incorporate a margin of 3 against rupture due to gross overloading.

The overturning moment on the TF coils is reacted principally by the intercoil support structure, although some torsional stress is developed in the bucking post. The amount of torque resisted by the bucking post can be estimated with a simple hand calculation (this estimate is consistent with finite element results), from which it follows that the torsional stress on the bucking post is only about 0.6 ksi, compared to an allowable $0.6\ S_m = 40$ ksi.

The estimated torque on the bucking post is also used as the basis for sizing the bolts which connect adjacent axial segments of the bucking post. For each joint between axial segments, 20 bolts of 3 cm diameter are used; the shear stress on the bolts due to torsional loading on the bucking post is 52 ksi, which is just at the allowable of 0.6 S_m for the 310 S bolt material.

Intercoil support structure

The intercoil support structure (ISS) is in the form of box-type modules consisting of an inner and outer shell plus circumferential stiffening ribs. These modules are bolted to the TF coil cases as noted in Section 4.1.2. In addition, there are gusset support assemblies which reinforce the 9 m span of TF coil in the outboard region against out-of-plane loads.

Because of the complexity of the support structure, machine-aided structural analysis is required. The PAFEC general-purpose finite element program has been used for this purpose. The structural analysis explicitly models one complete TF coil plus the ISS extending to the midplane between the TF coil being modeled and the adjacent TF coil on either side. The bucking post and pedestal supports are also included. Periodic boundary conditions are applied in the two midplanes through the ISS, meaning that similarly located node points in the two planes have the same deflections and rotations when measured in and normal to the respective plane, although these motions are not known a priori. Use of periodic boundary conditions restricts the model to loading conditions in which the loads on any one TF coil are the same as on any other TF coil. This restricted class of loadings includes the loads which occur during usual pulsed-field operation but does not include TF coil current-imbalance conditions or horizontal seismic loads. Use of the periodic boundary conditions, as opposed to explicit modeling of all 10 TF coils, greatly reduces the size of the structural model and the cost of the analysis.

Figure 4-35 shows two perspective views of the structural model, prepared using the PAFEC computer graphics package. The model contains

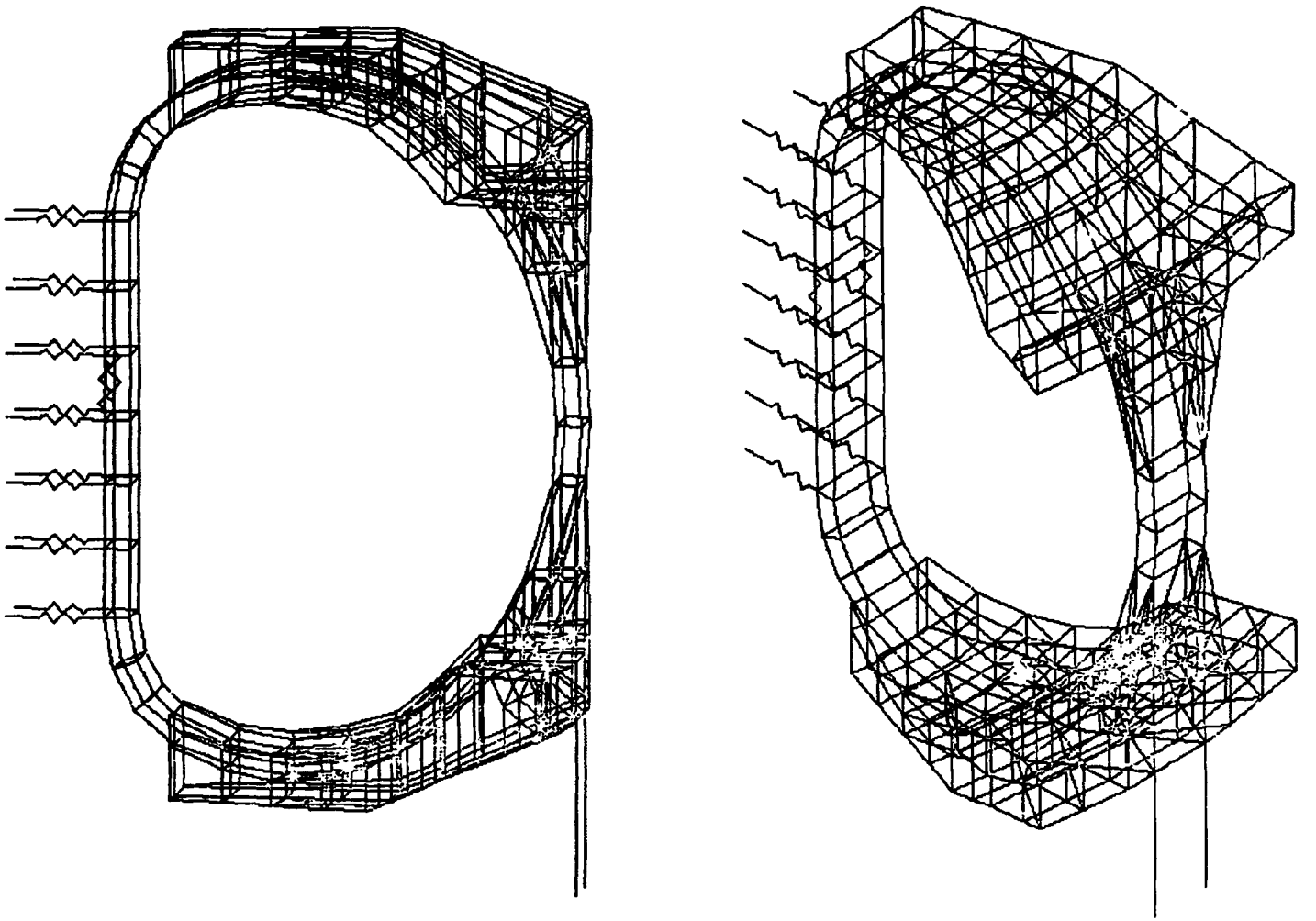

Fig. 4-35. PAFEC finite element model of FED TF coil.

about 2300 degrees of freedom. Each run uses about 30 min CPU time on a DEC PDP-10 computer.

The TF coil case and the ISS members are modeled with thin plate elements which carry membrane and bending loads. The dilational stiffness of the winding pack is included in the form of beam elements which carry axial load, but no bending loads. The bucking post is represented by spring elements which simulate both the radial and torsional stiffness. The pedestal support is modeled with beam elements.

The finite element model has been used to evaluate the stress distribution in the ISS and in the gusset supports which reinforce the outboard portion of the TF coil case. Initially, the analysis was performed assuming 5 cm thick panels throughout the ISS. The gusset support modules, described in Section 4.1.2, use 7.5 cm thick plate stock in the vertical ribs and in the external cover plate. PAFEC results indicate that stresses are within allowable levels throughout most of the ISS; in fact, many ISS panels could be made thinner without exceeding stress allowables. In the gusset support assemblies, there are local overstress conditions; for example, in the vertical triangular ribs which are normal to the plane of the TF coil, local stresses are about 50% in excess of the fracture mechanics allowable. This degree of non-compliance can be corrected by thickening the overstressed members a small amount. The overall conclusion is that with reasonable design changes, the stress allowables can be satisfied. The present results suffice to indicate the feasibility of the proposed support concept.

Ground supports

The pedestal supports are in the form of hollow cylinders of mean diameter 1 m and thickness 3.8 cm, fabricated from cylindrically wrapped layers of epoxy-impregnated fiberglass cloth.

The pedestal supports are sized to carry the weight of the TF coils plus the weight of other components which are supported off the TF coils, such as the ohmic heating coil, the bucking cylinder, the inter-coil support structure, and the two outboard superconducting ring coils. In addition to carrying the dead weight of these components, the supports are sized to withstand a 1 g vertical plus 1 g horizontal seismic loading.

Since the pedestal supports penetrate the magnet vacuum vessel, one end is at room temperature. Therefore, the allowable stress is based upon room temperature properties of G-10. Based upon a compressive ultimate strength of 54 ksi, the allowable stress under seismic (abnormal) conditions is 1.5 S_m = 27 ksi. The actual stress in the pedestals under the assumed loading condition is 26.3 ksi.

Assuming one end of the pedestal support at 4 K and one end at 300 K, and a thermal conductivity of 0.2 W/m-K, the combined heat leak through all of the pedestal supports is 35 W, which is insignificant compared to eddy current heat loads on the system.

Summary of stresses

Table 4-19 summarizes the structural analysis results which have been reported for the components listed above.

Coolant channels

If the eddy current losses which occur in the TF coil case and intercoil support structure were permitted to pass into the winding, the helium in the winding would be insufficient to remove heat loads of this magnitude. Consequently, these losses are intercepted by helium coolant tubes embedded in the TF coil structure and ISS.

The cooling tube arrangement used in the TF coil case is shown in Fig. 4-36. There is a standoff region between the inside surface of the case and the winding, which is partially filled with strips of low thermal conductivity polyimide alumina. About one-third of the standoff perimeter is taken up by the strips, based on limiting the compressive stress in the inserts to S_m = 26.7 ksi. The remainder of the standoff perimeter is sufficient to allow 236 square coolant tubes, 1 cm on a side. The case heat load is $\sim$ 4 kW per coil, and it is desirable to maintain the case temperature at about 4 K; the latter objective is imposed to limit the heat leak to the winding. If the coolant tube length is equal to the coil perimeter, a mass flow rate of 2900 g/s will remove 4 kW, without exceeding the case temperature constraint. The coolant conditions are 3.1 K, 4 atm for the inlet and 4 K, 3.7 atm

Table 4-19. Summary of TF coil system structural analysis results

Component		Calculated Result	Allowable Result
Winding Insulation	• Compressive stress due to in-plane loading (steady)	39.5 ksi	S_m = 40 ksi
	• Compressive stress due to out-of-plane loading (cyclic)	36.2 ksi	S_m = 40 ksi
	• Fatigue usage factor due to 250,000 8-T shots plus 25,000 10-T shots	0.22	1.0
Conductor Support Channel	• Bending stress at root of fillet in U-shaped channel (including stress concentration)	14.6 ksi	20 ksi[a]
	• Combined stress (stress intensity) due to compression and longitudinal dilation	52.4 ksi	S_m = 75 ksi
Conductor Conduit	• Membrane-plus-bending stress due to 218 atm quench pressure	115 ksi	1.5 S_m = 112.5 ksi
Coil Case	• Plate bending stress in sidewall due to out-of-plane loading (pulsed)	16.6 ksi	16.6 ksi[a]
	• Plate bending stress in outside wall due to in-plane loading (steady)	88 ksi	1.5 S_m = 100 ksi
	• Tensile stress in case wall due to in-plane dilational loads (steady)	17.2 ksi	S_m = 66.7 ksi
Bucking Post	• Compressive hoop stress	31 ksi	S_m = 40 ksi (insulator) S_m = 66.7 ksi (metal)
	• Margin against elastic buckling	6.9	$\geq$5.0
	• Torsional stress on bucking post	0.6 ksi	0.6 S_m = 40 ksi
	• Shear stress on bolts connecting axial segments	52 ksi	0.6 S_m = 52 ksi[a]

Table 4-19. Summary of TF coil system structural analysis results (continued)

Component		Calculated Result	Allowable Result
Intercoil support structure, gusset support modules	• Peak normal stress due to out-of-plane loads acting alone	25.6 ksi	16.6 ksi[a]
Pedestal supports	• Axial stress due to dead weight plus 1 g horizontal and vertical seismic load	26.3 ksi	1.5 S_m = 27 ksi

[a]Limit derived from crack growth and fracture mechanics considerations.

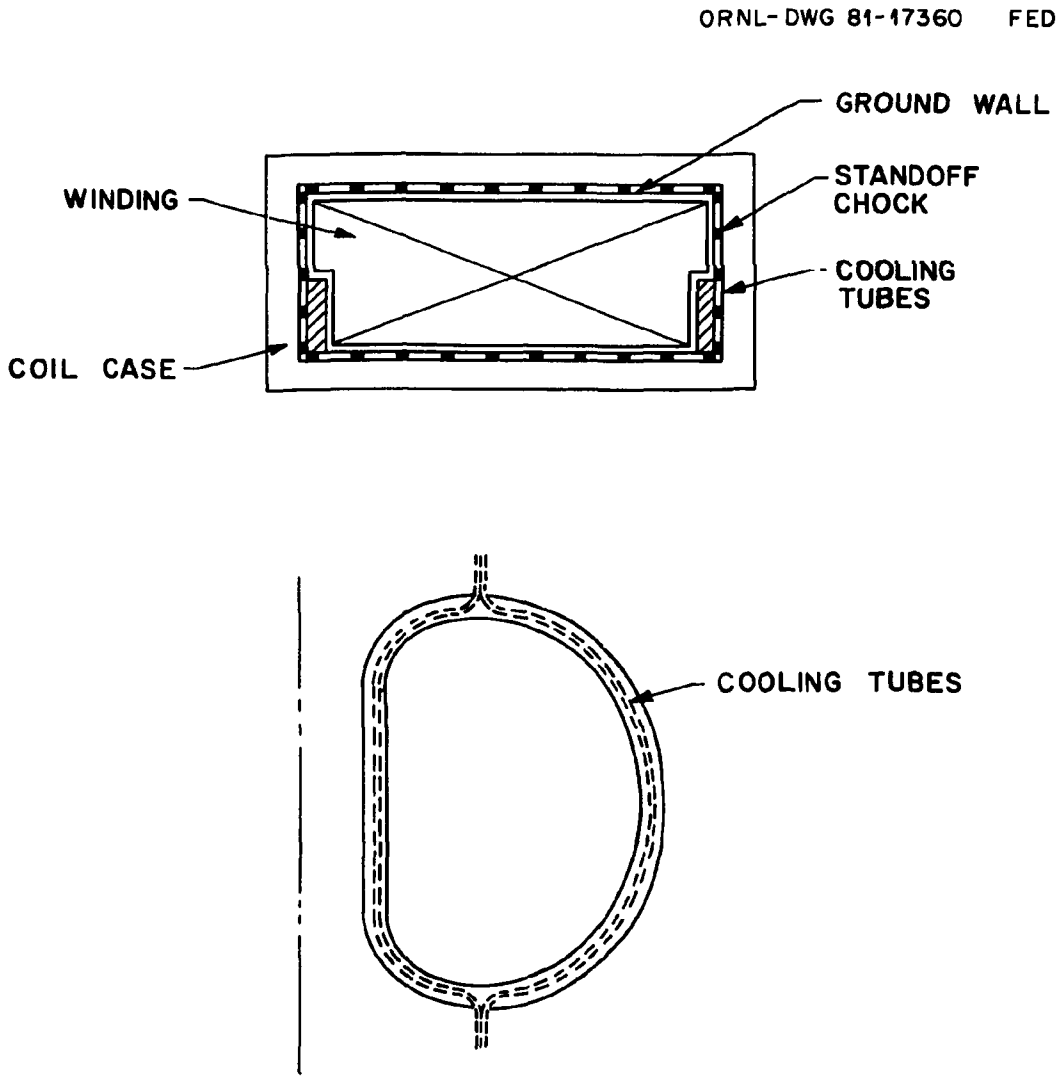

Fig. 4-36. Cooling tube configuration for the TF coil case.

for the outlet. The heat leak to the winding is ∿20 W per coil. The winding helium discharge will be directed through the case coolant tubes, supplemented as necessary by helium from the refrigerator.

Similar cooling tubes are embedded in the ISS for removing the ISS losses. The tube placement is shown in Fig. 4-37. A helium mass flow rate of 180 g/s is needed in the ISS coolant tubes for each TF coil. Helium inlet and outlet temperature and pressure conditions are 15 K at 2.5 atm and 20 K at 2.4 atm, respectively.

4.1.7 Future Work – TF Coil System

The purpose of the present preconceptual design effort has been to demonstrate feasibility of one plausible design concept and to develop that design in enough detail to permit a meaningful cost estimate to be made. Future work should examine some of the alternate concepts (discussed in Section 4.1.3) in comparable detail, in order to provide a firm basis for selection of a conceptual design.

In several instances, such as the selection of allowable discharge voltage and the assumption of initial flaw size, reasonable assumptions had to be made on the basis of engineering judgement and a small amount of experimental data. For preconceptual design, this approach is often satisfactory for purposes of demonstrating feasibility. For example, the assumption of a 0.1-in. initial flaw size is considered by some to be overly optimistic, but whether 0.1 in. or 0.25 in. is the correct size, the design calculations based on assumed flaw size clearly show that fatigue and fracture mechanics is a design driver that significantly affects the sizing of several key components.

As the design becomes more firmly defined, many of the assumptions made during preconceptual design will have to be reviewed and perhaps revised. From the standpoint of TF coil design, however, a high priority effort for future work is to define a workable PF coil system. The amp-turns and locations of the PF coils affect not only the design of the PF coils themselves but the design of other components also, including the TF coils. The location and size of the PF coils determines the eddy

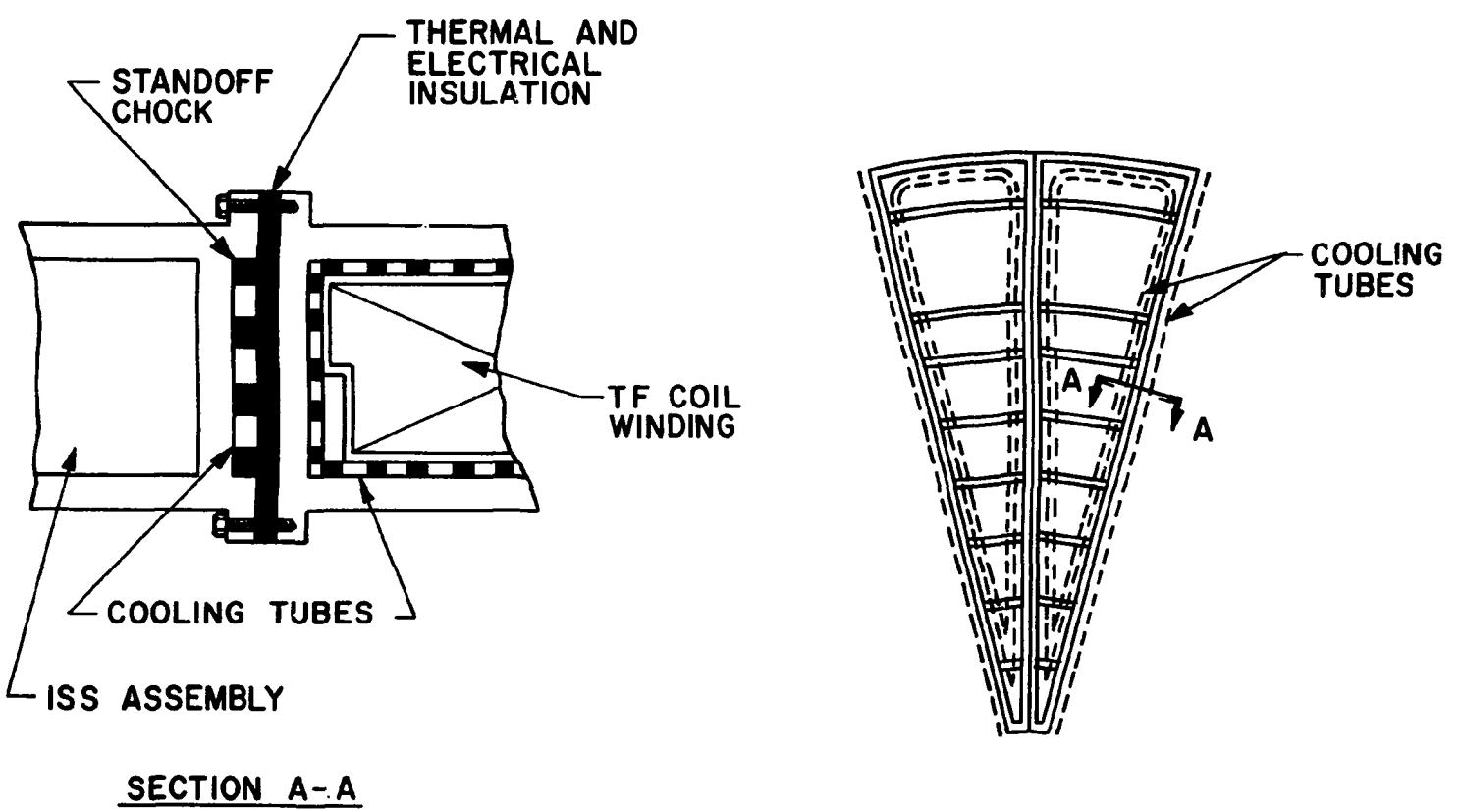

Fig. 4-37. Cooling tube configuration for the intercoil support structure.

current loss and the out-of-plane force profiles on the TF coils. The force distribution directly affects the design of many components in the TF coil system.

The design effort to date has focused relatively little attention on the response to fault loads, such as TF coil current imbalance conditions. In the case of current imbalance loads, just what constitutes a credible degree of current imbalance has not been clearly defined. Since the allowable stress levels for fault conditions are much higher than the fracture mechanics stress limits which size many of the TF coil system components, it is likely that current imbalance loads will not be a design driver, but this needs to be quantitatively verified.

There is a continuing need for material property data at cryogenic temperatures. Particularly scarce is fatigue life data for epoxy composites at liquid helium temperature. Fatigue life for epoxy composites is not only a function of temperature but a function of specimen configuration and mode and direction of loading.

The winding design discussed here, as well as alternate options, involve operation at temperatures below 4 K in order to be able to operate at 10-T peak field. There is presently very little material property data at these reduced temperatures, and it is not evident that 4 K data is necessarily applicable at lower temperatures.

In view of the large amount of welding involved in the fabrication of the TF coil system components, future work should address the effect of residual stresses upon design allowables, since such large structures cannot be stress relieved.

The internally cooled cabled superconductor (ICCS) proposed for the present design has been scaled and based on stability, heat transfer, and quench characteristic measurements at 7 T for a single triplex (three strands). It would be necessary to measure these characteristics and ac losses for the proposed conductor at 10 T to verify the scaling parameters for the reliable design and operation of the TF coils.

4.2 POLOIDAL FIELD COIL SYSTEM

4.2.1 PF Coil System Major Design Considerations

The poloidal field (PF) coils include several coil sets. Together, these coils provide the functions of plasma initiation, heating, shaping, and equilibrium. From a configuration standpoint they are grouped as a solenoid (long compared to diameter) and ring coils (diameter large compared to coil cross section).

System function summary

Equilibrium field (EF) coils shape the plasma in cross section and provide the vertical field necessary to maintain it in equilibrium. The function of ohmic heating (OH) coils is to inductively heat the plasma and to provide the volt-seconds to sustain the plasma current. Control coils are used in conjunction with feedback control circuits to control the position of the field null for plasma initiation and to control the plasma position radially and vertically during the cycle.

In early design studies, there was separation of function from coil to coil. Ohmic heating was provided by the solenoid, aided by ring coils carrying modest current (1-3 MAT) near the top and bottom of the solenoid to ensure that the solenoid flux linked the plasma. Larger diameter ring coils with larger current ratings (4-10 MAT), both exterior and interior to the bore of the TF coils, provided the EF function. Ring coils of small (<1 MAT) capacity placed inside the bore of the TF coils provided the control function.

Following numerous design and trade-off studies, the separation of function has largely disappeared. As PF system configuration is optimized to a greater degree, coils now fulfill two and sometimes three functions. The solenoid still has primarily an OH function; however the central portion of the solenoid, comprising 20% of the total number of turns, performs an EF function. The two large superconducting ring coils (EF_2 and EF_3 in Fig. 4-38), outboard of the plasma and external to the bore of the TF coils, are primarily EF in function, but the current waveform has

an OH component superposed on the EF component. The two large normal ring coils (EF_1 and EF_4), inboard of the plasma and inside the bore of the TF coils, are also primarily EF in function but carry an OH component of current as well as providing a 25 V per turn startup current. The four control coils (C_1 through C_4) provide an initial null field and a control function.

Requirements summary

The PF coil locations and coil current ratings for the baseline configuration are listed in Table 4-20 and illustrated in Fig. 4-38.

Table 4-20. PF system configuration

Coil	Maximum Coil Current, MAT[a]	Location of Centroid	
		Z, m[b]	R,m
EF_1[c]	4.3	4.10	3.85
EF_2	-6.1	4.75	9.5
EF_3	-9.1	-5.90	9.5
EF_4[c]	3.7	-3.80	3.05
EF_5	-12	0	1.17
OH_1	-24	3.18	1.17
OH_2	-24	-3.18	1.17
C_1	$\pm$0.35	3.95	4.2
C_2	$\pm$0.35	3.45	7.1
C_3	$\pm$0.35	-4.7	7.2
C_4	$\pm$0.35	-3.9	3.45

[a]Maximum currents in EF and OH coils occur at end of burn, t = 112 s; all currents are for 10-T operation.
[b]Height relative to plasma centerline.
[c]These coils will carry the blip voltage for plasma initiation.

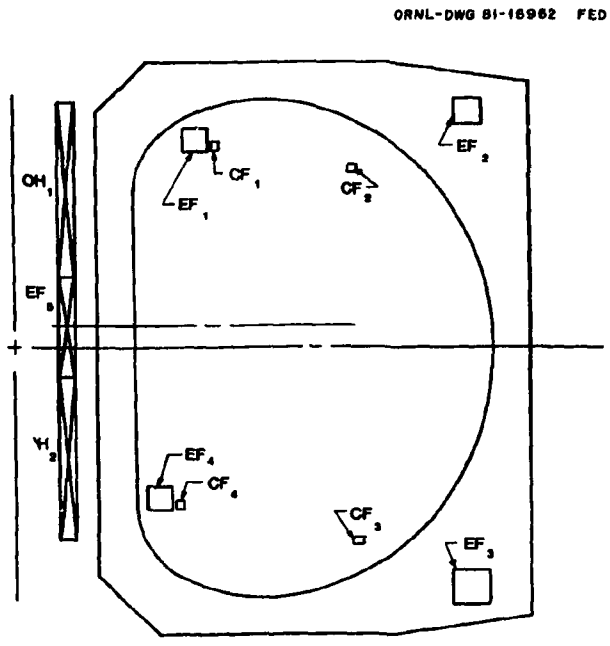

Fig. 4-38. PF system configuration.

The baseline configuration has evolved from numerous design studies to a configuration which simultaneously meets a variety of requirements:

- meet plasma system requirements
  - satisfy MHD stability criteria
  - provide the 95 volt-seconds for startup and 7 volt-seconds for burn*
  - provide plasma loop voltage of 25 volts to initiate plasma
  - control currents sufficient for adequate plasma control
- maximum filed in any superconducting coil is limited to 7 T for conductor stability
- superconducting coils must be cryogenically stable for operational heat loads
  - winding losses
  - eddy current loss in the case
  - lead and joint losses

*Volt-second requirements are given for 10-T operation; volt-second requirements for 8-T operation are slightly less.

- heat radiated from cold shield
- heat due to transient conductor motion

- structurally adequate for applied mechanical loads
  - magnetic loads
  - dead weight
  - 1 g seismic load (0.25 g ground motion, structural amplification of 4), laterally and vertically
  - operating pressure differentials
- superconducting coils must be capable of being rapidly discharged from the fully charged state without any permanent damage.

The design must withstand 250,000 8-T tesla and 25,000 10-T operations of the device. For the ring coils, with one load cycle for each cycle of operation, there will be a total of 275,000 load cycles. However, the solenoid experiences two peak-to-peak load cycles for each operating cycle and must be designed for 550,000 load cycles. The PF coils must survive all credible fault conditions without damage. All of the PF coils are categorized as semipermanent structures, i.e., they are to be designed for the life of the device and are not intended to be replaced or repaired. Nevertheless, the design must be such that coils can be replaced if necessary. Sufficient shielding will be provided to permit contact operations for preventive or corrective maintenance 24 hours after reactor shutdown. Neither neutron heating nor irradiation-induced material damage is a practical concern for the PF coils because of the attenuation of irradiation provided by the torus shielding and (for the solenoid) the TF coils and the bucking post.

Structural analysis and sizing calculations use the design allowables summarized previously (Sections 4.1.1 and 4.1.6) in this report.

4.2.2 Solenoid Layout

The conceptual design of the FED solenoid duplicates, to the maximum extent practical, the LANL design for the 20-MJ pulsed coil program. The 20-MJ coil will have been built and operated prior to

construction of FED, and it is deemed prudent to rely on that design unless future experience dictates otherwise. The major parameters of the solenoid are summarized in Table 4-21, and a layout is given in Fig. 4-39.

Key features of the FED solenoid design are

- double pancake winding layout
- modular design, with modules powered by separate leads
- glass epoxy helium vessel to avoid induced currents
- leads located in central bore minimize space required at OD
- solenoid supported off toroidal field intercoil support structure.

Conductor

The conductor for the solenoid is a 50-kA NbTi, copper stabilized, pool boiling liquid helium cooled, flat cable. The conductor (Fig. 4-40) consists of 36 subcables, each 0.6374 cm diameter, cabled around a central core consisting of two strips of Nitronic 40, each 11.21 cm by 0.282 cm. The use of two strips makes the core more flexible than a single thickness strip would be, facilitates winding, and reduces eddy current losses when an insulating material sheet is sandwiched between the two strips.

Each subcable consists of six insulated superconducting strands, each 0.213 cm diameter, stranded around a stainless steel strand of the same diameter. The stainless steel strand increases the tensile strength of the subcable.

Each strand has a central region of NbTi filaments imbedded in a copper matrix. This region is separated from the copper stabilizer surrounding it by a barrier of CuNi. The barrier provides high electrical resistance to inhibit eddy current paths between the superconductor filaments within and the copper stabilizer without. At the same time the barrier will permit heat transfer away from and current shunting around any normal region that develops in the superconductor. To inhibit eddy currents circulating through the copper stabilizer around the

Table 4-21. Central solenoid design parameters

Geometric	
Helium vessel dimensions	
Inside radius, m	0.733
Outside radius, m	1.450
Coil dimensions	
Inside radius, m	0.863
Outside radius, m	1.405
Height, m	10.45
Winding dimensions	
Inside radius, m	0.939
Outside radius, m	1.339
Weight, 10^3 kg	147
Electromagnetic	
Maximum field at winding, T	7
Ampere turns, MA	60
Conductor rating, A	50
Number of turns	1200
Number of pancakes	60
Current density	
Winding, A/cm^2	1435
Overall coil, A/cm^2	1059
Performance	
Maximum rate of change of field T/s	2.3
Discharge time, s	6
Stored energy at 50 kA, MJ	1000

ORNL-DWG 81-17044 FED

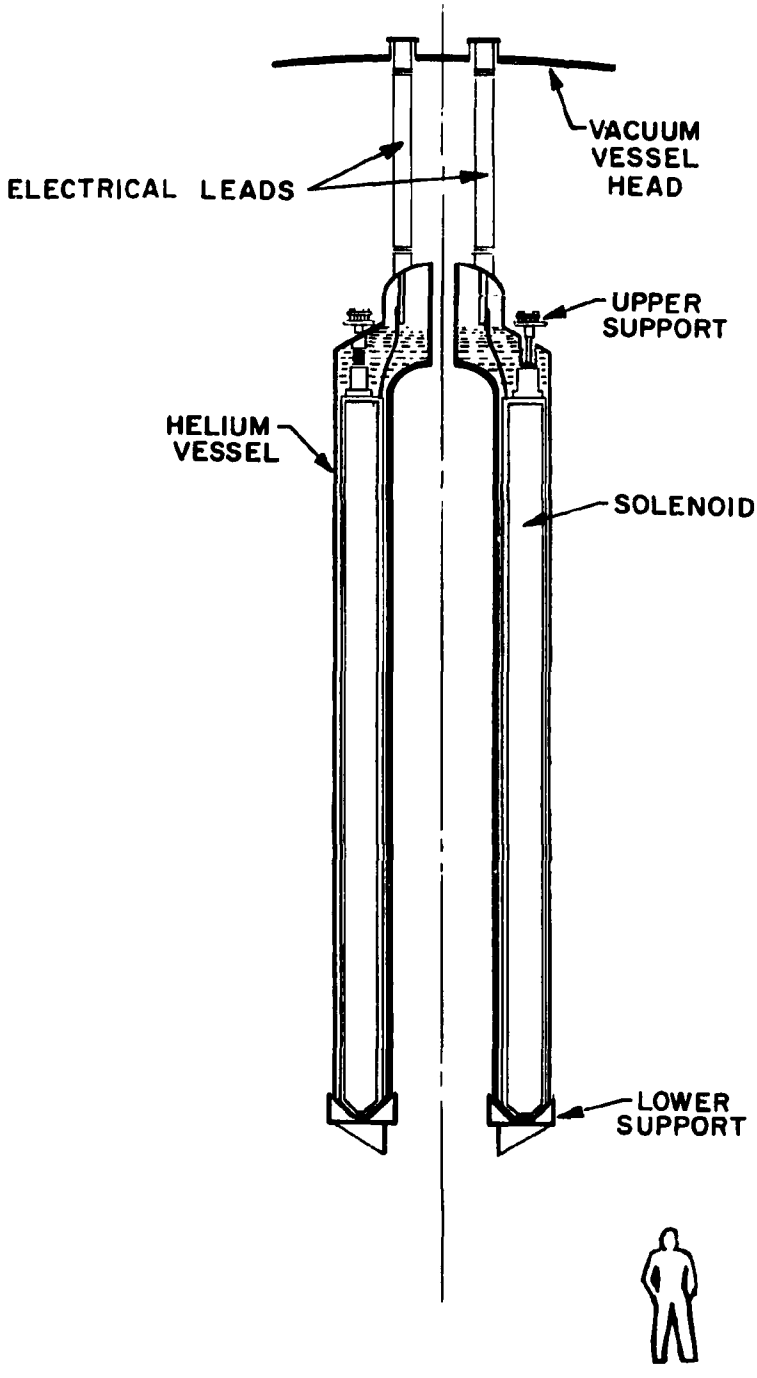

Fig. 4-39. Solenoid conceptual design.

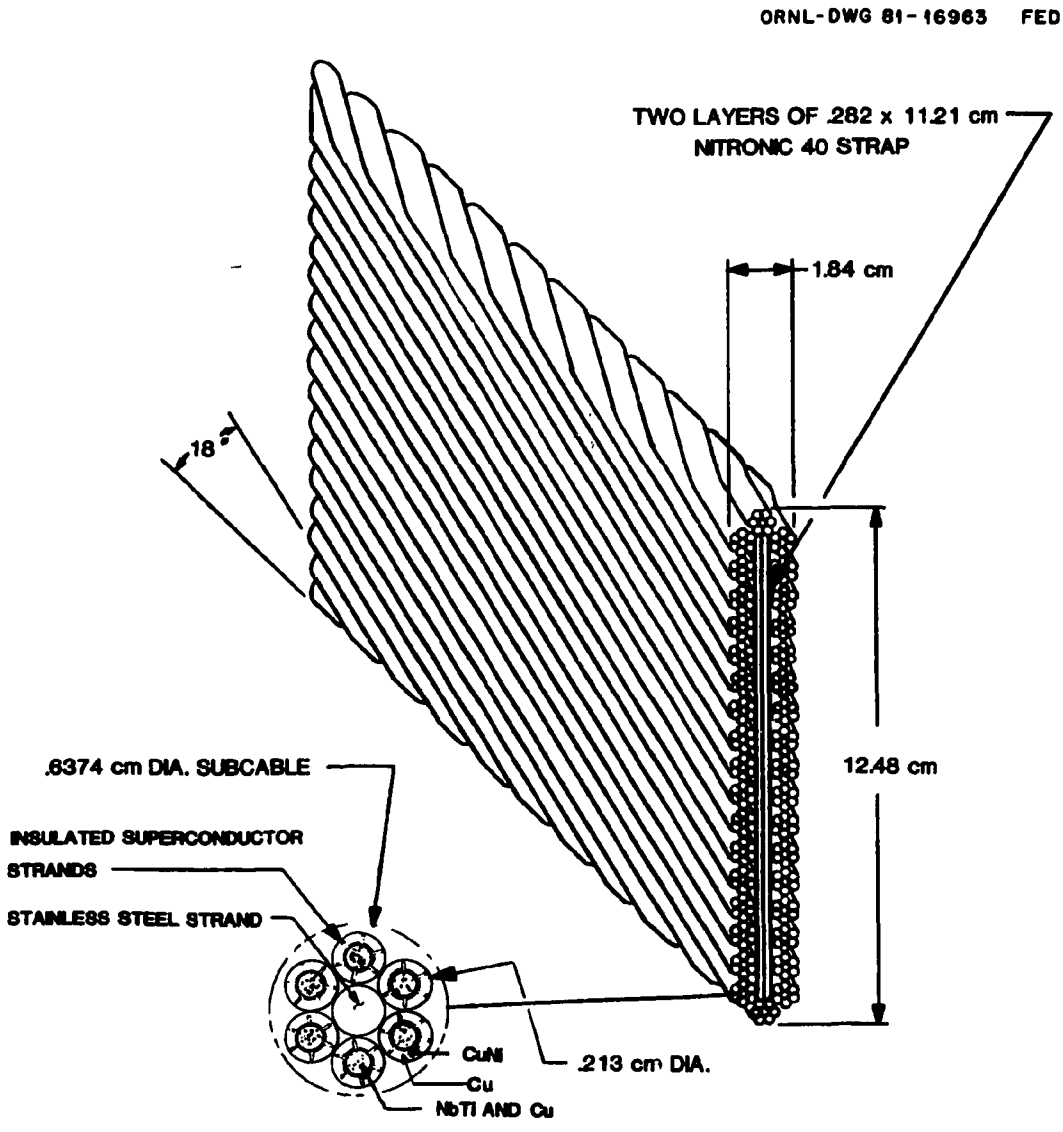

Fig. 4-40. 50 kA PF conductor.

superconducting region, six CuNi fins extend out into the stabilizer region from the barrier.

The turn-to-turn insulation consists of "railroad" spacers co-wound with the conductor. The spacers (Fig. 4-41) consist of 12.48 cm by 0.16 cm G-10 CR strips, held in position C.125 cm apart by glass tape. The construction permits free flow of helium coolant in the axial and azimuthal directions.

Winding layout

The basic structure of the coil winding employs double pancakes (Fig. 4-42) similar to the LANL 20-MJ coil. Pancake to pancake insulation is provided by a G-10 plate which also serves to support the out-of-plane magnetic loads on each pancake. The support plates are supported at their inner and outer edges by the coil former and support blocks, respectively, transferring axial magnetic load so it does not accumulate from pancake to pancake. The support plates have channel grooves sloped upwards at 7° to the horizontal to assure helium bubble clearing and migration through the winding.

The solenoid consists of a total of 60 pancakes with 20 turns per pancake. The central 12 pancakes (a total of 12 MAT) is designated EF_5 and represents the EF portion of the solenoid. OH_1 and OH_2, each consisting of 24 pancakes (a total of 24 MAT in each of OH_1 and OH_2), are the OH portion of the solenoid.

The voltage induced in the solenoid due to the blip (for plasma initiation) is 3 kV. Since the current requirements in the OH and EF portions of the solenoid are different, the solenoid will be divided into three modules, the modules being OH_1, OH_2, and EF_5 portions of the solenoid. The pancakes within each module will be connected in series and then connected to a separate pair of current leads. Wired in this way, the maximum voltages on the solenoid modules OH_1, OH_2, and EF_5 during discharging are 4 kV, 4 kV, and 2 kV, respectively. These voltages are less than the maximum allowable terminal voltage of 10 kV; the rather high (10 kV) allowable terminal voltage reflects the fact that the solenoid is encased in a fiberglass helium vessel. Voltages induced in these

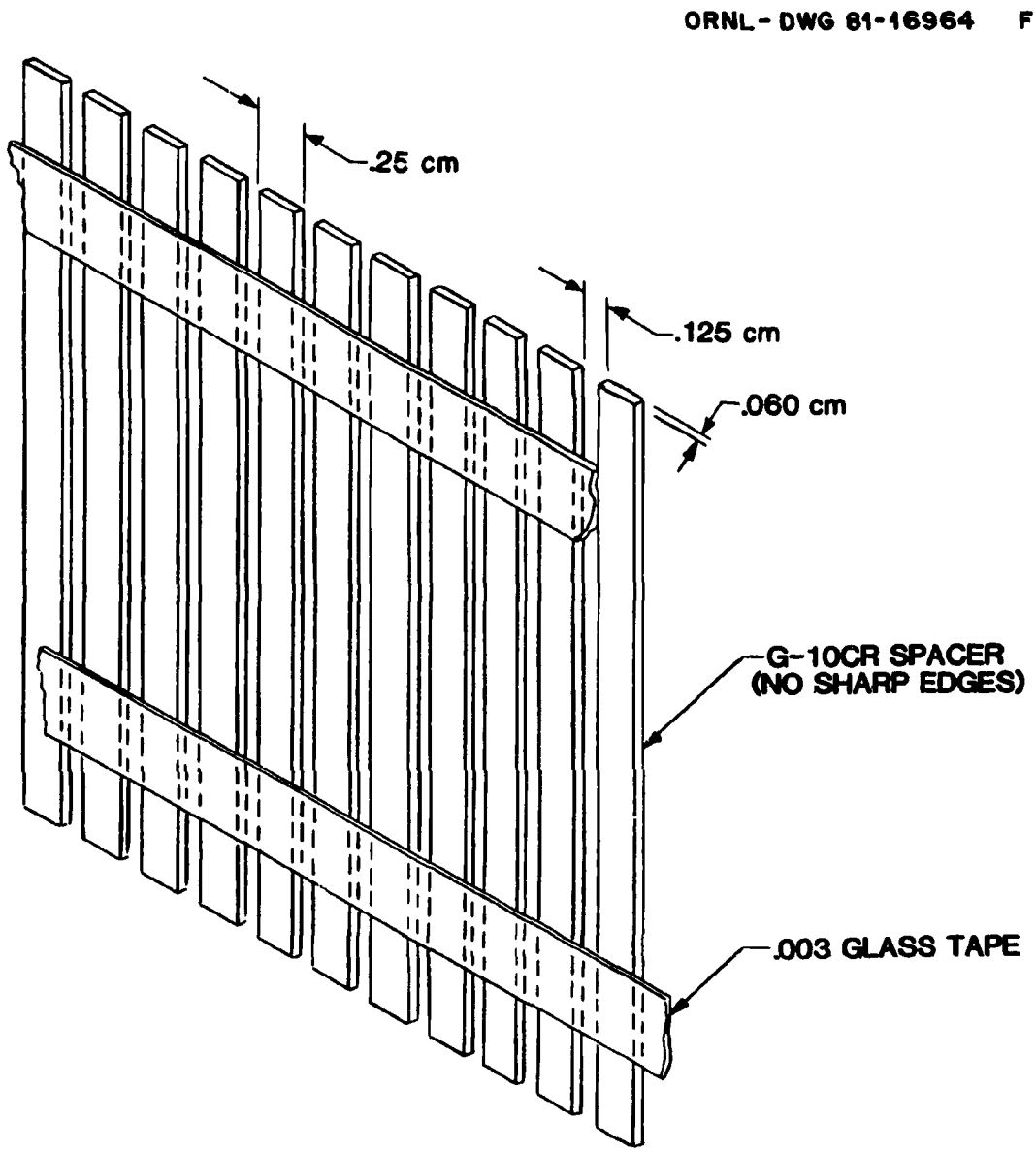

Fig. 4-41. Railroad spacer.

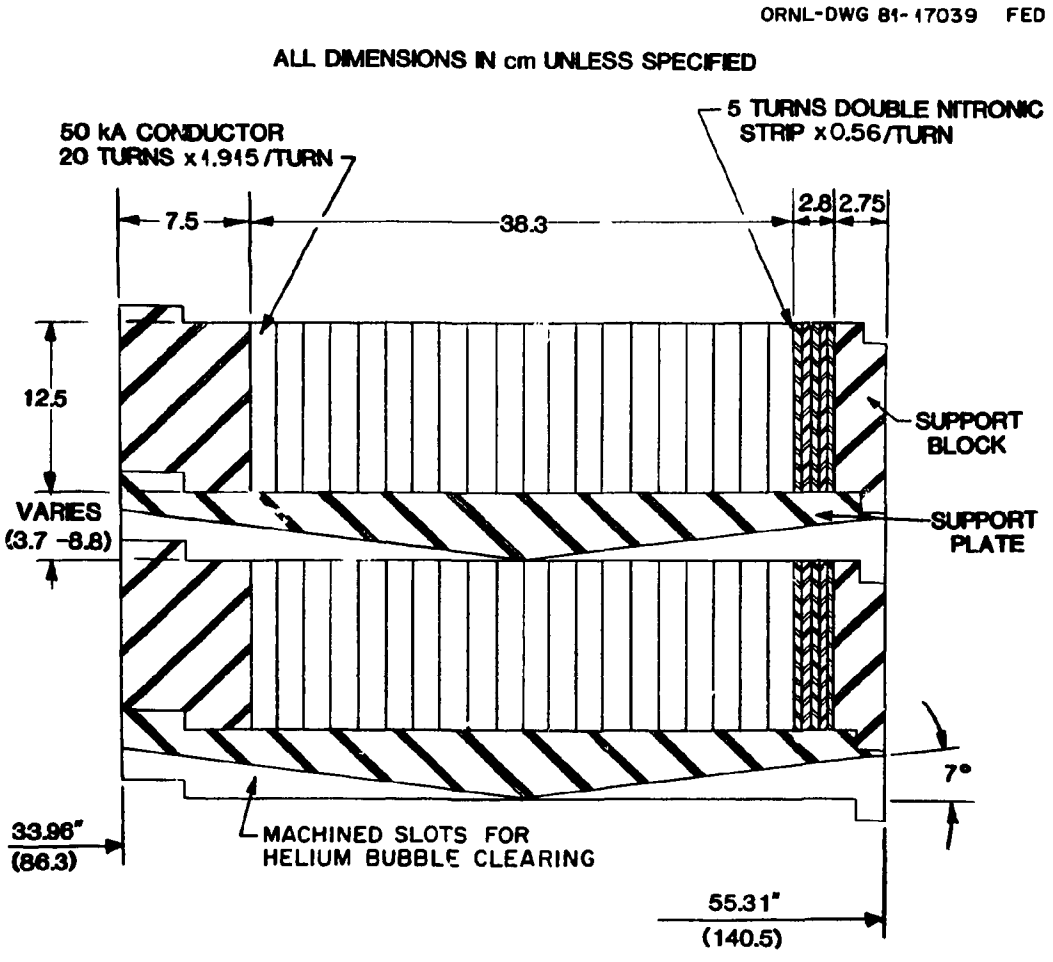

Fig. 4-42. Typical solenoid double pancake.

modules following a plasma disruption are less than the voltages induced during normal pulsed operation. The voltages induced by the control coils C_1 through C_4 have not yet been evaluated but are expected to be small.

Joints and lead routing

After 20 turns of full winding of each pancake, all the subcables of the 50 kA cable are separated from the central stainless strap of the cable and bent toward the upper and lower G-10 support plate of the pancake coil, where the joints are made. All the cable joints between pancake coils are located in every other G-10 support plate of the pancake coil. The central strap, without its insulation, makes additional turns for radial support of the coil and is terminated by welding.

The leads are routed into the inner radius region to avoid additional buildup in the outer radius region. Additional ac losses and loading in leads in the high field inner radius region will not be significant. Each lead will be restrained by G-10 plate and connected to two 25 kA vapor cooled current leads in the upper region of the cryostat.

Helium vessel

The helium vessel for the solenoid is a double walled cylinder made of glass epoxy to preclude eddy current losses due to induced poloidal currents.

Support structure

Details of the solenoid support are shown in Fig. 4-43. The helium vessel is supported by a ring support attached to the lower end of the TF coil nose region; the ring support also supports the bucking cylinder. The solenoid is inserted into the annulus of the double walled helium vessel and rests on the bottom in a tapered fitting which gives lateral support to the lower end of the solenoid. A vertical restraint is provided at the top of the solenoid to prevent liftoff. Resultant upward magnetic load could be caused by fault conditions such as failure

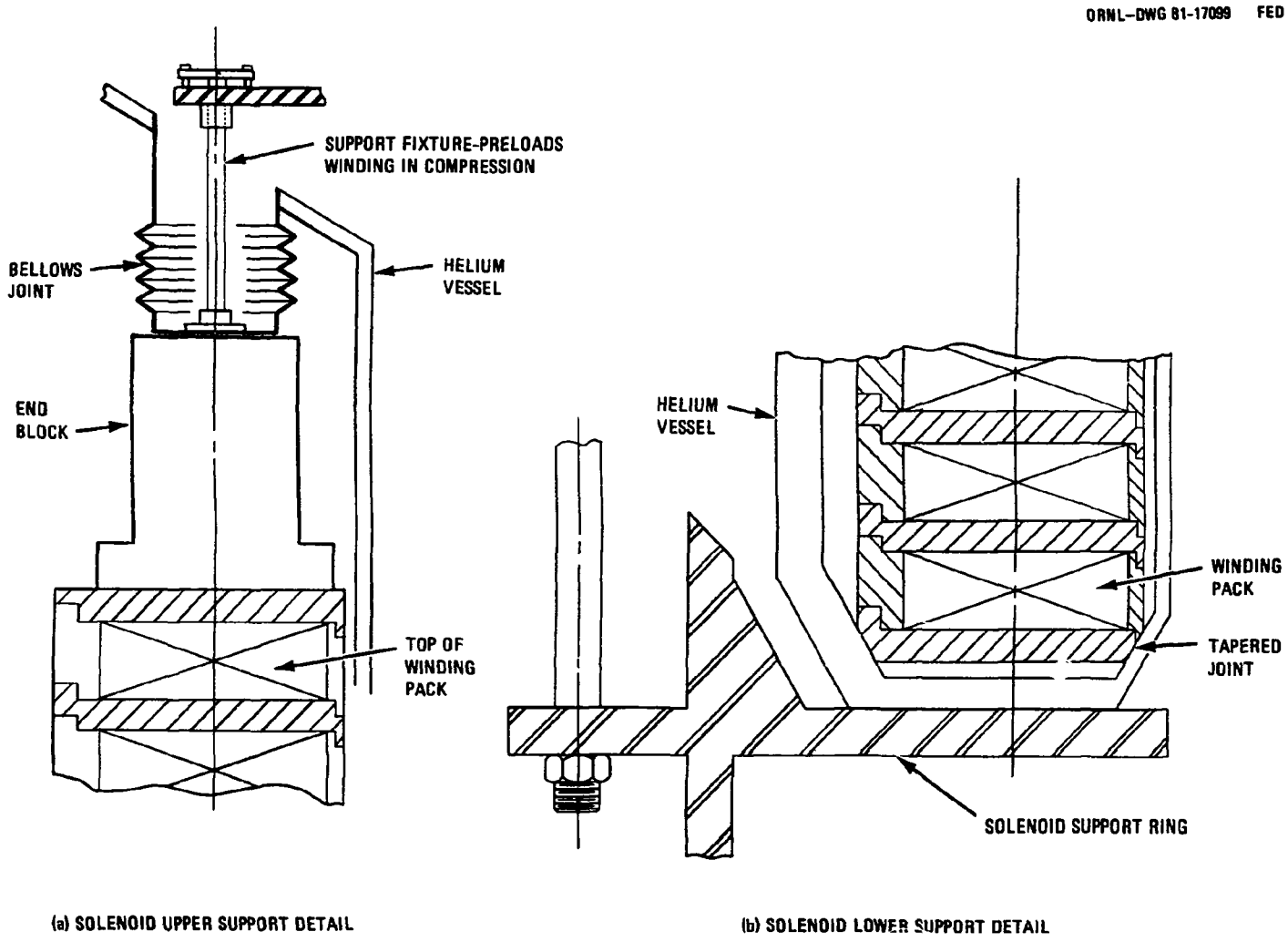

Fig. 4-43. Solenoid support details.

of lower EF coils (EF_3 and EF_4). Also, the design must be capable of equilibrating a 1 g vertically upward seismic load.

A fixture, internal to the bore of the helium vessel is used to support the solenoid, as an assembly, during erection or for removal during the life of the plant.

4.2.3 Exterior (Superconducting) Ring Coil Layout

The exterior ring coils will be superconducting so as to eliminate (almost) their ohmic power consumption. The major design parameters for these coils are summarized in Table 4-22. A conceptual drawing for the ring coils is shown in Fig. 4-44.

Key design features of the superconducting ring coils are

- 50 kA cable conductor
- pancake winding
- stainless steel, ring stiffened case to provide structural support and contain helium
- sliding pedestal supports transmit dead weight seismic loads and resultant out-of-plane magnetic load to intercoil support structure; coil case designed to equilibrate magnetic bursting load and magnetic bending loads
- dielectric breaks in the case to reduce induced poloidal currents; joints sealed by welded omega seals or double "O" rings

Conductor

The conductor being used for the superconducting ring coils is similar to that chosen for the solenoid, i.e., the 50-kA bath-cooled (by liquid helium at atmospheric pressure), cabled NbTi conductor, already discussed in Section 4.2.2. The only difference between the conductor for the ring coils and the conductor for the solenoid is the thickness of the Nitronic 40 strap. For the solenoid, it was chosen to be thick enough that each turn is free-standing. As discussed below, this is not

Table 4-22. Superconducting ring coil design parameter

Parameter	Coil EF_2[a]	Coil EF_3[a]
General		
Mean radius, m	9.50	9.50
Radial build, m		
Winding	0.71	0.82
Overall	1.27	1.79
Axial build, m		
Winding	0.78	0.96
Overall	0.92	1.14
Weight, 10^3 kg		
Winding	1090	1150
Structure	512	447
Electromagnetic		
Maximum field at winding, T	4.7	5.4
Conductor rating, kA	50	50
Winding type	Pancake	Pancake
Number of pancakes	4	5
Total number of turns	124	185
Current density, A/cm^2		
Winding	1090	1150
Overall	512	447
Performance		
Charge time, s	6	6
Design voltage/turn, V	35	45
Stored energy, MJ	900	900

[a]See Fig. 4-38 for coil locations.

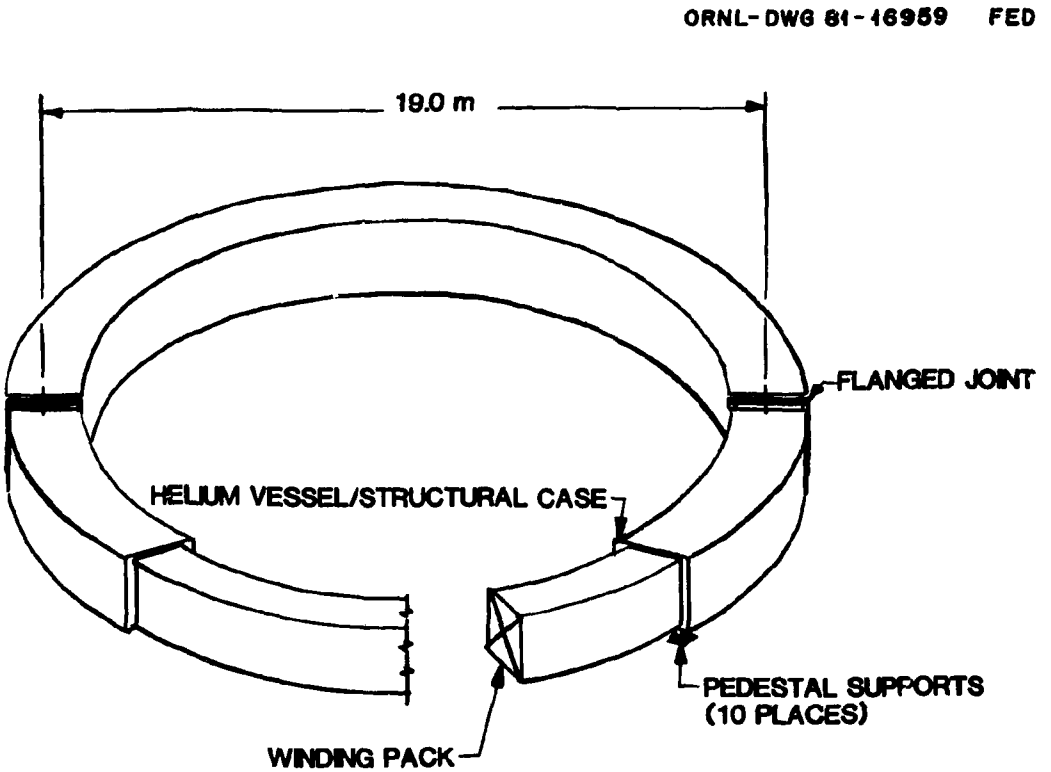

Fig. 4-44. Superconducting ring coil concept.

practical for the ring coils; therefore strap thickness was left at the 0.256 cm used in the conductor for the LANL 20-MJ coil.

Winding layout

The winding layout for coil EF_2 is illustrated in Fig. 4-45. The layout for coil EF_3 is similar, differing only in details such as number of turns, pancakes, etc. The conductor is spirally wound into pancakes separated by G-10 axial support plates, which in turn are axially supported at their edges by G-10 support rings. Pertinent winding pack parameters for the baseline coils are given in Table 4-22.

The peak voltages experienced by coils EF_2 and EF_3 occur during startup and are 4,400 V and 8,400 V, respectively. It is necessary to limit peak voltages on these coils to ~2,500 V because their pool boiled windings are encased in metallic (electrically grounded) support structure. Accordingly, coil EF_2 is grounded at the winding midpoint to make coil terminal voltages $\pm$2,200 V with respect to ground. This coil has therefore three current leads. Coil EF_3 is divided into two separate parts. As is the case for coil EF_2, each part is grounded at the winding midpoint to make the terminal voltages $\pm$2,100 V with respect to ground. This coil has six current leads. Voltages induced in these coils following a plasma disruption are less than voltages induced during startup. The voltages induced by the control coils have not yet been evaluated.

Helium vessel

The winding pack is enclosed in a stainless steel helium vessel of rectangular cross section which also acts as a structural case for the coil. A sketch illustrating the case concept is given in Fig. 4-46. The case cross section is shown in Fig. 4-47; in Fig. 4-47, details of the case are drawn for coil EF_2, coil EF_3 being similar in concept but different in detail. The top and bottom plates of the helium vessel extend radially inboard and outboard and are welded to circumferential

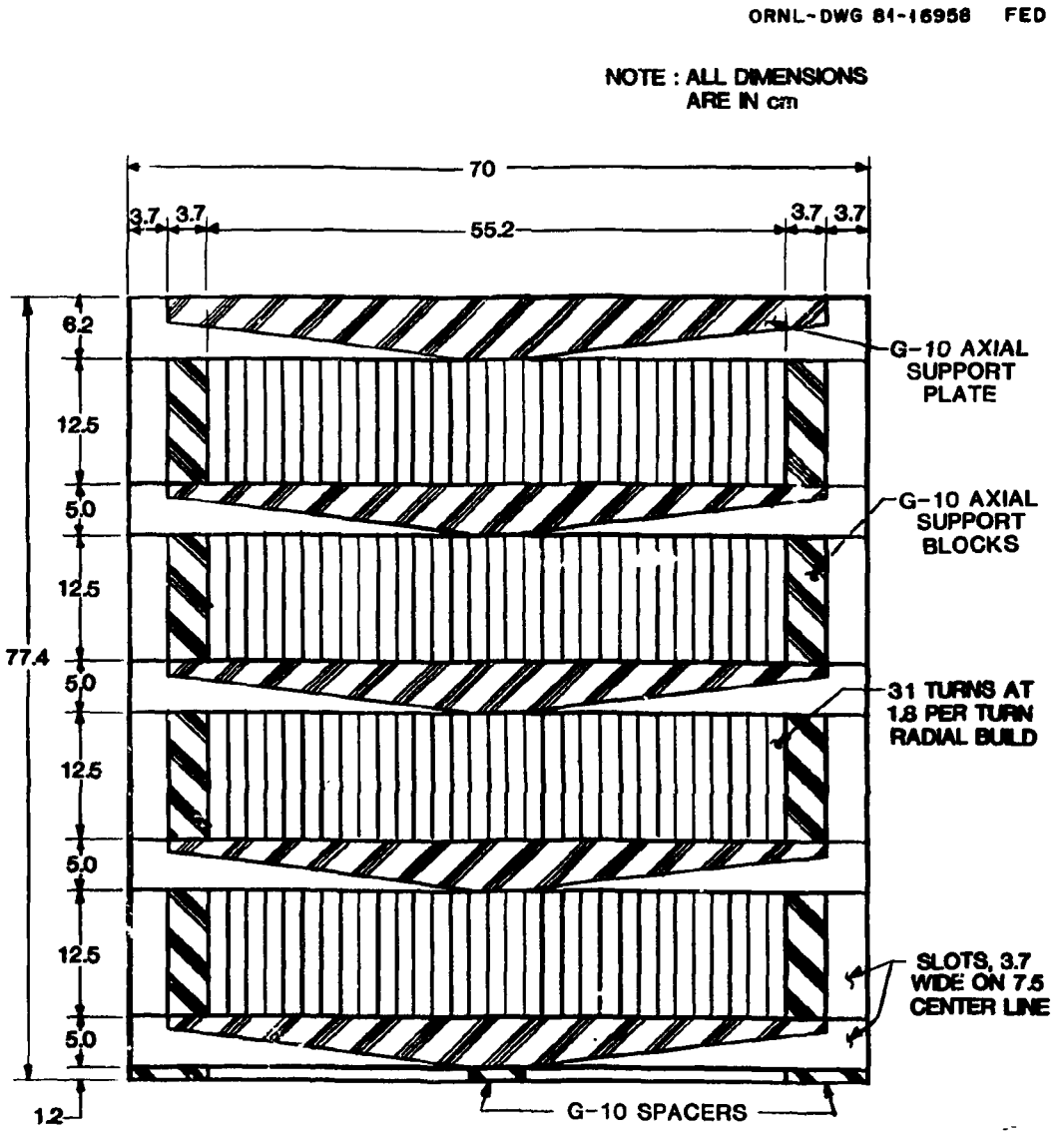

Fig. 4-45. Coil EF_2 winding pack layout.

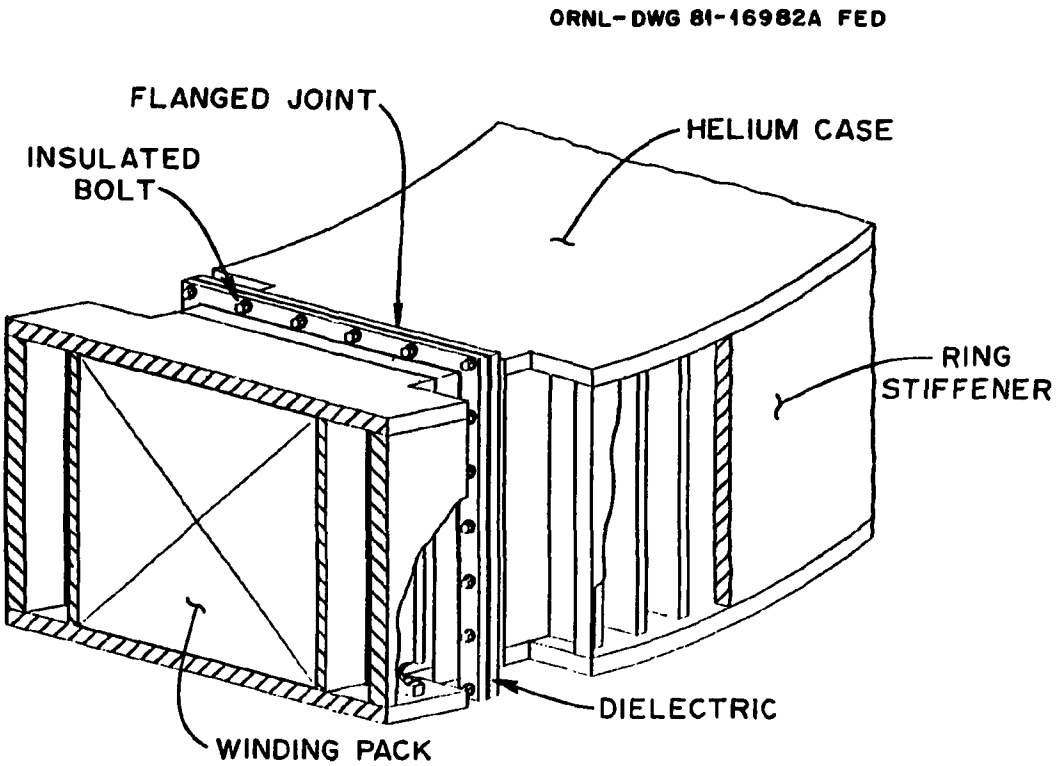

Fig. 4-46. Superconducting ring coil case concept.

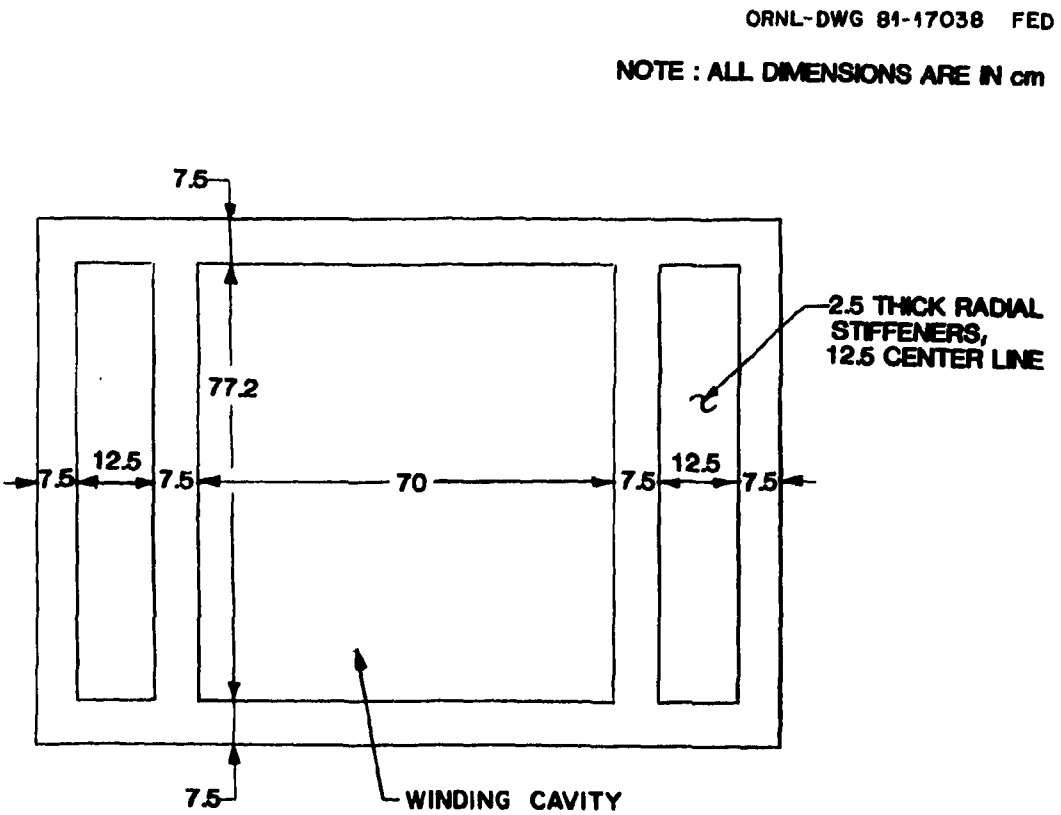

Fig. 4-47. Coil EF_2 case cross section.

cover plates both inboard and outboard, the whole producing a hollow circular beam of rectangular cross section stiffened by rings on its inboard and outboard faces. The rings are necessary to achieve the flexural rigidity in the structural case required to equilibrate the in-plane and out-of-plane magnetic bending loads on the coil. Radial stiffeners between the sides of the helium vessel and the cover plate, both inboard and outboard, stabilize the stiffening ring cross sections and also provide support to the inboard and outboard walls of the helium vessel, these walls being loaded by distributed force from the in-plane magnetic loads on the winding. Out-of-plane distributed magnetic load on each pancake is transmitted in bending of the support plates to the axial support blocks, through the support blocks in compression, and finally to the case in shear.

The ring stiffened helium vessel is designed to equilibrate those magnetic loads which are self-equilibrating in nature, i.e., produce no net force or moment when integrated over the coil. These include the uniform radial pressure tending to dilate the coil as well as the circumferentially varying (periodic) in-plane and out-of-plane loads caused by the fringing field of the TF coils.

Dielectric breaks

Calculation of the eddy current loss in the casing of one ring coil, based on the coil case cross section being uniform around the full circumference of the coil, has resulted in an order of magnitude estimate of the loss which is unacceptably high (~500 kW averaged over the cycle) from which it is concluded that a high resistance case is needed to reduce the poloidal current and associated loss. Consequently, the baseline configuration features flanged connections in the case, insulated to provide the break, as illustrated in Fig. 4-46.

The flanged breaks will be circumferentially spaced to occur at the locations of the TF coils. Because of periodicity in the magnetic loads, case bending moment is a minimum directly over each TF coil, and it is therefore easier to size a flange capable of transmitting case loads across the joint at this location. The baseline concept includes

two such breaks, diametrically opposed. One is sufficient to reduce the eddy current loss from 500 kW to 4 kW per superconducting ring coil, averaged over the cycle. A second break further reduces this loss only about 10%. Nevertheless, a second break is desirable to provide a degree of redundancy in the sense that shorting out of one of the breaks during a casualty condition will not produce a sudden, dramatic increase in the cryogenic requirements.

Two alternate concepts for sealing the joint are included in the baseline because both are developmental in nature. They are illustrated in Fig. 4-48 and both are compatible with the flanged break. The double "O" ring concept features two teflon coated steel seal rings with the space between the seals tapped and piped to a vacuum pumping system. The omega seal concept features an epoxy insert bonded into the metallic seal to interrupt poloidal current.

Structural support

The gravity support of the PF coils will be to the TF intercoil support structure. For the reasons discussed in Section 4.2.6, the support is designed to structurally decouple the PF coils from the TF structure as much as practical. The PF gravity supports are sized to equilibrate only the loads which produce resultant force on the PF coil — dead weight, seismic load, and out-of-plane resultant magnetic load. The supports are specifically designed to prevent transfer of load to the TF support structure due to uniform dilation of the PF coil or in-plane and out-of-plane magnetic bending loads.

A sliding support system which accomplishes these objectives is depicted in Fig. 4-49.

Helium bath

One of the potentially difficult technical problems associated with the baseline design is assurance of maintaining an adequate supply of liquid helium to the coil. This subject has not yet had quantitative

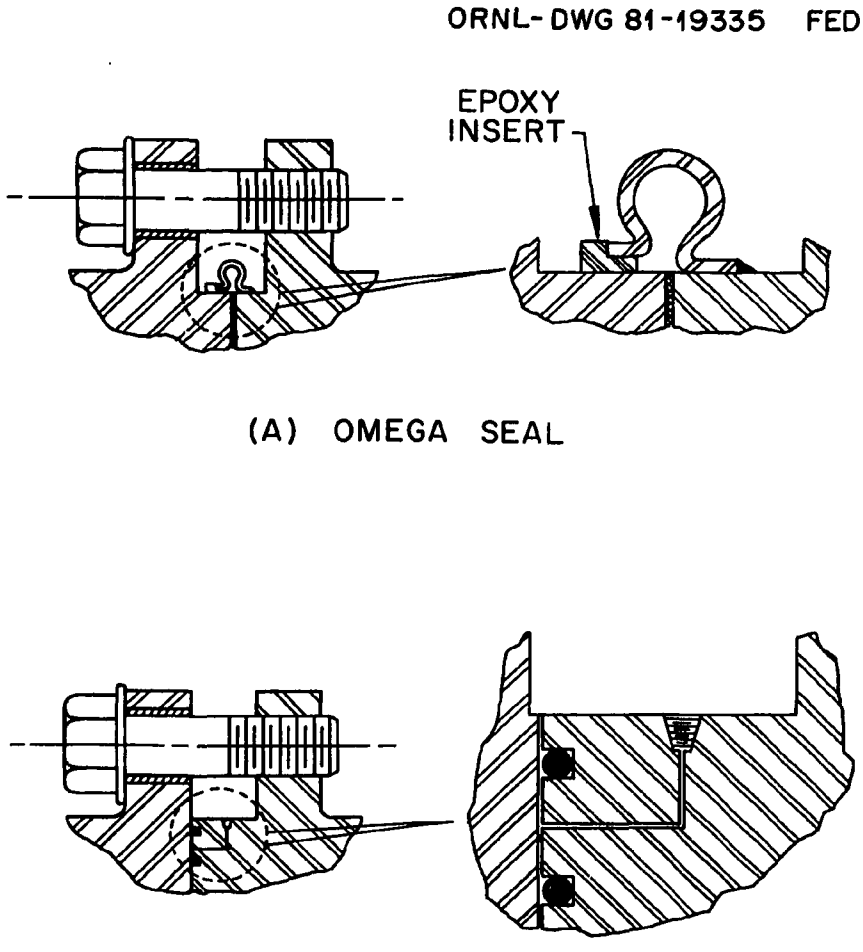

Fig. 4-48. Flanged joint seals.

ORNL-DWG 84-17042 FED

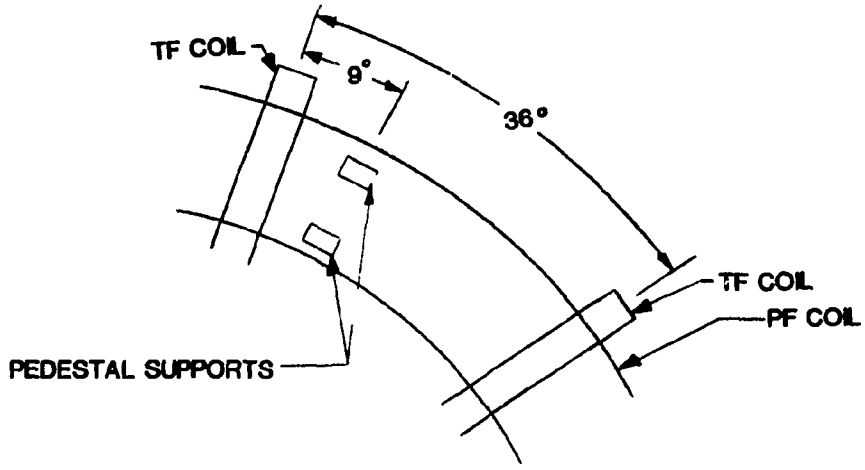

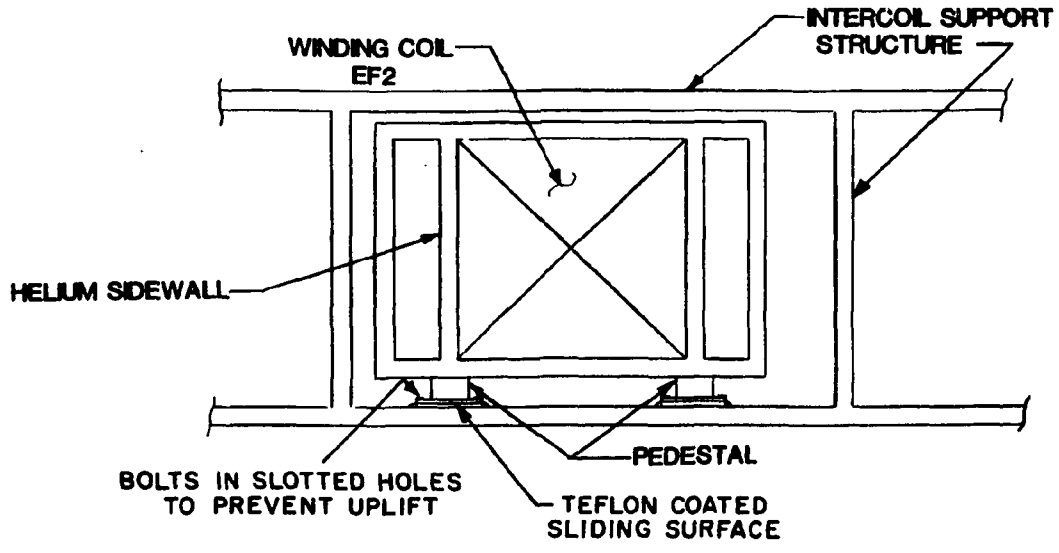

Fig. 4-49. Sliding pedestal supports.

evaluation. There are several concerns. The first is to assure helium bubbles will rise to the top of the winding pack and not pocket inside the winding. The second is venting of the bubbles from the top of the winding cavity.

Helium bubble clearing to the top of the winding is provided in the same manner as in the solenoid and is judged adequate. Slots on the undersides of the axial support plates are sloped upwards at 7° to direct the bubbles to the outer edges where they rise through vertical slots in the edges of the support plates and support rings.

Clearing of helium vapor from the top of the coil is a more serious concern. The size (9.5 m radius coil) and orientation of the PF superconducting ring coils (horizontal plane) present a long (∿60 m) horizontal surface which can trap the bubbles, forming vapor pockets and leading to a coil quench. Because of its location, coil EF_3 is especially difficult to adequately vent. The only available space for vertical risers is the annular gap between the unsupported outboard legs of the TF coils and the magnetic system vacuum vessel, so there can be, at most, ten risers to vent the vapor, which means the horizontal distance to a vent path can be as much as 3 m. Analysis is needed to ascertain if it is reasonable to expect the bubbles to migrate that far without pocketing.

Leads

It is planned that the leads be routed up the annulus between the TF coil case and the magnetic vacuum vessel in the outer leg region.

4.2.4 Internal (Normal) Ring Coils

The internal normal ring coil design reflects the requirement for demountable mechanical joints to facilitate initial assembly and coil replacement (if necessary). For the reasons discussed in Section 4.2.6, the internal ring coils EF_1 and EF_4 will be normal coils. The major design parameters for coils EF_1 and EF_4 are summarized in Table 4-23. The need for control coils C_1 through C_4 has only recently been identified,

Table 4-23. Normal ring coil design parameters

	Coil EF_1[a]	Coil EF_4[a]
Mean radius, m	3.85	3.05
Radial build, m	0.9	0.75
Axial build, m	0.58	0.58
Total current, Meg-amp	4.3	3.7
Number of turns	36	30
Number of pancakes	2	2
Power consumption, MW	17.4	11.8
Conductor current density, A/cm^2	1000	1000
Weight 10^3 kg	103	68

[a]See Fig. 4-38 for coil locations.

and no component design has been developed for these coils; this will be addressed in FY 82.

Key features of the internal ring coils are

- water cooled copper conductor
- two bolted joints per turn
- structural support from the torus permanent spool.

Conductor

The conductor cross section is depicted in Fig. 4-50. The cross section has been chosen to be as large as can be pratically drawn with extruded holes so as to minimize the number of joints. Discussions with Kabelmetal have confirmed that the shape can be manufactured, but there is some question if it can be manufactured in the desired lengths. The manufacturer has agreed to evaluate this further.

Winding pack

The conductor is spirally wound into two pancakes separated by a pancake to pancake insulating sheet. The conductor is wrapped with turn-to-turn insulation prior to winding or an insulating strip can be co-wound with the conductor. The winding layout for coil EF_1 (coil EF_4 is similar) is shown in Fig. 4-50.

Joints

Two joints per turn are planned so that the coils can be initially assembled in the bore of the TF coils. Should replacement be necessary the space constraints in the bore of the TF coils with torus assembled dictate more joints in the replacement coil, of the order of 8-10.

The joint concept for a single turn is illustrated in Fig. 4-51. The joint is bolted, with the conductor on either side of the joint scarfed to provide the overlap.

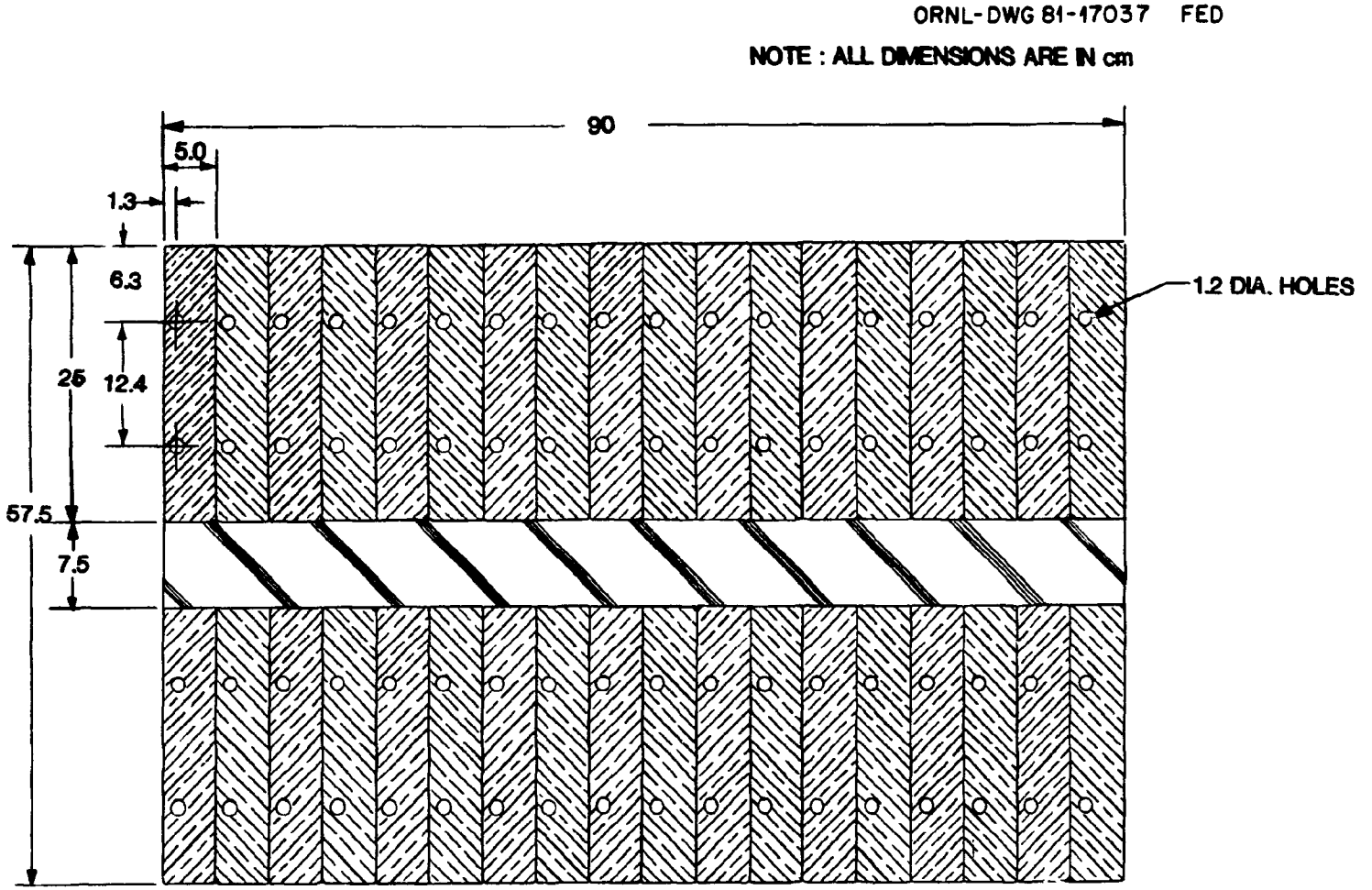

Fig. 4-50. Coil EF_1 winding layout.

ORNL-DWG 81-16981 FED

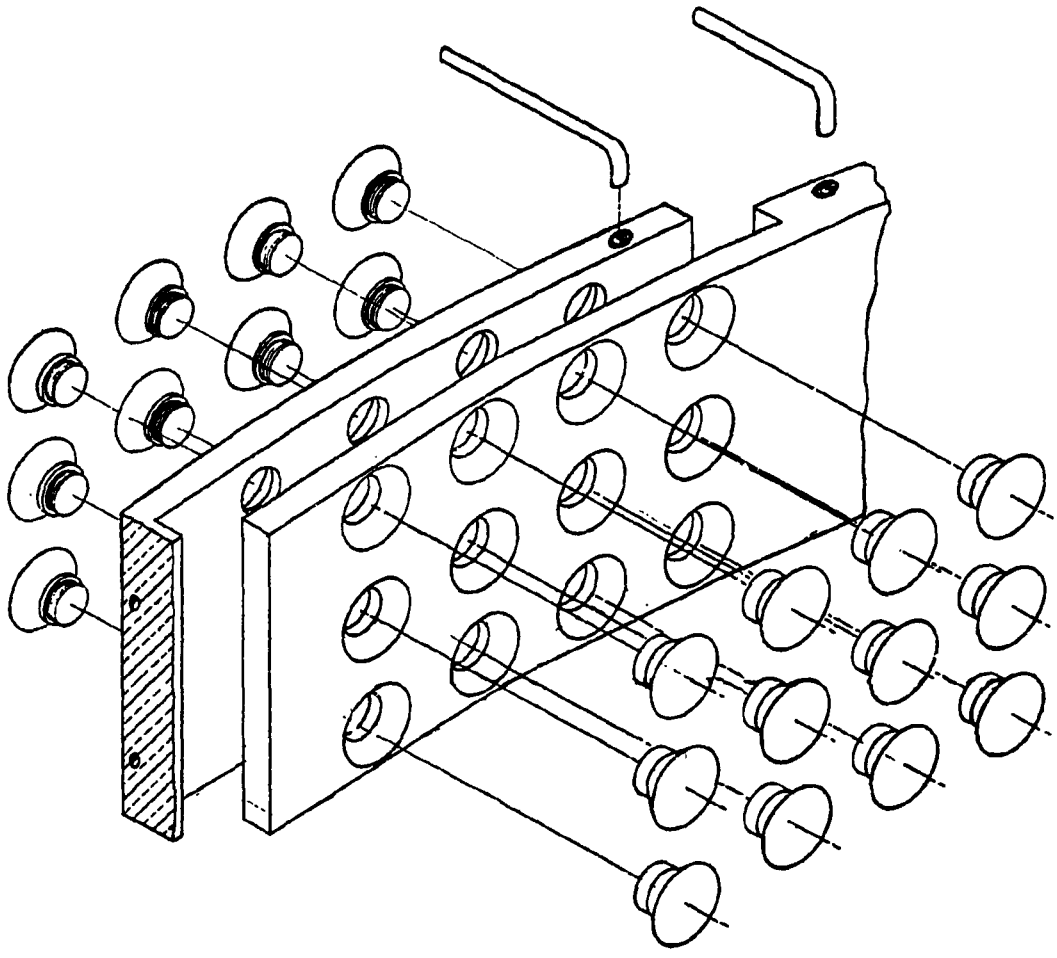

Fig. 4-51. Normal coil joint design.

Conductor cooling

The length of the cooling channel is one-half turn, or approximately 12 meters for the larger coil (coil EF_1). As shown in Fig. 4-51, copper tubing is brazed to the sides of the conductor at the joint to connect the conductor to supply and return headers. A plan of the coolant supply and return tubing is shown in Fig. 4-52.

In the event an internal ring coil needs to be replaced in service there will be 8-10 joints per coil, as discussed above. In this case there will still be two, diametrically opposed joints where coolant tubing is run into and out of the joint. Copper jumper tubes would be brazed in place at the other joints to carry coolant from one side of the joint to the other.

Lead Routing

The two pancakes are spirally wound, one clockwise and the other counterclockwise, so that a pancake to pancake connection can be made at the ID. Leads are brought into and out from the OD radially through the window between outboard legs of the TF coils.

Structural support

The conductors are capable of equilibrating the radial loads with no external support. Structural supports must be provided to equilibrate the axial load. Simple U-shaped brackets around the coil pack which bolt to the permanent torus spool support the coil. There are ten brackets equally spaced with 8 wide-flange 24 vertical legs and an 8 wide-flange 58 horizontal leg adequate for the coil loads.

4.2.5 PF Coil System Design

The poloidal field (PF) coils consist of equilibrium field (EF) and ohmic heating (OH) coil sets. Many engineering design issues are directly related to the configuration of these coil sets. These issues arise, for example, from the conflict between desirable coil location (for

ORNL-DWG 84-16965 FED

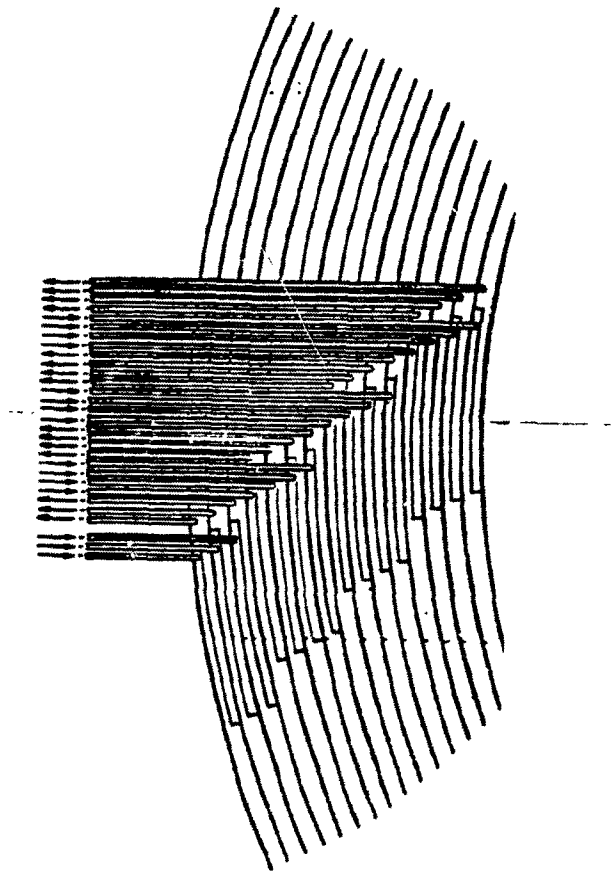

Fig. 4-52. Normal coil coolant line layout.

minimum ampere-turns) and the space and access requirements of other components of FED; the relatively large pulsed poloidal fields and out-of-plane forces on the TF coils; and the excessive local fields resulting from a juxtaposition of large coil bundles and currents. This section describes design evolution leading to selection of a hybrid EF coil configuration as a baseline for the FED.

Configuration and engineering considerations

Initially, FED plasma system baseline goals were 1.6 elongation, 0.5 triangularity, and 5.5% beta. Various PF coil configurations were considered for satisfying the above goals. The alternative configurations were also evaluated on the basis of estimated capitalized costs. Normal and superconducting coil costs were estimated using the procedure described below.

Cost estimation algorithms

For the purpose of trade-off analysis, capitalized cost of the normal and superconducting coils is determined on the basis of the initial cost of the coil, power supplies, refrigerator, and operating energy cost.

Copper coil cost

The cost of a copper coil, based on a current density of 1000 A/cm^2 and a unit cost of \$30/kg, is \$0.168 IR, where I and R are the coil current (A) and mean radius (m).

Electricity cost

The operating cost to make up for the power dissipated, based on a current density of 1000 A/cm^2 and unit costs of \$5.67/kW/month demand charge and \$0.02138/kW/hr for energy consumption (both per TVA cost schedule for 1980), is \$1.35 IR.

Superconducting coil cost

The cost of the superconducting coil is \$0.256 IR. This is based on an assumed current density of 2600 amp/cm^2, unit cost of NbTi conductor of \$90/kg, structure cost which is 15% of the winding cost and refrigerator cost which is 15% of the coil cost.

Power supplies cost

The cost of power supplies is based on formulas scaled from TFTR and simplified for this report by ignoring the cost of bus-bars and instrumentation. The modified formula for calculating the cost (C_{PS}) of power supplies is:

$$C_{PS}(MP) = 0.022\ MVA_{SU} + 0.0011\ MJ + 0.11\ MVA_{burn}$$

Where MVA_{SU} and MVA_{burn} are MVA during startup and burn, and MJ is the stored energy in the coil (MJ).

Comparison of EF coil configurations for triangularity of 0.5

An attempt was made to specify all EF coils internal to the toroidal field (TF) coil bore, for triangularity of 0.5 (the baseline goal).

All-internal EF configurations were found which satisfied the physics requirements; all of these required some EF coils placed inboard of the plasma (between plasma and TF coil straight legs). These coils would have to be embedded into the plasma vessel wall, would be highly irradiated, and hands-on maintenance on them would not be practical. Moreover, any repair or maintenance of these coils may require removal of plasma vessel segments, which is likely to be time consuming and expensive. Because of these considerations, it was felt inadvisable to consider EF coils buried in the plasma vessel.

Hybrid configurations, with the EF coils previously located between the plasma and TF coil nose region moved inboard of the TF coil nose region, were evaluated in an attempt to find solutions which meet both physics and engineering requirements. Two possibilities exist. One is

to move the ir[illegible] coils to be placed between the ohmic heating solenoid and t[illegible] coil nose region -- this produces too high a field at the OH solenoid. The other possibility is to incorporate the inboard EF coils into the solenoid -- this reduces solenoid capability to the point where startup is doubtful.

The Physics Branch reconsidered the objective of triangularity of 0.5 and agreed to a reduction to 0.3. All further PF system studies were based on achieving a triangularity of 0.3.

EF coil configurations for 0.3 triangularity

Effectiveness of specific coil locations was studied for producing the desired magnetic field configuration in the plasma region. Four possible PF coil configurations are shown in Fig. 4-53. An all-internal (inside TF coil bore) EF configuration is shown in Fig. 4-53(a). These coils can be divided into two separate groups — D and O as shown in the figure. Unlike the 0.5 triangularity EF system, this configuration does not require any coils inboard of the plasma. Two sleeve type EF coils were considered for the ohmic heating (OH) solenoidal region for studying their impact on the total ampere-turn requirements of the EF coil system [Fig. 4-53(b)]. The sleeve EF coils were found ineffective for reducing the ampere-turn requirements of the D-group of coils. One external coil was added to each group as shown in Fig. 4-53(c). The external 8 MA coil was not found very effective in reducing the ampere-turn requirements of the D-group of coils. The external coil in Fig. 4-53(c) requires 8 MA turns for replacing 1 MA turns in the internal coils in group D. However, the external coil added to the O-group is more effective. The external coil in this group requires 2.3 MA turns for replacing 1 MA turns in an internal coil. It can, therefore, be concluded that in an optimal EF system, the D-group coils must be placed inside the TF coil bore. External coil in the O-group could be justified on the basis of easing vacuum vessel maintenance. Following this approach, a hybrid EF coil configuration was proposed and is shown in Fig. 4-53(d).

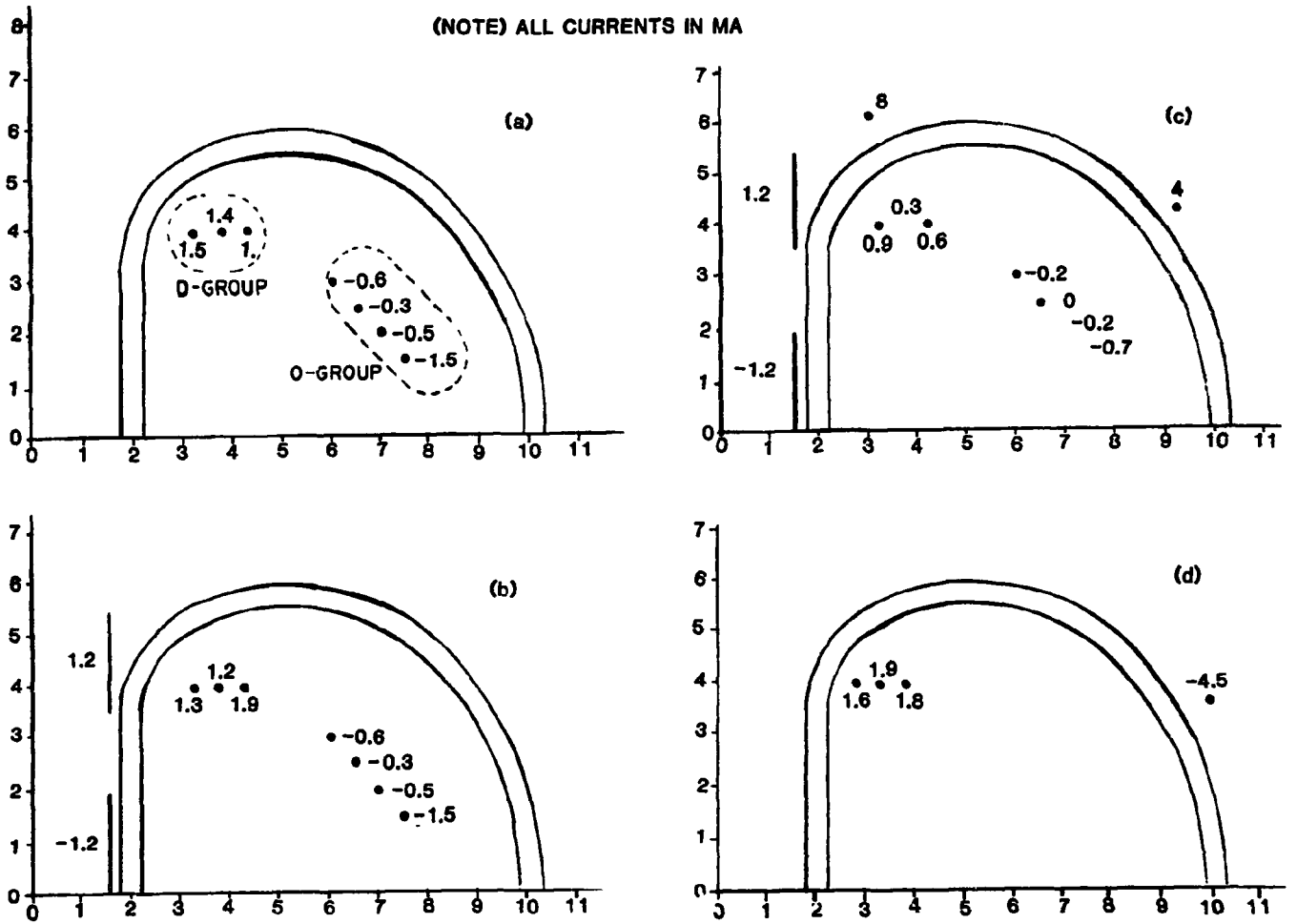

Fig. 4-53. PF coil configuration development.

Adoption of the selected EF concept to FED configuration

Once a preferred EF configuration [Fig. 4-53(d)] was selected, further optimization was achieved by placing the EF coils in more feasible locations in relation to other FED hardware.

In the preferred EF coil configuration, the three EF coils inside the TF coil bore were replaced by an equivalent coil. Thus, the whole EF coil system has two D-group coils inside the TF coil bore and two O-group coils outside the TF coil bore [see Fig. 4-54(a)]. Two variations of the preferred concept were generated by placing the four EF coils in various locations (see Fig. 4-54), an all-external configuration [Fig. 4-54(b)], and an all-internal configuration [Fig. 4-54(c)].

The initial and operating cost of each of the three concepts is summarized in Table 4-24, calculated using formulas discussed previously. The cost data supports the selection of the preferred configuration [Fig. 4-54(a)]. This concept was therefore defined as the baseline concept. To minimize the number of PF coils, it was later decided to use the EF coils as OH trim coils for assisting the solenoid.

4.2.6 PF Coil Alternate Concepts

The baseline configuration is depicted in Sections 4.2.2 through 4.2.4. The major alternative concepts that were considered in the development of the baseline are summarized in Table 4-25 and discussed below.

Internal ring coil options

As discussed above, the result of design studies for the optimum PF system configuration has been to select a hybrid configuration for the ring coils — two internal and two external to the bore of the TF coils. Coils internal to the bore of the TF coils must either be wound in place or have mechanical joints that they may be disassembled. On the basis of a preliminary evaluation of the feasibility of winding coils in place, it was concluded that this method of construction would require the bore of the TF coils to be dedicated to ring coil winding for the

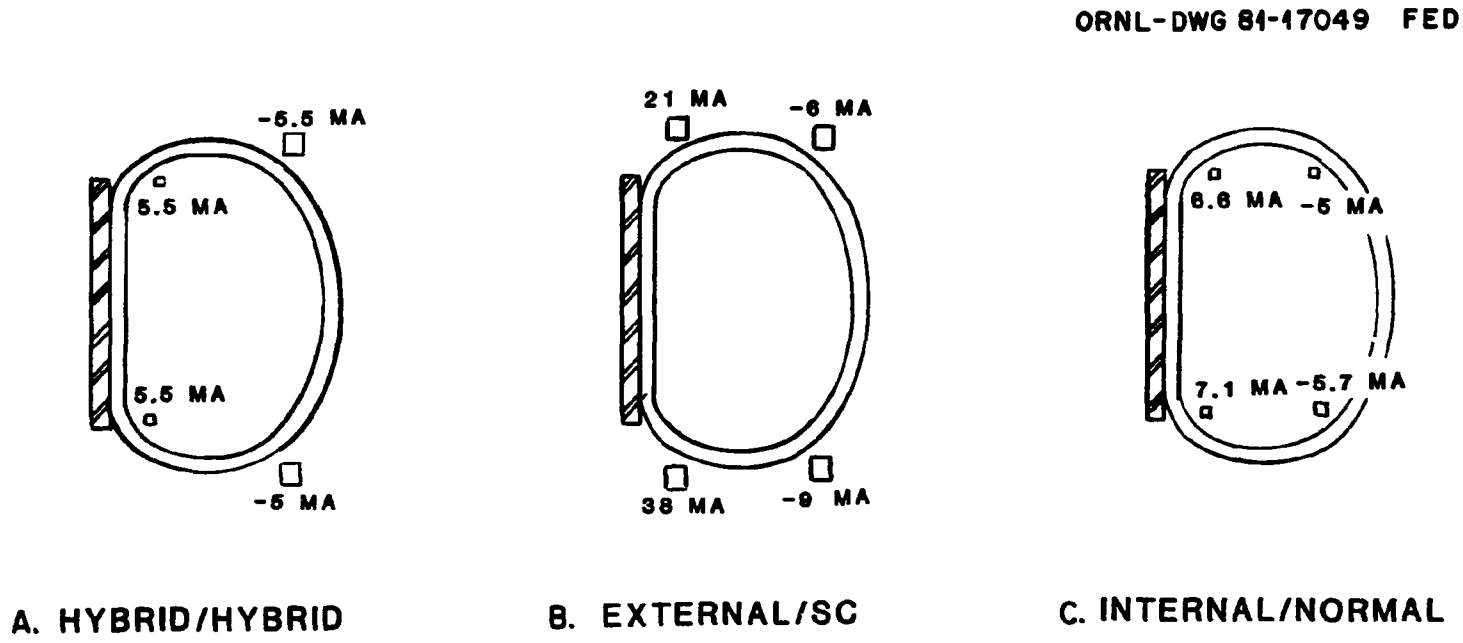

Fig. 4-54. Alternate PF coil concepts for 0.3 triangularity.

Table 4-24. Cost of EF coil concepts

Concept	Capital cost (M$)			Operating Power (MW)	Cost of Power (M$)[a]	Total life cycle cost (M$)
	Coils	Power Supplies	Total			
1 (Hybrid/hybrid)	32	22	54	52	55	109
2 (External/SC)	78	53	131	10	10	141
3 (Internal/normal)	22	45	67	168	178	245

[a]Based on 20% availability and 10 years of operation.

Table 4-25. Alternate design studies

Ring coils

- System configuration studies to consider relative merits of all-external and all-internal ring coil configurations as well as the baseline hybrid configuration.
- Wound-in-place as opposed to jointed internal ring coils.
- Glass epoxy superconducting ring coil helium vessel/case.
- Solid superconducting ring coil case instead of ring stiffened case.
- Thin stainless steel helium bladder for superconducting ring coils, backed by heavy structure with dielectric breaks.
- Continuous structural support of the superconducting ring coils by the TF intercoil support structure.
- 100 kA conductor for superconducting ring coils.

Solenoid

- Solenoid interleaved with bucking cylinder.
- Layer winding, rather than pancake winding.
- 100 kA conductor.

time it takes to assemble the winding table and wind the coils, estimated to take up to six months. Construction which precludes any significant parallel effort in the TF bore is in the critical construction path and, therefore, strongly objectionable. For this reason, the baseline concept adopted for the internal PF ring coils employs joints. The decision to use jointed internal ring coils is tantamount to a decision to use resistive coils for the internal ring coils since reliable superconducting coils with demountable (low resistance) mechanical joints are not considered feasible.

Resistive breaks

It has been found that steel superconducting ring coil cases will have unacceptably high eddy current losses due to induced poloidal currents if the cases are continuous around the circumference of the coil. Consequently, it is necessary to include joints with high electrical resistance designed to break up the poloidal path, or to design the superconducting ring coil cases to be constructed of dielectric material. Of these two alternatives, the latter was rejected as being too developmental in nature.

As discussed in 4.2.3, two seal concepts for the flanged joint concepts are being carried with the baseline. A thin, circumferentially continuous stainless steel bladder inside the heavy structural case has been considered as an alternate means of preventing helium leaks at the joints. The thin steel helium bladder concept is appealing because it eliminates helium leaks. However, the bladder must be extremely thin ($\sim$0.025 cm) in order that the losses be acceptable. The seal concepts described in the baseline and the thin bladder will all present fabrication difficulties. The seals are judged to be less difficult to fabricate, hence are shown in the baseline, but the helium bladder remains as a potential alternative should the development of leak tight seals for liquid helium in the large size required prove to be impractical.

Superconducting ring coil case options

The superconducting ring coils are pool boiling cooled by liquid helium and require a leak tight case to contain the coolant. The magnetic axial and radial running loads are transmitted through the winding pack to the case and must be borne by the case. Axial loads are transmitted in bending by support plates to support rings at the I.D. and O.D. of the pack, then in compression to be transmitted in shear to the top and bottom walls of the case. The top and bottom walls are sized by this shear load. Radial loads are equilibrated by turn to turn radial pressure which accumulates from turn to turn with the last turn bearing against the side of the helium case which supports the uniformly distributed bearing load in plate bending.

In order that the side wall bending stresses remain within allowable, the side walls must be very thick (up to 12 to 15 in.). As an alternative to thick lateral walls on the case, externally stiffened walls were considered with radial gussets welded to a continuous cover plate providing the section to carry the bending.

The two options (A and B) for the helium case sidewalls are illustrated in Fig. 4-55. A detailed analysis of the structural requirements (weight, welding, overall current density) for the two options has resulted in the conclusion that the externally stiffened case option (option B) is superior. The total structural weight will be considerably less for option B — about 40% of the structural weight required by option A for FED ring coils. Although option B requires considerably more linear feet of welding, the volume of weld metal required (a better measure of the cost of welding) will be about the same, and if one considers that the massive welds in option A are more difficult to inspect and are likely to require much more repair welding, then option B is judged to be cheaper to fabricate. Finally, it was found that the total coil cross-sectional area, winding pack plus structure, was about the same for the two options.

ORNL-DWG 81-17041 FED

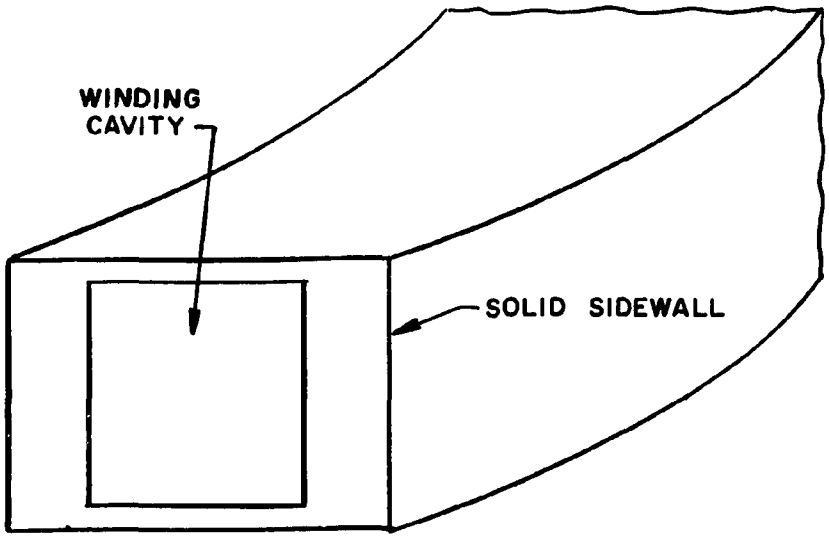

a) OPTION A—SOLID CASE

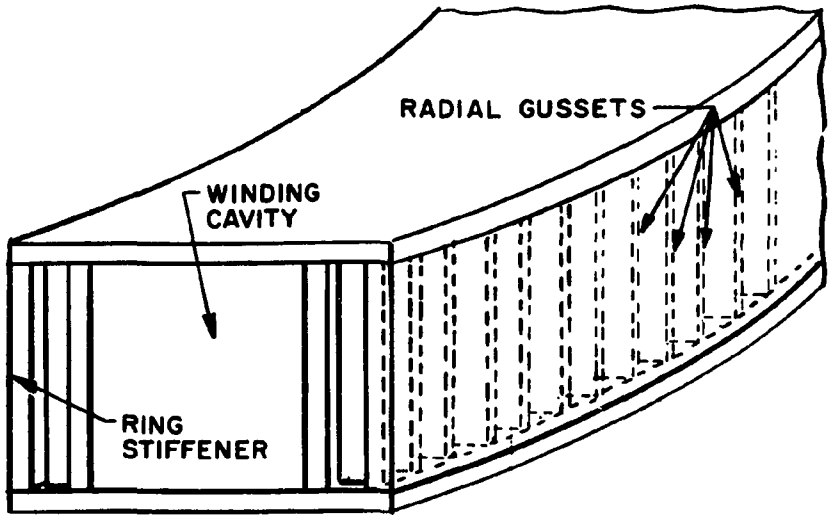

b) OPTION B—EXTERNALLY STIFFENED CASE

Fig. 4-55. Superconducting ring coil case options.

Structural support options — superconducting ring coils

The decision to support the superconducting ring coils from the TF coil/intercoil support structure (ISS) was made early and no alternatives were seriously considered. The TF system is physically close to the superconducting ring coils and is already a massive structure requiring little additional structural material to bear the ring coil loads. Furthermore, the TF system is cold structure and supporting the superconducting ring coils from this location requires no cold to warm mass transition.

Although the point of support was an early and relatively easy decision, the nature of the support was a subject of considerable study. The dead weight of the ring coils and the seismic loads must go into the supports, to satisfy equilibrium. However, not all of the magnetic load needs to be transmitted to the supports. Both the in-plane (radial) and out-of-plane (axial) magnetic running loads on the ring coils are of the same character — each has an axisymmetric component and a periodic component (approximately sinusoidal) with a period equal to the spacing of the TF coils. The uniform component of the axial magnetic running load produces a resultant axial load and it, too, must be transmitted to the supports. The remaining components of the magnetic load — the uniform component of the in-plane load and the periodic components of both the in- and out-of-plane loads are self-equilibrating in nature (produce no net force or torque when integrated over the coil) and can, theoretically, be borne by the coil case.

It has been found that the self-equilibrating magnetic loads can be borne by the coil case with only moderate increases in wall thickness above that determined by the basic coil case sizing, i.e., sizing top and bottom plates to carry axial running load in shear and sizing side plates with stiffeners to carry in-plane running load in bending (see discussion under "superconducting ring coil case options" above). The uniform component of the in-plane loads produces hoop membrane stress while the periodic axial and radial loads produce hoop bending.

The coil case is, therefore, sized so that the coil is free standing under the action of the self-equilibrating magnetic loads. The coil

case and the ring covers are thickened to provide the necessary cross-sectional area and flexural rigidity.

It was suggested at the FED Engineering Review that consideration be given to continuous support of the superconducting ring coils by the ISS to avoid the need for heavy walls necessary to support the radial running load in plate bending and provide sufficient section in the case that it may be self-supporting under the action of the self-equilibrating magnetic loads. This has been considered and rejected for two reasons. First, continuous support does not really eliminate much structure. The radial stiffeners and cover plates would still be required, whether they are part of the coil case or part of the ISS. Second, the fabrication problems associated with providing continuous support are significant. The ring coils are large enough in diameter that construction tolerances on coil dimensions would be large compared to allowable fit up gap between the coil case and its support. Perhaps by shimming the coil or by filling the space between the coil case and the support with a hardenable material, the support could be made continuous, but this does not appear to be attractive.

Solenoid winding alternatives

The winding concept chosen is pancake, as opposed to a layer wound coil. The pancake winding is deemed preferable because of greater modularity, structural superiority, higher current density, and better cooling. The potential advantage of a layer wound coil would be fewer joints. However, because of the pulsed nature of the FED machine, joint losses are small compared to ac losses.

PF superconductor design

Of many alternative concepts for conductor design, only differences in operating current and in load paths for radial forces are considered here. Of different possible cooling schemes, only cooling by pool boiling helium at 4.2 K is considered. The choice of a cable conductor over a monolithic conductor for a pulsed magnet is dictated by considerations of eddy current losses in the stabilizer. Similarly, the choice

of a flat cable (often called a Rutherford cable) is based on ease of coil winding and geometrical stability of the coil. Copper stabilizer and NbTi superconductor are chosen on the basis of extensive successful operation with them and on the lack of experience with other candidate materials.

Two operating currents were considered: 50 kA, which is well within the capacity of existing fabrication facilities, and 100 kA, which reduces problems with excessive voltages when the magnets are charged and discharged. Two concepts were also considered for radial load path (sometimes called substructure). In one, the radial forces are transferred through the conductor itself and through the electrical insulation separating neighboring turns. In the other concept, the cabled conductor lies in a channel, and radial force buildup is carried by the arms of the channel, not through the conductor itself.

Of the four possible combinations of current and radial load path, two are considered here: a 50-kA conductor with load path through the conductor and a 100-kA conductor with load path through a channel substructure. The pairings of current and load path are arbitrary except for the important consideration that a conductor of the 50 kA rating is under development at the Los Alamos National Laboratory (LANL). Test results from a 20-MJ coil using that conductor will be available before FED is built. For conciseness in what follows, we call the two conductors the 50-kA LANL type and the 100-kA channel type.

The 50-kA LANL type conductor was described in detail in Section 4.2.2.

The 100-kA channel type conductor design is a flat cable consisting of 36 basic cables, each 0.868 cm in diameter, cabled around a central pultruded fiberglass strip 13.9 cm by 0.159 cm, as shown in Fig. 4-56. The strip serves to ensure mechanical and dimensional stability during the conductor cabling and coil winding. Each basic cable consists of six copper and NbTi subcables, each 0.289 cm in diameter, stranded around a central multistrand stainless steel cable of the same diameter. The stainless steel increases the tensile strength of the basic cable. The subcables are weakly insulated from one another to reduce eddy current losses in the cable during charging and discharging. Each

ORNL-DWG 81-16960 FED

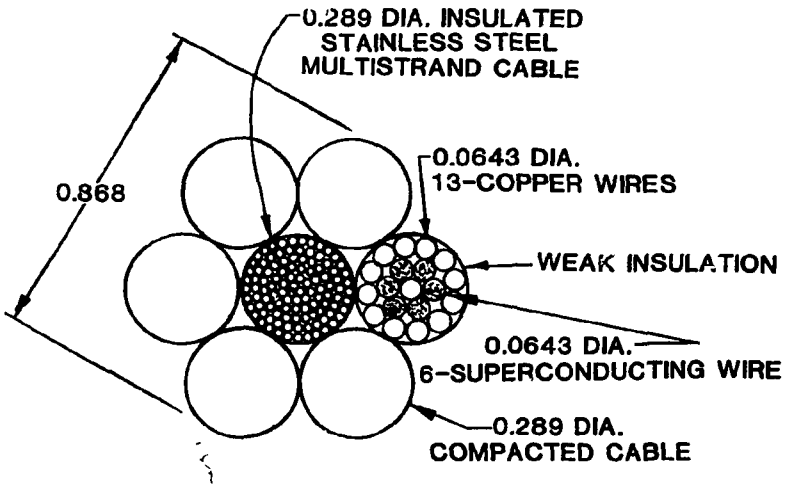

ENLARGED VIEW OF BASIC CABLE

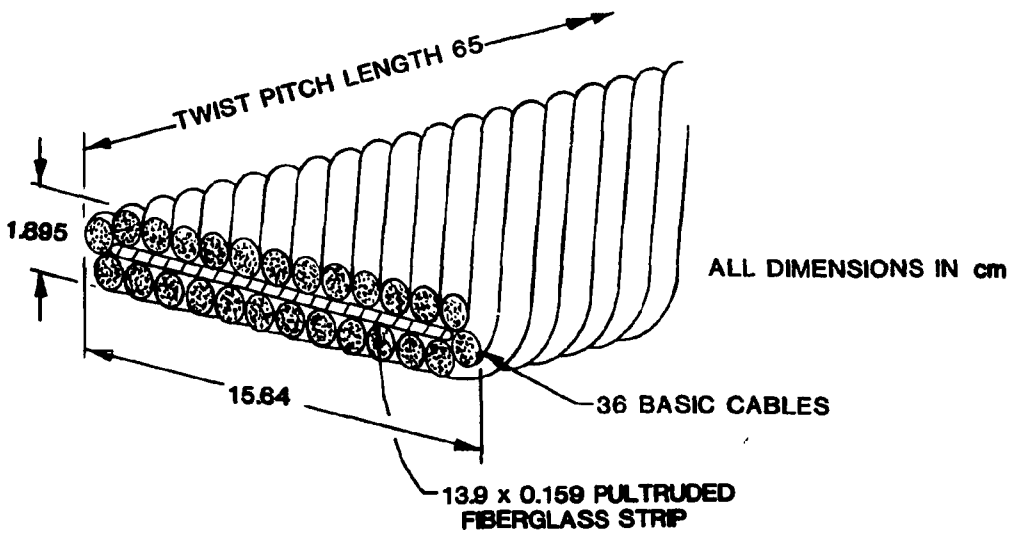

Fig. 4-56. 100-kA channel type conductor.

subcable consists of 19 strands; six 0.0643 cm in diameter superconducting strands, made up of NbTi filaments in a copper matrix, are stranded around a copper wire of the same size, and 12 additional copper strands are stranded around the superconducting ones. In this cable, the superconducting strands are all fully transposed; consequently, the transport current is equally shared among the strands, and there will be no large ac losses from circulating currents in the superconductor. Good electrical contact, achieved through compacting and soldering each subcable, insures cryostability, while the electrical insulation between subcables reduces eddy current losses. In this way, the cable provides the compromise between cryostability and low ac losses, which is required for a cryostable pulsed magnet. Each cable is enclosed at the top, bottom, and one side by a G-10 CR or insulated stainless steel channel, which transmits axial and radial force buildup (see Fig. 4-57). The channels are 2.54-cm long and separated by 0.635-cm gaps. On the other side of the conductor is a pultruded fiberglass band with longitudinal central groove and fully cut out "mouse holes" to permit free flow of helium coolant axially and azimuthally. Two Nitronic 40 bands are wound with the conductor to provide support against the hoop tension resulting from the magnetic forces.

A comparison of the two conductor designs is given in Table 4-26. Analysis shows that either conductor could be made to serve satisfactorily, and it is possible that neither is fully optimized for FED. There might be preference for a radial load path other than through the conductor itself, but the structure analysis shows that the stresses are not excessive. Conversely, it would be expected that the channel substructure would occupy more space, but the coil layouts show little difference in overall current density between the two.

Similarly, a 50-kA operating current might be preferable in that 50-kA conductors can be (and are being) fabricated with existing facilities, but a 100-kA conductor certainly can be wound also. While the 100-kA current would lead to a lower inductive voltage during charging or discharging, the conductor-to-ground voltage can be kept down to an acceptable value with the 50-kA conductor by dividing the solenoid into a number of sections and connecting separate power supplies between them.

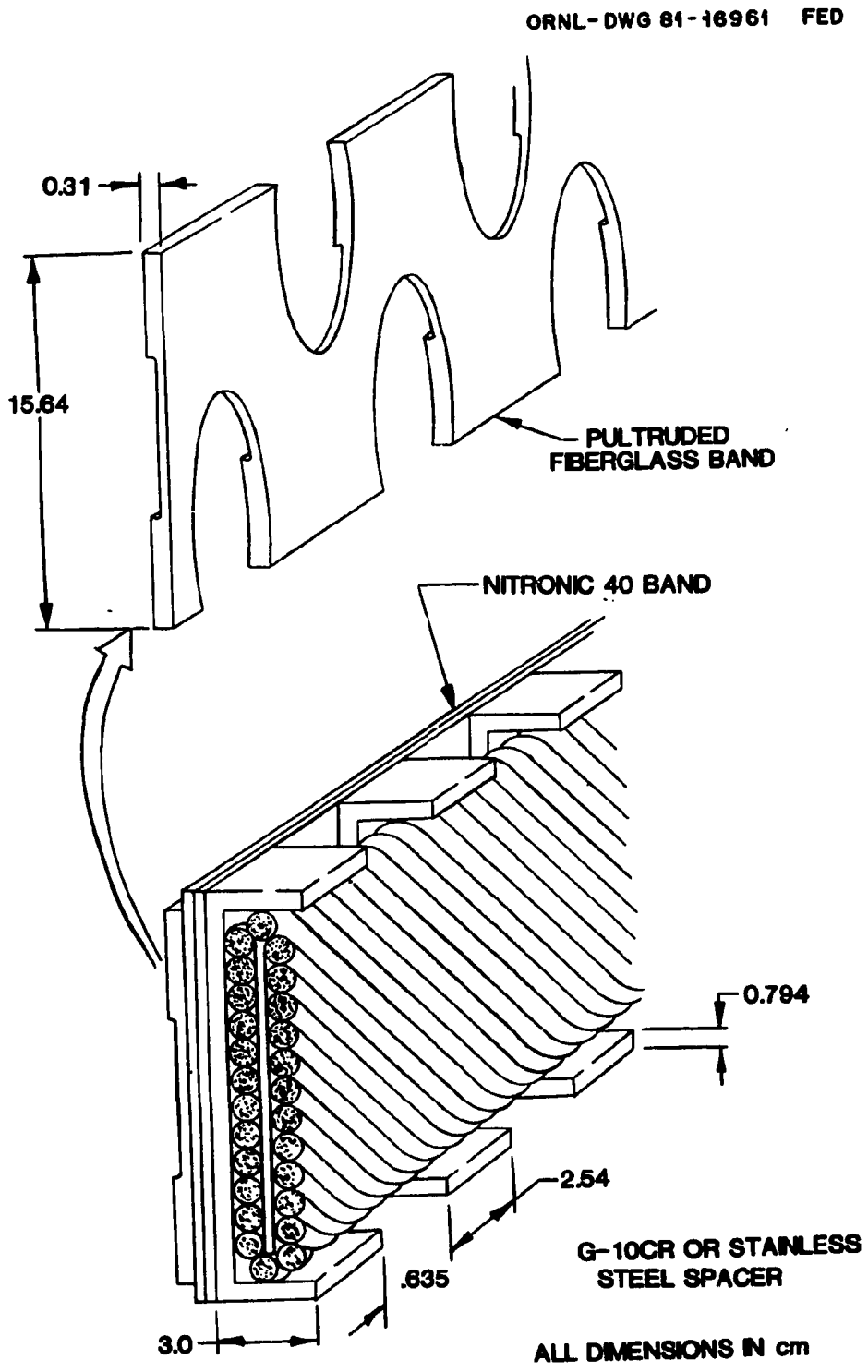

Fig. 4-57. 100-kA conductor channel support.

The 50-kA conductor was chosen for the reference design, and the 100-kA conductor designated as an alternative, because the 50-kA conductor is under development at LANL. Successful testing of the 20-MJ coil made of that conductor will lend confidence to construction of the PF system for FED.

Table 4-26. Comparison of solenoid conductor designs

	50-kA Conductor	100-kA Conductor
Geometry	flat cable	flat cable
Composition of Cable	36 subcables	36 basic cables
Composition of Sub-units	6 conducting strands around a SS strand	6 conducting subcables around a SS cable
Radial Force Transfer	across cable	through channel substructure
Overall Size of Cable	12.48 cm × 1.84 cm	15.64 cm × 1.895 cm

Solenoid interleaved with bucking cylinder

In most tokamak reactor design studies, the solenoid lies radially inward from the bucking cylinder, which in turn lies radially inward from the inner legs of the toroidal field coils. However, the GAC-ANL TNS (General Atomic Company — Argonne National Laboratory The Next Step) design studies featured an ohmic heating solenoid located between the bucking cylinder and the toroidal field (TF) coils. The solenoid was segmented; between each two segments was a G-10 ring to carry the centering force of the TF coils to the bucking cylinder. Locating the bucking cylinder inside the solenoid reduced the overall size of the reactor.

Such a system of interleaved solenoid and bucking cylinder deserves consideration for FED as well. However, locating the central solenoid near the TF coils is incompatible with the use of the central part of the cylinder as an equilibrium field coil as well as an ohmic heating solenoid. When the currents in neighboring segments of the solenoid are changing at different rates, there is a rapid change of field outside the solenoid where the segments meet. If the TF coils were located

there, they would experience large ac losses from these time varying fields.

Also, an internal solenoid would probably be far easier to install and remove than the interleaved solenoid and cylinder. Finally, the difficulty and long term value of developing an interleaved support and force transfer configuration must be considered; scoping studies suggest that the interleaved cylinder and solenoid would be of value only in reactors of FED size or smaller. On this basis the internal location for the central solenoid was chosen.

4.2.7 PF Coil Design Analysis

Fields and Forces

Each poloidal field coil experiences fields and forces from the toroidal field coils, from the plasma, and from all poloidal field coils. The field from the TF coils is constant in time throughout the cycle, is periodic in azimuthal angle with the 36° periodicity of the TF coil system itself, and has radial, axial, and azimuthal components. Because the current in the PF coils is azimuthal, the azimuthal component of field from the TF coils exerts no force on the PF coils. The radial and axial components exert forces that have the same 36° periodicity and vary throughout the cycle, being proportional to the varying current in each PF coil; the forces are a maximum when the currents attain their peak values.

The fields from the PF coils and the plasma are axisymmetric and have only radial and axial components. The field varies with time as the coil currents vary. For the current waveforms in the present baseline (see Fig. 4-24)) two extreme conditions exist, at time zero, when only the solenoid is charged, and at 112 s, when all the coils are fully charged. The former condition is more limiting for the solenoid and was used to calculate solenoid forces; the latter condition is more limiting for the ring coils and was used to calculate ring coil forces. The coil currents are given in Table 4-20.

The solenoid consists of two outer segments, each 4.26 m long, which serve as OH coils and an inner segment 1.93 m long, which combines

the function of OH and EF coils. Table 4-27 shows the variation in radial magnetic pressure along the solenoid, the axial force acting on 0.528 m axial segments (three pancakes) of solenoid, and the cumulative axial force. All are shown at zero time. Note that the net axial force on the solenoid is zero because the remaining EF coils are assumed to be carrying no current. However, a net downward force on the solenoid would result if all EF coils were also carrying current. This calculation has not been made yet.

The maximum field on a superconductor of the PF coil system is 7.2 T and occurs on the inner radius of the solenoid at time zero. The maximum rate of field change occurs during the startup (time 0 s to 6 s).

The four ring coils are designated (clockwise from the upper left) EF_1, EF_2, EF_3, and EF_4. Coils EF_2 and EF_3 are superconducting and located outside the TF coils. Coils EF_1 and EF_4 are normal-conducting and interlink the TF coils. At their exterior positions, coils EF_2 and EF_3 experience axisymmetric fields and forces primarily from themselves and the plasma, plus periodic forces from the fringe fields of the TF coils. At their more central locations, coils EF_1 and EF_4 experience fields and forces from all the coils. Although the support of normal-conducting and superconducting coils presents different problems and although normal-conducting materials do not exhibit the same sensitivity to high magnetic fields as superconductors do, the field and forces on all four coils will be described together here.

The forces from the TF coils are periodic around a ring coil, with period 36°. Fields were calculated at the center of each ring coil, over 18° of angle, and the force per unit circumferential length was calculated by multiplying the field components by the peak current. The peak forces so found are summarized in Table 4-28. In general, the forces can be treated as sinusoidal; but in coil EF_2, which experiences the highest forces from the TF coils, the peak force occurs at an angle of 12°, rather than at the 9° position predicted for a sinusoidal variation. The forces are calculated on the basis of a peak toroidal field of 10 T. For 8-T operation of FED, these forces should be scaled down by the ratio $(8/10)^2$.

Table 4-27. Forces on central solenoid at time zero

Axial Distance (m)	Loading		
	Radial Pressure (MN/m^2)	Axial force (MN)[a]	Cumulative Axial Force ΣF_2 (MN)
0.264	38.1	42.5	42.5
0.791	47.3	17.2	59.7
1.319	52.5	8.6	68.3
1.846	55.7	4.7	73.0
2.374	57.7	2.8	75.8
2.901	59.0	1.7	77.5
3.429	59.8	1.0	78.5
3.956	60.3	0.6	79.1
4.484	60.6	0.4	79.5
5.011	60.8	0.1	79.6
5.539	60.8	-0.1	79.5
6.066	60.6	-0.4	79.1
6.594	60.3	-0.6	78.5
7.121	59.8	-1.0	77.5
7.649	59.0	-1.7	75.8
8.176	57.7	-2.8	73.0
8.704	55.7	-4.7	68.3
9.231	52.5	-8.6	59.7
9.759	47.3	-17.2	42.5
10.286	38.1	-42.5	0

[a]Axial force on 0.528 m axial segments.

Table 4-28. Net forces on ring coils at time 112 s (End of burn phase)

Coil	Net Force per Unit Length (MN/m)[a]		
	From TF coils	From PF coils and plasma	Combined
	RADIAL		
EF_1	± 0.78	1.02	+0.24/+1.8
EF_2	± 3.85	2.75	-1.1/+6.6
EF_3	± 5.90	4.96	-0.94/+10.86
EF_4	± 0.03	1.16	+1.13/+1.19
	AXIAL		
EF_1	± 0.01	-0.22	-0.23/-0.21
EF_2	± 0.16	-0.20	-0.36/-0.04
EF_3	± 5.33	0.04	-5.29/+5.37
EF_4	± 0.09	0.20	+0.11/+0.29

[a] Assuming toroidal field of 10 T; for 8 T operation, multiply the numbers by $(8/10)^2$.

Structural evaluation - solenoid

The Nitronic strap in the conductor is sized to make a single turn self-supporting for the maximum radial magnetic load on the solenoid. This has resulted in a slight modification of the LANL 50-kA conductor (strap thickness 0.564 cm rather than 0.257 cm).

The G-10 support plates are sized in bending for the axial magnetic load. It is the nature of this load that it is largest in magnitude near the ends of the solenoid, diminishing to less than 5% of the peak value within 25% of the total height away from the ends. Therefore, the support plate thickness has been graded with distance from the end, diminishing in steps from a maximum of 8.75 cm at the end to 3.75 cm in the central 50% of the solenoid.

The former and the support blocks are not graded, being sized for the maximum axial force of 80 MN at the solenoid mid-height.

Because of the 1 g lateral seismic load, the coil must be capable of equilibrating beam bending type loads along its length. This has not been reflected as yet in the design, but will require the capability of carrying tension across former-to-former and support plate-to-support block joints.

Heat loads – superconductor

Losses in the ring coil and solenoid winding region are mainly coupling and eddy current losses in the superconducting strands, and hysteresis loss in the superconducting filaments.

Coupling and eddy current losses per unit volume of the strands can be expressed as

$$P_e = \left(\frac{\ell_p}{2\pi}\frac{R_f}{R_s}\right)^2 \frac{\dot{B}^2}{\rho_\perp} + \frac{1}{4}\left(1 - \frac{R_t^4}{R_s^4}\right)\frac{R_s^4}{\rho_{cu}}\dot{B}^2$$

where

ℓ_p is the twist pitch length,
R_s is the radius of the strand,
R_f is the radius of the core filament region,
R_t is the radius of the strand minus the outer shell thickness, and
ρ is the resistivity in the core region.

Hysteresis loss per unit volume of the filament can be obtained from

$$P_n = \frac{4}{3\pi} \gamma_c' \, d\dot{B}$$

where γ_c' is the critical current density in the filament and d is the filament diameter. Total ac losses in the ring coil and solenoid winding (cable + stainless steel strap) are roughly 182 kJ/cycle. Averaged over the 152 s cycle, the total heating is 1.20 kW. Losses due to the stainless steel straps are less than 20 kJ/cycle. The first six seconds produce the highest loads, 15 kW. Of the 182 kJ, the solenoid experiences 81 kJ.

Eddy current losses in the superconducting ring coil casing

When the PF coils are pulsed during each cycle, the vertical and radial field components of the poloidal field react with each PF coil. The vertical time-varying field component induces currents in all poloidal coils and their casings. Currents induced in the coil casing normally result in unacceptably high resistive losses, if the casing were azimuthally continuous. These eddy current losses are significantly reduced by introducing an electrical break to prevent the flow of current in the azimuthal direction.

However, the second level eddy currents can still induce significant eddy current loss. For example, field changes experienced by the coil casing of EF_2 (Fig. 4-47) are 0.08 tesla/second in the vertical direction and 0.01 tesla/second in the radial direction during the six-second startup. Similar field excursions are also experienced by the coil casing during shutdown phase. The eddy current loss calculations were made using the method discussed in Section 4.1.5. Losses during the

startup and shutdown phases are 4000 W (averaged over the cycle time of 152 seconds). Losses of similar magnitude will also occur in the lower superconducting ring coil (EF_3).

Structural evaluation - superconducting ring coils

The in-plane (radial) running load has an axisymmetric component and a component which is azimuthally periodic, with the period equal to the spacing between TF coils. It has been found that the 50-kA conductor developed for the LANL/ Westinghouse 20-MJ pulsed coil program and adapted for FED application cannot be modified to make it self-standing under the action of the in-plane magnetic load. Although the central strap could be thickened to carry the axisymmetric component of the in-plane load in hoop tension, it is not practical to increase it sufficiently to carry the hoop bending caused by the azimuthally periodic component of the load. As a consequence, the radial load must be permitted to accumulate from turn to turn with the winding pack bearing against, and receiving support from, the case. The inboard and outboard case walls are externally stiffened and sized to carry the maximum radial running load in plate bending, with the stiffened case wall evaluated as a pinned-pinned plate. The radial stiffeners are sized and spaced to support the case wall between stiffeners.

Out-of-plane (axial) loads on the pancakes are transmitted by bending of the G-10 support plates, evaluated as pinned-pinned, which then transmit loads through the support rings in bearing to the top or bottom of the case. The support plates and the support rings are sized for the maximum axial running load. The top and bottom plates of the case are sized for the maximum axial running load transmitted in shear to the case.

After preliminary sizing is complete, the resulting cross-sectional area and section modulus of the coil cross section are calculated and increased, if necessary, to insure that the hoop membrane and hoop bending stress in the case caused by in-plane axisymmetric load and in- and out-of-plane periodic loads do not exceed the allowable stress. Both coils EF_2 and EF_3 required thickening of the case steel to make the

coil self-supporting for the in- and out-of-plane bending loads and the axisymmetric in-plane load.

A summary of some of the more important structural design parameters is presented in Table 4-29. The allowable stresses are based on the discussions in Section 4.1.1.

Superconducting ring coil supports

The pedestal supports have been sized for a total of 6,000 tons of vertical load on the ten pairs of pedestals (5,000 tons representing the magnetic load, 500 tons dead weight, and 500 tons vertical shock) and 500 tons lateral shock. The calculated weight of coil EF_3 is 538 tons, so the pedestal sizing is slightly unconservative.

The direct compressive stress in the pedestal is limited to 20 ksi since the magnetic load is cyclic. Support bending stress due to lateral shock is limited by the primary stress limits of Section 4.1.1.

Power and cooling requirements - normal ring coils

For a current density of 1,000 amps/cm^2 = 6,250 amp/in.^{2}, the power consumed is 0.0266 IR watts, in which I is the coil current in amps and R is its mean radius in inches. For the sizes and currents in the baseline configuration, the power consumed by coils EF_1 and EF_4 is 17.4 and 11.8 MW, respectively. The lead losses, based on using a current density of 200 A/cm^2 with aluminum leads and a lead length of 200 m, are 1.3 MW for each normal ring coil. The total power required will, therefore, be 31.8 MW.

The coil is cooled by water flowing in two 1.25 cm diameter channels in each turn, with a coolant path length of one-half turn. With a 4.57 m/s coolant velocity, the pressure drop is 56 psig and the temperature rise is 96F°, indicating that process water supplied at a maximum inlet temperature of 100°F from a 100 psig system (typical for process water systems) is acceptable.

Table 4-29. Summary superconducting ring coil structural evaluation

Parameter	Coil EF_2	Coil EF_3
Radial magnetic load[a]		
$\bar{F}_r$, Kips/in.[b]	17.5	34.0
A, Kips/in.[b]	-23.6	37.1
Axial magnetic load[a]		
$\bar{F}_z$, Kips/in.[b]	-4.2	4.3
B, Kips/in.[b]	21.0	33.5
Winding pack maximum stress, ksi		
Conductor radial bearing (Allowable — 5 ksi)	2.3	3.2
Support plate bending (Allowable — 27 ksi)	26.6	27.3[c]
Case section properties		
Area, 10^2 in.^{2}	6.71	10.2
Moment of inertia, 10^5 in.^{4}		
I_r	1.16	2.74
I_z	1.79	5.30
Extreme fiber distance, in.		
C_r	18.4	22.4
C_z	25.0	35.2
Hoop stress		
(Allowable — 20 ksi)	19.1	20

[a] Loads are for the case of plasma disruption.

[b] A fair approximation of the azimuthal variation of load is $F_r = \bar{F}_r + A \sin(10\theta)\ \bar{F}_z + B \sin(10\theta)$ where θ is measured from a TF coil. Although only a fair approximation of load, the sinusoidal variation leads to an excellent approximation of maximum stress and has been used in the stress analysis.

[c] This slight overstress is considered acceptable, considering the preconceptual nature of the effort.

Structural evaluation - normal ring coils

The conductor is sufficiently strong to carry the radial magnetic forces without external support. For coil EF_1, the coil most highly stressed by the radial loads, the dilational force per turn is 160 lb/in., producing a hoop membrane stress of only 1230 psi. The bending component of the radial force per turn (approximately a sinusoid of 36° period and amplitude of 120 lb/in.) produces a hoop bending stress of 4298 psi for a combined hoop stress due to radial load of 5530 psi. Fatigue limits have not as yet been developed for copper; these stresses are moderate in comparison with yield for the material (15-18 ksi at room temperature), and they are judged acceptable. The axial periodic bending loads on the normal ring coils are equilibrated by the coils themselves and produce negligible bending stress.

The resultant axial load changes sign during the cycle. At the end of burn, the forces are such that EF_1 and EF_4 tend to move toward one another. The normal ring coils are supported by the permanent spool of the torus for axial loads in this direction. However, for $I_p = 0$ (the plasma disruption case), the normal ring coils tend to fly apart (axially) and will need supporting structure. The supports, consisting of simple U-type brackets around the coil pack and bolted to the permanent spool, have been sized for the axial loads during plasma disruption. The permanent spool structure has been confirmed to be sufficiently strong to support the loads.

Cooling and cryostability

Bath cooling by pool boiling liquid helium at 4.2 K has been chosen for the poloidal coils because of the extensive successful operation of large cryostable superconducting magnets with such cooling and because of the reserve cooling which bath cooling provides. The peak operational heat load is higher for the solenoid than for the ring coils. The peak operational required heat removal from the conductor of the solenoid is about 1.3 mW/cm^2, almost entirely due to ac losses from pulsing. However, the heat removal required for cryostability is 300 mW/cm^2, more than 200

times greater. With bath cooling, the greater reserve heat removal capacity is available whenever needed and is available without large pumping power needs.

Other cooling methods, e.g., forced flow and superfluid bath-cooled, are under development and show promise. These methods should be considered as possible alternatives to bath cooling with 4.2 K liquid.

The 50-kA LANL-type conductor has been analyzed for cryostability, using the ANL thermal analysis program TASS (Thermal Analysis for Safety and Stability). Normal operating conditions of the solenoid were assumed: 50-kA current, 4.2-K temperature, and 7.7-T peak field. The copper and NbTi in the conductor are equivalent to a rectangular monolithic conductor 6.0 cm by 1.05 cm, with copper to superconductor ratio 5.4:1. Two-thirds of each strand surface is assumed wetted by liquid helium; for the equivalent monolithic conductor, that is equivalent to a wetted perimeter 6.55 times the geometrical perimeter.

Analyses were carried out for initiating heat pulses of 150 J and 1200 J. Both are far larger than any heat pulse that might be expected from frictional motion or other occurrence of normal operation. The 150 J pulse was modeled by 2 cm of conductor initially at 50 K; the 1200 J pulse, by 16 cm of conductor initially at 50 K. Rapid replenishment of helium vapor by liquid was assumed.

For each value of the heat pulse, the stability limit was determined by computing the thermal response for values of the current. For the 150 J pulse, the normal region disappeared in 0.25 s for a current of 50 kA, grew without limit for a current of 70 kA or higher, and became a stable normal region for currents of 55 kA, 60 kA, and 65 kA. The normal region was approximately 0.5 m long with a temperature of approximately 10 K.

The thermal analysis program recalculates the current each iteration by decreasing the stored energy by the ohmic heating of the external dump resistor and of the resistance of the normal region of conductor. From the above analysis, it was determined that a persistent normal zone would develop if the current were higher than 51.3 kA. When the current is 51.3 kA, the normal region shrank and soon disappeared.

The analysis with a 1200 J heat pulse produced similar results. The normal region disappeared in 0.6 s for a current of 50 kA, but grew into a stable normal region for currents of 55 kA and 60 kA. When these currents decreased to 51.3 kA, the normal region again began to shrink and soon disappeared.

Conclusions of this analysis are that for currents below 51.3 kA, the conductor is stable against disturbances much larger than those which might be expected during normal coil operation, and will safely recover without quenching.

Stability criteria

Of the stability criteria suggested for the FED PF solenoid and ring coils,

1. no coil quench following an abrupt plasma disruption,
2. no coil quench during normal pulsed operation,
3. no coil quench if a half turn (alternatively a whole turn) goes normal,

the third is the most demanding. It was modelled in the TASS code with 4.2 m of conductor initially at 20 K and 7.8 T. Otherwise the parameters used were those described above. By symmetry, only half the length was considered, and it was modelled both by 105 elements 2 cm long and by 175 elements 1.2 cm long; the results were identical. The temperature profile assumed a stable normal form in less than half a second: the central region at 9.05 K and a transition region between 9.05 K and 4.2 K of length 0.7 m at either end. One might hypothesize that such a profile would develop for any normal length greater than about 1.5 m, but that was not tested. Likewise, the initial temperature of the normal region is probably not important, as long as it is in a temperature range (10 K to 50 K) in which the resistivity is largely temperature independent.

It is worth noting that the presence of that stable normal region depends upon the assumption that two-thirds of each strand surface of the cable is wetted by liquid helium. At the INTOR Meeting at Atlanta in March 1981, John Rogers of LANL reported that their stability measurement suggest 100% wetted perimeter of each strand. A recalculation

using this value (983% wetted surface of the equivalent monolithic conductor in TASS, rather than 655%) yields complete recovery of the half turn normal in 0.61 s. Clearly, additional experimental work is required on the stability of cabled conductors before FED is built.

By way of comparison, the second stability criterion, no coil quench during normal pulsed operation, is less severe. The ac heating is 8.8 W/m during the six seconds of rapid field changes. Six seconds is a long time to dissipate that heat, especially considering that if all 52.8 MJ/m were added instantaneously, it is less than one third the heat needed to raise the temperature to 20 K.

Protection

Protection of the PF coils is assured by controlled discharge through external discharge resistors connected in series with the coils. The protection system must be designed to limit discharge voltage and hot spot winding temperature to acceptable values. The maximum acceptable voltages during discharge will be taken to be the same values as the voltages permitted during normal operation of the coil, and previously discussed in Sections 4.2.2 and 4.2.3. The voltages are summarized in Table 4-30 for reference.

Table 4-30. PF coil discharge voltages

Coil	Maximum Acceptable Discharge Voltage, KV
EF_2	2.5
EF_3	2.5
EF_5	2
OH_1	4
OH_2	4

The maximum acceptable winding hot spot temperature rise during discharge is taken to be 200 K.

Protection analysis was performed for each of the superconducting PF coils using the TASS code as described previously in Section 4.1.5. It was found that if the dump resistor is sized so that the peak voltage during discharge is equal to the allowable value (Table 4-30) then the maximum hot spot temperature rise is approximately 30 K.

If a turn-to-turn short were to develop in the FED solenoid, then during the charging or discharging of the solenoid, inductively driven currents will occur in the shorted turn.

The effect of a shorted turn was studied with the ANL program SHORTURN, a modification of the ANL program TASS. Conductor and coil parameters were chosen as described in Sections 4.2.2 and 4.2.3. The effects of a shorted turn (peak temperature, peak current) depend strongly on two parameters, the discharge time τ and the electrical resistance of the short R_s. Calculations were carried out for discharge times of 6 s (the design value for the FED solenoid) and 10 s (discharge value for ring coils). The peak temperature reached in each case appears in Table 4-31. An exponential discharge was assumed in the analysis; but as the peak temperatures were reached within 0.13 s to 0.46 s, they appear to be insensitive to the exact time dependence of the discharge. Table 4-31 indicates that the peak temperature is approximately inversely proportional to the discharge time constant.

Table 4-31. Peak temperature reached in a shorted PF coil turn

Short Resistance, mΩ	Peak Temperature Reached, K	
	τ = 10 s	τ = 6 s
100	5	17
30	19	35
10	34	67
3	87	>100
1	>100	---

The computation was, in each case, discontinued when the temperature exceeded 100 K. In light of the many uncertainties involved it was felt that a peak temperature $\geq$100 K indicates the need for further theoretical and experimental analysis.

There is not much information on what values of short resistance might be expected. S.-T. Wang carried out experiments at ANL in which two pieces of monolithic conductor for the U-25 MHD magnet were pressed together over an area of about 1 cm^2 with a pressure of 5000 psi. The short resistance, both at room temperature and at 4.2 K, was several milliohm. When the two were soldered together, the resistance was about 0.1 mΩ. Note in Table 1 that for τ = 6 s, even a low resistance of 3 mΩ produces a peak temperature above 100 K. Similar experiments are recommended with the conductor to be used in FED, to determine expected short resistances.

4.2.8 Future Work — PF Coil System

Based on the work to date, it is concluded that an acceptable PF system is feasible. However, in the process of developing design detail in the selected baseline configuration, some new issues and unresolved problems remain. These are discussed below in order of decreasing priority.

New concepts

As discussed above, the need has been identified for control coils C_1 through C_4. Conceptual design of these must be developed, including the eddy currents and induced voltages produced by the coils.

Alternate concepts

Known weaknesses exist in the concepts discussed above. In these areas, suitable alternates must be developed. The perceived critical issues are:

- Helium clearing in superconducting ring coils - It is not known whether the large flat upper case of the coils will result in helium vapor being trapped and vapor locking of the coils resulting. Quantitative evaluation is necessary and a suitable alternate may be required (e.g., forced flow conductor).

- Solenoid helium vessel - The proposed glass epoxy helium vessel is considered to be not fabricable by a significant number of experts in the fusion community. Steel vessels with insulating breaks will be considered as an alternate.
- Normal ring coil - Because of the locations of these coils and the complexity of the mechanical joints, repair/replacement would be (at best) extremely difficult and time-consuming. Effort will be applied to define more suitable ring coil locations, while alternatives are considered for improving maintainability (e.g., wound-in-place coils, simpler joint design).

New issues

Aside from specific component problems addressed above, there are areas generic to all the coil sets which have not been addressed, which may significantly influence the coil design. The major concerns of this kind are:

- Off-normal condition - Structural evaluations have been limited to the loads related to normal operating conditions and one off-normal condition - plasma disruption. Future evaluations must consider the implications of other off-normal or casualty conditions, e.g., one coil shorted.
- Test requirements - A preliminary evaluation should be made of the acceptance test requirements and their effect on the coil designs.
- Instrumentation requirements - A preliminary evaluation should be made of the instrumentation requirements.

More detail in existing studies

There are numerous design specifics which should be addressed in the future. These include addressing issues such as the effect of mean stress on analysis for cyclic operation, the clenching forces on the ring coils, and resolution of a neutron streaming problem in the annular gap between the magnetic systems vacuum vessel and the TF coil cases in the nose region.

4.3 CRYOSTAT

4.3.1 Cryostat Major Design Considerations

Function summary

The function of the magnet cryostat is to maintain the superconducting magnets at a temperature sufficiently low that they retain the superconducting feature.

Requirements summary

An essential feature of the cryostat is that it be designed in such a manner that it permit access to the torus for maintenance, including removal of a shield segment. Accessibility to the torus has been established as a dominant design requirement for FED. In addition, the following requirements also apply.

1. Helium volume should be kept as small as practical so as to reduce capital cost, lessen personnel hazard due to a cryogen leak and limit internal pressure upon helium evaporation within containment due to a cryogen leak.
2. The thermal design of the cryostat must strike a reasonable compromise between capital cost and the operating cost due to heat leak from ambient to the cold interior of the cryostat.
3. The cryostat must be sized and supported sufficiently well to be structurally adequate under the following applied loads.
   - External pressure — 14.5 psig
   - Dead weight
   - Seismic load — 1 g laterally and vertically
   - Eddy current loads

4.3.2 Cryostat Layout and Principal Components

A sketch of the cryostat is shown in Fig. 4-58. The salient features are a vacuum vessel, a cold wall inside the vacuum vessel following the contours of the vacuum vessel, and individual helium vessels for each superconducting coil.

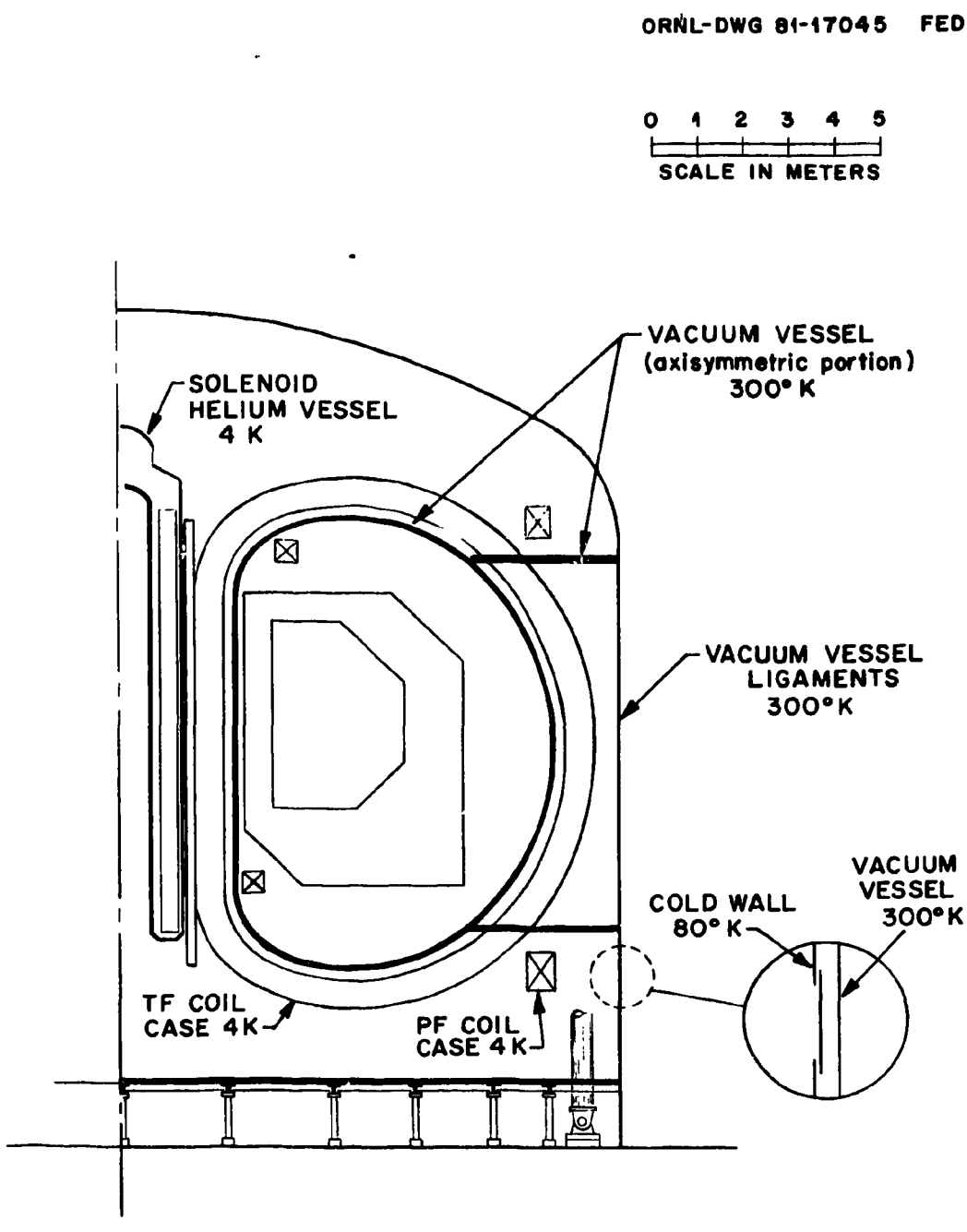

Fig. 4-58. Cryostat concept.

1. The vacuum vessel is a shell of revolution around the entire magnetic system except for a portion of the vertical legs of the TF coils at their outer extremity where openings are left to permit access to the torus; glove-like extensions of the vessel enclose these vertical legs.

   A single vacuum vessel (as opposed to many vacuum vessels, one enclosing each magnet and its associated helium vessel) has been chosen for ease and economy of construction and to minimize heat transfer surface area. Shells (cylindrical, toroidal, or torispherical) are used to the maximum extent practical rather than flat heads or rectangular walls to minimize structural material. Two exceptions are the flat plate on the bottom and the two annular flat horizontal plates connecting the outer shell to the inner shell in the area of the outer TF vertical legs. The bottom head was chosen to be flat to provide a usable surface on the bottom of the tank during construction and maintenance. Vertical support for the bottom head is provided by a grid of floor beams.

   The tank will be of welded construction. The torispherical head to outer wall joint will be flanged to permit easy removal of the head for access to the inside of the vacuum vessel. A flanged, circular hatch will be in the torispherical head sized large enough to permit removal of the central solenoid without removal of the entire head. Field welds will be required in the inner wall for assembly since toroidal field coils will be in place when the vacuum vessel is erected.

   The material will be 304 stainless steel. Preliminary calculations show that insulating breaks will not be needed.

   An external design pressure of 25 psig has been chosen for the vacuum vessel to allow for the possibility of a 10 psi overpressure in the containment building. Relief valves will be set to relieve at a slight positive internal pressure and the vessel designed for 0 psig internally. A seismic load of 1 g, laterally and vertically, has been chosen based on an assumed 0.25 g ground motion and structural amplification of 4. Preliminary sizing has been done in accordance with Section VIII of the ASME Boiler and Pressure Vessel

Code. Stresses due to dead weight, 1 g seismic load vertically and laterally, and magnetic forces are small compared to pressure stress.

2. The casings of the TF coils will also serve as helium vessels. An annular cylindrical vessel around the central poloidal field solenoid will serve as a helium vessel for that component. Other superconducting poloidal field coils will each have a helium vessel. The internal design pressure of the helium vessel is 40 psig and was chosen to accommodate redundancy of relief — first a relief valve, then a rupture disc with successively higher set pressures — to assure relief at cryogenic temperature. Relief valves are piped to relieve helium vapor to a collecting tank outside the containment building. The helium vessel for the central solenoid is sized so that membrane stress is limited to two-thirds yield. The superconducting poloidal field coils and the toroidal field coils have cases which provide structural support for the windings as well as contain the helium and sizing is dictated by magnetic loads rather than helium pressure.
3. A liquid nitrogen shield will be used. It will consist of panels affixed to the inside of the vacuum vessel. The panels will be formed to have curvature to conform to the inside surface of the cylinders or shells. In cross section, the panels are of double-wall construction with one wall flat and the other shaped to provide coolant channels with manifolds at inlet and outlet. One commercially available type of panel has the formed wall in a corrugated style with the corrugations providing the coolant channels.

4.3.3 Cryostat Alternate Concepts

Vacuum vessel topology

The alternative of many vacuum vessels, one enclosing each magnet (or a group of magnets) and associated helium vessel(s), was considered and rejected because of the complexity that is introduced. A single vacuum vessel permits all of the cold mass to be tied together and supported off a single set of support columns.

4.3.4 Cryostat Design Analysis

Structural analysis

Based on the results of the conceptual studies over the past several months, it has been concluded that it is feasible to meet the FED cryostat requirements. There are no apparent technical obstacles. Some details are presented below.

The vacuum vessel walls were sized in accordance with the ASME Boiler and Pressure Vessel Code for the ETF Design I vacuum vessel dimensions; since the FED vessel diameter and height are close to the corresponding ETF Design I dimensions, the sizing calculations were not repeated. The required wall thicknesses are given in Table 4-32. The thicknesses given are for unstiffened shells. By the use of external stiffeners, the wall thickness may be reduced, but the wall thicknesses given here are adequate for assessing feasibility.

Magnetic forces

Magnetic forces on the vacuum vessel structure during the current ramp have also been calculated. It was found that these forces produce an "equivalent" pressure load (normal magnetic force per unit area of vacuum vessel) which is small compared to the design pressure used for sizing the vessel.

Eddy current loss calculations

The cryostat structure forms a number of closed circuits as seen by the poloidal fields. Reaction currents are generated in these circuits whenever the poloidal field system is ramped up or down. These reaction currents produce joule heating.

Loss calculations for the cryostat were made for the U.S. INTOR design. The cryostat was simulated by the following three circuits:

1. Vertical cylindrical shell encircling the straight legs of the TF coils in the nose region.
2. Toroidal cap oblong in-bore TF coil surfaces (both top and bottom).

Table 4-32. Required wall thickness for cryostat

ORNL-DWG 81-17373 FED

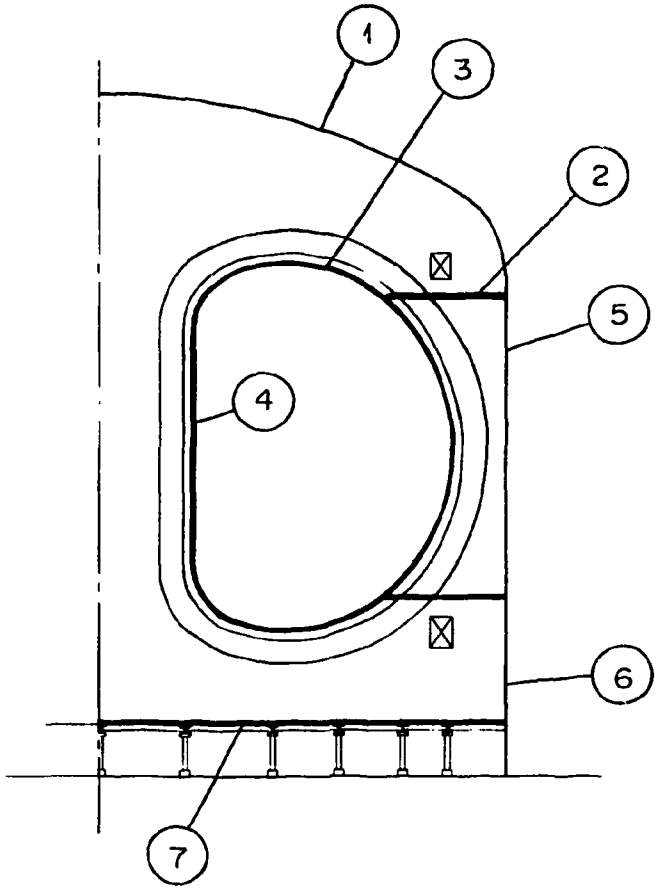

ITEM	DESCRIPTION	t, in (cm)
1	TORISPHERICAL CAP	2.75 (7.0)
2	FLAT PLATE	4.0 (10.2)
3	TOROIDAL SECTION	0.25 (0.64)
4	INNER CYLINDER	1.0 (2.54)
5	FINGERS	2.75 (7.0)
6	OUTER CYLINDER	2.375 (6.03)
7	BOTTOM HEAD	1.0 (2.54)

BASIS: SECTION VIII, ASME B&PV CODE

3. Torispherical cap outside the TF coil bore (both top and bottom).

Electrical losses only occur in room temperature components of the cryostat. These losses represent a very small surface heat flux (less than 2 joules/cm^2 in 6 seconds), and they can be easily dissipated into the environment. Because of the similarities in size and operation between FED and INTOR, and the fact that calculations for the INTOR design show the effect to be very small, the electrical losses are judged to be of no concern for FED either.

Heat load to helium vessels

Calculations were performed of the expected rate of heat transfer to the 4.2 K cold mass, by radiation from the 80 K cold shield and by conduction along the gravity supports from the 300 K floor. The radiation heat load was computed to be 300 W and the conduction heat load was computed to be 20 W.

4.3.5 Future Work — FED Cryostat

One of the results of the evaluation of refrigeration requirements for FED (see Chapter 8) is that the radiation heat load from the 80 K cold shield is small compared to other system heat loads. On the other hand, assembly and tightness testing of the cold shield is expected to be very time consuming and in the critical construction path. Consequently, a study will be made to determine if the cold shield can be eliminated, simply accepting the additional radiation heat load.

REFERENCES

1. J. R. Miller, "The Development of Forced-cooled Superconductor for Use in Large Magnets," paper presented at the 9th Cryogenic Eng. Conference, San Diego, to be published.
2. J. W. Lue and J. R. Miller, "Performance of an Internally Cooled Superconducting Solenoid," *Ibid*, 1981.
3. "Superconducting Magnet Coils for the Large Coil Program," Phase 2 final report to Union Carbide Corporation, Oak Ridge, TN, submitted by Westinghouse Electric Corporation, Vol I to IX, 1980.
4. C. A. Flanagan et al., *Initial Trade and Design Studies for the Fusion Engineering Device*, ORNL/TM-7777, June 1981.
5. S. S. Kalsi and R. J. Hooper, "Calculation of Eddy Current Losses in Toroidal Field Coil Casing," Proc. 9th Symposium on Engineering Problems of Fusion Research, Chicago, Illinois, October 1981.
6. R. J. Roark and W. M. Young, *Formulas for Stress and Strain*, 5th ed., McGraw Hill, 1975.
7. R. E. Peterson, *Stress Concentration Factors*, John Wiley & Sons, New York, 1974.
8. M. S. Walker et al., "Superconducting Design and Loss Analysis for a 20-MJ Induction Heating Coil," *IEEE Trans* MAG-17 908, 1981.
9. L. R. Turner, "Safety of Superconducting Magnets for Fusion, Thermal Analysis of Large Cryostable Magnets," *IEEE TRANS* MAG-17 463, 1981.

ORNL/TM-7948/V1
Dist. Category UC-20 c,d

INTERNAL DISTRIBUTION

1. R. G. Alsmiller, Jr.
2. S. E. Attenberger
3. R. J. Barrett
4. E. E. Bloom
5. T. G. Brown
6. E. H. Bryant
7. B. A. Carreras
8. R. E. Clausing
9. R. W. Derby
10. R. A. Dory
11. C. A. Flanagan
12. G. M. Fuller
13. G. E. Gorker
14. P. N. Haubenreich
15. L. M. Hively
16. J. A. Holmes
17. W. A. Houlberg
18. S. S. Kalsi
19. J. Kirchner
20. T. S. Kress
21. J. F. Lyon
22. M. S. Lubell
23-24. D. H. Metzler
25. W. D. Nelson
26. R. L. Reid
27. J. A. Rome
28. M. W. Rosenthal
29. P. H. Sager
30. M. J. Saltmarsh
31. R. T. Santoro
32. T. E. Shannon
33. J. Sheffield
34. G. E. Smith
35. P. T. Spampinato
36. D. Steiner
37. D. J. Strickler
38. N. A. Uckan
39. J. S. Watson
40. F. W. Wiffen
41. J. B. Wilgen
42. K. F. Wu
43-44. Laboratory Records Department
45. Laboratory Records, ORNL-RC
46. Document Reference Section
47-48. Central Research Library
49-50. Fusion Energy Division Library
51. Fusion Energy Division Reports Office
52. ORNL Patent Office

EXTERNAL DISTRIBUTION

53. M. A. Abdou, Associate Director, FPP/207, Argonne National Laboratory, 9700 South Cass Avenue, Argonne, IL 60439
54. N. A. Amherd, Fusion Power Program, Advanced Systems Department, Electric Power Research Institute, P.O. Box 10412, Palo Alto, CA 94304
55. J. L. Anderson, CMB-3, Mail Stop 348, Los Alamos National Laboratory, P.O. Box 1663, Los Alamos, NM 87544
56. M. Anderson, Tennessee Valley Authority, 1300 Commerce Bank Bldg., Chattanooga, TN 37401
57. D. J. Anthony, Manager, Advanced Energy Systems, Energy Systems Programs Department, Building 23, Room 290, General Electric Company, Schenectady, NY 12345
58. C. C. Baker, FPP/208, Argonne National Laboratory, 9700 South Cass Avenue, Argonne, IL 60439
59. T. H. Batzer, L-536, Lawrence Livermore National Laboratory, P.O. Box 808, Livermore, CA 94550
60. J. E. Baublitz, Office of Fusion Energy, Department of Energy, Mail Stop G-256, Washington, DC 20545

61. W. Bauer, Physical Research Division, Sandia Laboratories-Livermore, Livermore, CA 94550
62. J. F. Baur, General Atomic Company, P.O. Box 81608, San Diego, CA 92138
63. D. S. Beard, Office of Fusion Energy, Department of Energy, Mail Stop G-256, Washington, DC 20545
64. R. J. Beeley, ETEC, Rockwell International, P.O. Box 1449, Canoga Park, CA 91304
65. D. C. Berkey, Vice President and General Manager, Energy System and Technology Division, General Electric Company, P.O. Box 7600, Stamford, CT 06904
66. K. L. Black, McDonnell Douglas Astronautics Co., Dept. E452, P.O. Box 516, St. Louis, MO 63166
67. R. Botwin, C47-05, Grumman Aerospace Corporation, Bethpage, NY 11714
68. W. B. Briggs, McDonnell Douglas Astronautics Company, P.O. Box 516, St. Louis, MO 63166
69. G. Bronner, Princeton Plasma Physics Laboratory, P.O. Box 451, Princeton, NJ 08540
70. J. N. Brooks, FPP/207, Argonne National Laboratory, 9700 South Cass Avenue, Argonne, IL 60439
71. S. C. Burnett, General Atomic Company, P.O. Box 81608, San Diego, CA 92138
72. J. D. Callen, Department of Nuclear Engineering, University of Wisconsin, Madison, WI 53706
73. J. F. Clarke, Office of Fusion Energy, Office of Energy Research, Department of Energy, Mail Station G-256, Washington, DC 20545
74. R. G. Clemmer, Fusion Power Program, Argonne National Laboratory, 9700 South Cass Avenue, Argonne, IL 60439
75. D. R. Cohn, Massachusetts Institute of Technology Plasma Fusion Center, 167 Albany Street, Cambridge, MA 02139
76. R. W. Conn, School of Chemical, Nuclear and Thermal Engineering, Boelter Hall, University of California, Los Angeles, CA 90024
77. J. W. Coursen, C36-05, Grumman Aerospace Corporation, Bethpage, NY 11714
78. J. G. Crocker, EG&G Idaho, Inc., P.O. Box 1625, Idaho Falls, ID 83401
79. A. E. Dabiri, Energy Systems & Conservation Division, Science Applications, Inc., P.O. Box 2351, La Jolla, CA 92038
80. C. C. Damm, L-441, Lawrence Livermore National Laboratory, P.O. Box 808, Livermore, CA 94550
81. R. C. Davidson, Massachusetts Institute of Technology, 77 Massachusetts Avenue, Cambridge, MA 02139
82. N. A. Davies, Office of Fusion Energy, Department of Energy, Mail Stop G-256, Washington, DC 20545
83. J. W. Davis, McDonnell Douglas Astronautics Company, E457, Building 81/1/B7, P.O. Box 516, St. Louis, MO 63166
84. M. J. Davis, Sandia Laboratories-Albuquerque, Org. 5830, P.O. Box 5800, Albuquerque, NM 87185
85. S. O. Dean, Director, Fusion Energy Development, Science Applications, Inc., 2 Professional Drive, Suite 249, Gaithersburg, MD 20760

86. J. F. Decker, Office of Fusion Energy, Department of Energy, Mail Stop G-256, Washington, DC 20545
87. D. DeFreece, McDonnell Douglas Astronautics Company, E451, Building 81/1/B7, P.O. Box 516, St. Louis, MO 63166
88. A. Deitz, Princeton Plasma Physics Laboratory, P.O. Box 451, Princeton, NJ 08540
89. D. A. Dingee, Program Manager, Fusion Technology, Pacific Northwest Laboratories, Battelle Boulevard, Richland, WA 99352
90. J. N. Doggett, L441, Lawrence Livermore National Laboratory, P.O. Box 808, Livermore, CA 94550
91. H. Dreicer, Division Leader, CRT, Los Alamos National Laboratory, P.O. Box 1663, Los Alamos, NM 87544
92. W. R. Ellis, Office of Fusion Energy, Department of Energy, Mail Stop G-256, Washington, DC 20545
93. B. A. Engholm, General Atomic Company, P.O. Box 81608, San Diego, CA 92138
94. H. P. Eubank, Princeton Plasma Physics Laboratory, P.O. Box 451, Princeton, NJ 08540
95. F. Farfaletti-Casali, Engineering Division, Joint Research Center, Ispra Establishment, 21020 Ispra (Varese), Italy
96. J. J. Ferrante, Manager, Large Superconducting Program, Building 36-241, General Electric Company, 1 River Road, Schenectady, NY 12345
97. J. File, Princeton Plasma Physics Laboratory, P.O. Box 451, Princeton, NJ 08540
98. H. K. Forsen, Bechtel Group, Inc., Research and Engineering, P.O. Box 3965, San Francisco, CA 94119
99. J. S. Foster, Jr., TRW, Inc., Building R4-2004, 1 Space Park, Redondo Beach, CA 90278
100. T. K. Fowler, Associate Director for MFE, L-436, Lawrence Livermore National Laboratory, P.O. Box 808, Livermore, CA 94550
101. J. W. French, EBASCO Services, Inc., Forrestal Campus, CN-59, Princeton, NJ 08540
102. H. P. Furth, Director, Princeton Plasma Physics Laboratory, P.O. Box 451, Princeton, NJ 08540
103. J. G. Gavin, Jr., President, A01-111, Grumman Aerospace Corporation, Bethpage, NY 11714
104. Gordon Gibson, Westinghouse Electric Corporation, Fusion Power Systems, P.O. Box 10864, Pittsburgh, PA 15236
105. J. R. Gilleland, Manager, Fusion Projects, General Atomic Company, P.O. Box 81608, San Diego, CA 92138
106. W. D. Goins, Tennessee Valley Authority, 1300 Commerce Union Bank Bldg., Chattanooga, TN 37401
107. R. Goldston, Princeton Plasma Physics Laboratory, P.O. Box 451, Princeton, NJ 08540
108. M. B. Gottlieb, Princeton Plasma Physics Laboratory, P.O. Box 451, Princeton, NJ 08540
109. R. W. Gould, Department of Applied Physics, California Institute of Technology, Pasadena, CA 91109
110. M. W. Griffin, McDonnell Douglas Astronautics Co., Dept. E236, P.O. Box 516, St. Louis, MO 63166

111. C. R. Head, Office of Fusion Energy, Department of Energy, Mail Stop G-256, Washington, DC 20545
112. C. D. Henning Mirror Program Office, L-644, Lawrence Livermore National Laboratory, P. O. Box 5511, Livermore, CA 94550
113. G. K. Hess, Office of Fusion Energy, Department of Energy, Mail Stop ER-701, Washington, DC 20545
114. T. Hiraoka, Japan Atomic Energy Research Institute, JT-60 Project Office I, Tokai Research Establishment, Tokai-mura, Naka-gun, Ibaraki-ken, Japan
115. R. L. Hirsch, Manager, Synthetic Fuels Research, Exxon Research and Engineering Company, P.O. Box 4255, Baytown, TX 77520
116. J. J. Holmes, Westinghouse-Hanford Engineering Development Laboratory, P.O. Box 1970, Richland, WA 99352
117. W. G. Homeyer, General Atomic Company, P.O. Box 81608, San Diego, CA 92138
118. J. C. Hosea, Princeton Plasma Physics Laboratory, P.O. Box 451, Princeton, NJ 08540
119. D. Hwang, Princeton Plasma Physics Laboratory, P.O. Box 451, Princeton, NJ 08540
120. G. J. Inukai, McDonnell Douglas Astronautics Co., Dept. E231, P.O. Box 516, St. Louis, MO 63166
121. D. L. Jassby, Princeton Plasma Physics Laboratory, P.O. Box 451, Princeton, NJ 08540
122. J. B. Joyce, Princeton Plasma Physics Laboratory, P.O. Box 451, Princeton, NJ 08540
123. E. E. Kintner, Director, Office of Fusion Energy, Department of Energy, Mail Stop G-256, Washington, DC 20545
124. R. A. Krakowski, CTR-12, Mail Stop 641, Los Alamos National Laboratory, P.O. Box 1663, Los Alamos, NM 87544
125. G. L. Kulcinski, University of Wisconsin, Department of Nuclear Engineering, Engineering Research Building, Room 439, 1500 Johnson Drive, Madison, WI 53706
126. D. L. Kummer, McDonnell Douglas Astronautics Company, 969 Executive Parkway, Bellerive Office Center, Creve Coeur, MO 63141
127. T. S. Latham, United Technologies Research Center, Mail Stop 44, Silver Lane, East Hartford, CT 06108
128. L. R. Ledman, Office of Fusion Energy, Department of Energy, Mail Stop G-256, Washington, DC 20545
129. L. M. Lidsky, Massachusetts Institute of Technology Plasma Fusion Center, Cambridge, MA 02139
130. E. F. Lowell, General Manager, Energy Systems Program Department, Building 2-455, General Electric Company, 1 River Road, Schenectady, NY 12345
131. D. G. McAlees, Manager, Program Development, Laser Enrichment Department, Exxon Nuclear Company, Inc., 600 108th Avenue, NE, Bellevue, WA 98009
132. D. J. McFarlin, United Technologies Research Center, Mail Stop 44, Silver Lane, East Hartford, CT 06108
133. R. McGrath, Fusion Power Program, Argonne National Laboratory, 9700 South Cass Avenue, Argonne, IL 60439

134. V. A. Maroni, Argonne National Laboratory, CEN/205, 9700 South Cass Avenue, Argonne, IL 60439
135. W. Marton, Office of Fusion Energy, Department of Energy, Mail Stop G-256, Washington, DC 20545
136. L. G. Masson, EG&G Idaho, Idaho National Engineering Laboratory, P.O. Box 1625, Idaho Falls, ID 83401
137. D. M. Meade, Princeton Plasma Physics Laboratory, P.O. Box 451, Princeton, NJ 08540
138. A. T. Mense, McDonnell Douglas Astronautics Co., Bldg. 107, Post B2, P.O. Box 516, St. Louis, MO 63166
139. L. Michaels, Princeton Plasma Physics Laboratory, P.O. Box 451, Princeton, NJ 08540
140. D. Mikkelsen, Princeton University, Plasma Physics Laboratory, P.O. Box 451, Princeton, NJ 08540
141. R. L. Miller, General Atomic Company, P.O. Box 81608, San Diego, CA 92138
142. R. G. Mills, Princeton Plasma Physics Laboratory, P.O. Box 451, Princeton, NJ 08540
143. J. T. D. Mitchell, Culham Laboratory, Abingdon, Oxon, OX14 3DB, United Kingdom
144. R. W. Moir, Lawrence Livermore National Laboratory, P.O. Box 808, Livermore, CA 94550
145. D. B. Montgomery, Massachusetts Institute of Technology Plasma Fusion Center, 170 Albany Street, Cambridge, MA 02139
146. K. Moses, TRW, Inc., R-1/1078, 1 Space Park, Redondo Beach, CA 90278
147. R. E. Muller, Aerojet Manufacturing Company, 601 South Placentia Avenue, P.O. Box 4210, Fullerton, CA 92934
148. A. E. Munier, Grumman Aerospace Corporation, Bethpage, NY 11714
149. M. R. Murphy, Office of Fusion Energy, Department of Energy, Mail Stop G-256, Washington, DC 20545
150. R. E. Nygren, FPP/207, Argonne National Laboratory, 9700 South Cass Avenue, Argonne, IL 60439
151. T. Ohkawa, General Atomic Company, P.O. Box 81608, San Diego, CA 92138
152. M. Okabayashi, Princeton Plasma Physics Laboratory, P.O. Box 451, Princeton, NJ 08540
153. D. Overskei, Massachusetts Institute of Technology Plasma Fusion Center, 167 Albany Street, Cambridge, MA 02139
154. R. R. Parker, Francis Bitter National Magnet Laboratory, 170 Albany Street, Cambridge, MA 02139
155. B. Pease, Culham Laboratory, Abingdon, Oxon, OX14 3DB, United Kingdom
156. M. Pelovitz, Princeton University, Plasma Physics Laboratory, P.O. Box 451, Princeton, NJ 08540
157. M. Petravic, Princeton University, Plasma Physics Laboratory, P.O. Box 451, Princeton, NJ 08540
158. D. E. Post, Princeton Plasma Physics Laboratory, P.O. Box 451, Princeton, NJ 08540
159. L. K. Price, Department of Energy, Oak Ridge Operations, P.O. Box E, Oak Ridge, TN 37830

160. R. E. Price, Office of Fusion Energy, Department of Energy, Mail Stop G-256, Washington, DC 20545
161. D. H. Priester, Office of Fusion Energy, Department of Energy, Mail Stop G-256, Washington, DC 20545
162. F. A. Puhn, General Atomic Company, P.O. Box 81608, San Diego, CA 92138
163. J. Purcell, General Atomic Company, P.O. Box 81608, San Diego, CA 92138
164. R. V. Pyle, University of California, Lawrence Berkeley Laboratory, Berkeley, CA 94720
165. J. M. Rawls, General Atomic Company, P.O. Box 81608, San Diego, CA 92138
166. P. J. Reardon, Princeton Plasma Physics Laboratory, P.O. Box 451, Princeton, NJ 08540
167. M. Roberts, Office of Fusion Energy, Department of Energy, Mail Stop G-256, Washington, DC 20545
168. F. L. Robinson, Tennessee Valley Authority, 1300 Commerce Bank Bldg., Chattanooga, TN 37401
169. J. D. Rogers, Los Alamos National Laboratory, P.O. Box 1663, Los Alamos, NM 87544
170. M. L. Rogers, Monsanto Research Corporation, Mound Facility, P. O. Box 32, Miamisburg, OH 45342
171. M. N. Rosenbluth, University of Texas, Institute for Fusion Studies, RLM 11.218, Austin, TX 78717
172. P. N. Rutherford, Princeton Plasma Physics Laboratory, P.O. Box 451, Princeton, NJ 08540
173. M. M. Sabado, EBASCO Services, Inc., Forrestal Campus, A Site, Building 1-A, Princeton, NJ 08540
174. J. A. Schmidt, Princeton Plasma Physics Laboratory, P.O. Box 451, Princeton, NJ 08540
175. J. Schultz, Massachusetts Institute of Technology, 167 Albany Street, Cambridge, MA 02139
176. F. R. Scott, Electric Power Research Institute, P.O. Box 10412, Palo Alto, CA 94304
177. G. Sheffield, Princeton Plasma Physics Laboratory, P.O. Box 451, Princeton, NJ 08540
178. C. E. Singer, Princeton Plasma Physics Laboratory, P.O. Box 451, Princeton, NJ 08540
179. T. J. M. Sluyters, Brookhaven National Laboratory, Accelerator Department, Upton, Long Island, NY 11973
180. D. Smith, Materials Science Division, Argonne National Laboratory, 9700 South Cass Avenue, Argonne, IL 60439
181. R. I. Smith, Board Chairman, Public Service Electric and Gas Company, 80 Park Place, Newark, NJ 07101
182. L. Southworth, General Atomic Company, P.O. Box 81608, San Diego, CA 92138
183. W. M. Stacey, Jr., Georgia Institute of Technology, School of Nuclear Engineering, Atlanta, GA 30332
184. E. Stern, Grumman Aerospace Corporation, Forrestal Campus, CN-59, Princeton, NJ 08540
185. L. D. Stewart, Princeton Plasma Physics Laboratory, P.O. Box 451, Princeton, NJ 08540

186. W. Stodiek, Princeton Plasma Physics Laboratory, P.O. Box 451, Princeton, NJ 08540
187. P. M. Stone, Office of Fusion Energy, Department of Energy, Mail Stop G-256, Washington, DC 20545
188. I. N. Sviatoslavsky, University of Wisconsin, Room 33, Engineering Research Building, 1500 Johnson Drive, Madison, WI 53706
189. T. Tamano, General Atomic Company, P.O. Box 81608, San Diego, CA 92138
190. R. E. Tatro, Manager, Energy Systems, General Dynamics, Convair Division, M.Z. 16-1070, P.O. Box 80847, San Diego, CA 92138
191. F. Tenney, Princeton Plasma Physics Laboratory, P.O. Box 451, Princeton, NJ 08540
192. F. Thomas, Grumman Aerospace Corporation, B-20-5, Bethpage, NY 11714
193. K. I. Thomassen, Lawrence Livermore National Laboratory, P.O. Box 808, Livermore, CA 94550
194. R. J. Thome, Massachusetts Institute of Technology, 170 Albany Street, Cambridge, MA 02139
195. S. L. Thomson, Bechtel Group Inc., P.O. Box 3965, San Francisco, CA 94119
196. C. Trachsel, McDonnell Douglas Astronautics Company, P.O. Box 516, St. Louis, MO 63166
197. J. R. Treglio, General Dynamics, Convair Division, P.O. Box 80847, San Diego, CA 92138
198. A. W. Trivelpiece, Office of Energy Research, Department of Energy, Washington, DC 20545
199. L. R. Turner, Fusion Power Program, Argonne National Laboratory, 9700 South Cass Avenue, Argonne, Il 60439
200. M. A. Ulrickson, Princeton Plasma Physics Laboratory, P.O. Box 451, Princeton, NJ 08540
201. T. C. Varljen, Westinghouse Electric Corporation, P.O. Box 10864, Pittsburgh, PA 15236
202. H. F. Vogel, Los Alamos National Laboratory, P.O. Box 1663, Los Alamos, NM 87544
203. A. Wait, Building 36-421, General Electric Company, 1 River Road, Schenectady, NY 12345
204. K. E. Wakefield, Princeton Plasma Physics Laboratory, P.O. Box 451, Princeton, NJ 08540
205. F. Weldon, Los Alamos National Laboratory, P.O. Box 1663, Los Alamos, NM 87544
206. J. C. Wesley, General Atomic Company, P.O. Box 81608, San Diego, CA 92138
207. S. Whitley, Tennessee Valley Authority, 1300 Commerce Bank Bldg., Chattanooga, TN 37401
208. W. R. Wilkes, Monsanto Research Corporation, Mound Laboratory, Miamisburg, OH 45342
209. J. E. Wilkins, EG&G Idaho, Idaho National Engineering Laboratory, Idaho Falls, ID 83401
210. H. Willenberg, Mathematical Sciences Northwest, P.O. Box 1887, Bellevue, WA 98009

211. J. E. C. Williams, Massachusetts Institute of Technology, 170 Albany Street, Cambridge, MA 02139
212. P. Willis, General Electric Company, 1 River Road, Building 23, Room 298, Schenectady, NY 12345
213. T. F. Yang, Massachusetts Institute of Technology Plasma Fusion Center, 167 Albany Street, Cambridge, MA 02139
214. H. H. Yoshikawa, Hanford Engineering Development Laboratory, W/A-62, P.O. Box 1970, Richland, WA 99352
215. K. M. Young, Princeton University, Plasma Physics Laboratory, P.O. Box 451, Princeton, NJ 08540
216. N. E. Young, EBASCO Services, Inc., Princeton Plasma Physics Laboratory, P.O. Box 451, Princeton, NJ 08540
217. K. M. Zwilsky, National Materials Advisory Board, National Academy of Sciences, 2101 Constitution Avenue, N.W., Washington, DC 20418
218. Office of Assistant Manager for Energy Research and Development, Department of Energy, Oak Ridge Operations Office, Oak Ridge, TN 37830
219-457. Given distribution as shown in TID-4500, Magnetic Fusion Energy (Distribution Category UC-20 c and d: Reactor Materials and Fusion Systems)

★ U.S. GOVERNMENT PRINTING OFFICE: 1981-546-067/379